UNIVERSITY OF COPENHAGEN

Exploring the High-Energy Transient Universe with Neutrinos

DOCTORAL THESIS

by

ERSILIA GUARINI

Supervised by Prof. Irene Tamborra

This thesis has been submitted to the PhD School of the Faculty of Science,

University of Copenhagen

December 31, 2023

Ai miei genitori e alle mie sorelle,

per aver creduto in me nelle ore più buie.

Ai miei nonni, che vorrei poter abbracciare tutti.

ABSTRACT

The advent of time-domain astronomy has led to the discovery of a plethora of energetic transient phenomena showcasing a wide range of luminosities and durations, the latter spanning from a few seconds to a few months. While photons remain our primary observational tool, at high-energy they can interact with matter and radiation in their journey from the source to Earth, therefore carrying limited information about distant sources. Consequently, unraveling the mechanism powering transients solely through electromagnetic radiation can pose significant challenges, and the nature of most of these sources remains puzzling. Yet astrophysical transients also act as cosmic accelerators, producing cosmic rays and high-energy neutrinos, and they can emit gravitational waves. As each of these messengers carries unique information about their source, only by combining them can we gain a deep understanding of the most powerful phenomena occurring in the cosmos. Within the vibrant landscape of multi-messenger astronomy, the focus of this thesis is on high-energy neutrinos. Due to their feeble interaction with matter, neutrinos can travel large distances almost unhindered and therefore stand out as unique probes of the high-energy sky. This thesis endeavors to assess the potential of high-energy neutrinos to unravel the enigmatic nature of some transient phenomena.

The first part of this thesis offers a broad overview of multi-messenger astronomy and its current status, followed by a discussion on particle acceleration and radiative processes in high-energy astrophysics. Next, relevant transient sources and their connection with high-energy neutrinos are outlined. Finally, the thesis provides an overview of the currently operating and forthcoming electromagnetic as well as high-energy neutrino telescopes. These introductory Chapters pave the road towards discussing the potential of combining multi-wavelength and high-energy neutrino data.

The second and third parts of the thesis showcase original results from the published works concluded during the doctoral studies of the Ph.D. candidate. The first work presented in the second part makes use of state-of-the-art general relativistic magneto-hydrodynamic simulations of collapsar jets to show that high-energy neutrino production in regions deeply embedded in the outflow is favored only if the jet is magnetized. Importantly, this work proves that the subphotospheric high-energy neutrino signal is highly sensitive to the jet magnetization and can be used to reveal the presence of a choked jet in the source. The

second work included in this part of the thesis investigates high-energy neutrino production at the optical jump, namely the sudden rebrightening observed in the optical lightcurve of some gamma-ray burst (GRB) afterglows. Notably, the findings of this work hint that high-energy neutrinos can enable us to test the medium surrounding the burst. The final work included in this part focuses on GRBs whose afterglow is observed at very-high-energy (VHE, $\gtrsim$ 100 GeV). By making use of multi-wavelength data and by requiring that the blastwave is transparent to $\gamma - \gamma$ pair production at the time of observation of VHE photons, this work hints that VHE GRBs may occur in low-density environments. These findings may have crucial implications for the progenitors of VHE GRBs.

High-energy neutrinos can also be combined with multi-wavelength data to probe the mechanisms powering emerging classes of high-energy transients, as outlined in the third part of the thesis. The first work presented in this part reveals that high-energy neutrinos can disentangle the mechanism powering Luminous Fast Blue Optical Transients (LFBOTs) while also constraining a region of the parameter space otherwise allowed by electromagnetic observations. Finally, we conclude this thesis with a work outlining the best strategy to carry out multi-messenger follow-up searches of transients stemming from collapsing massive stars. The key findings of this study prove that the neutrino signal is strongly correlated with the radio and X-ray bands if the transient is powered by interaction with a dense circumstellar medium and the spindown of a central magnetar, respectively. Importantly, this final work also proves that combining radio and X-ray data with the infrared-optical-ultraviolet lightcurve is pivotal to breaking the degeneracies in the transient parameter space.

As of today, high-energy neutrino astronomy is an extremely vibrant field. While the IceCube Neutrino Observatory successfully measured the diffuse flux of high-energy neutrinos, pinpointing their origin is extremely challenging due to the limited sensitivity of current instruments. Likewise, an increasing number of high-energy neutrinos is detected in association with astrophysical transients. Emerging neutrino telescopes such as IceCube-Gen2, KM3NeT, and GRAND anticipate a substantial enhancement in the detection capabilities of high-energy neutrinos, and they will finally give us the possibility to collect a large number of neutrino data. At the same time, the number of observed astrophysical transients is going to increase exponentially in the near future as high-cadence, wide-field surveys come online. With these encouraging developments on the horizon, we can expect to delve even deeper into the nature of the transient sources investigated in this thesis, unraveling further insights into their multi-messenger emission.

ABSTRAKT

Fremkomsten af tidsdomæne-astronomi har ført til opdagelsen af en overflod af energiske forbigående astrofysiske fænomener, kaldet *transienter*. Transienter kan have en bred vifte af lysstyrker og varierende tidsperioder fra få sekunder til få måneder. Fotoner er stadig vores primære observationsværktøj, men ved høj energi kan de vekselvirke med stof og stråling på deres rejse fra deres oprindelige astrofysiske kilde til Jorden, og derfor har de begrænset information om fjerne kilder. Derfor kan det være en udfordring kun at opklare den mekanisme, at forklare den mekanisme, der driver transienter, ved udelukkende at bruge elektromagnetisk stråling, og de fleste af dem er stadig gådefulde. Men astrofysiske transienter kan fungere som kosmiske acceleratorer, der producerer kosmisk stråling og højenergi-neutrinoer, og de kan også udsende gravitationsbølger. Da hver af disse budbringere bærer unik information om deres kilde, er det kun ved at kombinere dem, at vi kan få en dyb forståelse af de mest kraftfulde fænomener, der forekommer i kosmos. I det pulserende landskab af multi-messenger-astronomi er fokus i denne Ph.D.-afhandling på højenergi-neutrinoer. På grund af deres svage vekselvirkning med stof skiller neutrinoer sig ud som unikke sonder af højenergihimlen, da de kan rejse over store afstande næsten uhindret. Denne afhandling forsøger at vurdere potentialet i højenergi-neutrinoer til at opklare den gådefulde natur af transienter.

Den første del af denne Ph.D.-afhandling giver et bredt overblik over multi-messenger-astronomi og dens nuværende status, efterfulgt af en diskussion om partikelacceleration og strålingsprocesser i højenergi-astrofysik. Dernæst skitseres relevante transiente kilder og deres forbindelse til højenergi-neutrinoer. Endelig giver afhandlingen et overblik over de nuværende og kommende elektromagnetiske teleskoper samt højenergi-neutrinoteleskoper. Disse indledende kapitler baner vejen for at diskutere potentialet i at kombinere observationer af multi-bølgelængder med data for højenergi-neutrinoer.

Anden og tredje del af afhandlingen fremviser originale resultater fra de publicerede artikler, der blev afsluttet under Ph.D.-kandidatens studier. Den første artikel, der præsenteres i anden del, gør brug af state-of-the-art generelle relativistiske magneto-hydrodynamiske simuleringer af *collapsar jets* for at vise, at højenergi-neutrinoproduktion i regioner, der er dybt indlejret i udstrømningen, kun favoriseres, hvis strålen er magnetiseret. Dette studie beviser et meget vigtigt fænomen: det at det subfotosfæriske højenergi-

neutrinosignal er meget følsomt over for jetmagnetiseringen, og det kan bruges til at afsløre tilstedeværelsen af en kvalt jet i kilden. Den anden artikel i denne del af afhandlingen undersøger produktionen af højenergi-neutrinoer ved det optiske spring, nemlig den pludselige opblomstring, der er observeret i den optiske lyskurve for nogle eftergløder fra gammaglimt (GRB; *gamma-ray burst*). Resultaterne af dette arbejde antyder især, at højenergineutrinoer kan gøre det muligt for os at teste mediet omkring udbruddet. Det sidste arbejde, der er inkluderet i denne del, fokuserer på GRB'er, hvis efterglød observeres ved meget høj energi ($\gtrsim$ 100 GeV). Ved at gøre brug af data fra flere bølgelængder og ved at kræve, at eksplosionsbølgen skal være gennemsigtig for $\gamma - \gamma$ parproduktion på tidspunktet for observation af fotoner af meget høj energi (VHE; *very-high-energy*), antyder dette studie, at VHE GRBs kan forekomme i miljøer med lav densitet. Disse resultater kan have afgørende betydning for, hvordan VHE GRBs opstår.

Højenergi-neutrinoer kan også kombineres med multi-bølgelængdedata for at undersøge den mekanisme, der driver nye klasser af højenergi-transienter, som skitseret i tredje del af afhandlingen. Det første artikel, der præsenteres i denne del, afslører, at højenergi-neutrinoer kan opklare mekanismen bag *Luminous Fast Blue Optical Transients (LFBOTs)*, samtidig med at de begrænser et område af parameterrummet, der ellers er tilladt af elektromagnetiske observationer. Endelig konkluderer vi dette med en artikel, der skitserer den bedste strategi til at udføre multi-messenger opfølgningssøgninger af transienter, der stammer fra kollapsende massive stjerner. De vigtigste resultater af dette studie viser, at neutrinosignalet er stærkt korreleret med radio- og røntgenbåndene, hvis transienten er drevet af interaktion med henholdsvis et tæt circumstellart medium og *spindown* fra en central magnetar. Det er væsentligt, at det i denne artikel også bliver bevist, at kombinationen af radio- og røntgendata med den infrarød-optiske-ultraviolette lyskurve er afgørende for at bryde udartethederne i transientens parameterrum.

I dag er højenergi-neutrinoastronomi et ekstremt levende felt. Selvom IceCube Neutrino Observatory med succes har målt den diffuse flux af højenergi-neutrinoer, er det ekstremt udfordrende at lokalisere deres oprindelse på grund af den begrænsede følsomhed af de nuværende instrumenter. Ligeledes bliver et stigende antal højenergi-neutrinoer detekteret i forbindelse med astrofysiske transienter. Med udviklingen af nye neutrinoteleskoper som IceCube-Gen2, KM3NeT og GRAND forventes der en betydelig forbedring af detektionsmulighederne for højenergi-neutrinoer, forventes der en betydelig forbedring. Samtidig vil antallet af observerede astrofysiske transienter stige eksponentielt i den nærmeste fremtid, efterhånden som høj-kadence, *wide-field surveys* vil komme online. Med disse opmuntrende udviklinger i horisonten kan vi

forvente at dykke endnu dybere ned i naturen af de transiente kilder, der undersøges i denne afhandling, og afdække yderligere indsigt i deres multi-messenger udledning.

THESIS OUTLINE

The thesis is divided into five parts:

- Part i: Introduction
- Part ii: Multi-messenger emission from long gamma-ray bursts
- Part iii: Multi-messenger emission from emerging classes of high-energy transients
- Part iv: Summary and conclusions
- Part v: Appendices

Part i offers a broad introduction to multi-messenger astronomy, particle acceleration, and electromagnetic and high-energy neutrino production in astrophysical transients, as well as an overview of the transient phenomena discussed along the thesis. Parts ii and iii of this thesis consist of the reprints of the following journal articles published during the PhD studies:

1. **Ersilia Guarini**, Irene Tamborra, Ore Gottlieb, *State-of-the-art collapsar jet simulations imply undetectable subphotospheric neutrinos*, Phys. Rev. D 107 (2023) 2, 023001, arXiv:2210.03757
2. **Ersilia Guarini**, Irene Tamborra, Damien Bégué, Tetyana Pitik, Jochen Greiner, *Multi-messenger detection prospects of gamma-ray bursts afterglows with optical jumps*, JCAP 06 (2022) 06, 034, arXiv:2112.07690
3. **Ersilia Guarini**, Irene Tamborra, Damien Bégué, Annika Rudolph, *Probing gamma-ray bursts observed at very high energies through their afterglows*, Mon.Not.Roy.Astron.Soc. 253 (2023) 149-162, arXiv:2301.10256
4. **Ersilia Guarini**, Irene Tamborra, Raffaella Margutti, *Neutrino Emission from Luminous Fast Blue Optical Transients*, Astrophys. J. 935 (2022) 157, arXiv:2205.12282

5. **Ersilia Guarini**, Irene Tamborra, Raffaella Margutti, Enrico Ramirez-Ruiz, *Transients stemming from collapsing massive stars: The missing pieces to advance joint observations of photons and high-energy neutrinos*, Phys. Rev. D. 108 (2023) 8, 083035 , arXiv:2308.03840

Each chapter of the thesis corresponding to a given publication is followed by a section named *Critical Outlook*, which provides a brief overview of the project and critically outlines the findings of the corresponding publication from a state-of-the-art standpoint. Part ii consists of publications 1, 2, and 3, while Part iii consists of publications 4 and 5.

Part iv summarizes the main findings of this research, highlights some of its limitations, and suggests possible future directions of our work. Finally, Part v contains the appendices of each publication, not included in the main body of the thesis.

ACKNOWLEDGEMENTS

I have always gauged the significance of my life chapters by the robustness of human connections entwined within them. In this sense, the past three years have been rich and fulfilling, as many extraordinary people walked into my life and now are essential parts of it. This Section is dedicated to all the people who accompanied me along one of the most challenging journeys I have undertaken so far. Without you all the Ph.D. would lose all its meaning.

È d'obbligo cominciare con le mie colonne portanti, le persone che hanno creduto in me anche quando— in una piccola stanza nella fredda Copenhagen— piangevo aspettando di tornare nella mia amata Trani: i miei genitori e le mie sorelle. Da sempre siete stati la mia forza più grande e probabilmente l'unica ragione per cui sono arrivata intatta e forte alla fine del dottorato. Voi, mamma e papà, siete sempre stati la mia ispirazione. Con la vostra tenacia e determinazione, mi avete sempre mostrato che nella vita le difficoltà vanno affrontate di petto, senza paura. Mi avete trasmesso quello spirito di avventura che porta fino in fondo al tunnel: nonostante sia buio e ci si senta soli, alla fine la via d'uscita la si trova continuando a camminare. E voi, Giusy e Martina, siete state costantemente la boccata di aria fresca di cui avevo bisogno nelle ore più nere. Le vostre storie e i vostri drammi (ahimé, non più adoloscenziali) mi hanno riscaldato il cuore, e mi hanno fatta sentire parte del quotidiano che tanto manca quando si va via. Grazie ai miei zii, Rita, Salvatore e Mariangela, e ai miei cugini Sara, Michele, e cugini acquisiti Daniele e Mirella, per essere sempre stati presenti e aver reso i miei ritorni a casa sempre felici e pieni di vita. A mia nonna Ersilia, e tutti i nonni non più presenti, perché ognuno di voi mi ha insegnato che a volte nella vita bisogna solo aspettare con pazienza, tenendo il cuore sempre aperto.

I would like to express my gratitude to my supervisor, Irene Tamborra, for being a mentor and an inspiration during these three years. I am grateful she saw something special in me and gave me the chance to grow personally and academically when, four years ago, I asked her whether she was looking for Ph.D. students. The invaluable lessons I have learned will stay with me as I embark on my own path.

Y ahora tengo que agradecer a la persona que me salvó de todas las formas posibles estos tres años. Víctor, lo mejor que tengo es el amor que me das cada día. Eres mi hogar, la persona con la que quiero brindar por

todos los éxitos y con la que quiero compartir mis penas. Sin vosotros Dinamarca habría sido oscura y fría, pero contigo se ha convertido en el lugar más acogedor. También quiero agradecer a la familia de Lima, Teresa, Victor, Mayte, el dulce Mateo y la Fochi, por abrirme sus puertas como familia. Me mostraste tu hermoso país, y ahora el Perú es parte de mí.

I am very grateful for all the people I have met during my Ph.D journey: you have been not only my colleagues, but also friends I can trust. Thanks to Enrico Peretti, *l'importante*, the first person I met when I arrived in Copenhagen. He made things very clear since the beginning: at NBI we work hard and play hard, sometimes play more than work. He has been an important guide and mentor for me. I want to thank Damiano Fiorillo and Marina De Amicis for becoming my best friends in Copenhagen. I have survived the past years only because of our private tea times, gossip about Taylor Swift and Damiano's cellphone backgrounds. I truly love you guys. *Of course*, thanks to Tania Pitik, my academic sister, who became a dear friend I know I can always count on. Besides giving me trauma about my food habits, she has also been one of my biggest support and inspiration during the Ph.D. Thanks to Marie Cornelius Hansen, Annika Rudolph, Anna Suliga, Manuel Goimil García, Pablo Martínez Miravé, Rasmus Hansen, Yoann Genolini, Bernanda Telalovic, Kathrine Mørch Groth, Shashank Shalgar, and Evelyin-Andrea Ester; for making of NBI a place where we can laugh, cry and always find friendly faces. I want to express my gratitude also to the people who made Friday nights in Copenhagen wild and fun: Kevin Urquia, Antonio Capanema, Pedro Dedin, Tania Kozynets and Ian Padilla. I may still be hangover in three years because of you, guys.

In Copenhagen, I met many special ones far from the walls of NBI. Thanks to Salomé, Jordy, Delphine and Mads for the most random and yet amazing friendship I have ever had. I am still waiting to be updated about your homework for the pedagogy course, but three years already passed. Thanks to Azzurra, who has become a dear friend and confident over the past year, but above all has proven to be the perfect shopping mate. I am grateful that life led our paths to cross.

During the Ph.D., I have visited UC Berkely and UC Santa Cruz, where I had the pleasure and honor to work with Raffaella Margutti and Enrico Ramirez-Ruiz. Thanks both for being great mentors and collaborators, and for making my visit to the US exciting and fun. I also want to express my gratitude to Damien Bégué and Ore Gottlieb, who have taught me all I know about gamma-ray bursts. They have been amazing collaborators to me.

I must dedicate a special section to Alessandro Mirizzi, who has not only been a mentor throughout my entire academic journey but also a true friend. He was the first person to believe in me as a scientist and has consistently been there to encourage and motivate me through all the challenges that academia presented. I am thankful I have begun my academic journey with him.

Si vola di nuovo a Trani, perché torno sempre a lei. Tra ulivi e salsedine, i miei amici di una vita sono sempre lí ad aspettarmi dopo i miei viaggi intorno al mondo. Sono la rete di cui ho bisogno, quella che mi sorregge e mi fa sentire al sicuro. Nessun posto e nessun rapporto potranno mai sostituire il nostro. Un grazie speciale a Carlo, Giorgio L. e Francesco M. per accettare e ascoltare i miei momenti più critici con pazienza. Siete in grado di risollevarmi con la forza che solo l'amicizia di una vita conosce. Grazie alla mia seconda famiglia, *Amix*: Alessandro, Emilio, Betta, Consuelo, Giorgio T., Antonio, Alessandra, Nunzia, Francesco P.; ma anche alle mie *amiche di sempre*, Sabrina, Daniela, Doriana e Laura, per riuscire ad accorciare le distanze. Non importa quanto sparpagliate e sparpagliati siamo in Italia o nel mondo, quando ci rincontriamo sembra non essere passato un secondo dall'ultima volta. E infine, grazie ad Antonella, Giulia e Federica, praticamente mie sorelle acquisite, per essere le persone dolci e forti che sono, e per essermi vicine incondizionatamente. Conoscono i miei pensieri prima ancora che li comprenda io, e sono grata alla vita per averle portate e trattenute nella mia.

We made it!

CONTENTS

“ There are many reasons to treat each other
with great tenderness. One is
the sheer miracle that we are here together
on a planet surrounded by dying stars.”
Rosmerry Wahtola Trommer

“I believe in pink.”
Audrey Hepburn

Part I

INTRODUCTION

1

MOTIVATION

Since the dawn of time, humanity has been gazing at the night sky, amazed by the light emitted by stars. As technologies advanced, our ability to unravel the mysteries of the Universe also evolved. Once merely able to observe visible light, we can now detect photons across a wide range of wavelengths, accessing astrophysical sources through the radio, infrared, optical, ultraviolet, X-ray and gamma-ray wavebands [1, 2]. These remarkable advancements in the field reached their zenith with the advent of time-domain astrophysics. The unprecedented time and energy resolution reached by high-cadence and wide-field telescopes led to the discovery of a broad range of energetic astrophysical phenomena responsible for the production of bright bursts of particles [3]. The luminosity and durations of these *transients*— astrophysical sources with duration ranging from a few seconds to a few months— exhibit a large variety, however the nature of most of them remains elusive and puzzling.

Yet over the past century, we have witnessed one of the most exciting advancements in astronomy. First, the discovery of *cosmic rays* unveiled the existence of energetic protons and heavy nuclei accelerated in cosmic sources [4]. Subsequently, the detection of *neutrinos* from the Sun established the pivotal role of these elusive particles in astrophysics [5], a notion further strengthened by the thrilling observation of neutrinos of extragalactic origin from supernova SN 1987a [6, 7]. It was not until 2013 that high-energy (TeV-100 PeV) cosmic neutrinos were first detected, giving rise to the vibrant field of high-energy neutrino astronomy [8]. The latest breakthrough in astronomy unfolded in 2015 with the detection of gravitational waves [9]. No longer bound solely to photons, we can now explore the Universe through multiple messengers. These exciting discoveries collectively marked the dawn of the *multi-messenger astronomy* era.

In this dynamic landscape, high-energy particles offer the unprecedented opportunity to probe the extreme Universe in a novel way, by combining the unique information carried by each messenger. Yet decoding detailed information on Earth may be challenging due to the properties of the specific particle and the underlying detection techniques. For instance, high-energy photons undergo several absorption processes in the source and on their way to Earth before being detected, therefore they carry poor energy information [10,

11]. Similarly, cosmic rays are deflected multiple times before reaching the Earth, weakening the information on the direction of their source. In contrast, high-energy neutrinos stand out as unique probes of the extreme Universe. With their small cross section, nearly null mass, and neutral charge, these particles can escape very dense environments and reach terrestrial detectors almost unhindered, pointing back to their source.

The exceptionally high energy reached by cosmic rays, gamma-rays, and neutrinos hints that cosmic sources act as particle accelerators. Neutrinos and photons are expected to result from the decay of secondary particles, produced when accelerated protons undergo photo-hadronic ($p\gamma$) and hadronic (pp) interactions with the radiation and proton backgrounds in the source, respectively.

From the theoretical requirement that the source magnetic fields should be able to confine charged particles in order to accelerate them to high-energies, some sources appear to be ideal cosmic accelerators [12]. In particular, transients are very promising targets for multi-messenger astronomy searches due to their large luminosities and short durations. Importantly, a growing number of high-energy neutrinos is detected in the direction of astrophysical transients at the IceCube Neutrino Observatory, located in the South Pole [13]. Although a handful of transients have been suggested as factories of high-energy neutrinos, the origin of the most energetic particles ever observed remains largely unknown. On the other hand, both time-domain and multi-messenger astronomy are poised to experience a huge leap in the near future. New telescopes and detectors are on the horizon, promising unparalleled sensitivities both for photons and high-energy neutrinos. Among these, the Vera C. Rubin Observatory [14] and ULTRASAT [15] will provide us with the unprecedented opportunity to catch swiftly transients that evolve in few days. Furthermore, many (ultra-, $\geq$ 100 PeV) high-energy neutrino telescopes will come online soon, such as IceCube-Gen2 [16], the Giant Radio Array for Neutrino Detection (GRAND200k) [17], and the spacecraft Probe of Extreme Multi-Messenger Astrophysics (POEMMA) [18]. They will lead to an exponential growth in the number of known transients, and they will allow us to finally collect a large number of high-energy neutrino events.

As time-domain and multi-messenger astronomy herald a future of exciting discoveries, intense theoretical effort is needed to keep pace with the rapid advancements in observational techniques. The works contained in this thesis provide detailed modelling of particle acceleration and high-energy neutrino production processes in a variety of astrophysical transients. This thesis offers insights on the possibility of using neutrinos to disentangle the mechanism powering transients, whereas existing theoretical models for electromagnetic radiation are plagued by degeneracies. It also provides a valuable roadmap to carry out informed multi-

messenger searches of astrophysical transients by combining multi-wavelength and high-energy neutrino data. Our work proves that only by leveraging multi-messenger synergies can we shed light on the most energetic and puzzling phenomena occurring in our Universe.

2

THE LANDSCAPE OF MULTI-MESSENGER ASTRONOMY

The vibrant and growing field that combines different particles and messengers to explore the cosmos is called *multi-messenger astronomy*, and it will be introduced in this Chapter. In Section 2.1, we provide an overview of the history and properties of the different cosmic messengers. Subsequently, in Section 2.2 we highlight the state-of-the-art of multi-messenger astronomy and its biggest milestones achieved over the past years.

2.1 LOOKING AT UNIVERSE THROUGH MULTIPLE MESSENGERS

As of today, we can probe the Universe through photons, cosmic rays, neutrinos and gravitational waves. In the following, we give a brief overview of each of the four messengers.

– **Photons** still remain the primary source of information from astrophysical sources. It was not until the first half of the 20th century that radio astronomy developed [1], marking a significant leap in our observational capabilities, before limited to the optical light only. However, we had to wait for the second half of the century to access higher energy wavebands, with the first observations of X-rays and gamma-rays [2, 19]. The information about the electromagnetic diffuse flux detected on Earth across all the wavebands was first collected by Ressel and Turner, in the so called *Grand Unified Photon Spectrum*, shown in Fig.1.

  The inspection of the photon signal over multiple wavebands provides us with valuable insights into different processes, regions and timescales within the same astrophysical source. Different wavelengths also dictate the choice of observational technique, as the interaction of photons with their surrounding must be carefully taken into account.

  Electromagnetic spectra observed from astrophysical sources can be broadly classified into two main categories: *thermal* and *non-thermal*. Thermal spectra are generated by the motion of hot particles and

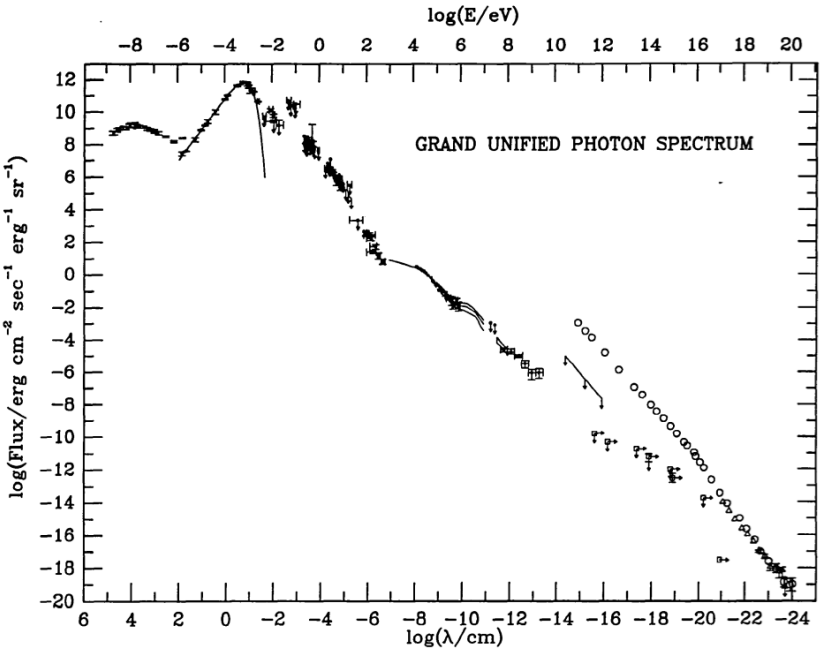

Figure 1: The Grand Unified Photon Spectrum, showing the diffuse flux of photons observed on Earth across all the accessible wavelengths. Figure from Ref [20].

are described by a black-body distribution. On the other hand, non-thermal photons typically exhibit a power-law distribution, shaped through the cooling of accelerated particles. We will provide an overview of both kinds of spectra in Chapter 4. While non-thermal photons could serve as probes of acceleration processes taking place within the source, our access to the high-energy sky is significantly limited by the opacity of the Universe above $\sim 10^{12}$ eV[21], as shown in Fig. 2. High-energy gamma-rays interact with the Cosmic Microwave Background (CMB) photons and undergo pair production and inverse Compton scattering processes, that is,

$$\gamma + \gamma_{\rm CMB} \longrightarrow e^+ + e^- \tag{2.1}$$

$$e^\pm + \gamma_{\rm CMB} \longrightarrow e^\pm + \gamma\,, \tag{2.2}$$

respectively. As a result, gamma-rays are scattered to lower energies. Over cosmic scales ($\sim$ Gpc), gamma-rays are also affected by interactions with the Extragalactic Background Light [22]. We conclude that, although photons effectively enable us to probe nearby sources, their suitability for exploring the edges of the Universe drastically diminishes at high energies [23].

– **Cosmic rays** are charged particles that continuously bombard the Earth. First discovered by Victor Hess in 1912 through balloon experiments [4], cosmic rays are currently detected over a wide range of energies and up to the ultra-high-energy scale (UHE, $\sim 10^{18}$ eV). However, their detection at the

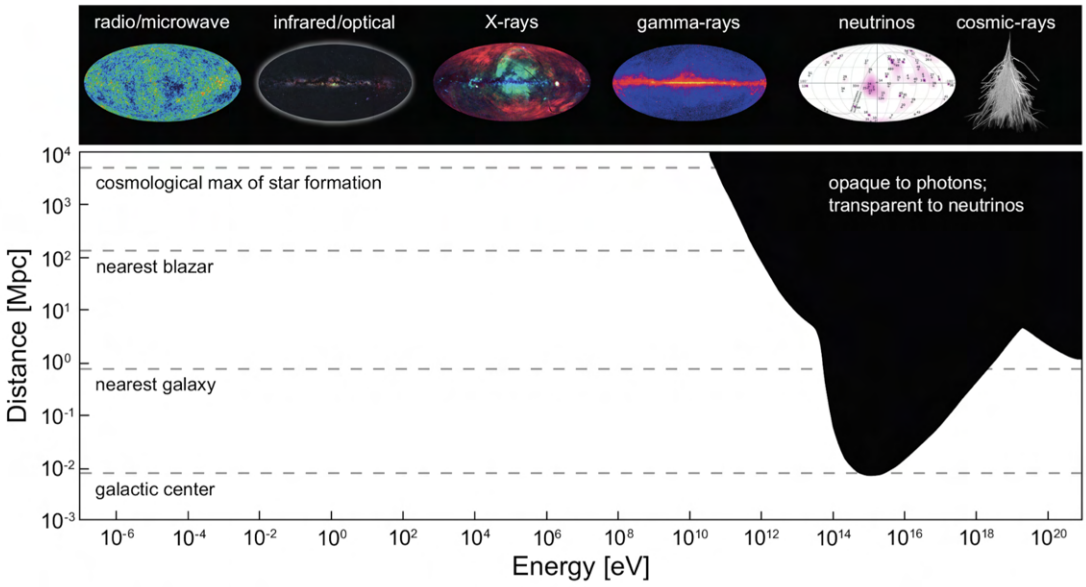

Figure 2: Distance at which the Universe becomes opaque to electromagnetic radiation, as a function of the photon energy. Figure from Ref. [16].

highest energies is challenging, due to their flux decreasing as $\propto E^{-2.7}$. Approximately, we receive 1 particle/m^2 s at 10^{11} eV, 1 particle/m^2 yr at 10^{16} eV and 1 particle/km^2 yr at 10^{18} eV.

Similarly to photons, different observation techniques must be employed to catch cosmic rays across multiple energy bands. Small space-based instruments are adequate for detection at low energies. Yet at UHE only indirect observations are possible, through the detection of hadronic air showers initiated when cosmic rays interact with particles in the atmosphere. A census of the detectors chasing for indirect observations of cosmic rays is shown in Fig. 3. Cosmic rays below $\sim 10^{15}$ eV are thought to be accelerated in the Milky Way, whereas above 10^{18} eV they cannot be effectively contained within our galaxy and they are therefore believed to have extragalactic origin. This constraint arises because the Larmor radius of cosmic rays becomes comparable to the thickness of the galactic disk, assuming a galactic magnetic field strength of approximately $\approx 3\mu$ G.

As depicted in Fig. 3, the cosmic ray spectrum reveals many transition features. Notably, the maximum energy achievable by galactic cosmic rays induces the *first knee*, which marks the transition to the extragalactic component. On the other hand, the *second knee* is related to the transition to heavy primaries. The transition to an extragalactic population of accelerated cosmic rays is marked by the *ankle* in the spectrum. Finally, the interaction between UHE cosmic rays with the CMB produces the high-energy cutoff in the spectrum, known as the *Greisen-Zatsepin-Kuzmin (GZK) cutoff* [25, 26].

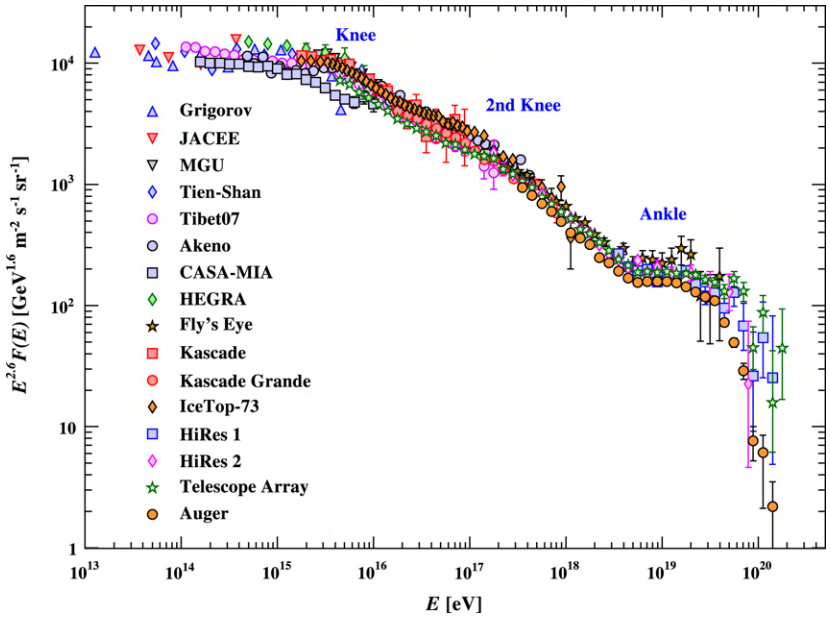

Figure 3: Cosmic ray spectrum $E^{2.6}F(E)$ as a function of their energy. Here, $F(E)$ is the number of particles per unit of energy, second and solid angle. Figure from Ref. [24].

Cosmic rays are the smoking gun of particle acceleration processes taking place within their source. However, due to their charge, these particles are deflected by galactic ($\sim O(\mu\text{G})$) and extragalactic ($\sim O(\text{nG})$) magnetic fields before reaching Earth. As our knowledge of these electromagnetic fields is poor, reconstructing the original direction of cosmic rays is challenging. Furthermore, UHE cosmic rays undergo pair production and photo-hadronic processes with the CMB photons, that is,

$$p + \gamma_{\text{CMB}} \longrightarrow p + e^+ + e^- \tag{2.3}$$

$$p + \gamma_{\text{CMB}} \longrightarrow \Delta^+ \longrightarrow \begin{cases} p + \pi^0 \\ n + \pi^+ \,, \end{cases} \tag{2.4}$$

respectively. Similarly to photons, we conclude that cosmic rays are not ideal probes of sources located far away from Earth.

– **Neutrinos** are neutral fermions whose existence was first proposed by Wolfgang Pauli in the context of beta decays [27]. The name *neutrino* appeared for the first time in Enrico Fermi's theory of beta decay [28], but due to their very small cross-section, these weakly interacting particles were not observed until 1956 [29]. Their extremely feeble interactions with matter allow neutrinos to travel large distances without being absorbed or deflected. Therefore, once they reach Earth they pinpoint their source. While these properties make neutrinos ideal candidates to probe the high-energy sky, they also pose substantial challenges to neutrino detection, as we will further discuss in the following.

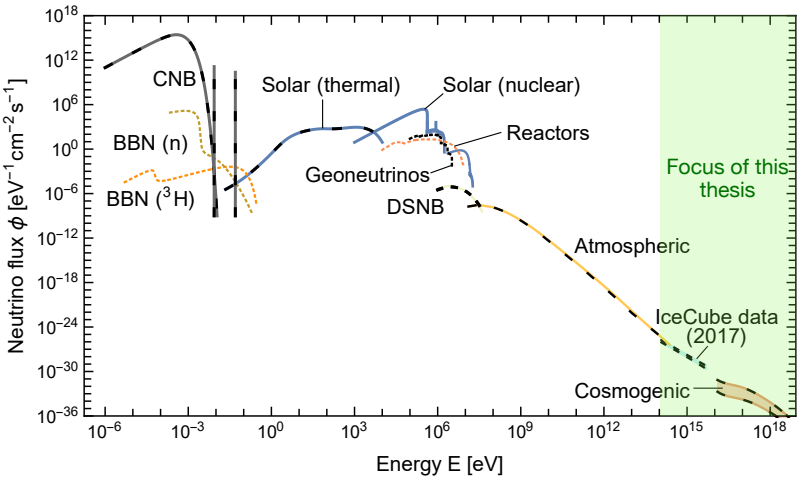

Figure 4: The Grand Unified Neutrino Spectrum at Earth per unit of energy, area and second. The green part highlights the energy range of interest for this thesis, namely neutrinos with energies $\geq$ TeV. Figure adapted from Ref. [32].

As of today, we know that neutrinos come in three flavors, one for each corresponding lepton: the electron neutrino (ν_e), the muon neutrino (ν_μ) and, finally, the tau neutrino (ν_τ). Being a quantum superposition of three mass states, neutrinos oscillate between different flavors while propagating from the source to Earth [30, 31].

These elusive particles are produced in a variety of experiments on Earth and astrophysical sources, spanning nuclear reactors, the Sun, Supernovae and the terrestrial mantle. Of particular interest for this thesis are high-energy neutrinos, produced as (ultra-)high-energy cosmic rays interact with radiation or matter backgrounds in astrophysical sources. Similar processes come into play when UHE cosmic rays interact with the Earth's atmosphere, producing atmospheric neutrinos. The latter serve as a background against which neutrinos of astrophysical origin with energies $\lesssim$ 100 TeV cannot be easily distinguished. Similarly to photons, the state-of-the-art knowledge on the neutrino diffuse flux across all the energy ranges is summarized in the *Grand Unified Neutrino Spectrum* [32], shown in Fig. 4. Throughout this thesis, we will focus on the highlighted region in Fig. 4, namely on neutrinos with energies $\geq$ TeV.

The crucial role of neutrinos in the interplay between particle physics and astrophysics became clear with the detection of neutrinos from the Sun [33], followed by supernova SN 1987a, the very first source outside the solar system to be seen through neutrinos [6, 7]. These discoveries marked the dawn of neutrino astronomy. Since then, gigantic detectors have been built to catch neutrinos at the highest energies, such as the IceCube Neutrino Observatory [34], which observed for the first time neutrinos in

the TeV–PeV range in 2013 [8]. Over 10 years of operations, IceCube detected hundreds of cosmic neutrinos with energies between 10^4 GeV and 10^7 GeV [35]. Yet the sources of the cosmic neutrino signal detected in the form of a diffuse flux remain unknown [36, 37], with a handful of candidates. Possible factories of high-energy neutrinos will be further discussed in Sec. 4.

Neutrinos with energies above 10^7 GeV are expected to be produced through the interaction of UHE cosmic rays with the intergalactic medium, as well as through hadronic and photo-hadronic interactions of UHE cosmic rays in cosmic accelerators. However, so far we have not observed neutrinos with such high energies and many upcoming detectors aim at pushing their sensitivity above $O(10^7)$ GeV, as we will discuss in Sec. 5.

– **Gravitational waves** are distortion of the space-time structure. Let us consider a space-time geometry that deviates from the Minkowski one ($\eta_{\mu\nu}$) only by a small perturbation, such that the metric can be written as

$$g_{\mu\nu}(x) \simeq \eta_{\mu\nu} + h_{\mu\nu}(x) \tag{2.5}$$

where $|h_{\mu\nu}(x)| \ll 1$, the indices μ, ν run over the values $0, 1, 2, 3$, with $x^0 = t$ and $\eta_{11} = \eta_{22} = \eta_{33} = -\eta_{00} = -1$.

In harmonic coordinates and for weak gravitational fields the linearized Einstein field equations read

$$\Box h^{\alpha}_{\nu} = -2\chi \left(T^{\alpha}_{\nu} - \frac{1}{2}\delta^{\alpha}_{\nu} T \right) , \tag{2.6}$$

where T^{α}_{ν} is the energy-momentum tensor, T is its trace and $\chi = 8\pi G/c^4$ is a constant controlling the coupling between matter and geometry, with G being the gravitational constant. Finally, $\Box = \eta^{\mu\nu}\partial_\mu\partial_\nu$ is the d'Alambert operator of the flat Minkowski space-time. Eq. 2.6 connects the space-time curvature to the energy-momentum density of the matter sources and it also holds when the perturbations $h_{\mu\nu}$ depend on time. In this case, Eq. 2.6 describes geometric fluctuations that propagate in vacuum at the speed of light, known as *gravitational waves*. It can be shown that the radiated gravitational power is controlled by the third derivative of the quadrupole moment of the source, that is $dE/dt \propto |\dddot{Q}|^2$. Therefore, gravitational waves can only be emitted by systems with a non-vanishing and non-constant quadrupole moment.

Originally predicted by Henri Poincaré and Albert Einstein at the beginning of the 20$^{\text{th}}$ century, gravitational waves produced by the merger of two black holes were detected in 2015 (GW150914) by

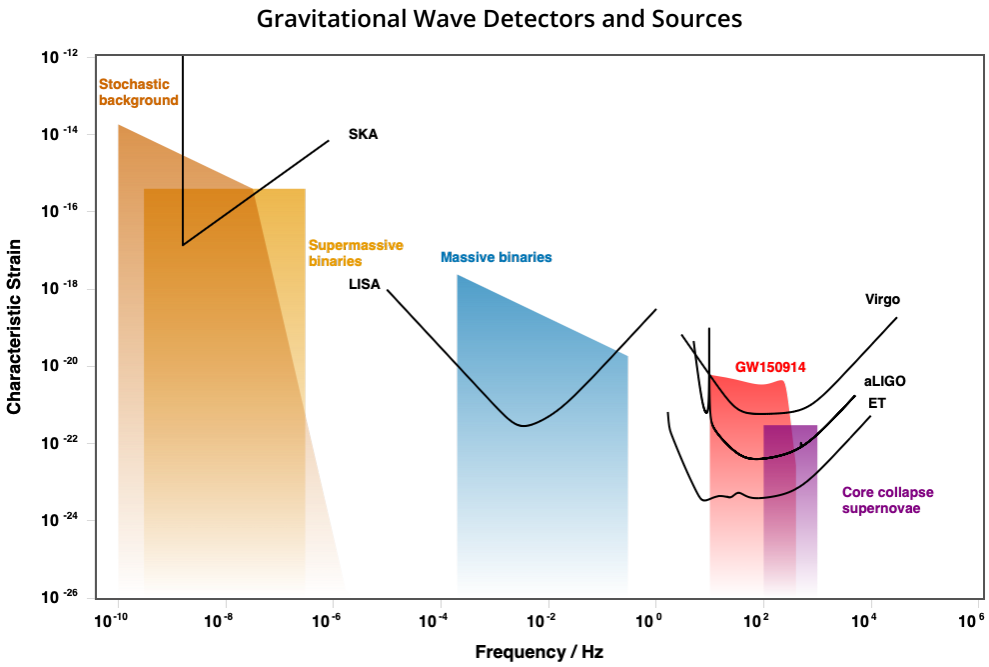

For details of the data and various conventions used, see this paper on the arXiv. For a less technical discussion, this blog post provides a good introduction.

Figure 5: The gravitational waves landscape as a function of frequency and strain. Figure produced with the Gravitational Wave Plotter.

the Laser Interferometer Gravitational-Wave Observatory (LIGO) and Virgo collaborations [9]. Current interferometers are sensitive to the frequency range corresponding to the merger of compact objects, such as black holes and neutron stars. Upcoming interferometers, such as the Einstein Telescope (ET), will unlock the unprecedented opportunity to detect gravitational waves from core-collapse supernovae [38]. Similarly, the proposed Laser Interferometer Space Antenna (LISA) will access lower frequencies, enabling the detection of gravitational waves from massive black hole binary inspirals [39]. Finally, at nanohertz frequencies the pulsar timing array SKA will be sensitive to the stochastic background of primordial gravitational waves [40]. A selected compilation of cosmic events observable in gravitational waves together with the sensitivity curves of current and upcoming instruments is shown in Fig. 5.

Gravitational waves are intriguing messengers, as proven by the detection of the gravitational wave event GW170817 in association with the multi-wavelength spectrum from a neutron star merger [41]. No neutrinos were detected in coincidence with this event [42, 43]. However, neutron star mergers are candidate factories of neutrinos across a wide range of energies, making the correlation existing between photons, neutrinos and gravitational waves extremely exciting for future perspectives.

2.2 RECENT HIGHLIGHTS IN MULTI-MESSENGER ASTRONOMY

Multi-messenger astronomy is a vibrant field that has witnessed significant breakthroughs over the past decade. Despite its remarkable advancements, to date no simultaneous detection of all the direct messengers (photons, neutrinos and gravitational waves) has been reported. In the following, we present a selected compilation of recent highlights in multi-messenger astronomy. We will distinguish between *steady sources* and *transient sources*, the latter exhibiting durations ranging from fractions of a second to a few months.

2.2.1 *Steady sources*

2.2.1.1 *Photon-neutrino correlation*

NGC 1068: Active Galactic Nuclei (AGN) are extremely bright regions at the center of a galaxy hosting a supermassive black hole. These compact sources have long been considered efficient cosmic accelerators, a conjecture which has been confirmed by the IceCube Neutrino Observatory with the detection of $\simeq 80$ neutrino events with $O(\text{TeV})$ energies from the *Squid Galaxy* NGC 1068 with a significance of 4.2σ [44]. The source is known to be a starburst galaxy hosting an AGN. To ensure consistency with the diffuse gamma-ray background detected by *Fermi*, neutrinos should be produced in a region that is opaque to $0.1 - 10$ GeV gamma-rays [45, 46]. In light of these constraints, it has been suggested that the observed neutrinos are produced in the vicinity of supermassive black holes surrounded by very optically thick dust or gas [47]. However, none of the existing models is able to accommodate simultaneously the electromagnetic and neutrino signals, underscoring the pressing need for a theoretical effort to accurately model particle production and acceleration mechanisms within AGN and starburst sources.

The galactic plane: Cosmic rays accelerated in the Milky Way and interacting with the interstellar medium produce neutral pions (π^0). In turn, these pions decay into gamma-rays with energies $\gtrsim O(\text{GeV})$, as we observe from our own galaxy. Charged pions are also produced in the interaction between cosmic rays and the Milky Way interstellar medium, and subsequently decay producing high-energy neutrinos. Over ten years of data, IceCube successfully identified such neutrino emission from the galactic plane, achieving a

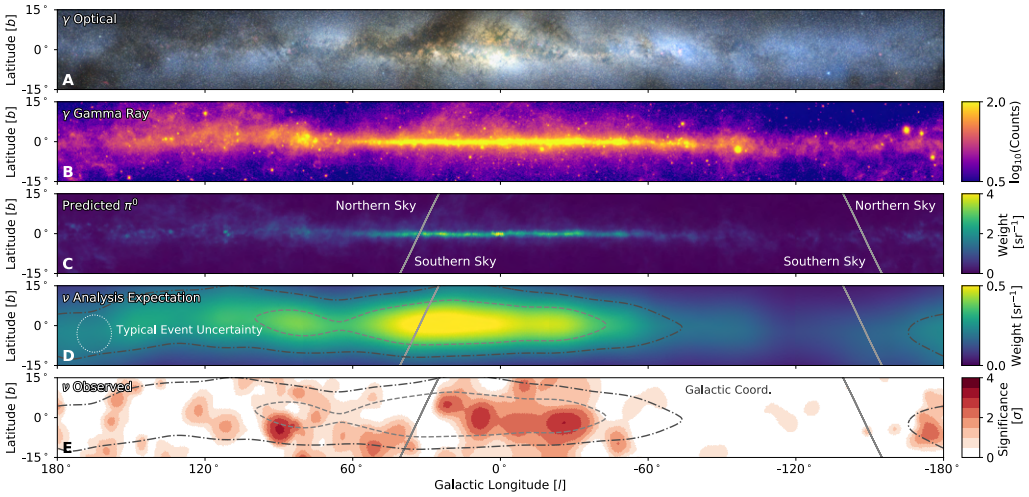

Figure 6: The galactic plane as seen in optical photons, gamma-rays and and high-energy neutrinos. Figure from Ref. [48].

significance level of 4.5σ [48]. A picture of the Milky Way as seen in optical photons, gamma-rays and high-energy neutrinos is shown in Fig. 6.

2.2.2 *Transient sources*

2.2.2.1 *Photon-neutrino correlation*

TXS 0506+056 and PKS 0735+178: Blazars are a rare subclass of AGNs whose black hole harbors a relativistic jet pointing towards Earth. The IceCube collaboration identified two neutrino point-like sources in the Northern sky, whose electromagnetic counterparts correspond to well known blazars: TXS 0506+056 and PKS 0735+178. The skymap of three high-energy neutrino hotspots identified by IceCube, namely TXS 0506+056, PKS 0735+178 and NGC 1068, is shown in Fig. 7.

In 2017 the IceCube collaboration reported the association between the IceCube 170922A high-energy neutrino event and the bright blazar TXS 0506+056 [49]. Notably, the astrophysical source was undergoing flaring activity at the time of the IceCube detection. Further analysis of archival data from 2015 revealed 13 ± 5 additional neutrino events in spatial and temporal coincidence with another flare event from the same source [50]. Following TXS 0506+056, in December 2021 IceCube [51], Baikal [52], Baksan [53] and KM3NeT [54] observed multiple high-energy neutrino events likely associated with the bright blazar PKS 0735+178. Concurrently, the blazar exhibited the most significant flaring activity ever recorded in the optical, ultraviolet, X-ray and gamma-ray bands.

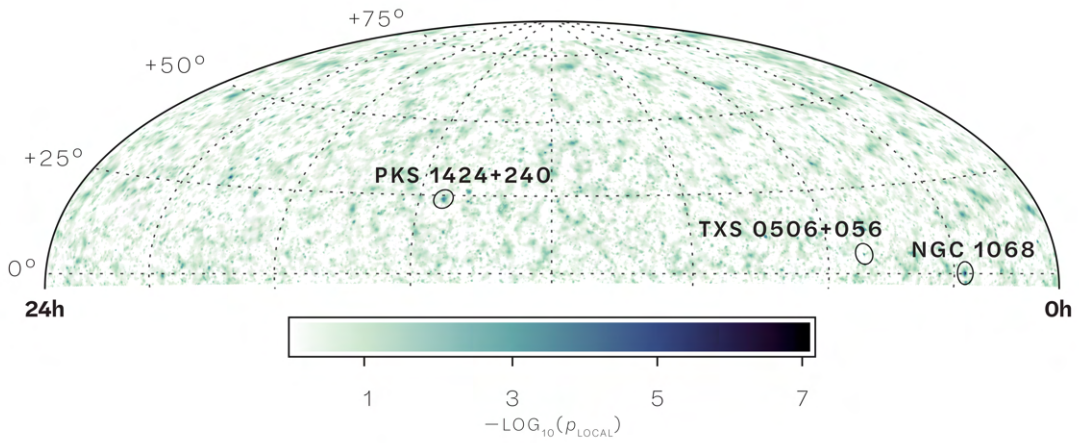

Figure 7: Skymap of neutrino point sources in the Northern Hemisphere. The black circles denote the three most significant objects identified in the searches performed by IceCube. Figure from [44].

The observed multi-wavelength emission from blazars is commonly explained by invoking lepto-hadronic or hadronic models, which associate the signal to both leptons and hadrons or hadrons only, respectively. However, when considering neutrinos and photons simultaneously in both models, fine tuning of the blazar parameters is needed [55–57]. Despite the interesting neutrino detection possibly associated with single sources, the contributions of blazars to the high-energy diffuse flux detected at IceCube is quite small ($\lesssim 10\%$ [58]).

AT2019fdr: The joint effort of IceCube and the Zwiky Transient Facility (ZTF) collaboration led to the observation of a handful of high-energy neutrino events associated with optical transients, some of which considered candidate tidal disruption events [59–61]. Of particular interest in the context of this thesis is the ZTF transient AT2019fdr [62, 63]. The neutrino event was detected approximately 300 days after the peak of the transient bolometric lightcurve. A first theoretical interpretation classified AT2019fdr as a tidal disruption event [60]. Nevertheless, the latest hypothesis of a hydrogen-rich superluminous supernova (SLSN) [64] seems more likely, also in light of the rebrightening observed in the lightcurve $\approx$ 70 days after the optical peak. The SLSN conjecture can also accommodate the IceCube high-energy neutrino event observed in coincidence with AT2019fdr without invoking jetted tidal disruption events, which may be a quite rare subclass [65].

AT2018cow: IceCube reported the detection of two neutrino events in the direction of AT2018cow, a source belonging to the emergent class of Luminous Fast Blue Optical Transients (LFBOTs) [66]. The neutrinos arrived during a time window of $\sim$ 3.5 days of exposure, spanning from the last confirmed

non-detection of the transient to its first optical observation. However, due to their $O(\mathrm{TeV})$ energies, these events fall in the energy range populated by the atmospheric background. Thus, it is challenging to discern whether those neutrinos are of astrophysical origin.

Irrespective of the specific nature of AT2019fdr and AT2018cow, the increasing number of neutrino detections in the direction of astrophysical transients supports the idea that these sources are intriguing high-energy multi-messenger targets. We will further discuss this topic in Sec. 4.

2.2.2.2 *Photon-gravitational wave correlation*

GW170817: One of the major breakthrough in multi-messenger astronomy has certainly been the detection of the gravitational wave event GW170817 in temporal and spatial association with the short gamma-ray burst GRB 170817A [41, 67, 68]. An extensive multi-wavelength campaign followed the observation of GW170817, revealing the existence of a kilo/macronova overlapped with the GRB afterglow [69, 70]. The fascinating event also confirmed the theoretical conjecture that elements heavier than iron are synthesized in neutron star mergers through neutron capture, the so called neutron capture process (r-process) [71, 72]. The association between short GRBs and neutron star mergers was a long-standing paradigm whose first confirmation has been the GW170817/GRB 170817A detection. However, we note that the theoretical association between kilonovae and short bursts has been recently challenged by the detection of two long GRBs followed by a kilonova [73, 74]. These observations may hint towards the existence of a third class of bursts, probably originating from different processes and yet associated with kilonovae.

3

PARTICLE ACCELERATION AND RADIATIVE PROCESSES IN ASTROPHYSICAL PLASMAS

From the overview on multi-messenger astronomy provided in Chapter 2 it emerges that high-energy particles are the smoking gun of particle acceleration processes taking place within astrophysical sources. In this Chapter, we briefly discuss the particle acceleration mechanisms invoked throughout this thesis. Subsequently, we provide an overview of the relevant radiative processes in high-energy astrophysics and highlight their interplay with acceleration mechanisms.

3.1 PARTICLE ACCELERATION

In the recipe for particle acceleration, the key ingredient is the presence of large scale magnetic fields capable of confining particles, ensuring that the Larmor radius of the latter does not exceed the size of the source. Some astrophysical sources naturally fulfill this requirement, with several processes invoked to account for particle acceleration within them, including shock acceleration (e.g. Ref. [75] for a review), shear acceleration [76] and magnetic reconnection [77]. While these models succeed in reproducing the non-thermal power-law spectrum observed from high-energy phenomena, there is no conclusive evidence favoring one over the others. For the purposes of this thesis, we will limit our discussion to shock acceleration and magnetic reconnection, while we refer the interested readers to the aforementioned references for details on other acceleration mechanisms.

3.1.1 *Fermi acceleration*

Two Fermi acceleration mechanisms have been formulated, known as *second-order* and *first-order* Fermi acceleration [78, 79]. Both these processes rely on a few key assumptions: (i) particles are continuously

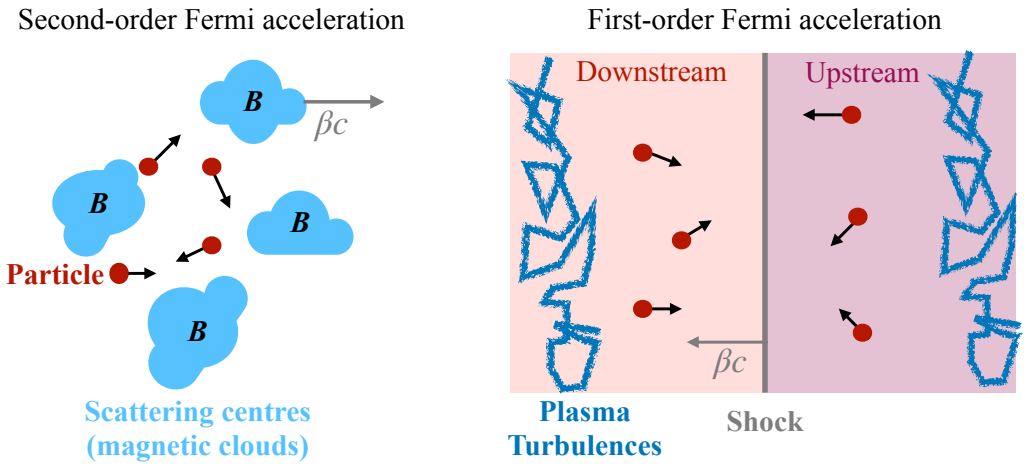

Figure 8: *Left panel*: Cartoon of the second-order Fermi acceleration process. Particles gain energy by scattering off centers (magnetic clouds, for instance) which are randomly distributed in the fluid. *Right panel*: Cartoon of the first-order Fermi acceleration process. Particles cross multiple time the shock front and scatter off plasma turbulences existing both in the downstream and in the upstream of the shock front (grey line).

injected into the fluid through some mechanism; (ii) some scattering centers exist within the fluid and isotropize the particle distribution. We discuss the details of both processes in the following.

3.1.1.1 *Second-order Fermi acceleration*

In its first version, the acceleration mechanism proposed by Fermi assumes that the scattering centers move randomly in the fluid, effectively acting as magnetic mirrors for particles. For instance, these centers could be interstellar clouds that reflect off particles multiple times. A cartoon of the second-order Fermi acceleration process is shown on the left panel of Fig. 8.

Let us consider scattering centers moving at mean speed βc and Lorentz factor Γ. It is possible to show that after one collision the energy gain of a particle is [80]

$$\frac{\Delta E}{E} = \Gamma^2(1 - \beta\cos\theta + \beta\cos\theta' - \beta^2\cos\theta\cos\theta') - 1 \,, \tag{3.1}$$

where θ and θ' are the angles between the particle speed entering and exiting the scattering region, respectively, and the speed of the scattering center.

By averaging on the angle distributions, the overall energy gain per collision is

$$\left\langle \frac{\Delta E}{E} \right\rangle = \frac{4}{3}\beta^2\Gamma^2 \simeq \frac{4}{3}\beta^2 \,, \tag{3.2}$$

where in the last step we have made the approximation $\Gamma \simeq 1$, namely the scattering centers are non-relativistic. Since the energy gain in one collision is proportional to β^2 the process is called *second-order acceleration*.

3.1.1.2 *First-order Fermi acceleration*

This mechanism is particularly relevant for astrophysical shocks, namely disturbances that propagate in the fluid faster than the sound. Within this framework, particles gain energy by crossing the shock front—assumed to be infinite and planar— multiple times. The crossing is induced by irregularities ahead of the shock front and turbulences behind it. A cartoon of the first-order Fermi acceleration process is shown in Fig. 8.

Let βc be the speed of the unshocked upstream region as seen by the shocked downstream region, and Γ the corresponding Lorentz factor. It can be shown that the energy gain over one cycle is the same as in Eq. 3.1. However, due to the assumption of infinite planar shock geometry the angle averaged energy gain is [80]

$$\left\langle \frac{\Delta E}{E} \right\rangle = \frac{4}{3}\beta\Gamma^2 + \frac{13}{9}\beta^2\Gamma^2 \simeq \frac{4}{3}\beta \,, \tag{3.3}$$

where the last approximation corresponds to the limits $\beta \ll 1$ and $\Gamma \simeq 1$. Since the energy gain in one collision is linear in β, this process is dubbed *first-order Fermi acceleration*.

Probabilistic arguments can be used to prove that the distribution of accelerated particles is a power-law. Given a particle with initial energy E_0, its energy after one collision reads $E = E_0\beta$. Therefore, the number of particles with energies $E = E_0\beta^n$ after n collision will be $N = N_0 P^n$, where P denotes the probability that the particle stays in the acceleration region after one collision. This probability reads $P \equiv 1 - P_{\rm esc} = 1 - 4/3\beta$, where we have denoted with $P_{\rm esc}$ the particle escape probability. We conclude that the particle energy spectrum expected from the process is [81]

$$N(E)\mathrm{d}E \propto E^{-1+\frac{\ln P}{\ln \beta}}\mathrm{d}E \simeq \mathrm{const} \times \mathrm{E}^{-2}\mathrm{dE} \,. \tag{3.4}$$

The second-order Fermi acceleration mechanism is of particular interest in the context of astrophysics, as shocks are expected to occur in a variety of astrophysical systems. We note that the underlined simple picture has been derived for non-relativistic shocks and several factors can alter it. For instance, the spectrum may be softened when diffusion within a finite medium is considered, whereas the resulting spectrum can be harder due to non-linear phenomena stemming from cosmic ray pressure. For ultra-relativistic shocks (where $\Gamma \gg 10$), the energy gain of particles during the first cycle increases by a factor Γ^2 compared to the one

calculated for non-relativistic shocks, whereas the energy gain is only a factor ≈ 2 [82] in the subsequent cycles. Under these conditions, particles can attain high energies if there is substantial amplification of magnetic power at small scales, thereby preventing the particles from escaping the source [83].

The inherent complexity of the particle acceleration problem at shocks requires sophisticated numerical methods to be employed. In this context, Particle-In-Cell (PIC) simulations have proven to be highly effective, even though it is important to note that they fall short in capturing the physics of the system on large scales. In the initial implementation of the PIC method, charged particles in the plasma only interacted with the electromagnetic fields produced by their own motion. Yet modern PIC simulations can meticulously track individual particles, capturing the kinetic of the plasma in full detail. Furthermore, they enable the modeling of various instabilities which may play a crucial role in particle acceleration at shocks [84, 85]. PIC simulations predict a power-law distribution $\propto E^{-k}$ for accelerated particles, with the spectral index being $k \approx 2.5$ for ultra-relativistic shocks [85]. However, shock compression and anisotropic scattering in the downstream medium can result in $k \approx 2.6 - 2.7$ [86].

3.1.1.3 *Collisionless shocks and sub-shocks*

Efficient particle acceleration can take place at *collisionless* shocks, namely shocks which are mediated by plasma instabilities rather than by radiation [87, 88]. On the contrary, photons that are produced in the downstream of *radiation mediated* shocks can diffuse upstream and interact with electrons and pairs. Consequently, acceleration is hindered as the protons upstream are decelerated by photons via their coupling with thermal electrons. In general, the shock is said to be collisionless when the upstream medium becomes optically thin to the shock, namely when its Thomson optical depth $\tau \lesssim c/v_{\rm sh}$ [87], where $v_{\rm sh}$ denotes the shock velocity.

When the shock propagates in a sufficiently magnetized plasma, collisionless sub-shocks may form within radiation mediated shocks [89]. The formation of the sub-shock can be qualitatively understood as follows. As hot photons from the downstream region diffuse into the upstream, they try to slow down the incoming upstream particles through scatterings. However, in a magnetized plasma, a fraction of the overall downstream energy is stored in the compressed magnetic field, and only the remaining fraction is stored in photons. Consequently, the latter can only moderately decelerate the incoming upstream flow. A thin sub-shock must form near the downstream side of the radiation mediated shock to fully dissipate the kinetic energy of the incoming particles. It can be shown that this sub-shock is collisionless and able to accelerate particles [89].

3.1.2 *Magnetic reconnection*

In an electrically conducting plasma, magnetic field lines are *frozen-in* to the plasma and move with its velocity field. As a result, oppositely directed magnetic field lines can rearrange their geometry, breaking and reconnecting. The altered magnetic field lines develop a pronounced curvature and form the typical X point feature. This process is called *magnetic reconnection* and it occurs in a variety of laboratory and astrophysical plasmas, including the Sun (see Ref. [90] for a review).

According to Faraday's equations, variations in the magnetic flux induce electric fields. As a response, the plasma attempts to screen the induced electric fields. The screening process is nearly perfect in an ideal plasma, where the induced fields set charges in motions and produce magnetic fields that cancel out the magnetic flux variations. Therefore, reconnection is hindered in ideal plasmas and non-ideal effects are crucial to initiate the process and to sustain the electric field induced by reconnection events. When two magnetic field lines are pushed together, cut at their intersection point, and subsequently reconnected, the system releases its energy, dissipating magnetic energy into kinetic energy.

The first theoretical formulation of magnetic reconnection was developed within a non-relativistic framework in the Sweet-Parker model [91, 92]. A magnetically neutral region develops between two anti-parallel magnetic field lines, where electric current density concentrates in current sheets and dissipation takes place in a planar geometry. The Sweet-Parker model does not take into account either three-dimensional or time-dependent effects, and it does not allow to reproduce the fast reconnection rates observed in some plasmas. On the contrary, the Petschek model broadens the outflow region and it introduces a slow shock near the X points, effectively boosting the rate of magnetic reconnection [93]. A cartoon of the Sweet-Parker and Petscheck models is shown in Fig. 9. Alternatively, the rate of reconnection can be boosted through plasma turbulences, which induce multiple reconnection events at the same time.

Of particular interest in the context of astrophysics is relativistic magnetic reconnection, taking place when the plasma magnetization parameter $\sigma \gg 1$ [95, 96]. The latter is defined as the ratio between the Poynting luminosity and the kinetic luminosity

$$\sigma = \frac{B'^2}{4\pi\rho' c^2} \,, \tag{3.5}$$

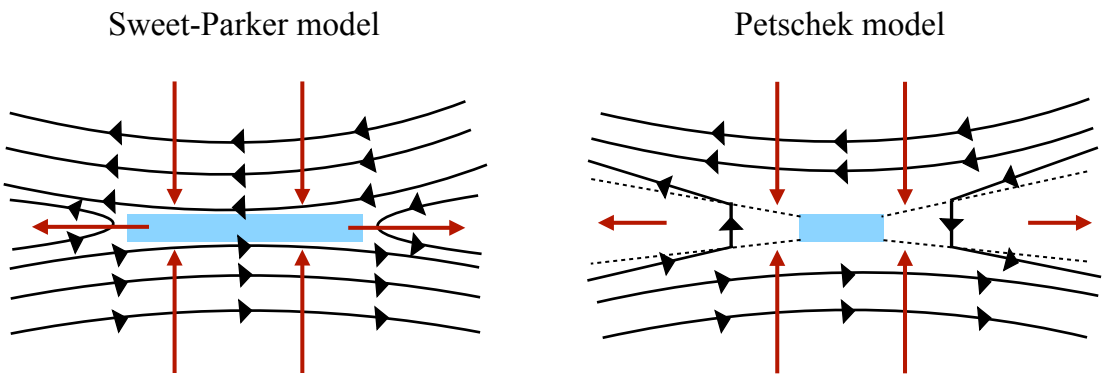

Figure 9: *Left panel*: Magnetic field line configuration in the Sweet-Parker model for magnetic reconnection. *Right panel*: Magnetic field line configuration in the Petscheck model for magnetic reconnection. In both cases, the shaded blue area denote the dissipation regions and the red long arrow denote the plasma velocity field. The dashed lines in the right panel represent slow shocks. Figure adapted from Ref. [94].

where B' is the magnetic field and ρ' is the baryon density, both measured in the comoving frame of the plasma [1].

PIC simulations have been employed to explore relativistic collisionless reconnection in electron-positron pair and electron-ion plasmas, underlying that approximately half of the dissipated magnetic energy is stored in kinetic plasma energy. Notably, the remaining half goes into particle acceleration [97–99]. Similarly to collisionless shocks, particles accelerated through magnetic reconnection follow a power-law distribution $N(E)\mathrm{d}E \propto E^{-k}$, whose spectral index k strictly depends on the fluid magnetization [99]. This acceleration mechanism is particularly appealing, as it naturally leads to hard spectra ($k < 2$) for $\sigma \gg 1$, which are consistent with the observed spectra of some astrophysical sources such as blazar flares [100–102].

3.2 RADIATIVE PROCESSES IN HIGH-ENERGY ASTROPHYSICS

Charged particles undergo many energy-loss processes in astrophysical environments. These processes can significantly limit the maximum energy achievable by accelerated particles in the source and have important consequences both on the observed electromagnetic and high-energy neutrino signals. In the following, we provide an overview of the physics underlying each radiative process, while we refer the reader to Refs. [103–105] for a detailed discussion.

1 Hereafter, we denote with X' and X the quantities measured in the fluid reference frame and in the observer frame, respectively.

3.3 THERMAL RADIATION

A body in thermodynamic equilibrium emits thermal radiation, resulting from the conversion of heat generated by the motion of charged particles in matter into electromagnetic radiation. In optically thick media, thermal radiation coincides with *black body radiation*, which is radiation emitted in thermal equilibrium with its environment by a perfect absorber, dubbed black body.

The specific intensity of black body radiation is given by the Planck law

$$B'_\nu = \frac{2h\nu'^3}{c^2}\frac{1}{e^{h\nu'/k_BT'}-1}\,, \tag{3.6}$$

where k_B is the Boltzmann constant and T' is the black body temperature, controlling the peak of the spectrum at $h\nu'_{\rm pk} = 2.82k_BT'$. The corresponding internal energy density is

$$e'_{\rm int} = \frac{4\pi}{c}\int_0^\infty B'_\nu d\nu = aT'^4\,, \tag{3.7}$$

where a is the radiation constant. Importantly, in thermal plasmas with a given surface and temperature, it is not possible to overtake the black body luminosity.

Of particular interest in the context of this thesis is the limit of the black body spectrum obtained for $h\nu' \ll k_BT'$, when Eq. 3.6 reduces to the *Wien spectrum*:

$$B'^{\rm Wien}_\nu = \frac{2h\nu'^3}{c^2}e^{-h\nu'/k_BT'}\,. \tag{3.8}$$

In astrophysical environments, radiation can be produced by charged particles through several processes, as we will detail in the following. When the source is optically thick, photons can achieve thermal equilibrium and redistribute to a pure black body spectrum. However, complete thermalization can only be sustained as long as the radiation sources generate a sufficient number of photons. A given radiative process freezes out at the radius $R_{\rm sup}$, obtained from the condition [106]

$$t'_{\rm ad}\dot{n}' \geq n'_{\gamma,\rm th}\,. \tag{3.9}$$

Here, $t'_{\rm ad}$ parametrizes the adiabatic expansion of the source, $\dot{n}'$ is the photon production rate due to a specific radiative process and $n'_{\gamma,\rm th} = 16\phi\zeta(3)(k_BT'/ch)^3$ is the photon number density obtained for a black body distribution. Finally, $\zeta(3) \approx 1.202$ is the Riemann zeta function. Above the freezing-out radius $R_{\rm sup}$ given in Eq. 3.9, radiative processes fail in ensuring complete thermalization and photons relax to a Wien distribution.

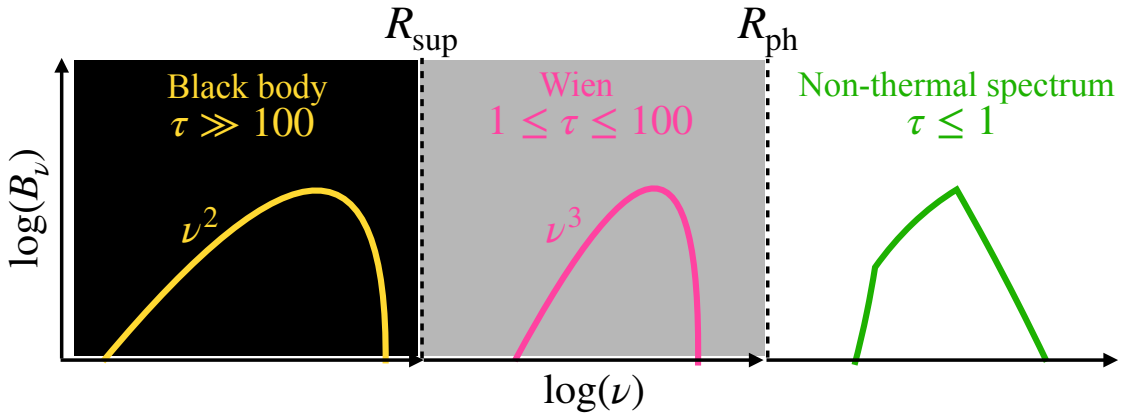

Figure 10: Schematic view of the three regions that can be broadly identified in astrophysical plasmas. In the black body region ($R < R_{\rm sup}$, left panel) radiative processes produce enough photons to ensure complete thermalization. In the Wien zone ($R_{\rm sup} < R < R_{\rm ph}$, middle panel), radiative processes can no longer sustain a black body distribution and photons relax to a Wien spectrum. Above the photosphere ($R > R_{\rm ph}$, right panel) non-thermal processes emerge in the observed spectrum.

The plasma becomes optically thin at the photospheric radius ($R_{\rm ph}$), where particle acceleration and non-thermal processes kick in and shape the observed spectrum. A schematic representation of the evolution of the spectrum (in logarithmic scale) is shown in Fig. 10. We stress that the spectral shaping process is considerably more intricate than the simplified framework outlined herein. Notably, non-thermal features may emerge in the photon distribution even below the plasma photosphere. However, for the purposes of this thesis, it is enough to distinguish between pure thermal spectra, Wien spectra, and non-thermal spectra.

3.4 LEPTONIC PROCESSES

3.4.1 *Synchrotron radiation*

Particles with charge Ze immersed in a pure magnetic field are accelerated along a curved orbit as effect of the Lorentz force, and they emit synchrotron radiation. A particle with mass m moving with velocity $\beta = v/c$ and forming a pitch angle θ' with the magnetic field $\mathbf{B}'$ will radiate a total synchrotron power $P'_{\rm synch}(\theta) = 2\sigma_T \beta^2 \gamma'^2 c U'_B \sin^2\theta'$. Here, σ_T is the Thomson cross section, $\gamma' = 1/\sqrt{1-\beta^2}$ is the particle Lorentz factor and $U'_B = B'^2/8\pi$ is the magnetic energy density. By averaging on an isotropic pitch-angle distribution we obtain

$$P'_{\rm sync}(\gamma') = \frac{4}{3}\sigma_T \left(\frac{m_e}{m}\right)^2 Z^4 \gamma'^2 c U'_B \,, \tag{3.10}$$

where m_e is the electron mass and we have assumed $\beta \simeq 1$ for relativistic particles. As the synchrotron power is $\propto (m_e/m)^2$, it is clear that synchrotron radiation from particles heavier than electrons is negligible in typical astrophysical environments.

Particles radiating synchrotron radiation cool on a timescale

$$t'_{\rm sync} = \frac{6\pi m^3 c}{\sigma_T m_e^2 Z^4 \gamma' B'^2} \,. \tag{3.11}$$

Therefore, after a time t' particles whose Lorentz factor is above

$$\gamma'_{\rm cool}(t) = \frac{6\pi m^3 c}{\sigma_T m_e^2 B'^2 t'} \tag{3.12}$$

have lost most of their energy through synchrotron losses, where we have assumed a population of particles accelerated to a power-law distribution. The Lorentz factor in Eq. 3.12 is dubbed *cooling Lorentz factor* and it is obtained by solving $t' = t'_{\rm synch}(\gamma'_{\rm cool})$

It is worth mentioning that in the presence of strong magnetic fields, the energy losses due to synchrotron radiation become particularly significant, causing the particle pitch angle to change rapidly.

3.4.1.1 *Synchrotron spectrum*

In the following we focus on electrons ($m = m_e$, $Z = 1$), however the listed results can be rescaled to the mass of other charged particles.

As mentioned in Sec. 3.1, both theory and PIC simulations predict a power-law distribution $N(\gamma'_e) \propto \gamma_e'^{-k_e}$ for accelerated electrons with $\gamma'_{e,\rm min} \leq \gamma'_e \leq \gamma'_{e,\rm max}$, where $\gamma'_{e,\rm min}$ and $\gamma'_{e,\rm max}$ are the minimum and the maximum Lorentz factors of the electron energy distribution, respectively. The synchrotron spectrum F'_ν emitted by such a population of electrons is characterized by the pitch angle averaged *critical frequency* $\nu'_{\rm crit} \simeq \gamma_e'^2 \nu'_L$, where $\nu'_L = eB'/2\pi m_e c$ is the Larmor frequency. It can be shown that the radiated synchrotron spectrum is

$$F'_\nu \propto \begin{cases} \nu'^{1/3} & \nu' < \nu'_{\rm min} \\ \nu'^{-(k_e-1)/2} & \nu'_{\rm min} < \nu' < \nu'_{\rm max} \\ \nu'^{1/2} e^{-\nu'/\nu'_{\rm max}} & \nu' > \nu'_{\rm max} \,, \end{cases} \tag{3.13}$$

where $\nu'_{\rm min} = \gamma'^2_{e,\rm min}\nu'_L$ and $\nu'_{\rm max} = \gamma'^2_{e,\rm max}\nu'_L$.

The treatment above does not take into account *synchrotron self-absorption* processes, namely the re-absorption of synchrotron photons by the electrons that produced them. The overall effect of synchrotron self-absorption is the introduction of an additional break in the photon spectrum at the self-absorption

frequency $\nu'_{\rm a}$. For $\nu'_{\rm min} \ll \nu' \ll \nu'_{\rm max}$ the synchrotron self-absorbed spectrum scales as $\nu'^{5/2}$, whereas for $\nu' \ll \nu'_{\rm min} \ll \nu'_{\rm max}$ the spectrum is $\propto \nu'^2$. The exact calculation of the self-absorption frequency requires detailed knowledge of the thermal electron distribution, and several methods can be employed to estimate it. We refer the readers to Ref. [107] for a detailed review.

3.4.2 *Inverse Compton scattering*

Compton scattering is the interaction of a photon with a free charged particle. The latter is at rest in the standard Compton scattering process, yet in astrophysical plasmas charged particles are often moving at relativistic speeds. When the energy of the charged particle exceeds the one of the incoming photon, a part of its energy can be transferred to the scattered photons. This process is called *inverse Compton scattering* (IC), and it can take place in two different regimes. If the photon energy in the particle rest frame is much smaller than the charged particle rest mass energy, the process occurs in the Thomson regime. In the opposite limit, the photon energy in the charged particle rest frame is much larger than the rest energy mass of the particle and the process takes place in the Klein-Nishina regime.

In the Thomson regime, it can be shown that the total energy loss rate is

$$P'_{\rm IC} = \frac{4}{3}\sigma_T \left(\frac{m_e}{m}\right)^2 Z^4 \gamma'^2 c U'_{\rm ph} \,, \tag{3.14}$$

where $U'_{\rm ph}$ is the energy density of the scattering photons. When relativistic charged particles are confined within a region where both radiation and magnetic field exist, they will undergo both IC and synchrotron losses. The ratio among the corresponding emitted powers $P'_{\rm sync}/P'_{\rm IC} = U'_B/U'_{\rm IC}$ determines which process dominates the cooling of the charged particle and it affects the shape of the emitted spectrum.

The cooling time due to IC losses is

$$t'_{\rm IC} = \frac{3m^3c^2}{4\sigma_T m_e^2 Z^4 \gamma' c U'_{\rm ph}} \,. \tag{3.15}$$

3.4.2.1 *Inverse Compton spectrum*

The IC spectrum depends on the details of the incident photon distribution and on the angle between the charged particle and the photon. However, it can be shown that a distribution of accelerated electrons

$N(\gamma'_e) \propto \gamma'^{-k_e}_e$ produces a photon spectrum $F'_\nu \propto \nu'^{-(k_e-1)/2}$, independently on the incident photon distribution.

In the Thomson regime, we can neglect the recoil of electrons and the process can be treated as a particle-particle scattering in the rest frame of the electron. If the latter is relativistic ($\gamma'_e \gg 1$) then the energy of the outgoing photon is $\epsilon'_{\gamma,\rm out} \simeq \gamma'^2_e \epsilon'_{\gamma,\rm in}$, being $\epsilon'_{\gamma,\rm in} = E'_{\gamma,\rm in}/m_e c^2$ the initial energy of the photon normalized to the electron mass energy.

In the Klein-Nishina regime, we should take into account both quantum effects and the recoil of the electron. However, for the purposes of this thesis, it is enough to mention that the overall effect is the suppression of the IC cross section. The energy of the outgoing photon is limited by energy conservation to values $\epsilon'_{\gamma,\rm out} \lesssim \gamma'_e$. As a result, in pure Klein-Nishina regime, the cooling rate of the charged particle is constant, rather than growing as $\propto \gamma'^2_e$ (Eq. 3.14).

3.4.3 *Synchrotron self-Compton*

The IC scattering of synchrotron photons on the same population of electrons that produced them is known as *synchrotron self-Compton* (SSC). The process is responsible for the double-hump feature in the νF_ν spectrum sometimes observed from astrophysical sources. The first peak is induced by synchrotron radiation, whereas the second peak is commonly linked to SSC processes. The latter may be particularly interesting for GRBs observed at very-high-energy, as shown in Fig. 11 for GRB 190829A. We will discuss this intriguing application of the SSC process in detail in Chapter 9.

To assess the relative importance of SSC losses in comparison to synchrotron losses, it is useful to introduce the Comptonization parameter

$$Y = \frac{U'_{\rm ph}}{U'_{\rm B}} \equiv \frac{U'_{\rm sync}}{U'_{\rm B}} \,. \tag{3.16}$$

If the SSC process dominates the overall cooling of electrons, namely if $Y > 1$, the cooling factor of the synchrotron spectrum defined in Eq. 3.12 is reduced by a factor $1 + Y$. In the opposite limit $Y < 1$, the cooling of electrons is mostly dominated by synchrotron processes and the cooling frequency in Eq.3.12 remains unchanged.

The synchrotron break frequencies $\nu'_{\gamma,j}$ translate into the breaks $\nu'^{\rm IC}_{\gamma,ij} = 2\gamma'^2_{e,i}\nu'_{\gamma,j}$ in the SSC spectrum, where the subscripts $i, j = a,\ \rm min,\ cool,\ max$ refer to the specific break. The exact shape of the radiated

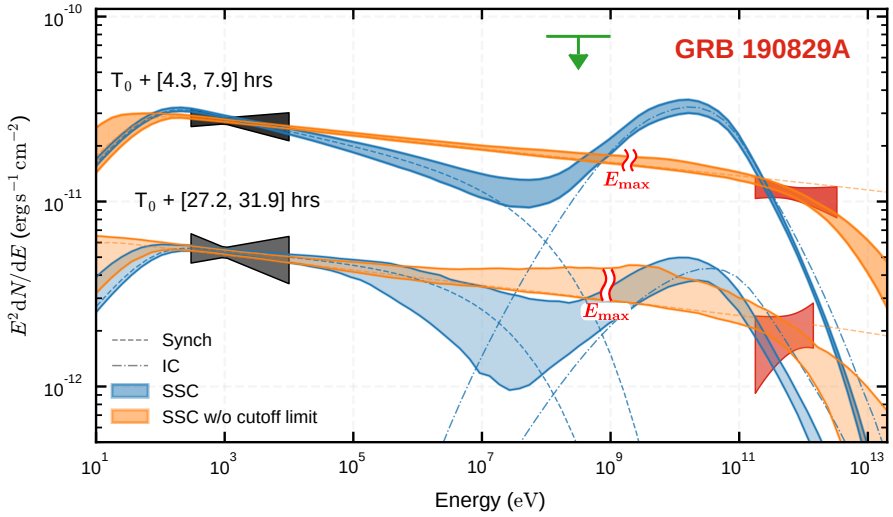

Figure 11: Theoretical multi-wavelength model for GRB 190829A. The first peak is associated to synchrotron radiation from a population of relativistic electrons, whereas the second peak may be explained through SSC radiation processes. Figure from Ref.[108].

spectrum depends on the relation between these break frequencies, see e.g. Refs. [109, 110] for a detailed discussion.

3.4.4 *Bremsstrahlung*

Bremsstrahlung, also known as free-free absorption process, is the interaction of an unbound electron with the Coulomb electric field of ionized atomic nuclei, resulting in the emission of photons. The electrostatic force decelerates the electron, inducing it to release part of its kinetic energy in the form of photons. As its radiation power is proportional to the plasma proton density ($P_{\rm brem} \propto n'_p$), bremsstrahlung becomes a relevant cooling mechanism for electrons in dense plasmas.

The most relevant case for the purposes of this thesis is *thermal bremsstrahlung*, occurring when particles have a thermal distribution of speeds. If the latter is isotropic, the probability dP that a particle has a speed in the range $[\mathrm{v}, \mathrm{v}+\mathrm{dv}]$ is

$$dP \propto \mathrm{v}^2 e^{-\frac{m_e \mathrm{v}^2}{2k_B T'_e}} \mathrm{dv}\,, \tag{3.17}$$

where T'_e is the electron temperature. It can be shown that the bremsstrahlung emission from a population of particles whose speed distribution follows Eq. 3.17 is

$$\frac{\mathrm{d}E'}{\mathrm{d}V'\mathrm{d}t'\mathrm{d}\nu'} = 6.8\times10^{-38} Z_i^2 n'_e n'_i T'^{-1/2}_e e^{-\frac{h\nu'}{k_B T'_e}} \bar{g}_{ff}\,, \tag{3.18}$$

where we are considering a plasma with electron number density n'_e and ions of charge Z_i with number density n'_i. The factor $\bar{g}_{ff}$ is the Gaunt factor, and is a function of the energy of the electron and the frequency of the emitted photon.

Bremsstrahlung photons can be absorbed by free electrons. This process is known as *free-free* absorption, whose effect is parametrized through the absorption coefficient of the plasma

$$\alpha_\nu^{\rm ff} = 3.7 \times 10^8 \frac{Z_i^2 n'_e n'_i}{T_e'^{1/2}} \frac{1 - e^{-h\nu'/k_B T'_e}}{\nu'^3} \bar{g}_{ff} \ . \tag{3.19}$$

The dependence on ν'^{-3} of the absorption coefficient implies that absorption is more relevant at low frequencies. In particular, the self-absorbed part of the bremsstrahlung spectrum ends when the plasma optical depth at frequency ν drops to unity, namely $\tau_\nu \simeq \alpha_\nu R' \approx 1$, where R' is the comoving size of the source. If $\tau_\nu > 1$ for all the frequencies, the medium is optically thick across all the wavebands and the bremsstrahlung spectrum is completely self-absorbed, reducing to the black body spectrum in Eq. 3.6.

3.4.5 *Photon-photon pair annihilation*

In non-thermal dense plasmas two photons of frequency ν'_1 and ν'_2 can annihilate into an electron-positron ($e^\pm$) pair, when the condition

$$h^2 \nu'_1 \nu'_2 (1 - \cos\theta') > 2(m_e c^2)^2 \ , \tag{3.20}$$

is fulfilled, where θ' is the angle between the colliding photons. The cross-section of the process peaks at $\approx 4 m_e^2 c^4$, and then it decays steeply. Consequently, this process is relevant close to its energy threshold.

Photon-photon pair annihilation constitutes the main absorption channel of high-energy photons in their source and on their way to Earth. We do not provide any further detail about this process, since the condition in Eq. 3.20 is the one we will use throughout this thesis.

3.5 HADRONIC PROCESSES

Protons are charged particles, therefore they also experience energy losses due to IC and synchrotron radiation on timescales obtained from Eqs. 3.11 and 3.15, respectively, properly accounting for the mass rescaling. However, protons emit significantly less luminosity through synchrotron and IC radiation compared to

electrons, due to their greater mass. This result holds in typical astrophysical environments, as long as the energy carried by protons is comparable to or smaller than the one carried by electrons. In the following, we discuss other relevant radiative processes for hadrons.

3.5.1 *Bethe-Heitler (photon-pair production)*

Bethe-Heitler (BH) pair production is the scattering of a photon with the virtual photon from the Coulomb field of a nucleus, resulting in the production of an electron-positron pair, that is the process

$$p\gamma \longrightarrow p + e^+ + e^- \,. \tag{3.21}$$

In the proton rest fame, the BH process can occur above the energy threshold $\gamma'_p E'_\gamma > m_e c^2$, where E'_γ is the photon energy and γ'_p is the proton Lorentz factor.

Protons undergo BH energy losses on a timescale

$$t'_{\rm BH} = \left[\frac{7 m_e \alpha \sigma_T c}{9\sqrt{2}\pi m_p \gamma'^2_p} \int_{\gamma'^{-1}_p}^{\frac{E'_{\gamma,\rm max}}{m_e c^2}} d\epsilon'_\gamma \frac{n'_\gamma(\epsilon'_\gamma)}{\epsilon'^2_\gamma} \times \left\{ (2\gamma'_p \epsilon'_\gamma)^{3/2} \left[\ln(\gamma'_p \epsilon'_\gamma) - \frac{2}{3} \right] + \frac{2^{5/2}}{3} \right\} \right]^{-1} \,, \tag{3.22}$$

where $\epsilon'_\gamma = E'_\gamma / m_e c^2$ and n'_γ is the comoving energy distribution of the photon field scattering on the nucleus.

3.5.2 *Photo-hadronic interactions*

Photo-hadronic ($p\gamma$) interactions are crucial in the context of high-energy astrophysics, as they are one of the channels for the production of secondary hadrons, mesons, gamma-rays and neutrinos. The simplest process reads

$$p + \gamma \longrightarrow p(n) + \pi^0(\pi^+) \,, \tag{3.23}$$

whose energy threshold is

$$E_{\rm th} = m_\pi + \frac{m_\pi^2}{2 m_{p(n)}} \,, \tag{3.24}$$

which is $E_{\rm th} \simeq 0.145$ GeV for π^0 production and $E_{\rm th} \simeq 0.150$ GeV for $\pi^\pm$ production.

Let us consider a photon with energy $E_r = \gamma'_p E'_\gamma (1 - \beta'_p \cos\theta')$ in the proton comoving frame, where β'_p is the velocity of the proton and θ' is the angle formed between the photon and the proton in the fluid comoving frame. Depending on the value of E_r, the interaction can take place through different channels:

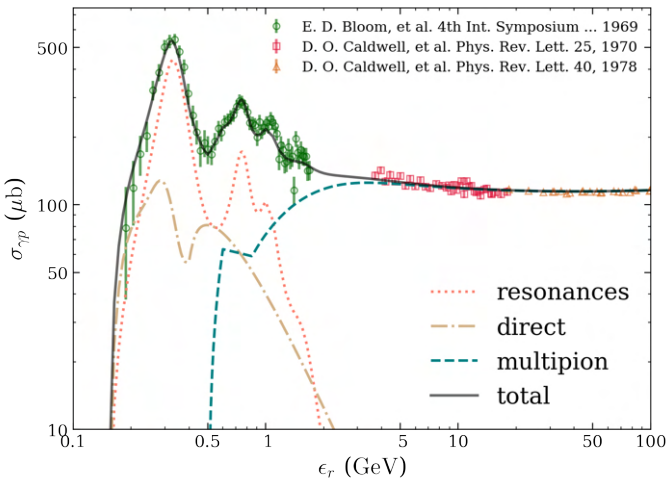

Figure 12: Cross section for $p\gamma$ interactions as a function of the photon energy measured in the comoving frame of the proton. Figure from Ref. [111].

- *Resonance production* of $\Delta^+(1232)$, that is:

$$p + \gamma \longrightarrow \Delta^+ \longrightarrow \begin{cases} n + \pi^+ & 1/3 \text{ of all cases} \\ p + \pi^0 & 2/3 \text{ of all cases} . \end{cases} \tag{3.25}$$

  This is the overall dominating channel for $p\gamma$ interactions, with the corresponding cross section peaking around $E_r \simeq 0.32$ GeV (see Fig. 12). Resonances more massive than Δ^+ also contribute.

- *Direct production* of the outgoing particles, namely $p + \gamma \longrightarrow n + \pi^+$. In this channel, the initial nucleon and γ exchange a meson instead of creating a virtual baryon resonance. For $E_{\rm th} \lesssim E_r \lesssim 0.25$ Gev direct production is the dominating channel, whereas it contributes to the $\sim 30\%$ of the total cross section up to $E_r \simeq 1$ GeV.

- *Multi-pion production*, which dominates the high-energy tail of the cross section ($E_r \gtrsim 1$ GeV). This channel leads to the production of two or more pions.

Protons cool through $p\gamma$ interactions on a timescale

$$t'_{p\gamma} = \left[\frac{c}{2\gamma'^2_p} \int_{E_{\rm th}}^{\infty} dE'_\gamma \frac{n'_\gamma(E'_\gamma)}{E'^2_\gamma} \int_{E_{\rm th}}^{2\gamma'_p E'_\gamma} dE_r E_r \sigma_{p\gamma}(E_r) K_{p\gamma}(E_r) \right]^{-1} , \tag{3.26}$$

where

$$K_{p\gamma}(E_r) = \begin{cases} 0.2 & E_{\rm th} < E_r < 1 \text{ GeV} \\ 0.6 & E_r > 1 \text{ GeV} \end{cases} \tag{3.27}$$

is the $p\gamma$ inelasticity and $\sigma_{p\gamma}$ is the cross-section [24].

3.5.3 *Hadronic interactions*

Hadronic (pp) interactions are of particular relevance in astrophysical environments with large matter densities. The interaction takes place when a high-energy proton (or nucleon) collides with a non-relativistic proton (or a nucleus made of A nucleons, being A the mass number of the nucleus). The simplest channel is the inelastic collision

$$p + p \longrightarrow N_\pi(\pi^+ + \pi^- + \pi^0) + X \tag{3.28}$$

where N_π is the pion multiplicity and X denotes any kind of secondary particle that can be produced during the interaction. The proton cooling time due to pp interactions reads

$$t'_p = (n'_p \sigma_{pp} c K_{pp})^{-1} , \tag{3.29}$$

where n'_p is the target proton density, σ_{pp} is the cross-section for pure hadronic interactions and $K_{pp} \simeq 0.5$ is the inelasticity of the interaction channel.

3.6 MAXIMUM ENERGY ACHIEVABLE BY ACCELERATED PROTONS

3.6.1 *The Hillas criterion*

A particle with charge Ze can be accelerated in a source with magnetic field B as long as it is confined within the source. Based on this underlying requirement, the Hillas criterion allows to estimate the maximum energy achievable by charged particles accelerated in astrophysical sources.

Let us consider a particle of charge e and energy E' immersed in an electric field $\boldsymbol{\mathcal{E}}'$. This particle is accelerated on a timescale $t'_{\rm acc} = E'/e\mathcal{E}'c$. In an almost perfectly conducting plasma moving with velocity $\mathbf{v}$ the electric field is linked to the magnetic field through $\boldsymbol{\mathcal{E}}' = -\mathbf{v} \times \mathbf{B}'/c$, implying $\mathcal{E}' \leq B'$. Therefore, the acceleration timescale of a proton can be simply related to its Larmor radius

$$t'_{\rm acc} \equiv t'_L = E'/ceB' \ . \tag{3.30}$$

According to the Hillas criterion, the particle Larmor radius r_L must not exceed the size of the source R, namely $r_L = E\beta_{\rm acc}/ZeB \leq R$ [12], where $\beta_{\rm acc} = v_{\rm acc}/c$ is the speed of the acceleration region. In light of

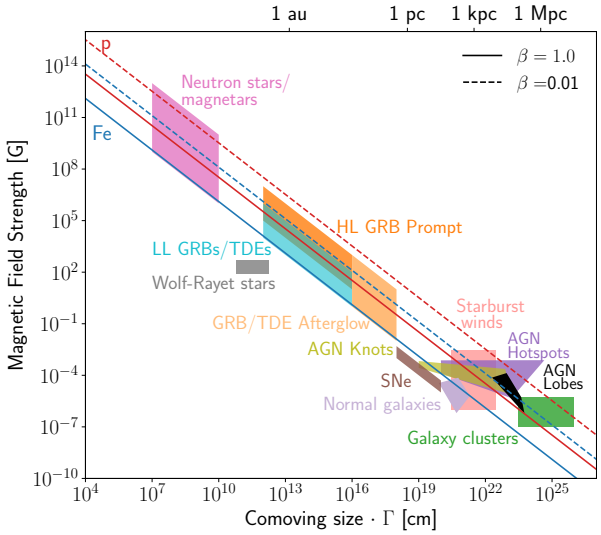

Figure 13: Hillas plot (from Ref. [12]), showing different astrophysical sources in the space spanned by their size $R'\Gamma$ and magnetic field strength B'. Above the red (blue) line, sources can accelerate protons (iron) above $E_{\rm max} \simeq 10^{20}$ eV.

this simple constraint, the maximum energy achievable by the charged particle is $E_{\rm max} \simeq \beta_{\rm acc} ZeBR$. For a relativistic source moving with Lorentz factor Γ the criterion reads $E_{\rm max} \simeq ZeB'R'\Gamma$, where B' and R' are the comoving magnetic field and comoving size of the source, respectively. The Hillas criterion is illustrated in Fig. 13 for various astrophysical sources.

3.6.2 *The interplay between acceleration and interacion*

The Hillas criterion provides a conservative upper limit on the maximum energy achievable by accelerated protons. However, it does not account for the effect of energy losses through the radiative processes described above. When interactions are taken into account, the maximum energy achievable by accelerated protons can be estimated by comparing their acceleration timescale with the total cooling timescale, that is

$$t'_{\rm acc} = t'_{\rm cool} \equiv \left(t'^{-1}_{\rm ad} + t'^{-1}_{\rm BH} + t'^{-1}_{\rm IC} + t'^{-1}_{\rm sync} + t'^{-1}_{p\gamma} + t'^{-1}_{pp} \right)^{-1} \tag{3.31}$$

where $t'_{\rm ad}$ is the adiabatic cooling time, related to the adiabatic expansion of the acceleration region, while $t'_{\rm BH}, t'_{\rm IC}, t'_{\rm sync}, t'_{p\gamma}, t'_{pp}$ are the BH, IC, synchrotron, $p\gamma$, and pp cooling times defined in Secs. 3.4 and 3.5.

4

HUNTING FOR HIGH-ENERGY NEUTRINO SOURCES

In this Chapter, we mostly focus on the main characters of this thesis: high-energy neutrinos. With energies between few TeV and few PeV, these particles have been detected in the form of a diffuse flux by the IceCube Neutrino Observatory [112]. Phenomenological considerations allow us to pinpoint candidate factories of high-energy neutrinos, yet their origin remains unknown. Intriguingly, similar diffuse fluxes of high-energy gamma-rays [113] and UHE cosmic-rays [114] are observed. If all the high-energy particles stem from the same source classes, their cosmic energy density should be linked. On the other hand, as outlined in Chapter 2, the number of high-energy neutrinos detected in spatial and temporal coincidence with specific point-like sources is increasing. Importantly, some of these sources are emerging classes of transients, whose number is expected to grow exponentially with the advent of new telescopes.

In the following, we discuss high-energy neutrino production in astrophysical sources, we outline possible sources of their diffuse flux and their connection with the diffuse fluxes of other high-energy messengers. Subsequently, we highlight a selected compilation of emerging transients within the array of potential sources of high-energy neutrinos.

4.1 PRODUCTION OF HIGH-ENERGY PARTICLES IN ASTROPHYSICAL SOURCES

In astrophysical sources, both $p\gamma$ and pp interactions (see Chapter 3) lead to the production of neutrinos and gamma-rays. Notably, neutral pions (π^0) and charged pions ($\pi^{\pm}$) are unstable and they decay through the channels $\pi^0 \longrightarrow 2\gamma$ and $\pi^+ \longrightarrow \mu^+ + \nu_\mu$, the latter followed by the muon decay: $\mu^+ \longrightarrow \bar{\nu}_\mu + \nu_e + e^+$. We conclude that both high-energy gamma-rays and high-energy neutrinos are produced when accelerated protons interact with radiation or non-relativistic proton targets within the source. Many existing models in the literature treat photo-hadronic and hadronic interactions both semi-analytically (see e.g., Ref. [115–117]) and numerically (see e.g., Ref. [57, 118, 119]). Even though a full numerical treatment is needed to account

for a precise description of the interaction processes, semi-analytical approximations lead to quite accurate estimates.

Basic properties of high-energy gamma-rays and high-energy neutrinos resulting from $p\gamma$ and pp interactions can be obtained through simple arguments, as detailed in the following.

- *High-energy gamma-rays*. Pions carry on average about $1/5$ of the energy of the parent proton E_p, that is $E_\pi \simeq 1/5 E_p$. In turn, each gamma-ray resulting from the π^0 decay is expected to receive half of the pion energy, implying $E_\gamma \simeq 1/2 E_\pi \simeq 1/10 E_p$. The latter does not necessarily correspond to the energy measured on Earth, since gamma-rays can undergo several interaction processes before being detected. They can be absorbed within their source if this is thick enough, and their flux can be further attenuated en route to Earth due to interactions with the CMB and the Extragalactic Background Light. As a result, we cannot receive PeV gamma-rays from sources located outside the Milky Way, whereas at TeV energies no photons can reach us from sources beyond a few hundred Mpc.

- *High-energy neutrinos*. Each neutrino receives on average $1/4$ of the energy of the parent pion, namely $E_\nu \simeq 1/4 E_\pi \simeq 1/20 E_p$. Note that this result holds as long as energy losses of secondary mesons are negligible. If this is the case, the neutrino plus antineutrino flavor ratio at the source is $(\nu_e : \nu_\mu : \nu_\tau) \simeq (1 : 2 : 0)$, whereas the observed signal is a composition $(\nu_\mu : \nu_e : \nu_\tau) \simeq (1 : 1 : 1)$ due to neutrino flavor oscillations en route to Earth.

If the cooling of secondary mesons is negligible, the neutrino and gamma-ray fluxes obey the simple relation:

$$\frac{1}{3} \sum_\alpha E^2_{\nu_\alpha} Q_{\nu_\alpha + \bar{\nu}_\alpha} \simeq \frac{K_\pi}{4} \left[E^2_\gamma Q_\gamma(E_\gamma) \right]_{E_\gamma = 2E_\nu} , \tag{4.1}$$

where Q is the production rate of the specific particle and $K_\pi = N_{\pi^+ + \pi^-}/N_{\pi^0}$ is the ratio of charged-to-neutral pions produced at the interactions.

Several caveats can alter the simplified framework outlined above. For instance, gamma-rays may be produced through different radiative processes which only involve leptons. Alternatively, $p\gamma$ and pp interactions may take place in opaque regions, effectively hiding the gamma-ray counterpart of the high-energy neutrino signal.

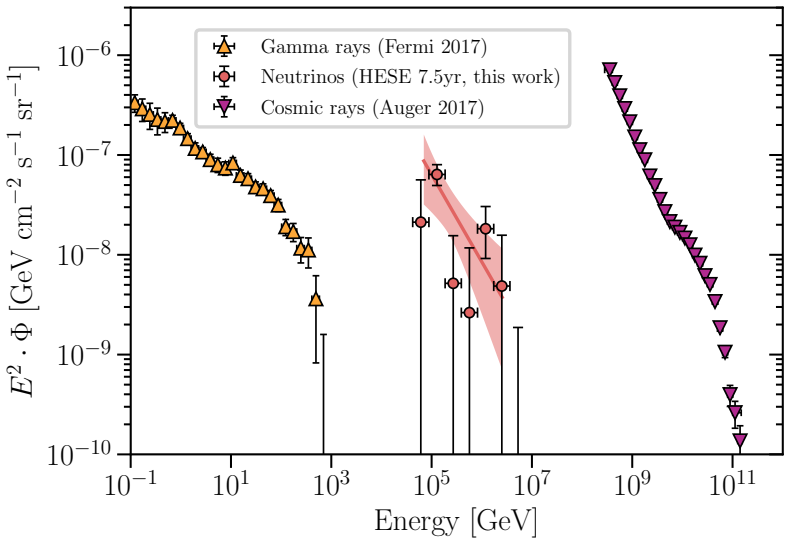

Figure 14: Isotropic fluxes of high-energy gamma-rays (data from *Fermi* [113]), high-energy neutrinos (data from IceCube [112]) and UHE cosmic rays (data from the Pierre Auger Observatory [114]). Figure from Ref. [112].

4.1.1 *Multi-messenger connection at high-energy*

As both neutrinos and gamma-rays are produced when accelerated protons interact with a radiation or matter target, it appears clear that there is a special connection between the high-energy messengers. As shown in Fig. 14, the differential energy fluxes measured by *Fermi* for high-energy gamma-rays [113], by IceCube for high-energy neutrinos [112] and by the Pierre Auger Observatory for UHE cosmic rays [114] are comparable. At first, the similarity in the energy budget of the three high-energy messengers prompted the hypothesis that they are produced by a common source [37].

In principle, TeV–PeV neutrinos should pinpoint the factories of UHE cosmic rays, however no clear smoking gun has been found yet [120]. Assuming that the observed diffuse flux of cosmic rays above 3×10^9 GeV and cosmic high-energy neutrinos are produced by the same source, Waxman and Bachall obtained the so-called *Waxman and Bachall bound*: $E^2\Phi_\nu < 6 \times 10^{-8}$ GeV cm $^{-2}$ s^{-1} sr^{-1}. The latter sets an upper limit on the neutrino flux from the sources of UHE cosmic rays [121].

Let us now turn to the link between high-energy neutrinos and gamma-rays. Intriguingly, the excess of neutrinos compared to the gamma-ray flux between 10 TeV and 100 TeV challenges the common origin hypothesis. Therefore, the current data cannot be interpreted by invoking the same composition of sources and the common origin hypothesis is ruled out.

One appealing way to address the issue involves the existence of *hidden sources*, namely sources that are opaque to gamma-rays but transparent to neutrinos [122]. This scenario can be realized in extremely dense environments, where gamma-rays are trapped whereas neutrinos can escape without hindrance. For instance, jets launched by collapsing massive stars and then choked within the stellar mantle have been considered among the most promising candidates. We will further inspect this conjecture in Chapter 7. Alternatively, the ejecta of core-collapse supernovae (SNe) interacting with the circumstellar medium could explain the high-energy neutrino diffuse flux without violating the *Fermi* data [123]. These transients would naturally produce the different high-energy neutrino and high-energy gamma-ray fluxes in the 10 – 100 TeV energy range, relaxing the constraint on opaque sources.

4.1.2 *Candidate sources of the diffuse flux of high-energy neutrinos*

The diffuse flux of neutrinos from extragalactic sources can be approximately expressed as [121]

$$\Phi_\nu \simeq \xi \frac{L_\nu n_s R_H}{4\pi} \,, \tag{4.2}$$

where the factor $\xi = 2 - 3$ for sources whose redshift evolution follows the star-formation rate, L_ν is the neutrino luminosity of the source, n_s is the source density and $R_H \simeq 400$ Mpc is the Hubble radius. The high-energy neutrino diffuse flux observed by IceCube is $\Phi_\nu^{\rm IceCube} \simeq 2.8 \times 10^{-8}$ GeV cm^{-2} s^{-1} sr^{-1}, which, compared with Eq. 4.2, leads to

$$n_s L_\nu \approx 10^{43} \frac{\rm erg}{\rm Mpc^3 yr} \,. \tag{4.3}$$

In the luminosity-density plane, this relation defines a line above which astrophysical sources need to sit to produce the diffuse flux detected at IceCube. An analogous relation can be established between the bolometric neutrino energy ε_ν and the local rate density $\dot{\rho}_s$ for transient sources. We recall that we call transients those astrophysical sources whose duration ranges from fractions of a second to a few months. The relation in Eq. 4.2 is shown in Fig. 15, together with some benchmark astrophysical sources. We note that high-energy neutrinos can be emitted by a plethora of sources, both steady and transient ones. In the following, we highlight specific transient sources shown in the right panel of Fig. 15, as these are relevant for the purposes of this thesis. We refer the reader to Refs. [32, 124, 125] for a detailed discussion on the potential steady sources of high-energy neutrinos.

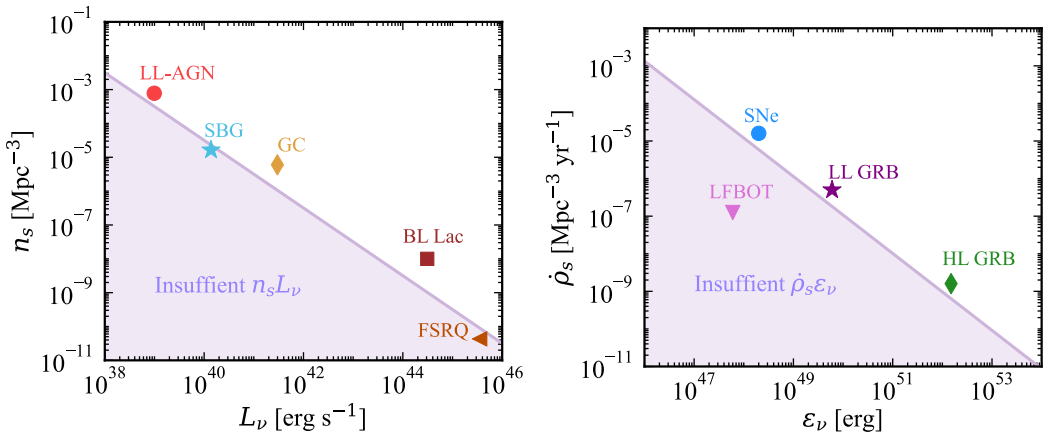

Figure 15: *Left panel*: Potential steady sources of high-energy neutrinos in the plane spanned by their neutrino luminosity L_ν and density n_s. Sources below the purple line do not have sufficient $n_s L_\nu$ to produce the high-energy diffuse flux detected at IceCube. We showcase some benchmark steady sources: low-luminosity AGN (LL-AGN), starburst galaxies (SBG), galaxy clusters (GC), BL Lacertae objects (BL-Lac) and flat-spectrum radio quasars (FSRQ). *Right panel*: Same as the left panel, but for selected benchmark transient sources: SNe, low-luminosity GRB (LL GRB), high-luminosity GRB (HL GRB) and LFBOTs. Figure adapted from Refs. [32, 124].

4.2 TRANSIENT PHENOMENA AS FACTORIES OF HIGH-ENERGY NEUTRINOS

Transient sources are energetic phenomena often characterized by bright and brief bursts of non-thermal particles, features that make them promising cosmic accelerators. The advent of time-domain astronomy unveiled the existence of a multitude of sources previously unknown, with some of them displaying puzzling features and evolving very quickly. Our knowledge of the transient sky is going to be further revolutionized as new high-cadence, wide-field surveys come online (see discussion in Chapter 5), leading to an exponential growth of the number of known transients.

With their intense bursts of energy release, transients may also be factories of high-energy neutrinos, which can be produced when accelerated protons undergo $p\gamma$ or pp interactions within the source. Besides being among the candidate sources of the high-energy neutrino diffuse flux detected at IceCube (right panel in Fig. 15), single transients are also ideal targets for neutrino searches, since their limited duration minimizes the atmospheric background within the observation time window. Furthermore, they can be localized in the sky with high precision through their multi-wavelength electromagnetic observations, facilitating follow-up multi-messenger searches in a given direction. Intriguingly, the possible link between transients and high-energy neutrinos is supported by the observation of a handful of IceCube events in spatial and temporal coincidence with point transient sources, including flaring blazars, tidal disruption events, SLSNe and LFBOTs (see discussion in Sec. 2). As new neutrino telescopes with improved sensitivity will come

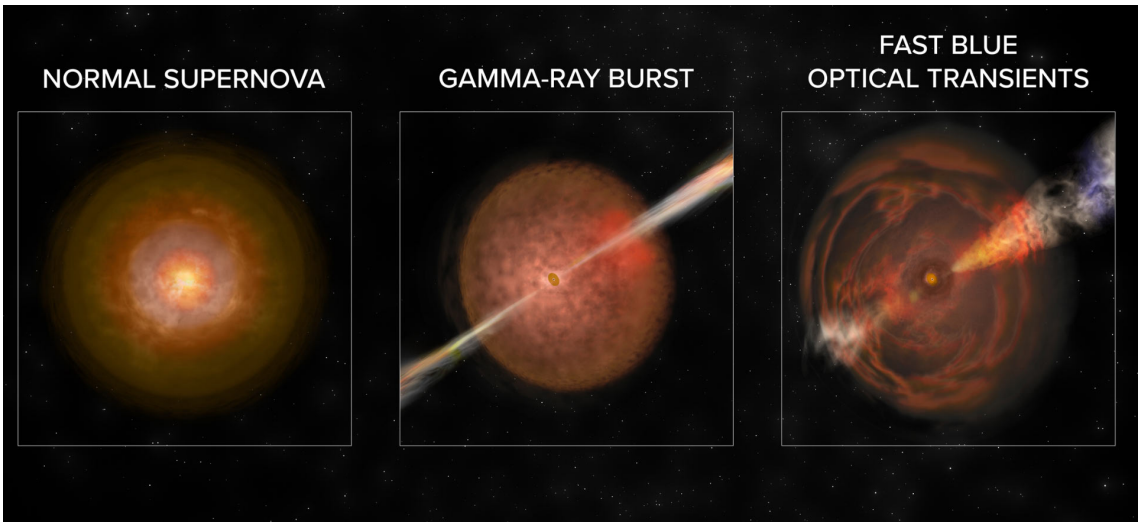

Figure 16: Transients considered throughout this thesis, possibly related to explosive massive stars. From left to right: core-collapse SNe, GRBs and LFBOTs. Image credit to Bill Saxton / NRAO / AUI / NSF.

online soon (see discussion in Chapter 5), we expect to observe a growing number of neutrino events in spatial and temporal coincidence with transients.

In preparation for the future of time-domain and high-energy neutrino astronomy, it is timely and crucial to investigate the production of high-energy neutrinos in transient phenomena. We provide a brief overview of the main properties and theoretical challenges of a selected compilation of astrophysical transients which we inspect throughout this thesis: SNe, GRBs and LFBOTs. However, we stress that many additional phenomena could potentially produce high-energy neutrinos. An artistic impression of these sources is depicted in Fig. 16.

- **Core-collapse SNe** are cataclysmic events marking the death of massive stars, and they are some of the oldest recorded transient events. Recently, we have also observed a subset of SN explosions with optical luminosities ten to hundred times larger than typical core-collapse SNe. These extraordinary explosions are known as superluminous SNe (SLSNe) [126]. The SN explosion mechanism has been extensively studied both analytically and numerically, see for instance Refs. [127, 128] for a review. Since our primary interest is the production of high-energy particles, we will not delve into the details of the explosion process, rather we focus on other relevant properties of these energetic phenomena.

  Both core-collapse SNe and SLSNe are broadly classified into two categories, depending on their spectra near maximum light: while Type II SNe show hydrogen lines in their spectra, Type I SNe do not. In all cases, the explosion leads to the ejection of matter which expands outward, cooling

adiabatically and emitting radiation. The light observed on Earth can be the intricate combination of a variety of physical processes that heat the ejecta, including radioactive decay of ^{56}Ni, hydrogen recombination and interaction of the outflow with the dense medium surrounding the progenitor star. Some subclasses of SNe and SLSNe might also harbor a central engine, namely a black hole or a rotating magnetar, a conjecture which would explain the extremely bright events occasionally observed [129]. In such cases, the ejecta is heated either through the fallback of matter onto the central black hole or through the spindown of the central magnetar.

SNe are factories of neutrinos, which can be copiously produced through different processes and across a wide range of energies (e.g., Ref. [130]). For the purposes of our thesis, we focus on the production of high-energy neutrinos, which can take place as protons are accelerated at the shock driven by the ejecta into the surrounding medium [65, 123, 131]. Alternatively, if the SN harbors a central magnetar hadron acceleration can take place in the wind surrounding the compact object [132]. Finally, we point out that some Type Ib/c SNe with broad line features in their spectra have been observationally associated with GRBs (that we discuss in the following), hinting that this class of SNe harbors relativistic jets. Yet it is not clear why only some of them produce long GRBs. While the angular momentum of the stellar core plays a crucial role in the successful launching of the jet, it may also be possible that a large fraction of these jets is not powerful enough to make it through the stellar mantle. High-energy neutrinos can be produced along the jet, both in the successful and choked scenario, as we will discuss in Chapter 7.

- **GRBs** are among the brightest transients ever observed, consisting of brief and intense bursts of radiation produced in relativistic collimated jets. The latter can be launched through the extraction of either gravitational or magnetic energy from a central compact object, which fuels the relativistic outflow for a limited time interval. Observations reveal the existence of a bimodal distribution in the burst durations, with bursts lasting less and more than 2 seconds classified as short and long GRBs, respectively. Short GRBs are usually associated with the merger of neutron stars, whereas long GRBs are believed to stem from the cataclysmic death of massive stars [133, 134]. In this thesis, our focus will be on the latter category.

  The prompt emission of GRBs consists in a non-thermal burst of X-rays/gamma-rays, usually well described by a smoothly-joining broken power-law known as *Band function*. A small fraction of bursts

also exhibits a thermal (or quasi-thermal) component, probably emerging from the photosphere of the relativistic jet. However, the mechanism responsible for the prompt emission remains puzzling, with several processes invoked to explain its origin [107, 135].

In this thesis, we are mostly concerned with the delayed emission following the burst and observed across all the wavebands, known as *afterglow*. The latter is broadly believed to result from the interaction of the jet with the surrounding environment [136–138]. The observed spectrum is consistent with synchrotron radiation emitted by a population of electrons accelerated at the shocks driven by the jet into the external medium. However, this standard picture cannot accommodate the rich set of additional features observed at late times in the afterglow lightcurve of some GRBs. For instance, a sudden rebrightening is sometimes observed in the optical lightcurve, possibly associated with a late activity of the central engine. This puzzling feature is called *optical jump*, and we will discuss it in Chapter 8. Our understanding of the afterglow emission has been further jeopardized by the observations of very high-energy photons ($\simeq O(\mathrm{TeV})$) at late times and deep in the afterglow of some GRBs. The very-high-energy component of the spectrum has been modeled by invoking either SSC radiation or proton synchrotron processes, yet its origin remains largely elusive, as we will discuss in Chapter 9.

GRBs have long been considered sources of UHE cosmic rays [139], and they are therefore promising factories of high-energy neutrinos. The latter can be produced both during the prompt phase, through photo-hadronic and hadronic interactions occurring inside the jet, and during the afterglow, when protons accelerated at the external shock driven by the jet in the surrounding medium interact with synchrotron photons produced by accelerated electrons. Yet no neutrino-GRB association has been reported to date, and upper limits on the expected neutrino signal from the prompt and afterglow phases have been set [140–142].

- **LFBOTs** are an emerging and puzzling class of transients, reaching optical peak luminosity $\gtrsim 10^{44}$ erg s^{-1} on timescales $\lesssim 3$ days [143–146]. To date, the landscape of FBOTs is populated by several candidates, but only six of them can be classified as luminous: CSS161010, AT2018cow, AT2018lug, AT2020xnd, AT2020mrf and AT2022tsd.

  Intriguingly, LFBOTs display properties that straddle SNe and GRBs. The detection of a highly variable X-ray signal suggests the presence of a central compact object [147, 148], similar to GRBs.

However, notably, LFBOTs do not display any gamma-ray counterpart. On the other hand, the radio signal associated with LFBOTs is consistent with self-absorbed synchrotron radiation produced through the interaction of an almost spherical outflow with the surrounding medium [147–152], remarking the case of radio SNe. The ejecta expand with mildly-relativistic velocities $0.1 \lesssim v \lesssim 0.6$ c, comparable to broad line SNe.

Many models have been invoked to accommodate all the observed features of LFBOTs. For instance, a jet may be harbored within a collapsing massive star that has not lost completely its hydrogen layer [153]. The jet may be either observed off-axis or choked within the extended hydrogen envelope, with stringent constraints existing on the jet properties in both cases. Alternatively, LFBOTs may arise from the merger between a Wolf-Rayet star and a black hole, following a common envelope phase. In this framework, the accretion disk surrounding the final black hole may launch a fast outflow in the polar direction [154]. Both scenarios successfully reproduce the observed optical radiation, but it is not clear yet whether they can explain the radio and X-ray signals. Furthermore, late UV and X-ray signals in the direction of AT2018cow have been reported at 2 and 3.7 years after its first detection, respectively. It is not yet understood which framework could better accommodate both the persistent UV and X-ray signals, as the latter was discovered after the two outlined models had been suggested. Intriguingly, the conjecture of a collapsing supergiant with the subsequent launching of a jet may be supported by the recent observations of the flaring LFBOT AT2022tsd [155]. However, the origin of LFBOTs remains largely elusive.

Independently on the nature of LFBOTs, high-energy neutrinos could be produced at the external shock developed at the interaction between the outflow and the surrounding medium. If these sources arise from collapsars, then an additional neutrino signal could be expected from the choked jet. We will discuss high-energy neutrino production in LFBOTs in detail in Chapter 10.

Fig. 17 compares the peak luminosities and durations of the transients detected by the Zwicky Transient Facility (ZTF), including SNe, SLSNe, afterglows and LFBOTs. The similarities in the observed properties of SNe, GRBs and LFBOTs hint at a common origin among these transients, possibly emerging from the aftermath of explosive massive stars which results in a variety of ejecta geometries and luminosities. However, this conjecture still awaits validation through additional observations and intense effort is needed to assess whether a *unified model* for explosive transients is possible. The aforementioned sources will be the

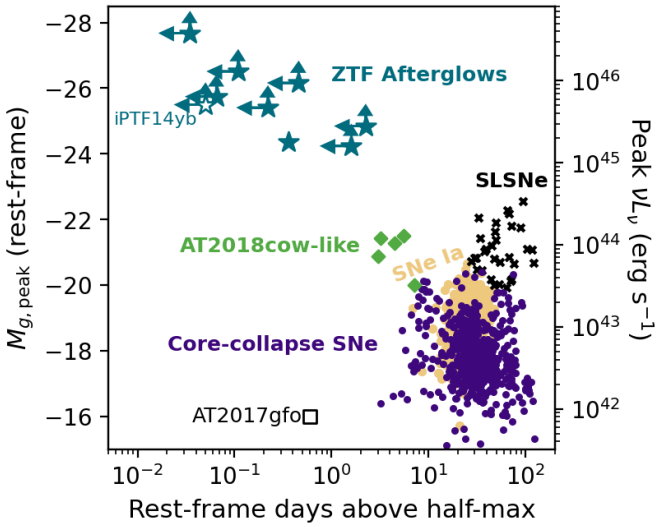

Figure 17: Duration and luminosity of fast evolving optical transients detected by ZTF. The similarity between SNe, SLSNe, GRBs and AT2018cow-like sources (LFBOTs) hint towards a common origin for these transients. Figure from Ref. [156].

protagonists of the following Chapters of this thesis, and we will delve into the details of each transient and their connection with high-energy neutrinos in Parts ii and iii.

5

CURRENT STATUS AND FUTURE PERSPECTIVES OF MULTI-MESSENGER DETECTORS

The remarkable milestones achieved in multi-messenger astronomy over the past decade have been possible thanks to the substantial progress in observational techniques. Upcoming instruments will lead to an exponential growth of the number of known transients and they will provide us with a deeper knowledge of the high-energy neutrino sky, shedding new light on the extreme Universe. In this Chapter, we highlight the telescopes we refer to throughout the thesis, both for electromagnetic radiation across different wavebands and for high-energy neutrinos. However, we stress that the detection landscape extends far beyond what is presented in this Chapter, which does not intend to provide an exhaustive overview.

5.1 ELECTROMAGNETIC TELESCOPES

Wide-field, high-cadence surveys are pivotal in the context of time-domain astronomy, as they enable us to catch swiftly transients evolving on short timescales. Among these surveys, the operating Zwicky Trantient Facility (ZTF) [157], the All-Sky Automated Survey for SuperNovae (ASAS-SN) [158], the Panoramic Survey Telescope and Rapid Response System (Pan-STARRS) [159] and the Young Supernova Experiment (YSE) [160] already pinpoint potential multi-messenger targets. They will keep providing us with unique insights on the transient Universe in the optical and near-infrared bands. The upcoming Vera C. Rubin Observatory [161] will guarantee an unprecedented coverage of the visible sky at regular intervals, generating astronomical catalogs that are thousands of times larger than any previously compiled over an operational period of ten years.

On the other hand, our knowledge of the hot transient sky will be soon revolutionized with the advent of the Ultraviolet Transient Astronomy Satellite (ULTRASAT) [15]. The latter will monitor a large patch of the sky in the near-ultraviolet, providing alerts to other telescopes within $\lesssim 15$ minutes and facilitating the serendipitous observations of transients across multiple wavelengths.

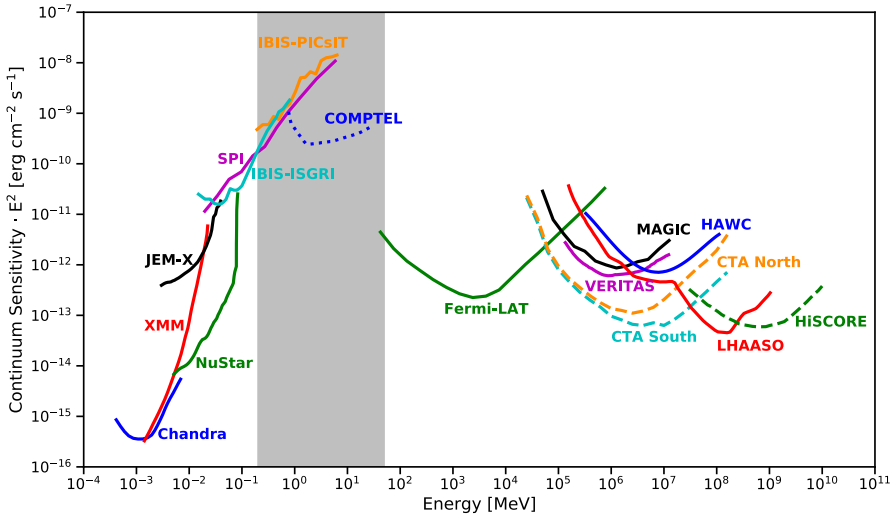

Figure 18: Sensitivity of X-ray and gamma-ray instruments. Currently operating telescopes are marked with continuous lines, whereas upcoming instruments are denoted with dashed lines. Figure from Ref. [172].

The radio and sub-millimeter bands are currently monitored by the Very Large Array Sky Survey (VLASS) [162]. However, VLASS only scans ≈ 80% of the Northern Hemisphere. A plethora of additional radio sources will be discovered through the coverage of the Southern Hemisphere with the upcoming Square Kilometer Array Observatory (SKA) [163]. The latter will have an unprecedented large field-of-view which, combined with its sensitivity, will be able to scan a large portion of the sky significantly faster than other radio telescopes.

As for the higher energy part of the electromagnetic spectrum, *Swift* [164] and the Gamma-Ray Burst Monitor onboard of the *Fermi* satellite (*Fermi*-GBM) [165] already provide us with key data in the X-ray band. Likewise, our access to the gamma-ray sky is possible with the Large Area Telescope (LAT) boarded on the *Fermi* satellite [166], together with ground-based Imaging Air Cherenkov Telescopes (IACTs). Currently operating IACTs include VERITAS [167], the High Energy Stereoscopic System (H.E.S.S.) [168], the Major Atmospheric Gamma Imaging Cherenkov (MAGIC) [169]. Our knowledge of the high-energy gamma-ray sky has already been transformed by the Large High Altitude Air Shower Observatory (LHAASO) [170], and it is poised to undergo a further expansion with the advent of the Cherenkov Telescope Array (CTA) [171]. The latter will consist of a combination of over 100 telescopes distributed both in the Northern and Southern hemispheres. Fig. 18 shows the sensitivity of current and upcoming telescopes in the X-ray and gamma-ray bands, providing insights into their comparative capabilities.

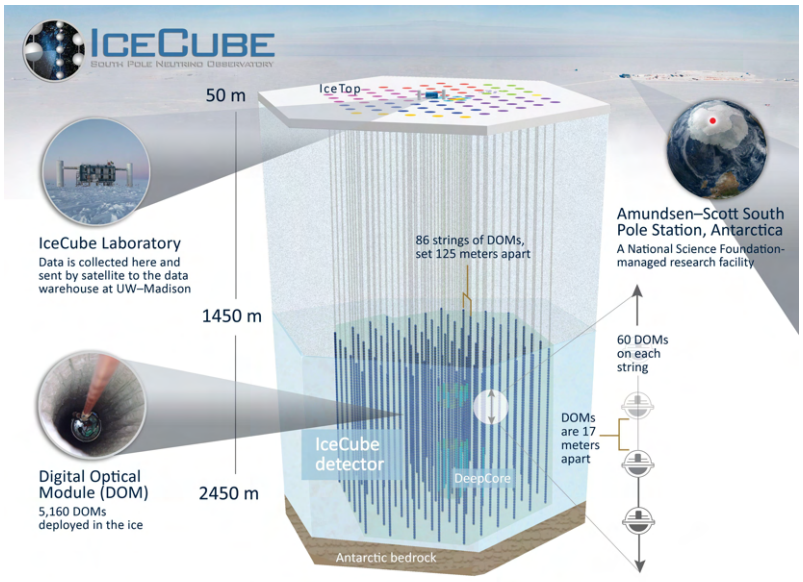

Figure 19: Schematic view of the IceCube Neutrino Observatory. Figure credit: IceCUbe/NSF.

5.2 HIGH-ENERGY NEUTRINO DETECTION

Detecting high-energy neutrinos is not an easy task, due to the elusive nature of these particles. The neutrino-nucleon cross section at high-energies is approximately $\sigma_{\nu N} \approx 10^{-35}\text{cm}^2\ (E_\nu/\text{GeV})^{0.36}$, while $N_N \approx 6\times10^{38}$ target nucleons are contained in 1 km^3 of water. This yields to $\sim$ 20 neutrino events at $\sim$ 100 TeV energies per year per km^3. Thus, it was understood quite soon that kilometer-scale detectors are needed to detect a few tens of neutrinos with energy above 100 TeV per year.

Neutrinos propagating in the detector medium undergo weak interactions and produce charged particles. Consequently, the widely used detection technique for high-energy neutrinos consists of catching the Cherenkov light produced by these secondary charged particles as they propagate in the detector. To date, the largest operating neutrino telescope is the cubic-kilometer IceCube Neutrino Observatory, made of Antarctic ice [13]. IceCube consists of 86 strings placed 125 apart and lying 1450 m below the ground. Each string carries 60 Digital Optical Modules, constituting the heart of the detector. The complementary in-fill array DeepCore extends the sensitivity of IceCube to energies from 10 GeV to 100 GeV [173]. A schematic view of IceCube is shown in Fig. 19.

With a volume $\simeq$ 8 times larger than IceCube, its upgrade IceCube-Gen2 will increase the number of detected events of a $O(10)$ factor [16]. An array of radio antennas is planned for IceCube-Gen2, which will detect neutrinos with energies $\gtrsim O(10)$ PeV. The design of IceCube-Gen2 radio is based on its

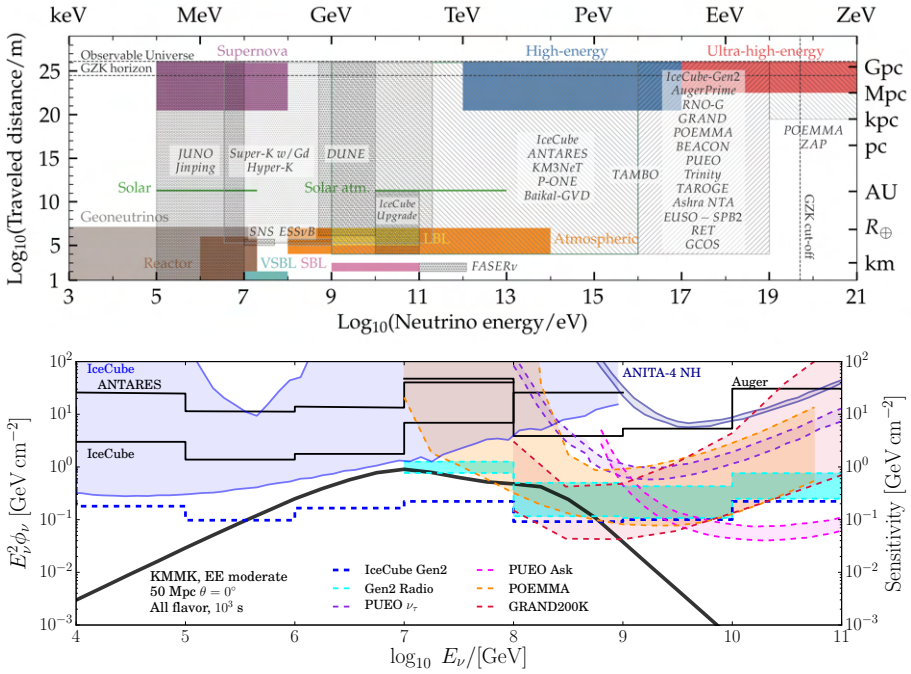

Figure 20: *Top panel*: Present and future telescopes aiming at detecting neutrinos from different sources and across a wide range of energies. *Bottom panel*: Sensitivity curves of different high-energy neutrino telescopes to transients lasting $\leq$ 1000 s. Figures from Ref. [183].

proof-of-concepts: the Antarctic Ross Ice-Shelf ANtenna Neutrino (ARIANNA) [174], the Askaryan Radio Array (ARA) [175] and the Radio Neutrino Observatory in Greenland (RNO-G) [176]. The aforementioned telescopes push their sensitivity to the UHE frontier ($\gtrsim 10^7$ GeV), together with the operating Antarctic Impulsive Transient Antenna (ANITA) [177], a balloon experiment expected to undergo several improvements in the next years. Other upcoming large-scale experiments aim at detecting UHE neutrinos are the Giant Radio Array for Neutrino Detection (GRAND)[17], the spacecraft Probe of Extreme Multi-Messenger Astrophysics (POEMMA)[18] and the Pacific Ocean Neutrino Experiment (P-ONE)[178].

Some detectors use the Cherenkov light produced as neutrinos cross the water rather than ice, such as KMK3NeT [179], built in the Mediterranean sea— of which ANTARES [180] can be considered the predecessor— and Baikal-GVD [181], placed in the lake Baikal in Russia. A next generation water Cherenkov detector operating in the MeV-GeV range will be Hyper-Kamiokande (Hyper-K), expected to be one order of magnitude larger than its predecessor Super-K [182], effectively increasing the statistics of expected events.

An overview of the currently operating and upcoming neutrino telescopes across different energy ranges is shown in the top panel of Fig. 20, whereas the bottom panel compares the sensitivity of different UHE neutrino telescopes to point transient sources lasting $\leq$ 1000 s.

5.2.1 *Spotlight on the IceCube Neutrino Observatory: events' morphology and detection techniques*

As of today, IceCube is the telescope with the highest sensitivity (to high-energy events) currently operating. Therefore, it is imperative to discuss in more detail its detection techniques and the morphology of the neutrino signals. Neutrinos crossing IceCube interact with the nuclei in the ice through deep inelastic scatterings. In charged current (CC) interactions a $W^{\pm}$ boson is exchanged, resulting in the creation of a charged lepton with the same flavor as the incoming neutrino. On the other hand, in neutral current interactions (NC) a neutral Z^0 boson is exchanged and the nucleus remains intact. The interaction process (CC or NC) and the outgoing lepton flavor determine the kind of signal detected at IceCube, as summarized in Fig. 21 and detailed in the following.

- *Muon neutrinos*: Before interacting or decaying, muons cross large paths in the ice and therefore produce a *track signal* of Cherenkov light. Tracks have excellent angular resolution and they can be used to reconstruct the direction of the incoming neutrino.

- *Electron neutrinos*: Contrarily to muons, electrons have a short length-scale and they interact many times within a volume completely confined within the detector. As a result, they produce a *cascade* of Cherenkov light whose energy resolution is high, making that kind of signals a powerful tool to reconstruct energy information.

- *Tau neutrinos*: The signal produced by tau neutrinos is particularly interesting: they produce a first cascade through CC interactions and a second one due to their decay into a lighter lepton. The result is a *double-bang* signal, which can be fully distinguished by a simple cascade only for the tau neutrinos with the highest energies[16].

As already mentioned, the detection of neutrinos of astrophysical origin is challenged below energies $\lesssim 100$ TeV, where the background is populated by atmospheric neutrinos produced when cosmic rays interact in the atmosphere [32]. However, the nature of the detected signal at IceCube can be disentangled through three different techniques. First, the Earth can shield atmospheric muons and one can select up-going track events only, a method known as *Through-Going Muon Track*. Alternatively, one can consider only neutrino interactions initiated within the detector— the so called *High-Energy Starting Events*— by using the outer region of IceCube as a veto system. Finally, since neutrinos of atmospheric origin are mostly muon neutrinos,

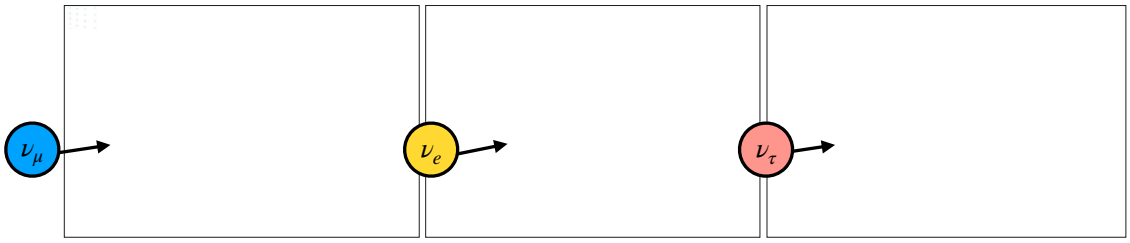

Figure 21: Morphology of the IceCube neutrino events, depending on the reaction channel of the incoming neutrino (NC or CC) and the flavor of the outgoing lepton. *Left panel*: A track signal from an incoming muon neutrino. *Center panel*: Cascade signal from an incoming electron neutrino. *Right panel*: Double-bang signal from an incoming tau neutrino. Figure from Ref. [16]

one can only look for cascade and double-bang events. For a more detailed discussion, we refer the reader to [184].

5.2.2 *Multi-messenger follow-up campaigns*

In order to capitalize on the power of multi-messenger astronomy, networks merging multiple instruments conduct real-time correlation searches and analyses of the signals across all the direct astronomical messengers: photons, neutrinos and gravitational waves. A simplified cartoon of a generic multi-messenger network of telescopes is shown in Fig.22. These networks effectively improve the collective sensitivity of different instruments, while also facilitating prompt follow-up searches of potential counterparts of the observed messenger. As mentioned in Chapter 2, the extensive multi-wavelength campaign following the observation of GW170817 enabled the detection of the whole electromagnetic spectrum of the short GRB associated with the gravitational wave events [41]. Follow-up searches of high-energy neutrinos were also carried out, however, no high-energy neutrino was detected in coincidence with the event [43]. Yet the serendipitous observation of a gravitational wave event alongside a short GRB underscores the pivotal role of telescope networks for multi-messenger follow-up searches of transients.

As our focus is on high-energy neutrinos and their connection with electromagnetic radiation, we mention some follow-up campaigns carried out for these two messengers:

- Target-of-opportunity searches for optical counterparts to the high-energy neutrinos detected at IceCube are carried out by ASAS-SN, ZTF and Pan-STARRS. In turn, IceCube looks for neutrinos in the direction of transients observed by optical surveys.

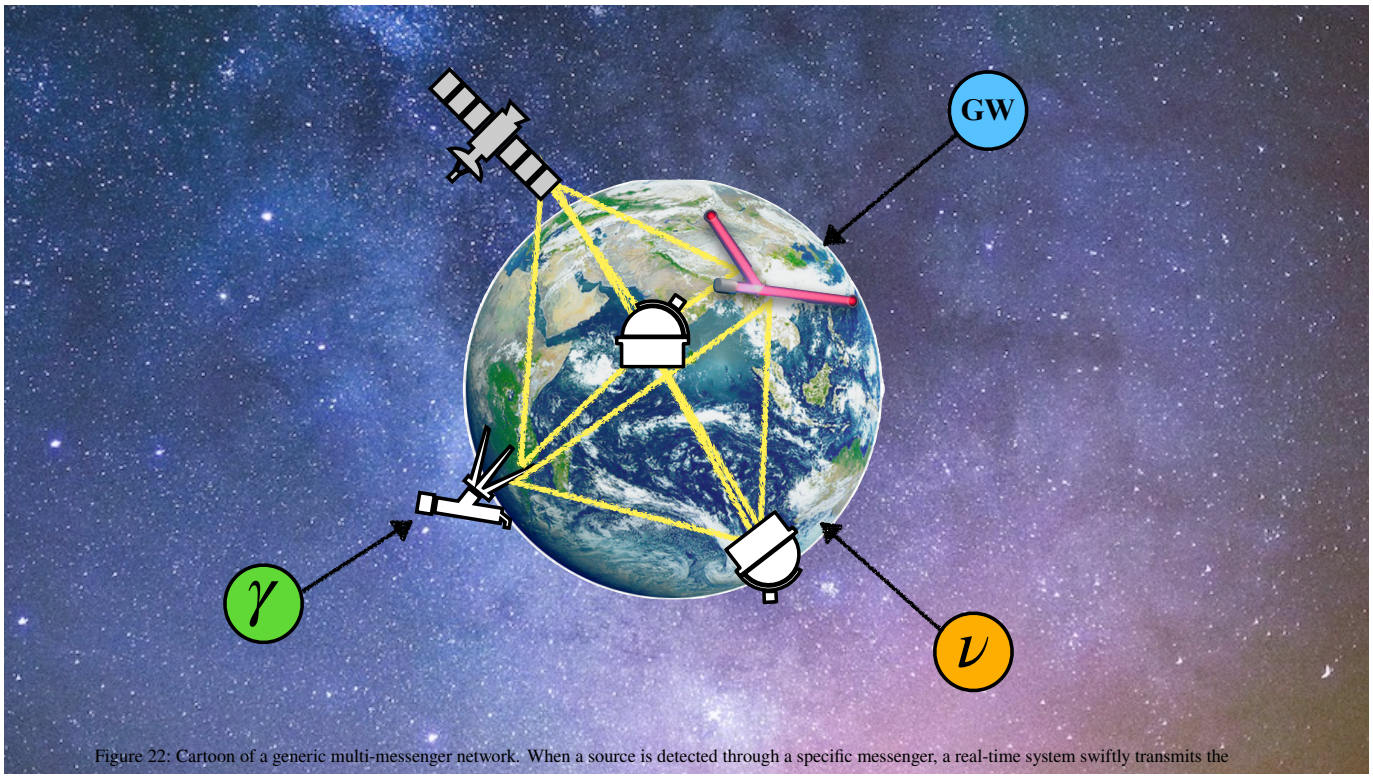

Figure 22: Cartoon of a generic multi-messenger network. When a source is detected through a specific messenger, a real-time system swiftly transmits the astronomical coordinates of the astrophysical source to other instruments.

- Due to the natural connection between high-energy neutrinos and high-energy gamma-rays, Fermi-LAT, the IACTs and IceCube look for high-energy gamma-rays in association with high-energy neutrino events.

6

INTERLUDE

The previous Chapters have offered an overview of the current status of multi-messenger astronomy. We now briefly outline the contents of this thesis and the way they contribute to addressing some open problems in the field. As our focus is on the connection between high-energy neutrinos and electromagnetic radiation from transients, we will not further discuss other messengers or astrophysical sources.

The exciting milestones in multi-messenger astronomy spur the development of increasingly advanced theoretical models, aimed at answering the pivotal questions raised by recent observations. The multitude of telescopes with improved sensitivity on the horizon introduced in Chapter 5 anticipates the discovery of an increasing number of transient phenomena, together with a surge in the number of high-energy neutrinos detected in coincidence with them. Therefore, it is timely and crucial to investigate the connection between the most enigmatic phenomena occurring in our Universe and the particles with the highest energy ever detected. *What can high-energy neutrinos teach us about the source? What are the most promising transients to target for high-energy neutrino searches?* In preparation for the bright future ahead of multi-messenger astronomy, in this thesis we tackle these questions. Our results highlight the potential of high-energy neutrinos as unique probes in astrophysics.

In Part ii we outline how neutrinos can shed light on GRBs. In Chapter 7 we explore optically thick regions of collapsar jets through high-energy neutrinos. Not only neutrinos can provide unique insight into the innermost regions of the outflow, but they can also be used to track the environments surrounding GRBs. We discuss this possibility in Chapter 8, where we inspect the unusual feature displayed by some GRB afterglows called optical jump. Likewise, in Chapter 9 we combine multi-wavelength data and high-energy neutrinos to investigate whether the environments of GRBs observed at very-high-energy at late time during their afterglows share common properties

In Part iii we combine multi-wavelength data and high-energy neutrinos to inspect the nature of emerging classes of high-energy transients. In Chapter 10, we prove that neutrinos may disentangle the process powering LFBOTs and exclude regions of the parameter space otherwise allowed by electromagnetic observations.

Finally, we note that although potential sources of high-energy neutrinos can be identified both theoretically and observationally, it is still poorly understood which electromagnetic waveband can be better correlated with neutrinos. This is an important problem in multi-messenger astrophysics, and its resolution would allow us to carry out informed follow-up observations of high-energy neutrino counterparts of astrophysical transients. We tackle this issue in Chapter 11.

Our findings not only advocate for intensified efforts to detect high-energy neutrinos stemming from transients, but also emphasize the need for more realistic modeling of particle acceleration and production in these sources, which can be achieved by relying on the outputs of advanced numerical simulations. This thesis offers insights into how neutrinos, combined with multi-wavelength data, can serve as guiding beacons in unraveling the nature of the most energetic and extraordinary phenomena occurring in our Universe.

Part II

MULTI-MESSENGER EMISSION FROM LONG GAMMA-RAY BURSTS

7

STATE-OF-THE-ART COLLAPSAR JET SIMULATIONS IMPLY UNDETECTABLE SUBPHOTOSPHERIC NEUTRINOS

Based on: **Ersilia Guarini**, Irene Tamborra, Ore Gottlieb, *State-of-the-art collapsar jet simulations imply undetectable subphotospheric neutrinos*, PRD 107 (2023) 2, 023001, arXiv:2210.03757

ABSTRACT Mounting evidence suggests that the launching of collapsar jets is magnetically driven. Recent general relativistic magneto-hydrodynamic simulations of collapsars reveal that the jet is continuously loaded with baryons, owing to strong mixing with the cocoon. This results in a high photosphere at $\gtrsim 10^{12}$ cm. Consequently, collisionless internal shocks below the photosphere are disfavored, and neutrino production in the deepest jet regions is prevented, in contrast to what has been assumed in the literature. We find that subphotospheric neutrino production could take place in the presence of collisionless sub-shocks or magnetic reconnection. Efficient particle acceleration is not possible in the cocoon, at the cocoon-counter cocoon shock interface, or at the shock driven by the cocoon in the event of a jet halted in an extended envelope. These subphotospheric neutrinos have energy $E_\nu \lesssim 10^5$ GeV for initial jet magnetizations $\sigma_0 = 15$–2000. More than one neutrino event is expected to be observed in Hyper-Kamiokande and IceCube DeepCore for bursts occurring at $z \lesssim O(0.1)$. Because of their energy, these neutrinos cannot contribute to the diffuse flux detected by the IceCube Neutrino Observatory. Our findings have implications on neutrino searches ranging from gamma-ray bursts to luminous fast blue optical transients.

7.1 INTRODUCTION

Relativistic jets are known to play a crucial role in a wide range of astrophysical transients, however many aspects of the jet physics remain poorly understood. For example, the mechanism powering short- and long-duration gamma-ray bursts (GRBs) is still puzzling [133, 134, 185], with hydrodynamic [186] or magnetized jets [187] being proposed. Relativistic jets have also been invoked to model the explosion of

some core-collapse supernovae as well as common envelope jet supernovae [188–190]. Intriguingly, also the emerging class of luminous fast blue optical transients (LFBOTs) may harbor relativistic jets, likely choked [153], as suggested by the asymmetry of the outflow responsible for the radiation observed in the ultraviolet, optical, infrared, radio, and X-ray bands [148, 152].

Independently on the source, the central engine of collapsar jets is expected to be a compact object (CO), which can either be a hyper-accreting black hole or a rapidly spinning magnetar [153, 154, 191–193]. The outflow is powered over a limited time interval, during which energy is extracted electromagnetically—by tapping into the rotational energy of the CO or the harbored magnetic field [187, 194]—or thermodynamically, through neutrino annihilation [195–197]. After its launch, the jet propagates through the stellar envelope and may break out or be choked, e.g. if it is too weak or the stellar envelope is too dense [198–200]. Independently of its fate, the jet inflates the cocoon, while piercing through the stellar mantle, and the cocoon inevitably breaks out from the stellar envelope [201–205].

Multi dimensional simulations of hydrodynamic jets contributed to shed light on the jet properties and evolution [206–213], though it is currently understood that, while energy deposition through neutrino annihilation can accelerate outflows with large Lorentz factors, if the baryon loading is low along the polar funnel, jet launching is more efficient if magnetically driven [214–216]. The first simulations of magnetized jets, e.g. Refs. [217–221], could not successfully follow the jet upon its breakout from the star, and the jet was artificially launched at the boundary of the simulation grid. More recently, Ref. [222] carried out the first 3D general relativistic magneto-hydrodynamic (GRMHD) simulation of a highly magnetized relativistic jet that breaks out from a star, expanding on the findings of Ref. [223] and illustrating the need for strong magnetic fields to allow for successful jet breakout with relativistic Lorentz factors.

Relativistic jets are deemed to be factories of ultra-high-energy cosmic rays and neutrinos up to $O(10^{10})$ GeV [36, 224–226]. Neutrinos could be produced in jets through photo-hadronic ($p\gamma$) [224, 225, 227] or hadronic (pp and pn) interactions (the latter are expected to be more efficient in the innermost regions of the outflow where the baryon density is large [228–230]), as pointed out through a number of analytical models [224, 231–242]. But before breakout, the jet is subject to strong mixing with the cocoon, which results in heavy baryon loading [222]; this reduces the Lorentz factor of the outflow and substantially increases its opaqueness, preventing the formation of collisionless shocks and potentially disfavoring neutrino production [222, 243–245]. In addition, the mixing between the highly magnetized jet with the weakly

magnetized stellar material leads to reduction of the jet magnetic energy, which also impacts neutrino production [231, 246].

Neutrinos with $\gtrsim O(10)$ TeV energy could be produced in optically thick regions of relativistic jets [234, 235, 237, 247–255]. Internal shocks occurring at large densities in the outflow, or in an extended envelope surrounding the star, have been deemed to lead to efficient neutrino production. Most of the aforementioned work relies on the criterion for the formation of collisionless shocks [247]; the latter is fulfilled by jets with low luminosity and reaching high Lorentz factors before undergoing collimation. However, such properties may not be common to all jet-powered transients, nor supported by numerical simulations of collapsar jets. Subphotospheric neutrino production has been explored in Ref. [236], in the context of short GRBs; it was found that the production of high energy neutrinos in the optically thick part of the outflow is highly suppressed, due to the large baryon density and magnetic field that limit the maximum energy up to which protons can be accelerated. Unsuccessful jets, dark in gamma-rays and producing neutrinos while still inside the stellar progenitor, have also been suggested as major contributors to the diffuse flux detected by the IceCube Neutrino Observatory [122, 235, 237, 256].

The non-thermal production of neutrinos could take place in the subphotospheric region through other poorly explored processes. Even though collisionless shocks are disfavored within the optically thick region of the outflow, collisionless sub-shocks may emerge in the outflow in the presence of mild magnetization [89]. Furthermore, Ref. [222] reveals that magnetic energy may be dissipated in the jet, while the latter is still embedded in the stellar envelope. Hence, magnetic reconnection may be another viable mechanism for particle acceleration in the optically thick regions [187, 257–260].

In this paper, for the first time, we carry out a realistic modeling of subphotospheric neutrino production by post-processing the outputs of the 3D GRMHD simulations presented in Ref. [222]. We find that neutrino production can occur in mildly-magnetized collisionless sub-shocks [89] and because of magnetic reconnection [187, 257, 258] in the innermost regions of the outflow. We also investigate possible neutrino production in the cocoon and at the interface between the cocoon and the counter-cocoon, showing that particle acceleration is hindered. To date, the simulations presented in Ref. [222] are among the most advanced ones of collapsar jets, yet affected by some limitations. A larger and more advanced simulation set would be needed to comprehensively assess subphotospheric neutrino production in collapsar jets.

Our work is organized as follows. In Sec. 7.2, we present our benchmark models of collapsar jets. In Sec. 7.3, we introduce the energy distributions of photons and protons produced at the acceleration sites, as well as neutrinos. In Sec. 7.4, we discuss viable acceleration mechanisms below the photosphere, namely sub-shocks and magnetic reconnection. In Sec. 7.5, we investigate subphotospheric production of neutrinos in the outer regions of the jet and show under which conditions the jet is halted in the stellar envelope or an extended outer envelope. The expected neutrino production from subphotospheric acceleration sites is summarized in Sec. 7.6, while the detection prospects are presented in Sec. 7.7. Finally, in Sec. 7.8 we draw conclusions on our findings. A discussion on the thermalization of the photon spectrum is reported in Appendix A.1, while Appendix A.2 summarizes the main proton and meson cooling times. Appendix A.3 explores possible acceleration sites linked to the cocoon, while we outline the production of neutrinos in successful jets in Appendix A.4 for reference.

7.2 JET MODEL

We rely on the 3D GRMHD simulations presented Ref. [222]. The simulations have been carried out through the code H-AMR [261] (we refer the interested reader to Refs. [222, 223] for details on the numerical implementation). The initial magnetic field configuration allows for a self-consistent jet launching and production of a long-lived jet, which breaks out from the stellar progenitor.

The CO powering the jet is a Kerr BH with mass $M_{\rm BH,0} = 4\ M_\odot$ and dimensionless spin $s_0 = 0.8$. The BH is embedded in a Wolf-Rayet star of mass $M_\star = 14\ M_\odot$, extended up to $R_\star = 4 \times 10^{10}$ cm. The initial magnetic field is uniform and vertical inside the magnetic core, which extends up to $\simeq 10^8$ cm; outside the core, the magnetic field profile decreases as $R^{-1.5}$, being R the distance from the CO. The simulation tracks the collapse of the stellar envelope onto the CO and subsequent formation of an accretion disk. A bipolar jet is launched a few milliseconds after the collapse, as shown from the snapshot in Fig. 23. The CO powering the jet exhibits an intrinsic variability on a timescale 10 ms $\lesssim t_v \lesssim$ 100 ms. The simulation runs for 18 s after the launching of the jet.

A jet with opening angle $\theta_j \simeq 0.1$ rad and time-varying luminosity $\tilde{L}_j$ forms. The jet is powered over the time interval $\tilde{t}_j$, so that the total energy the CO injects in it is $\tilde{E}_j = \int_0^{\tilde{t}_j} d\tilde{t} \tilde{L}_j(\tilde{t})$ [1]. The simulation reveals that

1 We adopt three different reference frames throughout this paper: the CO frame, the observer frame and the jet comoving frame. Quantities in each of these frames are denoted as: $\tilde{X}$, X, and X', respectively.

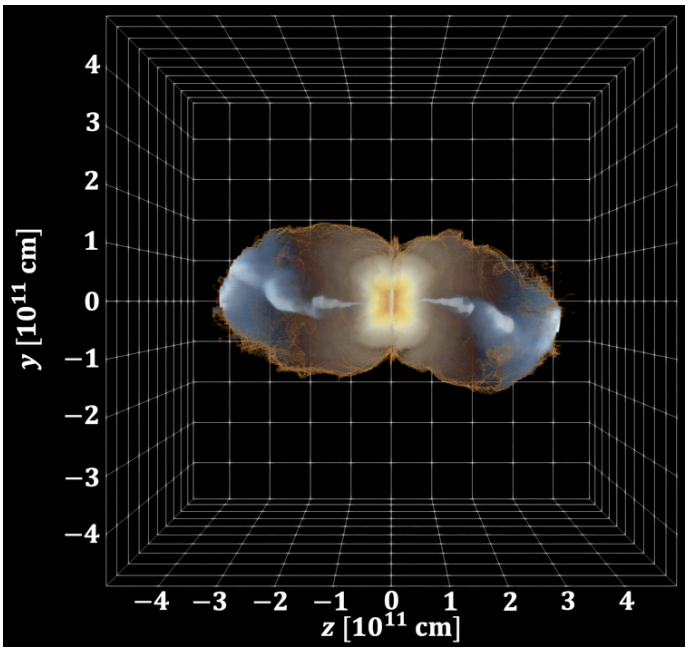

Figure 23: Isocontour of the matter density of the star (yellow) and the cocoon (white-brown) combined with the asymptotic proper velocity of the jet (grey/blue) for the simulation with $\sigma_0 = 15$ extracted when the jet head is at $R \simeq 10R_\star = 4 \times 10^{11}$. The jet is collimated by the cocoon, which breaks out from the star. A shock develops at the interface between the cocoon and the counter-cocoon (same colors as the cocoon, but on the opposite axis).

the disk-jet system develops misalignment relative to the CO axis. This results in the jet wobbling with an angle $\theta_w \simeq 0.2$ rad throughout its propagation. The effective opening angle of the jet is $\simeq \theta_j + \theta_w = 0.3$ rad. It is useful to define the total isotropic-equivalent luminosity of the jet $\tilde{L}_{\rm iso} = \tilde{L}_j / \left(\theta_j^2/2\right)$, since it is directly related to the observed quantities on Earth [134]. The post-breakout jet isotropic luminosity is $\tilde{L}_{\rm iso} \simeq 10^{54}$ erg $\rm s^{-1}$, although it might seem that this luminosity lies in the tail of the luminosity distribution of long duration GRBs [262], $\tilde{L}_{\rm iso}$ effectively observed would be smaller because of the jet wobbling and therefore within average or just above the peak of the luminosity distribution of long GRBs [262]; see Ref. [263] for a detailed discussion. Our benchmark simulation does not constrain the jet lifetime. Hence, we assume $t_j = 10$ s, which is representative of long GRBs [264]. Note that other sources of interest—such as LFBOTs or low luminosity GRBs—have typical luminosity smaller than the ones of long GRBs, see e.g. Refs. [147, 152, 265].

The magnetic field of the CO plays a crucial role in the launching of the jet. A fundamental quantity entering the dynamics of the outflow is its magnetization,

$$\sigma = \frac{B'^2}{4\pi\rho' c^2} \,, \tag{7.1}$$

where B' is the comoving magnetic field strength and ρ' is the comoving matter density in the jet. Simulations are performed for two initial magnetizations: $\sigma_0 = 15$ and $\sigma_0 = 200$. The initial magnetization of the jet

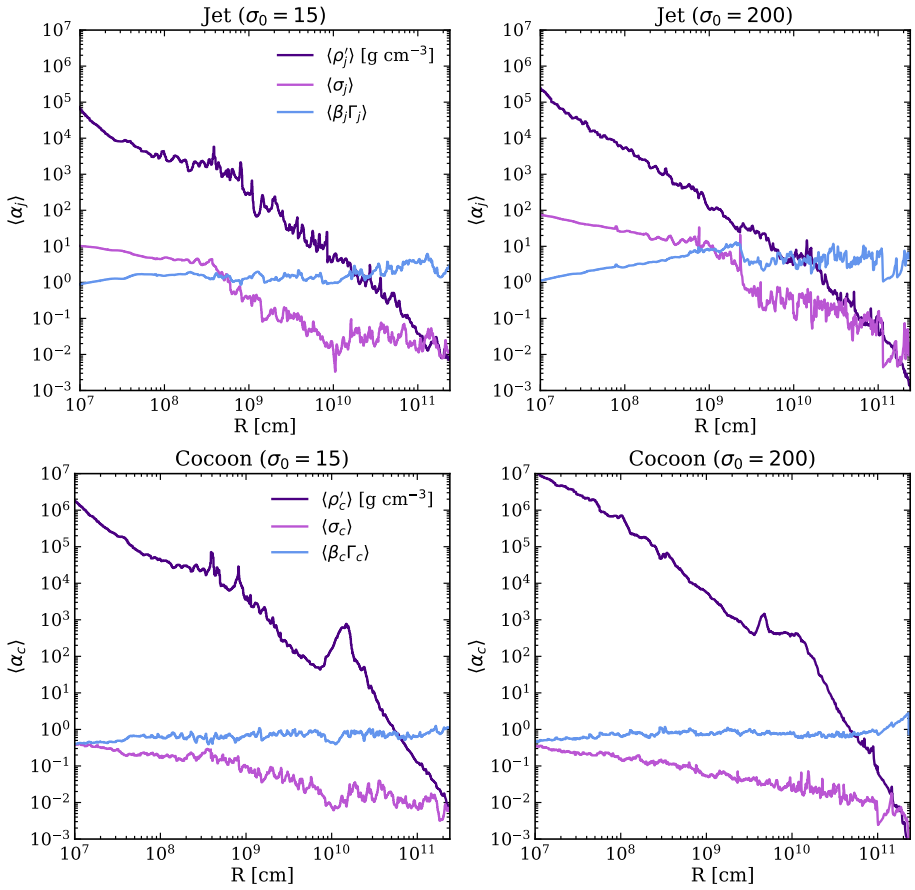

Figure 24: The top (bottom) panels show the radial profiles of the angle averaged proper velocity (blue line), magnetization (pink line) and matter density (purple line) in the jet (cocoon) for initial magnetization $\sigma_0 = 15$ (left panels) and $\sigma_0 = 200$ (right panels). These quantities have been extracted when the jet head is at $R \simeq 10 R_\star$ cm. The magnetization in the jet decreases, while its proper velocity increases as a function of the radius. This hints that magnetic energy is efficiently converted into kinetic energy of the jet up to $R \simeq 3 \times 10^8$ cm ($R \simeq 2 \times 10^9$ cm) for $\sigma_0 = 15$ ($\sigma_0 = 200$), where both the magnetization and the Lorentz factor start showing an erratic behavior. The cocoon has roughly constant magnetization and proper velocity $\langle\beta_c\Gamma_c\rangle \lesssim 1$ throughout the whole evolution.

corresponds to the maximum asymptotic velocity that each fluid element in the outflow can reach, if no mixing takes place.

Because the jet wobbles, it is convenient to describe the jet dynamics in terms of angle averaged quantities, namely the energy-flux weighted quantities. The top panels of Fig. 24 show the jet proper velocity $\langle\beta_j\Gamma_j\rangle$, magnetization $\langle\sigma_j\rangle$, and comoving matter density $\langle\rho'_j\rangle$, where the symbol $\langle ...\rangle$ denotes angle averaged quantities. Here, β_j and Γ_j are the dimensionless velocity and the Lorentz factor of the jet, respectively. The left (right) panel has been obtained for $\sigma_0 = 15$ ($\sigma_0 = 200$), and all quantities have been extracted when the jet head is at $R \simeq 10\ R_\star$. The magnetization of the jet $\langle\sigma_j\rangle$ decreases with the radius, a fraction of which is dissipated, while some is invested in accelerating the bulk motion, hence the increase in $\langle\beta_j\Gamma_j\rangle$. This hints towards efficient conversion of magnetic energy into kinetic energy, up to $R \simeq 3 \times 10^8$ cm ($R \simeq 2 \times 10^9$ cm)

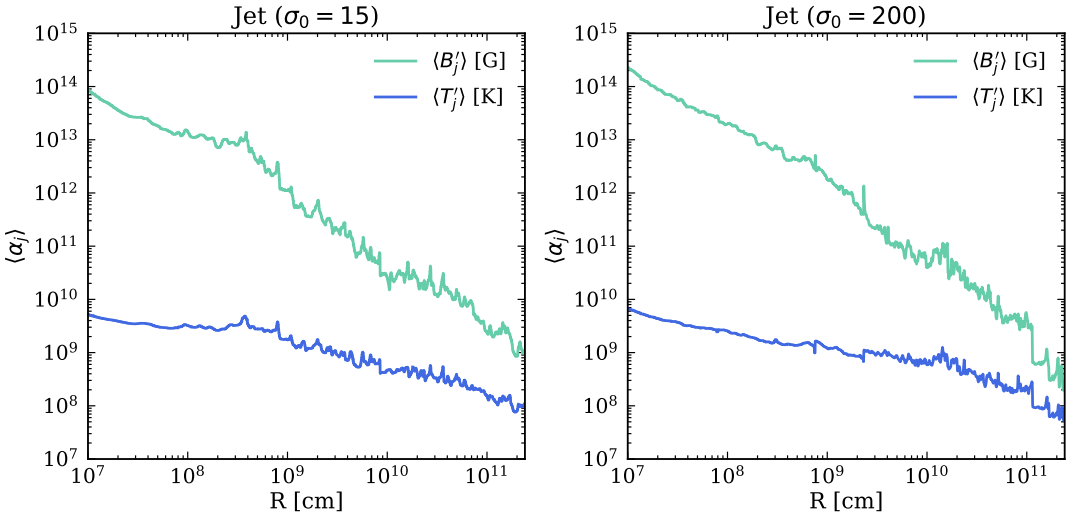

Figure 25: Angle averaged radial profile of the comoving temperature $\langle T'_j \rangle$ (blue line) and magnetic field magnitude $\langle B'_j \rangle$ (green line) for $\sigma_0 = 15$ (left panel) and $\sigma_0 = 200$ (right panel). These quantities have been extracted when the jet head is at $R \simeq 10 R_\star$.

for $\sigma_0 = 15$ ($\sigma_0 = 200$). At this distance from the CO, both $\langle \sigma_j \rangle$ and $\langle \beta_j \Gamma_j \rangle$ start showing an erratic behavior, induced by the entrainment of stellar material from the cocoon in the jet. In Fig. 25 we show the comoving angle averaged temperature $\langle T'_j \rangle$ and magnetic field $\langle B'_j \rangle$ along the jet, when the jet head reaches $R = 6 R_\star$, as in Fig. 24. The temperature and the magnetic field profiles are similar for both initial configurations with $\sigma_0 = 15$ and $\sigma_0 = 200$.

While it propagates through the star, the jet inflates a high pressure region, the cocoon, which plays a fundamental role in the collimation of the jet [201–205]. The cocoon, see also Fig. 23, is characterized by the average proper velocity $\langle \beta_c \Gamma_c \rangle$, magnetization $\langle \sigma_c \rangle$, and comoving matter density $\langle \rho'_c \rangle$, whose radial profiles are shown in the bottom panels of Fig. 24. The cocoon magnetization is $\langle \sigma_c \rangle \lesssim 0.1$ throughout its whole evolution. The cocoon propagates at non-relativistic to mildly relativistic velocities, with $\langle \beta_c \Gamma_c \rangle \lesssim 1$. The isocontour in Fig. 23 shows the existence of the counter-cocoon (white/brown region), which collides with the cocoon outside the star at the distance $R \simeq 2 R_\star$.

The jet-cocoon mixing observed in Fig. 24 plays a crucial role in the definition of the outflow optical depth, since it increases the jet baryon density and it reduces the jet Lorentz factor. Hence, we show a contour plot of the Thompson optical depth τ of the outflow in Fig. 26. The latter is highly optically thick throughout the simulation duration, while we find that the jet becomes optically thin ($\tau \simeq 1$) at the photospheric radius $R_{\rm PH} \gtrsim 10^{12}$ cm, independently on the initial magnetization of the jet (see Ref. [153] for a discussion). The role of jet-cocoon mixing has been overlooked in the literature; this led to underestimate the optical depth of relativistic outflows, with consequent optimistic conclusions on particle acceleration efficiency [247].

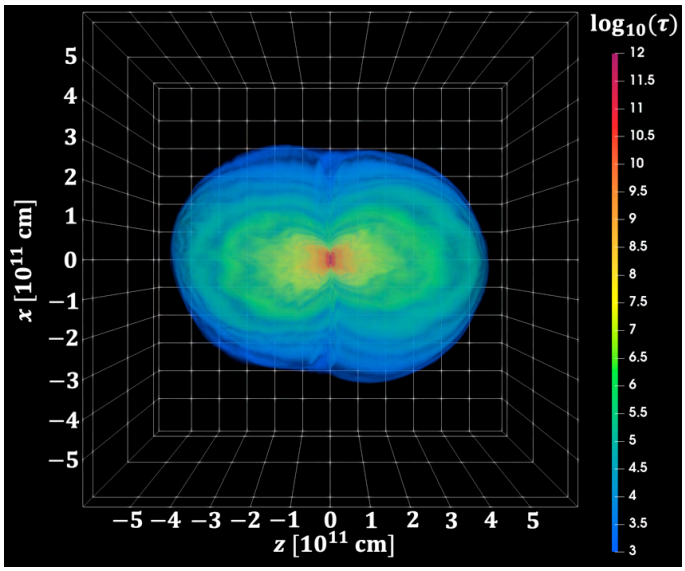

Figure 26: Isocontour of the outflow optical depth extracted when the jet head is at $R \simeq 10R_\star$. The jet is highly optically thick at all times, with $\tau \gtrsim 10^3$. From the simulation it can be extrapolated that the photosphere is located at $R_{\rm PH} \gtrsim 10^{12}$ cm, independently on the initial magnetization.

Lower baryon densities may be possible if the jet achieves Lorentz factors of $O(100)$ early on. In this scenario, optically thin regions may form deeply embedded in the star. However, state-of-the-art numerical simulations suggest that the jet is likely loaded with baryons as soon as collimation starts, both for low- and high-luminosity collapsar jets [212, 213, 243, 244]. Therefore, acceleration to ultra-relativistic Lorentz factors at small radii seems unlikely in collapsar jets. Further work is needed to shed light on possible exceptions.

7.3 ENERGY DISTRIBUTIONS OF PHOTONS, PROTONS, AND NEUTRINOS

The main goal of this paper is to investigate neutrino production below the photosphere in collapsar jets. We do so, by relying on the jet model outlined in Sec. 7.2. Neutrinos can be copiously produced through photo-hadronic ($p\gamma$) and hadronic (pp) interactions. The former take place when accelerated protons interact with a photon target, while the latter involve the collision of relativistic protons on proton targets in the outflow.

The process responsible for particle acceleration is still subject of active research. To date, the most commonly invoked mechanisms are diffusive shock acceleration [133, 134, 266, 267] and magnetic reconnection [268–270]. The outcome of both processes are non-thermal distributions of particles, which we introduce in this section.

7.3.1 *Photon energy distribution*

Both in diffusive shock acceleration and magnetic reconnection processes, accelerated electrons are expected to cool by emitting synchrotron radiation [259, 260, 271]. Since dissipation of energy occurs in a highly optically thick region (see Fig. 26), synchrotron photons quickly thermalize to a black-body distribution [259]. The timescale over which the synchrotron spectrum thermalizes is much faster than any other relevant timescale for photon interactions, see Appendix A.1. Hence, the photon energy distribution in the region of interest is given by [in units of $\mathrm{GeV}^{-1}\ \mathrm{cm}^{-3}$]:

$$n'_\gamma(E'_\gamma) = A'_\gamma \frac{E'^2_\gamma}{e^{E'_\gamma/k_B\langle T'_j\rangle} - 1}\ , \tag{7.2}$$

where k_B is the Boltzmann constant and $A'_\gamma = a\langle T'^4_j\rangle \left[\int_0^\infty dE'_\gamma E'_\gamma n'_\gamma(E'_\gamma)\right]^{-1}$, with a being the radiation constant. The radial profile of the comoving temperature $\langle T'_j\rangle$ is extracted from our benchmark jet simulations and it is shown in Fig. 25. The photon distribution in Eq. 7.2 is evaluated at each radius R where photons are produced.

Note that synchrotron photons might not be abundant enough to ensure complete thermalization. In this case, photons would resemble a Wien distribution rather than a black-body one [106, 272]. The photon spectrum may adjust to a Wien distribution also because of pair production, which maintains the photon bath at a comoving temperature $T'_W \simeq 50$ keV [211]. This result holds for hydrodynamic jets and it is yet to be proven for magnetized outflows [222]. However, since the optical depth in the region of interest is extremely large, as shown in Fig. 26, we assume that deviations from the black-body distribution (Eq. 7.2) are negligible in the region of interest. This approximation is also justified as we have tested that the neutrino distribution is not sensitive to differences between the black-body and Wien distributions (results not shown here; see also Sec. 7.3.3).

7.3.2 *Proton energy distribution*

The non-thermal proton energy distribution is [in units of $\mathrm{GeV}^{-1}\ \mathrm{cm}^{-3}$]:

$$n'_p(E'_p) = A'_p E'^{-k_p}_p \Theta\left(E'_p - E'_{p,\mathrm{min}}\right) \exp\left[-\left(E'_p/E'_{p,\mathrm{max}}\right)^{\alpha_p}\right]\ , \tag{7.3}$$

where k_p is the proton spectral index, $\alpha_p = 2$ takes care of the exponential cutoff [115], and Θ is the Heaviside function. $E'_{p,\rm min}$ is the minimum energy of accelerated protons and $E'_{p,\rm max}$ is the maximum energy at which protons can be accelerated. The latter is fixed by requiring that the proton acceleration rate $t'^{-1}_{p,\rm acc}$ is smaller than the total cooling rate $t'^{-1}_{p,\rm cool}$, with the proton cooling rates being outlined in Appendix A.2.

The normalization constant $A'_p = \varepsilon_p \varepsilon_d e'_k \left[\int_{E'_{p,\rm min}}^{E'_{p,\rm max}} dE'_p E'_p n'_p(E'_p)\right]^{-1}$, with ε_d being the dissipation efficiency and ε_p the fraction of the dissipated kinetic energy stored in accelerated protons. Finally, $e'_k = \langle \rho'_j \rangle c^2 (\langle \Gamma_j \rangle - 1)$ is the kinetic energy density of the outflow. The specific values for the parameters entering in Eq. 7.3 depend on the mechanism responsible for particle acceleration; we introduce their values in Sec. 7.4.

7.3.3 *Neutrino energy distribution*

Neutrinos can be produced through $p\gamma$ or pp interactions. In the following, we introduce these interaction channels and the resultant neutrino distributions.

7.3.3.1 *Neutrino production through $p\gamma$ interactions*

When accelerated protons interact with the photons thermalized in the jet, efficient $p\gamma$ interactions take place (see Appendix A.2). Hereafter, unless otherwise specified, we do not distinguish between neutrinos and antineutrinos and we refer to their sum $\nu_\alpha \equiv \nu_\alpha + \bar{\nu}_\alpha$, where $\alpha = e, \mu, \tau$ is the neutrino flavor. The main channels for $p\gamma$ interactions are

$$p + \gamma \rightarrow \Delta \rightarrow n + \pi^+, p + \pi^0 \tag{7.4}$$

$$p + \gamma \rightarrow K^+ + \Lambda/\Sigma\,. \tag{7.5}$$

Subsequently, neutral pions decay into gamma rays: $\pi^0 \rightarrow 2\gamma$. Neutrinos are produced through the charged pion (kaon) decay chain $\pi^+(K^+) \rightarrow \mu^+ + \nu_\mu$, followed by the muon decay $\mu^+ \rightarrow \bar{\nu}_\mu + \nu_e + e^+$, and $n \rightarrow p + e^- + \bar{\nu}_e$, and the related antiparticle decay channels.

In order to compute the neutrino distribution, we rely on the photo-hadronic model of Ref. [115]. For the given injected energy distribution of protons $n'_p(E'_p)$ and distribution of target photons $n'_\gamma(E'_\gamma)$, secondary mesons l (with $l = \pi^\pm, \pi^0, K^\pm$) are produced in the comoving frame at a rate [in units of GeV^{-1} cm^{-3} s^{-1}]:

$$Q'_l(E'_l) = c \int_{E'_l}^{\infty} \frac{dE'_p}{E'_p} n'(E'_p) \int_{E_{\rm th}/2\gamma'_p}^{\infty} dE'_\gamma n'_\gamma(E'_\gamma) R(x,y) \,, \tag{7.6}$$

where $x = E'_l/E'_p$ is the fraction of the proton energy which goes in the secondaries, $y = \gamma'_p E'_l$, and $R(x,y)$ takes into account the interaction physics. The photon and proton distributions are given by Eqs. 7.2 and 7.3.

Charged mesons l undergo energy losses, quantified by the cooling time $t'^{-1}_{l,\rm cool}$. Energy losses of secondaries are particularly important when the magnetic field and the baryon density are very large, as shown in Appendix A.2. The spectrum of mesons at decay is:

$$Q'^{\rm dec}_l(E'_l) = Q'_l(E'_l)\left[1 - \exp\left(-\frac{t'_{l,\rm cool} m_l}{E'_l \tau'_l}\right)\right] , \tag{7.7}$$

with τ'_l being the lifetime of the meson l. The comoving neutrino production rate from decayed mesons is [in units of GeV^{-1} cm^{-3} s^{-1}]:

$$Q'_{\nu_\alpha}(E'_\nu) = \int_{E'_\nu}^{\infty} \frac{dE'_l}{E'_l} Q'^{\rm dec}_l(E'_l) F_{l\to\nu_\alpha}\left(\frac{E'_\nu}{E'_l}\right) , \tag{7.8}$$

where α is the neutrino flavor at production and $F_{l\to\nu_\alpha}$ is provided in Ref. [273]. The cooling of secondaries affects the resulting neutrino spectral energy distribution [273]. In particular, when kaons cool before decaying they contribute significantly to the neutrino spectrum at high energies [238, 274–276].

7.3.3.2 *Neutrino production through pp interactions*

Because of the large proton densities in the innermost regions of the outflow, pp interactions copiously contribute to sub-photospheric neutrino production. Accelerated protons interact with the static proton target in the jet, producing charged and neutral pions in equal numbers.

At each radius along the jet, the proton number density is given by

$$n'_{p,j} = \frac{\langle \rho'_j \rangle}{2m_p} \,, \tag{7.9}$$

where we assume an equal amount of baryons and leptons in the jet. The radial profile of the angle averaged matter density $\langle \rho'_j \rangle$ is shown in Fig. 24.

As for the modeling of pp interactions, we rely on Ref. [116] and, in particular, focus on $E'_p < 0.1$ TeV. This is justified, since the contribution of pp interactions dominates over $p\gamma$ interactions for $E'_p \lesssim 10^2$ GeV, as shown in Appendix A.2.

The comoving pion production rate [in units of $\mathrm{GeV}^{-1}\ \mathrm{cm}^{-3}\ \mathrm{s}^{-1}$] is given by

$$Q'_\pi(E'_\pi) = \tilde{n}\frac{cn'_{p,j}}{K_\pi}\sigma_{pp}\left(m_p + \frac{E'_\pi}{K_\pi}\right)n'_p(E'_p)\ , \tag{7.10}$$

where $n'_{p,j}$ is defined in Eq. 7.9 and $n'_p(E'_p)$ is the energy distribution of accelerated protons in Eq. 7.3. The free parameters are assumed to be: $\tilde{n} \simeq 1$ and $K_\pi \simeq 0.17$; the former is a valid approximation [116], the latter is the pion multiplicity for $E'_p \leq 0.1$ TeV [277]. Finally, σ_{pp} is the energy-dependent cross-section for pp interactions, which is provided in Ref. [277].

Since secondaries are affected by strong energy losses in the optically thick region, the cooling of pions must be taken into account. The pion spectrum at decay can be approximated as in Eq. 7.7, using the initial rate in Eq. 7.10. The production rate of muon neutrinos from pion decay reads [in units of $\mathrm{GeV}^{-1}\ \mathrm{s}^{-1}\ \mathrm{cm}^{-3}$]:

$$Q'_{\pi\to\nu_\mu}(E'_\nu) = \int_{E'_{\rm min}}^{\infty}\frac{dE'_\pi}{\sqrt{E'^2_\pi - m^2_\pi c^4}}Q'^{\rm dec}_\pi(E'_\pi)f^{(1)}_{\nu_\mu}\left(\frac{E'_\nu}{E'_\pi}\right)\ , \tag{7.11}$$

where $E'_{\rm min} = E'_\nu + m^2_\pi/4E'_\nu$ is the minimum energy of pions and $f^{(1)}_{\nu_\mu}$ is a function given in Ref. [116].

As for muons from pion decay, the treatment in Ref. [116] does not include their cooling before decaying and producing neutrinos. We therefore follow Ref. [238] and assume that the cooling of muons results in an additional term in the neutrino spectrum approximated by $\left[1 - \exp\left(-t'_{\mu,\rm cool}m_\mu/E'_\mu\tau'_\mu\right)\right]$, with $E'_\nu \approx E'_\mu/3$ [2].

The neutrino production rate from muon decay is [in units of $\mathrm{GeV}^{-1}\ \mathrm{s}^{-1}\ \mathrm{cm}^{-3}$]:

$$Q'_{\mu\to\nu_\mu}(E'_\nu) = 2\left[1 - \exp\left(-\frac{t'_{\mu,\rm cool}m_\mu}{E'_\mu\tau'_\mu}\right)\right]\int_{E'_{\rm min}}^{\infty}\frac{dE'_\pi}{\sqrt{E'^2_\pi - m^2_\pi c^4}}Q'^{\rm dec}_\pi(E'_\pi)f^{(2)}_{\nu_\mu}\left(\frac{E'_\nu}{E'_\pi}\right)\ , \tag{7.12}$$

$$Q'_{\mu\to\nu_e}(E'_\nu) = 2\left[1 - \exp\left(-\frac{t'_{\mu,\rm cool}m_\mu}{E'_\mu\tau'_\mu}\right)\right]\int_{E'_{\rm min}}^{\infty}\frac{dE'_\pi}{\sqrt{E'^2_\pi - m^2_\pi c^4}}Q'^{\rm dec}_\pi(E'_\pi)f_{\nu_e}\left(\frac{E'_\nu}{E'_\pi}\right)\ , \tag{7.13}$$

where the functions $f^{(2)}_{\nu_\mu}$ and f_{ν_e} are given in Ref. [116]. The total production rates of muon and electron neutrinos are

$$Q'_{\nu_\mu}(E'_\nu) = Q'_{\pi\to\nu_\mu}(E'_\nu) + Q'_{\mu\to\nu_\mu}\ , \tag{7.14}$$

$$Q'_{\nu_e}(E'_\nu) \equiv Q'_{\mu\to\nu_e}\ . \tag{7.15}$$

2 Muons are produced by the cooled population of pions and then they undergo further energy losses. As a consequence, the spectrum of neutrinos from muon decay is highly suppressed compared to the one produced in the direct decay of pions. Hence, the approach adopted in Ref. [238] is a good approximation to our purposes, since we do not expect muons to contribute significantly to the neutrino signal, see also Sec. 7.6.

7.3.4 *Neutrino flux at Earth*

Neutrinos undergo flavor oscillation on their way to Earth [278, 279]. Hence, the resulting observed fluence for the flavor α is [in units of GeV^{-1} cm^{-2}]:

$$\Phi_{\nu_\alpha}(E_\nu, z) = V' t_j \frac{(1+z)^2}{4\pi d_L^2(z)} \sum_\beta P_{\nu_\beta \to \nu_\alpha}(E_\nu) Q'_{\nu_\beta}\left(\frac{E_\nu(1+z)}{\langle\Gamma_i\rangle}\right) ,$$

where z is the redshift of the source harboring the jet, $i = j, c$ depending on the neutrino production site (i.e. the jet or the cocoon), $Q'_{\nu_\beta}(E_\nu(1+z)/\langle\Gamma_i\rangle)$ is the comoving neutrino production rate for $p\gamma$ or pp interactions, given by Eq. 7.8 and Eqs. 7.14-7.15, respectively. The comoving volume of the interaction region is $V' \simeq 2\theta_i^2 \pi R_{\rm int}^3/(2\langle\Gamma_i\rangle)$ [280], where $R_{\rm int}$ is the distance from the CO where the interaction takes place. The outflow lifetime measured on Earth is $t_j = \tilde{t_j}(1+z)$. The neutrino oscillation probabilities, $P_{\nu_\beta \to \nu_\alpha} = P_{\bar{\nu}_\beta \to \bar{\nu}_\alpha}$, are given by [279]:

$$P_{\nu_e \to \nu_\mu} = P_{\nu_\mu \to \nu_e} = P_{\nu_e \to \nu_\tau} = \frac{1}{4}\sin^2 2\theta_{12} , \tag{7.16}$$

$$P_{\nu_\mu \to \nu_\mu} = P_{\nu_\mu \to \nu_\tau} = \frac{1}{8}(4 - \sin^2\theta_{12}) , \tag{7.17}$$

$$P_{\nu_e \to \nu_e} = 1 - \frac{1}{2}\sin^2 2\theta_{12} , \tag{7.18}$$

where $\theta_{12} \simeq 33.5°$ [277, 281].

In a standard flat ΛCDM cosmology, the luminosity distance is

$$d_L(z) = (1+z)\frac{c}{H_0}\int_0^z \frac{dz'}{\sqrt{\Omega_\Lambda + \Omega_M (1+z')^3}} , \tag{7.19}$$

where we adopt $H_0 = 67.4$ km s^{-1} Mpc^{-1}, $\Omega_M = 0.315$, and $\Omega_\Lambda = 0.685$ [277]. In the following, unless otherwise specified, we assume that the source harboring the collapsar jet is located at $z = 2$, namely at the peak of the redshift distribution of long GRBs [282].

7.4 INNER SUBPHOTOSPHERIC PARTICLE ACCELERATION SITES

As discussed in Sec. 7.3, efficient neutrino production occurs where particles can be accelerated efficiently. In this section, we outline two possible mechanisms for particle acceleration in the optically thick region of collapsar jets: magnetic reconnection and collisionless mildly magnetized sub-shocks emerging within radiation mediated shocks, and present the corresponding neutrino fluence. We stress that our results are

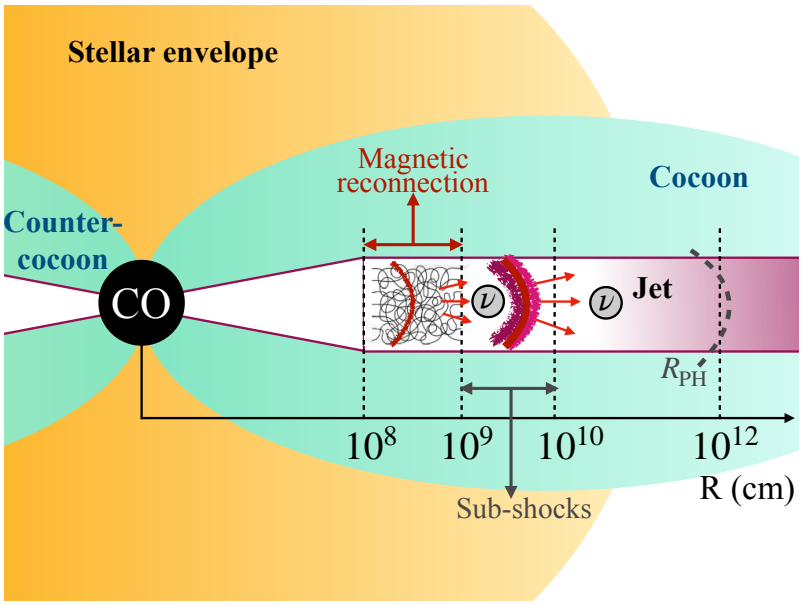

Figure 27: Sketch of the particle acceleration sites in the optically thick regions of the jet shown Fig. 23 (not in scale). The jet (white-purple) is launched by the CO (black) and it inflates the cocoon (aqua region) and the counter-cocoon while propagating in through the star (yellow); the photosphere radius is marked for orientation. Magnetic reconnection is efficient deep in the outflow ($R \simeq 10^8$–10^9 cm), where the magnetic energy is dissipated and converted into kinetic energy of the jet. At larger radii ($R \simeq 10^9$–10^{10} cm) particles can be accelerated at the collisionless sub-shocks where the outflow is mildly magnetized. Both magnetic reconnection and sub-shocks lead to neutrino production.

based on the physics of our benchmark jet model [222]. Nevertheless, ours is a first step towards a more realistic modeling of particle acceleration in collapsar jets. A schematic summary of the particle acceleration regions is displayed in Fig. 27. We rely on the angle averaged profiles shown in Figs. 24 and 25.

7.4.1 *Magnetic reconnection*

When the central engine hosts a highly variable magnetic field, particle acceleration can take place through magnetic reconnection [101, 283–285]. In the standard picture, magnetic energy is gradually dissipated along the jet, starting below the photosphere and extending over a wide range of radii [257, 258].

The central engine powering the outflow changes polarity on a length scale λ. When magnetic lines of inverse polarity reconnect, magnetic energy is dissipated. Half of the dissipated energy is converted into kinetic energy of the jet. The remaining half is believed to go into particle acceleration. Magnetic reconnection is no longer efficient when the magnetization of the outflow drops to $\sigma_j \simeq 1$, where the jet stops accelerating. For a review on the analytical modelling of magnetic reconnection see, e.g., Refs. [259, 260].

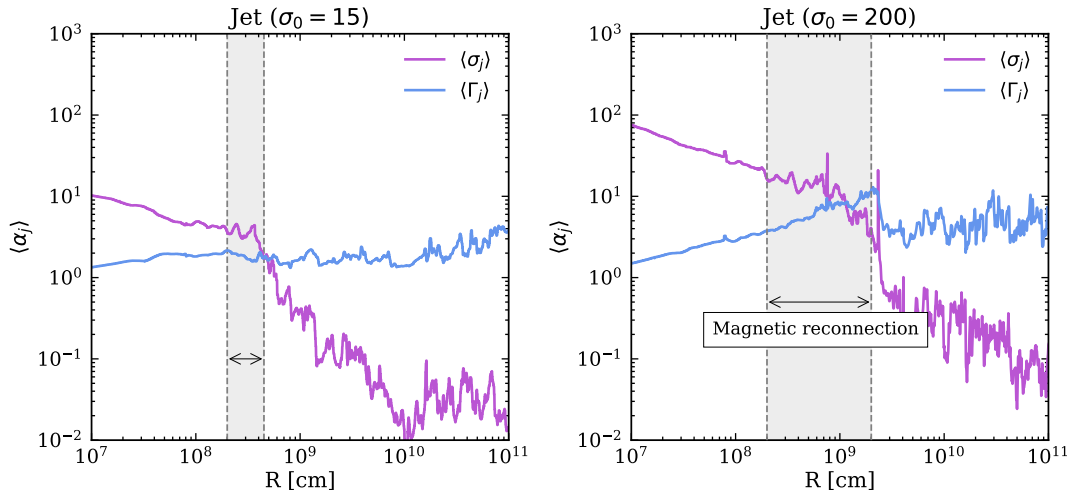

Figure 28: Radial profiles of the angle averaged magnetization $\langle\sigma_j\rangle$ and Lorentz factor $\langle\Gamma_j\rangle$ in the jet, for $\sigma_0 = 15$ (left panel) and $\sigma_0 = 200$ (right panel), same as the top panels of Fig. 24. Magnetic reconnection can efficiently occur from $R \equiv \lambda \simeq 2\times10^8$ cm (namely the length scale over which the magnetic field inverts polarity) through the radius such that $\langle\sigma_j\rangle \simeq 1$. This corresponds to the following radial ranges: $R \in [2\times10^8, 3.5\times10^8]$ cm for $\sigma_0 = 15$ (gray shaded region in the left panel) and $R \in [2\times10^8, 2\times10^9]$ cm for $\sigma_0 = 200$ (gray shaded region in the right panel). Magnetic reconnection is not efficient for the jet with $\sigma_0 = 15$.

Our two benchmark jet simulations show polarity inversion of the magnetic field lines over a typical length scale $\lambda \simeq 2\times10^8$ cm, both for $\sigma_0 = 15$ and $\sigma_0 = 200$. This length scale is in very good agreement with the one usually adopted in the literature (i.e. $\lambda \simeq 10^8$–10^9 cm) [259]. Magnetic energy is efficiently converted in kinetic energy along the outflow, as shown in Fig. 24 and discussed in Sec. 7.2.

The left panel of Fig. 28 shows the radial evolution of the jet Lorentz factor and the magnetization for $\sigma_0 = 15$. One can see that particle acceleration through magnetic reconnection can only occur over a very narrow radial range, since the jet magnetization drops to unity at $R \simeq 3.5\times10^8$ cm. We conclude that magnetic reconnection is therefore inefficient for $\sigma_0 = 15$. On the other hand, the right panel of Fig. 28 shows that the jet Lorentz factor increases up to $R \simeq 2\times10^9$ cm for $\sigma_0 = 200$, where its magnetization approaches $\langle\sigma_j\rangle \simeq 1$. This hints that magnetic energy is efficiently dissipated up to this radius, where $\langle\Gamma_j\rangle$ starts displaying an erratic behavior and the jet becomes mildly magnetized. Hence, magnetic reconnection can take place over the range $R \simeq 2\times10^8$–2×10^9 cm, outlined with a gray shaded band in Fig. 28. We warn the reader that the range of radii highlighted in Fig. 28 is sensitive to the initial magnetization of the jet: a larger σ_0 may stretch the region over which magnetic reconnection occurs, since the jet would reach $\langle\sigma_j\rangle \simeq 1$ at $R \gg 10^9$ cm. On the other hand, the erratic behavior of $\langle\Gamma_j\rangle$ could inhibit magnetic reconnection before the jet magnetization drops below unity.

When protons are accelerated through magnetic reconnection, the proton energy distribution (Eq. 7.3) depends on the outflow magnetization. The proton spectral index is parametrized as [99] [3]:

$$k_p \approx 1.9 + \frac{0.7}{\sqrt{\langle\sigma_j\rangle}} \,. \tag{7.20}$$

The fraction of dissipated energy stored in accelerated protons is [99]

$$\varepsilon_p = 1 - \frac{1}{4}\left(1 + \sqrt{\frac{\langle\sigma_j\rangle}{10 + \langle\sigma_j\rangle}}\right) \,, \tag{7.21}$$

where σ_j is shown in Fig. 28. Finally, following Ref. [231], we assume that protons are accelerated with a minimum energy

$$E'_{p,\rm min} = m_p c^2 \max\left[1, \langle\sigma_j\rangle \frac{\varepsilon_p}{2}\frac{k_p - 2}{k_p - 1}\right] \,. \tag{7.22}$$

7.4.2 *Neutrino fluence from magnetic reconnection*

Figure 29 shows the muon neutrino fluence originating from magnetic reconnection for our jet with $\sigma_0 = 200$ (no neutrino production due to magnetic reconnection occurs for $\sigma_0 = 15$). The neutrino distribution is determined by $p\gamma$ interactions for $E_\nu \gtrsim 50$ GeV and pp interactions for $E_\nu \lesssim 50$ GeV. The bump in the high-energy tail of the energy distribution comes from kaon decay, as expected due to the large magnetic fields and baryon densities along the jet, see Figs. 24 and 28.

The large density in the jet substantially limits the proton maximum energy, as discussed in Appendix A.2. Hence, the neutrino signal extends up to $E_\nu \simeq 3 \times 10^4$ GeV. We note that the proton spectral index in Eq. 7.20 becomes shallower as the radius increases, and the corresponding proton number density decreases, causing a quick drop in the neutrino flux as the energy increases.

3 We assume that the proton and the electron spectral indexes are the same: $k_p = k_e$. This result is motivated by particle-in-cell simulations of magnetic reconnection with $\sigma \gg 1$ [102], albeit it has yet to be proven for $\sigma \approx 1$ [101]

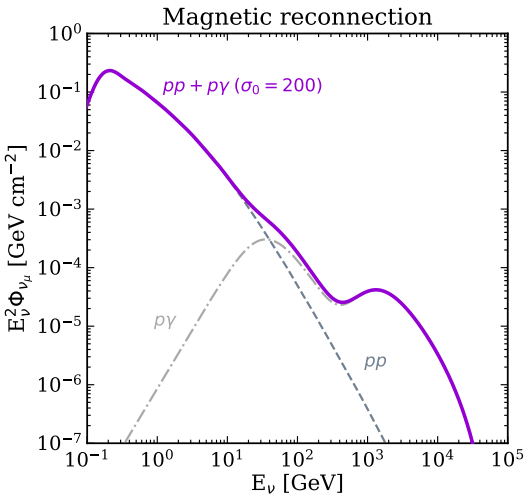

Figure 29: Muon neutrino fluence on Earth for a collapsar jet at $z = 2$ resulting from magnetic reconnection for our benchmark jet with $\sigma_0 = 200$. The spectral shape is determined by pp interactions (dark gray dashed line) below $E_\nu \simeq 50$ GeV, and $p\gamma$ interactions (light gray dot-dashed line) for $E_\nu \gtrsim 50$ GeV. The bump at $\simeq 5 \times 10^3$ GeV is due to kaon decay, the spectrum has a cutoff at $E_\nu \simeq 3 \times 10^4$ GeV. Magnetic reconnection is not efficient for the jet with $\sigma_0 = 15$ and therefore no neutrinos are produced.

7.4.3 *Internal sub-shocks*

As mentioned in Sec. 7.2, the central engine powering the relativistic outflow exhibits intermittency on time scales 10 ms $\lesssim t_v \lesssim$ 100 ms. It follows that the jet is not homogeneous, but it is made up of several shells of plasma moving with different velocities. These shells can collide at the internal shock radius [286]:

$$R_{\rm IS} = \frac{2\langle\Gamma_j\rangle^2 t_v c}{1+z} \,. \tag{7.23}$$

Internal shocks can efficiently accelerate particles only if they are collisionless, namely when they are mediated by collective plasma instabilities, rather than collisions [287]. Collisionless shocks can form within regions of the outflow that are optically thin (i.e. where the Thompson optical depth is $\tau \lesssim 1$). Figure 26 shows that the outflow is highly optically thick for $R \lesssim 4 \times 10^{11}$ cm. Hence, even though the CO variability allows for the formation of internal shocks at $R_{\rm IS} \lesssim R_\star$, it is unlikely that these shocks are collisionless.

If the jet is mildly magnetized ($\langle\sigma_j\rangle \gtrsim 10^{-1}$), however, Ref. [89] showed that collisionless sub-shocks may form within radiation mediated shocks when the following condition is fulfilled:

$$\chi \equiv \frac{p'_{\rm th}}{p'_{\rm mag}} \lesssim 2 \,. \tag{7.24}$$

In Eq. 7.24, $p'_{\rm mag} = \langle B'^2_j\rangle/8\pi$ is the comoving magnetic pressure, with $\langle B'_j\rangle$ being the comoving magnetic field shown in Fig. 25; $p'_{\rm th} = (\hat{\gamma} - 1)e'_{\rm th}$ is the thermal pressure, related to the comoving internal energy of

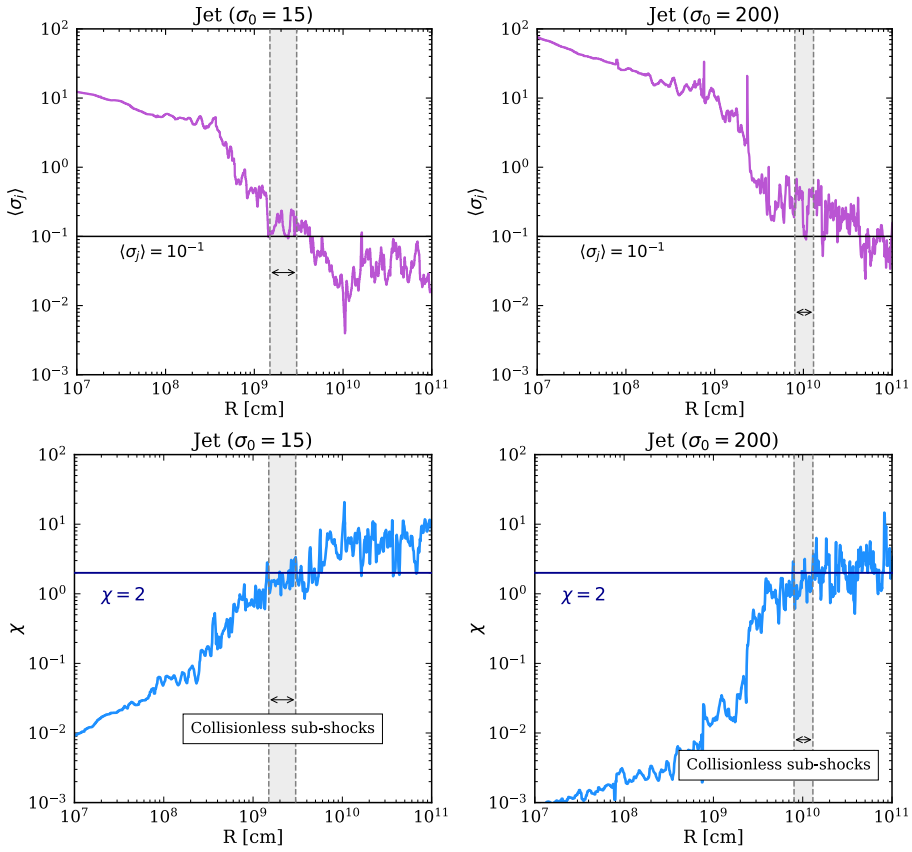

Figure 30: Radial profiles of $\langle\sigma_j\rangle$ (top panels) and of the parameter χ (Eq. 7.24, bottom panels) for $\sigma_0 = 15$ (left) and $\sigma_0 = 200$ (right). The black horizontal line in the top panels marks the condition $\langle\sigma_j\rangle = 10^{-1}$, whereas the blue horizontal line in the bottom panels marks the condition $\chi \lesssim 2$, for which strong collisionless sub-shocks can occur within radiation mediated shocks. Collisionless sub-shocks can take place for 1.5×10^9 cm $\lesssim$ R $\lesssim 3\times10^9$ cm when $\sigma_0 = 15$ and 8×10^9 cm $\lesssim$ R $\lesssim 1.2\times10^{10}$ cm for $\sigma_0 = 200$; each of these radial regions is highlighted by a shaded gray band.

the outflow $e'_{\rm th} = a\langle T'^4_j\rangle$; $\hat{\gamma} = 4/3$ is the adiabatic index for an ideal polytropic fluid and $\langle T'_j\rangle$ is the comoving temperature displayed in Fig. 25. The radial profiles of B'_j and T'_j are displayed in Fig. 25.

Figure 30 shows the radial profiles of $\langle\sigma_j\rangle$ and χ (Eq. 7.24); the horizontal lines mark the radii for which $\langle\sigma_j\rangle = 10^{-1}$ and $\chi = 2$, respectively. By combining the information in the top and bottom panels of Fig. 30, we deduce that collisionless sub-shocks may occur within radiation mediated shocks for 1.5×10^9 cm $\lesssim$ R $\lesssim 3\times10^9$ cm when $\sigma_0 = 15$ and 8×10^9 cm $\lesssim$ R $\lesssim 1.2\times10^{10}$ cm for $\sigma_0 = 200$. As for protons accelerated at collisionless sub-shocks, we assume $k_p = 2$, which is appropriate for mildly relativistic shocks [85]. The minimum energy of shock accelerated protons is $E'_{p,\rm min} = m_p c^2 \simeq 1$ GeV.

For mildly relativistic sub-shocks, we rely on particle-in-cell simulations of collisionless shocks in electron-ion plasma and fix $\varepsilon_p = 0.1$ [288]. We also assume constant dissipation efficiency, $\varepsilon_d = 0.2$ for mildly magnetized and mildly relativistic shocks [289, 290]. Note that since the region where collisionless

sub-shocks occur is rather small, we rely on a one-zone model [289, 290], even though ε_d may depend on the details of the collision [291, 292]. Hence, we fix the sub-shock radius $R_{\rm SS} = 2.5 \times 10^9$ cm for $\sigma_0 = 15$ and $R_{\rm SS} = 10^{10}$ cm for $\sigma_0 = 200$, where $0.1 \lesssim \langle \sigma_j \rangle \lesssim 1$ (see Fig. 24).

7.4.4 *Neutrino fluence from collisionless sub-shocks*

Figure 31 displays the muon neutrino fluence from collisionless sub-shocks for our jets with $\sigma_0 = 15$ and $\sigma_0 = 200$. For $\sigma_0 = 15$, pp interactions dominate the signal below $E_\nu \lesssim 1$ GeV, while $p\gamma$ interactions shape the spectrum for $E_\nu \gtrsim 10$ GeV. For $\sigma_0 = 200$, pp interactions are important for $E_\nu \lesssim 10$ GeV, while $p\gamma$ interactions dominate above $E_\nu \gtrsim 10^2$ GeV. The first bump in the neutrino energy distribution is due to the transition from the pp-dominated regime to the $p\gamma$-dominated one, while the second bump (for $E_\nu \gtrsim 10^2$ GeV) is due to kaon decay. The neutrino energy distribution has a cutoff at $E_\nu \lesssim 10^3$ GeV ($E_\nu \lesssim 2 \times 10^4$ GeV) for $\sigma_0 = 15$ ($\sigma_0 = 200$).

The differences between the two initial magnetizations can be understood as follows. The neutrino production rate in the comoving frame obtained for $\sigma_0 = 200$ (see Eqs. 7.8, 7.14 and 7.15) is comparable to the one for $\sigma_0 = 15$. Nevertheless, the volume of the interaction region V' (Eq. 7.16) for $\sigma_0 = 200$ is larger than the one for $\sigma_0 = 15$, resulting in a larger fluence in the former case. Furthermore, the neutrino signal is boosted to higher energies for $\sigma_0 = 200$, due to the larger values of $\langle \Gamma_j \rangle$ reached in the jet; see Fig. 24.

7.5 OUTER SUBPHOTOSPHERIC PARTICLE ACCELERATION SITES

In the context of subphotospheric particle acceleration, it is relevant to discuss unsuccessful jets, which are smothered in the stellar envelope or within an extended envelope. A cartoon displaying the possible jet fate is shown in Fig. 32. We discuss the conditions that must be fulfilled in order to produce an unsuccessful jet and the relevant particle acceleration sites. Note that both in the case of successful and unsuccessful jets, the high-pressure cocoon breaks out from the star and the extended envelope, if any. However, particle acceleration is not efficient at these sites; we refer the interested reader to Appendix A.3 for an overview of the acceleration sites in the cocoon.

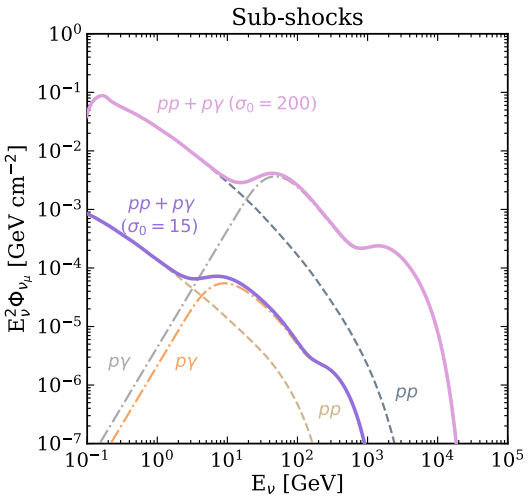

Figure 31: Muon neutrino fluence on Earth for a collapsar jet at $z = 2$ originating from collisionless sub-shocks for our benchmark jets with $\sigma_0 = 15$ (solid purple line) and $\sigma_0 = 200$ (solid orchid line). For $\sigma_0 = 15$, pp interactions (sand dashed line) dominate for $E_\nu \lesssim 1$ GeV, while $p\gamma$ (orange dot-dashed line) interactions shape the spectrum for $E_\nu \gtrsim 10$ GeV. For $\sigma_0 = 200$, pp interactions (dark gray dashed line) dominate for $E_\nu \lesssim 10$ GeV, while $p\gamma$ interactions (light gray dot-dashed line) are important for $E_\nu \gtrsim 10^2$ GeV. In both cases, the transition from the pp-dominated regime to the $p\gamma$-dominated one produces a bump in the neutrino spectral distribution. The second bump in the energy spectrum is due to kaon decay. The neutrino signal is limited to energies $E_\nu \lesssim 10^3$ GeV ($E_\nu \lesssim 2 \times 10^4$) GeV for $\sigma_0 = 15$ ($\sigma_0 = 200$).

7.5.1 *Motivation*

A short-lived engine can generate a jet that does not break out from the stellar core and it is halted (see left panel of Fig. 32). Another instance for which jets could be unsuccessful occurs when the progenitor star has not shed apart the hydrogen layer completely and retains an extended massive envelope engulfing its core, as sketched in the middle panel of Fig. 32. This could happen, for example, for partially stripped supernovae [200, 294, 295]. If this is the case, even when the jet breaks out from the stellar core, it fails to pierce through the external extended envelope. This scenario is of particular interest, since some GRBs or LFBOTs may harbor relativistic jets, which do not break out successfully.

For example, it has been proposed that low- and high-luminosity GRBs share the same explosion mechanism, with the difference that low-luminosity GRB progenitors retain an extended low-mass envelope [199, 200]. The envelope smothers the jet, which drives a mildly relativistic shock leading to a low-luminosity GRB. Choked jets could be harbored within LFBOTs as well [143–146, 296]. The lack of gamma-ray associations with known LFBOTs [297] and the observation of broad hydrogen lines in some of their spectra [148, 149, 152] may hint towards a jet smothered in the extended hydrogen envelope [153]. The jet inflates the cocoon responsible for the observed electromagnetic emission in the optical and radio bands. The existence of a jet in

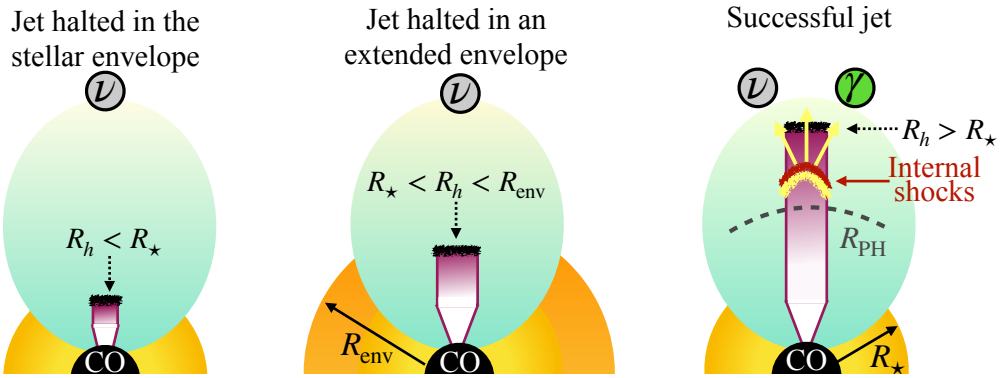

Figure 32: Sketch of the fates of collapsar jets. *Left panel*: The jet is halted in the stellar core ($R_h < R_\star$) at the end of the jet lifetime. The only particle acceleration sites are the ones displayed in Fig. 27. *Middle panel*: The jet is halted in an extended outer envelope (dark-orange region) engulfing the star ($R_\star < R_h < R_{\rm env}$). If the jet is magnetized, the acceleration sites are the ones drawn in Fig. 27. *Right panel*: The jet is successful and breaks out from the stellar envelope (orange). The jet head is above the stellar radius ($R_h > R_\star$) when the CO activity stops. The jet reaches the photosphere, where further energy dissipation and particle acceleration may take place. In all three scenarios, the cocoon (aqua) breaks out from the star and the extended envelope, if any. The case of a jet breaking out from the extended envelope is not considered, since this is not supported by observations [293].

LFBOTs would also explain the asymmetry observed in the outflow [148]. We refer the reader to Refs. [234, 298] for a discussion on the acceleration sites.

Jets which manage to pierce through the extended envelope are not supported by observations: successful jets should produce GRBs, whose progenitors do not exhibit any hydrogen line in their spectra [293]. Hence, this case is not of interest to our discussion.

Our benchmark simulations focus on jets breaking out from the stellar core, with no extended envelope engulfing the progenitor star. Hence, the jet freely propagates up to its photosphere. To date, numerical simulations tracking the dynamics of magnetized jets that break out in an extended stellar envelope are lacking. However, the outflow dynamics mimics the one of hydrodynamic jets above $R_\star$ [222]. Even though numerical simulations would be required, we rely on previous work on hydrodynamic jets to investigate the propagation of our benchmark jets in a massive envelope. Since the jet lifetime is not constrained by the simulation, we intend to explore the allowed parameter space and compute the value of $\tilde{t}_j$ required for halting jets resembling the simulated ones in the extended envelope. The goal of this section is to expand on the results of Sec. 7.4 to unsuccessful jets.

7.5.2 *Conditions for halting the jet*

We assume that the star has a core of radius $R_\star$ and an envelope extending up to $R_{\rm env}$. The stellar core is described by the following radial density profile [210, 222, 299]:

$$\rho_\star(R) = \rho_0 R^{-2}\left(1-\frac{R}{R_\star}\right)^3 , \tag{7.25}$$

where the normalization constant is fixed by the stellar mass, namely $\rho_0 = M_\star/\left[\int_0^{R_\star} dR' 4\pi R'^2 \rho_\star(R')\right]$. As for $M_\star$ and $R_\star$, we adopt the same values used in the simulation and listed in Sec. 7.2.

The radial density profile of the extended envelope is assumed to be [200]:

$$\rho_{\rm env}(R) = \rho_{0,\rm env} R^{-2} , \tag{7.26}$$

where $M_{\rm env}$ is its mass and $\rho_{0,\rm env} = M_{\rm env}/\left[\int_{R_\star}^{R_{\rm env}} dR 4\pi R^2 \rho_{\rm env}(R)\right]$. Inspired by partially stripped supernovae, we fix $R_{\rm env} = 10^{13}$ cm and we consider two representative cases for the envelope mass: $M_{\rm env} = 0.1 M_\odot$ and $M_{\rm env} = 5 M_\odot$ [199, 200, 294, 295, 300]. Overall, the density profile of the star is parametrized as

$$\rho(R) = \max\left[\rho_\star(R), \rho_{\rm env}(R)\right] . \tag{7.27}$$

The propagation of a hydrodynamic relativistic jet in dense media has been modeled analytically [201] and semi-analytically [210]. In both cases, the jet dynamics is completely determined once its luminosity $\tilde{L}_j$, duration $\tilde{t}_j$, initial opening angle θ_j, and the density profile of the medium $\rho(R)$ are fixed. Hence, in order to infer whether the jet is successful or not, we follow the temporal evolution of its head R_h.

We stress that we rely on hydrodynamic jets, generally different from the magnetically dominated jets considered so far. However, since the simulated jets become weakly magnetized above $R_\star$, this is a fair approximation. The jet dynamics is obtained by relying on the semi-analytical model presented in Ref. [210] (we refer the interested reader to Ref. [210] for details on the calculation). The model allows to calculate, at each time, the position of the jet head R_h, its proper velocity $\beta_h\Gamma_h$, and the breakout time $\tilde{t}_{\rm BO,\star(env)}$ from $R_\star$ ($R_{\rm env}$).

Since the jet head is relativistic, while propagating through the stellar envelope (Eq. 7.27), the time over which the engine has to power the jet in order to allow for its breakout from the star (envelope) is

$$\tilde{t}_j = \tilde{t}_{\rm BO,\star(env)} - \frac{R_{\star(\rm env)}}{c} . \tag{7.28}$$

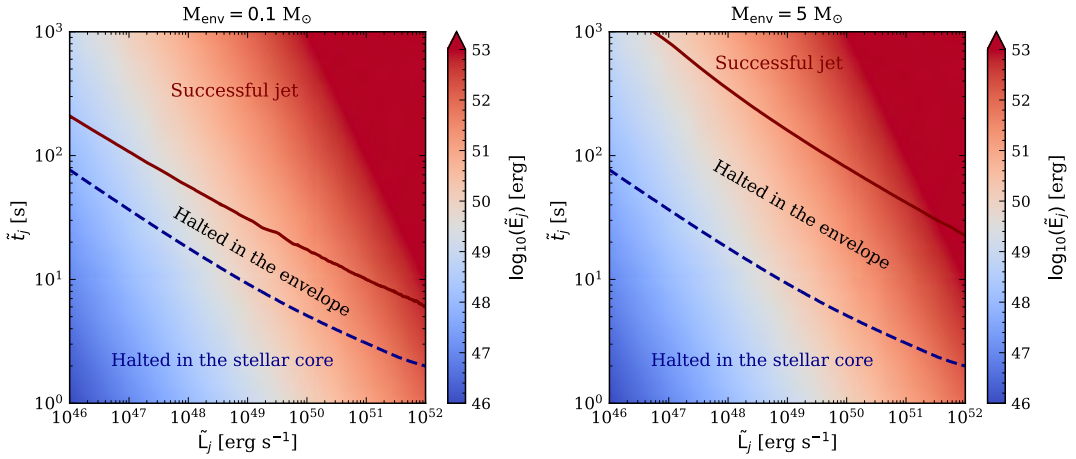

Figure 33: Contour plot of the energy injected in the jet by the central engine ($\tilde{E}_j = \tilde{L}_j \tilde{t}_j$) in the plane spanned by the luminosity and engine lifetime. The jet propagates in an envelope with radius $R_{\rm env} = 10^{13}$ cm and mass $M_{\rm env} = 0.1 M_\odot$ (left panel) or $M_{\rm env} = 5 M_\odot$ (right panel). The region of the parameter space below the dashed blue line corresponds to jets halted within the stellar core, for which $R_h < R_\star$ at the end of the jet lifetime. The region above the solid brown line corresponds to successful jets, namely jets that breakout both from the stellar core and the extended envelope for which $R_h > R_{\rm env}$. Between the blue and brown isocontours, the pairs $(\tilde{L}_j, \tilde{t}_j)$ lead to jets which breakout from the star, but are halted in the extended envelope, i.e. $R_\star < R_h < R_{\rm env}$ at the end of the jet lifetime.

For a given pair $(\tilde{L}_j, \tilde{t}_j)$, when $\tilde{t}_j < \tilde{t}_{\rm BO,\star} - R_\star/c$ the jet is halted in the stellar core. If, instead, $\tilde{t}_{\rm BO,\star} - R_\star/c < \tilde{t}_j < \tilde{t}_{\rm BO,env} - R_{\rm env}/c$, the jet breaks out from the stellar core, but it is halted in the envelope. Figure 33 shows the parameter space of the pairs $(\tilde{L}_j, \tilde{t}_j)$ corresponding to the same energy $\tilde{E}_j$ injected in the jet. The mass of the envelope is assumed to be $M_{\rm env} = 0.1 M_\odot$ (left panel) and $M_{\rm env} = 5 M_\odot$ (right panel). The region below the dashed blue line corresponds to jets halted in the stellar core, i.e. $R_h < R_\star$ at the end of the jet lifetime. This region is not of interest for the reference simulations of Ref. [222], since the jets are very energetic and likely to break out from $R_\star$ in any case.

The area between the dashed blue and solid brown lines in Fig. 33 corresponds to jets halted in an extended envelope. In this case, at the end of the jet lifetime, $R_\star < R_h < R_{\rm env}$. Our simulated jets, with total luminosity $\tilde{L}_j \simeq 5 \times 10^{51}$ erg s^{-1} (at the time when the snapshots in Fig. 24 are taken), break out from the star for $\tilde{t}_j \gtrsim 2$ s. The result is consistent with the simulations, since the central engine is still active and powering the outflow at 2 s. Our benchmark jets may be halted in the extended envelope if $\tilde{t}_j \lesssim 6$ s ($\tilde{t}_j \lesssim 25$ s), for $M_{\rm env} = 0.1 M_\odot$ ($M_{\rm env} = 5 M_\odot$), and we would not observe any jet-powered gamma-ray bursts.

Finally, the region above the brown line in Fig. 33 corresponds to jets able to drill out from the star, for which $R_h > R_{\rm env}$. As expected, massive envelopes require long living engines in order to produce successful jets. Furthermore, for a fixed engine duration, jets less powerful than our simulated ones are halted within the extended envelope more easily.

7.5.3 *Neutrino production in unsuccessful jets*

From Fig 33, we deduce that jets can be unsuccessful only for some $(\tilde{L}_j, \tilde{t}_j)$ pairs. Particle acceleration in unsuccessful jets has been discussed in the literature, both at the collimation shock [247] and at internal shocks occurring either in the outflow or at the jet head [234, 237, 247, 248, 251, 253]. These works rely on the criterion outlined in Ref. [247] for the formation of collisionless shocks and they all assume hydrodynamic jets.

GRB like jets are expected to undergo intense mixing due to interactions with the cocoon [213]. Hence, the criterion proposed in Ref. [247], which is given for idealized jets, has been shown to do not be satisfied in regions of the jet still embedded in the stellar core ($R \lesssim R_\star$) in numerical simulations, since the mixing slows down the jet and increases its baryon density [213, 245]. Indeed, we find that the optical depth of the outflow is substantially larger than the one obtained from analytical estimations, see Fig. 26. We conclude that particle acceleration at internal shocks occurring deep in the stellar core or at the collimation shock is disfavored, contrary to what concluded in Ref. [247] (see also the discussion in Ref. [236]).

The picture above could change in the presence of a massive envelope surrounding the star, investigated in Refs. [234, 235, 248]. Nevertheless, if the jet is magnetized, the results of Refs. [234, 235, 248] may no longer hold, being the underlying jet dynamics different and highly non-linear. The extended envelope would affect the jet dynamics above $R_\star$ and it may increase the effect of the jet-cocoon mixing, which would be relevant up to radii larger than the ones reached in the simulation. As a result, the outflow may become optically thin at $R_{\rm PH} \gg 10^{12}$ cm, possibly even above $R_{\rm env}$. Even though particle acceleration at internal shocks approaching the jet head seems unlikely in magnetized jets, dedicated numerical simulations are desirable. Therefore, in the following, we limit our discussion to radii below the edge of the envelope ($R \lesssim O(10^{12})$ cm).

This scenario could be relevant, for example, for neutrino production in LFBOTs [153, 234]. In the case of a magnetized unsuccessful jet, the discussion on particle acceleration in Sec. 7.4 should apply. Since the energy of LFBOTs is expected to be smaller than the one obtained for the jet simulations presented in Ref. [236], the overall normalization of the neutrino fluences in Figs. 29 and 31 should be affected. Yet, we expect the neutrino fluence produced from a magnetized unsuccessful jet to be limited to energies

$E_\nu \lesssim 10^5$ GeV. Intriguingly, this signal would be very different from the one predicted for a hydrodynamic [4] choked jet, which instead peaks at $E_\nu \simeq 10^5$ GeV [234]. Hence, neutrinos could contribute not only to disentangle the mechanism powering LFBOT sources—as suggested in Ref. [234]—but also to discern the nature of unsuccessful jets. The signal calculated in Sec. 7.4 is typical of magnetized jets, while it is not expected from hydrodynamic jets, which are optically thick below $R_\star$ and do not have magnetization to sustain nor sub-shocks or magnetic reconnection [212, 213, 243, 244].

Another outer particle acceleration site for hydrodynamic jets (or jets which mimic hydrodynamic ones) may be the shock which develops at the interface between the cocoon and the envelope. This shock becomes collisionless at the shock-breakout radius $R_{\rm BO,env}$ defined as

$$\tau_{\rm env}(R_{\rm BO,env}) = \int_{R_{\rm BO,env}}^{R_{\rm env}} dR \rho(R) k_{\rm es} = \frac{c}{v_{\rm sh,env}} \,. \tag{7.29}$$

where $\rho(R)$ is given by Eq. 7.27, $v_{\rm sh,env}$ is the speed of the shock and $k_{\rm es}$ is the electron scattering opacity. Here we adopt $k_{\rm es} = 0.34$, assuming solar abundances [301]. Since the cocoon fastest component moves with mildly relativistic velocities ($\langle \Gamma_c \rangle \lesssim 2$), it enters the envelope with a mildly relativistic shock, i.e. $c/v_{\rm sh,env} \simeq 1$. Our goal is to assess whether there is a part of the parameter space for which $R_{\rm BO,sh} \ll R_{\rm env}$. This case would resemble the propagation of a mildly-relativistic shock in the circumstellar medium, see e.g. Ref. [302], but acceleration of particles would start deep in the envelope rather than at its edge and would occur over a wide range of radii inside the star. Efficient particle acceleration when $R_{\rm BO,env} \simeq R_{\rm env}$ is possible (see, e.g., Refs. [200, 236]), but we do not further investigate this case since it is beyond the main focus of this work.

Figure 34 shows the parameter space of the $(R_{\rm env}, M_{\rm env})$ pairs having the same shock-breakout radius $R_{\rm BO,env}$, as defined in Eq. 7.29. For most of the envelope masses $M_{\rm env}$ and radii $R_{\rm env}$, the shock-breakout occurs very close to the edge of the envelope, in particular at $R \gtrsim 0.7 R_{\rm env}$. The breakout could occur at smaller radii only for envelopes with large extension ($R_{\rm env} \gg \times 10^{13}$ cm) and small masses ($M_{\rm env} \lesssim 5 \times 10^{-4} M_\odot$), as visible from the right bottom corner of the parameter space in Fig. 34. Such envelopes are not dense enough to halt relativistic jets and are poorly motivated theoretically [199, 200, 294, 295, 300].

Combining the results from Figs. 33 and 34, we deduce that small envelope masses require fine tuning of the jet lifetime and luminosity to simultaneously smother the jet and allow for neutrino production in the range $R_\star \lesssim R \lesssim R_{\rm env}$. Therefore, particle acceleration at the shock between the cocoon of unsuccessful

4 We stress that we intend to highlight the mechanism responsible for the jet launching through the wording "hydrodynamic jet." Even though our magnetized jets resemble hydrodynamic ones after the breakout from the star, their evolution is different at the initial phase of the jet lifetime.

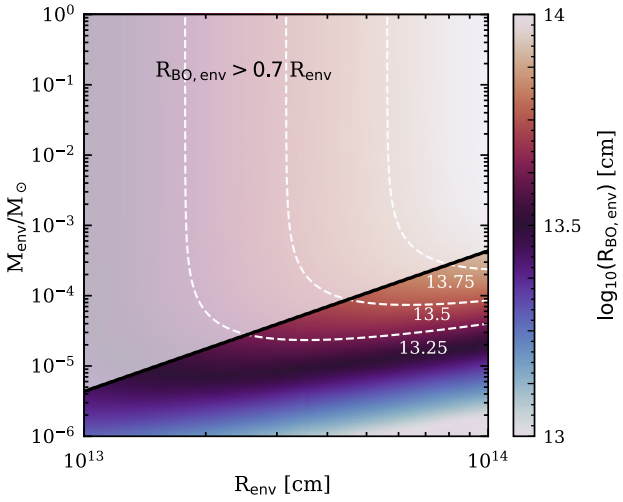

Figure 34: Contour plot of the shock-breakout radius at the envelope $R_{\rm BO,env}$ (Eq. 7.29) in the plane spanned by the radius $R_{\rm env}$ of the envelope and its $M_{\rm env}$. The dashed white lines display representative values of $\log_{10}\left(R_{\rm BO,env}\right)$ to guide the eye. The shadowed region corresponds to pairs $(R_{\rm env}, M_{\rm env})$ for which the envelope becomes optically thin close to its edge, for $R_{\rm BO,env} > 0.7\ R_{\rm env}$. The shock-breakout occurs deep in the envelope only for the right bottom corner of the parameter space, for which $M_{\rm env} < 5 \times 10^{-4} M_\odot$ and $R_{\rm env} \gg 10^{13}$ cm; these parameters are quite unusual and would require fine tuning of the initial conditions of the jet for halting it within the envelope. We conclude that in most cases the shock break out occurs very close to the edge of the envelope.

jets and the envelope is either inhibited or it occurs in a very narrow range of radii, making it a subleading process for neutrino production in the region $R \ll R_{\rm env}$.

We conclude that, if a magnetized jet is halted in the extended envelope, neutrino production is possible at the sites discussed in Sec. 7.4. For instance, if the simulated jets were to breakout from the stellar core in an envelope with $R_{\rm env} = 10^{13}$ cm and $M_{\rm env} = 5 M_\odot$, for the fixed lifetime $t_j = 10$ s, the neutrino fluence from magnetic reconnection processes and collisionless sub-shocks would be the same as the one displayed in Figs. 29 and 31, respectively, with the results being sensitive to the initial magnetization of the jet. As for jets which are hydrodynamically launched and choked in the extended envelope, neutrino production may occur at the sites discussed in Refs. [234, 248, 253]. It is still to be proven whether further particle acceleration can occur in magnetized unsuccessful jets at the same sites, namely at $R_{\rm IS} \simeq R_h \lesssim R_{\rm env}$.

If the jet head is halted in the extended envelope at the position R_h, the neutrino signal produced at the acceleration sites discussed in Sec. 7.4 can be attenuated because of neutrino propagation in matter between R_h and $R_{\rm env}$. The attenuation factor for the neutrino fluence scales approximately as $f_{\rm att} \simeq \exp[-\int_{R_h}^{R_{\rm env}} \rho(R)/(2m_p)\sigma_\nu^{\rm CC}(E_\nu)]$, where $\rho(R)$ is given in Eq. 7.27 and $\sigma_\nu^{\rm CC}$ is the cross section for neutrino-charged current interactions which is the dominant process in the GeV–TeV energy range of interest [303]. Attenuation is relevant when $f_{\rm att} \ll 1$; for the density profile in Eq. 7.27, we find that this

condition is fulfilled for $E_\nu \gtrsim 100$ TeV, i.e. it is negligible for the scenarios investigated in this paper. Neutrino flavor conversion may also occur in choked jets [304–306], nevertheless for our collapsar scenarios the flavor composition at Earth is not substantially altered [307]. Further attenuation of the neutrino signal may be caused by the increase of the jet-cocoon mixing in the presence of a massive envelope, which cannot be analytically estimated. Hence, the results presented in Sec. 7.4 for the subphotospheric neutrino signal expected on Earth still shall be interpreted as an upper limit for a magnetized jet halted in an extended envelope.

7.6 EXPECTED SUBPHOTOSPHERIC NEUTRINO EMISSION

By relying on the findings of Secs. 7.4 and 7.5, in this section we present the total fluence expected for subphotospheric neutrinos produced in collapsar jets. We also compare our finding with the existing literature. Our results are sensitive to the underlying reference simulations. Yet they urge to move towards a more robust modelling than the one provided by analytical treatments.

7.6.1 *Neutrino fluence*

Figure 35 shows the total subphotospheric muon neutrino fluence, where the lower limit is set by $\sigma_0 = 15$ and the upper limit by $\sigma_0 = 200$. In the former case, only internal sub-shocks are a viable mechanism for neutrino production, since the magnetization along the jet is not large enough to sustain magnetic reconnection; see Fig. 31. In the latter scenario, both sub-shocks and magnetic reconnection contribute to shape the neutrino energy distribution from the optically thick region; see Figs. 29 and 31. The neutrino fluence has a cutoff at $E_\nu \simeq 4 \times 10^4$ GeV ($E_\nu \simeq 10^3$ GeV) for $\sigma_0 = 200$ ($\sigma_0 = 15$). This is due to the large baryon density in the outflow, which substantially limits the maximum energy at which protons can be accelerated.

As pointed out in Ref. [222], GRB jets may have initial magnetization larger than the ones considered in this paper ($\sigma_0 \gtrsim 1000$) in order to reach the observed Lorentz factors of a few hundreds. Because of numerical limitations, jet simulations with such large σ_0 are not yet available. Nevertheless, we extrapolate the radial profiles of the jet characteristic quantities ($\langle \rho'_j \rangle$, $\langle \sigma_j \rangle$, $\langle \Gamma_j \rangle$) for a relativistic jet with $\sigma_0 = 2000$ by assuming a constant scaling ratio on the basis of the simulations with $\sigma_0 = 15$ and $\sigma_0 = 200$ (see Fig. 24),

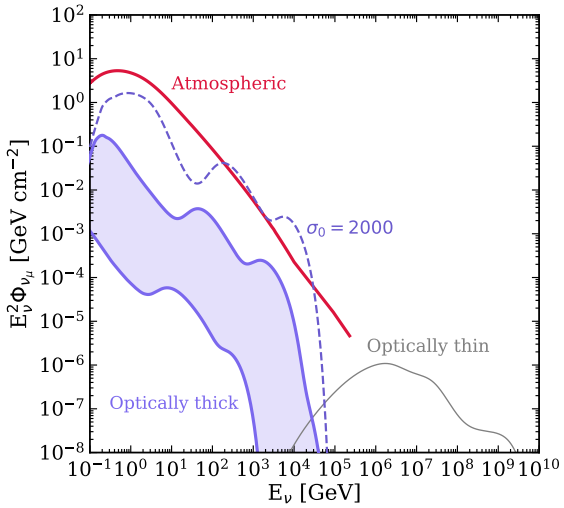

Figure 35: Muon neutrino fluence on Earth for a collapsar jet at $z = 2$. The purple band represents the range of variability of the subphotospheric neutrino production (optically thick region); the lower limit corresponds to the fluence obtained for $\sigma_0 = 15$ (as displayed in Fig. 31), while the upper limit is obtained for $\sigma_0 = 200$ (see Figs. 29 and 31). The purple dashed line corresponds to the neutrino fluence expected for $\sigma_0 = 2000$; see main text for details. For comparison, we show the benchmark muon neutrino fluence from the optically thin region (above the photosphere) of a successful collapsar jet, namely a GRB (see Appendix A.4). The red line represents the atmospheric background expected during the jet lifetime [308–310]. The neutrino signal in the optically thick region of the outflow extends up to $E_\nu \simeq 4 \times 10^4$ GeV ($E_\nu \simeq 10^3$ GeV) for $\sigma_0 = 200$ ($\sigma_0 = 15$) and it lies below the atmospheric background. For $\sigma_0 = 2000$, the neutrino signal extends up to $E_\nu \lesssim 7 \times 10^4$ GeV and it is comparable in intensity to the atmospheric background.

while the temperature is kept unchanged. The corresponding neutrino fluence increases up to one order of magnitude compared to the one obtained for $\sigma_0 = 200$, as shown in Fig. 35 (dashed purple line). Yet, the larger baryon density and magnetic field in the jet are such that the neutrino spectrum extends up to energies $\lesssim 7 \times 10^4$ GeV. While this result should be interpreted as an order of magnitude computation and may change if it were to be obtained by relying on self-consistent jet simulations, it provides a good insight on what to expect.

For comparison, the neutrino fluence produced above the photosphere (optically thin region) in the case of a successful jet is also shown in Fig.35; see also Appendix A.4. We compute this fluence by assuming that the target photon energy distribution is shaped by a dissipative photosphere and internal shocks occur above the photosphere, as discussed in Appendix A.4. The photospheric efficiency of the jet is $\epsilon_{\rm PH} \simeq 0.1$, which is the fraction of the jet isotropic energy energy emerging from the photosphere. The radiative efficiency at the photosphere is obtained by solving the hydrodynamic equations for the fireball model, within the assumption that the jet is almost hydrodynamic; see e.g. Ref. [211]. Our benchmark simulations hint that $\epsilon_{\rm PH} \gtrsim 10\%$ could be reached for jets with $\sigma_0 \gtrsim 1000$. All other jet parameters follow the ones adopted in Ref. [231], chosen to match GRB observations (see Ref. [231] and references therein). We can see that the neutrino

fluence from the optically thin region has a lower overall normalization, but it extends up to $E_\nu \simeq 10^9$ GeV. We stress that this result is only shown to favor a direct comparison between the subphotospheric neutrino signal and the one produced above the jet photosphere, if the jet is successful.

In Fig. 35, we also show the expected fluence of atmospheric muon neutrinos during the jet lifetime [308–310]. Our neutrino fluence from the optically thick region of the outflow lies below the atmospheric background both for $\sigma_0 = 200$ and $\sigma_0 = 15$, while it becomes comparable to the atmospheric one for a jet launched with $\sigma_0 = 2000$.

7.6.2 *Comparison with existing literature*

Our findings are in contrast with existing literature. In fact, under the assumption of collisionless internal shocks taking place in parts of the jet deeply embedded in the stellar envelope, Refs. [237, 247, 252, 255] conclude that TeV–PeV neutrinos could be produced. The main difference with our work is that the aforementioned papers overlooked the role of jet-cocoon mixing, underestimating the optical depth of the outflow; we find that shocks in the innermost parts of the jet are likely radiation mediated when the role of mixing is consistently accounted for in the jet dynamics [222]. As mentioned in Sec. 7.2, low baryon densities may be allowed if the jet accelerates at small radii to large Lorentz factors. This might favor acceleration of particles through internal shocks [247]. Nevertheless, such large Lorentz factors seem to be disfavored from state-of-the-art numerical simulations of collapsar jets.

Our results are in agreement with Ref. [236], which investigated the neutrino production at internal sub-shocks in the optically thick region of short GRBs, by relying on the outputs of numerical simulations artificially launching the jet. Yet, the self-consistent jet launching of our benchmark jet simulations [222] affects the jet fate.

Intriguingly, subphotospheric production of neutrinos in the same energy range displayed in Fig. 35 can occur if collisional heating is considered as the mechanism responsible for energy dissipation in collapsar jets [311, 312]. In this scenario, neutrinos are produced through neutrino-proton interactions along the outflow.

7.7 DETECTION PROSPECTS

The subphotospheric neutrino fluence shown in Fig. 35 spans an energy range below $O(100)$ TeV, where the IceCube Neutrino Observatory is most sensitive to astrophysical neutrinos. Hence, contrarily to the conclusions drawn in Refs. [228, 237, 247, 255, 256] for hydrodynamic jets, unsuccessful magnetized jets cannot contribute to the diffuse neutrino flux detected by the IceCube Neutrino Observatory [8, 313]. These conclusions might change if the jet should be halted in an extended envelope and neutrino production should take place close to the jet head, at $R \lesssim 10^{13}$ cm [235, 248, 253]. As extensively discussed in Sec. 7.5, we expect this scenario to be unlikely for magnetized jets.

The detection of subphotospheric neutrinos is hampered by the atmospheric neutrino flux, as discussed in Sec. 7.6; however, we investigate whether astrophysical neutrinos could be discriminated from the atmospheric background by exploiting the directionality of the incoming astrophysical neutrinos. To this purpose, we rely on the Hyper-Kamiokande neutrino detector [182] and IceCube DeepCore, designed to detect neutrinos with energy as low as $E_\nu \simeq 10$ GeV [173].

As for Hyper-Kamiokande, the event directionality can be reconstructed by relying on the elastic scattering of neutrinos on electrons: $\nu_\alpha + e^- \to \nu_\alpha + e^-$ ($\bar{\nu}_\alpha + e^- \to \bar{\nu}_\alpha + e^-$) [5]. The dominant contribution to the $\nu_\alpha e^-$ elastic scattering channel comes from the electron flavor, while the contribution from muon or tau flavors is subleading (see e.g. Refs. [303, 314] for a review). Hence, we only consider $\alpha = e$ at Hyper-Kamiokande. The total number of subphotospheric neutrino events is [315]

$$N_{\nu_e+\bar{\nu}_e}(z) = \epsilon N_e \int dE_\nu [\sigma_{\nu_e+e^-}(E_\nu)\Phi_{\nu_e}(E_\nu, z) + \sigma_{\bar{\nu}_e+e^-}(E_\nu)\Phi_{\bar{\nu}_e}(E_\nu, z)] \,,$$

where $\sigma_{\nu+e^-}$ [$\sigma_{\bar{\nu}+e^-}$] is the cross-section for the neutrino (antineutrino)–electron elastic scattering [303] and ϵ is the detector efficiency, which we optimistically assume to be 1. The total number of electron targets is $N_e = 1.13 \times 10^{34}$ for a water Cherenkov detector with a fiducial volume of 0.188 Mton [316]. The number of atmospheric neutrino events is calculated through Eq. 7.30, by using the neutrino atmospheric flux in Refs. [308–310].

For IceCube-DeepCore, the total number of subphotospheric neutrino events is

$$N_{\nu_\mu+\bar{\nu}_\mu} = \int_{10\ \mathrm{GeV}}^{100\ \mathrm{GeV}} dE_\nu A_{\mathrm{eff}}(E_\nu)\Phi_{\nu_\mu+\bar{\nu}_\mu}(E_\nu, z) \,, \tag{7.30}$$

5 Note that in this case we need to distinguish between neutrinos and antineutrinos, since the respective cross-sections are different.

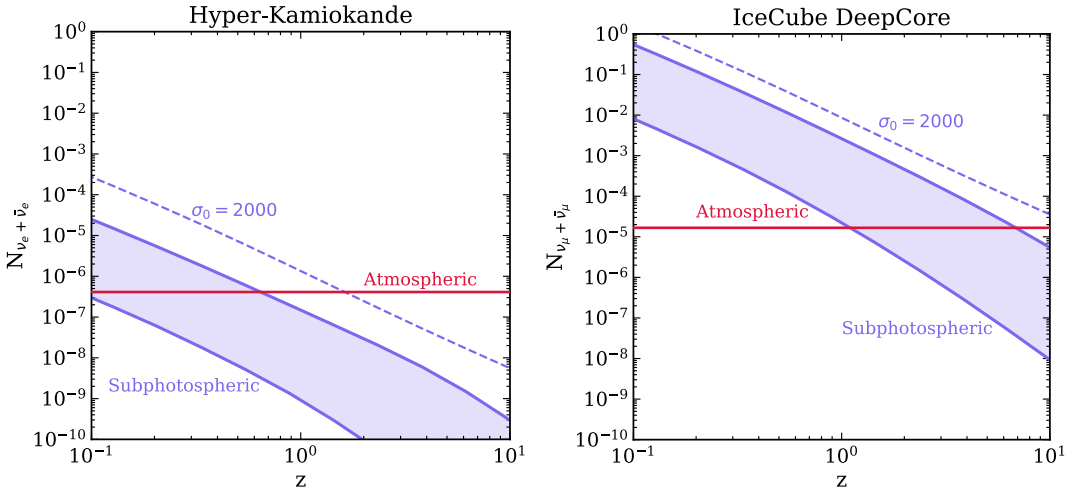

Figure 36: Number of subphotospheric neutrino events (purple band) expected at Hyper-Kamiokande (left panel) and IceCube DeepCore (right panel). The upper and lower solid lines of each band correspond to $\sigma_0 = 200$ and $\sigma_0 = 15$, respectively. We also show the expected number of neutrinos extrapolated for a jet with $\sigma_0 = 2000$ (dashed purple line). For comparison, the background of atmospheric neutrino events is plotted (solid red line). The number of suphotospheric neutrino events is larger than the atmospheric ones in Hyper-Kamiokande, if the source is placed at $z \lesssim 0.8$ ($z \lesssim 0.1$) for a jet with $\sigma_0 = 200$ ($\sigma_0 = 15$). While for IceCube DeepCore, this should happen for a jet located at $z \lesssim 7$. As for the initial magnetization $\sigma_0 = 2000$, the number of suphotospheric neutrino events is larger than the atmospheric ones for $z \simeq 2$ for Hyper-Kamiokande and for $z \gtrsim 10$ for IceCubeDeep Core.

where $A_{\rm eff}$ is the energy-dependent effective area of the detector [173]. The rate of atmospheric neutrinos in the 10–100 GeV range is obtained from Ref. [317].

Figure 36 shows the total number of subphotospheric neutrino events expected at Hyper-Kamiokande (on the left) and IceCube DeepCore (on the right) as a function of the source redshift, for our benchmark jets. For comparison, the number of atmospheric neutrino events is also plotted in Fig. 36. We can see that the number of events expected at Hyper-Kamiokande is significantly lower than the one observable at IceCube DeepCore, due to the smaller cross-section.

The number of events from subphotospheric neutrinos would be larger than the atmospheric neutrino number of events at Hyper-Kamiokande for a jet at $z \lesssim 0.8$ ($z \lesssim 0.1$) for $\sigma_0 = 200$ ($\sigma_0 = 15$). On the other hand, in principle, the astrophysical signal may be larger than the atmospheric one for sources at $z \lesssim 7$ at IceCube DeepCore. As for the jet with initial magnetization $\sigma_0 = 2000$, the astrophysical signal becomes comparable to the atmospheric one at $z \simeq 2$ ($z \gtrsim 10$) in Hyper-Kamiokande (IceCube DeepCore).

The detection of $N_{\nu_\alpha+\bar{\nu}_\alpha} \gtrsim 1$ might be possible if the magnetized collapsar jet is located within $z \lesssim 0.1$ for all σ_0's considered in this work. These findings are in agreement with Ref. [312], that investigated the detection of neutrinos in a similar energy range for collisionally heated GRBs. While the detection horizon is limited, the existence of bright GRBs at fairly moderated redshift is not ruled out—see, e.g., GRB 221009A

which occurred at $z \simeq 0.151$ [318]. These detection prospects may further improve with the upcoming IceCube Upgrade [319, 320], expected to lead to a more accurate event reconstruction in the energy region where IceCube DeepCore is sensitive. Moreover, as also pointed out in Ref. [312], stacking searches of collapsar jets could enhance the detection chances of subphotospheric neutrinos; dedicated forecast work on stacking searches is left as future task, as it would require a large set of GRMHD simulations.

7.8 CONCLUSIONS

A realistic modelling of relativistic jets and their related particle production is not only relevant for interpreting electromagnetic observations of a growing number of astrophysical transients, but also for investigating the associated high-energy neutrino production. While analytical treatments hold in the optically thin region of the outflow, they are no longer adequate to describe the evolution of the jet in the optically thick regime. This is due to the large jet–cocoon mixing revealed in a range of numerical simulations, both for hydrodynamic and magnetized jets.

In this work, we explore neutrino production in the optically thick region of relativistic jets by relying on the numerical simulations carried out in Ref. [222], with initial magnetization $\sigma_0 = 15$ and $\sigma_0 = 200$. As the jet propagates through the star, it efficiently converts magnetic into kinetic energy. While the formation of collisionless shocks seems to be disfavored due to the large optical depth, the mild magnetization $\langle \sigma_j \rangle \lesssim 0.1$ reached at $R \simeq 10^9$–10^{10} cm could sustain the formation of collisionless sub-shocks for both σ_0. The intrinsic magnetization of the jet may also trigger magnetic reconnection events, especially for jets with $\sigma_0 = 200$. Hence, both sub-shocks and magnetic reconnection are viable particle acceleration mechanisms.

Our findings reveal that the subphotospheric neutrino signal spans an energy range with $E_\nu \lesssim 10^4$ GeV (10^5 GeV) for $\sigma_0 = 15$ ($\sigma_0 = 200$). This result also holds for larger initial magnetizations of the jet, e.g. $\sigma_0 = 2000$, for which we extrapolate the dynamics from the two simulated jets with lower σ_0. The maximum neutrino energy is limited due to the large baryon density and high magnetic field, which causes the cooling of secondary mesons and it is consistent with the results of Ref. [236]. These findings are in contrast with the ones previously reported in Refs. [237, 247, 252, 255], where TeV—PeV neutrinos were produced in the star under the assumption of collisionless internal shocks, which we show are unlikely because of the large optical depth of the outflow determined by the jet-cocoon mixing.

If the jet is halted in an extended envelope engulfing the progenitor star, the same conclusions concerning neutrino production hold, if the jet is magnetized. We find that no particle acceleration can occur at the shock developing at the cocoon front as it propagates in the extended envelope, unless the properties of the envelope and the jet are fine-tuned. Extreme conditions, which are not physically motivated, are required to simultaneously halt the jet and allow for particle acceleration.

Because of their low energies and based on our benchmark simulated jets, subphotospheric neutrinos from magnetized jets unlikely contribute to the high-energy diffuse neutrino flux observed by the IceCube Neutrino Observatory, contrarily to what suggested in the literature [247]. Yet, we investigate the detection perspectives in the upcoming water Chereknov detector Hyper-Kamiokande and IceCube DeepCore. The subphotospheric signal could be discriminated by the atmospheric background by exploiting the directional information of the astrophysical neutrinos, with the expected number of neutrino events being larger than the atmospheric one for a jet located at $z \lesssim 0.8$ ($z \lesssim 0.1$) for $\sigma_0 = 200$ ($\sigma_0 = 15$) in Hyper-Kamiokande and $z \lesssim 7$ ($z \lesssim 1$) for $\sigma_0 = 200$ ($\sigma_0 = 15$) in IceCube DeepCore.

Our results might not hold if a hydrodynamic jet is launched and halted in an extended envelope. In this case, particle acceleration at internal shocks approaching the jet head cannot be ruled out, albeit numerical simulations of this scenario are lacking. This might be the case for choked jets accompanying some Type-II supernovae [248] and LFBOTs [234].

In conclusion, our work highlights the importance of an advanced modeling of particle production and acceleration in collapsar jets, which takes into account the jet dynamics and related non-linearities. As shown in this work, such modeling may largely affect previous conclusions on the subphotospheric neutrino detection prospects.

NOTE ADDED.— While this project was in its final stages of completion, we became aware of work in progress by Carpio et al. [321, 322], which focuses on high-energy neutrino emission from magnetized jets propagating in different stellar progenitors. Reference [321, 322] relies on an analytic model with magnetization at the base of the jet growing as a function of time. This is intrinsically different from our work, which is based on post-processing of realistic 3D GRMHD collapsar jet simulations. Reference [321, 322] also overlooks the effects of jet-cocoon mixing and it considers neutrino production in uncollimated jets in collapsars, while our benchmark jets are naturally collimated by the cocoon. Uncollimated jets imply jet

energies that are orders of magnitude higher that those observed among GRBs and are thus not supported by observations.

7.9 CRITICAL OUTLOOK

In this section, we critically motivate our research from a state-of-the-art standpoint and provide an overview of our key findings. We also discuss possible future directions of our work.

7.9.1 *Overview and main findings*

As we outlined in Chapter 4, the differential energy fluxes measured by *Fermi* for high-energy gamma-rays [113], by IceCube for high-energy neutrinos [112] and by the Pierre Auger Observatory for UHE cosmic rays [114] are comparable. In principle, these observations hint towards a natural link between the diffuse fluxes of the high-energy messengers. Yet the excess of neutrinos compared to the gamma-ray flux between 10 TeV and 100 TeV disfavors the hypothesis that their high-energy diffuse fluxes originate from the same composition of sources.

To tackle the puzzle, jets launched by collapsing massive stars and choked within the stellar mantle have long been considered ideal candidate factories of the high-energy diffuse flux detected at IceCube. [122, 235, 237, 256]. The large radiation and matter densities inside the star naturally imply a large likelihood of producing neutrinos through $p\gamma$ and pp interactions, while effectively ensuring the absorption of high-energy gamma-rays throughout the entire jet lifetime.

The jet inhomogeneity causes fast shells to catch up and collide with slower ones, giving rise to internal shocks along the jet which, if collisionless, can accelerate particles. Shocks are said to be collisionless when they are mediated by plasma instabilities rather than by collisions, that is when the optical depth in the shock upstream $\tau \simeq \sigma_T n'_p R/\Gamma \lesssim 1$, where n'_p is the jet comoving baryon density and Γ is its Lorentz factor [247]. However, advanced GRMHD simulations of collapsar jets shed light on the highly non-linear evolution of the outflow inside the star. This behavior— attributed to the mixing between the jet and the cocoon— has been ignored in previous analytical models [222]. *In light of these insights, what is the neutrino signal produced*

by optically thick collapsar jets? Can these sources contribute to the diffuse flux of high-energy neutrinos when their non-linear evolution is taken into account? In our work, we tackle these questions.

Our research is a pioneering effort towards modeling neutrino production in opaque collapsar jets within a self-consistent framework. We achieve this by relying on the realistic evolution of the jet properties derived from state-of-the-art simulations, which naturally account for the complex interplay between the jet and the cocoon. Notably, this is the first time the neutrino signal from the innermost regions of collapsar jets is calculated by post-processing the outputs of GRMHD simulations.

As mentioned above, particle acceleration at internal shocks can take place when the upstream optical depth drops below unity, namely when $\tau \lesssim 1$. However, we find that the optical depth of the jetted outflow is $\gtrsim O(10^{11})$ up to radii $R \gtrsim 10^{12}$ cm, well above the stellar radius ($R_\star = 4 \times 10^{10}$ cm). We attribute this result to the jet-cocoon mixing, since the cocoon continuously loads the jet with baryons, effectively increasing the jet density n'_p and decreasing its Lorentz factor Γ. We conclude that particle acceleration is hindered at internal shocks occurring below the jet photosphere. Instead, we identify sub-shocks and magnetic reconnection as viable mechanisms for accelerating protons in this region. The former occur in the region $R \simeq 10^9 - 10^{10}$ cm, the latter can be triggered and sustained at radii $R \simeq 2 \times 10^8 - 2 \times 10^9$ cm.

Our findings yield pivotal advancements in several key areas. Firstly, the large magnetic fields and large radiation and baryon densities below the jet photosphere significantly limit the maximum energy achievable by accelerated protons. Likewise, secondary mesons undergo drastic cooling, resulting in the production of neutrinos with energies $\lesssim O(10^5)$ GeV. Importantly, our work reveals that subphotospheric neutrinos from collapsar jets are unlikely to produce the bulk of the high-energy neutrino diffuse flux detected at IceCube. This is in contrast with what was suggested in previous works which analytically model neutrino production in opaque collapsar jets, highlighting the importance of realistic models based on GRMHD simulations. Instead, we suggest that the search for these neutrinos could be successful with Hyper-Kamiokande IceCube DeepCore, where we expect to detect more than one neutrino event for bursts occurring at $z \lesssim O(0.1)$. Furthermore, the subphotospheric neutrino signal stands as a compelling smoking gun of jet magnetization, given that sub-shocks and magnetic reconnection can only occur in magnetized jets. Therefore, our study highlights the unique potential of subphotospheric neutrinos to unravel the enigmatic nature of collapsar jets.

7.9.2 *Future research directions*

Our work highlights the need for more accurate high-energy neutrino production models in future research. Possible directions to strengthen our results are outlined in the following:

1. *Increasing the initial jet magnetization.* Due to numerical instabilities, state-of-the-art numerical simulations cannot achieve initial jet magnetizations $\gtrsim O(100)$. However, in order to reproduce $\simeq O(100)$ Lorentz factors— typical of long GRBs, for instance— initial magnetizations $\gtrsim O(1000)$ are needed. Future works may overcome this limitation and provide more realistic insights into neutrino production in opaque jets.

2. *Modelling of magnetic reconnection in the optically thick regime.* The dependence of the magnetic reconnection rate on the outflow parameters in this regime is unclear, and existing works focus on collisionless plasmas. Our work highlights the importance of exploring PIC simulations of magnetic reconnection in the optically thick regime. Such studies could potentially offer fresh insights into the dependence of the proton spectral index and the fraction of energy stored in accelerated protons on the magnetization.

3. *Combining different GRMHD simulations*. The calculations presented in our work are carried out by relying on a single GRMHD simulation, whose jet is not representative of the whole population of collapsar jets. Post-processing more and different GRMHD simulations would allow us to explore a larger part of the parameter space, leading to broader conclusions.

4. *Simulating collapsars with an extended envelope surrounding the stellar core.* As mentioned in Sec. 7.5, realistic modeling of particle acceleration in this scenario is currently constrained by the limitations of state-of-the-art numerical simulations, which cannot track the jet above $\approx 10^{11}$ cm. Several transients may harbor jets choked in extended envelopes surrounding the stellar core, therefore we encourage performing GRMHD simulations within this set-up.

In summary, our research has paved the way for substantial improvements in the study of high-energy neutrino production below the photosphere of collapsar jets. Despite its limitations, our work is the first attempt of realistic modeling of particle acceleration in regions that are deeply embedded in the outflow. It also encourages searches of subphotospheric neutrinos with IceCube DeepCore and Hyper-Kamiokande,

in order to unlock the unique chance of probing the nature of collapsar jets. Further efforts in the outlined directions will significantly deepen our understanding of neutrino production in optically thick regions of the jet and will shed new light on the contribution of these sources to the high-energy neutrino flux detected at IceCube.

8

MULTI-MESSENGER DETECTION PROSPECTS OF GAMMA-RAY BURST AFTERGLOWS WITH OPTICAL JUMPS

Based on: **Ersilia Guarini**, Irene Tamborra, Damien Bégué, Tetyana Pitik, Jochen Greiner *Multi-messenger detection prospects of gamma-ray burst afterglows with optical jumps*, JCAP 06 (2022) 06, 034, arXiv:2112.07690

ABSTRACT Some afterglow light curves of gamma-ray bursts (GRBs) exhibit very complex temporal and spectral features, such as a sudden intensity jump about one hour after the prompt emission in the optical band. We assume that this feature is due to the late collision of two relativistic shells and investigate the corresponding high-energy neutrino emission within a multi-messenger framework, while contrasting our findings with the ones from the classic afterglow model. For a constant density circumburst medium, the total number of emitted neutrinos can increase by about an order of magnitude when an optical jump occurs with respect to the self-similar afterglow scenario. By exploring the detection prospects with the IceCube Neutrino Observatory and future radio arrays such as IceCube-Gen2 radio, RNO-G and GRAND200k, as well as the POEMMA spacecraft, we conclude that the detection of neutrinos with IceCube-Gen2 radio could enable us to constrain the fraction of GRB afterglows with a jump as well as the properties of the circumburst medium. We also investigate the neutrino signal expected for the afterglows of GRB 100621A and a GRB 130427A-like burst with an optical jump. The detection of neutrinos from GRB afterglows could be crucial to explore the yet-to-be unveiled mechanism powering the optical jumps.

8.1 INTRODUCTION

Gamma-ray bursts (GRBs) are among the brightest and most poorly understood transients occurring in our Universe [133, 134, 185]. There are two classes of GRBs; the short ones, lasting less than 2 s, and the long ones [323, 324]. The latter are the focus of this work. They are thought to be harbored within collapsing

massive stars [325–327]. The isotropic equivalent energy release in gamma-rays spans 10^{49}–10^{55} erg and it occurs within a few tens of seconds [133, 328]. The observed spectrum is non-thermal, typically peaking in the 10–10^4 keV energy band [329–331].

The delayed emission following the prompt phase of GRBs—observed in the X-ray, optical/infrared, radio and as of recently TeV bands [108, 136, 332, 333]—is the so-called afterglow. It is observed for several weeks after the trigger of the burst and, in some cases, up to months or even years, making GRBs electromagnetically detectable across all wavebands. The afterglow emission results from the interaction between the ejecta and the circumburst medium (CBM). The physical mechanism responsible for the multi-wavelength observation is broadly believed to be synchrotron radiation from the relativistic electrons accelerated at the external shock, developing when the relativistic outflow expands in the CBM [136–138, 334].

Observations in the X-ray and optical bands show a rich set of additional features, not described by the simplest afterglow model. At X-rays, data from the Gehrels Swift Observatory display a rapid decline during the first few hundred seconds [335–337], strong X-ray flaring during the first few thousand seconds [338, 339], and a shallow decay up to ten-thousand seconds. A canonical view of GRB afterglow is presented in e.g. [340, 341]. In the optical band, the forward [e.g., 342] and reverse shocks [e.g., 343, 344] dominate during the first thousand seconds, together with plateaus in the majority of afterglows, and with X-ray flares, occasionally accompanyied by optical flares [345, 346]. At later times [i.e., at about 7–$10(1+z)$ days, with z being the redshift], the supernova signal emerges [347, 348] [1]. In this context, one of the biggest surprises was the observation of sudden rebrightenings in the afterglow light curve occurring at one to few hours after the prompt emission, primarily visible in the optical band (hereafter called optical jump) [349–353]. These optical jumps are very rare, as opposed to e.g. X-ray flares occurring in about 50% of all GRB afterglows. The optical jump can be very large in amplitude (>1 mag) and is typically brighter than the one observed in X-rays. So far, about 10 out of 146 GRBs with well sampled optical light curves collected between February 1997 and November 2011 have displayed an optical jump [354]; for half of these, the brightness at the jump peak is comparable to the peak of the afterglow associated to the forward shock.

Several theoretical models attempt to explain such optical jumps. For instance, they might be due to CBM inhomogeneities generated by anisotropic wind ejection of the GRB progenitor or interstellar turbulence [355, 356]; however, numerical simulations of spherical explosions exhibit rather regular features and, in addition, density fluctuations of the CBM cannot give rise to significant time variability in the

1 It is worth highlighting that we are only listing typical values for all the aforementioned timescales.

afterglow light curve [357–359]. Alternatively, the late variability of the afterglow light curve could be explained by invoking a late energy injection in the first blast wave emitted by the central engine. In this picture, the central engine undergoes intermittent late explosions, producing multiple shells of matter that propagate and collide with the slower ones previously emitted, as proposed in Ref. [360]. The origin of the late time activity of the central engine is unclear [361]. For example, it might be related to the disk fragmentation due to gravitational instabilities in the outer regions of the disk, with the resulting fragments being accreted into the central compact object over different timescales, and causing the observed time variability in the afterglow light curve [362]. Despite the uncertain origin of the central engine late time activity, this model predicts that the second blast wave emitted by the central engine injects new energy in the initially ejected one, causing the observed rebrightening in the light curve [363, 364]. Even though there is to date no smoking-gun signature favoring a specific mechanism to explain the appearance of optical jumps, the late collision of two relativistic shells [360] is appealing in light of its ability to successfully fit the light curves of some GRBs with optical jumps [352, 365].

These peculiar features of the light curve of GRB afterglows raise questions on the possibly related neutrino emission. In fact, GRBs have been proposed as sources of ultra-high energy cosmic rays and high-energy neutrinos [36, 224, 225]. In the prompt phase, a copious amount of neutrinos could be produced by photo-hadronic ($p\gamma$) [224, 225, 227] or hadronic interactions (pp or pn), the latter being more efficient in the innermost regions where the baryon density is large [228–230, 247]. The neutrinos produced during the prompt GRB phase in the optically thin region have TeV–PeV energies, and their spectral distribution strongly depends on the emission mechanism [224, 231, 246, 366–369].

High energy neutrinos could also be produced during the afterglow phase through $p\gamma$ interactions in the PeV–EeV energy range. Protons can be accelerated in the blastwave through Fermi acceleration [139, 370] and interact with the synchrotron photons produced by accelerated electrons. Within the framework of the classic afterglow model, the neutrino emission from GRB afterglows has been computed by considering the interaction of the GRB blastwave with the external medium in two possible scenarios: the forward shock one, according to which particles are accelerated at the shock between the blastwave and the CBM [226, 232, 371, 372] and the reverse shock model, that assumes acceleration of particles at the reverse shock propagating back towards the ejecta [373].

Since the neutrino production during the GRB afterglow phase strictly depends on the photon distribution, an increase of the photon flux as observed for late time jumps in the light curve should result in an increased neutrino flux, potentially detectable by current and future high energy neutrinos facilities. In fact, optical photons are ideal targets for the production of PeV neutrinos. The detection prospects with the IceCube Neutrino Observatory, which routinely observes neutrinos with energies up to a few PeV [37, 112, 374, 375], of GRB afterglows displaying an optical jump have not been investigated up to now. In addition, the possibly higher neutrino flux could be detectable by upcoming detectors, such as IceCube-Gen2 and its radio extension [16], the Radio Neutrino Observatory in Greenland (RNO-G) [176] and the full planned configuration of the Giant Radio Array for Neutrino Detection (GRAND200k) [17]. The orbiting Probe of Extreme Multi-Messenger Astrophysics (POEMMA) spacecraft may also have promising perspectives for the detection of neutrinos from GRB afterglows [376].

If a jump is observed in the optical light curve of a GRB, what is its signature in neutrinos? Can we use neutrinos to learn more about this enigmatic feature of some GRBs? In this paper, we address these questions and explore the corresponding neutrino detection prospects. Our reference model is the late collision of two relativistic shells [352, 360, 365]. Nevertheless, we stress that our goal is not to prove that the shell collision is the main mechanism explaining the GRBs light curves displaying jumps; rather, this scenario provides us with the framework within which we aim explore the associated neutrino signal.

This paper is organized as follows. In Sec. 8.2, we present the theoretical model for the late collision of two relativistic shells that we consider to be the mechanism responsible for the sudden jump in the afterglow light curve. Section 8.3 focuses on the modeling of the electromagnetic signal from GRB afterglows in the presence of optical jumps, while Sec. 8.4 is centered on the proton distribution in the blastwave and the resulting neutrino signals. Section 8.5 presents our findings on the neutrino and photon signals expected during the GRB afterglow phase, in the absence as well as in the presence of optical jumps; while Sec. 8.6 investigates the neutrino detection prospects in the context of quasi-diffuse and point source searches. In particular, we discuss the neutrino detection prospects for the well studied GRB 100621A [352] and a burst with model parameters inspired by GRB 130427A [377–379] having a hypothetical optical jump. Finally, our findings are summarized in Sec. 8.7. The analytical model on the late collision and merger of two relativistic shells is detailed in Appendix B.1, a discussion on the degeneracies among the parameters of our model is

reported in Appendix B.2, while Appendix B.3 focuses on the cooling times of protons and mesons of our GRB afterglow model.

8.2 MODELLING OF THE MERGER OF TWO RELATIVISTIC SHELLS

In this section, we outline the blastwave physics, introducing the scaling relations describing the temporal evolution of the radius and Lorentz factor of the blastwave. By relying on the late activity scenario for the central engine [341, 361, 380, 381], our model on the late collision of two relativistic shells is then presented.

8.2.1 *Physics of the blastwave*

According to the standard picture, the relativistic GRB jet propagates with half opening angle θ_j and Lorentz factor $\Gamma \gg 100$ [324] in the reference frame of the central engine. As long as $\Gamma^{-1} < \theta_j$, the emitting region can approximately be considered spherical. In order to investigate the afterglow physics, it is useful to introduce the isotropic equivalent energy of the blastwave, $\tilde{E}_{\rm iso}$ [2]. We denote with $\tilde{E}_{k,\rm iso}$ the isotropic equivalent kinetic energy of the blastwave, defined as $\tilde{E}_{k,\rm iso} = \tilde{E}_{\rm iso} - \tilde{E}_{\gamma,\rm iso}$ and representing the energy content of the outflow after $\tilde{E}_{\gamma,\rm iso}$ has been released in γ-rays during the prompt phase.

Two shocks develop at the interaction front between the burst and the CBM: a reverse shock, that propagates towards the core of the jet, and a forward shock propagating in the CBM. After the reverse shock crosses the relativistic ejecta, the blastwave enters the so-called Blandford and McKee self-similar regime [382] (dubbed BM hereafter). In the following, we focus on the BM phase, during which the emission is associated with the forward shock only. The particle density profile of the CBM is assumed to scale as a function of the distance from the central engine as $n \propto R^{-k}$. In this work, we consider two CBM scenarios: a constant density profile resembling the one of the interstellar medium ($k = 0$, ISM) and a stellar wind one ($k = 2$, wind).

We assume that the ejecta initially have isotropic kinetic energy $\tilde{E}_{k,\rm iso}$ and Lorentz factor Γ_0. Two extreme scenarios for the hydrodynamical evolution of the blastwave can be described analytically: fully adiabatic

2 We adopt three reference frames: the blastwave comoving frame, the center of explosion (i.e. the central compact object) frame, and the observer frame (the Earth). Quantities in these frame are denoted as X', $\tilde{X}$ and X, respectively. Energy, for example, transforms as $\tilde{E} = (1+z)E = \mathcal{D}E'$. Here z is the redshift and $\mathcal{D} = [\Gamma(1-\beta\cos\theta)]^{-1}$ is the Doppler factor, where $\beta = \sqrt{1-1/\Gamma^2}$ and θ is the angle of propagation of an element of the ejecta relative to the line of sight.

and fully radiative [382, 383]. In the former case, the blastwave does not radiate a significant amount of energy while propagating. On the contrary, it quickly cools in the latter scenario, radiating all the internal energy released in the shock while being decelerated by the CBM. Observational evidence suggests that GRB afterglow blastwaves are in the adiabatic regime rather than in the radiative one [107]. Therefore, in this paper we focus on the adiabatic scenario.

Within the assumption of a thin shell (for which the reverse shock is mildly relativistic at most), if propagation occurs through a CBM with constant density $n = n_0$, the blastwave starts to be decelerated at [107, 382]:

$$T_{\rm dec,ISM} = \left[\frac{3\tilde{E}_{k,\rm iso}(1+z)^3}{64\pi n_0 m_p c^5 \Gamma_0^8}\right]^{1/3} ; \tag{8.1}$$

while if it occurs in a wind profile, $n = AR^{-2}$, the deceleration occurs at [384]:

$$T_{\rm dec,wind} = \frac{\tilde{E}_{k,\rm iso}(1+z)}{16\pi A m_p c^3 \Gamma_0^4} , \tag{8.2}$$

where $A = \dot{M}_w/(4\pi v_w m_p) = 3.02\times10^{35} A_\star$ cm^{-1}, with $A_\star = \dot{M}_{-5}/v_8$ corresponding to the typical mass loss rate $\dot{M}_{-5} = \dot{M}/(10^{-5} M_\odot)$ yr^{-1} and wind velocity $v_8 = v_w/(10^8$ cm s$^{-1})$ [372, 385] [3]. Here $c = 3\times10^{10}$ cm s^{-1} is the speed of light and $m_p = 0.938$ GeV c^{-2} is the proton mass.

After the deceleration begins, the Lorentz factor of the shell decreases with time as [382–384, 386]:

$$\Gamma_{\rm ISM} = \Gamma_0\left(\frac{T_{\rm dec,ISM}}{4t}\right)^{3/8} ; \tag{8.3}$$

$$\Gamma_{\rm wind} = \Gamma_0\left(\frac{T_{\rm dec,wind}}{4t}\right)^{1/4} ; \tag{8.4}$$

The radius of the blastwave evolves with time according to [372]:

$$R = \frac{\zeta\Gamma^2 tc}{(1+z)} , \tag{8.5}$$

where the correction factor ζ depends on the hydrodynamical evolution of the shock; we assume $\zeta = 8$ [372, 383, 387].

In this work we are mainly interested in estimating the neutrino signal, whose accuracy is mainly dominated by other local uncertainties (e.g. the proton acceleration efficiency and the fraction of the blastwave internal energy that goes into accelerated protons, that we introduce in Sec. 8.4.1). Hereafter, we adopt the uniform

3 Care should be taken when comparing our definition of the density profile for a wind CBM (which follows the convetion adopted in e.g. Ref. [133]) with the one often adopted in the literature, i.e. $\rho = AR^{-2}$, where $A = 5\times10^{-11}$ g cm^{-1} A$_\star$ and $A_\star = \dot{M}_{-5}/v_8$. The difference between the two definitions is the normalization in units of proton mass.

shell approximation of the BM solution, as presented in this section. This assumption suits our purposes, since the particle density of a BM shell quickly drops outside the region of width $\propto R/\Gamma^2$ behind the forward shock and thus the corresponding neutrino emission is negligible.

8.2.2 *Merger of two relativistic shells*

The late merger of two relativistic shells has been investigated through hydrodynamical simulations [360] and applied to fit the light curve of GRB 100621A [352]. However, a simplified analytical modeling aiming to estimate the corresponding neutrino signal is presented in this paper for the first time. We assume that the first shell is launched by the central engine. At the onset of its deceleration, it is heated up, as its kinetic energy $\tilde{E}_{k,\mathrm{iso}}$ is converted in internal energy $\tilde{W}$. From now on, we refer to this shell as the "slow shell." Its dynamics is described by the simplified BM solution in the uniform blastwave approximation introduced in Sec. 8.2.1, its Lorentz factor Γ and radius R evolve by following Eq. 8.3 and Eq. 8.5, respectively.

Assuming that the central engine undergoes late activity, a second shell with energy $\tilde{E}_f$ is emitted with a time delay Δ_T with respect to the slow one, see the left panel of Fig. 37. We refer to this second shell as the "fast shell." This shell propagates in an almost empty environment since most of the matter has been swept up by the slow shell [360]. Thus, the fast shell moves with a constant Lorentz factor Γ_f, eventually reaches the slow shell, and merges with it, as sketched in the middle and right panels of Fig. 37. Details on the analytical model describing the shell merger and the related conserved quantities are reported in Appendix B.1.

In order for the collision to happen at a given time T_{coll}, the slow and fast shells must be at the same position at $t = T_{\mathrm{coll}}$: $R(T_{\mathrm{coll}}) = R_f(T_{\mathrm{coll}})$. As extensively discussed in Appendix B.2, this condition gives rise to a degeneracy between Γ_f and Δ_T (see also Appendix C of [365] for a similar discussion). Indeed, a shell launched with a large delay and large speed could reach the slow shell at the same time of a slower shell launched with a smaller time delay. Understanding this degeneracy among the characteristic shell parameters is important, since Γ_f directly affects the dynamics of the collision between the two shells.

As the slow and fast shells collide, two shocks develop: a reverse shock, propagating back towards the fast shell, and a forward shock, propagating through the slow shell. A detailed modeling of the collision between the fast and the slow shell is not necessary to estimate the production of neutrinos. Therefore, we assume that both the forward and reverse shocks created in the shell collision instantly cross the slow (forward shock) and

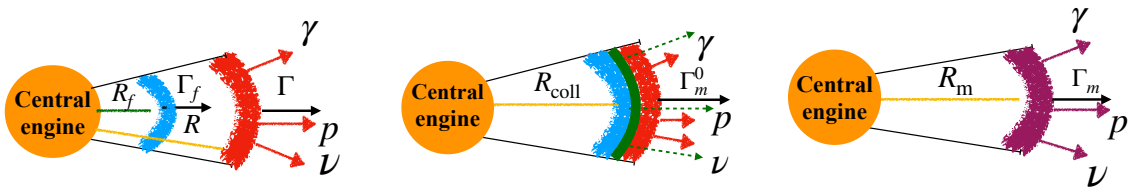

Figure 37: Sketch of the collision and merger of two relativistic shells (not in scale). *Left panel*: The slow shell (marked in red) is launched by the central engine and decelerated by the interaction with the external medium. A shock develops at the contact surface, leading to the classic afterglow emission. The fast shell (marked in blue) is launched by the central engine with a temporal delay Δ_T and propagates freely. *Middle panel* : The fast shell reaches the slow BM blastwave. Two shocks develop at the collision (marked in green); the internal energy released in this process is emitted through radiation of secondary particles. *Right panel:* The merged shell (plotted in purple) propagates through the external medium, emitting afterglow radiation.

the fast (reverse shock) shell, which thus merge in a single shell at $T_{\rm coll}$. In other words, when the collision occurs, a hot "merged" shell instantaneously forms as described in Appendix B.1; see the right panel of Fig. 37. Despite the simplifying assumption of instantaneous merger between the two shells, our overarching goal of computing the time-integrated neutrino event rate is not affected since the neutrino emission during the merger interval is overall negligible, see discussion in Sec. 8.5.

In order to characterize the properties of the merged shell, we apply the energy-momentum conservation equations, expanding on the model describing the collision of two relativistic shells for the internal shock scenario employed to model the prompt phase [291, 292]. The main difference with respect to the internal shock scenario [291, 292] is that our slow shell is hot and is sweeping up material from the external medium. Thus, we need to include the internal energy of the slow shell and the swept up mass in our calculation. As discussed in Appendix B.1, the following equations are obtained within the assumption of instantaneous merger. Therefore, we evaluate the quantities describing the slow and the fast shells at time $t = T_{\rm coll}$. The initial Lorentz factor of the merged shell is

$$\Gamma_m^0 \simeq \sqrt{\frac{m_f \Gamma_f + m_{\rm eff}\Gamma}{m_f/\Gamma_f + m_{\rm eff}/\Gamma}}\,, \tag{8.6}$$

where $m_f = \tilde{E}_f/(\Gamma_f c^2)$ is the mass of the fast shell and $m_{\rm eff} = m + \hat{\gamma}W'/(c^2)$ is the effective mass of the slow shell. Here $\hat{\gamma} = 4/3$ is the adiabatic index in the relativistic limit (which holds since the slow shell is hot) and m is the mass of the slow shell, i.e. the sum between the initial mass of the ejecta $m_0 = \tilde{E}_{\rm iso}/(\Gamma_0 c^2)$ and the swept up mass from the CBM up to the radius R,

$$m = m_0 + 4\pi \int_0^R dR' R'^2 n(R') m_p\,. \tag{8.7}$$

Furthermore, at the collision, the internal energy $\tilde{W}_m^0$ is generated:

$$\tilde{W}_m^0 \equiv \Gamma_m^0 W_m'^0 = \frac{1}{\hat{\gamma}} \left[(m_f \Gamma_f + m\Gamma)c^2 - (m + m_f)\Gamma_m^0 c^2 \right] + \Gamma W' \,. \tag{8.8}$$

In the last stage of evolution, the merged shell moves in the CBM and interacts with it, giving rise to the standard afterglow radiation. Note that another degeneracy occurs. In fact, the same value of Γ_m^0 can be obtained for different pairs of $(\tilde{E}_{k,\rm iso}, n_0)$ or $(\tilde{E}_{k,\rm iso}, A_\star)$. Thus, different initial conditions can lead to the same initial setup of the merged shell, nevertheless as discussed in Appendix B.2 and in Sec. 8.3, this degeneracy is not reflected in the observed photon flux.

The dynamics of the slow shell depends on the comoving dynamical time [372],

$$t'_{\rm dyn} \simeq \frac{R}{8\Gamma c} \,, \tag{8.9}$$

and the related comoving width is [382]

$$l' \simeq c t'_{\rm dyn} = \frac{R}{8\Gamma} \,, \tag{8.10}$$

where the radius R is defined in Eq. 8.5.

The fast shell propagates with constant Lorentz factor $\Gamma_f \gg 1$, thus its radius evolves as [133]:

$$R_f = \frac{2\Gamma_f^2 (t - \Delta_T) c}{(1+z)} \,. \tag{8.11}$$

The comoving dynamical time of the fast shell is given by

$$t'_{\rm dyn,f} \simeq \frac{R_f}{2\Gamma_f c} \,, \tag{8.12}$$

and its comoving width is

$$l'_f \simeq c t'_{\rm dyn,f} = \frac{R_f}{2\Gamma_f} \,. \tag{8.13}$$

The initial width of the merged shell is approximated as

$$l_m'^0 \simeq \Gamma_m^0 \left(\frac{l'_f}{\Gamma_f} + \frac{l'}{\Gamma} \right) ; \tag{8.14}$$

while the dynamical time characterizing the merged shell at the collision is

$$t'^0_{\rm dyn,m} \simeq \frac{l_m'^0}{c} \,, \tag{8.15}$$

where we have considered the Lorentz transformation for the length between the comoving and laboratory frames.

After a transient phase during which the merged shell relaxes, it is decelerated by the CBM and enters the BM regime. Since we neglect the time needed by the merged shell to relax soon after the merger, a sharp jump results in the light curve; this treatment is not adequate for realistic fits of the electromagnetic signal, see Sec. 8.3.2 for a discussion, but such task is beyond the scope of this paper. The semi-analytical treatment of the hydrodynamics of the collision, also taking into account the reverse shock crossing the fast shell was obtained in Ref. [363]; considering such a treatment would not substantially affect the neutrino signal, since current and future neutrino telescopes may only be sensitive to the time-integrated spectral distribution in the most optimistic scenarios (see Sec. 8.6).

Once the merged shell enters the BM regime, its Lorentz factor Γ_m evolves as described by Eqs. 8.3, by replacing $\Gamma_0 \rightarrow \Gamma_m^0$ and using the appropriate deceleration time. Indeed, even though the dynamics of the merged shell resembles the BM solution, there are some important and non trivial precautions to take into account for the definition of its deceleration radius and time , see Appendix B.1. This is due to the fact that the merged shell is already hot and contains swept-up material. Once the deceleration time of the merged shell is properly defined, its radius R_m follows Eq. 8.5 by replacing $\Gamma \rightarrow \Gamma_m$. Finally, the width and dynamical time of the merged shell after its deceleration are given by Eqs. 8.9 and 8.10, with $\Gamma \rightarrow \Gamma_m$ and $R \rightarrow R_m$.

8.3 PHOTON ENERGY DISTRIBUTION AND LIGHT CURVE

In this section, we introduce the main ingredients for the modeling of the emission of electromagnetic radiation during the classic afterglow and at the shell merger which produces the optical jump. In the following, we consider a generic shell with Lorentz factor Γ for the sake of simplicity, however our treatment holds for the afterglow generated both by the slow and the merged shell. The proper Lorentz factor has to be taken into account for each case, i.e. Eqs. 8.3 and 8.4 for the slow and the merged shell during the afterglow with the appropriate initial Lorentz factor and deceleration time, as discussed in Sec. 8.2.2. As for the collision, the relevant Lorentz factor is given by Eq. 8.6.

8.3.1 *Photon energy distribution during the afterglow*

It is assumed that particles undergo Fermi acceleration [139, 370, 388] at the forward shock. The synchrotron radiation coming from shock accelerated electrons is broadly considered to be the origin of the observed afterglow light curve [383]. For the modeling of the synchrotron photon spectrum, we follow Refs. [383, 385, 389]. The internal energy density of the blastwave is given by the shock jump conditions (Eqs. B.3 and B.4). Therefore, the internal energy density generated by the forward shock is [382]:

$$w' = 4m_p c^2 \Gamma(\Gamma - 1) n \,, \tag{8.16}$$

where $n = n_0$ and $n = AR^{-2}$ for the ISM and wind scenarios, respectively. A fraction ϵ_e of this energy goes into accelerated electrons, a fraction ϵ_B into magnetic field, while protons receive the fraction $\epsilon_p \lesssim 1 - \epsilon_e - \epsilon_B$. Thus, the magnetic field generated by the shock at the BM blastwave front is

$$B' = \sqrt{32\pi m_p c^2 n \Gamma(\Gamma - 1)\epsilon_B} \,. \tag{8.17}$$

Electrons are expected to be accelerated to a power-law distribution $N_e(\gamma_e) \propto \gamma_e^{-k_e}$, where k_e is the electron spectral index. The resulting electron distribution has three characteristic Lorentz factors: minimum ($\gamma'_{e,\rm min}$), cooling ($\gamma'_{e,\rm cool}$), and maximum ($\gamma'_{e,\rm max}$) ones. The minimum Lorentz factor corresponds to the minimum injection energy of electrons in the blastwave; the cooling Lorentz factor characterizes the energy of electrons that have time to radiate a substantial fraction of their energy in one dynamical time; the maximum Lorentz factor corresponds to the maximum energy that electrons can achieve in the acceleration region [107, 383]. These characteristic Lorentz factors are given by [383]:

$$\gamma'_{e,\rm min} = \epsilon_e \frac{m_p}{m_e} \frac{(k_e - 2)}{(k_e - 1)} (\Gamma - 1) \,, \tag{8.18}$$

$$\gamma'_{e,\rm cool} = \frac{6\pi m_e c}{\sigma_T B'^2} \frac{(1+z)}{t\Gamma} \,, \tag{8.19}$$

$$\gamma'_{e,\rm max} = \left(\frac{6\pi e}{\sigma_T B' \xi} \right)^{1/2} \,, \tag{8.20}$$

where $\sigma_T = 6.65 \times 10^{-25}$ cm^{-2} is the Thompson cross section, ξ represents the number of gyroradii needed for accelerating particles, $m_e = 5 \times 10^{-4}$ GeV c^{-2} is the electron mass and $e = \sqrt{\alpha \hbar c}$ is the electron charge, where $\alpha \sim 1/137$ is the fine-structure constant and $\hbar \simeq 6.58 \times 10^{-25}$ GeV s is the reduced Planck constant.

We take $\xi \equiv 10$ [390]. The three characteristic Lorentz factors result into three observed characteristics break energies $E_{\gamma,\rm min}$, $E_{\gamma,\rm cool}$ and $E_{\gamma,\rm max}$, in the synchrotron photon spectrum at Earth:

$$E_\gamma \equiv h\nu_\gamma = \frac{3}{2}\frac{B'}{B_Q} m_e c^2 {\gamma'_e}^2 \frac{\Gamma}{(1+z)} \,, \tag{8.21}$$

where $B_Q = 4.41 \times 10^{13}$ G. The electrons are in the "fast cooling regime" when $\nu_{\gamma,\rm min} > \nu_{\gamma,\rm cool}$, while the "slow cooling regime" occurs when $\nu_{\gamma,\rm min} < \nu_{\gamma,\rm cool}$.

For the picture to be complete, the synchrotron self-absorption (SSA) frequency should be considered as well. However, properly accounting for the SSA requires detailed information about the shell structure and the eventual thermal electron distribution [391]. Since this frequency is expected to be in the radio band [107], and since its inclusion does not change the results presented herein, we neglect SSA in the rest of this paper.

We are interested in the comoving photon density in the blastwave [in units of $\rm GeV^{-1}\ cm^{-3}$]. In the fast cooling regime, it is given by [383, 392]:

$$n'_\gamma(E'_\gamma) = A'_\gamma \begin{cases} \left(E'_\gamma/E'_{\gamma,\rm cool}\right)^{-2/3} & E'_\gamma < E'_{\gamma,\rm cool} \\ \left(E'_\gamma/E'_{\gamma,\rm cool}\right)^{-3/2} & E'_{\gamma,\rm cool} \le E'_\gamma \le E'_{\gamma,\rm min} \\ \left(E'_{\gamma,\rm min}/E'_{\gamma,\rm cool}\right)^{-3/2} \left(E'_\gamma/E'_{\gamma,\rm min}\right)^{-(k_e+2)/2} \mathrm{e}^{-\frac{E'_\gamma}{E'_{\gamma,\rm max}}} & E'_{\gamma,\rm min} < E'_\gamma \le E'_{\gamma,\rm max} \end{cases} ; \tag{8.22}$$

while, in the slow cooling regime, it is

$$n'_\gamma(E'_\gamma) = A'_\gamma \begin{cases} \left(E'_\gamma/E'_{\gamma,\rm min}\right)^{-2/3} & E'_\gamma < E'_{\gamma,\rm min} \\ \left(E'_\gamma/E'_{\gamma,\rm min}\right)^{-(k_e+1)/2} & E'_{\gamma,\rm min} \le E'_\gamma \le E'_{\gamma,\rm cool} \\ \left(E'_{\gamma,\rm cool}/E'_{\gamma,\rm min}\right)^{-(k_e+1)/2} \left(E'_\gamma/E'_{\gamma,\rm cool}\right)^{-(k_e+2)/2} \mathrm{e}^{-\frac{E'_\gamma}{E'_{\gamma,\rm max}}} & E'_{\gamma,\rm cool} < E'_\gamma \le E'_{\gamma,\rm max} \end{cases} . \tag{8.23}$$

Here $E'_\gamma \equiv h\nu'_\gamma$ is the comoving photon energy. The normalization constant is

$$A'_\gamma = \frac{1}{2}\frac{L'_{\gamma,\rm max}}{4\pi R^2 c\ \min(E'_{\gamma,\rm min}, E'_{\gamma,\rm cool})} \,, \tag{8.24}$$

where $L'_{\gamma,\rm max} = N_e P'_{\rm max}(\gamma'_{e,\rm min})\phi_e/(E'_{\gamma,\rm min})$ is the comoving specific luminosity [in units of $\rm s^{-1}$], and $1/2$ is the geometrical correction coming from the assumption of isotropic synchrotron emission in the comoving frame [226]. The number of electrons in the blastwave is $N_e = 4/3\pi n_0 R^3$ in the ISM scenario and $N_e = 4\pi A R$ in the wind scenario, while $P'_{\rm max}(\gamma'_{e,\rm min})$ is the maximum synchrotron power emitted by electrons with Lorentz factor $\gamma'_{e,\rm min}$ and defined as $P'_{\rm max}(\gamma'_{e,\rm min}) = c\sigma_T {B'}^2 {\gamma'}^2_{e,\rm min}/(6\pi)$. Finally, $\phi_e \simeq 0.6$ is a constant depending on the spectral index k_e [393]; we adopt $k_e = 2.5$, as suggested from simulations of relativistic collisionsless shocks [85, 394]. This value is also consistent with that obtained from the study of X-ray

afterglows, see e.g. [395]. Note that for the classic afterglow, we consider the transition from fast to slow cooling through the time evolution of the blastwave. Indeed, at late times the blastwave is in the slow cooling regime, in agreement with observations (see e.g. [396, 397]).

8.3.2 *Photon energy distribution during the shell merger*

When the two shells collide, the internal energy $\tilde{W}^0_m$ is released, see Eq. 8.8[4]. Assuming that $\epsilon^0_{B,m}$ is the fraction of the internal comoving energy density released during the collision and going in magnetic energy density, the comoving magnetic field is

$$B'^0_m = \sqrt{8\pi\epsilon^0_{B,m} w'^0_m}\,, \tag{8.25}$$

where the comoving internal energy density is defined as

$$w'^0_m = \frac{\tilde{W}^0_m}{\Gamma^0_m V'_m} = \frac{\tilde{W}^0_m}{\Gamma^0_m 4\pi R(T_{\rm coll})^2 l'^0_m}\,, \tag{8.26}$$

where l'^0_m is given by Eq. 8.14 and $V'^0_m = 4\pi R(T_{\rm coll})^2 l'^0_m$ is the volume of the merged shell right after its creation.

We assume that, at the collision, electrons are accelerated with the same index as the one of the particles accelerated at the shock between the slow blastwave and the CBM ($k_e = 2.5$). The fraction $\epsilon^0_{e,m}$ of internal energy density released at the collision goes into accelerated electrons, which cool through synchrotron radiation. The characteristic energies of the resulting photon spectrum are $E^{m,0}_{\gamma,\rm min}$, $E^{m,0}_{\gamma,\rm cool}$ and $E^{m,0}_{\gamma,\rm max}$ and are defined as in Eq. 8.21 by replacing $\Gamma \rightarrow \Gamma^0_m$, and where the magnetic field is given by Eq. 8.25.

The shell collision and the afterglow are two distinct processes. The former involves a hot and a cold shell, the latter is related to the interaction between the slow, hot shell and the cold CBM. Therefore, the microphysical parameters $\epsilon^0_{e,m}$ and $\epsilon^0_{B,m}$ do not need to be the same as ϵ_e and ϵ_B. Moreover, while observations suggest a slow cooling regime for the classic afterglow at late times, electrons accelerated at the collision might be either in the fast or in the slow cooling regime, depending on the relevant parameters.

4 For the sake of clarity, we denote the physical quantities characteristic of shell collision with the apex "0", to distinguish them from the parameters describing the deceleration phase of the merged shell (marked with the subscript "m").

If for fixed initial conditions of the colliding shells and collision time the condition $\gamma'^{m,0}_{e,\min} > \gamma'^{m,0}_{e,\mathrm{cool}}$ is verified, then the spectral energy distribution at the collision is

$$n'^{m,0}_{\gamma}(E'_\gamma) = A'^{m,0}_{\gamma} \begin{cases} \left(E'_\gamma / E'^{m,0}_{\gamma,\mathrm{cool}}\right)^{-2/3} & E'_\gamma < E'^{m,0}_{\gamma,\mathrm{cool}} \\ \left(E'_\gamma / E'^{m,0}_{\gamma,\mathrm{cool}}\right)^{-3/2} & E'^{m,0}_{\gamma,\mathrm{cool}} \leq E'_\gamma \leq E'^{m,0}_{\gamma,\min} \\ \left(E'^{m,0}_{\gamma,\min} / E'^{m,0}_{\gamma,\mathrm{cool}}\right)^{-3/2} \left(E'_\gamma / E'^{m,0}_{\gamma,\min}\right)^{-(k_e+2)/2} \mathrm{e}^{-\frac{E'_\gamma}{E'^{m,0}_{\gamma,\max}}} & E'^{m,0}_{\gamma,\min} < E'_\gamma \leq E'^{m,0}_{\gamma,\max} \end{cases} , \tag{8.27}$$

where

$$A'^{m,0}_{\gamma} = \frac{\epsilon^0_{e,m} w'^0_m}{\int_{\gamma'^{m,0}_{\min}}^{\gamma'^{m,0}_{\mathrm{sat}}} dE'_\gamma n'^{m,0}_{\gamma}(E'_\gamma) E'_\gamma} . \tag{8.28}$$

If instead $\gamma'^{m,0}_{e,\min} < \gamma'^{m,0}_{e,\mathrm{cool}}$, then the photon density is properly described by a slow cooling spectrum

$$n'^{m,0}_{\gamma}(E'_\gamma) = A'^{m,0}_{\gamma} \begin{cases} \left(E'^{m,0}_{\gamma} / E'^{m,0}_{\gamma,\min}\right)^{-2/3} & E'_\gamma < E'^{m,0}_{\gamma,\min} \\ \left(E'^{m,0}_{\gamma} / E'^{m,0}_{\gamma,\min}\right)^{-(k_e+1)/2} & E'^{m,0}_{\gamma,\min} \leq E'_\gamma \leq E'^{m,0}_{\gamma,\mathrm{cool}} \\ \left(E'^{m,0}_{\gamma,\mathrm{cool}} / E'^{m,0}_{\gamma,\min}\right)^{-(k_e+1)/2} \left(E'_\gamma / E'^{m,0}_{\gamma,\mathrm{cool}}\right)^{-(k_e+2)/2} \mathrm{e}^{-\frac{E'_\gamma}{E'^{m,0}_{\gamma,\max}}} & E'^{m,0}_{\gamma,\mathrm{cool}} < E'_\gamma \leq E'^{m,0}_{\gamma,\max} \end{cases} . \tag{8.29}$$

where

$$A'^{m,0}_{\gamma} = \frac{\epsilon^0_{e,m} w'^0_m}{\int_{\gamma'^{m,0}_{\min}}^{\gamma'^{m,0}_{\mathrm{sat}}} dE'_\gamma n'^{m,0}_{\gamma}(E'_\gamma) E'_\gamma} \left(\frac{\gamma'^{m,0}_{e,\mathrm{cool}}}{\gamma'^{m,0}_{e,\min}}\right)^{(-k_e+2)} . \tag{8.30}$$

In the last expression we have taken into account the fact that only a fraction of electrons radiates.

8.3.3 *Light curve*

We now have all the ingredients for investigating the expected light curve if the merger of two relativistic shells occurs. We can distinguish between three time windows in the photon light curve: an "afterglow phase" ($T_{\mathrm{dec}} \leq t < T_{\mathrm{coll}}$), the "merging phase" responsible for the jump origin ($t = T_{\mathrm{coll}}$), and a "late afterglow phase" ($t > T_{\mathrm{dec},m}$, with $T_{\mathrm{dec},m}$ given by Eq. B.28).

In our simplified model, the photon lightcurve is a stepwise function obtained as follows. For $T_{\mathrm{dec}} \leq t < T_{\mathrm{coll}}$, the flux results from the interaction between the slow shell and the external medium. Therefore, it is described by the synchrotron spectrum introduced in Sec. 8.3.1. At $t = T_{\mathrm{coll}}$, the flux undergoes a sharp increase: this is obtained as the sum between the afterglow radiation generated by the slow shell at $t = T_{\mathrm{coll}}$ and the synchrotron radiation instantaneously emitted at the collision, see Sec. 8.3.2 for its description. Finally, for $t > T_{\mathrm{dec},m}$, the radiation comes from the deceleration of the merged shell. Thus, the light curve follows again

the predicted broken power-law for the classic afterglow. The relations derived in Sec. 8.3.1 hold by applying the temporal evolution of the Lorentz factor and the radius of the merged shell as prescribed in Appendix B.1.

Let $F_\gamma^s(E_\gamma)$ and $F_\gamma^m(E_\gamma)$ be the photon fluxes at Earth obtained from the photon distributions of the slow and merged shell, respectively, i.e. Eqs. 8.22–8.23, taken with the proper Lorentz factor and radius; $F_\gamma^{m,0}(E_\gamma)$ is instead the photon flux from electrons accelerated at the collision, corresponding to the photon distributions Eqs. 8.27–8.29. Therefore, the resulting flux at Earth $F_\gamma(E_\gamma)$ reads as

$$F_\gamma(E_\gamma) = \begin{cases} F_\gamma^s(E_\gamma) & T_{\rm dec} \leq t < T_{\rm coll} \\ F_\gamma^s(E_\gamma, t = T_{\rm coll}) + F_\gamma^{m,0}(E_\gamma) & t = T_{\rm coll} \\ F_\gamma^m(E_\gamma) & t \geq T_{\rm dec,m} \end{cases} . \tag{8.31}$$

This prescription does not aim to fit the afterglow light curves in the presence of a jump. Rather, it is a qualitative parametrization useful for contrasting the neutrino signal in the presence of a jump with the classic afterglow case.

We conclude by observing that we cannot model the transition phase $T_{\rm coll} < t < T_{\rm dec,m}$ analytically. Indeed, we should take into account the time needed by the merged shell to relax before starting its deceleration; on the contrary, we are assuming an instantaneous merger. This approximation may lead to overestimate or underestimate the photon flux in the aforementioned time window. Even though this is may be problematic for the electromagnetic signal, it does not affect the neutrino forecast substantially, as discussed in Sec. 8.5.

8.4 ENERGY DISTRIBUTIONS OF PROTONS AND NEUTRINOS

In this section, the energy distribution of protons is introduced together with the most relevant cooling timescales. The steps followed to compute the neutrino flux expected at Earth are also outlined.

8.4.1 *Proton energy distribution*

We assume that protons are Fermi accelerated at the shock front, although the process responsible for particle acceleration is still subject to debate, see e.g. Refs. [85, 101, 283–285]. Accelerated protons have a

non-thermal power-law plus exponential cutoff distribution defined in the frame comoving with the blastwave as

$$n'_p(E'_p) = A'_p E_p^{'-k_p} \exp\left[-\left(\frac{E'_p}{E'_{p,\max}}\right)^{\alpha_p}\right]\Theta(E'_p - E'_{p,\min}) \,, \tag{8.32}$$

where Θ is the Heaviside function, $\alpha_p = 2$ [115] and k_p is the proton spectral index. The proton spectral index resulting from non-relativistic shock diffusive acceleration theory is expected to be $k_p \simeq 2$ [398], while it is estimated to be $k_p \simeq 2.2$ from Monte Carlo simulations of ultra-relativistic shocks [85], assuming isotropic diffusion in the downstream. In this work, we assume $k_p = 2$. The normalization constant is $A'_p = \epsilon_p w' [\int_{E'_{p,\min}}^{E'_{p,\max}} dE'_p E'_p n'_p(E'_p)]^{-1}$, where $\epsilon_p + \epsilon_e + \epsilon_B \lesssim 1$ and w' is the comoving energy density of the blastwave. For the slow and merged shells, w' is given by Eq. 8.16, by considering the Lorentz factor and radius of the respective shell, while the energy density during the merger is given by Eq. 8.26. The minimum energy of accelerated protons is $E'_{p,\min} = \Gamma m_p c^2$ [226, 372, 373]. Finally, $E'_{p,\max}$ is the maximum energy up to which protons can be accelerated in the blastwave and is obtained by the constraint of the Larmor radius being smaller than the size of the acceleration region or imposing that the acceleration timescale,

$$t_{p,\rm acc}^{'-1} = \frac{ceB'}{\xi E'_p} \,, \tag{8.33}$$

is smaller than the total cooling timescale for protons. Similarly to the electrons, we assume that $\xi = 10$ for protons [390].

The total cooling timescale for protons, at a fixed time of the evolution of the blastwave, is

$$t_{p,\rm cool}^{'-1} = t_{\rm ad}^{'-1} + t_{p,\rm sync}^{'-1} + t_{p\rm fl}^{'-1} + t_{pp}^{'-1} + t_{p,\rm BH}^{'-1} + t_{p,\rm IC}^{'-1} \,, \tag{8.34}$$

where $t_{\rm ad}^{'-1}$, $t_{p,\rm sync}^{'-1}$, $t_{p\gamma}^{'-1}$, $t_{pp}^{'-1}$, $t_{p,\rm BH}^{'-1}$, $t_{p,\rm IC}^{'-1}$ are the adiabatic, synchrotron, photo-hadronic ($p\gamma$), hadronic (pp), Bethe-Heitler (BH, $p\gamma \rightarrow pe^+e^-$) and inverse Compton (IC) cooling timescales, respectively; these are defined as follows [103, 390, 399]:

$$t_{\rm ad}^{'-1} = \frac{8c\Gamma}{R} \,, \tag{8.35}$$

$$t_{p,\rm sync}^{'-1} = \frac{4\sigma_T m_e^2 E'_p B'^2}{3m_p^4 c^3 8\pi} \,, \tag{8.36}$$

$$t_{p\gamma}^{'-1} = \frac{c}{2\gamma_p'^2}\int_{E_{\rm th}}^{\infty} dE'_\gamma \frac{n'_\gamma(E'_\gamma)}{E'^2_\gamma}\int_{E_{\rm th}}^{2\gamma'_p E'_\gamma} dE_r E_r \sigma_{p\gamma}(E_r) K_{p\gamma}(E_r) \,, \tag{8.37}$$

$$t_{pp}^{'-1} = c n'_p \sigma_{pp} K_{pp} \,, \tag{8.38}$$

$$t_{p,\rm BH}^{'-1} = \frac{7 m_e \alpha \sigma_T c}{9\sqrt{2}\pi m_p \gamma_p'^2}\int_{\gamma_p'^{-1}}^{\frac{E'_{\gamma,\max}}{m_e c^2}} d\epsilon' \frac{n'_\gamma(\epsilon')}{\epsilon'^2}\left\{(2\gamma'_p\epsilon')^{3/2}\left[\ln(\gamma'_p\epsilon') - \frac{2}{3}\right] + \frac{2^{5/2}}{3}\right\} \,, \tag{8.39}$$

$$t_{p,\rm IC}^{'-1} = \frac{3(m_e c^2)^2 \sigma_T c}{16\gamma_p'^2(\gamma'_p - 1)\beta'_p}\int_{E'_{\gamma,\min}}^{E'_{\gamma,\max}} \frac{dE'_\gamma}{E'^2_\gamma} F(E'_\gamma, \gamma'_p) n'_\gamma(E'_\gamma) \,, \tag{8.40}$$

where $\gamma_p = E'_p/m_p c^2$, $\epsilon' = E'_\gamma/m_e c^2$, $E_{\rm th} = 0.150$ GeV is the threshold for photo-pion production, and $\beta'_p \approx 1$ for relativistic particles. The function $F(E'_\gamma, \gamma'_p)$ is given in Ref. [400], with the replacement $m_e \longrightarrow m_p$. The cross sections for $p\gamma$ and pp interactions, $\sigma_{p\gamma}$ and σ_{pp}, are defined following Ref. [277]. The function $K_{p\gamma}(E_r)$ is the $p\gamma$ inelasticity, given by Eq. 9.9 in [103]:

$$K_{p\gamma}(E_r) = \begin{cases} 0.2 & E_{\rm th} < E_r < 1 \text{ GeV} \\ 0.6 & E_r > 1 \text{ GeV} \end{cases} \tag{8.41}$$

where $E_r = \gamma'_p E'_\gamma (1 - \beta'_p \cos\theta')$ is the relative energy between a proton with Lorentz factor γ'_p and a photon with energy E'_γ, moving such that they form an angle θ' in the comoving frame of the blastwave. The comoving proton density in the blastwave, n'_p, is obtained from the jump conditions (see Appendix B.1) and is such that $n'_p = 4n\Gamma$. The inelasticity of pp interactions is $K_{pp} \simeq 0.8$ [231] and $n'_\gamma(E'_\gamma)$ is the photon target for accelerated protons.

8.4.2 *Neutrino energy distribution and flux expected at Earth*

The blastwave is rich of photons radiated by shock accelerated electrons, which are ideal targets for protons co-accelerated at the shock. This results in efficient neutrino production through $p\gamma$ interactions, mostly dominated by the Δ^+ resonance:

$$p + \gamma \longrightarrow \Delta^+ \longrightarrow \begin{cases} n + \pi^+ & 1/3 \text{ of all cases} \\ p + \pi^0 & 2/3 \text{ of all cases .} \end{cases} \tag{8.42}$$

Neutral pions decay in two photons: $\pi^0 \longrightarrow 2\gamma$; while charged pions can produce neutrinos through the decay chain $\pi^+ \longrightarrow \mu^+ + \nu_\mu$, followed by the muon decay $\mu^+ \longrightarrow \bar{\nu}_\mu + \nu_e + e^+$. Note that, since the number of photons in the blastwave is much larger than the number of protons swept up from the CBM by the blastwave, we can safely neglect the contribution to the neutrino emission due to pp interactions. Indeed, the cooling timescales satisfy $t_{pp}^{-1} \ll t_{p\gamma}^{-1}$ for typical GRB afterglow parameters, as shown in Appendix B.3.

In order to compute the neutrino spectral energy distribution resulting from $p\gamma$ interactions, we rely on the semi-analytic photo-hadronic model described in Ref. [115]. This model is based on SOPHIA [118], which takes into account the Δ^+ channel in Eq. 8.42, as well as the N resonances, the multi-pion and direct-pion production channels.

The procedure adopted to compute the neutrino energy distribution is the same for all three time windows of our GRB afterglow model, after taking into account the corresponding distributions of photons and protons. Given the comoving photon energy distribution, $n'_\gamma(E'_\gamma)$, and the comoving proton energy distribution $n'_p(E'_p)$ [both in units of GeV^{-1} cm^{-3}], the rate of production of secondary particles $l = \pi^\pm, \pi^0, K^+$ in the comoving frame [in units of GeV^{-1} cm^{-3} s^{-1}] is given by [115]:

$$Q'_l(E'_l) = c \int_{E'_l}^{\infty} \frac{dE'_p}{E'_p} n'(E'_p) \int_{E_{\rm th}/2\gamma'_p}^{\infty} dE'_\gamma n'_\gamma(E'_\gamma) R(x,y) \,, \tag{8.43}$$

where $x = E'_l/E'_p$ is the fraction of proton energy that goes into the secondary particles, $y = \gamma'_p E'_l$ and $R(x,y)$ is the response function, which contains information on the interaction, i.e. cross section and multiplicity.

Before decaying, charged mesons undergo energy losses. Their energy distribution at decay is approximated by:

$$Q_l^{'\rm dec}(E'_l) = Q'_l(E'_l)\left[1 - \exp\left(-\frac{t'_{l,\rm cool} m_l}{E'_l \tau'_l}\right)\right] , \tag{8.44}$$

where $t'_{l,\rm cool}$ is the cooling time scale of the l meson, m_l its mass and τ'_l its lifetime. Finally, mesons decay and the resulting neutrino comoving spectrum [in units of GeV cm^{-3} s^{-1}] is

$$Q'_{\nu_\alpha}(E'_\nu) = \int_{E'_\nu}^{\infty} \frac{dE'_l}{E'_l} Q_l^{'\rm dec}(E'_l) F_{l\to\nu_\alpha}\left(\frac{E'_\nu}{E'_l}\right) , \tag{8.45}$$

where $\alpha = e, \mu$ is the neutrino flavor at production and $F_{l\to\nu_\alpha}$ is a function defined as in Ref. [273]. Kaons suffer less from radiative cooling compared to charged pions, due to their larger mass and shorter lifetime. Thus, their contribution to the resulting neutrino spectrum is always sub-leading at lower energies, but may become dominant at higher energies [238, 274–276].

For a source at redshift z, the flux of neutrinos of flavor α expected at Earth [in units of GeV^{-1} cm^{-2} s^{-1}] is:

$$\Phi_{\nu_\alpha}(E_\nu, z) = \frac{(1+z)^2}{4\pi d_L^2(z)} V'_{\rm shell} \sum_\beta P_{\nu_\beta\to\nu_\alpha}(E_\nu) Q'_{\nu_\beta}\left[\frac{E_\nu(1+z)}{\Gamma}\right] , \tag{8.46}$$

where $V'_{\rm shell} = 4\pi R^2 l'$ is the volume of the emitting shell [280] and l' its width. The neutrino oscillation probability $P_{\nu_\beta\to\nu_\alpha}(E_{\nu_\alpha})$ is such that $P_{\nu_\beta\to\nu_\alpha} = P_{\bar\nu_\beta\to\bar\nu_\alpha}$ and is given by [279]:

$$P_{\nu_e\to\nu_\mu} = P_{\nu_\mu\to\nu_e} = P_{\nu_e\to\nu_\tau} = \frac{1}{4}\sin^2 2\theta_{12} \,, \tag{8.47}$$

$$P_{\nu_\mu\to\nu_\mu} = P_{\nu_\mu\to\nu_\tau} = \frac{1}{8}(4 - \sin^2\theta_{12}) \,, \tag{8.48}$$

$$P_{\nu_e\to\nu_e} = 1 - \frac{1}{2}\sin^2 2\theta_{12} \,, \tag{8.49}$$

Table 1: Characteristic parameters assumed for our benchmark GRB afterglow in the ISM and wind CBM scenarios.

	$\tilde{E}_{k,\rm iso}$ (erg)	Γ_0	n_0 (cm^{-3}) or $A_\star$	ϵ_e	ϵ_B	$\epsilon^0_{e,m}$	$\epsilon^0_{B,m}$	$T_{\rm coll}$ (s)	$\tilde{E}_f$ (erg)	k_e	k_p
ISM	10^{53}	300	1.0	0.1	0.1	0.1	0.1	5×10^3	2×10^{53}	2.5	2
Wind	10^{53}	100	0.1	0.1	0.1	0.1	0.1	5×10^3	2×10^{53}	2.5	2

with $\theta_{12} \simeq 33.5°$ [281]. The luminosity distance in a standard flat ΛCDM cosmology is

$$d_L(z) = (1+z)\frac{c}{H_0}\int_0^z \frac{dz'}{\sqrt{\Omega_\Lambda + \Omega_M (1+z')^3}}\,, \tag{8.50}$$

where we adopt $H_0 = 67.4$ km s^{-1} Mpc^{-1}, $\Omega_M = 0.315$, and $\Omega_\Lambda = 0.685$ [401].

8.5 AFTERGLOW SIGNALS

In this section, we present our findings on the particle distributions expected at Earth from the GRB afterglow. We explore the photon light curve as well as the temporal evolution of the neutrino spectral energy distribution in three time windows: the afterglow generated by the first shell launched by the central engine, the time at which the fast shell collides and merges with the slow one, and the afterglow generated by the merged shell.

8.5.1 *Particle emission in the absence of a late shell collision*

We consider a benchmark GRB with characteristic parameters as in Table 1 and located at $z = 1$. The chosen value for the isotropic kinetic energy is motivated by post-Swift observations reporting an average isotropic energy emitted in photons $\tilde{E}_{\gamma,\rm iso} = O(10^{52})$ erg [402] and assuming a conversion efficiency of $\sim 10\% \tilde{E}_{\rm iso}$ into gamma-rays, therefore leading to the isotropic kinetic energy $\tilde{E}_{k,\rm iso} \sim 10^{53}$ erg. Moreover, we rely on the standard microphysical parameters reported in Ref. [383]. Since there is no evidence for the values of typical microphysical parameters characteristic of the collision, we fix $\epsilon^0_{e,m} = \epsilon_e$ and $\epsilon^0_{B,m} = \epsilon_B$. Finally, as for the CBM densities, we follow Refs. [383, 385].

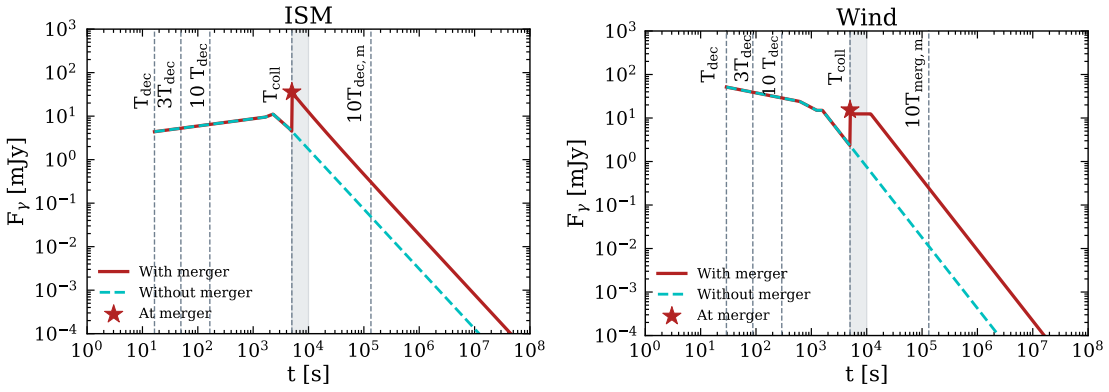

Figure 38: Light curves expected at Earth for our benchmark GRB at $z = 1$ for the classic afterglow scenario (cyan dashed line) and in the presence of an optical jump (brown solid line) for an observed photon frequency $\nu_\gamma = 6 \times 10^{14}$ Hz. The brown star marks the flux generated at $T_{\rm coll}$. At the merger and after it, the observed flux is larger than the one expected from the classic afterglow. The gray shadowed region ($T_{\rm coll} < t < T_{\rm dec,m}$) is excluded from the computation of the neutrino signal since we cannot treat this transition phase analytically (see the main text for details). We assume a photon spectral index $k_e = 2.5$. In order to guide the eye, the vertical grey dashed lines mark the times at which we show snapshots of the spectral energy distribution of photons and neutrinos (see Figs. 39 and 40). These light curves should be considered for illustrative purposes only, since we assume the instantaneous shell collision for simplicity.

Concerning the fast shell, we fix Γ_f by taking $\Delta_T \ll T_{\rm coll}$, so that $\Gamma_f \simeq 2\Gamma(T_{\rm coll})$ (see Appendix B.2). Since there are no theoretical constraints on the energy $\tilde{E}_f$, we fix the latter by following Ref. [360]. We choose $\tilde{E}_f = 2\tilde{E}_{\rm iso}$ relying on the results of "case 4" of Ref. [360], for which the strongest rebrightening is obtained. Moreover, we fix $T_{\rm coll} = 5 \times 10^3$ s both for the ISM and the wind scenarios. At this time the light curve is decreasing in both scenarios, and it has been chosen consistently with the observation of jumps between a few hundred seconds and ~ 1 day after the onset of the burst [346, 352–354].

In the classic afterglow scenario, the time evolution of the photon light curve at Earth, computed as described in Sec. 8.3.1, for our benchmark GRB is shown in Fig. 38 (cyan dashed line). The light curve is computed for an observed photon frequency $\nu_\gamma = 6 \times 10^{14}$ Hz, i.e. in the optical band. For both the ISM and wind scenarios, the breaks in the light curve are determined by the times at which the break frequencies $\nu_{\gamma,\rm min}$ and $\nu_{\gamma,\rm cool}$ cross the observed one ν_γ, and $\nu_{\gamma,\rm min} = \nu_{\gamma,\rm cool}$.

The photon and neutrino fluxes expected at Earth (see Sec. 8.4.2) are shown in Fig. 39 for $t = T_{\rm dec}$, $3T_{\rm dec}$, and $10T_{\rm dec}$ (marked with vertical lines in Fig. 38) for the ISM and wind scenarios. We refer the interested reader to Appendix B.3 for a discussion on the characteristic cooling times of protons and mesons affecting the neutrino distributions. For both CBM cases, the flux at Earth decreases with time, as expected [383]. Moreover, the peak of the photon energy distribution and its energy breaks shift to lower energies as time

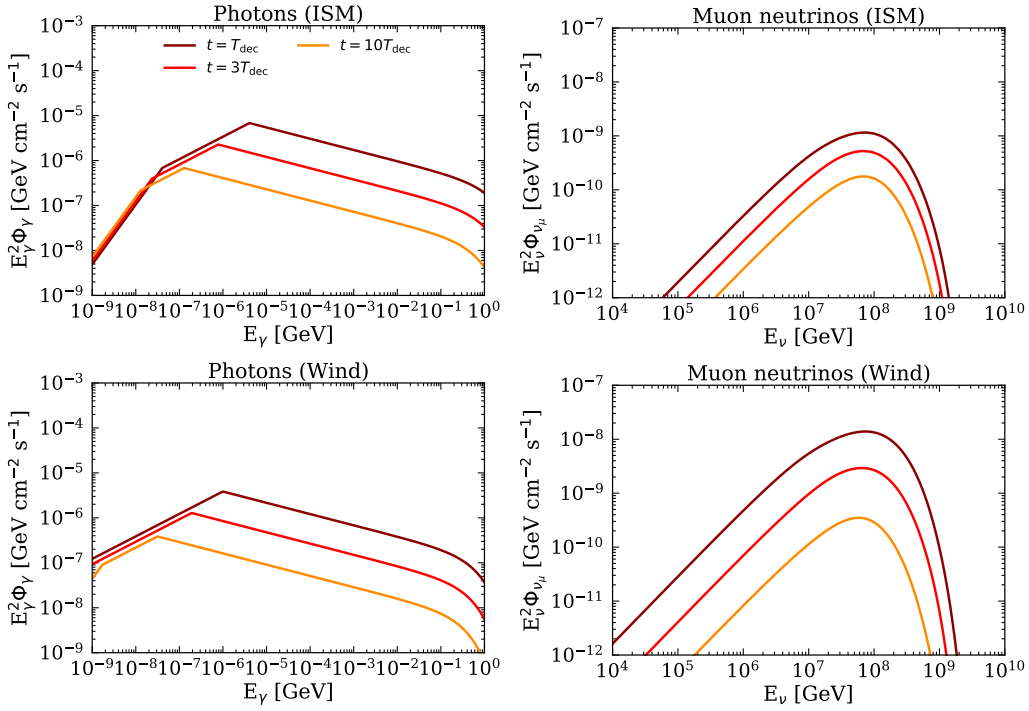

Figure 39: *Left:* Synchrotron photon flux expected at Earth for the classic afterglow scenario for $t = T_{dec}$, $3T_{dec}$, and $10T_{dec}$ (see the gray vertical lines in Fig. 38) for our benchmark GRB in Table 1 at $z = 1$. *Right:* Corresponding neutrino flux expected at Earth. Both fluxes for the wind scenario decrease faster than for the ISM scenario.

increases. This is due to the fact that the minimum and cooling energies scale with time as $E_{\gamma,\rm min} \propto t^{-3/2}$ $E_{\gamma,\rm cool} \propto t^{-1/2}$, respectively [383].

In the right panels of Fig. 39, we show our results concerning the neutrino flux. In the wind scenario, the neutrino flux peaks at $E_\nu^{\rm peak} \simeq 8.1 \times 10^7$ GeV for $t = T_{\rm dec}$ and then decreases up to $E_\nu^{\rm peak} \simeq 6.3 \times 10^7$ GeV for $t = 10T_{\rm dec}$. For the ISM scenario, the neutrino flux peaks at $E_\nu^{\rm peak} \simeq 7.7 \times 10^7$ GeV and at $E_\nu^{\rm peak} \simeq 7.3 \times 10^7$ GeV for $t = 10T_{\rm dec}$. The effect of kaon cooling is not visible, since as shown in Appendix B.3 (see Fig. 68) kaons cool at energies larger than the maximum energy of protons in the blastwave. Note that both the photon and the neutrino fluxes are larger in the wind scenario than in the ISM one, but they decreas faster in the wind case [372]. This is due to the fact that higher densities of the external medium can be initially reached within the wind profile. At such densities, the blastwave decelerates faster, leading to a rapidly decreasing flux [372]. The higher densities in the wind scenario also allow for higher magnetic fields, which cause the shift of the cooling frequency in the photon spectrum at energies lower than the ISM case. Of course, this is a direct consequence of the value adopted for ϵ_B.

The standard afterglow scenario has been already investigated in the literature for what concerns neutrino emission. Nevertheless, there are some relevant differences with respect to the results presented in this

section. Our classic afterglow model resembles the one investigated in Refs. [372, 392]. However, by using the benchmark input parameters of Refs. [372, 392], we find a neutrino flux that is almost 5 orders of magnitude larger, but with an identical shape. This discrepancy might be caused by several reasons. First, there is a missing factor $(E'_{\gamma,\rm min}/E'_{\gamma,\rm cool})^{-1/2}$ in the photon distribution in Eq. 11 of Ref. [372]; second, in the definition of the proton flux of Ref. [372] there is a factor $1/[4\pi(1+z)^2]$ in excess, which contributes to further lower the corresponding neutrino flux. On the other hand, our results on the photon and neutrino fluxes are in agreement with the ones in Refs. [226, 383], respectively.

The afterglow flux produced by the reverse shock has been investigated in Ref. [373], while we focus on the contribution from the forward shock. The neutrino flux obtained in Ref. [373] strictly depends on the assumptions on the thickness of the shell. For example, in the case of a thin shell with $\tilde{E}_{\rm iso} = 4 \times 10^{52}$ erg and propagating in an ISM with $n_0 = 0.5$ cm^{-3}, the estimated flux peaks at $E_\nu^{\rm peak} \simeq 10^{10}$ GeV, where it should reach about 10^{-10} GeV cm^{-2} s^{-1} for a GRB at $z = 1$. This result is comparable with our maximum flux $\simeq 2 \times 10^{-9}$ GeV cm^{-2} s^{-1}, considering that the isotropic energy adopted in Ref. [373] is one order of magnitude smaller than the one we adopt in this work. Nevertheless, the neutrino flux peaks at energies higher than ours in Ref. [373]. Indeed, our fluxes peak at $E_\nu \simeq 10^8$ GeV, in contrast with the peak at $\simeq 10^{10}$ GeV in [373], probably because of the different initial Γ_0 and because protons are expected to be accelerated at higher energies at the reverse shock. The most optimistic case considered in Ref. [373] is a thick shell propagating in a wind environment. In the latter scenario, the afterglow flux reaches an amplitude about ~ 2 orders of magnitude larger than ours at the peak energy $E_\nu \sim 10^9$ GeV, which is shifted by ~ 1 order of magnitude with respect to ours. Also for the wind scenario, the differences are mainly due to the energy of the ejecta, assumed to be ~ 4 times larger than ours, and the density of the environment up to 10 times larger than our benchmark value. Moreover, we rely on the thin shell assumption rather than the thick one, hence the results are not directly comparable. Finally, note that the emission from the reverse shock lasts longer than the emission from the forward shock.

8.5.2 *Particle emission in the presence of a late shell collision*

In the presence of an optical jump, we model the afterglow light curve through the late collision of two relativistic shells. At $t = T_{\rm coll}$, we compute the neutrino flux as described in Sec. 8.4.2 and by using the photon

distribution introduced in Sec. 8.3.2. After the merger, the resulting merged shell starts to be decelerated by the external medium, emitting radiation with the standard features expected during the afterglow, as discussed in Sec. 8.5.1, but with the parameters characteristic of the merged shell. Since energy has been injected in the slow shell during the merger, the merged shell is more energetic than the slow one. Thus, we obtain a higher photon flux as shown in Fig. 38 (brown continuous line). The star denotes the flux at $t = T_{\rm coll}$, given by the sum of the afterglow radiation (see Sec. 8.5.1) generated by the slow shell and the radiation from the shocks developing at the collision. For our choice of parameters, electrons accelerated at the collision are in the slow cooling regime both in the ISM and wind scenario (see Appendix B.1 and figures therein). Therefore, the appropriate photon distribution is given by Eq. 8.29.

Since it is assumed that the merger occurs instantaneously at the collision time, we are not taking into account the time needed by the merged shell to relax before being decelerated to the BM solution. Because of this approximation, we neglect the neutrinos produced for $T_{\rm coll} < t < T_{\rm dec,m}$, since an analytic treatment in this transition phase is not feasible, as already mentioned in Sec. 8.3.3. The time window excluded from our calculations of the neutrino signal corresponds to the gray shadowed area in Fig. 38. Note that, for most of the initial configurations of the slow shell, we find $T_{\rm dec,m} \simeq 2\, T_{\rm coll}$. The exclusion of such a time window in our calculation negligibly affects the overall time-integrated neutrino signal, which is the main goal of this work (see Sec. 8.6).

Figure 40 shows the photon and muon neutrino fluxes at $t = T_{\rm coll}$ and after the merger at $t = 10 T_{{\rm dec},m}$ for the ISM and wind scenarios. These times are marked in Fig. 38 by vertical lines. For comparison, we also show the photon and neutrino fluxes that would be generated at $t = 10 T_{{\rm dec},m}$ if no merger occurred. In both CBM scenarios, the neutrino flux increases in the presence of a jump, as expected, due to the denser photon field leading to more efficient $p\gamma$ interactions (see also the cumulative number of muon neutrinos plotted as a function of time in Fig. 41).

The peak of the neutrino distribution at late times in Fig. 40 is shifted at higher energies compared to the case without merger. This is explained because the energy density content of the merged shell is larger than the one of the slow shell, thus the corresponding magnetic field is larger as well. This results into a greater maximum energy of protons in the merged blastwave since $E'_{p,\rm max}$ depends linearly on the magnetic field; indeed, the acceleration time (see Eq. (8.33)) limits the maximum energy of protons. Finally, the quantities

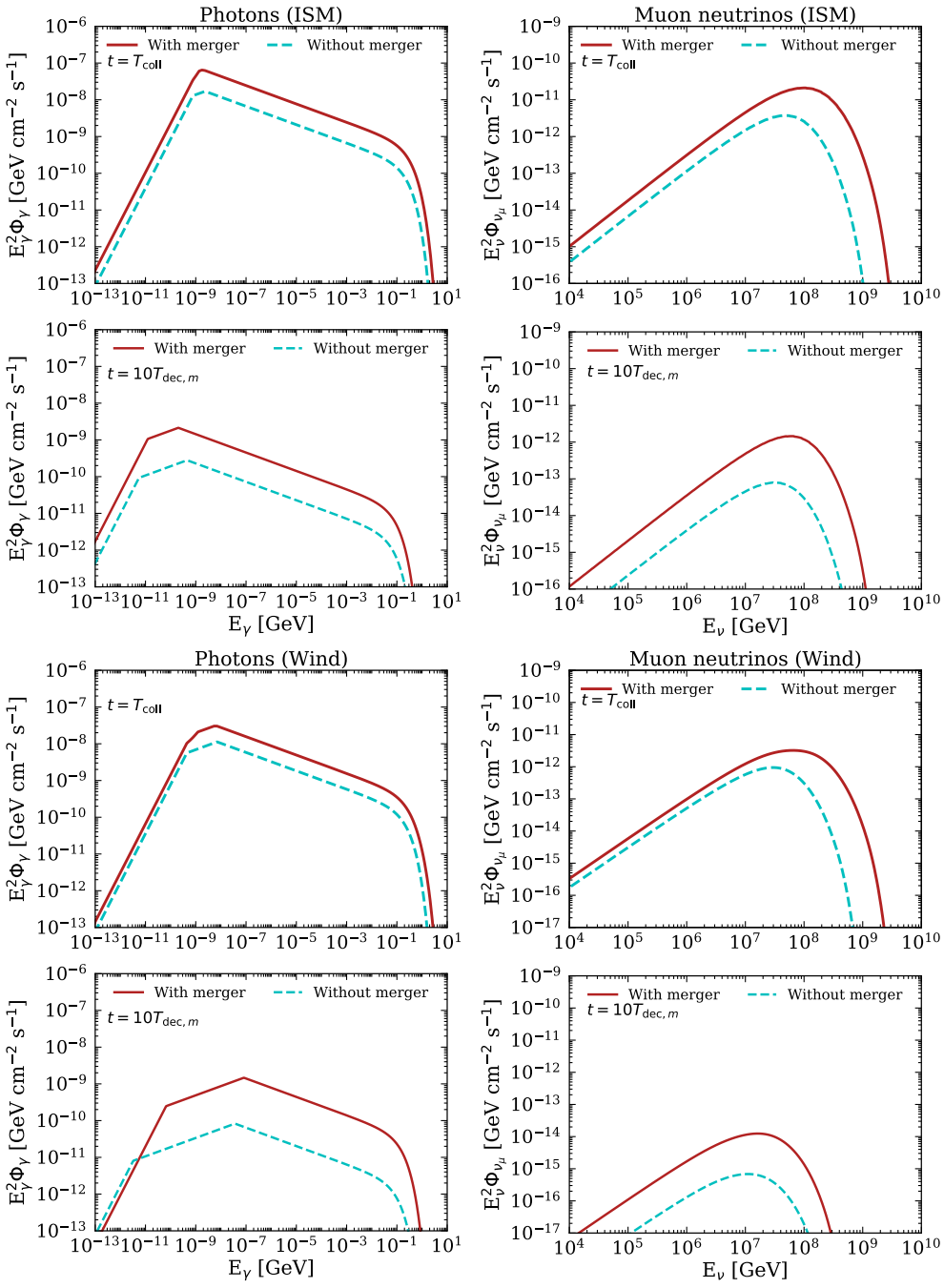

Figure 40: Photon (on the left) and neutrino (on the right) fluxes expected at Earth as functions of the particle energy from the afterglow when the merger of two relativistic shells occurs for the ISM (top two panels) and wind (bottom two panels) scenarios for our benchmark GRB in Table 1 at $z = 1$. For each CBM scenario, the fluxes are shown at $t = T_{\rm coll}$ and 10 $T_{{\rm dec},m}$ (see vertical lines in Fig. 38). The brown lines display the total expected flux in the presence of a merger, while the cyan lines represent the flux that would be observed in the absence of a jump. The late shell merger enhances the photon and neutrino fluxes compared to the standard afterglow scenario and shifts the peak of the energy distributions at larger energies.

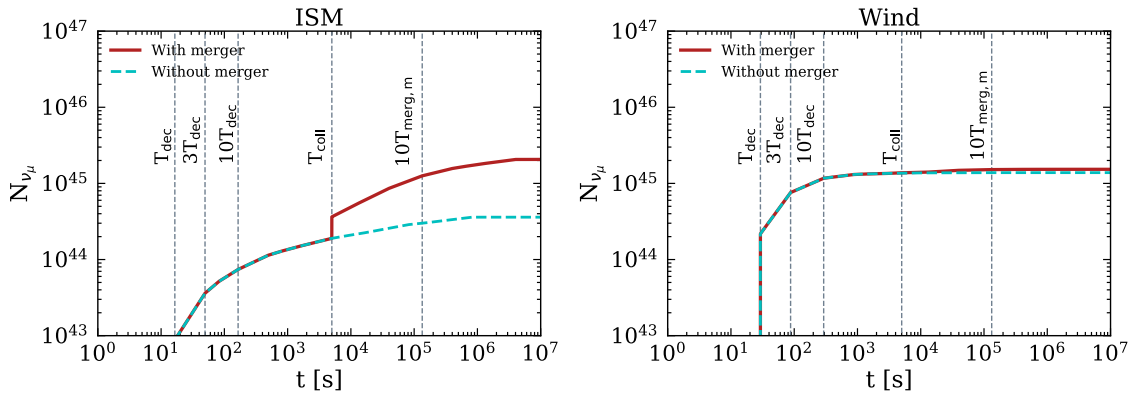

Figure 41: Cumulative number of muon neutrinos expected at Earth for the ISM (left panel) and wind (right panel) scenarios as a function of time for our benchmark GRB (Table 1) at $z = 1$. The brown solid line represents the number of muon neutrinos produced when the shell merger occurs, while the cyan dashed line corresponds to the case of the classic afterglow. In order to guide the eye, the gray vertical lines mark the times at which we show the neutrino flux at Earth for the classic afterglow scenario (Fig. 39) and when a jump occurs (Fig. 40). In the ISM environment, the jump significantly increases the cumulative number of neutrinos, while the difference between the two scenarios is negligible in the wind case.

entering the Lorentz transformation of the flux at Earth (e.g. the Lorentz factor) are larger for the merged shell than for the slow one.

From Fig. 41, we can see that the number of neutrinos at $T_{\rm coll}$ is given by the sum of the neutrinos produced at the shock front between the slow shell and the CBM and the neutrinos produced at the collision between the slow and fast shells. After the merger, the only contribution comes from the afterglow of the merged shell. By comparing the left and right panels of Fig. 41, we note that a larger efficiency in the neutrino production is achieved in the ISM scenario in the presence of shell merger. In particular, for the ISM scenario the number of neutrinos increases by a factor of 6. This result is justified in light of the fact that the neutrino flux rapidly decreases for a wind-like CBM. Thus, the early time emission dominates the time-integrated neutrino flux. Motivated by these results, in the next section we discuss the detection prospects for neutrinos produced during the GRB afterglow when a jump occurs in the light curve.

8.6 NEUTRINO DETECTION PERSPECTIVES

In this section, we explore whether the increase in the number of neutrinos expected in the presence of an optical jump could reflect improved detection perspectives at ongoing and future generation neutrino telescopes. We explore the detection prospects for the all-sky quasi-diffuse flux as well as point source

searches. Finally, we forecast the expected neutrino fluence from GRB 100621A and for a second hypothetical GRB with parameters inspired by the bright GRB 130427A.

8.6.1 *All-sky quasi-diffuse flux*

The average isotropic kinetic energy from the catalogue of the Gehrels Swift Observatory is $\tilde{E}_{k,\rm iso} \simeq 10^{53}$ erg [262] and the redshift distribution peaks at $z \simeq 2$ [282]. Hence, we compute the all-sky quasi-diffuse flux by placing our benchmark GRB at $z = 2$ and assuming that its flux is representative of the GRB population. For a GRB rate of $\dot{\rm N} \sim 700\ {\rm yr}^{-1}$ [140, 403, 404] and an isotropic distribution of all the sources in the sky, the all-sky quasi-diffuse flux is:

$$F_{\nu_\mu}(E_\nu) = \frac{\dot{\rm N}}{4\pi} \int dt\ \Phi_{\nu_\mu}(E_\nu, z = 2)\ , \tag{8.51}$$

being Φ_{ν_μ} defined as in Eq. 8.46. In the case of the afterglow generated by the slow and the merged shells, we perform the time integration for $t \in [T_{\rm dec}, T_{\rm Sedov}]$, where $T_{\rm Sedov}$ marks the Sedov time when the blastwave becomes non-relativistic and enters the Newtonian regime. At $T_{\rm coll}$ the integration over time is replaced by the product with $t^0_{\rm dyn,m} = t'^0_{{\rm dyn},m}(1+z)/\Gamma^0_m$, where $t'^0_{{\rm dyn},m}$ is given by Eq. (8.15), since the collision is considered to be an instantaneous process.

The top panels of Fig. 42 show the all-sky quasi-diffuse neutrino flux in the absence of shell merger, i.e. if the light curve resembles the standard afterglow scenario, for the ISM and wind scenarios. For the ISM scenario, the band corresponds to $1 \lesssim n_0 \lesssim 10\ {\rm cm}^{-3}$; while for the wind scenario, the band includes $0.01 \lesssim A_\star \lesssim 0.1$.

So far, the IceCube Neutrino Observatory has detected neutrinos with energies up to a few PeV [37, 112, 374, 375]. Even though several sources have been proposed to explain the origin of high-energy neutrinos [32, 279, 366–368], only a handful of possible associations have been presented between neutrinos and active galactic nuclei, tidal distruption events (TDEs), and superluminous supernovae [49, 59, 65, 405–410]. In particular, limits on the quasi-diffuse neutrino flux from GRBs have been placed by the IceCube Collaboration by taking into account the prompt emission [140], while a similar analysis on the afterglow phase is missing. A statistical analysis aiming to look for temporal and spatial coincidences between GRB afterglows and neutrinos detected by the IceCube Neutrino Observatory has been carried out in Ref. [403]. In agreement with the findings of Ref. [403], our quasi-diffuse flux does not overshoot existing upper limits on the prompt

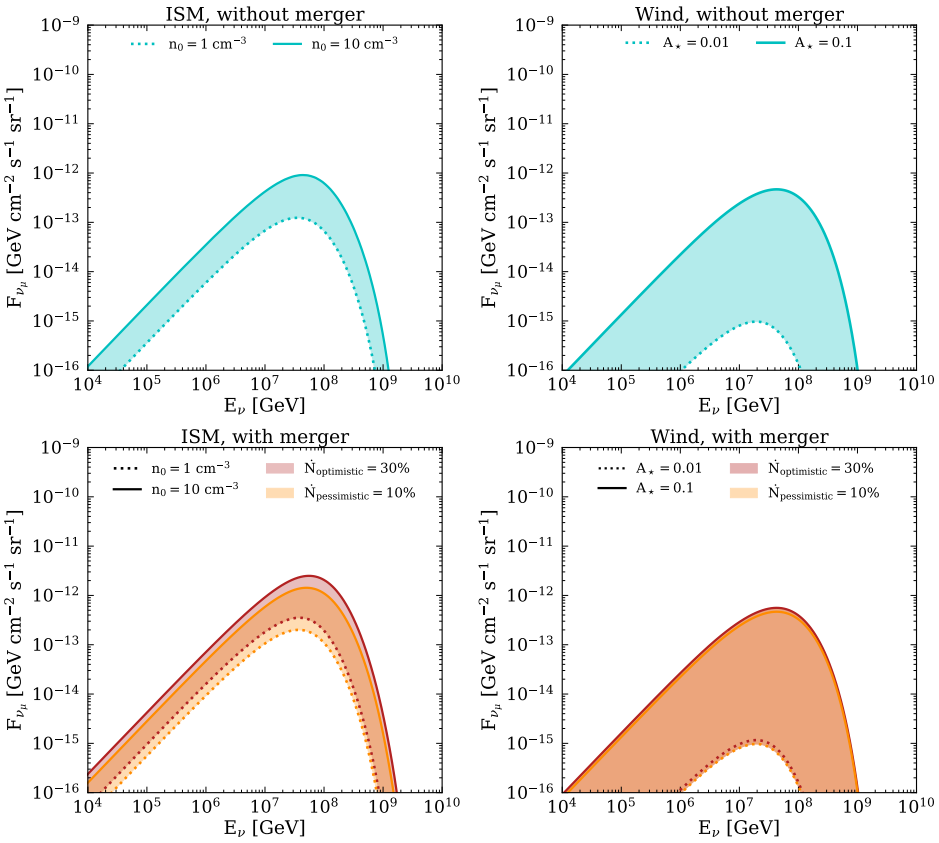

Figure 42: All-sky quasi-diffuse muon neutrino flux from GRB afterglows for the constant density (left panels) and wind (right panels) CBM scenarios, for the standard GRB afterglow (top panels) and the case with optical jumps (bottom panels). For the ISM scenario, the band is defined by $1 \lesssim n_0 \lesssim 10$ cm^{-3} (dotted and solid lines, respectively). For the wind scenario, the band is defined by $0.01 \lesssim A_\star \lesssim 0.1$. For the bottom panels, the quasi-diffuse neutrino flux is computed for the optimistic scenario with $\dot{N}_{\rm optimistic} = 30\%\dot{N}$ (brown shadowed region) and $\dot{N}_{\rm pessimistic} = 10\%\dot{N}$ (orange shadowed region). In the presence of optical jumps, the all-sky quasi-diffuse flux slightly increases for the ISM scenario, while negligible changes occur for the wind case. For the wind environment, there is no difference between the optimistic and pessimistic cases since the classic afterglow always dominates the neutrino fluence. In the cases with and without shell merger, the all-sky quasi-diffuse neutrino flux is in agreement with the results on GRB afterglow neutrino searches reported in Ref. [403] and it does not overshoot the IceCube limits on the GRB prompt emission [140], as well as the limits placed by the ANTARES collaboration [411] and the expected ones for KM3NeT [179].

emission reported by IceCube [140] and by the ANTARES collaboration [411], as well as the ones expected for KM3NeT [179]. Despite differences in the theoretical modeling of the expected signal, our conclusions are also consistent with the detection prospects for the GRB afterglow neutrinos outlined in Ref. [412]. Assuming that jumps occur in the afterglow light curve, the corresponding all-sky quasi-diffuse muon neutrino flux is shown in the bottom panels of Fig. 42 for the two CBM scenarios. Since the fraction of GRB afterglows having optical jumps is largely uncertain [346, 354], we consider an optimistic (pessimistic) case such that the rate of GRBs per year with jumps is 30% (10%) of $\dot{N}$ (see Eq. 8.51). The "pessimistic" fraction of GRBs with optical jumps is extrapolated by the analysis carried out in Ref. [354], where they estimate that

10 out of 146 GRBs with well resolved optical light curves displayed a jump. The "optimistic" fraction of GRBs with optical jumps is obtained by considering that the actual fraction of GRBs with optical jumps is not known and existing constraints may be plagued by observational biases, most notably the missing complete coverage over the first few hours. Therefore, we assume an upper limit of $\sim 30\%$ of the GRB population displaying a jump in the light curve.

The all-sky quasi-diffuse neutrino flux for the ISM scenario is enhanced by a factor ~ 3 by assuming that 30% of the GRB afterglows shows jumps. On the contrary, for the wind scenario, the variation is basically null since the neutrino fluence is dominated by the early-time flux, i.e. the neutrino emission expected from the standard afterglow. This is due to the fact that, as mentioned in Sec. 8.4.2, the flux quickly decreases for the wind profile. Thus, at the time of the shell collision, the flux is already small and does not contribute to the quasi-diffuse emission substantially. Even though the presence of optical jumps slightly enhances the all-sky quasi-diffuse flux, the latter is still below the limit for the prompt phase of IceCube and is consistent with the results of Ref. [403].

The neutrino diffuse emission associated with late optical jumps has been investigated in [413] for optical flares occurring after 1 day from the onset of the prompt emission, thus at times larger than the ones considered in this work. Moreover, Ref. [413] carries out an approximated theoretical modeling of the jump and uses fixed values for the radius of the outflow and its Lorentz factor, while we embed the temporal evolution of the blastwave and consistently model the shell merger. In Ref. [413], a distance of $R \simeq 10^{13}$ cm with Lorentz factor $\Gamma \simeq 10$ at $t = 1$ day is assumed. Through our approach and for the same luminosity, we obtain for the ejecta (that we assumed to be the slow shell) $R \simeq 10^{17}$ cm for $\Gamma \simeq 4$. In the light of these differences, we conclude that our results are not directly comparable to the ones in Ref. [413]. Furthermore, the estimation reported in Ref. [413] is based on Ref. [414], where the expected neutrino signal from the X-ray flares is computed by assuming the late internal shock scenario of Ref. [415]. This model assumes that shock heated electrons in the BM shell are cooled through external inverse Compton scattering. On the other hand, in this work, we only consider synchrotron emission. Despite the major differences in the modeling with respect to this work, Ref. [413] also concludes that the optical jump leads to an increase in the expected number of neutrinos.

8.6.2 *Point source searches*

Figure 43 shows the fluence S_{ν_μ} for our benchmark GRB (Table 1) with an optical jump assuming a distance of 40 Mpc (brown-shadowed region) for the ISM (on the left) and wind (on the right) scenarios. We also assume a band for $1 \lesssim n_0 \lesssim 10$ cm^{-3} (ISM density) and $0.1 \lesssim A_\star \lesssim 0.01$ (wind). We compare the expected muon neutrino fluence with the most optimistic sensitivity of IceCube-Gen2 radio expected for the declination angle of the source in the sky ($\delta = 0°$) [416], the sensitivity of IceCube for a source located at $\delta = -23°$ [416, 417], the sensitivity of RNO-G for a source at $\delta = 77°$ [176], the sensitivity of GRAND200k for $|\delta| = 45°$ [17], and the full range time-averaged sensitivity of POEMMA [376] [5] .

Other radio neutrinos detectors have already been operating in the past years, such as the Askaryan Radio Array (ARA) [175, 418], the Antarctic Ross Ice-Shelf ANtenna Neutrino Array (ARIANNA) [419, 420] and the Antartic Impulsive Transient Antenna (ANITA) [177, 421]. Nevertheless, in the energy region where the afterglow fluence peaks these detectors have worse sensitivity compared to the ones displayed in Fig. 43 and thus we did not consider them in our analysis. Note also that, at these energies, the neutrino background could also be populated by cosmogenic neutrinos [422–424], neutrinos from TDE [425], newborn pulsars and millisecond magnetars [132, 426], in addition to GRB afterglow neutrinos [372, 373].

For a source at $d_L = 40$ Mpc, no detection of neutrinos is expected neither at IceCube—consistently with current non-observations—nor at GRAND 200k and RNO-G for both CBM scenarios. On the contrary, a successful detection could be possible with the radio extension of IceCube-Gen2 for the ISM scenario. In principle, in this case through the detection of neutrinos with IceCube-Gen2 radio, we could be able to constrain the CBM through neutrinos as well as probe the mechanism powering the optical jump. Indeed, the results presented in this paper are based on the assumption of a late collision between two shells, but other mechanisms may lead to different signatures in the neutrino signal. Furthermore, if no neutrino event is detected in temporal and spatial coincidence with the GRB event, constraints could be set on the parameters describing the jump in the afterglow light curve.

5 The declination angles for the detectors are not the same for all instruments since they have been chosen to guarantee the most optimistic conditions for detection. In addition, GRAND200k and POEMMA are designed to be sensitive to showers initiated by tau neutrinos. Nevertheless, the following flavor composition $(\nu_e : \nu_\mu : \nu_\tau) \simeq (1 : 1 : 1)$ [278] is expected at detection. Thus, the fluence of tau neutrinos expected at Earth is comparable to the one of muon neutrinos.

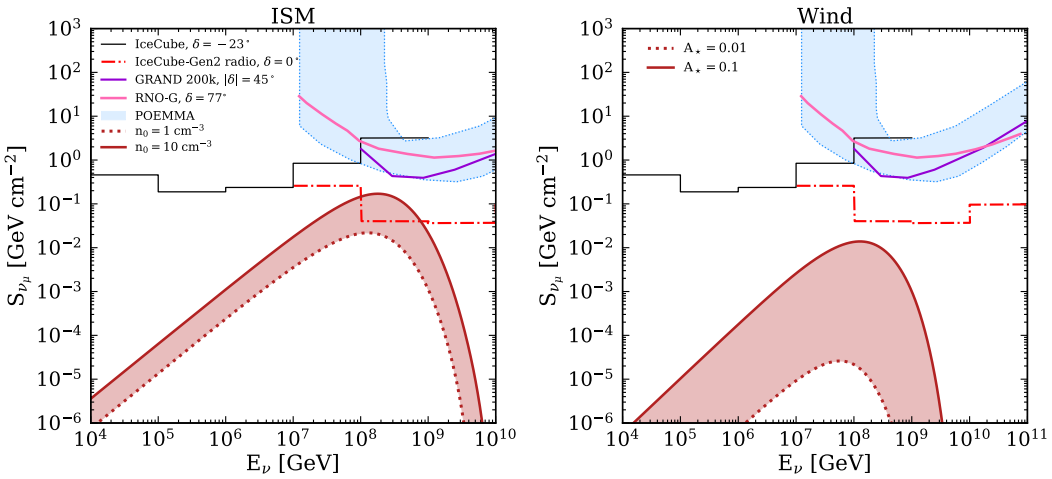

Figure 43: Muon neutrino fluence for our benchmark GRB afterglow with an optical jump at $d_L = 40$ Mpc (brown shadowed region) for the ISM (left panel) and wind (right panel) scenarios. The fluence bands correspond to $1 \lesssim n_0 \lesssim 10$ cm^{-3} and $0.1 \lesssim A_\star \lesssim 0.01$ (dotted and solid lines for the lower and upper bounds, respectively). The expected fluence is compared with the estimated sensitivities of IceCube-Gen2 radio for a source at $\delta = 0°$ [416], IceCube for a source located at $\delta = -23°$ [416, 417], RNO-G for a source at $\delta = 77°$ [176], GRAND200k for a source at $|\delta| = 45°$ [17], and the full range time-averaged sensitivity of POEMMA [376]. For the ISM scenario, IceCube-Gen2 radio shows promising detection prospects.

8.6.3 *Detection prospects for GRB 100621A and a GRB 130427A-like burst*

We now explore the neutrino detection prospects for GRB 100621A, whose optical jump [352] has been detected in seven channels simultaneously with GROND [427]. We also investigate the detection prospects for a second GRB whose parameters are inspired by the bright and nearby GRB 130427A [377–379]. An optical jump has not been observed for GRB 130427A, however we assume that it has one (hereafter GRB 130427A-like). The model parameters inferred for these two GRB afterglows and related uncertainties are summarized in Table 2. We fix $T_{\rm coll} = 5 \times 10^3$ s for GRB 100621A, according to observations. As for GRB 130427A-like, we choose $T_{\rm coll} = 1 \times 10^4$ s for the ISM and wind scenarios, in order to have the light curves decreasing at $T_{\rm coll}$ in both scenarios.

For GRB 100621A, we fix $\epsilon^0_{e,m}$ and $\epsilon^0_{B,m}$ by matching the amplitude of the jump in the light curve. For GRB 130427A-like, we fix $\epsilon^0_{e,m} = \epsilon_e$ and we choose $\epsilon^0_{B,m}$ in order to get the same rebrightening both for the ISM and wind scenarios. We note that there is a substantial freedom in the choice of $\epsilon^0_{e,m}$ and $\epsilon^0_{B,m}$.

The wind scenario has been excluded for GRB 1000621A, thus we perform the calculations only for the ISM case. For our GRB 130427A-like, instead, we explore the detection perspectives both for the ISM [377] and wind [377, 378] scenarios.

Table 2: Parameters characteristic of GRB 100621A [352] (second column) and GRB 130427A-like (inspired by GRB 130427A [377–379], third and fourth columns). For GRB 100621A, only the wind scenario is considered, while both CBM scenarios are investigated for GRB 130427A-like, see main text for more details.

	GRB 100621A (ISM)	GRB 130427A-like (ISM)	GRB 130427A-like (wind)
$\tilde{E}_{k,\mathrm{iso}}$ (erg)	2.8×10^{53}	3.8×10^{54}	4.2×10^{53}
z	0.54	0.34	0.34
$n_0(\mathrm{cm}^{-3})$ or $A_\star$	1–100	$(2\text{–}7)\times10^{-3}$	$(1\text{–}5)\times10^{-3}$
Γ_0	60–104	850	430
ϵ_e	$(2\text{–}6)\times10^{-2}$	0.3	0.3
ϵ_B	6×10^{-6}–6×10^{-4}	10^{-4}	3×10^{-2}
$\epsilon^0_{e,m}$	0.1	0.3	0.3
$\epsilon^0_{B,m}$	10^{-4} – 10^{-3}	10^{-4}	0.1

The expected neutrino fluences are shown in Fig. 44. For both GRBs, the detection of neutrinos seems unlikely. Thus, if GRBs with properties similar to GRB 100621A or GRB 130427A-like should be observed, no associated neutrino signal should be expected, unless the burst propagates in an ISM with n_0 larger than the one inferred for GRB 130427A [377] or the bursts occur at smaller distances.

8.7 CONCLUSIONS

The light curve of some gamma-ray burst afterglows exhibits a sudden intensity jump in the optical band between about one hour and one day after the prompt emission. The origin of this peculiar emission is not known yet, nor the fraction of GRBs displaying this feature. In this paper, we assume that the optical jump results from the late collision of two relativistic shells, as proposed in Ref. [360].

After modeling the shell merger analytically, we compute the neutrino emission from the GRB afterglow within a multi-messenger framework by considering two scenarios for the circumburst medium: a constant density case (ISM) and a stellar wind profile. We find that the presence of an optical jump can increase the number of produced neutrinos by about an order of magnitude.

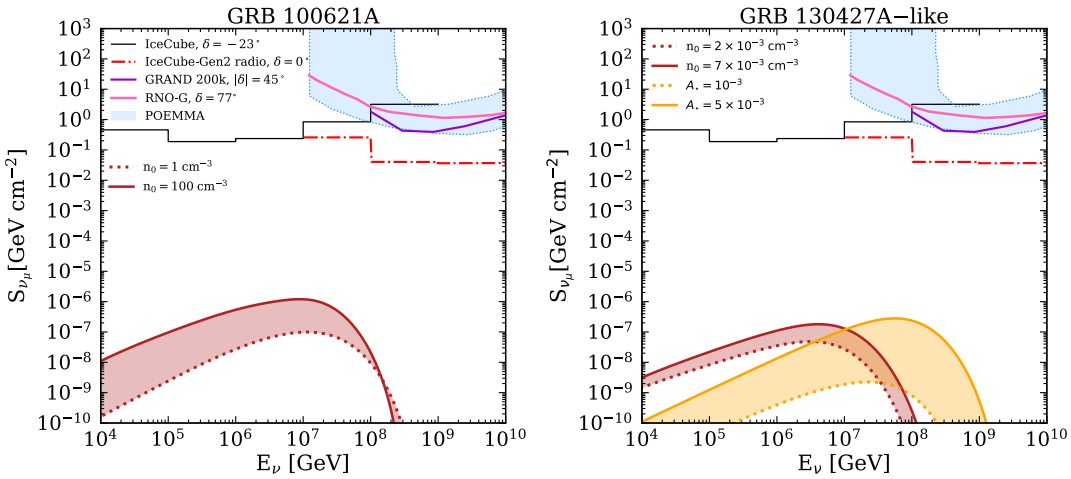

Figure 44: Neutrino fluence for GRB 100621A (left panel) and GRB 130427A-like (right panel) for the parameters in Table 2. The brown (orange) bands represent the ISM (wind) scenario. For GRB 100621A, the dotted (solid) line corresponds to $n_0 = 1$ cm^{-3} ($n_0 = 100$ cm^{-3}). For GRB 130427A-like, the dotted lines correspond to $n_0 = 2 \times 10^{-3}$ cm^{-3} (ISM) and $A_\star = 10^{-3}$ (wind), while the solid lines refer to $n_0 = 7 \times 10^{-3}$ cm^{-3} (ISM) and $A_\star = 5 \times 10^{-3}$ (wind). The expected fluence is compared with the estimated sensitivities of IceCube-Gen2 radio for a source at $\delta = 0°$ [416], IceCube for a source at $\delta = -23°$ [416, 417], RNO-G for a source at $\delta = 77°$ [176], GRAND200k for a source located at $|\delta| = 45°$ [17], and the full range time-averaged sensitivity of POEMMA [376]. For both GRBs, the neutrino fluence lies below the point source sensitivities for all detectors.

The expected quasi-diffuse flux of afterglow neutrinos falls below the upper limits placed by the non-detection of neutrinos during the GRB prompt phase. IceCube-Gen2 radio shows the most promising detection prospects for point source searches, potentially being able to constrain the mechanism powering the optical jump as well as the properties of the circumburst medium through neutrinos; for a source at $d_L = 40$ Mpc, a successful detection could be possible with IceCube-Gen2 radio for the ISM scenario.

We also explore the neutrino emission from GRB 100621A and a burst similar to GRB 130427A but with an optical jump, assuming both these GRBs as benchmark cases given their respective luminosity and redshift. However, because of their distance, the neutrino detection prospects from the afterglow of GRBs similar to these ones could not be probed with next generation neutrino telescopes.

This work shows that the (non)-detection of neutrinos from GRB afterglows could offer an independent way to explore the mechanism powering the jump as well as the properties of the circumburst medium, if a GRB occurs relatively nearby or is especially bright.

8.8 CRITICAL OUTLOOK

In this Section, we provide an overview of the pivotal results and implications of our study. We also outline possible future directions to strengthen our results.

8.8.1 *Overview and main findings*

The delayed emission following the prompt phase of GRBs and observed across all the wavebands is called *afterglow*. The latter is broadly believed to be associated with the synchrotron radiation of electrons accelerated at the external shock resulting from the interaction of the GRB jet with the CBM. However, observations of GRB afterglows have unveiled several unexpected features, which cannot be accommodated within the standard afterglow model introduced in Sec. 8.5.1. Among these, one of the biggest surprises was the observation of a sudden and pronounced increase in the brightness of the optical afterglow lightcurve at late times, a feature dubbed *optical jump*.

The existence of the optical jump raises questions about the corresponding high-energy neutrino signal. A sharp rise in the afterglow photon density should reflect in a larger likelihood of producing *high-energy neutrinos* through $p\gamma$ interactions taking place at the shock between the jet and the CBM. While the high-energy neutrino signal produced during GRB afterglows has been extensively investigated in the standard scenario [226, 232, 371, 372], the way it is modified in the presence of an optical jump remains unexplored and we study it in this work for the first time.

We assume that the central engine responsible for the emission of the GRB jet undergoes delayed activity, ejecting a fast shell of plasma. The latter can catch up with the shell initially ejected, which, at the time of the second explosion, is being decelerated by the CBM and radiating standard afterglow emission. Within this framework, the optical jump is due to the late collision of two relativistic shells. Following the collision, the two shells merge into a single one that in turn interacts with the CBM and produces standard afterglow radiation. The model successfully fits the lightcurve of some GRBs displaying an optical jump, such as GRB 100621 as shown in Fig. 45.

While numerical simulations of the late collision and merger of two relativistic shells exist in the literature [360], our study provides the first analytical parametrization of this process. We combine the

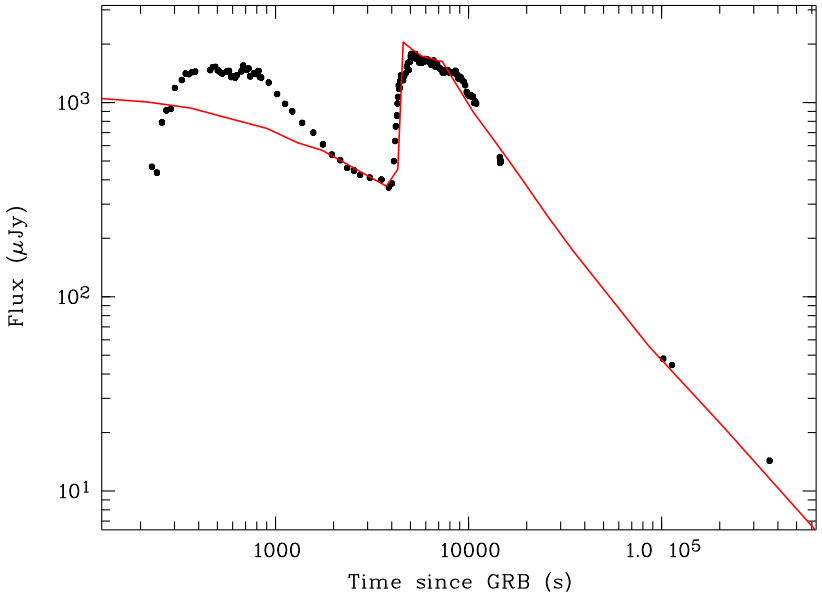

Figure 45: Optical lightcurve of GRB 100621 (black points) fitted with the model for the late collision of two relativistic shells developed in Ref. [360]. Figure from Ref. [352].

hydrodynamic shock jump conditions of ultra-relativistic shocks with general relativity tools and obtain analytical expressions of the characteristic parameters of the merged shell. Subsequently, we employ our analytical model to calculate the signature induced by the optical jump in the corresponding high-energy neutrino signal. Importantly, we find that the neutrino signal is sensitive to the optical jump only when the burst propagates in a constant density CBM. In this case, the number of neutrino events is expected to increase up to one order of magnitude with respect to the standard afterglow scenario. The result is very encouraging, as it significantly boosts the detection prospects of high-energy neutrinos from GRB afterglows.

Should the burst propagate in a constant density CBM, successful detection of neutrinos associated with the afterglow optical jump may be possible with IceCube-Gen2 radio. If this detection were to happen, our findings prove that we could probe the medium surrounding the GRB through neutrinos, since the jump in the neutrino curve is not expected if the burst propagates in a wind-like medium. Furthermore, the intensity of the rebrightening is sensitive to the CBM density. Notably, our findings would change if a different framework were to be adopted to model the optical jump. Therefore, we conclude that neutrinos could also be used to test the mechanism powering the jump.

8.8.2 *Future research directions*

Possible pathways for strengthening of our model are outlined in the following:

- *Energy injection across all the wavebands.* The injection of energy from the fast shell into the slow one should result in the increase of the electromagnetic flux across all the wavebands. However, bright jumps have been observed in the optical lightcurve only, with a dimmer jump sometimes observed in the X-ray band. The lack of multi-wavelength observations may be attributed to experimental constraints. The afterglow flux is quite dim by the time the jump is observed, and it possibly falls below the sensitivity thresholds of instruments looking at wavelengths other than the optical range. Upcoming telescopes in the radio and X-ray bands will provide further insights into this puzzling phenomenon.

- *Including the reverse shock in the model.* We assume that the reverse shock instantaneously crosses the merged shell. This simplified picture does not affect the expected number of neutrinos, however it produces the sharp lightcurves shown in Fig. 38. An analytical model including both the reverse and forward shock contributions will allow us to obtain more accurate forecasts of the electromagnetic signal associated with optical jumps.

- *Uncertainty on the rate of optical jumps.* The all-sky quasi-diffuse flux outlined in Sec. 8.6 is affected by the large uncertainties on the number of GRB afterglows with optical jumps. Currently operating and upcoming optical surveys, such as ZTF and the Vera C. Rubini Observatory, respectively, will potentially enable us to observe additional optical jumps, improving our knowledge of the fraction of long GRBs displaying this feature.

In summary, our research highlights the potential of high-energy neutrinos to probe the CBM surrounding GRB jets, while also testing the mechanism powering the optical jump. At the same time, our results advocate for the development of more advanced theoretical models to better account for the wide array of features observed during GRB afterglows. As high-cadence surveys with enhanced sensitivity will come online soon, they will detect an increasing number of well sampled optical lightcurves of GRB afterglows. Therefore, we expect additional optical jump data to become available in the near future, shedding new light on this puzzling feature.

9

PROBING GAMMA-RAY BURSTS OBSERVED AT VERY HIGH ENERGIES THROUGH THEIR AFTERGLOW

Based on: **Ersilia Guarini**, Irene Tamborra, Damien Bégué, Annika Rudolph, *Probing gamma-ray bursts observed at very high energies through their afterglow*, Mon. Not. Roy. Astron. Soc. 253 (2023) 149-162, arXiv:2301.10256

ABSTRACT A growing number of gamma-ray burst (GRB) afterglows is observed at very-high energies (VHE, $\gtrsim$ 100 GeV). Yet, our understanding of the mechanism powering the VHE emission remains baffling. We make use of multi-wavelength observations of the afterglow of GRB 180720B, GRB 190114C, and GRB 221009A to investigate whether the bursts exhibiting VHE emission share common features. We assume the standard afterglow model and microphysical parameters consistent with a synchrotron self-Compton (SSC) scenario for the VHE radiation. By requiring that the blastwave should be transparent to γ–γ pair production at the time of observation of the VHE photons and relying on typical prompt emission efficiencies and data in the radio, optical and X-ray bands, we infer for those bursts that the initial energy of the blastwave is $\tilde{E}_{k,\rm iso} \gtrsim O(10^{54})$ erg and the circumburst density is $n_0 \lesssim O(10^{-1})$ cm^{-3} for a constant circumburst profile [or $A_\star \lesssim O(10^{-1})$ cm^{-1} for a wind scenario]. Our findings thus suggest that these VHE bursts might be hosted in low-density environments, if the SSC radiation is responsible for the VHE emission. While these trends are based on a small number of bursts, the Cherenkov Telescope Array has the potential to provide crucial insight in this context by detecting a larger sample of VHE GRBs. In addition, due to the very poor statistics, the non-observation of high-energy neutrinos cannot constrain the properties of these bursts efficiently, unless additional VHE GRBs should be detected at distances closer than 15 Mpc when IceCube-Gen2 radio will be operational.

9.1 INTRODUCTION

Gamma-ray bursts (GRBs) are among the most powerful explosions in our Universe [133, 134, 185]. They exhibit a non-thermal spectrum with typical peak energies in the keV–MeV range [331, 428, 429]. We focus on long-duration GRBs, which release an isotropic energy in gamma-rays of about 10^{49}–10^{55} ergs within a few $O(10)$ s [133, 328]. The pulse of gamma-rays released during the prompt phase is followed by a delayed, long-lasting emission: the afterglow. Being detected from the radio to the X-ray bands, the afterglow makes GRBs electromagnetically accessible across all wavebands [e.g., 136].

Afterglow detections at high energy (HE, $\gtrsim 1$ GeV) have been reported for more than a decade, e.g. by the Large Area Telescope (LAT) onboard of the *Fermi* satellite [166]. In the past few years, such observations have been complemented by the detection of very high energy (VHE, $\gtrsim 100$ GeV) emission from an increasing number of GRBs, with photons with $O(\mathrm{TeV})$ energy being detected several hours after the burst trigger [108, 332, 333, 430–432]. Among these puzzling bursts, the recently discovered GRB 221009A represents an extraordinary event, being located close-by ($z \simeq 0.15$), very bright in gamma-rays ($\tilde{E}_{\gamma,\mathrm{iso}} \gtrsim 3 \times 10^{54}$ ergs) [1], and detected with photons up to $O(10)$ TeV by the Large High Altitude Air Shower Observatory (LHAASO) [433].

The VHE emission associated with the GRB afterglow was theoretically predicted [133, 134, 434–436], and then observed thanks to ground-based Cherenkov telescopes, such as the High Energy Stereoscopic System (H.E.S.S.) and the Major Atmospheric Gamma Imaging Cherenkov (MAGIC). The detection rate of GRB photons with energies $\gtrsim O(\mathrm{TeV})$ is expected to further improve with LHAASO [433] and the upcoming Cherenkov Telescope Array (CTA) [171]; hence, it is timely to investigate under which conditions VHE emission should be expected.

Up to HE, the multi-wavelength emission of the GRB afterglow is broadly considered to be generated by the synchrotron radiation produced by the electrons accelerated at the external shock as the latter expands in the circumburst medium (CBM) [136–138, 334, 383]. Yet, this standard afterglow picture cannot accommodate the production of TeV photons, unless electrons are accelerated above the synchrotron cut-off energy—see, e.g., [108].

1 We use three different reference frames throughout this paper: the observer frame, the central engine frame, and the blastwave comoving frame. In each of these frames, quantities are denoted with $X, \tilde{X}, X'$, respectively.

A possibility proposed to explain the VHE emission is the synchrotron self-Compton (SSC) scenario, according to which synchrotron photons inverse-Compton scatter the electrons that produced them [109, 226, 387, 437–443]. Alternatively, the acceleration of baryons together with electrons at the external shock can be considered. In this case, the mechanism responsible for the VHE emission may be proton synchrotron radiation or the decay of secondaries produced in photo-pion and photo-pair processes [e.g., 444–448]. Photohadronic processes have also been invoked for modeling the VHE emission [e.g., 449, 450].

While the number of GRBs detected in the VHE regime in the afterglow increases, our understanding of the physics underlying these bursts remains superficial. Do GRBs with VHE emission share common properties? Can we use VHE observations to infer properties of the CBM? In this paper, we intend to infer the characteristic features of GRBs exhibiting VHE emission and explore whether these bursts occur in environments with similar properties, possibly different from the ones expected from typical Wolf-Rayet stars observed in our Galaxy [e.g. 451, 452].

This paper is organized as follows. Section 9.2 presents an outline of the properties of the bursts detected in the VHE regime. In Sec. 9.3, we review the afterglow model, the blastwave dynamics and the related synchrotron radiation. We present constraints on the GRB energetics and the initial Lorentz factor in Sec. 9.4, while constraints on the non-observation of neutrinos from these bursts are presented in Sec. 9.5. A discussion on our findings is reported in Sec. 9.6, before concluding in Sec. 9.7. The modeling of the photon energy distribution is summarized in Appendix C.1, while the physics of hadronic interactions is outlined in Appendix C.2. Appendix C.3 provides additional insight on the properties of the CBM for our VHE GRB sample in comparison with GRBs without VHE emission.

9.2 SAMPLE OF GAMMA-RAY BURSTS OBSERVED AT VERY HIGH ENERGIES

The GRBs detected with VHE emission can be broadly grouped in two classes based on the isotropic energy emitted in gamma-rays during the prompt phase: GRBs with intermediate to low isotropic energy [$\tilde{E}_{\gamma,\mathrm{iso}} \lesssim 10^{50}$ erg, i.e. GRB 201015A [431] and GRB 190829A [108]] and energetic events with isotropic energy larger than typically observed ($\tilde{E}_{\gamma,\mathrm{iso}} \gtrsim 10^{53}$ erg). We limit our analysis to the latter group.

The class of bursts detected in the VHE regime and with large $\tilde{E}_{\gamma,\mathrm{iso}}$ is populated by:

Table 3: Properties of the sample of VHE GRBs considered in this work. For each GRB we list the redshift (z), the inferred emitted isotropic energy of the prompt phase in the source frame ($\tilde{E}_{\gamma,iso}$), the duration of the prompt emission (T_{90}), the time of detection of the VHE photon ($T_{\gamma,\mathrm{VHE}}$), the electron spectral index (k_e) and the CBM type (wind or ISM). The following references are quoted in the table: [1] [460], [2] [453], [3] [333], [4] [332], [5] [430], [6] [461], [7] [332], [8] [462], [9] [433], [10] [457], [11] [463], [12] [464].

Event	Redshift	$\tilde{E}_{\gamma,iso}$ [erg]	T_{90} [s]	T_{VHE} [days]	k_e	CBM	References
GRB 180720B	0.653	6×10^{53}	49	0.5	2.4	ISM	[1, 2, 3]
GRB 190114C	0.4245	2.5×10^{53}	25	6×10^{-3}	2.2–2.45	ISM	[4, 5, 6, 7, 8]
GRB 221009A	0.151	3×10^{54}	300	0.3	2.5	Wind	[9, 10, 11, 12]

- GRB 180720B detected with $\tilde{E}_{\gamma,\mathrm{iso}} \simeq 6\times10^{53}$ erg [453]. The H.E.S.S. Collaboration reported the observation of photons with energy between 0.11 TeV and 0.44 TeV at about $\sim$ 10 hours after the trigger [333].

- GRB 190114C, whose isotropic energy is estimated to be $\tilde{E}_{\gamma,\mathrm{iso}} \simeq 2.5\times10^{53}$ [454]. MAGIC observed 0.3–1 TeV photons [332, 430] from this burst, starting approximately one minute after its trigger. From Fig. 3 of [430], we infer that a large number of photons of energy up to 1 TeV is still observed at late times, around 520 s, when the emission can be associated with the afterglow.

- GRB 221009A observed with isotropic energy $\tilde{E}_{\gamma,\mathrm{iso}} \gtrsim 3\times10^{54}$ erg [318, 455, 456]. This is an interesting burst with photons with energy up to 18 TeV reported by LHAASO within 2000 s post GBM trigger [433, 457]. The distribution in energy and time of the VHE photons is not yet available,while upper limits on the VHE flux at very late times have been published by H.E.S.S. [458]. On the contrary, the photon with energy $\simeq$ 0.4 TeV detected 0.4 days after the trigger of the burst by *Fermi*-LAT can be safely associated with the afterglow emission [457].

Note that VHE emission has been observed from GRB 201216C as well, whose prompt isotropic energy is $\tilde{E}_{\gamma,\mathrm{iso}} \simeq 4.7\times10^{53}$ erg [459]. Since the published data is sparse to date [432], we do not consider this GRB in our analysis. The properties of the sample of GRBs that we consider throughout this paper are summarized in Table 3.

9.3 AFTERGLOW MODEL

In this section, we review the dynamics of the GRB blastwave as it propagates in the CBM. We also introduce the synchrotron spectrum invoked to model the standard afterglow emission.

9.3.1 *Blastwave dynamics*

Throughout the prompt phase, the Lorentz factor of GRB outflows is $\Gamma \gg 100$ [324]. During the afterglow, $\Gamma^{-1} \lesssim \theta_j$, being θ_j the jet half-opening angle. Therefore, it is safe to model the afterglow radiation through isotropic equivalent quantities [133]. We introduce the kinetic isotropic energy of the blastwave, $\tilde{E}_{k,\rm iso} = \tilde{E}_{\rm iso} - \tilde{E}_{\gamma,\rm iso}$, corresponding to the energy left in the outflow after the isotropic energy $\tilde{E}_{\gamma,\rm iso}$ has been released in gamma-rays during the prompt emission.

In the standard picture, the onset of the afterglow coincides with the beginning of the blastwave deceleration, occurring as the mass swept-up from the CBM becomes comparable to the initial mass of the outflow [e.g., 107, and references therein]. The CBM is assumed to have particle density profiles scaling as $n \propto R^{-k}$, where R is the distance from the central engine. Two asymptotic scenarios are usually considered in the literature [451]: $k = 0$, corresponding to a constant density interstellar medium (hereafter named ISM), and $k = 2$, corresponding to a wind-like CBM (hereafter dubbed wind).

As the blastwave expands, it interacts with the cold CBM. Two shocks form: the forward shock, which propagates in the cold CBM, and the reverse shock, propagating in the relativistic jet, in mass coordinates. We focus on the self-similar phase, starting when the reverse shock has crossed the ejecta and the electromagnetic emission is mainly due to the forward shock. In this phase, the blastwave dynamics is well described by the Blandford-McKee (BM) solution [382].

The deceleration time of the blastwave depends on the particle density profile of the CBM. Assuming that the outflow is launched with initial Lorentz factor Γ_0 in the ISM scenario [107, 382]:

$$T_{\rm dec,ISM} = \left[\frac{3\tilde{E}_{k,\rm iso}(1+z)^3}{64\pi n_0 m_p c^5 \Gamma_0^8}\right]^{1/3}, \tag{9.1}$$

where $n = n_0$ is the ISM density, z is the redshift of the source, c is the speed of light, and m_p is the proton mass. As for the wind scenario, the number density of the CBM is parametrized as $n = AR^{-2}$.

Here, $A = \dot{M}_w/(4\pi v_w m_p) = 3.02 \times 10^{35} A_\star$ cm^{-1}, where $A_\star = \dot{M}_{-5}/v_8$ is given for the typical mass loss rate $\dot{M}_{-5} = \dot{M}/(10^{-5} M_\odot$ yr$^{-1})$ and wind velocity $v_8 = v_w/(10^8$ cm s$^{-1})$ of Wolf-Rayet stars [372, 385]. According to this [384]:

$$T_{\rm dec,wind} = \frac{\tilde{E}_{k,\rm iso}(1+z)}{16\pi A m_p c^3 \Gamma_0^4} \,. \tag{9.2}$$

After the deceleration starts, the Lorentz factor of the blastwave decreases with time [382–384]:

$$\Gamma_{\rm ISM} = \Gamma_0 \left(\frac{T_{\rm dec,ISM}}{4t}\right)^{3/8} , \tag{9.3}$$

$$\Gamma_{\rm wind} = \Gamma_0 \left(\frac{T_{\rm dec,wind}}{4t}\right)^{1/4} , \tag{9.4}$$

for the ISM and wind scenarios, respectively.

Finally, the radius of the blastwave evolves as [372]:

$$R = \frac{\zeta \Gamma^2 t c}{(1+z)} \,, \tag{9.5}$$

where Γ decreases with time according to Eqs. 9.3 or 9.4, and we recall that the time t is measured in the observer frame. The parameter ζ depends on the hydrodynamics of the blastwave. It is usually assumed to be constant, but its value is very uncertain [e.g., 372, 383, 387, 465, 466]; throughout this work, we adopt $\zeta = 8$ [372].

We assume the uniform shell approximation of the BM solution. This is a fair assumption, since we are not interested in the hydrodynamics of the blastwave. Furthermore, the particle density of the BM shell quickly drops outside the region of width $\propto R/\Gamma^2$ behind the forward shock. Hence, particle emission from outside this region is negligible.

9.3.2 *Synchrotron spectrum*

As the fireball expands in the cold CBM, the forward shock at its interface converts the kinetic energy of the blastwave into internal energy, whose density is given by [382]

$$u' = 4 m_p c^2 n \Gamma (\Gamma - 1) \,, \tag{9.6}$$

where $n = n_0$ for the ISM scenario and $n = A R^{-2}$ in the wind scenario. Equation 9.6 directly follows from the shock-jump conditions at the forward shock.

A fraction ε_B of the internal energy density in Eq. 9.6 is stored in the magnetic field, whose comoving strength is

$$B' = \sqrt{32\pi m_p c^2 n \varepsilon_B \Gamma(\Gamma-1)}\,. \tag{9.7}$$

The forward shock driven by the ejecta into the CBM is collisionless, meaning that it is mediated by collective plasma instabilities rather than collisions [287]. Hence, it can accelerate particles through the Fermi mechanism [139, 370, 388]. In particular, we assume that electrons are accelerated to a power-law distribution $N(\gamma_e) \propto \gamma_e^{-k_e}$, where k_e is the electron spectral index. The resulting non-thermal population of accelerated electrons is assumed to carry a fraction ε_e of the energy density (Eq. 9.6).

Three characteristic Lorentz factors define the distribution of shock-accelerated electrons: the minimum ($\gamma'_{e,\rm min}$), the cooling ($\gamma'_{e,\rm cool}$), and the maximum ($\gamma'_{e,\rm max}$) ones. These are given by [134, 384, 389]:

$$\gamma'_{e,\rm min} = \frac{\epsilon_e}{\xi_e}\frac{m_p}{m_e}\frac{(k_e-2)}{(k_e-1)}(\Gamma-1)\,, \tag{9.8}$$

$$\gamma'_{e,\rm cool} = \frac{6\pi m_e c}{\sigma_T B'^2}\frac{(1+z)}{t\Gamma}\,, \tag{9.9}$$

$$\gamma'_{e,\rm max} = \left(\frac{6\pi e}{\sigma_T B' \varphi}\right)^{1/2}\,, \tag{9.10}$$

where σ_T is the Thompson cross section, ξ_e is the fraction of accelerated electrons, $e = \sqrt{\alpha\hbar c}$ is the electron charge, with $\alpha = 1/137$ being the fine-structure constant, and $\hbar$ the reduced Planck constant. Finally, φ is the number of gyroradii required to accelerate particles [390]. The maximum Lorentz factor $\gamma'_{e,\rm max}$ is obtained by equating the electron cooling time $t'_{e,\rm cool} = 6\pi m_e c/(\sigma_T \gamma'_e B'^2)$ and the acceleration time $t'_{\rm acc} = 2\pi\gamma'_e m_e c^2 \varphi/(ecB')$.

The synchrotron break frequencies in Eqs. 9.8–9.10 should take into account SSC losses of electrons, usually modeled through a correction factor depending on the Comptonization parameter Y [for more details, see *e.g.* 109]. For all considered GRBs, observations show that the flux normalizations in the X-ray and VHE bands are comparable, hinting that synchrotron and SSC processes equally contribute to the cooling of electrons at the time of VHE emission. Since the Y parameter decreases with time [109], and our analysis mainly considers epochs $t > T_{\rm VHE}$, we can safely neglect SSC corrections in Eqs. 9.8-9.10; see Sec. 9.4.1.

The characteristic Lorentz factors of electrons introduce three energy breaks in the observed spectrum of synchrotron photons, namely $E_{\gamma,\rm min}$, $E_{\gamma,\rm cool}$ and $E_{\gamma,\rm max}$, defined as [383]:

$$E_\gamma \equiv h\nu_\gamma = \frac{3}{2}\frac{B'}{B_Q} m_e c^2 {\gamma'_e}^2 \frac{\Gamma}{(1+z)}\,, \tag{9.11}$$

where $B_Q = 4.41 \times 10^{13}$ G.

The synchrotron self-absorption (SSA) Lorentz factor should be included for a complete treatment of synchrotron radiation. The corresponding break frequency is expected in the radio band [107]. However, detailed knowledge on the thermal electron distribution and on the structure of the emitting shell is needed to account for the SSA process [391]. We neglect this characteristic Lorentz factor and corresponding break frequency and discuss how this choice affects our findings in Sec. 9.4.2.

Electrons can be in two distinct radiative regimes: the "fast cooling regime" (if $\nu_{\gamma,\rm min} > \nu_{\gamma,\rm cool}$) or the "slow cooling regime" (for $\nu_{\gamma,\rm min} < \nu_{\gamma,\rm cool}$). In the former case, all the electrons efficiently cool down via synchrotron to the cooling Lorentz factor $\gamma_{e,\rm cool}$. In the latter case, synchrotron cooling is inefficient and it takes place for electrons with $\gamma_e > \gamma_{e,\rm cool}$ only.

In the fast cooling regime, the synchrotron photon energy density [in units of $\rm GeV^{-1}\ cm^{-3}$] is [383]:

$$n'^{\rm sync}_{\gamma}(E'_\gamma) = A'_\gamma \begin{cases} \left(\frac{E'_\gamma}{E'_{\gamma,\rm cool}}\right)^{-\frac{2}{3}} & E'_\gamma < E'_{\gamma,\rm cool} \\ \left(\frac{E'_\gamma}{E'_{\gamma,\rm cool}}\right)^{-\frac{3}{2}} & E'_{\gamma,\rm cool} \le E'_\gamma \le E'_{\gamma,\rm min} \\ \left(\frac{E'_{\gamma,\rm min}}{E'_{\gamma,\rm cool}}\right)^{-\frac{3}{2}} \left(\frac{E'_\gamma}{E'_{\gamma,\rm min}}\right)^{-\frac{k_e+2}{2}} & E'_{\gamma,\rm min} < E'_\gamma \le E'_{\gamma,\rm max} \end{cases} . \tag{9.12}$$

On the other hand, in the slow cooling regime, the synchrotron photon energy density is:

$$n'^{\rm sync}_{\gamma}(E'_\gamma) = A'_\gamma \begin{cases} \left(\frac{E'_\gamma}{E'_{\gamma,\rm min}}\right)^{-\frac{2}{3}} & E'_\gamma < E'_{\gamma,\rm min} \\ \left(\frac{E'_\gamma}{E'_{\gamma,\rm min}}\right)^{-\frac{(k_e+1)}{2}} & E'_{\gamma,\rm min} \le E'_\gamma \le E'_{\gamma,\rm cool} \\ \left(\frac{E'_{\gamma,\rm cool}}{E'_{\gamma,\rm min}}\right)^{-\frac{k_e+1}{2}} \left(\frac{E'_\gamma}{E'_{\gamma,\rm cool}}\right)^{-\frac{k_e+2}{2}} & E'_{\gamma,\rm cool} < E'_\gamma \le E'_{\gamma,\rm max} \end{cases} . \tag{9.13}$$

The normalization constant is given by [226, 383]

$$A'_\gamma = \frac{L'_{\gamma,\rm max}}{4\pi R^2 c\ \min(E'_{\gamma,\rm min}, E'_{\gamma,\rm cool})} , \tag{9.14}$$

where $L'_{\gamma,\rm max} = N_e P'_{\rm max}(\gamma'_e)/E'_\gamma$ is the comoving specific luminosity [in units of $\rm s^{-1}$]. The total number of radiating electrons in the blastwave is $N_e = 4\pi n_0 \xi_e R^3/3$ in the ISM scenario, while it is given by $N_e = 4\pi A \xi_e R$ in the wind scenario. Finally, the synchrotron power radiated by the electrons with Lorentz factor $\gamma'_e = \min(\gamma'_{e,\rm min}, \gamma'_{e,\rm cool})$ is $P'_{\rm max}(\gamma'_e) = c\sigma_T B'^2 \gamma'^2_e/(6\pi)$.

Given the photon energy density in Eqs. 9.12 and 9.13, the photon synchrotron spectrum observed at Earth is [in units of $\rm GeV\ cm^{-2}\ s^{-1}\ Hz^{-1}$]:

$$\Phi^{\rm sync}_{\nu_\gamma}(E_\gamma; z) = \frac{(1+z)^2}{4\pi d_L(z)^2} n'^{\rm sync}_{\gamma} \left(\frac{E_\gamma(1+z)}{\Gamma}\right) \frac{1}{\nu_\gamma} \frac{V'_\gamma(1+z)}{t\Gamma} , \tag{9.15}$$

where $V'_\gamma = 4\pi R^3/8\Gamma$ is the comoving emitting volume of the blastwave and $d_L(z)$ is the luminosity distance of the source at redshift z. We assume a flat ΛCDM cosmology with $H_0 = 67.4\ \rm km\ s^{-1}\ Mpc^{-1}$, $\Omega_M = 0.315$,

and $\Omega_\Lambda = 0.685$ [277]. The modeling of the (V)HE spectrum complementing the synchrotron one is described in Appendix C.1.

9.4 CONSTRAINTS ON THE ENERGETICS AND INITIAL LORENTZ FACTOR

In this section, we present constraints on the blastwave energy and the surrounding CBM properties by exploiting the observed radio, optical and X-ray fluxes, and the opacity to γ–γ pair production. By combining the observation of VHE photons with the duration of the prompt emission, we also infer upper and lower limits on the initial Lorentz factor Γ_0. We stress that we rely on the standard afterglow model outlined in Sec. 9.3. Hence, our constraints hold within this framework only.

Among the GRBs listed in Table 3, we select GRB 221009A and GRB 190114C to carry out our analysis. These GRBs are the closest ones and we consider them as representative of our sample in terms of energetics, see Sec. 9.2 and Table 3. Furthermore, they are good examples of the main models invoked to explain the VHE emission: SSC for GRB 221009A [467] and proton synchrotron for GRB 190114C [448]. The parameters listed in Table 3 are fixed in our analysis, while we consider $\tilde{E}_{k,\rm iso}$, n, ε_e, and ε_B as free parameters in the model.

9.4.1 *Multi-wavelength observations*

As discussed in Sec. 9.3, the dynamics of the blastwave is independent of the initial Lorentz factor Γ_0, and it is completely determined by the isotropic kinetic energy $\tilde{E}_{k,\rm iso}$ and the CBM density n. Hence, by requiring that Eq. 9.15 matches the fluxes observed across different wavebands, we can constrain the allowed $\tilde{E}_{k,\rm iso}$ and n.

For GRB 221009A and GRB 190114C, the radio, optical and X-ray fluxes are extracted at the observation time $T_{\rm obs}$ where the data in the three wavebands are available. $T_{\rm obs}$ considered for each burst and the corresponding observed fluxes are listed in Table 4. Multi-wavelength light-curves and tables of data are provided in [462] for GRB 190114C and in [467] for GRB 221009A; see also references therein for observations with different instruments. The X-ray fluxes are obtained from the [468].

Table 4: Multi-wavelength fluxes used in our analysis for the bursts listed in Table 3. For each GRB, we list the considered observation time ($T_{\rm obs}$), as well as the correspondent radio flux ($F^{\rm obs}_{\nu,\rm rad}$), optical flux ($F^{\rm obs}_{\nu,\rm opt}$), and X-ray flux ($F^{\rm obs}_{\nu,\rm X}$); each at its corresponding frequency or bands, as specified in parenthesis. The following references are quoted in the table: [1] [469], [2] [470], [3] [468], [4] [462], [5] [467], [6] [471]; see also references therein for the extrapolated fluxes.

Burst	$T_{\rm obs}$ [days]	$F^{\rm obs}_{\nu,\rm rad}$ [Jy]	$F^{\rm obs}_{\nu,\rm opt}$ [Jy]	$F^{\rm obs}_{\nu,\rm X}$ [Jy]	References
GRB 180720B	2	10^{-3} (15.5 GHz)	4×10^{-5} (R-band)	1.24×10^{-7} (10 keV)	[1, 2, 3]
GRB 190114C	1.424	1.930×10^{-3} (5.5 GHz)	3.9×10^{-5} ($R-$band)	5.98×10^{-8} (10 keV)	[3, 4]
GRB 221009A	2.3	9×10^{-3} (6 GHz)	2.016×10^{-3} ($R-$ band)	2.19×10^{-6} (10 keV)	[3, 5, 6]

We assume that the evolution of the emitting blast-wave is adiabatic, and that the micro-physical parameters of the emission are constant with time. Note that a different choice of $T_{\rm obs}$ would lead to the same order of magnitude estimation that we present here for $\tilde{E}_{k,\rm iso}$ and n. For convenience, we carry our analysis out at $T_{\rm obs}$ when radio, optical and X-ray data are simultaneously available for each GRB; see Table 4.

The left panels of Fig. 46 display the pairs of $(\tilde{E}_{k,\rm iso}, n)$ for which Eq. 9.15 reproduces the fluxes observed in the radio, optical and X-ray bands, respectively, for GRB 190114C (top and middle panels) and GRB 221009A (bottom panel). For GRB 190114C we calculate the theoretical synchrotron flux for two values of the electron spectral index: $k_e = 2.2$ (top panels), which is obtained by inspecting the spectral energy distribution [448], and $k_e = 2.45$ (middle panels), which instead reproduces the slope of the lightcurve [462]. For GRB 221009A, we only consider $k_e = 2.6$ [467]; see Table 3. In all cases, we fix $\xi_e = 1$ throughout our analysis. The line colors in the left panels of Fig. 46 correspond to different values of ε_B, which we vary in the range 10^{-5}–10^{-1}. For each ε_B we select a value of ε_e that allows for solutions, namely $\varepsilon_e = 0.1$ (stars) and $\varepsilon_e = 0.5$ (diamonds) for GRB 190114C and GRB 221009A, respectively. The intersection among the three lines in each of the left panels of Fig. 46, marked by a star (diamond), corresponds to the values of $\tilde{E}_{k,\rm iso}$ and n which simultaneously reproduce the observed flux across the three wavebands for given pairs of $(\varepsilon_e, \varepsilon_B)$.

The choice $\xi_e = 1$ naturally excludes the proton synchrotron process for the modeling of the VHE emission, whereas it is consistent with the SSC scenario. The latter also requires $\varepsilon_e \gtrsim \varepsilon_B$, with typical parameters being $\varepsilon_e \simeq O(10^{-1})$ and $\varepsilon_B \lesssim O(10^{-2})$ [e.g., 109]; the relation between ε_e and ε_B is inverted in the proton synchroton scenario, that is to say $\varepsilon_e \ll \varepsilon_B$ [e.g. 446, 448]. Our assumptions are thus consistent with the

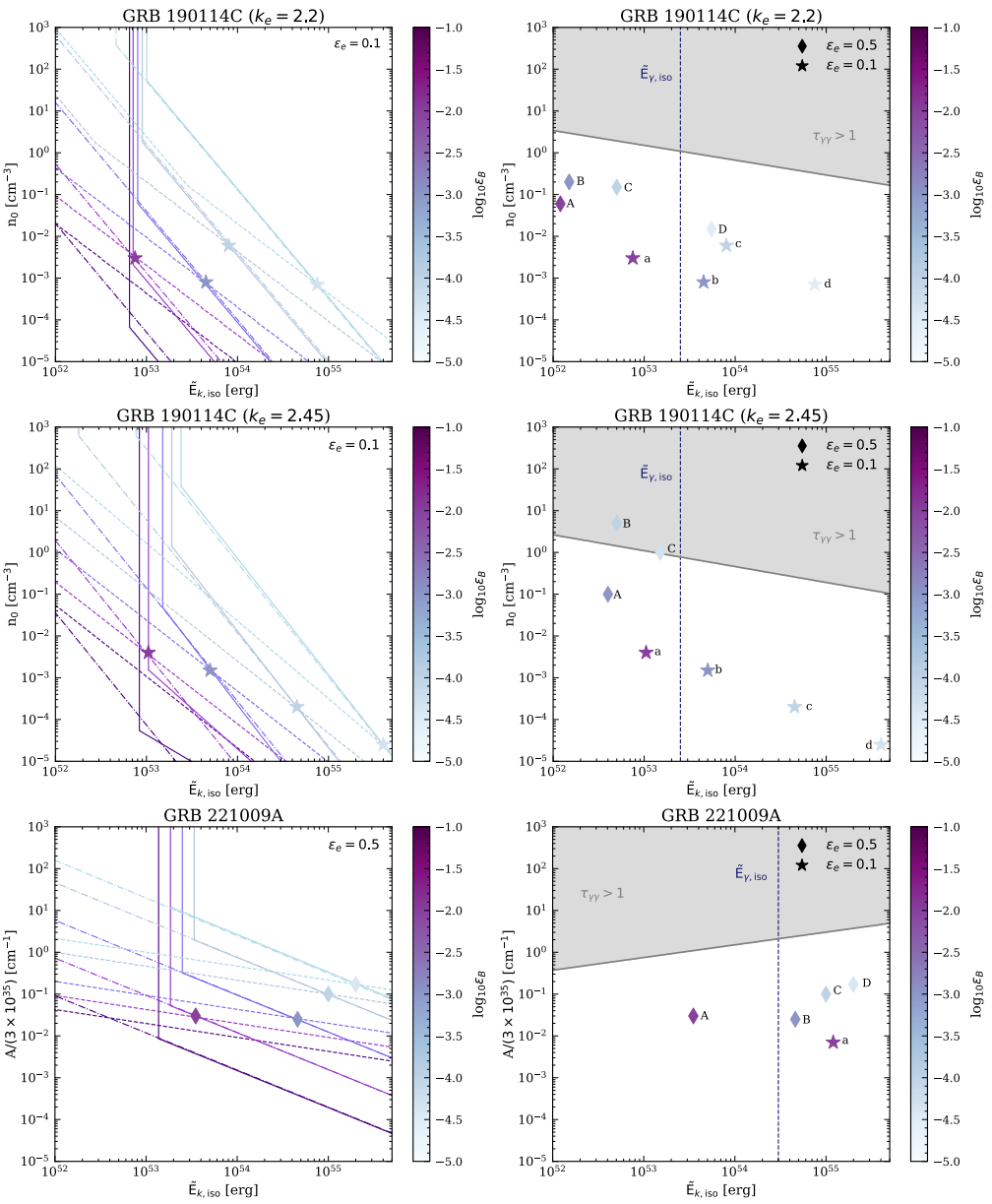

Figure 46: Isotropic kinetic energy $\tilde{E}_{k,\rm iso}$ and density n_0 $[A/(3\times10^{35})]$ compatible with the radio, optical and X-ray fluxes for GRB 190114C (top and middle panels) and GRB 221009A (bottom panels). *Left panels*: $(\tilde{E}_{k,\rm iso}, n)$ pairs for which the computed synchrotron flux (Eq. 9.15) matches the observed one in the radio (dashed lines), optical (dotted-dashed lines) and X-ray (continuous lines), as listed in Table 4. For each burst, the line colors are defined by the value of $\varepsilon_B \in [10^{-5}, 10^{-1}]$ (see colorbar). For GRB 190114C, we fix $\varepsilon_e = 0.1$ and $k_e = 2.2$ in the top panels, while $k_e = 2.45$ in the middle panels. For GRB 221009A, $\varepsilon_e = 0.5$ and $k_e = 2.6$; see main text for details. The intersection among the lines for each value of ε_B is marked by a star ($\varepsilon_e = 0.1$) or a diamond ($\varepsilon_e = 0.5$). Results are shown for the value of ε_e which guarantees solutions for ε_B in the considered range. *Right panels*: Same as the left panels, but highlighting the pairs of $(\tilde{E}_{k,\rm iso}, n)$ that simultaneously match radio, optical and X-ray data both for $\varepsilon_e = 0.1$ (stars) and $\varepsilon_e = 0.5$ (diamonds). The shadowed gray region is excluded from the transparency argument, i.e. $\tau_{\gamma\gamma} > 1$ at $T_{\rm VHE}$ (Table 3). The dashed blue line marks the value of $\tilde{E}_{\gamma,\rm iso}$ for both bursts. Combining the transparency argument, the typical prompt emission efficiencies, and multi-wavelengths data, the preferred region of the parameter space for GRB 190114C [GRB 221009A] is the one with $2.5\times10^{53} \lesssim \tilde{E}_{k,\rm iso} \lesssim 10^{55}$ erg $[3\times10^{54} \lesssim \tilde{E}_{k,\rm iso} \lesssim 5\times10^{55}$ erg] and $6\times10^{-4} \lesssim n_0 \lesssim 2\times10^{-2}$ cm^{-3} $[7\times10^{-3} \lesssim A/(3\times10^{35}) \lesssim 10^{-1}$ cm$^{-1}]$. Note that the upper limit set for the kinetic energy is implied by the requirement that ε_B cannot be too small in collisionless shocks. The letters mark the selected $(\tilde{E}_{k,\rm iso}, n)$ pairs for which the corresponding initial Lorentz factor Γ_0 is reported in Table 5.

SSC interpretation of the VHE emission. We discuss how this may affect our results in the following; see Sec. 9.4.2 and Sec. 9.6.

Note that we neglect any uncertainty on the observed fluxes and the microphysical parameters for simplicity, and the lines in the left panels of Fig. 46 are obtained by considering nominal values for the involved quantities. Furthermore, we rely on two approximations. First, we do not consider the exact hydrodynamics of the blastwave and adopt the uniform BM shell dynamics, as outlined in Sec. 9.3. Second, our results are sensitive to the constant ζ appearing in the definition of the blastwave radius, i.e. Eq. 9.5. However, we expect the error introduced by these two approximations to be below a factor of 2. Hence, the results in Fig. 46, although approximated, provide good insights into the features of our VHE GRB sample, if the standard afterglow model is adopted to explain multi-wavelength data.

9.4.2 *Blastwave opacity to γ–γ pair production*

The synchrotron model, outlined in Sec. 9.3 and adopted in Sec. 9.4.1, cannot explain the VHE radiation observed during the afterglow, if the energy cutoff of relativistic electrons is taken into account [108]. Nevertheless, the energy cutoff cannot be neglected, and it is not clear under which conditions electrons can be accelerated up to PeV energies within the blastwave.

To model the VHE emission, SSC has been invoked [109, 387, 435, 437–442] or mechanisms involving either proton-synchrotron radiation or the decay of secondaries produced in photo-pion and photo-pair processes [e.g., 444–448]. Both these scenarios assume that the photons observed with $\sim$ TeV energy are produced in the same decelerating fireball as the synchrotron ones [382, 383, 472]. Hence, in order to allow for VHE photons to escape the production region [e.g., 473, 474], the blastwave should be transparent to γ–γ pair production for $O(\mathrm{TeV})$ photons for $t \gtrsim T_{\rm VHE}$, $T_{\rm VHE}$ being the detection time of the VHE photon [e.g., 473, 474].

The blastwave opacity to γ–γ annihilation is parameterized through the γ–γ optical depth:

$$\tau_\gamma(E'_{\gamma,\rm VHE}) \simeq 0.1 \sigma_T E'_\star n'^{\rm sync}_\gamma(E'_\star) \frac{R}{\Gamma} \lesssim 1 \,, \tag{9.16}$$

where $E'_\star = (2m_e c^2)^2/E'_{\gamma,\rm VHE}$, $E'_{\gamma,\rm VHE}$ is the energy of the detected VHE photon, R/Γ is the compactness of the blastwave, and $n'^{\rm sync}_\gamma$ is the energy density of synchrotron photons (see Eqs. 9.12 and 9.13) [2]. Note that Eq. 9.16 evaluates the blastwave opacity at the peak of the γ–γ annihilation cross section [see e.g. 475].

As mentioned in Sec. 9.4.1, the dynamics of the blastwave only depends on its isotropic kinetic energy $\tilde{E}_{k,\rm iso}$ and on the CBM density. Therefore, Eq. 9.16 further constrains the $(\tilde{E}_{k,\rm iso}, n)$ pairs allowing VHE photons to escape from the blastwave, independently on the model adopted for explaining the VHE emission.

The right panels of Fig. 46 show the region of the parameter space that does not fulfill Eq. 9.16 at $T_{\rm VHE}$ and for the observed $E_{\gamma,\rm VHE}$, both different for each burst (see Table 3). In addition, a summary of the constraints obtained by combining the radio, optical and X-ray observations discussed in Sec. 9.4.1 is also displayed. We stress that we do not aim to fit the multi-wavelength data and we do not include VHE fluxes in Fig. 46. Rather, we only require that the VHE photon escapes the blastwave at $T_{\rm VHE}$, according to Eq. 9.16; this argument is different than the one adopted in Sec. 9.4.1. As already discussed in Sec. 9.4.1, the choice $T_{\rm obs} = T_{\rm VHE}$ would not change the results in Fig. 46. Since the radio data are not available at $T_{\rm VHE}$ for all the bursts, we list the observed time when radio, optical and X-ray data are simultaneously available in Table 4.

In Fig. 46, we show results for $\varepsilon_e = 0.1$ and 0.5, while we verified that smaller values of ε_e do not allow to reproduce simultaneously the radio, optical and X-ray fluxes for any value of ε_B. This might depend on the fact that we neglect the SSA frequency, which would introduce an additional break in the photon distribution and shift the radio flux to larger values [391]. However, the considered bursts are expected to be in the weak-absorption regime at $T_{\rm obs}$ considered in our analysis, cf. Table 4 [470, 476], while to date no information is available for GRB 221009A. Hence, neglecting the SSA process in the synchrotron spectrum may be a valid approximation.

Our results depend on $\xi_e = 1$. Smaller values of this parameter could allow $\varepsilon_e < 0.1$ and would lead to larger values of n_0 or $A/(3\times10^{35})$, typically inferred when the proton synchrotron model is adopted to explain the VHE emission, see e.g. [448, 477]. Therefore, the results in Fig. 46 are consistent within the SSC scenario, but no longer hold in the proton synchrotron one, as previously discussed in Sec. 9.4.1. Given the large number of degeneracies in the afterglow model, we limit our discussion to the case with $\xi_e = 1$ and leave a detailed investigation of the dependence of our findings on this assumption to future work.

2 In principle, the whole photon energy distribution, including the VHE component, should be used. Nevertheless, $E'_\star$ falls between the optical and X-ray bands for the VHE photons we are interested in. Hence, in order to simplify the calculation, it is safe to consider the synchrotron component only.

The transparency argument is particularly powerful for GRB 190114C when the spectral index $k_e = 2.45$ is adopted. In this case, some pairs $(\tilde{E}_{k,\rm iso}, n_0)$ which reproduce the flux across different wavebands are excluded by the requirement that the VHE photons do not undergo γ–γ pair-production at $t \lesssim T_{\rm VHE}$.

The allowed parameter space can be further constrained by considering the radiative efficiency of the prompt phase. Despite the latter being a topic of debate and potentially varying depending on the event, we here adopt a typical efficiency of $\simeq 10\%$ [e.g. 478]. Since $\tilde{E}_{\gamma,\rm iso} \sim 2.5 \times 10^{53}$ erg [$\tilde{E}_{\gamma,\rm iso} \gtrsim 3 \times 10^{54}$ erg] for GRB 190114C [GRB 221009A], we expect the region of the parameter space with $2.5 \times 10^{53} \lesssim \tilde{E}_{k,\rm iso} \lesssim 10^{55}$ erg [$3 \times 10^{54} \lesssim \tilde{E}_{k,\rm iso} \lesssim 5 \times 10^{55}$ erg] and $6 \times 10^{-4} \lesssim n_0 \lesssim 2 \times 10^{-2}$ cm^{-3} [$7 \times 10^{-3} \lesssim A/(3 \times 10^{35}) \lesssim 10^{-1}$ cm^{-1}] to be preferred, as indicated by the dashed blue line in the right panels of Fig. 46.

The inclusion of SSA in our treatment could shift the densities to larger values. However, as already mentioned, GRB 190114C may be in the weak-absorption regime at the considered time [470, 476]. Our CBM densities for GRB 190114C are much smaller than the ones inferred in [448], which finds $n_0 \simeq O(10$–$100)$ cm^{-3}. This is due to our assumption $\xi_e = 1$, whereas $\xi_e \simeq O(10^{-2})$ is required in [448] in the context of the proton synchrotron model for the VHE emission.

As for GRB 221009A, our results are consistent with the ones of [467], which obtains $A_\star = 1.2 \times 10^{-2}$ for $\tilde{E}_{k,\rm iso} = 6.8 \times 10^{54}$ erg, $\varepsilon_e = 0.2$ and $\varepsilon_B = 2 \times 10^{-3}$. On the contrary, for GRB 190114C, we obtain $n_0 \lesssim 2 \times 10^{-2}$ cm^{-3}, which is a factor $O(10)$ smaller than $n_0 = 0.3$ cm^{-3} obtained in [479]. This discrepancy may be due to the fact that [479] does not take into account data in the radio band. As it can be seen in the left-middle panel of Fig. 46, when only the optical and X-ray fluxes are used, we recover $n_0 \simeq O(10^{-1})$ cm^{-3}, if we assume $\tilde{E}_{k,\rm iso} = 6 \times 10^{53}$ erg, $\varepsilon_e = 0.1$ and $\varepsilon_B = 10^{-4}$, i.e. for parameters compatible with the ones adopted in [479]. Thus, more solutions are possible if the radio data are not included in the analysis since the optical and X-ray data are degenerate for a large part of the $(\tilde{E}_{k,\rm iso}, n_0)$ space.

For GRB 180720B, the compactness argument is not constraining. In fact, a signal in the energy range $E_{\gamma,\rm VHE} = 0.11$–$0.44$ TeV has been reported for this GRB at the time considered in Table 3. At such late times, we expect the blastwave to be already transparent to γ–γ pair production. Hence, we do not show plots for this burst. Nevertheless, exploiting the multi-wavelength data, our approach enables us to break the degeneracies involved in the standard afterglow model and to obtain $6 \times 10^{53} \lesssim \tilde{E}_{k,\rm iso} \lesssim 10^{55}$ erg and $4 \times 10^{-5} \lesssim n_0 \lesssim 10^{-1}$ cm^{-3}. For this burst, our parameters are similar to those inferred in [479], namely $\tilde{E}_{k,\rm iso} = 10^{54}$ erg and $n_0 = 0.1$ cm^{-3}.

Additional inputs on $\tilde{E}_{\gamma,\rm iso}$ may further restrict the allowed parameter space shown in Fig. 46, when typical prompt efficiencies are taken into account [478]. Our results hold if the multi-wavelength radiation observed from this class of bursts is modelled within the standard afterglow framework outlined in Sec. 9.3. More complex jet geometries [480], time-varying microphysical parameters [462, 481], the assumption of two-zone models [443] or other more complex models [e.g., 482] would affect our conclusions. Intriguingly, a low-density wind environment is inferred for GRB 221009A in [482], even though they suggest that the standard assumptions of the afterglow theory may be violated by this burst.

9.4.3 *Initial Lorentz factor*

As discussed in Sec. 9.3, the afterglow dynamics is independent of the initial value of the blastwave Lorentz factor (Γ_0), if the shell is in the self-similar regime [382, 383]. Therefore, the afterglow onset (i.e., the deceleration time $T_{\rm dec}$) can be used to infer Γ_0. Assuming that the VHE photon detected at $T_{\rm VHE}$ is associated with the afterglow, the blastwave should start to decelerate at $T_{\rm dec} \lesssim T_{\rm VHE}$. From Eqs. 9.1 and 9.2, this translates in a lower limit (LL) for Γ_0:

$$\Gamma_{0,\rm ISM}^{\rm LL} = \left[\frac{3\tilde{E}_{k,\rm iso}(1+z)^3}{64\pi n_0 m_p c^5 T_{\rm VHE}^3}\right]^{1/8}, \tag{9.17}$$

$$\Gamma_{0,\rm wind}^{\rm LL} = \left[\frac{\tilde{E}_{k,\rm iso}(1+z)}{16\pi A m_p c^3 T_{\rm VHE}}\right]^{1/4}, \tag{9.18}$$

for the ISM and wind scenarios, respectively.

Even though there is no significant correlation between the onset of the afterglow $T_{\rm dec}$ and the duration of the prompt emission T_{90} [483], the assumption of a thin shell—for which the reverse shock is at most mildly relativistic—implies $T_{\rm dec} \gtrsim T_{90}$. Within this approximation, most of the energy of the ejecta has been transferred to the blastwave at the onset of deceleration [484]. This condition provides us with upper limits (UL) on Γ_0:

$$\Gamma_{0,\rm ISM}^{\rm UL} = \left[\frac{3\tilde{E}_{k,\rm iso}(1+z)^3}{64\pi n_0 m_p c^5 T_{90}^3}\right]^{1/8}, \tag{9.19}$$

$$\Gamma_{0,\rm wind}^{\rm UL} = \left[\frac{\tilde{E}_{k,\rm iso}(1+z)}{16\pi A m_p c^3 T_{90}}\right]^{1/4}, \tag{9.20}$$

for the ISM and wind scenarios, respectively.

Table 5: Upper and lower limits on $\Gamma_{0,\mathrm{ISM(wind)}}$ obtained for the points of the parameter space selected through the criteria illustrated in the right panels of Fig. 46 and marked by a letter therein.

Burst	Symbol	$\Gamma^{\mathrm{LL}}_{0,\mathrm{ISM(wind)}}$	$\Gamma^{\mathrm{UL}}_{0,\mathrm{ISM(wind)}}$
GRB 190114C ($k_e = 2.2$)	a	312	961
	b	180	555
	c	216	665
	d	146	450
	A	153	472
	B	85	262
	C	71	218
	D	80	246
GRB 190114C ($k_e = 2.45$)	a	575	1797
	b	337	1054
	c	199	622
	d	145	454
	A	76	237
	B	55	170
	C	50	156
GRB 221009A	a	173	313
	A	50	160
	B	47	154
	C	55	180
	D	27	90

For fixed isotropic kinetic energy and CBM density, $\Gamma^{\mathrm{LL}}_{0,\mathrm{ISM(wind)}}$ can be obtained by rescaling $\Gamma^{\mathrm{UL}}_{0,\mathrm{ISM(wind)}}$ by $(T_{90}/T_{\mathrm{VHE}})^{3/8}$, if the burst propagates in a constant density medium, or by $(T_{90}/T_{\mathrm{VHE}})^{1/4}$ in the wind scenario. For each point marked in the right panels of Fig. 46 through a letter, the range of allowed values of $\Gamma_{0,\mathrm{ISM(wind)}}$ is listed in Table 5.

Our limits complement the estimates obtained from the prompt emission for GRB 221009A [485–487]. Furthermore, they are in agreement with [488], which obtains $\Gamma_0 = 719 \pm 59$ for GRB 190114C. Note that the lower limits $\Gamma^{\mathrm{LL}}_{0,\mathrm{wind}}$ for GRB 221009A are quite small and hence not constraining, due to the large T_{VHE} (see Table 3). The results in Table 5 and Fig. 46 hint that a very energetic blastwave propagating in a low density medium implies large Γ_0. This could be justified by considering that weaker winds extract less

angular momentum from the GRB progenitors. In this scenario, the core collapse may be driven by faster rotation, which favors the formation of highly collimated jets, compatible with the large Γ_0 and isotropic energies in low-density CBMs [484]. Similar conclusions on the high collimation of GRB 221009A have been reached also in [482].

9.5 CONSTRAINTS FROM THE NON-OBSERVATION OF HIGH-ENERGY NEUTRINOS

Provided that protons are co-accelerated at the forward shock, the GRB afterglow is expected to emit neutrinos with PeV–EeV energy [138, 226, 233, 371–373]. Neutrinos are predominantly produced through photo-hadronic ($p\gamma$) interactions of the protons accelerated at the external shock and photons produced as the blastwave decelerates, as summarized in Appendix C.2.

The IceCube Neutrino Observatory detects neutrinos in the TeV–PeV range [375, 416]. Nevertheless, so far no neutrino detection has been reported in connection to electromagnetic observations of GRBs [140], with upper limits set on the prompt [141] and the afterglow emission [142, 489]. Yet, upcoming neutrino facilities, such as IceCube-Gen2 and its radio extension [416], the Radio Neutrino Observatory [176], the Giant Radio Array for Neutrino Detection (GRAND200k) [17], as well as the spacecraft Probe of Extreme Multi-Messenger Astrophysics (POEMMA) [376] are expected to improve the detection prospects of afterglow neutrinos.

The non-observation of neutrinos from GRB 221009A [490] allows to constrain the GRB properties as well as the mechanism powering the prompt emission [485–487, 491]. We intend to investigate whether complementary constraints can be obtained through the current non-detection of neutrinos from the afterglow of VHE GRBs. To this purpose, we model the neutrino signal expected from the afterglow of GRB 190114C, since multi-wavelength interpretations invoking both SSC and proton synchrotron have been proposed [448, 479]. We focus on the SSC model, since the results outlined in Sec. 9.4.2 are consistent with this interpretation, and briefly discuss the proton synchrotron case. We expect the correspondent neutrino signal to be representative for all other GRBs in our sample (Table 3). However, more detections in the VHE band would allow to make more accurate predictions.

The time-integrated neutrino signal from $p\gamma$ interactions is calculated following Sec. 4 of [233], using as input the total photon distribution (defined in Eq. C.1) and the proton distribution (Eq. C.5). The parameters

adopted for computing the neutrino signal within the SSC model are summarized in Table 6 , corresponding to [479] [3]. For protons we fix $\xi_p = 1$—in order to obtain an optimistic estimation of the resulting neutrino

Table 6: Assumed model parameters for GRB 190114C resulting from the multi-wavelength modeling of the photon distribution outlined in [479].

Parameter	SSC fit
$\tilde{E}_{k,\mathrm{iso}}$ [erg]	6×10^{53}
n_0 [cm^{-3}]	0.3
Γ_0	300
ξ_e	1
ξ_p	1
ε_e	0.07
ε_B	4×10^{-5}
ε_p	0.8
φ	10
k_e	2.5
k_p	2.2
δ	−26°

flux— and $\varepsilon_p = 1 - \varepsilon_e - \varepsilon_B$ and $k_p = 2.2$ [85]. As a consequence, the neutrino flux computed in the SSC scenario represents an upper limit to the actual flux for the considered $\tilde{E}_{k,\mathrm{iso}}$, since no constraints can be derived on the fraction of energy going into accelerated protons nor on the fraction of accelerated protons.

The left panel of Fig. 47 shows the time-integrated muon neutrino flux, Φ_{ν_μ}, from the afterglow GRB 190114C for the SSC model. For comparison, we also show the sensitivity of IceCube to a source located at the declination $\delta \simeq -23°$ [416, 417]. In order to investigate future detection prospects, we plot the most optimistic sensitivity of IceCube-Gen2 radio for a source at $\delta = 0°$ [416], the one of RNO-G for a source at $\delta = 77°$ [176], as well as the sensitivity of GRAND200k for a source at $|\delta| = 45°$ [17] and the full-range time-integrated sensitivity of POEMMA [376]. We consider an error band $\Delta\Phi_{\nu_\mu}/\Phi_{\nu_\mu} = \pm 2$, according

3 Note that we rely on the findings of [479] only in this section, since their work performs a multi-wavelength fit including the VHE component. Our discussion in Sec. 9.4.1 is independent on [479]. The microphysical parameters obtained in [479] are consistent with ours, while the density n_0 is a factor $O(10)$ larger than the one obtained in Sec. 9.4.1 for GRB 190114C. As a consequence, the neutrino signal presented in this section is an upper limit with respect to the one we would obtain using the results of Sec. 9.4.1.

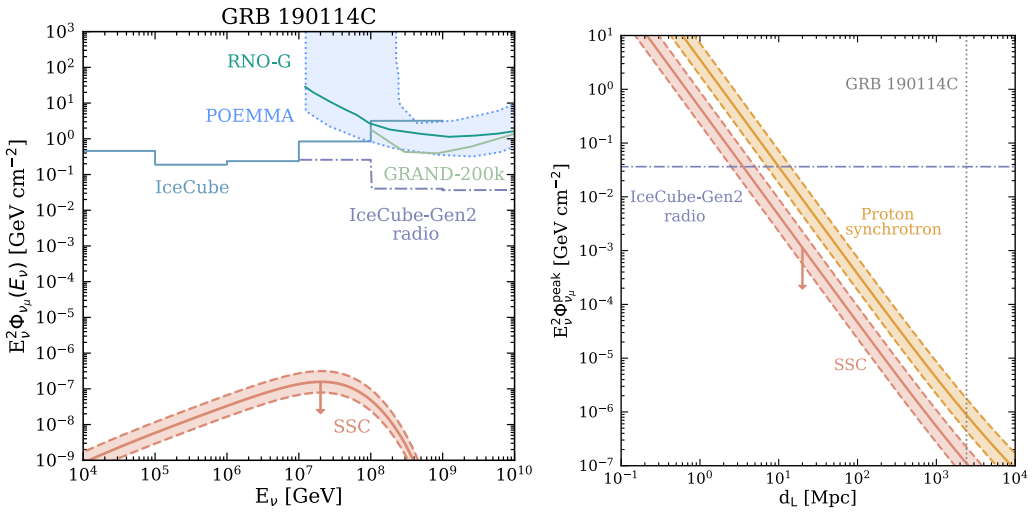

Figure 47: Time-integrated muon neutrino flux expected from the afterglow of GRB 190114C. *Left panel*: Time-integrated muon neutrino flux for the SSC model (pink shadowed area). This flux represents an upper limit for the real one (for the here considered $\tilde{E}_{k,\rm iso}$), as denoted by the pink arrow. The error in the flux prediction is assumed to be a factor $\Delta\Phi_{\nu_\mu}/\Phi_{\nu_\mu} = \pm 2$, due to the uncertainties in the analytical prescription of the photon flux; see main text. For comparison, the sensitivity of IceCube for a source located at the declination $\delta = -23^\circ$ [416, 417] is shown as well as the most optimistic ones of IceCube-Gen2 radio for a source at $\delta = 0^\circ$ [416], RNO-G for $\delta = 77^\circ$ [176], GRAND200k for a source at $|\delta| = 45^\circ$ [17], and the full-range time-integrated sensitivity of POEMMA [376]. The neutrino signal lies well below the sensitivity curves of current and upcoming VHE neutrino telescopes. Even though this result depends on the assumed parameters, we expect these conclusions to hold for different sets of parameters within current uncertainties. *Right panel*: Peak of the time-integrated muon neutrino flux (plotted in the left panel) as a function of the luminosity distance for a bursts with the same properties of GRB 190114C, except for its distance. The arrow for the SSC model is the same as the left panel. For comparison, we show the same result for the proton synchrotron model (yellow shadowed area), by relying on the parameters inferred in [448]. We also plot the sensitivity of IceCube-Gen2 radio for the optmistic case of a source located at $\delta = 0^\circ$ [416]. Note that since the peak of the time-integrated neutrino flux occurs for $E_\nu \simeq 10^7$–10^8 GeV for all the redshifts, we approximate the sensitivity of IceCube-Gen2 radio to be constant. In particular, we take the minimum value of the sensitivity to get the most optimistic prediction. For comparison, the dotted grey line indicates GRB 190114C. The peak of the time-integrated neutrino flux becomes comparable to the sensitivity of IceCube-Gen2 radio for $d_L \lesssim 5$ Mpc ($d_L \lesssim 15$ Mpc) for the SSC model parameters (proton synchrotron). As expected, at each distance the neutrino signal in the case of the proton synchrotron model is larger than the SSC one, since the former naturally requires larger values of n_0 and $\tilde{E}_{k,\rm iso}$.

to the uncertainties intrinsic to the analytical model, as discussed in Sec. 9.4.2. The main uncertainties come from the choice of parameters listed in Table 6. Nevertheless, the neutrino signal lies well below the sensitivity curves also for optimistic values of ε_e and ε_B—see also [233]. These findings imply that the non-detection of neutrinos from the afterglow of GRBs with VHE emission is expected and does not allow to further constrain the properties of the bursts. Conversely, detection of VHE neutrinos in coincidence with VHE GRB afterglows would be challenging to explain in the context of the standard afterglow model.

The right panel of Fig. 47 shows the peak of the time-integrated neutrino flux (plotted in the left panel) as a function of the luminosity distance, assuming a burst with properties identical to the ones of GRB 190114C. For comparison, we also show the peak of the time-integrated neutrino flux when the proton synchrotron model is assumed. We rely on the parameters inferred in [448]. We warn the reader that they are not comparable with the ones obtained in Sec. 9.4.1 due to our assumption $\xi_e = 1$ and the requirement $\xi_e \ll 1$ for a proton synchrotron model. Hence, the main goal of the right panel of Fig. 47 is to assess whether the neutrino detection perspectives from VHE bursts depend on the selected model for the VHE emission. Since the proton synchrotron model naturally requires larger values of n_0 and $\tilde{E}_{k,\mathrm{iso}}$, the resulting neutrino flux is larger than in the SSC scenario.

Comparing the peak of the neutrino flux to the sensitivity of IceCube-Gen2 radio [416], which is expected to be the most competitive facility (see left panel), we obtain that the peak of the neutrino flux becomes comparable to the sensitivity of IceCube-Gen2 radio for $d_L \lesssim 5$ Mpc ($d_L \lesssim 15$ Mpc) for the SSC model parameters (proton synchrotron). Such distances are too small, considering the distribution of long GRBs as a function of the redshift [282]. Therefore, we conclude that the detection of neutrinos from GRB afterglows displaying VHE emission is not a promising tool to infer GRB properties within a multi-messenger framework. Our conclusions are consistent with the ones of [448] for GRB 190114C, which finds that the photo-hadronic interaction rate accounts for inefficient energy extraction.

9.6 DISCUSSION

Our constraints on the VHE GRB properties are summarized in Table 7 for our benchmark bursts, GRB 180720B, GRB 190114C and GRB 221009A (see also Fig. 46). While our sample is small, such findings

Table 7: Summary of the model parameter constraints derived in this work from the afterglow of GRB 180720B, GRB 190114C and GRB 221009A (see also Fig. 46). The range preferred for the kinetic isotropic energy ($\tilde{E}_{k,\rm iso}$), the CBM density (n_0 $[A/(3\times10^{35})]$), and the initial Lorentz factor ($\Gamma_{0,\rm ISM(wind)}$) is reported.

GRB	$\tilde{E}_{k,\rm iso}$ [erg]	n_0 or $A/(3\times10^{35})$	$\Gamma_{0,\rm ISM(wind)}$
GRB 180720B	6×10^{53}–10^{55}	4×10^{-5}–10^{-1} cm^{-3}	80 – 1276
GRB 190114C	2.5×10^{53}–10^{55}	3×10^{-5}–2×10^{-2} cm^{-3}	50–1797
GRB 221009A	3×10^{54}–5×10^{55}	7×10^{-3}–10^{-1} cm^{-1}	$\lesssim 313$

raise questions on the nature of the progenitors and the sites hosting VHE bursts, if microphysical parameters compatible with the SSC scenario are assumed.

The initial Lorentz factor of our VHE bursts falls within the average expected for GRBs, see Sec. 9.4.3 and e.g. Secs. 5 and 6 of [483]. With the caveat that we have observed VHE emission for a few bursts only, our results seem to suggest that these VHE GRBs exhibit isotropic kinetic energy towards the higher tail of the distribution expected for GRBs, see e.g. Fig. 19 of [428]. This result might be biased by the sensitivity of existing telescopes, as well as the viewing angle. In the future, CTA may detect fainter bursts in the VHE regime, providing better insight on the population features and the fraction of GRBs with VHE emission.

As discussed in Sec. 9.4, VHE GRBs might preferentially occur in a low-density CBM–independently on the microphysics of the shock, the compactness argument requires that $n_0 \lesssim 1$ cm^{-3} and $A/(3\times10^{35}) \lesssim 1$ cm^{-1}. If microphysical parameters typical of SSC radiation are adopted [e.g., 492], even more stringent constraints are obtained. Intriguingly, we reach similar conclusions following the method outlined in [493] that relies on the simplifying assumption that all the bursts can be modelled with the same set of microphysical parameters and have a prompt emission efficiency $\simeq 50\%$. Following [493], we find that the VHE GRBs cluster in the low-density region of the parameter space $[n_0(A/(3\times10^{35})) \lesssim 10^{-1}$ cm^{-3} (cm^{-1})]. On the contrary, the bursts not displaying VHE emission analyzed in [493] are uniformly distributed in the $(\tilde{E}_{k,\rm iso}, n)$ space; we refer the interested reader to Appendix C.3 for additional details.

A CBM with low density is usually favored by the synchrotron closure relations [e.g. 494], that are found not to be fullfilled for all bursts; hence our findings might be affected by the simplifications intrinsic to these relations. Yet, these results are in agreement with the expectation that low-density environments favor a

transparent blastwave in the afterglow. Furthermore, larger densities may reprocess the VHE photons and emit electromagnetic radiation in other wavelengths. In addition, low density CBMs have been associated to long GRBs [e.g. 493, 495]. For example, a wind with $A_\star \simeq 4 \times 10^{-3}$ has been inferred for GRB 130427A [377], as a result of a multi-wavelength fit of the GRB lightcurve. [377] suggests that the weak wind could be a consequence of the GRB progenitor being hosted in a superbubble [496, 497]. Similarly, [484] finds that the winds of some GRB progenitors are weaker than the ones observed for Wolf-Rayet stars in our Galaxy ($A_\star \simeq 1$). This might be linked to the low metallicity of the progenitors [498] and their host galaxies [e.g. 499], which is anyway still under debate [e.g. 500]. Low CBM densities may also be caused by reduced mass-loss rate at the time of the stellar collapse [484]. Recently, [501] studied bursts with a plateau phase in their afterglow. In order to explain this feature, a small wind density consistent with our findings and a small outflow Lorentz factor are required, the latter implying a lack of VHE (and even HE) emission for those bursts, which [501] argues is the case.

Our results hold within the assumption that the multi-wavelength radiation is generated by the decelerating blastwave, whose dynamics is outlined in Sec. 9.3. Such conclusions may substantially change if more complex jet geometries [480], time-varying microphysical parameters [481] or two-zone models [443] should be invoked, as in the case of GRB 190114C [462]. Furthermore, low-density CBMs are obtained for $\xi_e = 1$, whereas smaller fractions of accelerated electrons naturally lead to larger densities [e.g. 448]. Thus, if a dense CBM should be inferred, e.g. via the SSA frequency in the radio band, it may hint towards a proton synchrotron model. In this sense, determining the CBM density can provide constraints on the mechanism powering the VHE emission. Our results are based on the SSC scenarios, rather than proton synchrotron ones. Since the value of ξ_e is largely uncertain, an analysis of the dependence of our conclusions on this parameter is left to future work. Additional input on these parameters may also come from numerical simulations of particle acceleration at the external shock.

Future observations of GRBs in the VHE regime with CTA [171] will be crucial to pinpoint the mechanism powering the VHE emission during the afterglow. However, CTA might have better detection prospects for large CBM surrounding these bursts, as suggested in [502]. The latter assumes a SSC origin of the VHE emission, although neglecting the cutoff introduced by γ–γ pair production. The SSC efficiency largely depends on the Compton parameter, which is maximized for large blastwave energies and CBM densities. As a consequence, [502] obtains CBM densities larger than the ones we infer, since the transparency argument

alone is sufficient to limit $n_0 \lesssim 1$ cm^{-3} $[A/(3\times10^{35}) \lesssim 1$ cm$^{-1}]$. We stress that the relation used for the opacity argument (Eq. 9.16) is approximate; therefore, detailed modeling of the energy cutoff and fit to the spectral energy distributions are required to draw robust conclusions from a larger burst sample. Yet, we do not expect the constraint $n < 1$ cm^{-1} to change drastically.

9.7 CONCLUSIONS

While the number of GRBs detected in the VHE regime during the afterglow will increase in the near future with the advent of CTA, our understanding of the mechanism powering the VHE emission is very preliminary. The standard synchrotron model, which well explains the afterglow data from the radio to the X-ray bands, cannot account for the emission of O(TeV) photons detected at late times.

In this paper, we focus on GRB 180720B, GRB 190114C and GRB 221009A, with the goal to infer the properties of the blastwave and the burst environment. By requiring that the plasma in the blastwave shell is transparent to γ–γ pair production at the time of the observation of the VHE photons, we obtain that the CBM density should be $n_0 \lesssim 1$ cm^3 $[A/(3\times10^{35})$ cm$^{-1}]$. A tentative interpretation of the radio, optical and X-ray data hints towards even lower CBM densities, with $n_0 \lesssim O(10^{-1})$ cm^{-3} $[A/(3\times10^{35}) \lesssim O(10^{-1})$ cm$^{-1}]$, if the microphysical parameters of the shock are taken to be consistent with SSC mechanism. Furthermore, we obtain constraints on the initial Lorentz factor of the blastwave by requiring that the deceleration of the fireball starts before the observation of VHE photons and after the GRB prompt emission, finding $10^2 \lesssim \Gamma_0 \lesssim 10^3$. While the initial Lorenz factors are within average in the context of long GRBs, we find that (assuming a typical prompt-phase efficiency of 10%) the kinetic blastwave energy is large, $\tilde{E}_{k,\rm iso} \gtrsim \times O(10^{54})$ erg (see also Table 7). Albeit such large energies could be due to an observational bias towards detection efficiency. Whether these conclusions are generally valid for VHE GRBs will be confirmed by future CTA observations.

Finally, we investigate the neutrino signal expected from the afterglow of VHE GRBs, focusing on GRB 190114C as representative burst. The non-observation of high-energy neutrinos from VHE GRBs is consistent with our theoretical predictions. The detection prospects for high-energy neutrinos from VHE GRBs with upcoming neutrino telescopes are equally poor, except for bursts closer than 15 Mpc. This suggests that neutrinos from the GRB afterglow may not be promising messengers to unveil the properties of the VHE emitting bursts.

Our findings hint at arising trends characterizing the properties of VHE GRBs, if the afterglow of these bursts can be modelled within the standard scenario. Additional data on bursts exhibiting VHE emission will shed light on the engine powering such transients and provide valuable insight on the characteristics of their host environments.

9.8 CRITICAL OUTLOOK

In this section, we critically scrutinize our research from a state-of-the-art standpoint and we provide an overview of our main findings. We also discuss future directions to improve our analysis. Notably, similar topics have been addressed in Sec.9.6 of the published paper.

9.8.1 *Overview and main findings*

In Chapter 8, we already pointed out that our understanding of the GRB afterglow has been undermined by the observation of several features that cannot be accommodated within the standard picture introduced in Sec. 9.3. Among these features, the observation of VHE emission (i.e., photons with energies $\gtrsim$ 100 GeV) at late times and deep in the GRB afterglow was certainly one of the most exciting and yet puzzling discovery. Several processes have been invoked to model the VHE component of the afterglow spectrum, including SSC scattering of accelerated electrons on the afterglow synchrotron photons or synchrotron radiation from a population of accelerated protons. Yet it remains largely uncertain whether the bursts observed in the VHE regime possess distinctive properties. In particular, *do they occur in similar CBM and do they share common properties?* These open questions serve as motivation for our work. Our findings may have important implications on the environment where GRBs with VHE afterglow emission occur and on their progenitors.

In the hypothesis where VHE radiation is produced by the same blastwave responsible for the emission at lower energies, VHE photons must be able to escape the blastwave at the time of observation. We translate this argument in the constraint on the blastwave compactness

$$\tau_\gamma(E'_{\gamma,\mathrm{VHE}}) \simeq 0.1\sigma_T E'_\star n'^{\mathrm{sync}}_\gamma(E'_\star)\frac{R}{\Gamma} \lesssim 1\ , \tag{9.21}$$

where $E'_{\gamma,\rm VHE}$ is the detected energy of the VHE photon, $E'_\star = (2m_e c^2)^2/E'_{\gamma,\rm VHE}$, $n'^{\rm sync}_\gamma$ is the energy density of synchrotron photons and R/Γ is the blastwave compactness.

Among the sample of GRBs detected with VHE emission, we focus on the ones displaying large isotropic energy. Thus, for each burst, we infer the doublets of blastwave isotropic kinetic energy $\tilde{E}_{k,\rm iso}$ and CBM density n that simultaneously reproduce observed data in the radio, optical and X-ray, while also fulfilling the compactness argument in Eq. 9.21. We assume that the afterglow spectrum spanning from the radio to the X-ray wavebands is shaped through standard synchrotron radiation. While we do not model explicitly the VHE part of the lightcurve, we carry out our analysis by assuming microphysical parameters which are consistent with SSC radiation.

Intriguingly, our findings hint that, if VHE photons are produced through SSC processes by the same electron population shaping the synchrotron spectrum across radio to X-ray wavelengths, GRBs displaying VHE emission may occur in low-density environments, with $n_0 \lesssim O(10^{-1})$ cm^{-3} or $A_\star \lesssim O(10^{-1})$ cm^{-1} for a constant density and wind-like CBM, respectively. Our results may have important implications for the nature of this class of GRBs. For instance, small CBM densities may imply progenitors and host galaxies with low metallicity. Likewise, low-density winds may imply a reduced mass-loss rate of the GRB progenitor at the time of the stellar collapse.

We also calculate the high-energy neutrino signal expected from GRBs displaying VHE emission. However, the non-observation of high-energy neutrinos from these bursts does not provide any further constraint on the $(\tilde{E}_{k,\rm iso}, n)$ parameter space, due to poor statistics. Importantly, our results are consistent with the constraint in Eq. 9.21, as the production of high-energy neutrinos inherently requires a blastwave with large compactness.

Should the upcoming IceCube-Gen2 radio detect neutrinos from nearby VHE GRBs, this detection would enable us to disentangle the proton synchrotron and SSC radiation processes. Therefore, our study highlights the importance of combining multi-wavelength observations and high-energy neutrino data to shed light on the VHE afterglow emission.

9.8.2 *Future research directions*

Our work may provide interesting insights on VHE GRBs and their environments. In the following we outline possible future directions to strengthen our model:

1. *Relaxing the dependence on the microphysical parameters*. Our analysis relies on microphysical parameters valid if the VHE emission is shaped through SSC radiation, in particular we assume that the fraction of accelerated electrons $\xi_e = 1$. However, a smaller ξ_e is required in the context of proton synchrotron radiation, for which we expect larger CBM densities. More general results could be obtained in two ways:

   - The same analysis could be carried out by assuming microphysical parameters which are consistent with proton synchrotron radiation;
   - A more general analysis could be performed by relaxing any constraint on the microphysical parameters and treating them as free parameters.

   Both approaches would enable us to explore a larger part of the parameter space.

2. *Including VHE data in the analysis.* We explicitly model the VHE part of the afterglow spectrum through SSC radiation to calculate the corresponding high-energy neutrino signal, whereas the exact shape of VHE spectrum does not affect our results on the allowed $(\tilde{E}_{k,\mathrm{iso}}, n)$ doublets. For our purposes, it suffices to treat the Klein-Nishina regime as an exponential cut-off in the photon distribution at the Klein-Nishina energy. In future research, the VHE part of the spectrum and corresponding data may be incorporated in the analysis. In such cases, proper modeling of the Klein-Nishina regime will be essential for accuracy.

3. *Including the self-absorption frequency in the synchrotron spectrum.* We neglect the break introduced by synchrotron self-absorption processes in the standard afterglow lightcurve. This simplification aligns with observational data of the considered sample of bursts. However, it is plausible that the latter is not representative of the whole population of VHE GRBs. Therefore, it is not straightforward that all the VHE GRBs are in a weak absorption regime. As synchrotron self-absorption strongly affects the spectrum at radio frequencies, it should be included in the analysis of future VHE GRBs.

We conclude this section by pointing out that the LHAASO data above 10 TeV for GRB 221009A have been recently made public [503], and analyses including these data may provide new insights on the VHE component of the spectrum.

In summary, our work hints towards the existence of intriguing patterns in the properties of VHE GRBs, provided their afterglow from radio to X-ray energies can be modeled within the standard scenario. Therefore,

we emphasize the importance of observing additional GRBs with VHE emission. The sample of GRBs analyzed in this work may be biased by the sensitivity of existing telescopes, which restrict our knowledge to bursts with exceptionally large isotropic kinetic energy. In this context, the upcoming CTA will play a pivotal role in collecting a larger sample of VHE GRBs, shedding new light on these intriguing bursts.

Part III

MULTI-MESSENGER EMISSION FROM EMERGING CLASSES OF HIGH-ENERGY TRANSIENTS

10

NEUTRINO EMISSION FROM LUMINOUS FAST BLUE OPTICAL TRANSIENTS

Based on: **Ersilia Guarini**, Irene Tamborra, Raffaella Margutti, *Neutrino Emission from Luminous Fast Blue Optical Transients*, Astrophys. J. 935 (2022) 2, 157, arXiv:2205.12282

ABSTRACT Mounting evidence suggests that Luminous Fast Blue Optical Transients (LFBOTs) are powered by a compact object, launching an asymmetric and fast outflow responsible for the radiation observed in the ultraviolet, optical, infrared, radio, and X-ray bands. Proposed scenarios aiming to explain the electromagnetic emission include an inflated cocoon, surrounding a jet choked in the extended stellar envelope. In alternative, the observed radiation may arise from the disk formed by the delayed merger of a black hole with a Wolf-Rayet star. We explore the neutrino production in these scenarios, i.e. internal shocks in a choked jet and interaction between the outflow and the circumstellar medium (CSM). If observed on-axis, the choked jet provides the dominant contribution to the neutrino fluence. Intriguingly, the IceCube upper limit on the neutrino emission inferred from the closest LFBOT, AT2018cow, excludes a region of the parameter space otherwise allowed by electromagnetic observations. After correcting for the Eddington bias on the observation of cosmic neutrinos, we conclude that the emission from an on-axis choked jet and CSM interaction is compatible with the detection of two track-like neutrino events observed by the IceCube Neutrino Observatory in coincidence with AT2018cow, and otherwise considered to be of atmospheric origin. While the neutrino emission from LFBOTs does not constitute the bulk of the diffuse background of neutrinos observed by IceCube, detection prospects of nearby LFBOTs with IceCube and the upcoming IceCube-Gen2 are encouraging. Follow-up neutrino searches will be crucial for unravelling the mechanism powering this emergent transient class.

10.1 INTRODUCTION

The advent of time-domain astronomy has led to the discovery of intriguing new classes of transients that evolve on time-scales $\lesssim$ 10 days [e.g. 143, 144, 504–506]. Among these, Fast Blue Optical Transients (FBOTs) [143–146, 296] exhibit unusual features. They have a rise time of a few days in the optical—$t_{\rm rise}$ up to 3 days, i.e. much faster than typical supernovae (SNe; e.g. [144, 146, 507])—and their spectrum remains blue and hot throughout the whole evolution.

We focus on the subclass of optically luminous FBOTs (hereafter denoted with LFBOTs), with absolute peak magnitude $M_{\rm peak} < -20$ [146, 152, 265]. LFBOTs have a rate in the local Universe $\lesssim 300$ Gpc^{-3} yr^{-1}, i.e. $\lesssim 0.4 - 0.6\%$ of core-collapse SNe ([146, 152, 265]). To date, radio emission has been detected for five FBOTs, all belonging to the LFBOTs category: CSS161010, AT2018cow, AT2018lug, AT2020xnd, and AT2020mrf. LFBOTs have been detected in the hard X-ray band as well, though not yet in gamma-rays (i.e. with energies > 200 keV) [147, 148, 150–152, 265].

The radio signal associated with LFBOTs is consistent with synchrotron radiation in the self-absorption regime, arising from the forward shock developing when the ejecta interact with the circumstellar medium (CSM). Broad hydrogen (H) emission features have been observed in the spectra of some LFBOTs, i.e. AT2018cow [148, 149] and CSS161010 [152]. Moreover, combined observations in the optical and radio bands suggest that the fastest component of the outflow is moving with speed $0.1c \lesssim v_{\rm f} \lesssim 0.6c$ [147–151].

As for X-rays, the spectrum exhibits a temporal evolution and a high variability that is challenging to explain by invoking external shock interaction. Rather, the X-ray emission might be powered by a rapidly evolving compact object (CO), like a magnetar or a black hole, or a deeply embedded shock [147, 148]. In addition, interaction with the CSM cannot simultaneously explain the ultraviolet, optical, and infrared spectral features, e.g. the rapid rise of the light curve and its luminosity ($L_{\rm opt} \simeq 10^{44}$ erg s^{-1}), as well as the receding photosphere observed for AT2018cow at late times [149] and typically associated with an increase of the effective temperature. In the light of this growing set of puzzling data, multiple sites might be at the origin of the observed electromagnetic emission across different wavebands, together with an asymmetric outflow embedding the CO [148]. An additional piece of evidence of the presence of a CO might be the persistent ultraviolet source observed at the location of AT2018cow [508]. The presence of a CO may also be supported by the observation in AT2018cow of high-amplitude quasi periodic oscillations in soft X-rays [509].

Several interpretations of LFBOT observations have been proposed, such as shock interaction of an outflow with dense CSM (e.g. [510–513][1]); reprocessing of X-rays emitted from a central engine within a polar outflow (e.g. [148, 149, 514–519]); a neutron star engulfed in the extended envelope of a massive red supergiant, leading to common envelope evolution and formation of a jetted SN [520] or a related impostor [521]; emission from the accretion disk originating from the collapse of a massive star into a black hole [522, 523] or from the electron-capture collapse to a neutron star following the merger of a ONeMg white dwarf with another white dwarf [524, 525]. Each of the aforementioned scenarios may only reproduce some of the observed features of LFBOTs.

Recently, two models have been proposed in the attempt of explaining the multi-wavelength emission of AT2018cow. [153] invoke the collapse of a massive star, possibly not completely H-stripped, which launches a jet. The jet may be off-axis or choked in the extended stellar envelope and, therefore, not directly visible; to date, direct associations between jets and LFBOTs are lacking and constraints have been set for AT2018cow [297]. The jet interacts with the stellar envelope, inflating the cocoon surrounding the jet; the cocoon expands, breaks out of the star and cools, emitting in the ultraviolet, optical, and infrared. [154] considers a delayed Wolf-Rayet star–black hole merger following a failed common envelope phase. This leads to the formation of an asymmetric CSM, dense in the equatorial region, and less dense in the polar one. The scenarios proposed by [153] and [154] successfully fit the ultraviolet, optical and infrared spectra of AT2018cow; [154] also provides a fit to the X-ray data of AT2018cow. However, it is yet to be quantitatively proven that the off-axis jet scenario of [153] is consistent with radio observations; no fit to the radio data is provided in [154]. It is unclear whether these models could explain the late time hot and luminous ultraviolet emission ($L_{\rm UV} \gtrsim 2.7 \times 10^{34}$ erg s^{-1}) detected in the proximity of AT2018cow [508]. [154] provides a possible explanation to this persistent emission as the late time radiation from the accretion disk surrounding the black hole resulting from the Wolf-Rayet star–black hole merger. Further observations in the direction of AT2018cow will eventually confirm this conjecture.

In order to unravel the nature of the engine powering LFBOTs, a multi-messenger approach may provide a fresh perspective. In particular, the neutrino signal could carry signatures of the mechanisms powering LFBOTs. Since the first detection of high-energy neutrinos of astrophysical origin by the IceCube Neutrino Observatory, follow-up searches are ongoing to pinpoint the electromagnetic counterparts associated to

1 We note, however, that the broad-band X-ray spectrum of AT2018cow is unlike the thermal spectra of interacting SNe, and shows instead clear non-thermal features.

the IceCube neutrino events [407, 526–529]. A dozen of neutrino events have been associated in likely coincidence with blazars, tidal distruption events or superluminous supernovae [49, 59, 65, 405–410]. As for LFBOTs, the IceCube Neutrino Observatory reported the detection of two track-like muon neutrino events in spatial coincidence with AT2018cow in the 3.5 days following the optical detection. These neutrino events could be statistically compatible with the expected number of atmospheric neutrinos–0.17 events [66].

As the number of LFBOTs detected electromagnetically increases, the related neutrino emission remains poorly explored. [530] pointed out that, if AT2018cow is powered by a magnetar, particles accelerated in the magnetar wind may escape the ejecta at ultrahigh energies. Within the models proposed in [153, 154], additional sites should be taken into account for what concerns neutrino production. For example, if a choked jet powered by the central CO is harbored within the LFBOT [153], we would not observe any prompt gamma-ray signal. Nevertheless, efficient proton acceleration could take place leading to the production of TeV–PeV neutrinos [200, 235, 237, 239, 247, 248, 252, 253, 255, 531, 532]. In addition, [153, 154] predict fast ejecta propagating in the CSM with velocity $v_{\rm f} \gtrsim 0.1c$. Protons may be accelerated at the shocks between the ejecta and the CSM leading to neutrino production, similar to what foreseen for SNe [65, 123, 131, 533–539] or trans-relativistic SNe [302, 540], probably powered by a choked jet as it may be the case for LFBOTs. Neutrinos produced from LFBOTs could be detectable by the IceCube Neutrino Observatory and the upcoming IceCube-Gen2, aiding to pin down the mechanisms powering LFBOTs [298, 541].

Our work is organized as follows. In Sec. 10.2, we discuss the most promising particle acceleration sites for the models proposed in [153] and [154] (a choked jet and/or a fast outflow emitted by the CO that propagates outwards in the CSM). Section 10.3 summarizes the model parameters inferred for AT2018cow and CSS161010 from electromagnetic observations. Section 10.4 focuses on the production of high-energy neutrinos. In Section 10.5, we present our findings for the neutrino signal expected at Earth from AT2018cow and CSS161010 and discuss the corresponding detection prospects. The contribution of LFBOTs to the neutrino diffuse background is presented in Sec. 10.6. Finally, we conclude in Sec. 10.7. The most relevant proton and meson cooling times are outlined in Appendix D.1.

10.2 PARTICLE ACCELERATION SITES

In this section, we outline the mechanisms proposed in [153] (hereafter named "cocoon model") and [154] (hereafter "merger model") for powering LFBOTs that could also host sites of particle acceleration. First, we consider a jet launched by the central engine and choked in the extended stellar envelope. Then, we focus on the interaction between the fast ejecta and the CSM.

10.2.1 *Choked jet*

[153] propose that LFBOTs arise from the collapse of massive stars that result in the formation of a central CO, possibly harboring a relativistic jet, as shown in the left panels of Fig. 48. If the jet were to successfully drill through the stellar envelope, it would break out and give rise to a gamma-ray bright signal. Nevertheless, no prompt emission has been detected in association with LFBOTs, suggesting that a successful jet could be disfavored [148, 152]. The non detection of gamma-rays hints that an extended envelope, probably not fully H-depleted in order to explain the broad emission features observed in some LFBOT spectra [AT2018cow [148, 149] and CSS161010 [152]], may engulf the stellar core, extending up to $R_\star \simeq 10^{11}$ cm [153]. In this case, the jet could be choked, as displayed in the middle left panel of Fig. 48.

We consider a collapsing star that has not lost its H envelope completely and it is surrounded by an extended shell of radius $R_{\rm env} \simeq 3 \times 10^{13}$ cm and mass $M_{\rm env} \simeq 10^{-2} M_\odot$ [235]. The modeling of the extended H envelope mass is inspired by partially stripped SNe [e.g. 200, 294, 295]. We fix the value of $M_{\rm env}$ to avoid to deal with several free parameters (see Sec. 10.3) and leave to future work the assessment of the dependence of the neutrino signal on the mass of the extended envelope. For the extended envelope we consider the following density profile [200]:

$$\rho_{\rm env}(R) = \rho_{\rm env,0} \left(\frac{R}{R_{\rm env}} \right)^{-2} , \tag{10.1}$$

where $\rho_{\rm env,0} = M_{\rm env} \left[\int^{R_{\rm env}} dR 4\pi R^2 \rho_{\rm env}(R) \right]^{-1}$ and R is the distance from the CO. We assume a fixed density profile for the extended envelope due to the lack of knowledge on its features; further investigations on the impact of this assumption on the neutrino signal is left to future work. Nevertheless, we expect that neutrino

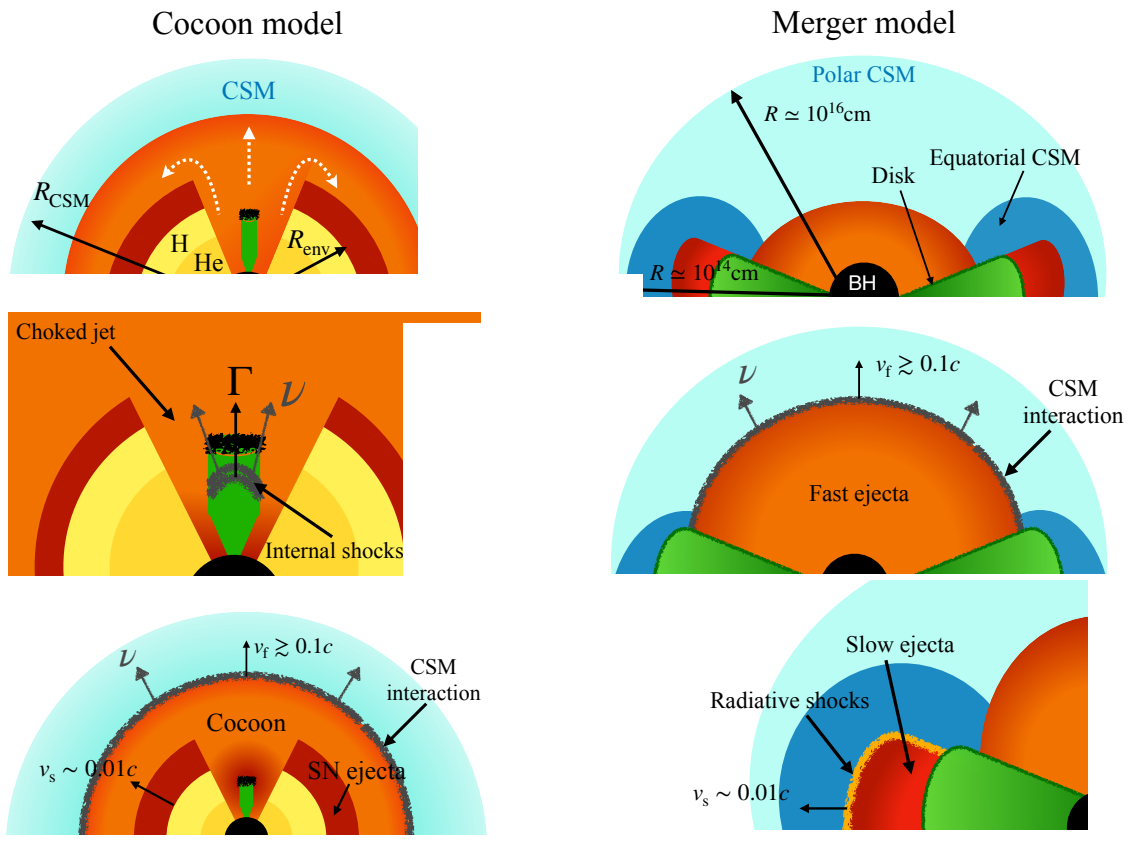

Figure 48: Cartoons of the cocoon model (left panels, [153]) and merger model (right panels, [154]), not to scale. For the sake of simplicity, we show only the upper half section of the FBOT. *Top left panel*: A massive star collapses, forming a CO (black region). The CO is surrounded by helium (He) and H envelopes (regions with yellow hues). The progenitor core ($R_\star \sim 10^{11}$ cm) is surrounded by an extended envelope (of radius $R_{\rm env}$). *Middle left panel*: The jet (green) is launched near the surface of the CO and it is choked in the extended envelope. Internal shocks occur in the proximity of the jet head (gray), where neutrinos can be produced. *Bottom left panel*: The jet inflates the cocoon (orange region); the latter breaks out from the stellar surface and interacts with the CSM (aqua outer region). The fastest component of the cocoon moves with $v_{\rm f} \gtrsim 0.1c$, while its slow component (red region; SN ejecta) propagates with $v_{\rm s} \simeq 0.01c$ in the equatorial direction. While the fast component of the cocoon propagates into the CSM, collisionless shocks take place (gray line surrounding the cocoon); here, neutrinos may be produced. Even though the geometry of the cocoon is not perfectly spherical, we assume spherical symmetry for the sake of simplicity in the analytical treatment of the problem; see main text. *Top right panel*: As a result of the Wolf-Rayet star-black hole merger, a black hole forms (BH; black), surrounded by an accretion disk (green region). The equatorial dense CSM (blue region) extends up to $\simeq 10^{14}$ cm, while the polar (aqua region) CSM extends up to $\simeq 10^{16}$ cm. *Middle right panel*: The disk emits a fast outflow (orange region) propagating in the polar direction with $v_{\rm f} \simeq 0.1c$ into the CSM. Here, collisionless shocks (gray line) occur and neutrino production takes place. *Bottom right panel*: The slow outflow (red shell) is emitted from the disk in the equatorial direction, and it propagates with $v_{\rm s} \simeq 0.01c$ into the dense equatorial CSM. Here, radiative shocks take place (orange line) and neutrino production is negligible with respect to the one from the polar outflow.

telescopes will not be sensitive to this dependence, see e.g. [532]. The jet is launched near the surface of the CO [2], with luminosity $\tilde{L}_j$, narrow opening angle θ_j.

For fixed θ_j, the dynamics of the jet only depends on the isotropic equivalent quantities. Hence, it is convenient to define the isotropic equivalent luminosity of the jet: $\tilde{L}_j^{\rm iso} = \tilde{L}_j/(\theta_j^2/4)$. Note that the isotropic equivalent quantities are always defined in the CO frame; for the sake of clarity we keep the twiddle notation throughout the paper.

While the jet pierces through the stellar envelope, two shocks develop: a reverse shock, propagating back to the core of the jet, and a forward shock, propagating into the external envelope. The region between the two shocks constitutes the jet head. Denoting with Γ the Lorentz factor of the un-shocked jet plasma (i.e., the bulk Lorentz factor of the jet) and with Γ_h the one of the jet head, the relative Lorentz factor is [248]:

$$\Gamma_{\rm rel} = \Gamma\Gamma_h(1-\beta\beta_h)\ , \tag{10.2}$$

where $\beta = \sqrt{1-1/\Gamma^2}$ and $\beta_h = \sqrt{1-1/\Gamma_h^2}$. For a non relativistic jet head: $\Gamma_h \simeq 1$, which implies $\Gamma_{\rm rel} \simeq \Gamma$; this assumption is valid for the region of the parameter space of interest, as discussed in Sec. 10.3.

From the shock jump conditions, the energy density in the shocked envelope region and in the shocked jet plasma at the position of the jet head $\tilde{R}_h \equiv R_h$, respectively, are [382, 542]:

$$e_{\rm sh,env} = (4\Gamma_h+3)(\Gamma_h-1)\rho_{\rm env}(R_h)c^2\ , \tag{10.3}$$

$$e_{\rm sh,j} = (4\Gamma_{\rm rel}+3)(\Gamma_{\rm rel}-1)n'_j(R_h)m_pc^2\ . \tag{10.4}$$

Here $n'_j = \tilde{L}_j^{\rm iso}/(4\pi R^2 m_p c^3\Gamma^2)$ is the comoving particle density of the un-shocked jet. Equating $e_{\rm sh,ext} = e_{\rm sh,j}$ and expanding around Γ_h for the non-relativistic case, we obtain the speed of the jet head:

$$v_h \simeq \left[\frac{\tilde{L}_j^{\rm iso}}{(4\Gamma_h+3)\pi c\rho_{\rm env}(R_h)R_h^2}\right]^{1/2}\ . \tag{10.5}$$

Since the jet head is non relativistic, its position at the time t is $R_h \simeq v_h t/(1+z) = v_h\tilde{t}$, where z is the redshift of the source [3]. Plugging the last expression in Eq. 10.5 we obtain the position of the jet head at the end of the jet lifetime $\tilde{t}_j$,

$$R_h \simeq \left[\frac{\tilde{t}_j^2\tilde{L}_j^{\rm iso}}{(4\Gamma_h+3)\pi c\rho_{\rm env,0}R_{\rm env}^2}\right]^{1/2}\ . \tag{10.6}$$

2 We rely on three different reference frames throughout this paper: the CO frame, the observer frame and the jet comoving frame. In order to distinguish among them, each quantity in each of these frames is denoted as $\tilde{X}, X, X'$, respectively.

3 In the literature a geometrical correction factor of 2 is often considered in the relations between the radius of the head and the time, see e.g. [248]; nevertheless, this does not affect our findings.

If $R_h < R_{\rm ext}$, the jet is choked inside the stellar envelope.

The jet consists of several shells moving with different velocities. This implies that internal shocks may take place in the jet at $R_{\rm IS} \lesssim R_h$, when a fast shell catches up and merges with a slow shell. If $\Gamma_{\rm r} \simeq \left(\Gamma_{\rm fast}/\Gamma_{\rm merg} + \Gamma_{\rm merg}/\Gamma_{\rm fast}\right)/2$ is the relative Lorentz factor between the fast (moving with $\Gamma_{\rm fast}$) and the merged shell (moving with $\Gamma_{\rm merg}$) in the jet, efficient particle acceleration at the internal shock takes place only if [247]

$$n'_p \sigma_T R_{\rm IS}/\Gamma \lesssim \min\left[\Gamma_{\rm r}^2, 0.1 C^{-1}\Gamma_{\rm r}^3\right] , \tag{10.7}$$

where $C = 1 + 2\ln\Gamma_{\rm r}^2$ is a constant taking into account pair production and $n'_p \simeq n'_j$ is the proton density of the un-shocked jet material. If Eq. 10.7 is not satisfied, the internal shock is radiative and particle acceleration is not efficient [247]. We assume that internal shocks approach the jet head, i.e. $R_{\rm IS} \simeq R_h$ [248].

10.2.1.1 *Photon energy distribution*

Electrons can be accelerated at the reverse shock between the shocked and the un-schocked jet plasma. Then, they heat up and rapidly thermalize due to the high Thomson optical depth of the jet head

$$\tau_{T,h} = n_{e,{\rm sh,j}} \sigma_T \frac{R_h}{\Gamma_h} \gg 1 , \tag{10.8}$$

where $n_{e,{\rm sh,j}} = (4\Gamma_h + 3) n'_j$ is the electron number density of the shocked jet plasma. Therefore, the electrons in the jet head lose all their energy ($\epsilon_e^{\rm RS} e_{\rm sh,j}$) through thermal radiation, with $e_{\rm sh,j}$ defined as in Eq. 10.4 and $\epsilon_e^{\rm RS}$ being the fraction of the energy density that goes into the electrons accelerated at the reverse shock. The temperature of the emitted thermal radiation, in the jet head comoving frame, is [237, 399]

$$k_B T_h \simeq \left(\frac{30\hbar^3 c^2 \epsilon_e^{\rm RS} \tilde{L}_j^{\rm iso}}{4\pi^4 R_h^2}\right)^{1/4} , \tag{10.9}$$

with k_B being the Boltzmann constant. Thus, the head appears as a blackbody emitting at temperature $k_B T'_{\rm IS} = \Gamma_{\rm rel} k_B T_h$ in the comoving frame of the un-shocked jet. The density of thermal photons in the jet head is

$$n_{\gamma,h} = \frac{19\pi}{(hc)^3} (k_B T_h)^3 . \tag{10.10}$$

As the internal shock approaches the head of the jet, a fraction $f_{\rm esc} = 1/\tau_{T,h}$ of thermal photons escapes in the internal shock [247], where their number density is boosted by $\Gamma_{\rm rel}$:

$$n'_{\gamma,{\rm IS}} \simeq \Gamma_{\rm rel} f_{\rm esc} n_{\gamma,h} . \tag{10.11}$$

The resulting energy distribution of thermal photons in the un-shocked jet comoving frame is [in units of $\mathrm{GeV}^{-1}\ \mathrm{cm}^{-3}$]:

$$n'_\gamma(E'_\gamma) = \frac{\mathrm{d}^2 N_\gamma}{\mathrm{d}E'_\gamma \mathrm{d}V'} = A'_{\gamma,j} \frac{E'^{-2}_\gamma}{e^{E'_\gamma/(k_B T'_{\rm IS})} - 1} \,, \tag{10.12}$$

where $A'_{\gamma,j} = n'_{\gamma,\rm IS} \left[\int_0^\infty dE'_\gamma n'_\gamma(E'_\gamma)\right]^{-1}$.

10.2.1.2 *Proton energy distribution*

Protons are accelerated to a power law distribution at the internal shock, even though the mechanism responsible for particle acceleration is still under debate (e.g. [85, 101, 283–285]). The injected proton distribution in the jet comoving frame is [in units of $\mathrm{GeV}^{-1}\ \mathrm{cm}^{-3}$]

$$n'_p(E'_p) \equiv \frac{\mathrm{d}^2 N'_{\rm p}}{\mathrm{d}E'_{\rm p} \mathrm{d}V'} = A'_p E_p^{'-k_p} \exp\left[-\left(\frac{E'_p}{E'_{p,\rm max}}\right)^{\alpha_p}\right] \Theta(E'_p - E'_{p,\rm min}) \,, \tag{10.13}$$

where k_p is the proton spectral index, $\alpha_p = 1$ simulates an exponential cutoff [543], and Θ is the Heaviside function. The value of k_p is highly uncertain: it is estimated to be $k_p \simeq 2$ from non-relativistic shock diffusive acceleration theory [398], while it is expected to be $k_p \simeq 2.2$ from Monte Carlo simulations of ultra-relativistic shocks [85]. In this work, we assume $k_p \simeq 2$.

The normalization constant is $A'_p = \epsilon_p \epsilon_{\rm d} e'_j \left[\int_{E'_{p,\rm min}}^{E'_{p,\rm max}} dE'_p E'_p n'_p(E'_p)\right]^{-1}$, where $\epsilon_{\rm d}$ is the fraction of the comoving internal energy density of the jet $e'_j = \tilde{L}^{\rm iso}_j/(4\pi R^2_{\rm IS} c\Gamma^2)$ which is dissipated at the internal shock, while ϵ_p is the fraction of this energy that goes in accelerated protons. We rely on a one-zone model for the emission from internal shocks and omit any radial evolution of the properties of the colliding shells. Hence, we assume that the dissipation efficiency $\epsilon_{\rm d}$ is constant [e.g. 231, 544]. Note, however, that $\epsilon_{\rm d}$ depends on the details of the collision, i.e. the relative Lorentz factor between the colliding shells and their mass (see e.g. [291, 292]).

The minimum energy of accelerated protons is $E'_{p,\rm min} = m_p c^2$, while $E'_{p,\rm max}$ is the maximum energy up to which protons can be accelerated at the internal shock. The latter is fixed by the condition that the proton acceleration timescale $t'^{-1}_{p,\rm acc}$ is smaller that the total cooling timescale $t'^{-1}_{p,\rm cool}$. For details on the cooling timescales of protons, see Appendix D.1. At the internal shock, the fraction ϵ_B of the dissipated jet internal energy is given to the magnetic field: $B' = \sqrt{8\pi\epsilon_B \epsilon_{\rm d} e'_j}$.

10.2.2 *Interaction with the circumstellar medium*

While the presence of a choked jet is uncertain because of the lack of electromagnetic evidence [297], the existence of fast ejecta launched by the central engine and moving with $v_f \gtrsim 0.1c$ is supported by observations in the radio band [4]. The origin of the ejecta is still unclear and under debate. In the following, we discuss several viable mechanisms for the production of a fast outflow expanding outwards in the CSM.

- In the cocoon model presented in [153] (see left panels of Fig. 48), as the jet propagates in the stellar envelope (Sec. 10.2.1), a double-layered structure, the cocoon, forms around the jet, see e.g. [201]. The cocoon breaks out from the star and expands in the surrounding CSM [223]. The interaction between the CSM and the cocoon is responsible for the observed radio signal. It is expected that the cocoon's ejecta are stratified in velocity, and the fastest component propagates with $v_f \gtrsim 0.1c$. Since we assume that the jet is choked in the extended stellar envelope and far from the stellar core, the fast component of the cocoon does not have any relativistic component moving with Lorentz factor $\Gamma_f \sim 3$ [223]. In addition to the fast ejecta, the outflow contains a slow component moving with $v_s \lesssim 0.01c$. This component might be the slow part of the SN ejecta accompanying the jet launching. Note that there might be a faster component of the SN ejecta, but the radio signal is probably dominated by the cocoon emission [153].

- The merger model proposed in [154] (see right panels of Fig. 48) invokes a Wolf-Rayet–black hole merger following a failed common envelope phase. This leads to a highly asymmetric CSM: a very dense region extends up to $R \simeq 10^{14}$ cm around the equator and a less dense component extends up to $R \simeq 10^{16}$ cm in the polar direction. The asymmetric CSM is clearly required by electromagnetic observations of AT2018cow [148] and the energetics of the fastest ejecta of CSS161010 [152]. An accretion disk forms as a result of the merger; slow ejecta in the equatorial direction move with $v_s \simeq 0.01c$, and the fast component in the polar plane has $v_f \simeq 0.1c$.

Other two models have been proposed in the literature with features similar to the ones of the scenarios described above for what concerns the neutrino production. [525] suggests that LFBOTs arise from the accretion induced collapse of a binary white dwarf merger. In this case, neutrinos may be produced at the

4 It is worth noticing that the speed for the ejecta is very similar to the one of core-collapse SNe. Nevertheless, LFBOTs have been observed with fast ejecta speeds up to $v_f \simeq 0.6c$, see e.g. [152]. This feature makes these transients different from core-collapse SNe.

highly magnetized and highly relativistic wind termination shock, responsible for the observed radio emission. In this scenario, we expect a neutrino signal similar to the one of the cocoon model (from CSM interaction only), because of the similarity with the model parameters considered in [525]. [521] invokes a common envelope phase between a red supergiant and a CO. This mechanism shares common features with the one proposed in [153]. Nevertheless, while the former predicts baryon loaded jets, the latter invokes relativistic jets. Neutrino production from the jet model proposed in [521] may mimic the results obtained in [254]. Moreover, as for the scenario of [154], a common envelope phase, during which an asymmetric CSM forms, is proposed. The parameters obtained in the common envelope jet SN impostor scenario are similar to the cocoon model as for the total energy and mass of the ejecta, as well as for the CSM properties. Results similar to the ones of the cocoon model should hold for the common envelope jet SN impostor scenario, when taking into account CSM interaction. Hence, in the following we focus on the cocoon and merger models only.

Independently of its origin, the fast outflow propagates outwards in the surrounding CSM, giving rise to the observed radio spectrum. Observations suggest a certain degree of asymmetry in the LFBOTs outflows [148, 150, 152]. Nevertheless, for the sake of simplicity, we consider a spherically symmetric geometry both for the ejecta and the CSM. We parametrize the CSM with a wind profile

$$n_{p,\mathrm{CSM}}(R) = \frac{\dot{M}}{4\pi m_p v_w R^2} \,, \tag{10.14}$$

where $\dot{M}$ is the mass-loss rate of the star and v_w is the wind velocity. The CSM extends up to R_{CSM} and its mass is obtained by integrating Eq. 10.14 over the volume of the CSM shell, $\mathrm{d}V_{\mathrm{CSM}} = 4\pi R^2 \mathrm{d}R$. Note however that radio observations of AT2018cow indicate a steeper density profile for the CSM, see e.g. [545]. Here, we assume a standard wind profile for a general case.

As the outflow expands in the CSM, forward and reverse shocks form—propagating in the stellar wind and back to the ejecta in mass coordinates, respectively. Both the forward and reverse shocks contribute to neutrino production. On the basis of similarities with the SN scenario, the forward shock is expected to be the main dissipation site of the kinetic energy of the outflow [e.g., 546–551]; hence, we focus on the forward shock only, which moves with speed $v_{\mathrm{sh}} \simeq v_{\mathrm{f}}$.

If the outflow expands in a dense CSM with optical depth τ_{CSM}, the forward shock is radiation mediated as long as $\tau_{\mathrm{CSM}} \gg 1$ and particle acceleration is not efficient [88, 131, 552]. Radiation escapes at the

breakout radius $R_{\rm bo}$, when the optical depth drops below $v_{\rm sh}/c$. The breakout radius is obtained by solving the following equation:

$$\tau_{\rm CSM} = \int_{R_{\rm bo}}^{R_{\rm CSM}} dr\ \sigma_T n_{p,\rm CSM}(R) = \frac{c}{v_{sh}}\ . \tag{10.15}$$

Existing data suggest that the LFBOT ejecta were possibly slowly decelerating during the time of observations [e.g., 152]. Nevertheless, this behavior is not well probed and the treatment of deceleration of a mildly-relativistic blastwave is not straightforward [553]. Hereafter, we assume that the shock freely moves with constant speed $v_{\rm sh}$ up to the deceleration radius

$$R_{\rm dec} = R_{\rm bo} + \frac{M_{\rm ej}}{4\pi m_p n_{p,\rm bo} R_{\rm bo}^2}\ , \tag{10.16}$$

where $M_{\rm ej}$ is the mass of the ejecta and $n_{p,\rm bo} = n_{p,\rm CSM}(R_{\rm bo})$. At this radius, the ejecta have swept-up a mass comparable to $M_{\rm ej}$ from the CSM.

10.2.2.1 *Proton energy distribution*

Diffusive shock acceleration of the CSM protons occurs at $R \gtrsim R_{\rm bo}$ and accelerated protons are assumed to have a power-law energy distribution. For a wind-like CSM, the proton distribution reads [in units of $\rm GeV^{-1}$ $\rm cm^{-3}$]

$$\tilde{n}_p(\tilde{E}_p) \equiv \frac{{\rm d}^2\tilde{N}_p}{{\rm d}\tilde{E}_p {\rm d}\tilde{V}} = \tilde{A}_p \tilde{E}_p^{-k_p} \Theta(\tilde{E}_p - \tilde{E}_{p,\rm min})\Theta(\tilde{E}_{p,\rm max} - \tilde{E}_{\rm p})\ ; \tag{10.17}$$

as for the choked jet scenario, we fix the proton spectral index $k_p = 2$. Moreover, the minimum energy of protons is $\tilde{E}_{p,\rm min} = m_p c^2$, since these shocks are not relativistic. The maximum energy of shock-accelerated protons is fixed by the condition that the acceleration timescale is shorter than the total cooling timescale, i.e. $\tilde{t}_{\rm acc}^{-1} \leq \tilde{t}_{\rm cool}^{-1}$ (see Appendix D.1). Note that for CSM interaction there is no difference between the comoving frame of the shock and the CO frame, since the involved speeds are sub-relativistic. Hence, the primed quantities are equivalent to the twiddled ones.

$\tilde{A}_p = 9\epsilon_p n_{p,\rm CSM}(R) m_p c^2/[8\ln(\tilde{E}_{p,\rm max}/\tilde{E}_{p,\rm min})](v_{\rm sh}/c)^2$ is the normalization constant. Here, ϵ_p is the fraction of the post-shock internal energy, $\tilde{e}_{\rm th} = 9 m_p c^2 (v_{\rm sh}/c)^2 n_{p,\rm CSM}(R)/8$, that goes in accelerated protons. The fraction ϵ_B of $\tilde{e}_{\rm th}$ is instead stored in the magnetic field generated at the forward shock: $\tilde{B} = \sqrt{9\pi\epsilon_B m_p c^2 (v_{\rm sh}/c)^2 n_{p,\rm CSM}(R)}$. We stress that the quantities introduced so far for CSM interaction evolve with the radius of the expanding outflow, and hence with time.

Electrons are expected to be accelerated together with protons at the forward shock and produce the synchrotron self-absorption spectrum observed in the radio band. The electron population responsible for the

radio emission is still under debate [146, 554]. Nevertheless, we verified that $p\gamma$ interactions are negligible for a wide range of parameters, consistently with the results reported in [131, 298]. Hence, we do not introduce any photon distribution and neglect neutrino production through $p\gamma$ interactions in the context of CSM-ejecta interaction (see Sec. 10.4).

10.3 BENCHMARK LUMINOUS FAST BLUE OPTICAL TRANSIENTS: AT2018COW AND CSS161010

In this section, we provide an overview on the parameters characteristic of AT2018cow and CSS161010. We select these two transients as representative of the detected LFBOTs for two reasons. First, they are the closest ones ($d_L \simeq 60$ Mpc for AT2018cow and $d_L \simeq 150$ Mpc for CSS161010; d_L is the luminosity distance, defined as in Sec. 10.4.3); second, while these two LFBOTs share similar CSM densities, extension of the CSM, ejecta mass and kinetic energy as the population of LFBOTs, their fastest ejecta span the entire range of values inferred. AT2018cow showed $v_{\rm f} \simeq 0.1$–$0.2c$ [147, 148, 545], while CSS161010 is the fastest LFBOT observed to date with $v_{\rm f} \simeq 0.55c$ [152]. We fix the speed of the fastest component of the outflow as measured from observations. The other characteristic parameters are still uncertain, hence we vary them within an uncertainty range. The parameters adopted for the choked jet (opening angle θ_j, Lorentz factor Γ, and lifetime $\tilde{t}_j$) are fixed on the basis of theoretical arguments as justified below. The typical parameters adopted for the choked jet and for CSM interaction are summarized in Table 8. As for the cocoon model harboring a choked jet, $\tilde{E}_j = \tilde{L}_j \tilde{t}_j$ corresponds to the physical energy injected by the central engine into the jet, whose opening angle is assumed to be $\theta_j = 0.2$ rad (e.g. [133, 556]). Since the jet is choked, all of its energy is transferred to the cocoon, i.e. the cocoon breaks out with energy $\tilde{E}_{\rm ej} \simeq \tilde{E}_j$; note that, in principle, we should consider that a fraction of the jet energy is dissipated at the internal shocks, nevertheless this fraction is small enough to be negligible [$\sim 10\%$ [292]]. The kinetic energy $\tilde{E}_k$ of the ejecta interacting with the CSM has been estimated from the radio data and it represents a lower limit on the total energy of the outflow, $\tilde{E}_{\rm ej}$ (see "CSM interaction, cocoon model" in Table 8). The upper limit on the total energy of the outflow is not directly inferred from observations, but estimations of its range of variability have been attempted. Thus, we vary the energy injected in the jet in the interval spanned by the lower and upper limits of the outflow energy, obtained by combining observations and theoretical assumptions (see "choked jet" in Table 8 and

Table 8: Benchmark input parameters characteristic of AT2018cow and CSS161010 adopted in this work. Some parameters are inferred from observations, while others denote typical values derived on theoretical grounds or combining observations and theoretical arguments. The following references are quoted in the table: [1] [555], [2] [152], [3] [149], [4] [556], [5] [133], [6] [545], [7] [148], [8] [153], [9] [557], [10] [558], [11] [531], [12] [559], [13] [292], [14] [544], [15] [560], [16] [248], [17] [561], [18] [147], [19] [562], [20] [154].

Parameter	Symbol	AT2018cow	CSS161010	References
Luminosity distance	d_L	60 Mpc	150 Mpc	[1, 2]
Declination	δ	22°	−8°	[2, 3]
	Choked jet			
Opening angle	θ_j	0.2	0.2	[4, 5, 6]
Isotropic energy	$\tilde{E}_j^{\rm iso}$ (erg)	10^{50}–10^{52}	10^{50}–10^{52}	[2, 7, 8]
Jet lifetime	$\tilde{t}_j$ (s)	10–10^6	10–10^6	[9, 17]
Lorentz factor	Γ	10–100	10–100	[10, 11, 12]
Dissipation efficiency (IS)	$\epsilon_{\rm d}$	0.2	0.2	[13, 14]
Accelerated proton energy fraction (IS)	$\epsilon_{\rm p}$	0.1	0.1	[15]
Magnetic energy density fraction (IS)	$\epsilon_{\rm B}$	0.1	0.1	[15]
Accelerated electron energy fraction (RS)	$\epsilon_e^{\rm RS}$	0.1	0.1	[16]
	CSM interaction, cocoon model			
Fast outflow velocity	$v_{\rm f}$	$0.2c$	$0.55c$	[2, 6, 7, 18]
Ejecta energy	$\tilde{E}_{\rm ej}$ (erg)	4×10^{48}–10^{51}	6×10^{49}–10^{51}	[2, 7, 18]
Mass-loss rate	$\dot{M}$ ($M_\odot$ yr^{-1})	10^{-4}–10^{-3}	10^{-4}–10^{-3}	[2, 7, 18]
Ejecta mass	$M_{\rm ej}(M_\odot)$	1×10^{-4}–3×10^{-2}	2.2×10^{-4}–4×10^{-3}	[2, 7, 18]
Wind velocity	v_w (km s^{-1})	1000	1000	[2, 7, 18]
CSM radius	$R_{\rm CSM}$ (cm)	1.7×10^{16}	3×10^{17}	[2, 18]
Accelerated proton energy fraction	ϵ_p	0.1	0.1	[19]
Magnetic energy density fraction	ϵ_B	0.01	0.01	[2, 6, 7, 18]
	CSM interaction, merger model			
Fast outflow velocity	$v_{\rm f}$	$0.2c$	0.55 c	[2, 6, 7, 18]
Ejecta energy	$\tilde{E}_{\rm ej}$ (erg)	4×10^{48}–10^{51}	6×10^{49}–10^{51}	[2, 7, 20]
Mass-loss rate	$\dot{M}$ ($M_\odot$ yr^{-1})	7×10^{-6}–7×10^{-5}	7×10^{-6}–7×10^{-5}	[2, 7, 20]
Ejecta mass	$M_{\rm ej}(M_\odot)$	10^{-4}–3×10^{-2}	2.2×10^{-4}–4×10^{-3}	[2, 7, 20]
Wind velocity	v_w (km s^{-1})	10	10	[20]
CSM radius	$R_{\rm CSM}$ (cm)	3×10^{16}	3×10^{16}	[20]
Accelerated proton energy fraction	ϵ_p	0.1	0.1	[19]
Magnetic energy density fraction	ϵ_B	0.01	0.01	[2, 6, 7, 18]

references therein). As mentioned in Sec. 10.2.1, the dynamics of the jet is conveniently described by the isotropic equivalent quantities; we refer to the isotropic equivalent energy of the jet: $\tilde{E}_j^{\rm iso} = \tilde{E}_j/(\theta_j^2/4)$.

The Lorentz factor of the jet is not measured. Hence, we rely on two extreme cases: $\Gamma = 10$ and 100. This choice is due to the fact that numerical simulations and semi-analytical models suggest that the jet propagates in the stellar core with $\Gamma \simeq 1$–10 [210, 558]. Nevertheless, when the jet pierces the stellar core at $R_\star \simeq 10^{11}$ cm and enters the extended envelope, it may be accelerated up to $\Gamma \lesssim 100$ because of the sudden drop in density [300, 559].

The jet lifetime is linked to the CO physics. The CO harboring relativistic jets can be either a black hole [223, 523] or a millisecond magnetar [563]. If we assume that the central engine of LFBOTs is a magnetar with initial spin period P_i, magnetic field $B_{\rm m}$ and mass $M_{\rm m} = 1.4 M_\odot$ then the upper limit on the jet lifetime is set by the spin-down period [557]:

$$\tilde{t}_{\rm sd} = 2.0 \times 10^5 \ {\rm s} \left(\frac{\rm P_i}{10^{-3} \ {\rm s}}\right)^2 \left(\frac{\rm B_m}{10^{14} \ {\rm G}}\right)^2 . \tag{10.18}$$

Following [530], for $P_i = 10$ ms and $B_{\rm m} = 10^{15}$ G, we obtain $\tilde{t}_j \lesssim \tilde{t}_{\rm sd} = 2 \times 10^5$ s. If the CO is a black hole, the upper limit on the jet lifetime is set by the free-fall time of the stellar material [561]:

$$\tilde{t}_{\rm ff} \simeq 1.7 \times 10^7 \ {\rm s} \left(\frac{\rm R_{BH}}{10^{13.5} \ {\rm cm}}\right)^{3/2} \left(\frac{\rm M_{BH}}{\rm M_\odot}\right)^{-1/2} , \tag{10.19}$$

where $M_{\rm BH}$ is the black hole mass and $R_{\rm BH}$ the distance from it. Since the nature of the CO powering LFBOTs as well as the presence of a jetted outflow are uncertain, we vary the jet lifetime in $\tilde{t}_j \in \left[10, 10^6\right]$ s. Note, however, that a short lifetime ($\tilde{t}_j < 10^3$ s) may require an amount of energy released by the CO larger than the sum of the observed radiated energy and the kinetic energy of the ejecta. This consideration arises when extrapolating the X-ray light-curve—likely associated with the CO powering LFBOTs [e.g. 148, 152]—back to early times ($\tilde{t} \sim \tilde{t}_j$). Nevertheless, there is no robust signature that allows to confidently exclude shorter CO lifetimes. Hence, we choose to span a wide range for $\tilde{t}_j$. Finally, the microphysical parameters ϵ_B, ϵ_p, and $\epsilon_e^{\rm RS}$ are fixed to typical values of choked jets; see "choked jet" in Table 8 and references therein.

Note that the same energy $\tilde{E}_j$ can be injected from the CO for different $(\tilde{L}_j, \tilde{t}_j)$ pairs. Since our main goal is to explore viable mechanisms for neutrino production in LFBOTs, not all $(\tilde{L}_j, \tilde{t}_j)$ pairs are allowed, as shown in Fig. 49. In fact, the $(\tilde{L}_j, \tilde{t}_j)$ pairs that do not satisfy, simultaneously, the choked jet condition ($R_h < R_{\rm ext}$, with R_h given by Eq. 10.6) as well as the acceleration constraint in Eq. 10.7 are excluded. Examples of the allowed $(\tilde{L}_j, \tilde{t}_j)$ pairs are shown in Fig. 49 for $\Gamma = 10$ and 100. We also exclude the $(\tilde{L}_j, \tilde{t}_j)$

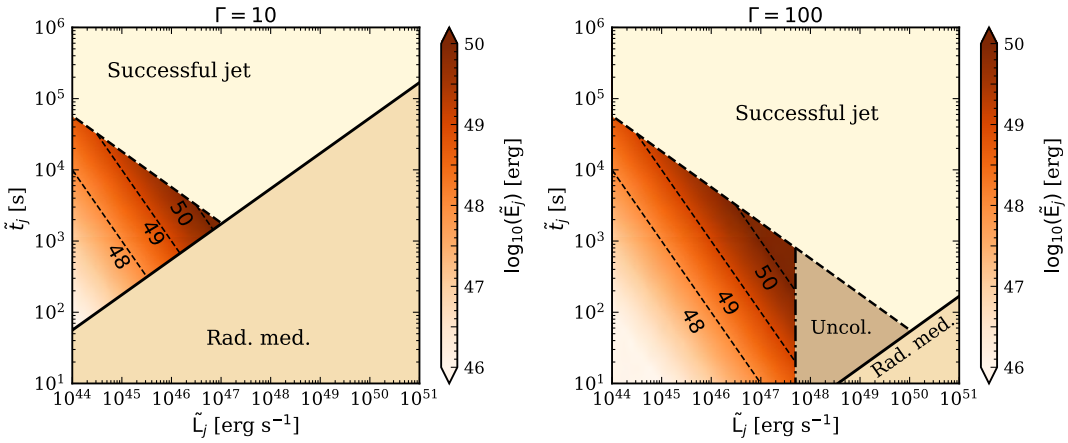

Figure 49: Contour plot of the energy injected in the jet by the central engine ($\tilde{E}_j = \tilde{L}_j \tilde{t}_j$) in the plane spanned by $\tilde{L}_j$ and $\tilde{t}_j$ for $\Gamma = 10$ (left panel) and $\Gamma = 100$ (right panel). The light yellow region is excluded since it would give rise to a successful jet. The light-brown region in the right lower corner is excluded because the jet would be radiation mediated ("Rad. med."; see Eq. 10.7). For $\Gamma = 100$, we exclude an additional region corresponding to an uncollimated jet ("Uncol"; brown region in the right panel). In the allowed region of the parameter space, the black-dashed lines are meant to guide the eye and correspond to $\tilde{E}_j = 10^{48}, 10^{49}, 10^{50}$ erg.

pairs leading to an uncollimated jet in the extended envelope for the fixed θ_j, as suggested by numerical simulations and implied by observations [153], see [201, 532] for details[5]. Uncollimated outflows are ruled out by energetic considerations, since they would require a total energy of the ejecta, $\tilde{E}_{\rm ej} \simeq 10^{53}$ erg, much larger than the one estimated for LFBOTs, i.e. $\tilde{E}_{\rm ej} \simeq 10^{50}$–$10^{51}$ erg [147, 152, 265]. In Fig. 49, we consider isocontours of the isotropic energy $\tilde{E}_j$ in the $(\tilde{L}_j, \tilde{t}_j)$ parameter space . Note that, for $\Gamma = 10$, the region excluded from the collimation argument overlaps with the area already excluded; therefore, we do not show it explicitly.

Concerning CSM interaction occurring in the cocoon model, if $v_{\rm f}$ is the speed of the fastest component of the cocoon responsible for the observed radio emission and $E_k = \tilde{E}_k/(1+z)$ its kinetic energy, its mass $M_{\rm ej}$ can be obtained through the following relation

$$v_{\rm ej} = \sqrt{\frac{2E_k}{M_{\rm ej}}} \, . \tag{10.20}$$

We then vary $M_{\rm ej}$ in the range corresponding to the upper and lower limits on the kinetic energy of the outflow. The former is obtained by assuming that all the energy of the ejecta is converted into kinetic energy, i.e. $\tilde{E}_k = \tilde{E}_{\rm ej}$; the latter is constrained from observations. The range of variability of $M_{\rm ej}$ is shown in Table 8 for AT2018cow and CSS161010 (see under "CSM interaction, cocoon model"). The mass-loss rate $\dot{M}$ spans

5 We assume a density profile of the stellar core $\rho_\star(R) = M_\star/(4\pi R_\star)R^{-2}$, valid up to the He envelope; this profile follows [299, 532] for progenitors harboring choked jets. For the mass of the stellar core and its radius we use $M_\star = 4M_\odot$ and $R_\star = 6 \times 10^{11}$ cm, respectively, inspired by [153] that reproduces the lightcurve of AT2018cow.

the range hinted from radio data, while the CSM radius is fixed from the latest radio observations; see "CSM interaction, cocoon model" in Table 8 and references therein.

For the merger model, we fix the upper limit on the total energy of the ejecta at the theoretical value estimated by [154]. We instead vary the mass of the fast ejecta by using Eq. 10.20, following the argument reported above concerning the upper and lower limits on the kinetic energy. Finally, the mass-loss rate spans a range obtained from theoretical predictions of the model, while the extension of the CSM is fixed from theoretical estimations [154]. All the aforementioned parameters and their variability ranges are listed in the section "CSM interaction, merger model" of Table 8.

10.4 NEUTRINO PRODUCTION

In this section, we summarize the viable mechanisms for neutrino production in LFBOTs. In particular, we discuss interactions between shock accelerated protons and target photons at the internal shocks ($p\gamma$ interactions) in the choked jet and interactions between shock-accelerated protons and a steady target of protons (pp interactions), taking place when the outflow expands in the CSM. In both cases, we present the procedure adopted to compute the high-energy neutrino flux at Earth.

10.4.1 *Neutrino production via proton-photon interactions*

Protons accelerated at the internal shocks interact with thermal photons escaping from the jet head and going back to the unshocked jet. Efficient $p\gamma$ interactions take place at the internal shock, mainly through the Δ^+ channel

$$p+\gamma \longrightarrow \Delta^+ \longrightarrow \begin{cases} n+\pi^+ & 1/3 \ \text{ of all cases} \\ p+\pi^0 & 2/3 \ \text{ of all cases}\,, \end{cases} \tag{10.21}$$

while we can safely neglect pp interactions at the internal shocks, since they are subleading (see Appendix D.1). The reaction channel in Eq. 10.21 is followed by the decay of neutral pions into photons: $\pi^0 \longrightarrow 2\gamma$. At the same time, neutrinos can be copiously produced in the decay chain $\pi^+ \longrightarrow \mu^+ + \nu_\mu$, followed by the muon decay $\mu^+ \longrightarrow \bar{\nu}_\mu + \nu_e + e^+$.

We rely on the photo-hadronic model presented in [115]. Hence, given the injected energy distribution of protons $[n'_p(E'_p)]$ and the distribution of target photons $[n'_\gamma(E'_\gamma)]$, the rate of production of secondary particles l (with $l = \pi^\pm, \pi^0, K^+$) in the comoving frame of the unshocked jet is given by [in units of $\mathrm{GeV}^{-1}\ \mathrm{cm}^{-3}\ \mathrm{s}^{-1}$]:

$$Q'_l(E'_l) = c \int_{E'_l}^{\infty} \frac{dE'_p}{E'_p} n'(E'_p) \int_{E_{\rm th}/2\gamma'_p}^{\infty} dE'_\gamma n'_\gamma(E'_\gamma) R(x,y)\ , \tag{10.22}$$

where $x = E'_l/E'_p$ is the fraction of proton energy which is given to secondary particles, $y = \gamma'_p E'_l$ and $R(x,y)$ is the response function, which contains the physics of the interaction. The initial distributions of protons and photons are given by Eqs. 10.13 and 10.12, respectively.

Before decaying, each charged meson l undergoes energy losses, parametrized through the cooling time $t'^{-1}_{l,\rm cool}$, see Appendix D.1. Therefore, the spectrum at the decay is

$$Q'^{\rm dec}_l(E'_l) = Q'_l(E'_l)\left[1 - \exp\left(-\frac{t'_{l,\rm cool} m_l}{E'_l \tau'_l}\right)\right], \tag{10.23}$$

where τ'_l is the lifetime of the meson l. The comoving neutrino spectrum from decayed mesons is [in units of $\mathrm{GeV}^{-1}\ \mathrm{cm}^{-3}\ \mathrm{s}^{-1}$]:

$$Q'_{\nu_\alpha}(E'_\nu) = \int_{E'_\nu}^{\infty} \frac{dE'_l}{E'_l} Q'^{\rm dec}_l(E'_l) F_{l\to\nu_\alpha}\left(\frac{E'_\nu}{E'_l}\right), \tag{10.24}$$

where $\alpha = e, \mu$ is the neutrino flavor at production and $F_{l\to\nu_\alpha}$ is provided in [273]. We use $\nu_\alpha \equiv \nu_\alpha + \bar{\nu}_\alpha$, i.e. we do not distinguish between neutrinos and antineutrinos.

Magnetic fields in the internal shock are not large enough to efficiently cool kaons, that have a larger mass and a shorter lifetime compared to pions and muons. Therefore, they suffer less energy losses and do not contribute significantly to the neutrino spectrum, even though they may become important at high energies [238, 274–276].

10.4.2 *Neutrino production via proton-proton interactions*

Similar to SNe, stellar outflows interacting with dense CSM can be neutrino factories [65, 123, 131, 533–539], when protons accelerated at the forward shock between the ejecta and the CSM interact with the steady target protons of the CSM.

Given the population of injected shock-accelerated protons in Eq. 10.17, the proton distribution evolves as [534, 564, 565]:

$$\frac{\partial \tilde{N}_{\rm p}(\tilde{\gamma}_{\rm p},R)}{\partial R} - \frac{\partial}{\partial \tilde{\gamma}_{\rm p}}\left[\frac{\tilde{\gamma}_{\rm p}}{R}\tilde{N}_{\rm p}(\tilde{\gamma}_{\rm p},R)\right] + \frac{\tilde{N}_{\rm p}(\tilde{\gamma}_{\rm p},R)}{v_{\rm sh}\tilde{t}_{pp}(R)} = \tilde{Q}(\tilde{\gamma}_p)\ , \tag{10.25}$$

where $\tilde{N}_{\rm p}(\tilde{\gamma}_{\rm p},R)$ is the total number of protons with Lorentz factor between $\tilde{\gamma}_p$ and $\tilde{\gamma}_p + d\tilde{\gamma}_p$ contained in the shell of shocked material at radius R and $\tilde{Q}(\tilde{E}_p) = \pi R_{\rm bo}^2 \tilde{n}(\tilde{E}_p/m_pc^2, R = R_{\rm bo})/(m_pc^2)$ is the proton injection rate at the breakout radius [in units of cm^{-1}]. The second term on the left-hand side of Eq. 10.25 parametrizes adiabatic losses due to the expansion of the shocked shell, while the third term corresponds to pp collisions, treated as an escape term [564].

The neutrino production rates for neutrinos of flavor α, Q_{ν_α} are given by [in units of GeV^{-1} cm^{-1}] [116]:

$$\tilde{Q}_{\nu_\alpha}(\tilde{E}_\nu,R) = \frac{4n_{p,\rm CSM}(R)m_pc^3}{v_{\rm sh}}\int_0^1 dx \frac{\sigma_{pp}(\tilde{E}_\nu/x)}{x}\tilde{N}_{\rm p}\left(\frac{\tilde{E}_\nu}{xm_{\rm p}c^2},R\right)F_{\nu_\alpha}(\tilde{E}_\nu,x)\ , \tag{10.26}$$

where $x = \tilde{E}_\nu/\tilde{E}_{\rm p}$ and the function F_{ν_α} is provided in [116]. Note that Eq. 10.26 is only valid for $E_{\rm p} > 0.1$ TeV, which is the energy range we are interested in.

10.4.3 *Neutrino flux at Earth*

On their way to Earth, neutrinos undergo flavor conversion. The observed distribution for the flavor ν_α (with $\alpha = e, \mu, \tau$) is [GeV^{-1} cm^{-2} s^{-1}]

$$F_{\nu_\alpha}(E_\nu,z) = \mathcal{T}\frac{(1+z)^2}{4\pi d_L^2(z)}\sum_\beta P_{\nu_\beta\to\nu_\alpha}(E_\nu)Q'_{\nu_\beta}(E_\nu\mathcal{L})\ , \tag{10.27}$$

with $Q'_{\nu_\beta}(E_\nu\mathcal{L})$ being the neutrino production rate in the comoving jet ($p\gamma$ interactions) or in the center of explosion (pp interactions) frame, given by Eqs. 10.24 and 10.26, respectively. The constant $\mathcal{T} = V'_{\rm iso} = 4\pi R_{\rm IS}^3/(2\Gamma)$ represents the isotropic volume of the interaction region [280] in the choked jet scenario, while $\mathcal{T} = v_{\rm sh}$ for CSM-ejecta interaction. Note that $\mathcal{T}$ has different dimensions in the choked jet scenario compared to the CSM-ejecta interaction case, because of the different dimensionality of the corresponding neutrino injection rates, see Eqs. 10.24 and 10.26. Moreover, the Lorentz conversion factor is $\mathcal{L} = (1+z)/\Gamma$ for the

choked jet and $\mathcal{L} = (1+z)$ for CSM interaction. The neutrino oscillation probability $P_{\nu_\beta \to \nu_\alpha} = P_{\bar{\nu}_\beta \to \bar{\nu}_\alpha}$ is given by [278, 279]:

$$P_{\nu_e \to \nu_\mu} = P_{\nu_\mu \to \nu_e} = P_{\nu_e \to \nu_\tau} = \frac{1}{4} \sin^2 2\theta_{12} \,, \tag{10.28}$$

$$P_{\nu_\mu \to \nu_\mu} = P_{\nu_\mu \to \nu_\tau} = \frac{1}{8}(4 - \sin^2 \theta_{12}) \,, \tag{10.29}$$

$$P_{\nu_e \to \nu_e} = 1 - \frac{1}{2} \sin^2 2\theta_{12} \,, \tag{10.30}$$

with $\theta_{12} \simeq 33.5°$ [277, 281]. The luminosity distance in a standard flat ΛCDM cosmology is:

$$d_L(z) = (1+z) \frac{c}{H_0} \int_0^z \frac{dz'}{\sqrt{\Omega_\Lambda + \Omega_M (1+z')^3}} \,, \tag{10.31}$$

where we use $H_0 = 67.4$ km s^{-1} Mpc^{-1}, $\Omega_M = 0.315$, and $\Omega_\Lambda = 0.685$ [277, 566].

The neutrino fluence at Earth is

$$\Phi_{\nu_\alpha}(E_\nu) = \int_{t_i}^{t_f} dt \; F_{\nu_\alpha}(E_\nu, t) \,, \tag{10.32}$$

where $F_{\nu_\alpha}(E_\nu, t)$ is given by Eq. 10.27, t_i and t_f are the onset and final times of neutrino production, respectively, measured by an observer at Earth. For the choked jet scenario, the integral in Eq. 10.32 is replaced by the product with the jet lifetime t_j. For CSM interaction, we fix the onset of our calculations $t_i \equiv t_{\rm bo} = (1+z) R_{\rm bo}/v_{\rm sh}$ and follow the neutrino signal up to $t_f \equiv t_{\rm ext} = (1+z) R_{\rm ext}/v_{\rm sh}$, where $R_{\rm ext} = \min[R_{\rm CSM}, R_{\rm dec}]$. In the last expression, $R_{\rm dec}$ is given by Eq. 10.16. This choice is justified because efficient particle acceleration takes place for $R \gtrsim R_{\rm bo}$ only; hence, no neutrinos can be produced before the breakout occurs. Second, for $R \gtrsim R_{\rm ext}$ either the CSM ends and there are no longer target protons for pp interactions to occur, or the ejecta start to be decelerated and the neutrino signal quickly drops as $\propto v_{\rm sh}^2$ [534]. Therefore, neutrino production is no longer efficient.

Both the cocoon model and the merger model predict the presence of slow ejecta, with $v_{\rm s} \simeq 0.01c$. Nevertheless, the fast component of the ejecta in the cocoon model sweeps up the CSM around the star; therefore, when the slow component emerges, there are no longer target protons for efficient pp interactions to occur (in the assumption of spherical symmetry). As for the merger model, the slow outflow propagates into a highly dense and compact CSM. However, shocks in the equatorial region are radiative, and neutrinos should be produced with a maximum energy lower than the one of neutrinos produced in the fast outflow–CSM interaction (see e.g. [298]). Furthermore, the equatorial CSM has a smaller extension than the polar one, and the corresponding neutrino production would last for a shorter time. As a consequence, we consider the neutrino signal from the fast outflow only.

10.5 NEUTRINO SIGNAL FROM NEARBY SOURCES

In this section, we present our forecasts for the neutrino signal for the the choked and CSM interaction models. We also discuss the number of neutrinos expected at the IceCube Neutrino Observatory as well as the detection perspectives at upcoming neutrino detectors, such as IceCube-Gen2.

10.5.1 *Neutrino fluence*

For the choked jet scenario (see Sec. 10.2.1), for fixed isotropic equivalent energy $\tilde{E}_j^{\rm iso}$, we consider an envelope containing the expected neutrino fluence for the allowed $(\tilde{L}_j, \tilde{t}_j)$ pairs. As for CSM interaction in the cocoon model, we fix $R_{\rm bo} = R_{\rm env} = 3 \times 10^{13}$ cm up to $R_{\rm ext}$. Indeed, in the hypothesis of an extended stellar envelope surrounding the core of the star, the CSM is already optically thin at the edge of the envelope and radiation can escape as soon as the cocoon breaks out. As already pointed out, in the merger model the breakout radius is calculated by using Eq. 10.15 and it does not occur too deep in the CSM, since the latter is not very dense.

Figure 50 shows the muon neutrino fluence expected from AT2018cow and CSS161010. The blue band corresponds to the neutrino fluence from the choked jet, while the orange and purple bands represent the neutrino signal from CSM interaction in the cocoon and merger models, respectively. Each band reflects the uncertainties on the model parameters discussed in Sec. 10.3 (see Table 8). The neutrino fluence for the choked jet scenario is displayed for the optimistic case of a jet observed on axis. If the jet axis should be perpendicular with respect to the line of sight of the observer, no neutrino is expected. In the following, we assume that the choked jet points towards the observer; this might have been the case for AT2018cow, since two neutrinos have been detected at IceCube in its direction [66, 567]—see discussion below. On the other hand, the emission from CSM interaction is approximately isotropic and hence observable from any viewing angle. This is consistent with electromagnetic observations of LFBOTs: if a choked jet is harbored, no electromagnetic emission is expected. The optical radiation is powered from the cooling of the cocoon, while the radio emission comes from the interaction of the cocoon with the CSM [153]. In the merger model, the fast outflow responsible for the high-energy neutrino emission likely covers about $\gtrsim 70\%$ of the solid angle 4π [154]; hence, its emission is quasi-isotropic and visible from along any observer direction.

Both for the cocoon and merger models, CSM interaction produce a smaller neutrino fluence than in the case of the choked jet model. Nevertheless, the merger model allows for a larger neutrino fluence compared to the cocoon one. This result is justified in the light of the larger CSM densities. Even though the stellar mass-loss rates are comparable, the wind speed is lower in the merger model than in the cocoon model (10 km s^{-1} and 1000 km s^{-1}, respectively; in the former model, it is generated by mass loss from the disk, while it is due to mass loss from the progenitor star prior to its explosion in the latter model). If a choked jet is harbored in LFBOTs and points towards the observer, then it dominates the neutrino emission. The neutrino emission from the choked jet model is in qualitative agreement with [235, 247, 248], which focused on forecasting the neutrino production in gamma-ray bursts instead. Our results concerning the neutrino signal from ejecta-CSM interaction are valid for every model invoking the emission of a fast outflow propagating outwards in the CSM. On the contrary, neutrino emission from the choked jet is model dependent. Recent numerical simulations show that efficient acceleration in jets can occur if the jet is weakly or mildly magnetized [236]; if this should be the case for LFBOTs, a dedicated investigation of the neutrino production in this scenario would be required. Furthermore, we have calculated the neutrino signal from the jet assuming that it is choked in the extended stellar envelope. As discussed in Sec. 10.3 and shown in Fig. 49, a choked jet may be harbored only for certain pairs of the jet luminosity and lifetime.

For comparison, in Fig. 50, we show the sensitivity of IceCube for point sources at the declination $\delta = 22°$ (for AT2018cow) and $\delta = -8°$ (for CSS161010) [568] and the projected sensitivity of IceCube-Gen2 for a point-like source at $\delta = 0°$ [16]. If a source similar to AT2018cow (or CSS161010) were to be observed in the future at this declination by IceCube-Gen2, the detection chances of neutrinos from the choked jet scenario would be comparable to the ones of IceCube. This is mainly due to the fact that the sensitivity of IceCube-Gen2 will be better than the one of IceCube in the PeV–EeV energy range but comparable at lower energies; the fluence from the choked jet peaks in the TeV–PeV range. As for the CSM interaction, the neutrino fluence lies well below the sensitivity curve of both IceCube and IceCube-Gen2.

Other neutrino detectors are planned to be operative in the future, such as GRAND 200k [17], RNO–G [176] and POEMMA [18]. These neutrino telescopes aim to probe ultra high energy neutrinos, but their sensitivity in the PeV–EeV energy range is worse than the one of IceCube-Gen2; therefore we do not show them in Fig. 50.

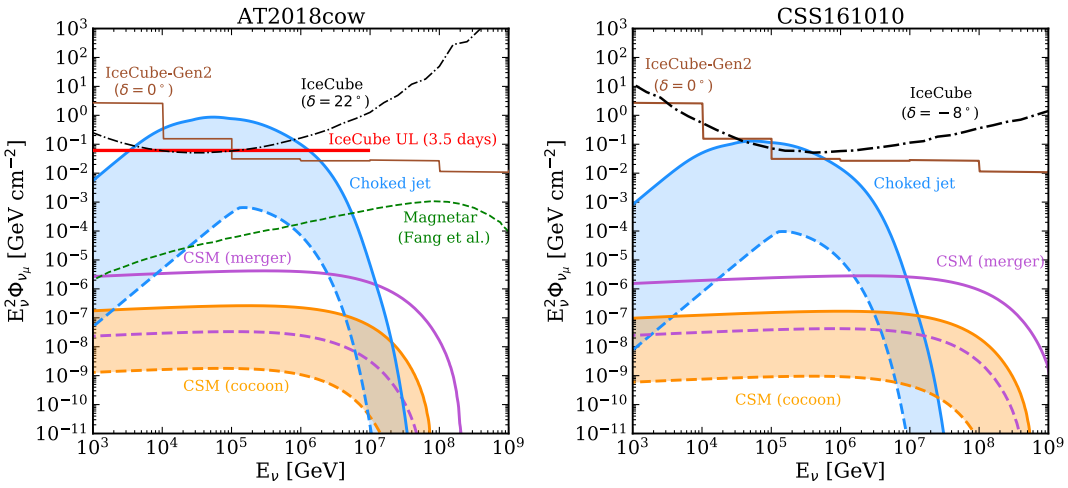

Figure 50: Muon neutrino fluence expected from AT2018cow (left panel, $z = 0.0141$, $\delta = 22°$) and CSS161010 (right panel, $z = 0.034$, $\delta = -8°$). The blue shaded region corresponds to the contribution to the neutrino signal from the choked jet, while the orange (purple) shaded region displays the signal from interaction between the CSM and the fast component of the outflow in the cocoon (merger) model. The continuous (dashed) lines are the upper (lower) limits on the neutrino fluence, corresponding to the ranges of parameter values listed in Table 8. The neutrino emission from the choked jet scenario is strongly dependent on the direction, while the one from the CSM scenarios is quasi-isotropic. The neutrino fluence in the choked jet scenario is shown in the most optimistic case of a jet oriented along the line of sight of the observer. For comparison, we show the results of [530] (green dashed line), corresponding to the neutrino fluence in the event that a magnetar powers AT2018cow. The sensitivity of IceCube for point sources is plotted at a declination $\delta = 22°$ and $\delta = -8°$ [568] (black dot-dashed lines), as measured for AT2018cow and CSS161010, respectively. The sensitivity of IceCube-Gen2 to a point source at $\delta = 0°$ is also shown (sienna line). The neutrino fluence from the choked jet harbored in LFBOTs—if the jet points towards the observer—is comparable with the sensitivities of IceCube and IceCube-Gen2. For AT2018cow, we show the upper limit set by IceCube on the time-integrated ν_μ fluence (IceCube UL, red line), corresponding to the observation of two neutrino events in coincidence with AT2018cow [66, 567].

In Fig. 50, we plot the upper limit set by IceCube on the muon neutrino fluence for AT2018cow. This upper limit corresponds to the observation of two IceCube neutrino events in coincidence with AT2018cow at 1.8σ confidence level within a time window of 3.5 days after the optical discovery [66, 567]. The envelope obtained for AT2018cow overshoots this limit for $\tilde{E}_j^{\rm iso} \gtrsim 10^{52}$ erg. Interestingly, $\tilde{E}_j^{\rm iso} \gtrsim 10^{52}$ erg falls in the range inferred by electromagnetic observations, see Table 8. This finding intriguingly suggests that existing neutrino data may further restrict the allowed parameter space shown in Fig. 49 for AT2018cow, as displayed in Fig. 51. No neutrino search has been performed in the direction of CSS161010 instead.

As discussed in Sec. 10.3, the CO of LFBOTs could be a magnetar. In this case, high-energy neutrinos could be produced in the proximity of the magnetar [132, 426, 569]. Protons (or other heavier nuclei) may be accelerated in the magnetosphere and then interact with photons and baryons in the ejecta shell surrounding the CO. Both $p\gamma$ and pp interactions can efficiently produce neutrinos in the PeV–EeV energy band. The neutrino production from a millisecond magnetar has been investigated in [298] for AT2018cow. We show the expected muon neutrino fluence at Earth obtained in [298] in Fig. 50 for comparison with the other scenarios explored in this paper. For CSS161010, we expect a neutrino fluence qualitatively similar to the one considered for AT2018cow.

If a magnetar is the central engine of LFBOTs, its contribution to the neutrino fluence would be relevant in the PeV–EeV band, at energies higher than the typical ones for neutrino emission from the choked jet and CSM interaction. Note that the comparison between the fluence from the magnetar and our results is consistent as for the energetics of the CO. Indeed, the set of parameters adopted by [530] leads to $\tilde{E} \simeq 10^{50}$–10^{51} erg injected by the magnetar in its spin-down time, $\tilde{t}_{\rm sd} \simeq 8.4 \times 10^3$–$8.4 \times 10^4$ s. If a jet is launched by the magnetar, then these quantities correspond to its energy and its lifetime, consistently with the ranges we are exploring in our work.

The radio extension of IceCube-Gen2 [16], as well as the neutrino facilities GRAND200k [17], POEMMA [18] and RNO-G [176] will be more sensitive than IceCube [16] for what concerns the emission of neutrinos in the magnetar scenario and they may detect neutrinos from sources similar to AT2018cow, occurring at a smaller distance.

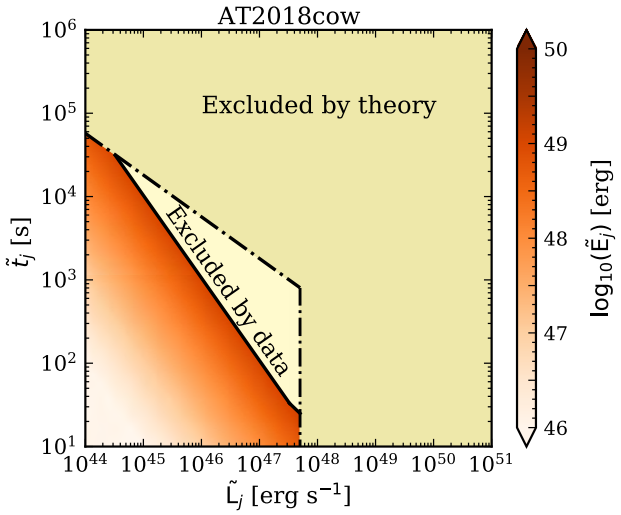

Figure 51: Contour plot of the jet energy $\tilde{E}_j$ in the parameter space spanned by $(\tilde{L}_j, \tilde{t}_j)$ for AT2018cow and $\Gamma = 100$. Part of the parameter space allowed in Fig. 49 is excluded by the IceCube neutrino data (light yellow region), since the correspondent neutrino emission would overshoot the upper limit set by IceCube on the time-integrated ν_μ flux from for AT2018cow [66, 567]. Another portion of the parameter space (dark yellow region) is excluded by theoretical arguments, as already shown in Fig. 49. For $\Gamma = 10$, the region of the parameter space excluded by the IceCube data is smaller and overlaps with the one excluded by theory. The region of the parameter space excluded by the IceCube data is obtained under the assumption of an on-axis choked jet, see discussion in the main text.

10.5.2 *Neutrino event rate*

Given the muon neutrino fluence up to the time t, $\Phi_{\nu_\mu}(E_\nu, t)$, the cumulative number of muon neutrinos expected at IceCube up to the same time is

$$N_{\nu_\mu}(t) = \int_{E_{\nu,\min}}^{E_{\nu,\max}} dE_\nu \Phi_{\nu_\mu,}(E_\nu, t) A_{\rm eff}(E_\nu, \delta) \ , \tag{10.33}$$

where $E_{\nu,\min} = 10^2$ GeV and $E_{\nu,\max} = 10^{10}$ GeV are the minimum and maximum neutrino energies, respectively, and $A_{\rm eff}(E_\nu, \delta)$ is the effective area as a function of energy and for a fixed source declination δ [141]. The background of atmospheric muon neutrinos can be estimated following [412]:

$$N_{\nu_\mu,\rm back}(t) = \pi \Delta\delta^2 \int_{E_{\nu,\min}}^{E_{\nu,\max}} dE_\nu A_{\rm eff}(E_\nu, \delta) \Phi^{\rm atm}_{\nu_\mu}(E_\nu, \theta, t) \ , \tag{10.34}$$

where $\Phi^{\rm atm}_{\nu_\mu}(E_\nu, \theta, t)$ is the fluence of atmospheric neutrinos at the time t, from the zenith angle θ and $\Delta\delta \simeq 2.5^\circ$ is the width of the angular interval within which is defined the effective area $A_{\rm eff}(E_\nu, \delta)$ of IceCube. For IceCube, the relation $\theta = 90^\circ + \delta$ holds [570]. We compute the atmospheric background by using the model presented in [571–573].

We show the cumulative number of neutrinos from the choked jet scenario (for a jet pointing towards the observer) and CSM interaction (both for the cocoon and merger models) as functions of time both for

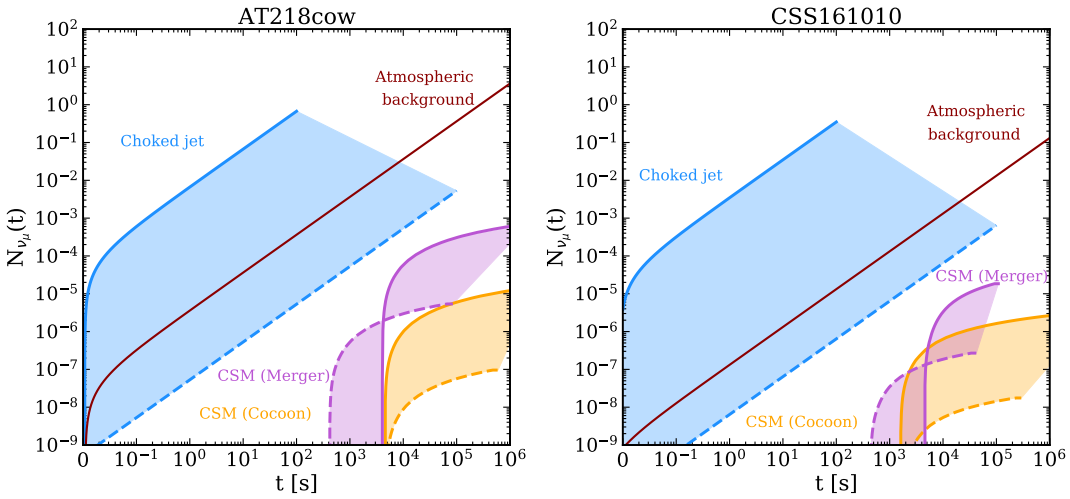

Figure 52: Cumulative number of muon neutrinos for AT2018cow (left panel) and CSS161010 (right panel) expected at the IceCube Neutrino Observatory; see Table 8. The blue shaded region corresponds to the contribution from the choked jet (when the latter is observed on-axis); the orange (purple) shaded region corresponds to neutrinos from CSM interaction in the cocoon (merger) model. The rate of neutrinos from the choked jet is expected to be constant in the approximation that N internal shocks occur in the jet during its lifetime and that each of them produces the same neutrino signal. Therefore, the neutrino signal grows linearly with time up to the end of the jet lifetime. For CSM interaction, the number of neutrinos rapidly increases and settles to a constant value since the proton injection is balanced by pp energy losses. The upper and lower limits of each band correspond to the same uncertainty ranges in Table 8 and Fig. 50, except for the upper limit for the choked jet scenario in AT2018cow for which we take $\tilde{E}_j^{\rm iso} = 10^{51}$ erg, consistently with the IceCube constraints–see Fig. 51. The brown line shows the cumulative number of atmospheric neutrinos (which constitutes a background for the detection of astrophysical neutrinos), which increases linearly with time.

AT2018cow and CSS161010 in Fig. 52. Note that for AT2018cow, the upper limit of the choked jet scenario is calculated by assuming $\tilde{E}_j^{\rm iso} = 10^{51}$ erg, in agreement with the allowed region of the parameter space shown in Fig. 51. The upper and lower limits for the cumulative number of neutrinos in the CSM interaction models for AT2018cow and for all the scenarios considered for CSS161010 are the same as the ones in Table 8. The thick lines denote the duration of the signal, which can last up to a few months for CSM interaction. As for the choked jet, the neutrino rate is expected to be constant during the jet lifetime, in the simple approximation that N internal shocks occur in the jet during this period and each of them produces the same neutrino signal. Hence, the cumulative neutrino rate from the choked jet grows linearly with time up to the jet lifetime. For CSM interaction, the number of neutrinos rapidly increases after the breakout and then reaches a plateau since the proton injection is balanced by pp energy losses. The atmospheric background neutrinos increase linearly with time. The background is expected to dominate over the signal from CSM interaction, both for the cocoon and merger models; on the contrary, the background becomes comparable to the choked jet signal at times larger than the jet lifetime.

10.5.3 *Detection prospects for AT2018cow and CSS161010*

The neutrino signal from LFBOTs overlaps in energy with the atmospheric neutrino background. In order to gauge the possibility of discriminating the LFBOT signal from the one of atmospheric neutrinos, we compare the total number of muon neutrinos of astrophysical origin $N_{\nu_\mu,\mathrm{astro}}$ with the total number of background atmospheric neutrinos $N_{\nu_\mu,\mathrm{back}}$. The former is given by the sum between contributions from the choked jet and CSM interaction in the cocoon model and by CSM interaction only in the merger model. Each contribution is computed by relying on Eq. 10.33 and integrating over the duration of the neutrino production, defined for each case in Sec. 10.4.3. The latter is obtained through Eq. 10.34, during the duration of neutrino production for each model.

Below 100 TeV, the astrophysical neutrino events need to be carefully discriminated against the atmospheric ones. Hence, we consider two scenarios: a conservative energy cutoff in Eq. 10.33, $E_{\nu,\mathrm{min}} = 100$ TeV (corresponding to the case when atmospheric neutrino events cannot be distinguished from the astrophysical ones below 100 TeV) and a low energy cutoff, $E_{\nu,\mathrm{min}} = 100$ GeV (representative of the instance of full discrimination of the events of astrophysical origin).

Our results are summarized in Table 9. The number of astrophysical neutrinos expected in the cocoon model is larger than the number of atmospheric neutrinos, both for AT2018cow and CSS161010, when the energy cutoff $E_{\nu,\mathrm{min}} = 100$ TeV is adopted. Hence, the detection chances of astrophysical neutrinos above 100 TeV may be promising, if a choked jet pointing towards the observer is harbored in LFBOTs. The number of astrophysical neutrinos may instead be smaller than or comparable to the atmospheric background for the merger model, therefore, the background signal cannot be fully discriminated; this is especially evident for $E_{\nu,\mathrm{min}} = 100$ GeV. In the event of detection of one or a few neutrinos from LFBOTs and depending on the number of undetected sources from the LFBOT population, the actual neutrino flux could be smaller than the one estimated by relying on the detected events. For this reason, we need to correct for the Eddington bias on neutrino observations [574]. Assuming that the local rate of LFBOTs is $\sim 0.4\%$ of the core-collapse SN rate [152], we consider the effective density integrated over the cosmic history of LFBOTs to be $O(10^4)$ Mpc^{-3}. The latter has been computed by assuming the density of core-collapse SNe equal to 1.07×10^7 Mpc^{-3} [32, 575] and the redshift evolution of LFBOTs identical to the one of the star formation rate. After aking into account these inputs, from Fig. 2 of [574], we find that the number of expected events

Table 9: Total number of astrophysical neutrinos ($N_{\nu_\mu,\mathrm{astro}}$) and atmospheric neutrinos ($N_{\nu_\mu,\mathrm{back}}$) in the cocoon (including choked jet and CSM interaction) and merger models, for $E_{\nu,\mathrm{min}} = 100$ TeV. The correspondent neutrino numbers obtained by adopting $E_{\nu,\mathrm{min}} = 100$ GeV are displayed in parenthesis. The range of variability corresponds to the upper and lower limits shown in Fig. 52.

N_{ν_μ}	AT2018cow	CSS161010
	Cocoon model	
$N_{\nu_\mu,\mathrm{astro}}$	3×10^{-3}–0.15 (7×10^{-3} – 0.67)	3×10^{-4}–0.23 (4×10^{-4} – 0.35)
$N_{\nu_\mu,\mathrm{back}}$	9×10^{-4} – 3×10^{-3} (2.23 – 9.71)	5×10^{-4} – 1.4×10^{-2} (2.6×10^{-2} – 0.64)
	Merger model	
$N_{\nu_\mu,\mathrm{astro}}$	1.5×10^{-6}–2.1×10^{-4} (1.5×10^{-6} – 2×10^{-4})	6.5×10^{-7}–4.5×10^{-5} (8×10^{-7} – 5×10^{-5})
$N_{\nu_\mu,\mathrm{back}}$	1×10^{-4} – 3×10^{-3} (0.32 – 8)	8×10^{-5} – 2×10^{-3} (3.7×10^{-3} – 9.2×10^{-2})

in Table 9 could be compatible with the observation of 1–3 neutrino events both from AT2018cow and CSS161010.

The IceCube Neutrino Observatory reported the detection of two track-like neutrino events in the direction of AT2018cow compatible with the expected number of atmospheric neutrino events [66]. Our findings hint that the observation of two neutrino events may also be compatible with the expected number of neutrinos of astrophysical origin. A dedicated neutrino search in the direction of CSS161010, during the time when the transient was electromagnetically bright, would be desiderable.

10.5.4 *Future detection prospects*

The rate of LFBOTs and its redshift dependence are still very uncertain. In oder to forecast the detection prospects in neutrinos for upcoming LFBOTs, we consider an LFBOT with properties similar to the ones of AT2018cow (see Table 8). Figure 53 shows the total number of neutrinos expected at the IceCube Neutrino Observatory in the choked jet scenario and for CSM interaction (both in the cocoon and merger models) as functions of the luminosity distance of the AT2018cow-like source; of course, similar conclusions would hold for an LFBOT resembling the CSS161010 source, see Figs. 50 and 52. We assume the upper and lower limits for AT2018cow listed in Table 8, since the neutrino constraints shown in Fig. 51 do not hold for this source. We assume that the source is at $\delta = 0°$, in order to guarantee the maximal effective area at IceCube [141],

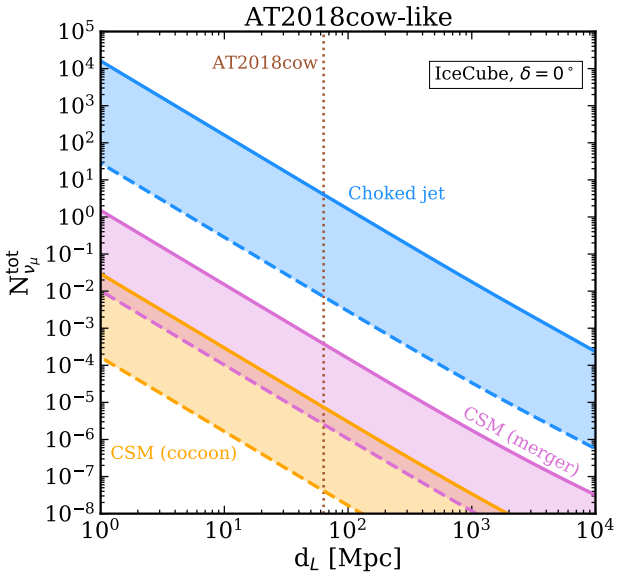

Figure 53: Total number of muon neutrinos expected at the IceCube Neutrino Observatory as a function of the luminosity distance for an AT2018cow-like source from the choked jet pointing towards the observer (blue shaded region) and CSM interaction in the cocoon and merger models (orange and purple shaded regions, respectively). The bands are obtained by adopting the parameter uncertainty ranges listed in Table 8 for AT2018cow. The source is placed at $\delta = 0°$. The brown vertical line marks the distance of AT2018cow to guide the eye. The number of neutrinos decreases as a function of the luminosity distance, as expected.

and perform the integral in Eq. 10.33 between the initial (t_i) and final (t_f) times of neutrino production as described in Sec. 10.4.3. Furthermore, we adopt the conservative lower energy cutoff $E_{\nu,\mathrm{min}} = 100$ TeV, in order to better discriminate neutrinos of astrophysical origin from atmospheric background neutrinos.

Figure 53 shows that the number of neutrinos expected in the choked jet scenario for an AT2018cow-like source located at 1 Mpc $\lesssim d_L \lesssim 10^4$ Mpc is $10^{-6} \lesssim N^{\mathrm{tot}}_{\nu_\mu} \lesssim 10^4$ if the jet points towards the observer. As for CSM interaction, the number of expected neutrinos for the same source located at 1 Mpc $\lesssim d_L \lesssim 10^4$ Mpc is for the cocoon model (merger model) is $2 \times 10^{-12} \lesssim N^{\mathrm{tot}}_{\nu_\mu} \lesssim 3 \times 10^{-2}$ ($10^{-10} \lesssim N^{\mathrm{tot}}_{\nu_\mu} \lesssim 2$). We expect comparable or better detection chances for IceCube-Gen2 (see Fig. 50). We stress that a detailed statistical analysis may provide improved detection prospects, but this is out of the scope of this work. Nevertheless, our results are an intriguing guideline for upcoming follow-up neutrino searches of LFBOTs.

10.6 DIFFUSE NEUTRINO EMISSION

Despite the growing number of neutrino events routinely detected at IceCube, the origin of the observed diffuse neutrino background is still unknown. Several source classes have been proposed as major contributors

to the observed diffuse flux, such as gamma-ray bursts, cluster of galaxies, star-forming galaxies, tidal distruption events, and SNe [32, 36, 37, 123, 231, 240, 242, 366–368, 576–579]. As discussed in Sec. 10.5, LFBOTs have favorable detection chances in neutrinos, hence we now explore the contribution of LFBOTs to the diffuse neutrino background.

The diffuse neutrino background is

$$F_\nu^{\rm back} = \frac{c}{4\pi H_0}\int_0^{z_{\rm max}} dz \frac{f_b R_{\rm SFR}(z)}{\sqrt{\Omega_M (1+z)^3+\Omega_\Lambda}}\phi_\nu(E'_\nu)\,, \tag{10.35}$$

where $z_{\rm max}=8$, $\phi_\nu(E'_\nu)$ is the differential neutrino number from a single burst (in units of GeV^{-1}; defined multiplying Eq. 10.32 by the luminosity distance), $E'_\nu = E_\nu(1+z)/\Gamma$ (where $\Gamma=1$ for CSM interaction). The beaming factor is given by $f_b = \Omega/4\pi \simeq \theta_j^2/2$ for the choked jet, while $f_b=1$ for CSM interaction. The factor takes into account the beaming of the jet within an opening angle θ_j. The beaming is not relevant in pp interactions, since they originate from the cocoon (or the polar fast outflow) whose opening angle is wider than the one of the jet [223]. Therefore, the geometry of the outflow can be assumed to be spherical.

So far, the luminosity function for LFBOTs is not available because only a few transients have been identified as belonging to this emerging class. Thus, we fix the isotropic equivalent energy of the choked jet $\tilde{E}_j^{\rm iso} = 10^{51}$ erg, its Lorentz factor $\Gamma=100$, and assume that it is representative of the whole population. For computing the contribution to the diffuse neutrino background from CSM interaction, we assume $M_{\rm ej}=10^{-2}M_\odot$, $\dot{M}=10^{-3}M_\odot$ yr^{-1}, $v_{\rm w}=1000$ km s^{-1}, and $v_{\rm sh}=0.3c$ as representative values.

We assume that the redshift evolution of LFBOTs follows the star formation rate, $R_{\rm SFR}(z)$ [575]:

$$R_{\rm SFR}(z) = R_{\rm FBOT}(z=0)\left[(1+z)^{-34}+\left(\frac{1+z}{5000}\right)^3+\left(\frac{1+z}{9}\right)^{35}\right]^{-1/10} \tag{10.36}$$

where the local rate of LFBOTs is assumed to be $R_{\rm FBOT}(z=0)\lesssim 300$ Gpc^{-3} yr^{-1} [146, 152].

Figure 54 shows the upper limit to the diffuse neutrino background resulting from the choked jet and CSM interaction (cocoon model; seagreen solid line). For comparison, we also show the upper limit on the total diffuse emission when we include the contribution from a millisecond magnetar, i.e. when we sum up the diffuse emission from choked jet, CSM interaction and the magnetar itself (light-brown dashed line). The diffuse emission from the magnetar only has been taken from [530] and it has been rescaled to the local rate assumed in this paper, referred to the subclass of LFBOTs. Note that here we consider the cocoon model only, since it includes both a choked jet and CSM interaction and thus it would lead to the most optimistic estimation of the expected neutrino background. If the merger model is adopted, the resulting diffuse neutrino

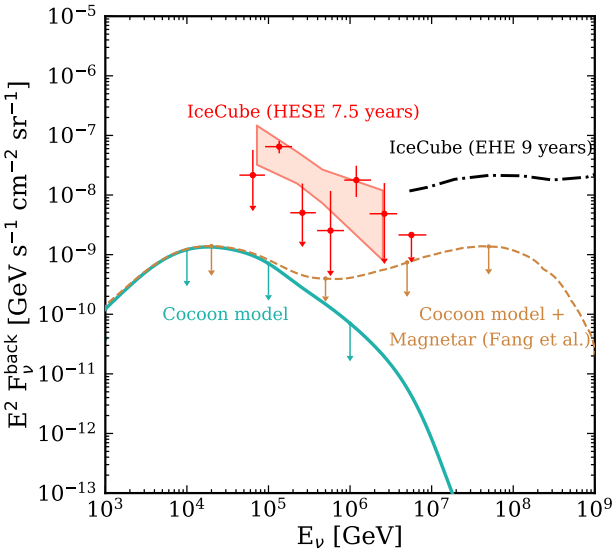

Figure 54: Upper limit on the all-flavor diffuse neutrino flux from LFBOTs obtained by including the contribution from a choked jet and CSM interaction (cocoon model; seagreen solid line) as a function of the neutrino energy. We show the cocoon model only, since it includes both the choked jet and CSM interaction; the merger model would give rise to a diffuse flux lying well below the seagreen line. For comparison, the upper limit obtained including both the cocoon model and the contribution from the magnetar (taken from [530]) is also shown (light-brown dashed line). The pink band corresponds to the fit to the 7.5 year IceCube high energy starting events (HESE), plotted as red datapoints [112]. The black dot-dashed line corresponds to the 9 year extreme-high-energy (EHE) 90% upper limit set by the IceCube Neutrino Observatory [580]. The diffuse neutrino background from LFBOTs lies below IceCube data.

background is flat at low energies, with an energy cutoff around 10^7 GeV; hence, the merger model would give rise to a diffuse emission below the seagreen line in Fig. 54 and consistent with the upper limit we are showing.

We compare our results with the flux constraints from the 7.5 year high-energy starting event data set (HESE 7.5yr) [112] and the 9 year extreme-high-energy (EHE) 90% upper limit set by the IceCube Neutrino Observatory [580] in Fig. 54. Our results suggest that LFBOTs do not constitute the bulk of the diffuse neutrino flux detected by the IceCube Neutrino Observatory. Nevertheless, typical energies of these objects might be larger that the ones assumed in this work, resulting in a larger diffuse neutrino emission.

10.7 CONCLUSIONS

Despite the growing number of observations of LFBOTs, their nature remains elusive. Multi-messenger observations could be crucial to gain insight on the source engine.

In this paper, we consider the scenarios proposed in [153] (cocoon model) and [154] (merger model) for powering LFBOTs and aiming to fit multi-wavelength electromagnetic observations and mounting evidence for asymmetric LFBOT outflows. In the cocoon model, neutrinos could be produced in the jet choked within the extended envelope of the collapsing massive star. The existence of a jet harbored in LFOBTs is highly uncertain, and certain conditions on its luminosity and lifetime must be satisfied for the jet to be choked. If a jet is launched by the CO and choked, it contributes to inflate the cocoon, the latter breaks out of the stellar envelope and interacts with the CSM; neutrinos could also be produced at the collisionless shocks occurring at the interface between the cocoon and the CSM. In the merger model, a black hole surrounded by an accretion disk forms as a result of the merger of a Wolf-Rayet star with a black hole. The disk outflow in the polar region propagates in the CSM, possibly giving rise to neutrino production.

By using the model parameters inferred from the electromagnetic observations of two among the most studied LFBOTs, AT2018cow and CSS161010, we find that neutrinos with energies up to $O(10^9)$ GeV could be produced in the cocoon and merger models. The neutrino signal from the choked jet would be detectable only if the observer line of sight is located within the opening angle of the jet. If this is the case, the upper limit on the neutrino emission set by the IceCube Neutrino Telescope on AT2018cow [66] already allows to exclude a region of the FBOT parameter space, otherwise compatible with electromagnetic observations. On the contrary, the existence of a fast outflow ($v_{\rm ej} \gtrsim 0.1$ c) interacting with the CSM is supported by electromagnetic observations. The results concerning the neutrino signal from CSM interaction are therefore robust and valid for any viewing angle of the observer, being the emission isotropic in good approximation.

We find that the neutrino emission from LFBOTs does not account for the bulk of the diffuse neutrino background observed by IceCube. Nevertheless, the neutrino fluence from a single LFBOT is especially large in the choked jet scenario, if the jet should be observed on axis, and is comparable to the sensitivity of the IceCube Neutrino Observatory and IceCube-Gen2, while it is below the IceCube sensitivity for the CSM interaction cases.

By taking into account the Eddington bias on the observation of cosmic neutrinos, we conclude that the two track-like events observed by IceCube in coincidence with AT2018cow may have been of astrophysical origin (similar conclusions would hold for CSS161010). In the light of these findings, a search for neutrino events in coincidence with the other known LFBOTs should be carried out.

In conclusions, the detection of neutrinos from LFBOTs with existing and upcoming neutrino telescopes will be crucial to probe the mechanism powering FBOTs. The choked jet and CSM interaction would generate very different neutrino signals: the former is direction dependent and peaks around $E_\nu \simeq 10^5$ GeV, the latter is quasi-isotropic and approximately flat up to $E_\nu \simeq 10^7$–10^8 GeV for our fiducial parameters. Current neutrino telescopes may not be able to clearly differentiate the signals from the choked jet and CSM interaction scenarios. Nevertheless, CSM interaction can produce neutrinos in the high energy tail of the spectrum. E.g. the detection of neutrinos with energies of $O(100)$ PeV may hint towards the CSM interaction origin; on the other hand, if a choked jet is harbored in LFBOTs and the jet is observed on-axis, a large number of neutrinos with $O(100)$ TeV energy is expected to be detected at IceCube and IceCube-Gen2. As the number of detected LFBOTs increases, neutrino searches have the potential to provide complementary information on the physics of these emergent transient class and their rate.

10.8 CRITICAL OUTLOOK

In this Section, we outline the key aspects of our study and provide an overview of our main results. We also highlight possible future directions of our work. Notably, similar topics have been addressed in Sec. 10.5.3.

10.8.1 *Overview and main findings*

As of today, core-collapse SNe stand as one of the most largely studied transient phenomena in astrophysics. As we stepped into the time-domain astronomy era, a plethora of transients previously unknown have been discovered. Notably, while standard SNe reach their peak luminosity on timescales $\gtrsim O(10)$ days, many of the observed transients evolve very quickly and reach their peak luminosity in $\lesssim 5$ days. Consequently, only some of the observed objects can be classified as SNe, while the nature of most of them remains unknown. Within the family of rapidly evolving transients, the emerging class of LFBOTs is particularly puzzling. Their outflow moves at mildly-relativistic ($\gtrsim 0.1$ c) velocities, akin to the ejecta of SNe Ib/c broad line. Likewise, the asymmetry observed in their outflow resembles the geometry of GRB explosions. However, the rapid rise time of their optical lightcurve and the lack of gamma-rays associated with them hint that LFBOTs form a novel class of explosive phenomena [148].

While the number of observed LFBOTs increases, the high-energy neutrino signal associated with these sources remains poorly explored. Yet the IceCube collaboration reported the detection of two high-energy neutrino events in the direction of AT2018cow, the first LFBOT ever observed [66]. Motivated by these intriguing observations, we investigate the high-energy neutrino signal from LFBOTs. Importantly, for the first time, we compare different LFBOT models— both capable of accommodating the multi-wavelength observations— in light of state-of-the-art multi-messenger observations. Our work paves the way for a multi-messenger approach to unravel the nature of these enigmatic transients.

We rely on the most promising LFBOT models to calculate the corresponding high-energy neutrino production. The first model invokes a collapsing massive star that launches a jet. The latter is subsequently choked within the extended hydrogen envelope surrounding the progenitor core, therefore we refer to this framework as *choked jet model*. The second model considers the delayed merger between a Wolf-Rayet star and a black hole, resulting in a final central black hole surrounded by an accretion disk. We refer to this scenario as *merger model*.

As for the choked jet model, we identify two regions where particle acceleration can take place: internal shocks occurring near the head of the choked jet and the external shock driven by the fast outflow in the surrounding CSM. On the contrary, the latter is the only possible particle acceleration site in the merger model. We carry out our analysis for AT2018cow and CSS161010, the two closest LFBOTs ever detected.

Our findings have crucial implications in several key areas. Firstly, our work reveals that existing neutrino data in the direction of AT2018cow already constrain the allowed parameter space in the choked jet model, excluding a region otherwise compatible with electromagnetic observations. Secondly, our results highlight that neutrinos can disentangle the mechanism powering LFBOTs. We find that, while a neutrino signal extending up to $\simeq O(10^8)$ GeV energies is expected from the interactions between the outflow and the CSM, the flux produced by the choked jet peaks at energies between $10^4 - 10^5$ GeV and it dominates the overall high-energy neutrino signal. In light of these findings, our work highlights that high-energy neutrinos provide pivotal complementary information to electromagnetic data.

Intriguingly, Ref. [530] investigates the scenario involving a central magnetar as the energy source of LFBOTs. The neutrino signal produced in the magnetar wind peaks around $\simeq 10^8$ GeV, thereby corroborating our finding that neutrinos can disentangle the mechanism powering LFBOT sources.

In preparation for future observations of LFBOTs, we also inspect the detection perspectives of high-energy neutrinos from transients resembling AT2018cow. Our findings hint that LFBOTs do not contribute to the bulk of the high-energy neutrino diffuse flux detected at IceCube. However, if a choked jet should be harbored within these sources and observed on-axis, we forecast the detection of $\simeq 10$ neutrinos at IceCube from AT2018cow-like sources. Therefore, we advocate for high-energy neutrino searches from LFBOTs as our work proves that their detection will be crucial to probe the mechanism powering these sources.

10.8.2 *Future research directions*

In the following, we suggest possible future directions to strengthen the results of our work.

1. *Model dependence of the choked jet scenario.* Our results for the choked jet scenario are model dependent, since specific conditions on the jet luminosity and lifetime must be satisfied to both choke the jet and allow for particle acceleration. Furthermore, the detectability of the neutrino signal depends on the alignment of the jet with respect to Earth. Should we sit outside the opening angle of the collimated outflow, the high-energy neutrino signal produced in the choked jet and merger models would appear nearly indistinguishable. Forthcoming observations of LFBOTs will be crucial to gain further insights into the origin of these enigmatic objects.

2. *Improving numerical simulations of choked jets.* Numerical simulations of jets choked in an extended envelope surrounding the stellar core will lead to more realistic modeling of high-energy neutrino production in this framework, as also urged by the results presented in Chapter 7.

3. *Including the velocity and energy distributions of the outflow in the analysis.* In our analysis, we consider a blastwave with fixed energy and expanding with constant velocity into the CSM. While this approximation does not affect the expected neutrino signal, both the energy and velocity distributions of the outflow should be taken into account to outline a unified model for the electromagnetic and neutrino radiation from LFBOTs.

We conclude this section with a discussion of recent developments in the understanding of LFBOTs since the publication of our work. Notably, a signal in the X-ray band has been observed in the direction of AT2018cow ≈ 3.7 years after its first observation [581], mirroring the previously reported persistent UV signal [508].

While the latter could be explained within the merger model, it is unknown whether this framework can accommodate the late X-ray signal as well. Furthermore, it has been recently suggested that LFBOTs may originate from the merger of a neutron star with a white dwarf [582]. High-energy neutrino production in LFBOTs should be scrutinized in light of recent theoretical models suggested in the literature.

Finally, we point out that a new fast evolving transient recently joined the family of LFBOTs: AT2022tsd. The source, which has been dubbed the *Tasmanian Devil*, exhibits energetic flares occurring over months. Intriguingly, the non-thermal nature of these flares favors the presence of a near-relativistic jet within LFBOTs and further supports the hypothesis of a central compact object powering these sources.

In summary, our research proves that LFBOTs are promising sources of high-energy neutrinos and it encourages neutrino follow-up searches from these transients with current and upcoming neutrino telescopes. Importantly, our work highlights the potential of high-energy neutrinos in disentangling the mechanism powering these transients. Future observations of LFBOTs and advanced numerical simulations in the outlined directions will further expand our understanding of these fascinating phenomena.

11

TRANSIENTS STEMMING FROM COLLAPSING MASSIVE STARS: THE MISSING PIECES TO ADVANCE JOINT OBSERVATIONS OF PHOTONS AND HIGH-ENERGY NEUTRINOS

Based on: **Ersilia Guarini**, Irene Tamborra, Raffaella Margutti, Enrico Ramirez-Ruiz, *Transients stemming from collapsing massive stars: The missing pieces to advance joint observations of photons and high-energy neutrinos*, arXiv:2308.03840

ABSTRACT Collapsing massive stars lead to a broad range of astrophysical transients, whose multi-wavelength emission is powered by a variety of processes including radioactive decay, activity of the central engine, and interaction of the outflows with a dense circumstellar medium. These transients are also candidate factories of neutrinos with energy up to hundreds of PeV. We review the energy released by such astrophysical objects across the electromagnetic wavebands as well as neutrinos, in order to outline a strategy to optimize multi-messenger follow-up programs. We find that, while a significant fraction of the explosion energy can be emitted in the infrared-optical-ultraviolet (UVOIR) band, the optical signal alone is not optimal for neutrino searches. Rather, the neutrino emission is strongly correlated with the one in the radio band, if a dense circumstellar medium surrounds the transient, and with X-rays tracking the activity of the central engine. Joint observations of transients in radio, X-rays, and neutrinos will crucially complement those in the UVOIR band, breaking degeneracies in the transient parameter space. Our findings call for heightened surveys in the radio and X-ray bands to warrant multi-messenger detections.

11.1 INTRODUCTION

A number of transients may be linked to the aftermath of collapsing massive stars, ranging from supernovae (SNe) and gamma-ray bursts(GRBs) [127, 324–327, 583] to exotic transients with puzzling properties, e.g. fast blue optical transients (FBOTs) [143–146, 296], superluminous supernovae (SLSNe) [126, 584] or

chameleon SNe [585, 586] among the ones detected electromagnetically. These objects are characterized by a range of time scales and peak luminosities [3, 129], albeit the mechanisms powering their emission remain uncertain.

In the next future, the theory behind such sources will progress through the exponential growth of the number of astrophysical transients detected across different wavebands with wide field, high cadence surveys, such as the Zwiky Transient Facility (ZTF) [157], the All-Sky Automated Survey for SuperNovae (ASAS-SN) [158], as well as the Panoramic Survey Telescope and Rapid Response System 1 (Pan-STARRS1) [159], and the Young Supernova Experiment (YSE) [160]. In addition, while our understanding of the UV emission from explosive transients has already been transformed thanks to *Swift*-UVOT [587], our ability to explore the hot and transient universe will soon be revolutionized by the upcoming Vera C. Rubin Observatory [161] and ULTRASAT [15].

Such transients are also expected to emit neutrinos with energy between $O(1)$ TeV and $O(100)$ PeV, as a result of particle acceleration [49, 59, 65, 410], as well as gravitational waves [70, 588]. The operating IceCube Neutrino Observatory [13], the Baikal Deep Underwater Neutrino Telescope (Baikal-GVD) [181] and the ANTARES neutrino telescope [180] routinely search for high-energy neutrinos from transient sources. In particular, neutrinos have been possibly observed in coincidence with a candidate hydrogen-rich SLSN [65, 410] as well as an FBOT [66, 234]. Our potential to explore the transient universe through non-thermal neutrinos will be further enhanced with upcoming neutrino telescopes such as IceCube-Gen2 [16], the Cubic Kilometre Neutrino Telescope (KM3NeT) [589], the Giant Radio Array for Neutrino Detection (GRAND200k) [17], the orbiting Probe of Extreme Multi-Messenger Astrophysics (POEMMA) [376], and the Pacific Ocean Neutrino Experiment (P-ONE) [178].

In order to address fundamental questions concerning the physics linked to high-energy particle emission, efficiency of particle acceleration, as well as the mechanisms powering these transients, it is key to exploit multi-messenger observations to break degeneracies in the parameter space of the transient properties otherwise hindering our understanding [234, 298, 590–592].

A number of programs are in place to explore transients through multiple messengers and across energy bands; for example, ASAS-SN, ZTF and Pan-STARRS1 carry out target-of-opportunity searches for optical counterparts of high-energy neutrino events [529, 593, 594], and in turn the IceCube Neutrino Observatory looks for neutrinos in the direction of the sources discovered by optical surveys, see e.g. Refs. [526, 595].

Follow-up searches of (very) gamma-ray counterparts of the high-energy neutrinos observed at the IceCube Neutrino Observatory are also carried out with Fermi-LAT [596, 597] and the Imaging Atmospheric Cherenkov Telescopes (IACTs) [527].

To capitalize on the promising multi-messenger detection prospects, it is necessary and timely to define a strategy to carry out informed follow-up searches of high-energy neutrinos and electromagnetic emission from transients. What electromagnetic waveband is better correlated with high-energy neutrinos? What fraction of the bulk of energy released in the collapse of massive stars is deposited across the different electromagnetic wavebands and neutrinos? In this paper, we address these questions performing computations of the energy budget of astrophysical transients stemming from collapsing stars. In our analysis, we consider both thermal and non-thermal processes that may power the electromagnetic emission and define a criterion for correlating electromagnetic observations at different wavelengths with the neutrino signal.

This paper is organized as follows. In Sec. 11.2, we outline the theoretical framework for calculating the energy budget in each electromagnetic waveband for non-relativistic outflows, while we focus on jetted relativistic outflows in Sec. 11.3. In Sec. 11.4, after introducing the distribution of accelerated protons, we outline the channels for neutrino production. Section 11.5 presents the energy budget across electromagnetic wavebands and in neutrinos of the astrophysical transients linked to collapsing massive stars. In Sec. 11.6, we investigate the most promising strategies to correlate electromagnetic and neutrino observations depending on the transient properties and the related detection prospects. Finally, we summarize our findings in Sec. 11.8. In addition, the cooling rates of protons accelerated in the magnetar wind, at CSM interactions as well as in a jetted outflow are discussed in Appendix E.1, while Appendix E.2 focuses on radiative shocks.

11.2 MODELING OF THE ELECTROMAGNETIC EMISSION: NON-RELATIVISTIC OUTFLOWS

After introducing the one-zone model adopted to compute the bolometric luminosity, in this section we outline the contribution to the electromagnetic emission, across wavebands, from different heating sources. For illustrative purposes we present the results for a benchmark transient in this section, whereas our findings for different transient classes are discussed in Sec. 11.5.

11.2.1 *Luminosity*

We rely on the one-zone model of Refs. [129, 598, 599] to compute the output bolometric luminosity from collapsing stars. This model only holds for spherical outflows and, since we are interested in the bulk of the emitted radiation, we focus on the properties of the bolometric light curve around its peak.

Our model is based on the following assumptions: 1. the ejecta are spherically symmetric and expand homologously; 2. the outflow is radiation dominated, namely the radiation pressure is larger than the electron and gas pressure (note that we do not consider radiation dominated outflows for the production of radio photons and neutrinos when the shock interacts with the CSM; see Secs. 11.2.2 and 11.4); 3. a central heating source is present [1]; 4. the ejecta propagate with a bulk constant velocity $v_{\rm ej}$, i.e.the injected energy is smaller than the kinetic energy of the ejecta.

Because of the hypothesis of homologous expansion, the radius of the ejecta evolves as $R_{\rm ej}(t) \simeq v_{\rm ej} t$. During the photospheric phase, which can last up to several weeks after the explosion depending on the ejecta mass [600], the ejecta are optically thick, i.e. their optical depth is $\tau_{\rm ej} \gg 1$. When and where $\tau_{\rm ej} \simeq 2/3$, radiation begins to diffuse from the outflow [599]. Since no significant kinetic energy is added to the outflow, one can assume that the photosphere expands with velocity $v_{\rm ph} \simeq v_{\rm ej}$.

The first law of thermodynamic can be written as (unless otherwise specified, we carry out our calculations in the reference frame of the expanding outflow):

$$\frac{{\rm d}E}{{\rm d}t} + \frac{{\rm d}P}{{\rm d}t} = \dot{q}_{\rm inj} - \frac{\partial L}{\partial m} \tag{11.1}$$

where $E = aT^4 V$ and $P = aT^4 V/3$ are the specific internal energy and pressure, respectively, L is the output luminosity and m is the mass of the fluid element, $V = \rho^{-1}$ is the specific volume with ρ being the density and T the temperature. The specific energy injection rate is $\dot{q}_{\rm inj}$.

For a photosphere which homologously expands, the solution of Eq. 11.1 is [599]:

$$L(t) = \frac{2}{t_d} e^{-\left(\frac{t^2}{t_d^2} + \frac{2R_0 t}{v_{\rm ej} t_d^2}\right)} \int_0^t dt' e^{-\left(\frac{t'^2}{t_d^2} + \frac{2R_0 t'}{v_{\rm ej} t_d^2}\right)} \left(\frac{R_0}{v_{\rm ej} t_d} + \frac{t'}{t_d}\right) L_{\rm inj}(t') + {\rm HS}\ , \tag{11.2}$$

1 The assumption of a central heating source does not hold for all the heating processes, in particular for interactions of the ejecta with a dense CSM surrounding the progenitor. Thus, this simplified model has several limitations, see Ref. [599] for a discussion. By comparing the analytical model with numerical simulations, Ref. [599] finds that the approximation of a central heating source reproduces the peak time of the bolometric lightcurve and its normalization within a factor $\simeq 2$ with respect to numerical simulations, which is acceptable for the purpose of this paper.

where $L_{\rm inj}$ is the luminosity injected by the central compact source (linked to $\dot{q}_{\rm inj}$ in Eq. 11.1), R_0 is the initial radius of the source, and $t_d = \sqrt{2\kappa M_{\rm ej}/\beta c v_{\rm ej}}$ is the time needed for the radiation to diffuse through the ejecta (assumed to be longer than the duration of the energy injection in our model) of mass $M_{\rm ej}$ and opacity κ—the latter is considered time-independent and independent on the ejecta composition; the geometrical factor is $\beta \simeq 13.7$ for a variety of diffusion density profiles [325], and HS is the homogeneous solution of Eq. 11.1 obtained requiring $\dot{q}_{\rm inj} = 0$.

The homogeneous solution is only relevant when the outflow expands adiabatically, with no energy source heating the ejecta. Assuming adiabatic expansion, the emitted luminosity is [129]

$$L_{\rm ad}(t) = \frac{E_{k,\rm ej}}{t_d} e^{-\left[t^2/t_d^2 + (2R_0 t)/(v_{\rm ej} t_d^2)\right]} , \tag{11.3}$$

where $E_{k,\rm ej}$ is the kinetic energy content of the ejecta.

When a dense CSM shell surrounds the transient, the outflow crashing with the nearly stationary CSM drives two shocks: one that propagates back in the ejecta and another one which propagates in the CSM. Both these shocks act as heating sources for the ejecta as their kinetic energy is converted into radiation. In this scenario, we assume that the shock efficiently radiates (i.e. $t_d = 0$), implying $L(t) \equiv L_{\rm inj}(t)$ [601]. This solution holds as long as the shock deceleration during the interaction with the CSM is negligible. The full self-similar solution including diffusion through the CSM has been calculated in Ref. [599]. However, since we are mostly interested in linking the electromagnetic emission to the neutrino one, with the production of the latter taking place in the optically thin part of the CSM, the simple model outlined in Ref. [601] is a fair approximation for our purposes. Note that we treat $E_{k,\rm ej}$ and $M_{\rm ej}$ as free parameters, and the ejecta velocity depends on these two quantities through $v_{\rm ej} \simeq \sqrt{2E_{k,\rm ej}/M_{\rm ej}}$.

11.2.2 *Heating sources*

For the purposes of this paper, we select the following heating processes [129]:

- fallback of matter on the black hole (BH);
- magnetar spin down;
- ^{56}Ni and ^{56}Co decay;
- hydrogen recombination;

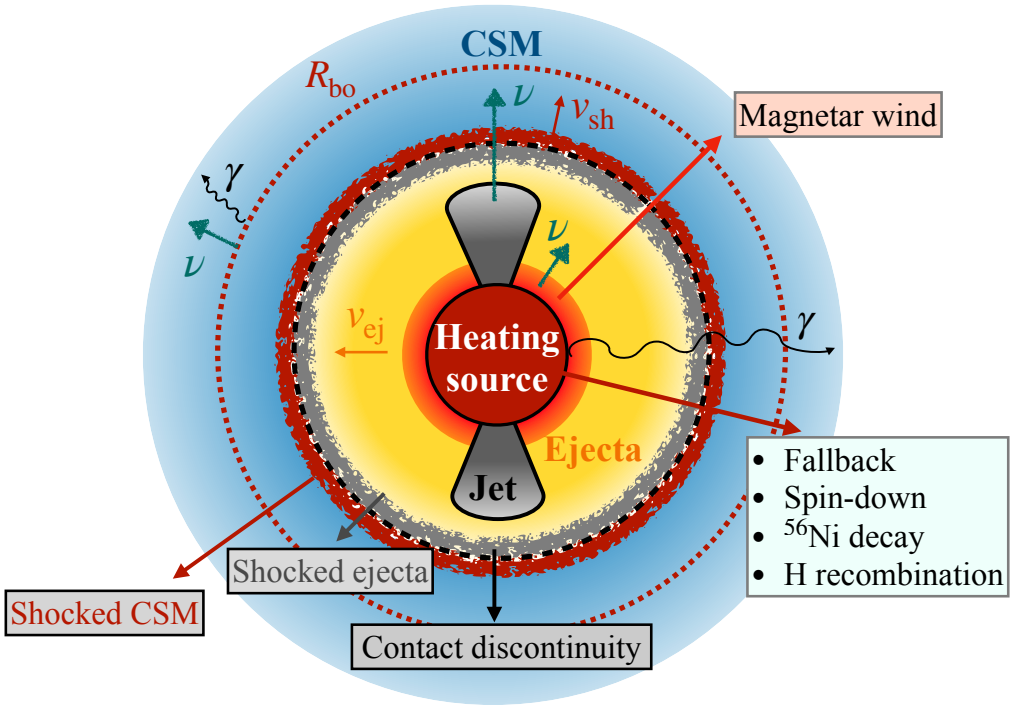

Figure 55: Sketch (not to scale) of the outflow (orange/yellow region) launched by the collapsing star and powered by a central heating source (red region), moving at velocity v_{ej}. The heating can be due to fallback material on the BH, spin-down of the magnetar, and/or ^{56}Ni decay, and hydrogen recombination. A jetted outflow can be harbored (gray region). The outflow expands and interacts with a dense CSM (blue region), forming a forward shock and a reverse shock. The former propagates outwards and it shocks the CSM (red outermost shell), the latter propagates inwards and it shocks the ejecta (light gray shell). The two shocked regions are separated by a contact discontinuity (black dotted line). The forward shock (moving at velocity v_{sh}) breaks out from the CSM at the breakout radius (R_{bo}, dotted red line), where non-thermal production of particles starts. Neutrino production can take place at the forward shock propagating in the CSM and eventually in the magnetar wind and/or in the jet.

- shock breakout from the stellar surface;

- interaction of the outflows with a dense CSM.

A sketch of the outflow evolution—including a jetted component—and the heating sources is provided in Fig. 55. Each process heats the ejecta for a duration t_{dur}. Unless otherwise specified, we assume that t_{dur} is the timescale such that the bolometric lightcurve luminosity has declined by 90% relative to its peak luminosity.

The duration of each heating process is shown in Fig. 56 for our benchmark transient, whose parameters are listed in Table 10. We assume that the progenitor star of our benchmark transient is a red supergiant. However, it is unlikely that all considered heating processes simultaneously power the outflow of a collapsing red supergiant. The parameters in Table 10 should be interpreted as representative of each process rather than of a specific transient source.

The total energy radiated by each heating source over the duration of its activity, $t_{\rm dur}$, in a specific waveband $[E_{\rm min}, E_{\rm max}]$ is

$$E_{\rm rad} = \int_{E_{\rm min}}^{E_{\rm max}} dE_\gamma \; E_\gamma n_\gamma(E_\gamma) \; , \tag{11.4}$$

where n_γ is the photon distribution resulting from the heating process under consideration. Note that we refer to the total energy radiated after photons diffuse through the ejecta mass. Throughout the paper, we consider the following wavebands:

- Radio: $[E_{\rm min}^{\rm Radio}, E_{\rm max}^{\rm Radio}] = [4\times10^{-15}, 4\times10^{-13}]$ GeV =[1, 100] GHz;
- Infrared (IR): $[E_{\rm min}^{\rm IR}, E_{\rm max}^{\rm IR}] = [4\times10^{-13}, 1.7\times10^{-9}]$ GeV = [0.75, 300] μm;
- Optical: $[E_{\rm min}^{\rm Opt}, E_{\rm max}^{\rm Opt}] = [1.7\times10^{-9}, 3.3\times10^{-9}]$ GeV = [320, 750] nm;
- Ultraviolet (UV): $[E_{\rm min}^{\rm UV}, E_{\rm max}^{\rm UV}] = [3.3\times10^{-9}, 1.2\times10^{-7}]$ GeV=[10, 320] nm;
- X-ray: $[E_{\rm min}^{\rm X-ray}, E_{\rm max}^{\rm X-ray}] = [3\times10^{-7}, 200\times10^{-6}]$ GeV= [0.3, 200] keV;
- Gamma-ray: $[E_{\rm min}^{\gamma-{\rm ray}}, E_{\rm max}^{\gamma-{\rm ray}}] = [200\times10^{-6}, 10^3]$ GeV.

Following Ref. [129], we assume that radiation quickly thermalizes and relaxes to a black-body distribution

$$n_\gamma^{\rm BB}(E_\gamma) = \int_0^{t_{\rm dur}} dt A_\gamma(t) \frac{E_\gamma^2}{e^{E_\gamma/k_B T_\gamma^{\rm BB}(t)}-1} \; , \tag{11.5}$$

with k_B being the Boltzmann constant, $A_\gamma(t) = L(t)/\left[\int_0^\infty dE_\gamma E_\gamma n_\gamma^{\rm BB}(E_\gamma, t)\right]$ the normalization constant and L the emitted luminosity given by Eq. 11.2, which depends on the type of heating source.

The blackbody temperature is

$$T_\gamma^{\rm BB}(t) \simeq \left[\frac{L(t)}{4\pi\sigma_{\rm SB} R_{\rm ph}(t)^2}\right]^{1/4} \; , \tag{11.6}$$

where σ_{SB} is the Stefan-Boltzmann constant and $R_{\rm ph} \simeq R_{\rm ej}$ is the photospheric radius in our approximation. Care should be taken for the photon spectrum resulting from CSM interactions; see Sec. 11.2.2.6.

The black-body assumption holds as long as the outflow is optically thick. Since the bulk of energy is emitted near the lightcurve peak with temperature $\simeq T_\gamma^{\rm BB}$, this is a fair approximation. Note that the total radiated energy in Eq. 11.4 is calculated in the reference frame of the star, without considering redshift corrections. For a source at redshift z, the observed energy is $E_{\rm obs} = E_{\rm rad}/(1+z)$.

Table 10: Characteristic parameters for our benchmark transient. Each parameter is defined in the main text for the corresponding heating source. We consider a red supergiant progenitor. These parameters are meant to represent individual heating processes; only a subset of them is expected to be at play for a specific transient source class.

Parameter	Symbol	Value
Ejecta energy	$E_{k,\mathrm{ej}}$	10^{51} erg
Ejecta mass	M_{ej}	$M_\odot$
Fallback time	t_{fb}	10^7 s
Fallback mass	M_{fb}	$10^{-2} M_\odot$
Jet efficiency	ϵ_j	10^{-2}
Density contributing to M_{fb}	$\bar{\rho}$	10^{-7} cm^{-3}
Spin-down period	P_{spin}	10 ms
Magnetar magnetic field	B	10^{14} G
Fraction of ejecta mass in ^{56}Ni	f_{Ni}	0.1
Progenitor radius	$R_\star$	500 $R_\odot$
Progenitor mass	$M_\star$	15 $M_\odot$
Mass-loss rate	M_w	5×10^{-3} $M_\odot$ yr^{-1}
Wind velocity	v_w	100 km s^{-1}
CSM radius	R_{CSM}	2×20^{16} cm
Jet isotropic energy	$E_{\mathrm{iso,j}}$	3.7×10^{54} erg
Jet lifetime	t_j	100 s
Jet Lorentz factor	Γ	300
Jet opening angle	θ_j	3°

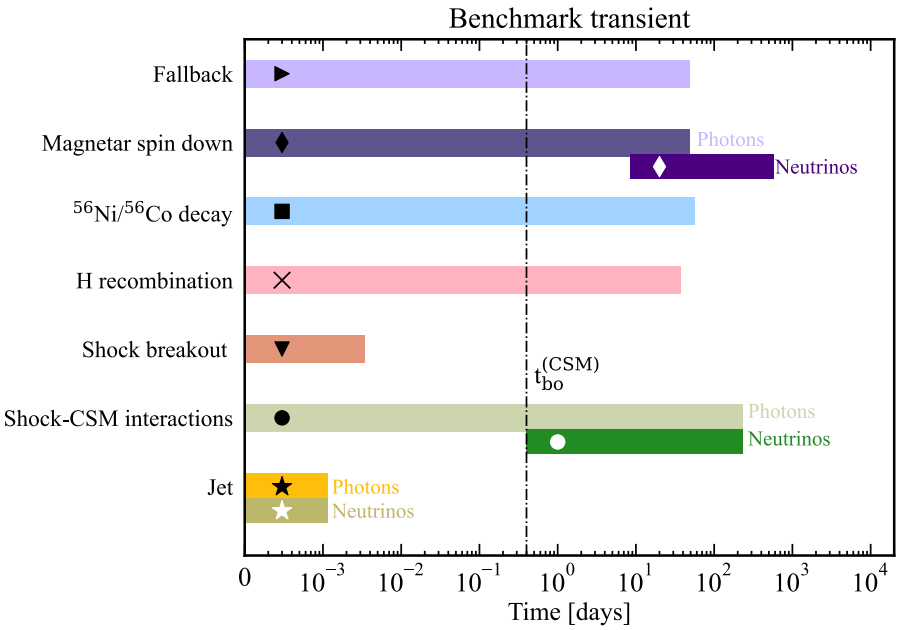

Figure 56: Duration of the bolometric lightcurve powered by different heating processes (Eq. 11.2). From top to bottom the observed luminosity is powered by: fallback of material onto a BH, magnetar spin down, ^{56}Ni and ^{56}Co decay, hydrogen recombination, shock breakout from the progenitor star, CSM interactions in the optically thick and thin regimes, and jet. The vertical line marks the time of breakout from the dense CSM shell (Eq. 11.19). The time intervals over which neutrino production occurs are displayed for the magnetar scenario, CSM interactions, and the jet. We mark each heating process with a different symbol. Black symbols denote photons, white ones denote neutrinos.

11.2.2.1 *Fallback*

When a massive star undergoes gravitational collapse its core collapses into a Kerr BH [326], as predicted by the collapsar model. Due to fast rotation, the outer layers of the collapsing star carry too much angular momentum to fall freely into the last stable orbit. Thus, an accretion disk forms, from which both gravitational and rotational energy can be extracted. Energy may also be released through neutrino cooling [195].

Besides the unbound mass ejected during the collapse, a comparable mass (e.g., from tidal tails) could remain bound to the central compact object and fallback onto it. The rate at which mass falls back onto the BH is [602–606]:

$$\dot{M}_{\rm fb}(t) = \frac{2}{3}\frac{M_{\rm fb}}{t_{\rm fb}}\frac{1}{\left(1+\frac{t}{t_{\rm fb}}\right)^{5/3}}\,, \tag{11.7}$$

where $M_{\rm fb}$ is the total accreted mass, $t_{\rm fb} = (3\pi/32G\bar{\rho})^{1/2}$ is the free-fall time scale [561], G is the gravitational constant, $\bar{\rho}$ is the mean density of the collapsing layer contributing to $M_{\rm fb}$. The injected luminosity from this heating process is [605]

$$L_{\rm inj}^{\rm fb}(t) = \epsilon_j \dot{M}_{\rm fb} c^2\,, \tag{11.8}$$

where ϵ_j is a constant factor representing the fraction of accreted energy which is used to power the disk

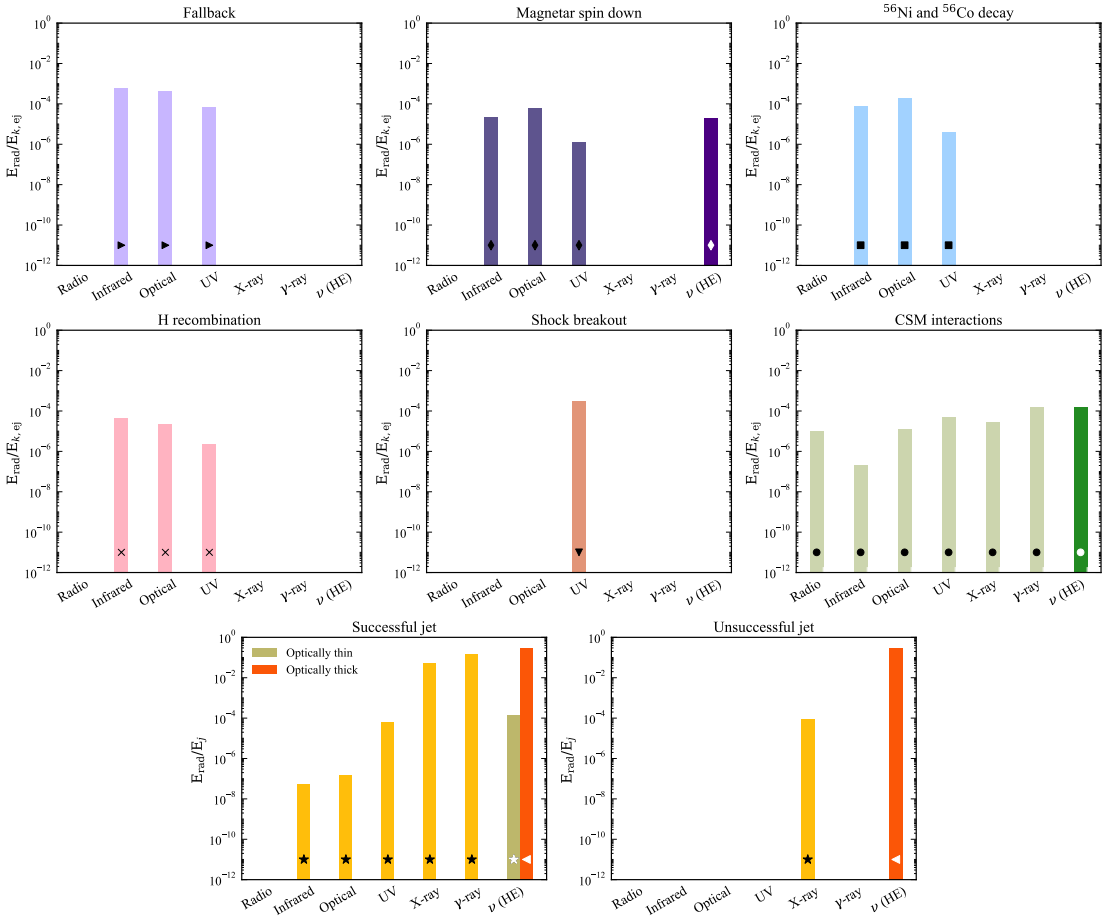

Figure 57: Ratio between the energy radiated across electromagnetic wavebands as well as neutrinos and the kinetic energy of the ejecta (or the energy of the jet for the bottom panels). The results are shown for our benchmark transient (see Table 10). The color code as well as the symbols denoting each heating process are the same as in Fig. 56. Heating from fallback material on the BH, magnetar spin down, ^{56}Ni, and ^{56}Co decay and hydrogen recombination lead to emission of radiation in the UVOIR band. The shock breakout produces a flash of light in the UV band. CSM interactions in the optically thin regime mostly radiate in the radio and X-ray bands, with a substantial energy fraction released in gamma-rays and neutrinos. A successful jet radiates in the X-ray and gamma-ray bands, whereas the only electromagnetic signature of unsuccessful jets is the flash of light from the shock breakout emitted in the X-ray/gamma-ray band, depending on the outflow and progenitor properties. The jet radiates energy in neutrinos both in the optically thin and thick regimes, the former component only existing for successful jets.

wind (or jetted outflow), namely its efficiency. The heating of the spherical ejecta occurs either because of a jet which becomes unstable and looses power [220] or a mildly-relativistic wind which is launched by the inner accretion disk and collides with the more massive outflow emitted at the explosion [607]. In both cases, the energy available to heat the collapsar outflow is given by Eq. 11.8; see also the discussion in Ref. [605].

For a red supergiant progenitor (Table 10), the collapsing layer has mean density $\bar{\rho} \simeq 10^{-7}$ g cm^{-3}, corresponding to the fallback time $t_{\rm fb} \simeq 10^7$ s [603]. The total mass accreted in this case is $M_{\rm fb} \simeq 10^{-2} M_\odot$ [608], resulting in a fallback rate $M_{\rm fb}/t_{\rm fb} \simeq 10^{-9} M_\odot$ s^{-1}. Figure 57 (top left panel) shows the energy radiated across the electromagnetic wavebands (Eq. 11.4) through fallback of matter on the BH, relative to

the kinetic energy of the ejecta $E_{k,\rm ej}$. For our benchmark transient, the bulk of radiation powered by fallback onto the BH is emitted in the infrared-optical-ultraviolet (UVOIR) band due to the opacity of the outflow. X-rays may become observable at later times, yet we do not consider this signal in our treatment as it would become relevant at larger times than the ones considered in this work; see [607] for details.

11.2.2.2 *Magnetar spin down*

Assuming a dipole configuration for the magnetic field, the injected luminosity from the spin down of the compact object is

$$L_{\rm inj}^{\rm sd}(t) = \frac{\epsilon_{\rm sd} E_{\rm sd}}{t_{\rm sd}\left(1+\frac{t}{t_{\rm sd}}\right)^2}\,, \tag{11.9}$$

where $E_{\rm sd} = I\Omega^2/2$ is the initial rotational energy of the magnetar, which depends on the moment of inertia (I) and angular velocity of the neutron star (Ω). The spin-down timescale $t_{\rm sd}$ is related to the neutron star magnetic field $B_{14} = B/(10^{14}G)$ and the spin period $P_{\rm spin} = 2\pi/\Omega \simeq 10\ [E_{\rm sd}/(2\times10^{50}\ {\rm erg})]^{-0.5}$ ms through [557]

$$t_{\rm sd} = 4\times10^7 \frac{P_{\rm spin,10}^2}{B_{14}^2}\ {\rm s}\,. \tag{11.10}$$

We consider the spin-down injection efficiency to be $\epsilon_{\rm sd} = 10\%$, relying on observations of the Crab Nebula [609]. Furthermore, we carry out our calculations for a neutron star with $I = 10^{45}$ g cm^{-2} g cm^{-2} [610].

Figure 57 (top central panel) shows the energy radiated (Eq. 11.4) through the magnetar spin down. The bulk of radiation powered by the spin down of the magnetar is emitted in the UVOIR band. Note that, during the the time interval that we consider, the outflow is optically thick, hence the non-thermal X-rays produced by the compact object are reprocessed in the optical/UV bands [132].

11.2.2.3 *Radioactive decay of nickel and cobalt*

Diffusion of radioactive energy produced by newly sinthetized ^{56}Ni and subsequently ^{56}Co was investigated in Refs. [598, 611, 612] analytically. The injected luminosity in Eq. 11.2 can be parametrized as

$$L_{\rm inj}^{\rm Ni}(t) = M_{\rm Ni}\left[\epsilon_{\rm Co} e^{-t/\tau_{\rm Co}} + (\epsilon_{\rm Ni}-\epsilon_{\rm Co}) e^{-t/\tau_{\rm Ni}}\right] \tag{11.11}$$

where $M_{\rm Ni} = f_{\rm Ni} M_{\rm ej}$ is the fraction of the ejecta mass that goes into ^{56}Ni, $\epsilon_{\rm Ni} = 3.9\times10^{10}$ erg s^{-1} g^{-1} ($\epsilon_{\rm Co} = 6.8\times10^9$ erg s^{-1} g^{-1}) and $\tau_{\rm Ni} = 8.8$ days ($\tau_{\rm Co} = 111.3$ days) are the energy generation rates and the decay rates of ^{56}Ni (^{56}Co), respectively.

Figure 57 (top right panel) displays the energy radiated across different wavebands (Eq. 11.4) through radioactive decay of ^{56}Ni and ^{56}Co. The bulk of radiation powered by these processes is emitted in the UVOIR band; also in this case, the resulting bulk of radiation depends on the assumption of optically thick ejecta.

11.2.2.4 *Hydrogen recombination*

When the collapsing massive star retains its hydrogen layer, the latter can be ionized by the SN shock. Hydrogen recombination takes place as the outflow cools to ≈ 5000 K, which is the ionization temperature of neutral hydrogen and it has been invoked to explain the plateau observed in the lightcurve of some SNe [613–616]. An analytical model for hydrogen recombination was presented in Refs. [129, 325, 615, 617–619].

The luminosity L_p and duration t_p of the plateau are [325]

$$L_p = 1.64 \times 10^{42} \frac{R_{\star,500}^{2/3} E_{k,51}^{5/6}}{M_{\rm ej,10}^{1/2}} \ {\rm erg\ s^{-1}}\ , \tag{11.12}$$

$$t_p = 99 \ \frac{M_{\rm ej,10}^{1/2} R_{\star,500}^{1/6}}{E_{k,51}^{1/6}} \ {\rm days}\,, \tag{11.13}$$

where $R_{\star,500} = R_\star/(500\ R_\odot)$, $E_{k,51} = E_{k,\rm ej}/(10^{51}\ {\rm erg})$ and $M_{\rm ej,10} = M_{\rm ej}/(10\ M_\odot)$ are the kinetic energy and the mass of the ejecta, respectively, with $R_\odot$ and $M_\odot$ being the solar radius and mass.

The injected luminosity from hydrogen recombination is [615]

$$L_{\rm inj}^{\rm H}(t) = \frac{L_p}{e^{-(13.1+0.47\ M_p)t}}\ , \tag{11.14}$$

where M_p is the peak magnitude, linked to the peak luminosity (L_p).

The energy radiated across different wavebands through hydrogen recombination is shown in Fig. 57 (middle left panel). The bulk of radiation powered by hydrogen recombination is emitted in the UVOIR band.

11.2.2.5 *Shock breakout*

A flash of light is expected when the forward shock driven by the outflow breaks out from the progenitor star. When the CSM surrounding the collapsing star is very dense, the shock breakout may however take place when the shock crosses the CSM.

The shock breakout theory has been developed in Refs. [620–622] for non-relativistic and (mildly-)relativistic shocks. The former is the regime expected for standard core-collapse SNe, while the latter is

relevant for engine-driven SNe. The models of Refs. [620, 621] are challenged by observations, as they cannot reproduce the duration and luminosity of the candidate SNe possibly displaying shock breakout, see e.g. Refs. [623–625]. Yet, an advanced shock breakout theory does not exist to date. In the light of these uncertainties, we do not adopt any spectral energy distribution for the shock breakout emission. Rather, we assume that photons with temperature $T_{\rm bo}$ are emitted over the time $t_{\rm bo}$, with total energy release $E_{\rm bo}$. These quantities depend on the stellar progenitor radius ($R_\star$) and mass ($M_\star$), as well as on the energy of the ejecta. For instance, in the case of a non-relativistic shock breakout from a red supergiant one has [620]:

$$T_{\rm bo} \simeq 25 \text{ eV } \mathrm{M}_{\star,15}^{-0.3}\, \mathrm{R}_{\star,500}^{-0.65}\, \mathrm{E}_{\rm k,ej,51}^{0.5} \,; \tag{11.15}$$

$$t_{\rm bo} \simeq 300 \text{ s } \mathrm{M}_{\star,15}^{0.21}\, \mathrm{R}_{\star,500}^{2.16}\, \mathrm{E}_{\rm k,ej,51}^{-0.79} \,; \tag{11.16}$$

$$E_{\rm bo} \simeq 9\times 10^{47} \text{ erg } \mathrm{M}_{\star,15}^{-0.43}\, \mathrm{R}_{\star,500}^{1.74}\, \mathrm{E}_{\rm k,ej,51}^{0.56} \,, \tag{11.17}$$

where $M_{\star,15} = M_\star/(15M_\odot)$, $R_{\star,500} = R_\star/(500R_\odot)$ and $E_{k,\rm ej,51} = E_{k,\rm ej}/(10^{51}$ erg). The analytical expressions of these parameters for other stellar progenitors are listed in Appendix A of Ref. [620] for non-relativistic shocks and Eq. 29 of Ref. [621] for (mildly-)relativistic shocks. Note that the flash of light produced at the breakout from the stellar surface should be followed by the cooling of the envelope [620, 621]. However, we neglect this contribution, as it is not correlated with neutrino emission and thus not of relevance for the purposes of this work.

Figure 57 (middle central panel) shows the energy radiated across different wavebands $E_{\rm rad}$ (Eq. 11.4) through shock breakout. For our benchmark transient, the non-relativistic shock breakout produces a burst of photons in the UV band.

11.2.2.6 *Interaction with the circumstellar medium*

Towards the end of their life, massive stars can undergo eruptive episodes, polluting the surrounding environment. As a consequence, the collapsing star could have a dense CSM shell. We assume that the CSM density follows a wind profile

$$\rho_{\rm CSM}(R) = \frac{\dot{M}_w}{4\pi R^2 v_w f_\Omega} \tag{11.18}$$

where $\dot{M}_w$ is the mass-loss rate of the star, v_w is the wind speed, and f_Ω is the fraction of the solid angle with dense CSM. Unless otherwise specified, we assume a spherically symmetric CSM ($f_\Omega = 1$), extended up to the external radius $R_{\rm CSM}$, where its density is assumed to drop sharply. As the outflow expands in the CSM, two shocks form: the forward shock, propagating outward and shocking the CSM material, and the

reverse shock propagating backward and shocking the ejecta (in mass coordinates) [626]. The forward shock is the main site of dissipation of kinetic energy, whereas the contribution of the reverse shock is expected to be subleading at the epochs considered in this work and for non-relativistic shocks [546–551]. The slow deceleration of the forward shock during its interaction with the CSM is not relevant to our purposes, as it would not affect substantially the neutrino emission; we assume that the interaction with the CSM has a total duration $t_{\rm dur} \simeq R_{\rm CSM}/v_{\rm sh}$, where $v_{\rm sh}$ is the velocity of the forward shock.

The forward shock breaks out from the CSM at the breakout radius $R_{\rm bo}$, defined through the following relation

$$\tau_{\rm CSM}(R_{\rm bo}) = \int_{R_{\rm bo}}^{R_{\rm CSM}} dR\, \rho_{\rm CSM}(R)\kappa_{\rm CSM} = \frac{c}{v_{\rm sh}}\,, \tag{11.19}$$

As the forward shock interacts with the CSM, its kinetic energy is converted into radiation. Within the approximation of constant shock velocity and efficient shock radiation, the injected and emitted luminosity coincide [601]:

$$L_{\rm inj}^{\rm CSM} \equiv L(t) = 2\pi\epsilon_{\rm eff}\rho_{\rm CSM}(t)R_{\rm sh}(t)^2 v_{\rm sh}^3, \tag{11.20}$$

where $\epsilon_{\rm eff}$ is the efficiency conversion factor of kinetic energy into radiation, $R_{\rm sh} = v_{\rm sh}t$ is the shock radius, and $\rho_{\rm CSM}$ is given by Eq. 11.18 and evaluated at $R_{\rm sh}(t)$. As the bulk of radiation from CSM interactions is radiated around $R_{\rm bo}$ [592], we assume that the total luminosity emitted in the range $R_0 \leq R \leq R_{\rm bo}$ is $L \simeq L_{\rm bo}$.

Within our simple framework, the effective temperature of the black-body distribution emerging at $R_{\rm bo}$ is [601, 627]:

$$T_\gamma^{\rm BB} = \left(\frac{18}{7a}\rho_{\rm CSM}(R_{\rm bo})v_{\rm sh}^2\right)^{1/4}\,. \tag{11.21}$$

Once the forward shock breaks out from the dense CSM, namely when Eq. 11.19 is fulfilled, it becomes collisionless. In this regime, photons are mainly produced through bremsstrahlung and emitted in the X-ray band for $v_{\rm sh} \gtrsim 10^4$ km s^{-1} [628]. The total emitted luminosity produced by the forward shock for $R_{\rm bo} \leq R \leq R_{\rm CSM}$ is given by [298, 628]

$$L^{\rm brem}(R_{\rm CSM}) = \min\left(0.3\frac{t_{\rm dyn}}{t_{\rm ff}}, 1\right) L_{\rm sh}\,, \tag{11.22}$$

where $t_{\rm dyn}$ and $t_{\rm ff}$ are the dynamical and free-free electron cooling times defined as in Appendix E.2. The shock kinetic power $L_{\rm sh}$ is also defined in Appendix E.2. Note that Eq. 11.22 is estimated at the edge of the CSM shell ($R_{\rm CSM}$).

After shock breakout from the CSM, the radiation due to CSM interactions no longer relaxes to a black-body distribution, hence the non-thermal photon spectrum is

$$n_\gamma^{\rm brem}(E_\gamma) = L^{\rm brem}\frac{E_\gamma}{k_B T_e}e^{-E_\gamma/k_B T_e}\ , \tag{11.23}$$

where $L^{\rm brem}$ is the total emitted luminosity given by Eq. 11.22 and T_e is the post-shock temperature of electrons, defined in Appendix E.2.

In the optically thin region of the CSM, particle acceleration leads to production of relativistic electrons. This case is particularly relevant when shocks are not radiative. As the forward shock expands in the CSM, it converts the kinetic energy of the blastwave into internal energy. The internal energy density is

$$u_{\rm int}(R) = \frac{9}{8}v_{\rm sh}^2\,\rho_{\rm CSM}\ , \tag{11.24}$$

where $\rho_{\rm CSM}$ is given by Eq. 11.18. A fraction ϵ_B of the internal energy density is stored in the post shock magnetic field $B_{\rm CSM} = \sqrt{8\pi\epsilon_B u_{\rm int}}$.

A fraction ϵ_e of Eq. 11.24 is given to accelerated electrons. The latter mostly cool through synchrotron radiation [629], whose spectrum for the non-relativistic and mildly-relativistic blastwave is provided in Ref. [628].

In Fig. 57 (middle right panel) we show the total energy radiated through CSM interactions. We also display the relative energy emitted in gamma-rays (see Sec. 11.4). The bulk of energy is radiated in the UVOIR band, whereas bremsstrahlung and synchrotron processes radiate energy mostly in the radio and X-ray bands.

11.2.2.7 *Multiple heating sources*

If more than one source contributes to heat the outflow as it expands, the total radiated luminosity is given by the sum of all contributions: $L^{\rm tot} = \sum_i L^i(t)$, where L^i corresponds to the luminosity radiated from the i-th heating source.

If the outflow propagates in a dense CSM, then the radiation produced by other heating sources (e.g., ^{56}Ni decay) has to propagate through the total mass $M_{\rm tot} = M_{\rm ej} + M_{\rm CSM,th}$, where $M_{\rm CSM,th} = \int_{R_\star}^{R_{\rm bo}} dR 4\pi R^2 \rho_{\rm CSM}(R)$ is the mass of the optically thick CSM.

11.3 MODELING OF THE ELECTROMAGNETIC EMISSION: JETTED RELATIVISTIC OUTFLOWS

In this section, we focus on the modeling of the electromagnetic emission in jetted relativistic outflows, which differs from the treatment outlined in Sec. 11.2 for the non-relativistic outflows. A bipolar jet may be harbored in the collapsing star and launched a few ms after the collapse. Given the jet luminosity L_j (assumed to be constant) and lifetime t_j, its injected energy is $E_j = L_j t_j$. The jet dynamics only depends on the jet isotropic equivalent energy $E_{\rm iso,j} = E_j/(\theta_j^2/4)$ and Lorentz factor Γ [266, 630], where θ_j is the jet opening angle. We parameterize the energy budget of the jet in terms of its energy E_j [583], rather than $E_{k,\rm ej}$ as we have considered for the non-relativistic outflows (see Fig. 57). Furthermore, our results refer to a jet observed on-axis (for a discussion on jets observed off-axis see, e.g., Ref. [631]).

Short living engines or progenitor stars which retain the hydrogen envelope, such as partially stripped SNe, are likely to produce unsuccessful jets [200, 294, 295, 602, 632]. In this case, the jetted outflow does not breakout from the stellar mantle or it is choked. If the jet is instead powered for sufficiently long time and is energetic enough, it breaks out from the star and produces a GRB.

11.3.1 *Successful jets*

The mechanism responsible for energy dissipation and shaping the observed non-thermal emission is still under debate, with particle acceleration possibly due to internal shocks [286, 291, 292] or magnetic reconnection [246, 257, 258, 269]. In both cases, the observed electromagnetic signal may originate both in the optically thick and thin regions of the jet. Following Ref. [231] [2], Fig. 57 (bottom left panel) shows the total energy radiated by a successful jet across the electromagnetic wavebands, assuming $t_{\rm dur} = 100$ s [324, 633]. We show the largest energy radiated among the GRB models considered in Ref. [231], in order to obtain an upper limit for the energy budget. Note that the relativistic component of the outflow moves with constant Lorentz factor Γ, hence the observed energy is $E_{\rm obs} = E_{\rm rad}\Gamma/(1+z)$.

2 Note that the calculations of Ref. [231] are carried out relying on isotropic equivalent quantities. In order to connect isotropic quantities with the observed ones, we correct the total isotropic energy by the beaming factor of the jet ($\theta_j^2/4$).

We do not consider the deceleration phase of the relativistic jetted component of the outflow. This is motivated by the fact that the neutrino emission during the afterglow is negligible with respect to the prompt one [233].

11.3.2 *Unsuccessful jets*

As the jet propagates through the stellar envelope, it inflates a high pressure region of shocked jet and stellar material, the cocoon [201, 203–205]. The jet dynamics is highly non-linear due to the mixing with the cocoon, which slows down the jet while increasing its baryon density [222] (see Ref. [201] for the analytical modeling of the propagation of a relativistic jet in the stellar mantle). Independently on the fate of the jet, the cocoon always breaks out from the star [201, 205].

If the jet is smothered within the stellar mantle, the only observable electromagnetic counterpart would be the shock breakout of the cocoon from the collapsing star. The breakout is expected to occur with mildly-relativistic velocities, with signatures of asymmetries in the outflow [213, 634]. The fraction of energy radiated from an unsuccessful jet is shown in Fig. 57 (bottom right panel), for the parameters used in Ref. [635].

11.4 NEUTRINO EMISSION

In this section, we summarize the processes leading to neutrino production, namely photo-hadronic ($p\gamma$) and hadronic (pp) interactions. Furthermore, we outline the methods adopted to calculate the neutrino signal.

11.4.1 *Proton spectral energy distribution*

The regions of the outflow where protons can be co-accelerated with electrons are the magnetar wind, the forward shock resulting from CSM interactions and the jet. We now introduce the resulting spectral energy distributions of protons.

MAGNETAR WIND. The injected proton energy distribution is [in units of GeV^{-1} cm^{-3}] [132]

$$n_p(E_p) \equiv \frac{\mathrm{d}^2 N_p}{\mathrm{d}E_p \mathrm{d}V} = A_p E_p^{-1} \,, \tag{11.25}$$

where the normalization constant is $A_p = 1.08 \times 10^{-5} B_{14}^{-1} t_{5.5}^{-3} M_{\mathrm{ej},-2}^{3/2} P_{\mathrm{spin},-3}^{3}$, with $t_{5.5} = t/10^{5.5}$ s, and the other quantities are defined as in Sec. 11.2.2. Note that the spectrum of protons accelerated in the magnetar wind is expected to be hard [$n_p(E_p) \propto E_p^{-1}$].

CSM INTERACTIONS. Protons can be accelerated at the forward shock as the SN ejecta cross the CSM. Efficient acceleration starts at $R \simeq R_{\mathrm{bo}}$ [123, 131, 231, 533, 552] and it proceeds over a wide range of radii, up to the outer radius $R_{\mathrm{out}} = \min[R_{\mathrm{CSM}}, R_{\mathrm{dec}}]$. Here, $R_{\mathrm{dec}} = M_{\mathrm{ej}} v_w / \dot{M}_w$ is the deceleration radius, corresponding to the distance from the center of explosion where the outflow has swept-up a CSM mass comparable to M_{ej}.

The injected proton energy distribution at the forward shock is [in units of GeV cm^{-3}]:

$$n_p(E_p) \equiv \frac{\mathrm{d}^2 N_p}{\mathrm{d}E_p \mathrm{d}V} = A_p E_p^{-k_p} \Theta(E_p - E_{p,\mathrm{min}}) \Theta(E_{p,\mathrm{max}} - E_{\mathrm{p}}) \,, \tag{11.26}$$

where $k_p = 2$ is the proton index for non-relativistic collisionless shocks [398]. The minimum proton energy for non-relativistic shocks is $E_{p,\mathrm{min}} = m_p c^2$ (for mildly-relativistic shocks, the minimum proton energy is $E_{p,\mathrm{min}} = \Gamma_{\mathrm{sh}} m_p c^2$, where $\Gamma_{\mathrm{sh}} = 1/\sqrt{1 - (v_{\mathrm{sh}}/c)^2}$ is the shock Lorentz factor; since for mildly-relativistic shocks $\Gamma_{\mathrm{sh}} \lesssim 2$, the correction to the minimum proton energy does not affect our results for the neutrino signal substantially), while the maximum energy $E_{p,\mathrm{max}}$ is obtained by the condition $t_{p,\mathrm{acc}}^{-1} = t_{p,\mathrm{cool}}^{-1}$, where $t_{p,\mathrm{acc}}^{-1}$ is the proton acceleration rate and $t_{p,\mathrm{cool}}^{-1}$ is the proton total cooling rate; see Appendix E.1 for the proton cooling rates.

The normalization constant is $A_p = 9\epsilon_p n_{p,\mathrm{CSM}}(R) m_p c^2 / [8 \ln(E_{p,\mathrm{max}}/E_{p,\mathrm{min}})] (v_{\mathrm{sh}}/c)^2$. Here, ϵ_p is the fraction of the blastwave internal energy expressed by Eq. 11.24 which is stored into accelerated protons. Finally, $n_{p,\mathrm{CSM}} = \rho_{\mathrm{CSM}}/m_p$ is the CSM proton number density.

JETTED OUTFLOWS. Protons accelerated in the jet follow a power-law spectrum [85]. The proton distribution in the comoving frame of the jet (we denote quantities in this frame as primed: X') reads [in units of GeV cm^{-3}]

$$n'_p(E'_p) = \frac{\mathrm{d}^2 N'_{\mathrm{p}}}{\mathrm{d}E'_{\mathrm{p}} \mathrm{d}V'} = A'_p E_p^{'-k_p} \exp\left[-\left(\frac{E'_p}{E'_{p,\mathrm{max}}} \right)^{\alpha_p} \right] \Theta(E'_p - E'_{p,\mathrm{min}}) \,, \tag{11.27}$$

where α_p mimics an exponential cutoff [543] and Θ is the Heaviside function. The minimum energy of accelerated protons is $E'_{p,\rm min} = m_p c^2$, while their maximum energy is obtained equating the proton acceleration rate with the proton cooling rate, namely $t'^{-1}_{p,\rm acc} = t'^{-1}_{p,\rm cool}$; see Appendix E.1 for the proton cooling rates in the jet. $A'_p = \epsilon_{j,d}\epsilon_{j,p}E'_{\rm iso,j}/(4\pi R_j^2 c t'_j)$ is the normalization constant, where $\epsilon_{j,p}$ is the fraction of the dissipated isotropic energy of the jet $\epsilon_{j,d}E'_{\rm iso}$ which is stored in accelerated electrons; R_j is the position along the jet where proton acceleration takes place, while $t'_j = t_j\Gamma$ is the comoving jet lifetime.

The microphysical parameters $\epsilon_{j,d}$ and $\epsilon_{j,p}$ depend on the process assumed to be responsible for energy dissipation along the jet. The spectral index is $k_p = 2.2$, if acceleration occurs at relativistic collisionless internal shocks or sub-shocks [85, 89], while it depends on the magnetization of the jet if protons are accelerated through magnetic reconnection [99].

11.4.2 *Neutrino production channels*

PROTON-PHOTON ($p\gamma$) INTERACTIONS. Electrons co-accelerated with protons cool producing a photon distribution which serves as a target for accelerated protons. Neutrinos are mainly produced through the Δ^+ resonance [115, 117]:

$$p+\gamma \longrightarrow \Delta^+ \longrightarrow \begin{cases} n+\pi^+ & 1/3 \ \text{ of all cases} \\ p+\pi^0 & 2/3 \ \text{ of all cases}\,. \end{cases} \tag{11.28}$$

Subsequently, neutral pions decay into gamma-rays $\pi^0 \longrightarrow 2\gamma$, while charged pions decay producing neutrinos $\pi^+ \longrightarrow \mu^+ + \nu_\mu \longrightarrow \bar{\nu}_\mu + \nu_e + e^+$. Unless otherwise specified, we do not distinguish between neutrinos and antineutrinos in the following.

PROTON-PROTON (pp) INTERACTIONS. Accelerated protons can interact with a target of non-relativistic protons, producing neutral and charged pions [116]. Subsequently, pions decay as detailed above for $p\gamma$ interactions. Throughout the paper, we consider the energy radiated in gamma-rays both through the electromagnetic processes discussed in Sec. 11.2 and through pp interactions.

11.4.3 *Expected neutrino emission*

Both $p\gamma$ and pp interactions can take place in the magnetar wind, at the external shock driven by the outflow in the CSM and in the jet. The duration of the expected neutrino signals in the wind of a central magnetar and at CSM interactions is summarized in Fig. 56 for our benchmark transient, whose parameters are listed in Table 10. Along the jet, neutrino production takes place throughout the whole jet lifetime t_j.

Both neutrinos and photons at CSM interactions are produced through the dissipation of kinetic energy of the blastwave as the forward shock expands within the optically thin CSM. Consequently, the duration of the electromagnetic and neutrino signals in Fig. 56 is similar. On the contrary, neutrino production in the magnetar wind starts when photopion production becomes efficient and it ceases when pion production freezes out [132]; these times are defined in Appendix E.1. As the processes producing photons and neutrinos in the magnetar wind are not correlated, their duration in Fig. 56 is different.

MAGNETAR WIND. Protons accelerated in the wind of the magnetar can undergo both $p\gamma$ and pp interactions. The injected proton energy distribution is given by Eq. 11.25, while thermal optical photons and non-thermal X-ray photons produced in the wind nebula serve as targets for $p\gamma$ interactions.

We calculate the total energy emitted in neutrinos in the magnetar wind following Ref. [132]:

$$E^{\nu}_{\rm tot} \simeq 1.7\times10^{41}\eta_{-1}^{2/3}B_{14}^{-4/3}M_{\rm ej,-2}^{-1/2}P_{\rm spin,-3}^{-1/2}\epsilon_{\rm mag,-2}^{-1/6}f^{p}_{\rm sup}f^{\pi}_{\rm sup}f^{\mu}_{\rm sup}\ {\rm erg}\ , \tag{11.29}$$

where $\eta_{-1}=\eta/10^{-1}$ is the acceleration efficiency in the magnetar wind nebula normalized to its nominal value, $\epsilon_{\rm mag,-2}=\epsilon_{\rm mag}/10^{-2}$ is the nebula magnetization parameter, whose nominal value is motivated by observations of the Crab Nebula [636]. Finally, $f^{p}_{\rm sup}$ is the suppression factor for pion creation, while $f^{\pi}_{\rm sup}$ and $f^{\mu}_{\rm sup}$ are the suppression factors for neutrino creation from $\pi^{\pm}$ and $\mu^{\pm}$ decays, respectively (see Appendix E.2). The fraction of the ejecta kinetic energy emitted in neutrinos in the magnetar wind is shown in Fig. 57 (top central panel) for our benchmark transient.

CSM INTERACTIONS. Accelerated protons follow the input energy distribution in Eq. 11.26 and can interact with the photon spectrum produced at the forward shock. Furthermore, accelerated protons undergo pp interactions with the non-relativistic CSM protons.

In most cases, $p\gamma$ interactions at the forward shock are subleading for non-relativistic and mildly-relativistic shocks [65, 123, 131, 233, 234, 533]. This result also holds when the shocks are radiative, as the energy threshold for $p\gamma$ interactions can be reached only when the CSM covers a small fraction of the solid angle ($f_\Omega \ll 1$), which is not the case for SNe [298, 637]. Therefore, we only consider pp interactions as a viable neutrino production channel at the forward shock. We calculate the total energy emitted in neutrinos through pp interactions following Refs. [116, 533]. The fraction of the ejecta kinetic energy radiated in neutrinos from CSM interactions for our benchmark transient is shown in Fig. 57 (middle right panel).

JETTED OUTFLOWS. In a magnetized jet, neutrino production begins in the optically thick part of the outflow [236, 635]. Hereafter we rely on the results of Ref. [635] for the expected neutrino signal. In particular, we consider the case with initial jet magnetization $\sigma_0 = 200$ of Ref. [635].

In the absence of jet magnetization, neutrino production below the jet photosphere may take place only if the jet is smothered in an extended envelope surrounding the progenitor core. We refer the interested reader to Refs. [234, 235] for the neutrino signal expected in this scenario, and we explicitly include it in our calculations in Sec. 11.5. However, in Fig. 57 (bottom right panel) we only show the case of a jet smothered in a Wolf-Rayet progenitor star.

In the optically thin region of the jet, the input proton distribution is given by Eq. 11.27. The non-thermal photon distribution that serves as target for $p\gamma$ interactions depends on the mechanism assumed for energy dissipation. We rely on Ref. [65] and take the maximum energy radiated in neutrinos across the different GRB models considered in the aforementioned reference. In the optically thin part of the jet, the baryon density is not large enough for pp interactions to be efficient [65]. Therefore, we only consider $p\gamma$ interactions as the viable channel for neutrino production.

In the bottom left panel of Fig. 57 we show the energy radiated by a successful jet in neutrinos both in the optically thick and thin regimes. However, we warn the reader that the results for the optically thick regime outlined in Ref. [635] are obtained for a jet with isotropic luminosity larger than the one assumed for the optically thin component in Ref. [231]; the comparison in the bottom left panel of Fig. 57 is intended to be representative.

11.5 TRANSIENTS FROM COLLAPSING MASSIVE STARS

In this section, we present the energy radiated through the mechanisms outlined in Sec. 11.2 across the electromagnetic wavebands as well as in neutrinos, for the transients originating from collapsing stars: SNe Ib/c as well as SNe Ib/c broad line (BL) and GRBs, SNe IIP, SNe IIn, SLSNe, and LFBOTs. The considered transient categories together with the characteristic parameters adopted for each of the heating processes are listed in Table 11. While a range of parameters should be considered [129], we aim to compute ballpark figures for the source energetics to gauge the best multi-messenger detection strategies.

One should also consider neutrinos from the shock breakout from the progenitor star. A calculation of the neutrino signal arising from the breakout of a (quasi) spherical outflow has been attempted in Ref. [236], which concluded that other dissipation mechanisms taking place within the outflow dominate the time integrated neutrino signal. Furthermore, the photon spectrum emerging from shock breakout is highly uncertain and it is challenging to reproduce observations. In the light of such uncertainties, we neglect neutrinos in the energy budget of shock breakout and leave this task to future work.

11.5.1 *Supernovae of Type Ib/c, Ib/c broad line and gamma-ray bursts*

Type Ib/c SNe and GRBs are thought to be linked to massive and compact hydrogen-depleted stars, which experience reduced mass loss ($\dot{M}_w \simeq 10^{-7}$–$10^{-4}\ M_\odot \mathrm{yr}^{-1}$) [638–640]. The wind velocities are typically $v_w \simeq 10^3$ km s^{-1} [586]. For Type Ib/c SNe, ^{56}Ni decay, CSM interactions and shock breakout of a non-relativistic outflow from a Wolf-Rayet star can contribute to heat the outflow.

Figure 58 (top left panel) shows the fraction of energy radiated across different electromagnetic wavebands and in neutrinos for SNe Ib/c. Radioactive decay of ^{56}Ni is the most relevant heating source for SNe Ib/c and it radiates the bulk of energy in the UVOIR band, with $E^{\mathrm{UVOIR}}/E_{k,\mathrm{ej}} \simeq 10^{-4}$.

The forward shock mediating CSM interactions is the only site of neutrino production for SNe Ib/c, as detailed in Sec. 11.4. Due to the small mass-loss rates of Wolf-Rayet stars [641], this class of SNe is not expected to radiate a bright neutrino signal ($E^{\nu}/E_{k,\mathrm{ej}} \lesssim 10^{-11}$), consistently with the findings of Ref. [123]. However, about 10% of SNe Ib/c show signs of late time interaction with a dense CSM [586], starting $\gtrsim$ 1 year after the explosion [SNe Ib/c late time (LT)]. SNe Ib/c LT can release an amount of energy in

Table 11: Characteristic parameters for each class of transients originating from the collapse of massive stars considered throughout this work.

Parameter	SNe Ib/c	SNe Ib/c BL with jet	SNe IIP	SNe IIn	SLSNe	LFBOTs
$E_{k,\rm ej}$ [erg]	10^{51}	10^{52}	10^{51}	10^{51}	10^{52}	10^{52}
$M_{\rm ej}$ [$M_\odot$]	1	1	5	2	5	10^{-1}
$M_{\rm fb}/t_{\rm fb}$ [$M_\odot$ s^{-1}]	N/A	5×10^{-4}	N/A	N/A	N/A	1.5×10^{-8}
ϵ_j	N/A	0.01	N/A	N/A	N/A	0.01
$\bar{\rho}$ [cm^{-3}]	N/A	100	N/A	N/A	N/A	10^{-7}
$P_{\rm spin}$ [ms]	N/A	N/A	N/A	N/A	5	1
B [G]	N/S	N/A	N/A	N/A	10^{15}	10^{15}
$f_{\rm Ni}$	0.1	0.15	10^{-3}	0.01	0.01	0.01
$R_\star$ [$R_\odot$]	4	4	500	434	434	434
M_w [$M_\odot$ yr^{-1}]	10^{-5}	10^{-5}	10^{-3}	10^{-2}	10^{-2}	10^{-3}
v_w [km s^{-1}]	1000	1000	15	100	100	1000
$\epsilon_{\rm eff}$	0.1	0.1	0.1	0.1	0.1	0.1
ϵ_e	10^{-1}	10^{-1}	10^{-1}	10^{-1}	10^{-1}	10^{-1}
ϵ_B	10^{-1}	10^{-2}	10^{-2}	10^{-2}	10^{-2}	10^{-2}
ϵ_p	10^{-1}	10^{-1}	10^{-1}	10^{-1}	10^{-1}	10^{-1}
$E_{\rm iso,j}$ [erg]	N/A	3.7×10^{54}	N/A	N/A	N/A	2.5×10^{53}
Γ	N/A	300	N/A	N/A	N/A	100
θ_j	N/A	3°	N/A	N/A	N/A	6°
$\epsilon_{j,d}$	N/A	0.2	N/A	N/A	N/A	0.2
$\epsilon_{j,p}$	N/A	0.1	N/A	N/A	N/A	0.1

neutrinos larger than standard SNe Ib/c. An investigation of the neutrino production due to CSM interactions for this class of SNe can be found in Refs. [123, 642].

The number of SNe observed with broad spectral features similar to the ones of SN 1998bw—dubbed SNe Ib/c broad line (BL)—is growing [643–645]. Many of these SNe are not observationally linked to GRBs [643], even though their ejecta move with mildly-relativistic velocity ($v_{\rm ej} \gtrsim 0.1c$), hinting that the explosion mechanism may be different from the one of standard core-collapse SNe. It has been suggested that the explosion of SNe Ib/c BL is not spherical, but either accompanied by an off-axis GRB [646] or a jet that barely fails to break out from the stellar mantle [199]. Due to the very high energies, SNe Ib/c BL and

GRBs are usually modeled by considering a spinning BH [325, 630, 647] or a magnetar [563, 648, 649] that powers the outflow.

For the class of SNe Ib/c BL, the contribution of fallback material onto the central compact object should be included as an energy source. The fraction of energy radiated across different electromagnetic wavebands and in neutrinos for SNe Ib/c BL is shown in Fig. 58 (top central panel). Fallback of matter on the BH constitutes the most important heating source for SNe Ib/c BL, with $E^{\rm UVOIR}/E_{k,\rm ej} \simeq 2\times10^{-4}$. If the central engine is not efficient then radiation is powered by ^{56}Ni decay only. Similarly to SNe Ib/c, CSM interactions are not an efficient neutrino production mechanism for SNe Ib/c BL ($E^{\nu}/E_{k,\rm ej} \lesssim 10^{-10}$).

Assuming that SNe Ib/c BL harbor an unsuccessful jet, shock breakout of the cocoon from a Wolf-Rayet star produces a burst of radiation in the X-ray band, with $E^{\rm X-ray}/E_j \simeq 10^{-6}$. A bright neutrino signal ($E^{\nu}/E_j \simeq 10^{-1}$) is expected only if the unsuccessful jet is magnetized and points towards Earth, as detailed in Sec. 11.4. If the jet is successful, as in the case of GRBs, the bulk of energy is emitted in the X-ray/gamma-ray band [$(E^{\rm X-ray}+E^{\gamma-\rm ray})/E_j \simeq 5\times10^{-2}$], as shown in Fig. 58 (top central panel). In this case, the expected neutrino ($E^{\nu}/E_j \simeq 5\times10^{-5}$) and electromagnetic signals are observable on Earth only if the jet is on-axis.

11.5.2 *Supernovae of Type IIP*

Type IIP SNe originate from red supergiants, massive stars which retain the extended hydrogen envelope. The abundance of hydrogen in their progenitor may cause the plateau of variable duration observed in the light curve of these SNe due to hydrogen recombination [613–616].

Typical values for the mass-loss rates of red supergiant stars are $\dot{M}_w \simeq 10^{-6}$–$10^{-5}\ M_\odot\ {\rm yr}^{-1}$, with wind velocity $v_w \simeq 10\ {\rm km\ s}^{-1}$ [586]. Nevertheless, larger CSM densities are inferred from the observation of SNe IIP, with $\dot{M}_w \simeq O(10^{-3})\ M_\odot\ {\rm yr}^{-1}$ [650–652]. Such large densities can be explained invoking eruptive mass loss of the progenitor star $\simeq O(1)$ year before the SN explosion [650, 653, 654]. Besides hydrogen recombination, ^{56}Ni decay can heat the SN outflow, together with CSM interactions. Recent work shows that $f_{\rm Ni} \equiv M_{\rm Ni}/M_{\rm ej} \lesssim 0.05$ [655], thus the contribution from the radioactive decay of ^{56}Ni is expected to be subleading.

The total energy radiated across all electromagnetic wavebands and the neutrino energy budget are shown in Fig. 58 (top right panel) for the parameters in Table 11. The bulk of energy radiated in the

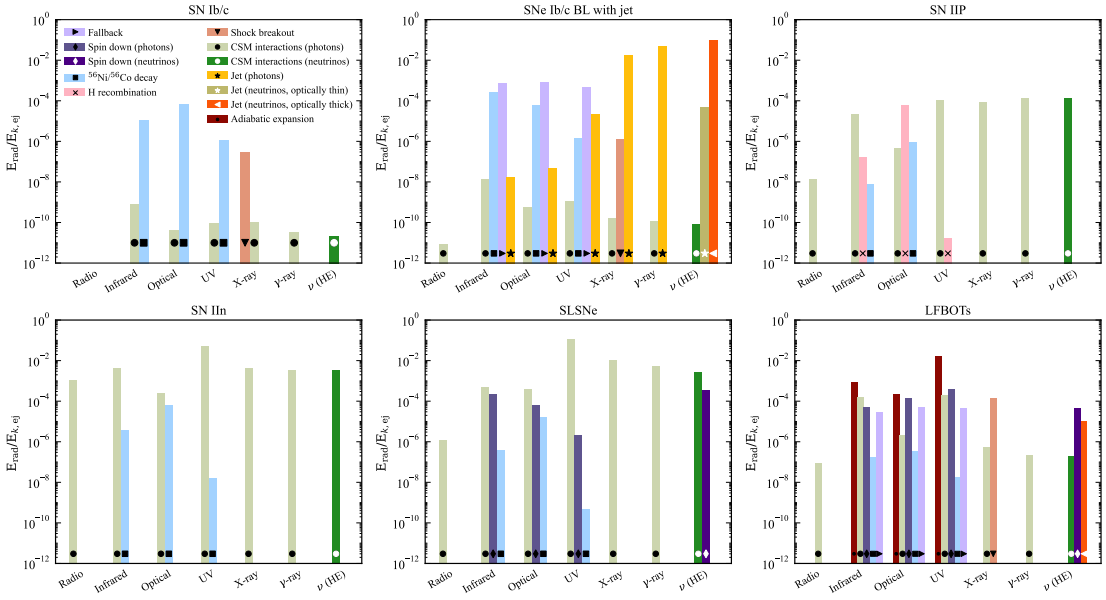

Figure 58: Ratio of the energy radiated across electromagnetic wavebands and in neutrinos (Eq. 11.4) and the kinetic energy of the ejecta (or energy of the jet) for SNe Ib/c, SNe Ib/c BL with jet, SNe II-P, SNe IIn, SLSNe and LFBOTs (from top left to bottom right, respectively). The color code for each process as well as the symbols denoting each heating process are the same as in Fig. 56. For each transient, we assume the fiducial parameters in Table 11. If the transient is engine driven, then the bulk of radiation is emitted in the UVOIR band through either fallback of matter onto the BH or the magnetar spin down. In the case of successful jet (GRB), most of the energy is emitted in the X-ray/gamma-ray bands, whereas a dimmer flash of light in the same bands resulting from shock breakout is expected for unsuccessful jets. If a dense CSM surrounds the collapsing star, then a significant fraction of energy is radiated in the UVOIR, radio and X-ray bands. In this case, also bright gamma-ray and neutrino signals are expected. Finally, when the heating source is either radioactive ^{56}Ni decay or H recombination, the outflow radiates energy in the UVOIR band.

UVOIR band is produced through CSM interactions ($E^{\rm UVOIR}/E_{k,{\rm ej}} \simeq 10^{-4}$) and hydrogen recombination ($E^{\rm UVOIR}/E_{k,{\rm ej}} \simeq 6\times10^{-5}$). Significant X-ray emission is also expected due to bremmsthralung as the ejecta propagate in the optically thin CSM ($E^{\rm X-ray}/E_{k,{\rm ej}} \simeq 7\times10^{-5}$). These results depend on the assumption of eruptive mass-loss episodes prior to the stellar collapse. If typical mass-loss rates of red supergiants were adopted, the energy in the UVOIR band would be radiated through hydrogen recombination and the X-ray energy would be a negligible fraction of the explosion energy. This may be the case for most of the SNe IIP, as suggested by the lack of X-ray bright SNe IIP [656]. Due to the large CSM density, neutrinos are produced with $E^{\nu}/E_{k,{\rm ej}} \simeq 10^{-4}$.

11.5.3 *Supernovae of Type IIn*

Type IIn SNe show clear signs of strong CSM interactions and some of them may linked to luminous blue variable, red supergiants or yellow hypergiant stars [657, 658]. The mass-loss rate of the surrounding CSM ranges between $\dot{M} = 10^{-4}$–$10\ M_{\odot}\ \mathrm{yr}^{1}$ [638, 659], with wind velocity $v_w \simeq 30$–$600\ \mathrm{km\ s}^{-1}$. As a result of the dense CSM, this class of SNe exhibits signs of strong CSM interactions.

We consider CSM interactions and ^{56} Ni decay as the main processes contributing to the heating of the outflow. The results are shown in Fig. 58 (bottom left panel) for the parameters in Table 11. The bulk of energy is emitted in the UVOIR band and it is produced by CSM interactions, with $E^{\mathrm{UVOIR}}/E_{k,\mathrm{ej}} \simeq 4 \times 10^{-2}$. A significant amount of energy is also emitted through non-thermal processes in the radio $E^{\mathrm{Radio}}/E_{k,\mathrm{ej}} \simeq 10^{-3}$ and X-ray bands $E^{\mathrm{X-ray}}/E_{k,\mathrm{ej}} \simeq 5 \times 10^{-3}$. Due to the large CSM density, $E^{\nu}/E_{k,\mathrm{ej}} \simeq 3.3 \times 10^{-3}$.

11.5.4 *Superluminous supernovae*

SLSNe are an emerging class of SN explosions whose optical luminosity is ten or more times larger than standard core-collapse SNe [126]. They can be broadly classified as H-poor (Type I) and H-rich (Type II) SLSNe; the lightcurve of many H-rich SLSNe is consistent with the interaction of the SN outflow with a dense CSM [660], similarly to the case of SNe IIn. The mechanism powering Type I SLSNe is not clear, even though observations suggest that these transients may be powered by a magnetar [607, 609], which would explain the observed large kinetic energy of the outflow and radiation output [584, 661]. On the contrary, Type II SLSNe exhibit signs of strong CSM interactions, like SNe IIn, and they are thought to be powered by CSM interactions [662]. Since hybrid mechanisms invoking magnetar spin down, CSM interactions and ^{56}Ni decay can also be considered for this class of transients, we include all these heating sources [663, 664].

The energy radiated across the electromagnetic wavebands and neutrinos is displayed in Fig. 58 (bottom central panel) for the parameters in Table 11. Most of the energy is radiated in the UVOIR band, thanks to interactions with the CSM ($E^{\mathrm{UVOIR}}/E_{k,\mathrm{ej}} \simeq 10^{-1}$) and spin down of the magnetar ($E^{\mathrm{UVOIR}}/E_{k,\mathrm{ej}} \simeq 2.4 \times 10^{-4}$). A significant amount of energy is also emitted in X-rays through bremmstrahlung ($E^{\mathrm{X-ray}}/E_{k,\mathrm{ej}} \simeq 10^{-2}$). Due to the large CSM density, a bright neutrino counterpart is expected. Furthermore, neutrinos can

be produced in the magnetar wind. The fraction of energy radiated in neutrinos is $E^\nu/E_{k,\rm ej} \simeq 2\times10^{-3}$ ($E^\nu/E_{k,\rm ej} \simeq 4\times10^{-4}$) for CSM interactions (for the magnetar wind).

11.5.5 *Luminous fast blue optical transients*

Luminous FBOTs (LFBOTs, namely FBOTs with optical luminosity $L_{\rm opt} \gtrsim 10^{44}$ erg s^{-1}) are an emerging SN-like class reaching peak luminosity in less than 10 days [143–145, 296], whose observed outflow asymmetry and variability of the X-ray light curve hint towards the presence of a compact object [147, 148, 153]. The latter should be responsible for the ejection of the observed asymmetric and fast outflow [148, 665].

One of the scenarios proposed to explain LFBOT observations invokes the collapse of a massive star, followed by the launch of a jet which inflates the cocoon [153]. The star may not be completely depleted of hydrogen, thus the jet may fail in breaking out and be choked in the stellar mantle. This scenario would explain the lack of direct association between gamma-rays and LFBOTs [297], as well as the asymmetric outflow and the hydrogen lines observed in the spectra of some LFBOTs [148, 149, 152].

Radio observations suggest that a fast blastwave drives the shock moving with $v_{\rm sh} \gtrsim 0.1c$ in the dense CSM, extended up to $R_{\rm CSM} \gtrsim 10^{16}$ cm. Even though observations reveal an asymmetric CSM, using the normalization in Eq. 11.18, $M_w \simeq 10^{-4}$–10^{-3} M$_\odot$ yr^{-1} is inferred, for a wind velocity $v_w \simeq 1000$ km s^{-1} [147, 148, 152].

The energy radiated across the electromagnetic wavebands and in neutrinos is shown in Fig. 58 (bottom right panel). We rely on the benchmark parameters in Table 11 and consider CSM interactions, ^{56}Ni decay, magnetar spin down, matter fallback, and shock breakout from a massive star that is not completely hydrogen stripped star. Additionally, we consider the possibility that radiation is emitted through the adiabatic expansion of the ejecta [153], whose output luminosity is described by the homogeneous solution in Eq. 11.3. However, we warn the reader that the mechanism powering LFBOTs is still uncertain and that they may not be linked to collapsing massive stars, see e.g. Ref. [154].

Following Ref. [234], we consider CSM interactions and a jet choked in an extended envelope surrounding the progenitor core as sites of neutrino production. We show the most optimistic scenario considered in Ref. [234] as a representative case, however the results are model dependent. The assumed total energy of

the explosion only holds if LFBOTs originate from the core collapse of a massive star, whereas different origin (e.g. cf. Ref. [154]) may affect the energy budget considered in this work.

From Fig. 58, we deduce that most of the energy is emitted in the UVOIR band, with $E^{\rm UVOIR}/E_{k,\rm ej} \simeq 1.6\times10^{-2}$ ($E^{\rm UVOIR}/E_{k,\rm ej} \simeq 5\times10^{-4}$), through adiabatic expansion of the outflow (magnetar spin down). Radioactive decay of ^{56}Ni does not contribute significantly to the emitted radiation in the UVOIR band [149]. This is consistent with the model outlined in Ref. [236], where most of the energy is radiated through the cooling of the cocoon inflated as the jet propagates in the stellar envelope. Consistently with observations, synchrotron radiation from accelerated electrons is responsible for the observed radio emission [147, 148, 152], with $E^{\rm Radio}/E_{k,\rm ej} \simeq 10^{-7}$. Neutrinos can be produced through CSM interactions and in the magnetar wind, with $E^{\nu}/E_{k,\rm ej} \simeq 2\times10^{-7}$ and $E^{\nu}/E_{k,\rm ej} \simeq 5\times10^{-5}$, respectively. For the assumed choked jet scenario, neutrinos are produced with $E^{\nu}/E_{k,\rm ej} \simeq 10^{-5}$.

11.6 CONNECTION BETWEEN ELECTROMAGNETIC EMISSION AND NEUTRINOS

In this section, we investigate the correlation between electromagnetic radiation and neutrinos from transient sources resulting from massive stars. Since neutrino emission is expected for sources powered by the magnetar spin down, CSM interactions or sources harboring a jet, we focus on these scenarios. The magnetar spin down could be applied to the case of SLSNe and LFBOTs. On the other hand, SNe IIn, IIp, SLSNe as well as LFBOTs may have efficient CSM interactions. Efficient neutrino production is also expected in GRB jets and in jets smothered in an extended envelope, which may be the case for LFBOTs.

If the CSM is not very dense, a small fraction of the ejecta kinetic energy is radiated in neutrinos and the neutrino counterpart is not bright enough to be detected. This may be the case for non-jetted SNe Ib/c or SNe IIP which do not show signs of strong CSM interactions. Therefore, if the observed transient is only powered by ^{56}Ni decay or hydrogen recombination and does not show any signs of engine or CSM interactions, we expect the corresponding neutrino signal to be negligible and do not discuss this case further.

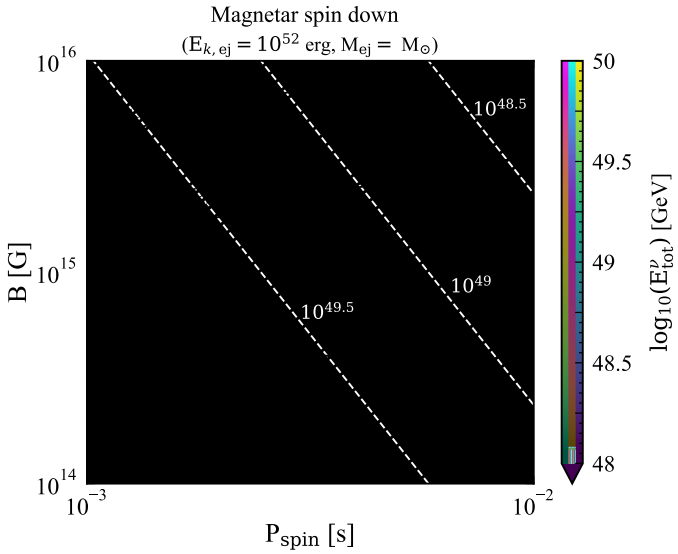

Figure 59: Isocontours of the total energy radiated in neutrinos $E^{\nu}_{\rm tot}$ (Eq. 11.29) for transients whose UVOIR lightcurve is powered by the magnetar spin down, in the plane spanned by the magnetar spin $P_{\rm spin}$ and magnetic field B. The brown dashed isocontours are displayed to guide the eye. The solid black isocontours mark benchmark values for the peak of the UVOIR luminosity, which is degenerate with respect to $(P_{\rm spin}, B)$. For a transient whose UVOIR lightcurve is powered by the magnetar spin down, the expected energy radiated in neutrinos can be inferred by localizing the transient in this plane.

11.6.1 *Magnetar spin down: Superluminous supernovae and fast blue optical transients*

A magnetar could power the emission of SLSNe and LFBOTs (see Fig. 58). As the spin down of the magnetar powers bright UVOIR radiation, we can correlate the neutrino signal with the electromagnetic signal.

Figure 59 shows contours for the total energy radiated in neutrinos from the magnetar wind (Eq. 11.29), in the plane spanned by the magnetar spin $P_{\rm spin}$ and the magnetic field B. The black solid lines mark the values of the peak bolometric luminosity in the UVOIR band for each $(P_{\rm spin}, B)$ pair. The results are shown for $E_{k,\rm ej} = 10^{52}$ erg and $M_{\rm ej} = M_\odot$, however Eq. 11.29 should be used for a given kinetic energy and mass of the ejecta. These parameters can be inferred from the bolometric lightcurve, which gives information on the photospheric velocity and the rise time; the former scales as $v_{\rm ph} \propto \sqrt{E_{k,\rm ej}/v_{\rm ej}}$, while the latter goes like $t_{\rm rise} \simeq t_{\rm d} \propto \sqrt{M_{\rm ej}}$.

The peak luminosity ($L^{\rm UVOIR}_{\rm pk}$) is degenerate with respect to the $(P_{\rm spin}, B)$ pairs. The only way to break this degeneracy is to complement the information from the UVOIR band with the non-thermal signal produced by the compact object observable in the X-ray band. To a first approximation, the total energy of non-thermal photons is proportional to the magnetic field $E_{\rm n-th} \propto B^{-2}$, whereas it is independent on the spin $P_{\rm spin}$ [132].

Note that we have not considered the non-thermal signal in Sec. 11.2, as its modeling is affected by large theoretical uncertainties (see Ref. [132] for details).

The total energy radiated in neutrinos ($E^{\nu}_{\rm tot}$) from a transient powered by the magnetar spin down can be obtained from Eq. 11.29, with the characteristic parameters inferred combining observations in the UVOIR and X-ray bands. From Fig. 59 we conclude that sources with a bright UVOIR signal consistent with the spin down of a magnetar are expected to produce a very bright neutrino counterpart. Intriguingly, if neutrinos should be detected in coincidence with the UVOIR signal, the total energy emitted in neutrinos can be combined with the peak of the bolometric UVOIR lightcurve to break the degeneracy between $P_{\rm spin}$ and B, as shown in Fig. 59.

Note that we consider time-integrated quantities, yet neutrino production in the magnetar wind starts later than the UVOIR radiation, at $t_{\nu,\rm in} \simeq 1.4 \times 10^5 \eta_{-1}^{8/25} B_{14}^{-18/25} M_{\rm ej,-2}^{9/50} P_{\rm spin,-3}^{9/25} \epsilon_{B,-2}^{8/25}$ s. The neutrino flux is expected to be maximum at $t_{\nu,\rm max} \simeq 9.3 \times 10^5 \eta_{-1}^{1/3} B_{14}^{-2/3} M_{\rm ej,-2}^{1/4} P_{\rm spin,-3}^{1/2} \epsilon_{B,-2}^{1/6}$ s. This time does not correspond to the peak of the UVOIR light curve, which is expected around 10–100 days [129]. For example, for the benchmark transient in Fig. 56, the neutrino signal peaks at $t \simeq 34$ days when the production of thermal UVOIR radiation already stopped. Therefore, the search for neutrinos from a magnetar-powered transient should be performed for $t_{\nu,\rm in} \lesssim t \lesssim t_{\nu,\rm max}$.

11.6.2 *Circumstellar interactions: Supernovae IIP, IIn, superluminous supernovae, and luminous fast blue optical transients*

When the observed transient exhibits strong signs of CSM interactions in the UVOIR light curve, bright radio and X-ray counterparts are expected— modulo absorption processes taking place in the CSM—together with high-energy neutrinos; see also Refs. [131, 552]. Here, we focus on the relation existing between the synchrotron radio and neutrino signals produced by the decelerating blastwave. This case is of relevance for SNe IIP and IIn, SLSNe, and LFBOTs (see Fig. 58).

For these transients a direct temporal correlation between the synchrotron radio and neutrino signals can be established, since both signals are produced through non-thermal processes in the proximity of the same

blastwave. As the outflow propagates in the dense CSM, the forward shock converts its kinetic energy into internal energy, whose density at each time t is given by Eq. 11.24. The energy density stored in protons is

$$u_p(t) \simeq E_p^2 \frac{\mathrm{d}N_p}{\mathrm{d}E_p \mathrm{d}V} \simeq \epsilon_p \frac{u_{\rm int}}{\ln(E_{p,\rm max}/E_{p,\rm min})} \ , \tag{11.30}$$

where we assume the injection spectrum given by Eq. 11.26.

Neutrinos are produced at the forward shock trough pp interactions (Sec. 11.4). The neutrino energy density in the blastwave at each radius R can be approximated as [298]

$$u_\nu(R) \approx \frac{1}{2} u_p \left(1 - e^{-\tau_{pp}}\right) \ , \tag{11.31}$$

where u_p is given in Eq. 11.30 and τ_{pp} is the optical depth of relativistic protons. The latter is given by $\tau_{\rm pp} \approx \sigma_{\rm pp} n_{p,\rm CSM} R_{\rm sh}$ for $E_p = E_{p,\rm max}$, while $\tau_{pp} = t_{\rm dyn}/t_{pp}$ for $E_p \ll E_{p,\rm max}$. Here, $E_{p,\rm max}$, $t_{\rm dyn}$ and t_{pp} are the maximum energy, the dynamical and pp interaction timescales of protons accelerated at the external shock, respectively; see Appendix E.1. Finally, the cross section for pp interactions is assumed to be independent of energy ($\sigma_{pp} \simeq 5 \times 10^{-26}$ cm^2).

The total energy emitted in neutrinos from the transient during its interaction with the CSM is

$$E^\nu_{\rm tot} = \int_{R_{\rm bo}}^{R_{\rm max}} dR 4\pi R^2 u_\nu(R) \ , \tag{11.32}$$

where $R_{\rm bo}$ is the breakout radius (Eq. 11.19) and $R_{\rm max}$ is the outer edge of neutrino production region defined as indicated in Sec. 11.4. From Eq. 11.32, we deduce that the total energy emitted by the blastwave in neutrinos is related to the upstream CSM density and the blastwave velocity at the considered time. The same dependence holds for the flux radiated in the radio band, which is produced through synchrotron losses [628].

While the total energy radiated in neutrinos scales with ϵ_p, the radio signal strongly depends on ϵ_B. Thus, the ratio $E^\nu_{\rm tot}/E^{\rm Radio} \propto \epsilon_p/\epsilon_B$. Typical values inferred from observations are $\epsilon_B \simeq 10^{-3}$– 10^{-2} [666], while the fraction of energy stored in protons accelerated at the forward shock is expected to be $\epsilon_p \lesssim 0.1$ [667, 668]. Therefore, when a bright radio source whose signal is consistent with synchrotron radiation is detected, its radio flux sets a lower limit on the total energy emitted in neutrinos by the expanding blastwave.

Figure 60 shows the contour plot of the total energy radiated in neutrinos, in the plane spanned by the upstream CSM density $n_{\rm CSM}$ and the blastwave dimensionless velocity $\beta_{\rm sh} = v_{\rm sh}/c$, both measured at $t = 100$ days. We use $\epsilon_p = \epsilon_e = 10^{-1}$ and $\epsilon_B = 10^{-2}$ in our calculations. Radio data allow to measure the CSM density at the time t, while the velocity of the fastest component of the ejecta $\beta_{\rm sh}$ can be inferred from radio data of the transient [629, 669]. A transient whose radio signal is produced through interactions of

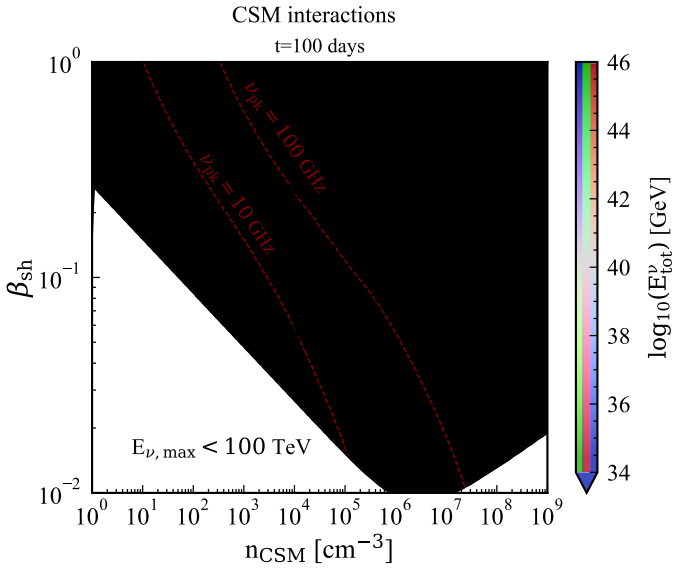

Figure 60: Isocontours of the total energy radiated in neutrinos (Eq. 11.32) through CSM interactions, in the plane spanned by the upstream density $n_{\rm CSM}$ and the shock adimensional velocity $\beta_{\rm sh} = v_{\rm sh}/c$, both measured at $t = 100$ days after the explosion. The solid black (dashed purple) lines mark the peak of the radio flux $L^{\rm Radio}_{\rm pk}$ (peak frequency $\nu_{\rm pk}$) for $\epsilon_B = 0.01$ and $\epsilon_e = 0.1$. We exclude the region of the parameter space producing neutrinos with energy $E_{\nu,\rm max} \lesssim 100$ TeV throughout the duration of CSM interactions; see main text for details. When a transient bright in radio is detected and its light curve is consistent with synchrotron radiation, the $(n_{\rm CSM}, \beta_{\rm sh})$ pair can be inferred and the expected energy radiated in neutrinos at a fixed time can be estimated from Eq. 11.32.

the outflow with the CSM can be located in the $(n_{\rm CSM}, \beta_{\rm sh})$ plane. Once the $(n_{\rm CSM}, \beta_{\rm sh})$ pair is fixed, the observed peak radio luminosity $L^{\rm Radio}_{\rm pk}$ and peak frequency $\nu_{\rm pk}$ can be obtained simultaneously only for a specific (ϵ_B, ϵ_e) pair and vice-versa [670].

The minimum luminosity radiated in neutrinos can be inferred from radio observation as $L^{\nu}_{\rm min} \simeq L^{\rm Radio}_{\rm pk}\nu_{\rm pk}$. The total energy in neutrinos $E^{\nu}_{\rm tot}$ can be estimated locating the transient in the plane in Fig. 60. Otherwise, once the $(n_{\rm CSM}, \beta_{\rm sh})$ pair is inferred from radio observations, the corresponding $E^{\nu}_{\rm tot}$ can be estimated from Eq. 11.32.

In summary, transients detected with a bright radio counterpart are expected to produce a bright neutrino signal. As neutrinos and radio photons are produced over the same time interval during CSM interactions (see Fig. 56), it is fundamental to identify radio sources at early times, in order to quickly initiate follow-up neutrino observations. However, we stress that the neutrino curve is expected to peak at a time likely shifted with respect to the one when the radio and optical light curves peak [231, 592]. The procedure outlined here can be performed at different times of radio observations.

We exclude in Fig. 60 the region of the parameter space leading to the production of neutrinos with maximum energy $E_{\nu,\rm max} \simeq 0.05 E_{p,\rm max} \lesssim 100$ TeV throughout the duration of CSM interactions. In fact, the

neutrino events detected below 100 TeV are contaminated by the atmospheric background and astrophysical neutrino detection would be challenging [32].

If neutrinos are produced as a result of CSM interactions, then a gamma-ray counterpart should be also expected [123, 642]. However, gamma-rays undergo γ-γ and Bethe-Heitler processes before reaching Earth, making the correlation with the corresponding neutrino signal less straightforward.

11.6.3 *Jetted transients*

The neutrino signal produced in the optically thin part of GRBs is strictly correlated with X-ray/gamma-ray radiation and its detectability has been extensively discussed in Ref. [65]. We refer the reader to the criterion outlined in Ref. [590] for the detectability of neutrinos from GRBs whether the bolometric X-ray/gamma-ray light curve is powered by internal shocks. The criterion does not hold if energy is dissipated through magnetic reconnection along the jet, and the correlation between neutrinos and photons is no longer trivial.

When a GRB is detected electromagnetically, correlated neutrino searches should be carried out also at energies $10^{-1} \lesssim E_\nu \lesssim 10^5$ GeV, since neutrinos may be produced in this energy range in the optically thick part of the jet [635]. Subphotospheric neutrinos could be easily differentiated from the prompt signal, as the latter peaks at energies $E_\nu \simeq 10^5 - 10^6$ GeV [231]. We note that neutrinos produced in the optically thick part of the jetted outflow do not have any direct electromagnetic counterpart, yet their detection in the direction of a GRB could be the smoking gun of the jet magnetization.

The only electromagnetic counterpart of unsuccessful jets would be the flash of light in the hard X-ray/soft gamma-ray band [200, 621] due to the shock breakout of the cocoon, as discussed in Sec. 11.3. Neutrinos with energy $10^{-1} \lesssim E_\nu \lesssim 10^5$ GeV [635] can be produced below the photosphere, if the jet is magnetized, while a neutrino signal peaking at $E_\nu \simeq 10^5$ GeV may exist if the jet is smothered in an extended envelope [234].

11.7 DETECTION PROSPECTS

In this section, we explore the detection prospects of neutrinos emitted from the transients considered throughout this paper (all of them already observed electromagnetically). Finally, we discuss the best strategy for follow-up searches of single transient sources and stacking searches.

11.7.1 *Expected number of neutrino events*

In order to compute the expected number of neutrino events, where suitable, we consider IceCube-Gen2 [16] for representative purposes because of its large expected rate. The number of muon neutrino events expected at IceCube-Gen2 [16, 141] for a source at redshift z is $N_{\nu_\mu}(z) = \int_{E_{\nu,\rm min}}^{E_{\nu,\rm max}} dE_\nu \Phi_{\nu_\mu}^{\rm obs}(E_\nu, z)\mathcal{A}_{\rm eff}(E_\nu, \delta)$, where $\mathcal{A}_{\rm eff}(E_\nu, \delta)$ is the detector effective area for a source at declination δ [671], $E_{\nu,\rm min}$ and $E_{\nu,\rm max}$ are the minimum and maximum neutrino energy, respectively. We fix $E_{\nu,\rm min} = 100$ TeV, in order to avoid the background of atmospheric neutrinos, and choose $\delta = 0°$ to maximize the effective area of the detector. The observed fluence of muon neutrinos is $\Phi_{\nu_\mu}^{\rm obs}(E_\nu, z)$ [in units of GeV^{-1} cm^{-2}], calculated as outlined in Sec. 11.4 for the model parameters in Table 11 and including neutrino flavor conversion [278, 279].

Figure 61 shows the number of muon neutrino events expected at IceCube-Gen2 as a function of the luminosity distance for SNe Ib/c BL harboring a jet, SNe IIP and IIn, SLSNe, as well as LFBOTs. For all source classes, we consider neutrino production through CSM interactions. For our fiducial parameters, CSM interactions produce neutrinos with $E_{\nu,\rm max} \lesssim 10^8$ GeV, in agreement with previous work [65, 123, 131, 234, 533, 536, 537, 592].

For SLSNe and LFBOTs, we also calculate the number of neutrino events expected from the magnetar wind. These neutrinos have energies larger than the ones produced through CSM interactions, with their signal expected to peak at $E_\nu \simeq 10^8$–10^9 GeV [132]. In this energy range the sensitivity of the radio extension of IceCube-Gen2 is better than its optical component [16], thus we estimate the detection perspectives of neutrinos from the magnetar wind at IceCube-Gen2 radio. In our simplified model, we assume that $N_{\nu_\mu} \simeq E_{\rm rad}^{\nu,\rm max}/10^{8.5}$ GeV$\mathcal{A}_{\rm eff}(10^{8.5}$ GeV), where $\mathcal{A}_{\rm eff}(10^{8.5}$ GeV) is the effective area of the radio extension IceCube-Gen2 at $\simeq 10^{8.5}$ GeV [671]. This is an approximation due to the fact that we do not consider the energy distribution of neutrinos from the magnetar.

As for SNe Ib/c BL harboring jets, we show the total number of events expected at IceCube-Gen2 in Fig. 61 from a successful jet, whereas the neutrino signal from CSM interactions only would be too small to be detected (see Sec. 11.5). If the jet is smothered in the Wolf-Rayet star progenitor, neutrinos with $E_\nu \lesssim 10^5$ GeV may be produced; the related detection prospects of subphotospheric neutrinos havew been explored in Ref. [635].

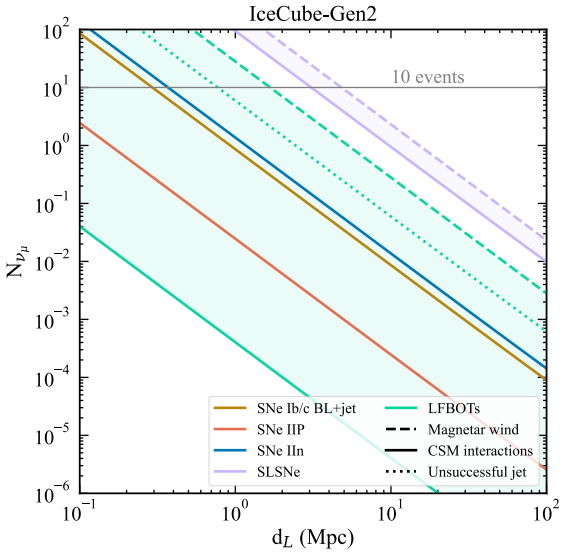

Figure 61: Expected number of muon neutrino and antineutrino events at IceCube-Gen2 as a function of the luminosity distance for SNe Ib/c BL harboring jets, SNe IIP, SNe IIn, SLSNe and LFBOTs. The gray horizontal line marks $N_{\nu_\mu} = 10$. We consider neutrinos from CSM interactions (solid lines), from the magnetar wind (dashed lines) and from jets (dotted lines). For SNe Ib/c BL harboring a jet, we display the total number of neutrinos given by CSM interactions and the jet; CSM interactions alone produce a number of neutrinos which falls below the plotted range. CSM interactions can produce $N_{\nu_\mu} \simeq O(10)$ at IceCube-Gen2 for SLSNe (SNe IIn) located at $d_L \lesssim 4$ Mpc ($d_L \lesssim 0.6$ Mpc). The magnetar wind can produce $N_{\nu_\mu} \simeq O(10)$ at IceCube-Gen2 radio for SLSNe (LFBOTs) located at $d_L \lesssim 5$ Mpc ($d_L \lesssim 2$ Mpc). $N_{\nu_\mu} \simeq O(10)$ is expected at IceCube-Gen2 from LFBOTs harboring unsuccessful jets and placed at $d_L \lesssim 1$ Mpc. Note that the number of neutrino events from jets, both successful and unsuccessful, is model dependent; see main text for details.

As outlined in Sec. 11.5, LFBOTs may harbor jets which are smothered in the extended envelope surrounding the progenitor core [153]. In this scenario, a signal peaking at $E_\nu \simeq 10^5$ GeV may be produced in the unsuccessful jet [234] (see also Ref. [235] for neutrino production in jets smothered in an extended envelope). In Fig. 61 we show the corresponding expected number of neutrino events, obtained by relying on the most optimistic model of Ref. [234].

From Fig. 61, we deduce that the expected number of neutrino events from CSM interactions is $N_{\nu_\mu} \simeq O(10)$ for SLSNe (SNe IIn) located at $d_L \lesssim 4$ Mpc ($d_L \lesssim 0.6$ Mpc). Large CSM densities may be possible around SLSNe and SNe IIn, with $M_w \lesssim 10 M_\odot$ yr^{-1} [638, 659]; in this case, the expected number of neutrino events from SLSNe and SNe IIn could be larger than considered here [592]. Neutrinos from magnetar winds show promising detection perspectives at IceCube-Gen2 radio, with $N_{\nu_\mu} \simeq O(10)$ for SLSNe and LFBOTs located at $d_L \lesssim 5$ Mpc and $d_L \lesssim 2$ Mpc, respectively. Unsuccessful jets in LFBOTs may produce $N_{\nu_\mu} \gtrsim O(10)$, if the source is at $d_L \lesssim 1$ Mpc. However, we note that the neutrino signal from the choked jet peaks at energies $E_\nu \simeq 10^5$ GeV and it quickly drops at larger energies [234], where the sensitivity of IceCube-Gen2 increases [16]. Thus, the most promising detection prospects for LFBOT sources are obtained with IceCube,

Table 12: Local rate ($\mathcal{R}_0$) of the sources considered throughout this paper including their error bands, relative to the local rate of core-collapse SNe [$\mathcal{R}_0^{\rm CCSN} = (1.25\times10^{-4})^{+70\%}_{-30\%}$ Mpc^{-3} yr^{-1}] [32, 575]. Note that the local rate of GRBs refers to GRBs beamed towards us. For reference, we also show the rate of low-luminosity (LL) GRBs as they are more abundant and might also be related to choked jets and/or shock breakouts.

Source	$\mathcal{R}_0/\mathcal{R}_0^{\rm CCSNe}$	Reference
SNe Ib/c	$(26\%)^{+5.1\%}_{-4.8\%}$	[672]
SNe Ib/c BL	$\lesssim 13\%$	[673]
SNe Ib/c BL with choked jet	Unknown	[673]
GRBs	$\lesssim 10^{-5}$	[674]
LL GRBs	$\lesssim 10^{-3}$	[675]
SNe IIP	$(48.2\%)^{+5.7\%}_{-5.6}$	[672]
SNe IIn	$(8.8\%)^{+3.3\%}_{-2.9\%}$	[672]
SLSNe	$\lesssim 2.8\times10^{-3}$	[676]
LFBOTs	$\lesssim 10^{-3}$	[152]

due to its sensitivity range [141] (see Fig. 6 in Ref. [234] for the expected number of neutrinos in this case). We stress that the results for both successful and smothered jets are model dependent and the number of events is calculated assuming that the jet is observed on-axis.

In order to assess the likelihood of finding such transients and contrast the local rate with the expected number of muon neutrino events, we assume that all these sources follow the star formation rate as a function of redshift. The local rates of the sources considered throughout this paper ($\mathcal{R}_0$) relative to the one of core-collapse SNe—$\mathcal{R}_0^{\rm CCSN} = (1.02\times10^{-4})^{+70\%}_{-30\%}$ Mpc^{-3} yr^{-1} [32, 199]—are listed in Table 12.

SLSNe and LFBOTs display the most promising chances of neutrino detections if powered by a magnetar, however these sources are the least abundant in the local universe. Using Table 12, $\simeq 4\times\mathcal{O}(10^{-7})$ Mpc^{-3} yr^{-1} [$\simeq 2\times\mathcal{O}(10^{-7})$ Mpc^{-3} yr^{-1}] SLSNe (LFBOTs) are expected at $d_L = 10$ Mpc (note that we consider the central values of the rates). On the contrary, SNe IIP are the most abundant sources locally, with $\mathcal{R}_0^{\rm SN\ IIP} = 1.1\times10^{-4}$ Mpc^{-3} yr^{-1}. Nevertheless, their neutrino signal is too weak to be detected at IceCube-Gen2. Jetted outflows are also expected to produce a significant number of neutrinos. Yet the probability that the jet points towards us is $\theta_j^2/4 \simeq \mathcal{O}(10^{-3})$ for typical opening angles (see Table 11). The beaming factor and the small local rate of GRBs, LFBOTs and SNe Ib/c BL which may harbor jets (Table 12) challenge the associated neutrino detection.

11.7.2 *Combining multi-messenger signals*

On the basis of our findings, we now outline a possible strategy to carry out multi-messenger observations of transients originating from collapsing massive stars. As outlined in Sec. 11.6.2, radio sources whose signal is consistent with synchrotron radiation are expected to have a bright neutrino counterpart. SLSNe, SNE IIn, LFBOTs and SNe IIP with eruptive episodes fall in the category of transients with strong CSM interactions, as shown in Figs. 58 and 61. The synchrotron signal is the signature of a collisionless shock expanding in a dense CSM and it plays a crucial role for multi-messenger searches. First, as neutrinos and radio photons are produced over the same time interval from CSM interactions (Fig. 56), early detection of the radio signal will be crucial to swiftly initiate follow-up neutrino searches. The latter can be guided by the criterion outlined in Sec. 11.6.2. Since gamma-rays are also expected to be produced together with neutrinos [117] (see Fig. 58), radio detection should also guide gamma-ray follow-up searches, e.g. with Fermi-LAT [596] or the Cherenkov Telescope Array (CTA) [677].

Sources emitting in X-rays due to bremsstrahlung emission are also hosted in a dense CSM, although this signal is produced through radiative shocks and may hint towards the existence of an asymmetric CSM [637]. Neutrinos produced at the same site of bremmsthralung radiation have energies below the sensitivity range of IceCube and IceCube-Gen2 [298] and we have not considered them throughout this work. Yet, X-ray data from bremmsthralung can be combined with synchrotron radio data to infer the CSM properties, that affect the expected neutrino signal [298, 592, 642].

If the UVOIR lightcurve shows signs of central magnetar activity, as it may be the case for SLSNe and LFBOTs, X-ray telescopes should look for a non-thermal and time variable signal. The latter may emerge at later times than the UVOIR light, due to the opacity of the outflow [148]. As detailed in Sec. 11.6.1, the non-thermal X-ray signal is key to disentangle the degeneracies plaguing the UVOIR lightcurve. Neutrino searches from this class of transients should start later than the UVOIR observations, and they should be carried out in the time window $[t_{\nu,\rm min}, t_{\nu,\rm max}]$ defined in Sec. 11.6.1, e.g. with IceCube-Gen2 radio.

Intriguingly, SLSNe and LFBOTs may be powered either by CSM interactions or magnetar spin down. While neutrinos from the former have energies $E_\nu < 10^8$ GeV, a signal peaking at $E_\nu \gtrsim 10^8$ GeV is expected from the latter. The time window during which neutrinos are radiated is different and it depends on the mechanism responsible for their production (see Fig. 56). Thus, the energies and the detection time of

neutrinos in the direction of the transient source can be combined with electromagnetic observations to disentangle the dominant mechanism powering the lightcurve.

Some sources, such as LFBOTs and SNe Ib/c BL, may harbor a choked jet pointing towards us. The resulting outflow has an asymmetry observable in the UVOIR and radio bands and it moves with middly-relativistic velocity, otherwise unreachable through symmetric explosions [634]. The electromagnetic signature of the choked jet would be a flash of light in the X-ray band [621]; see Fig. 58. Improving X-ray detection techniques to unambiguously detect shock breakouts will be crucial to model the associated neutrino signal.

If a mildly-relativistic outflow is inferred from radio observations, one should search for neutrinos in the direction of the transient hundred to thousand seconds before and after the first observation in the UVOIR band (see also Fig. 56). Indeed, if an unsuccessful jet is hidden in the source, neutrinos may be produced while the outflow is still optically thick and for a time $t^{\nu}_{\rm dur} \simeq t_j$. IceCube and IceCube-Gen2 could potentially detect neutrinos from a jet smothered in a red supergiant progenitor star, whereas IceCube DeepCore [173] is needed to observe neutrinos from a jet choked in Wolf-Rayet stars [234, 635]. A combined search may be promising for neutrinos from mildly-relativistic sources.

Finally, if the UVOIR lightcurve should mostly exhibit signs of ^{56}Ni decay or hydrogen recombination, the corresponding neutrino emission would be a negligible fraction [$\lesssim O(10^{-13})$] of the ejecta kinetic energy. Searches of neutrinos in the direction of sources only powered through these processes would not be successful.

11.7.3 *Follow-up searches for selected sources and stacking searches for a source class*

The detection prospects for follow-up searches of a selected source together with the best wavelength to correlate with neutrinos for each transient are summarized in Table 13. We list the luminosity distance (d_L) where $N_{\nu_\mu} = 10$ for our benchmark transients in Fig. 61, and the number of transients expected per year within d_L [$N_{\rm trans}(\leq d_L)$]. The bands reflect the uncertainty on the local core-collapse SN rate [678] and the fraction of SNe belonging to each class [672]. We do not include SNe Ib/c as the number of expected neutrinos from CSM interactions only is too low to be detected. For completeness, we also show the expected distance where $N_{\nu_\mu} = 10$ at IceCube DeepCore [173] for jets choked in Wolf-Rayet star progenitors, by relying on the results of Ref. [635].

Table 13: Summary of our results. We list the luminosity distance (d_L) where $N_{\nu_\mu} = 10$ for our benchmark transients (Fig. 61), the number of transients expected per year within d_L [$N_{\rm trans}(\leq d_L)$] and the best wavelength to correlate with neutrinos. The bands reflect the uncertainty on the local core-collapse SN rate [678] and on the fraction of SNe belonging to each class [672]. Note that for SNe Ib/c BL with a choked jet we calculate the number of neutrinos expected at IceCube DeepCore [173], by relying on the results in Ref. [635].

Source	Model	d_L [Mpc]	$N_{\rm trans}(\leq d_L)$ [yr^{-1}]	Best correlated wavelength
SLSNe	CSM interactions	4	$\lesssim 10^{-3}$	Radio
SLSNe	Magnetar wind	5	$\lesssim 2\times10^{-3}$	UVOIR+X-ray
SNe IIn	CSM interactions	0.6	$3.5\times10^{-3} - 2\times10^{-2}$	Radio
SNe IIP	CSM interactions	0.05	$6\times10^{-4} - 2\times10^{-3}$	Radio
LFBOTs	Magnetar wind	2	$\lesssim 2\times10^{-6}$	UVOIR+X-ray
LFBOTs with jet	Choked jet in extended envelope	1	$\lesssim 5\times10^{-7}$	X-ray/gamma-ray
GRBs	Envelope of more models (Ref. [65])	0.2	$\lesssim 2\times10^{-8}$	X-ray/gamma-ray
SNe Ib/c with choked jet	Choked jet in Wolf-Rayet star	90	Unknown	X-ray/gamma-ray

In order to carry out stacking searches of neutrinos from radio-bright transients, one can search through archival all-sky neutrino data for clusters of a few neutrino events in the direction of identified radio transients. To this purpose, it would be useful to compile catalogues of transients detected in the radio band, e.g. relying on data from the Very Larger Array Sky Survey (VLASS) [162]. Additional radio catalogues will be available in the near future, through the Square Kilometer Array Observatory (SKA), which will cover the Southern hemisphere [163]. Note, however, that an appropriate weighting of the sources relative to each other is recommended in order to optimize neutrino searches [592].

Another important factor in the search for neutrinos from radio sources is the time window. As extensively discussed in this work and shown in Fig. 56, the neutrino and radio signals are produced over the same window. The peak of the neutrino signal is expected to occur not too far from the breakout time of the forward shock from the CSM, or anyway around the peak of the optical lightcurve [592]. The same results do not hold for the radio signal, whose peak can occur much later than the optical one, depending on the properties of the CSM and the forward shock. Thus, it is crucial to combine UVOIR and radio data to optimize the time window for neutrino searches.

The atmospheric neutrino background increases when a long time window is chosen. Yet the criterion presented in Fig. 60 excludes the parameter space contaminated by atmospheric neutrinos, considering only

the $(n_{\rm CSM}, \beta_{\rm sh})$ pairs which allow for the production of neutrinos with $E_\nu \gtrsim 10^5$ GeV. Our findings provide guidance to identify the ideal time window to carry out radio and neutrino stacking searches. We also encourage to initiate radio follow-up observations of neutrino alerts [679]. In order to better assess the CSM properties, follow-up observations in the X-ray bands are needed to break the degeneracies in the $(n_{\rm CSM}, \beta_{\rm sh})$ space [628].

11.8 DISCUSSION AND CONCLUSIONS

In this work, we consider SNe Ib/c, SNe Ib/c BL harboring jets, SNe II-P, SNe IIn, SLSNe, as well as LFBOTs and compute the energy radiated across the observable electromagnetic wavebands and neutrinos. Our findings reveal that most of the energy is radiated in the UVOIR band. However, a significant fraction of the outflow kinetic energy can be emitted either in the radio or the X-ray bands through synchrotron or bremsstrahlung processes, when a dense CSM engulfs the collpasing star. Since the UVOIR light curve is degenerate with respect to the transient model parameters, a correlation of neutrino observations with this band alone is not sufficient, in agreement with the findings of Ref. [592]. However, one could combine UVOIR observations with radio data to infer upper and lower limits, respectively, on the ejecta energy $E_{\rm ej}$ and mass $M_{\rm ej}$ [147, 152, 629].

While the peak of the UVOIR luminosity of transients powered by the spin down of a magnetar is degenerate with respect to the spin period and magnetic field of the pulsar, multi-wavelength observations are fundamental to break these degeneracies. In particular, X-ray/non-thermal data can be combined with the thermal UVOIR ones to infer the spin and magnetic field [132] and allow to forecast the neutrino number of events. Neutrino observations could be instrumental to break the degeneracy between the spin period and the magnetic field. As the neutrino production starts (ends) when photopion processes become efficient (inefficient), neutrino searches should be carried out in a time window uncorrelated with the UVOIR lightcurve.

Our findings reveal that bright radio sources are promising high-energy neutrino factories. Opposite to the UVOIR signal, a correlation between the radio and optical signals exist. Radio photons and neutrinos are produced over the same time interval and therefore neutrino searches should be performed over the duration of the radio emission. The radio counterpart allows to infer the CSM density $n_{\rm CSM}$ and the shock velocity

$\beta_{\rm sh} = v_{\rm sh}/c$ at the observed time [629]. The minimum neutrino luminosity expected at each emission time from the transient can be computed considering the product of the radio peak luminosity and peak frequency $E^{\nu}_{\rm rad,min} \simeq L^{\rm Radio}_{\rm pk}\nu_{\rm pk}$, and the total energy radiated in neutrinos can be localized in the plane spanned by $n_{\rm CSM}$ and $\beta_{\rm sh}$.

For our fiducial parameters, IceCube-Gen2 will be able to detect neutrinos from SLSNe at $d_L \lesssim 4$ Mpc, when neutrinos are produced from CSM interactions. If SLSNe (LFBOTs) harbor a central magnetar, 10 neutrino events produced in the magnetar wind are expected in IceCube-Gen2 radio for sources at $d_L \lesssim 5(2)$ Mpc.

While transients linked to massive stars are routinely detected in the UVOIR band, our findings urge to optimize the detection opportunities in the radio and X-ray bands to swiftly identify CSM and magnetar powered transients. Furthermore, neutrino searches would be useful for mildly-relativistic transients, as neutrinos may signal the presence of a choked jet. Improving observational techniques in the UV/X-ray will be fundamental to detect the shock breakout light and model the corresponding neutrino signal. Neutrino searches from mildly-relativistic sources should be performed (10–1000) s before and after the first UVOIR signal.

In summary, in order to optimize the chances of joint detection of electromagnetic radiation and neutrinos from transients stemming from collapsing massive stars, follow-up programs solely based on UVOIR observations are not optimal. UVOIR data should be complemented by radio data tracing CSM interactions or X-ray data carrying imprints of the activity of the central engine, if any. Only exploiting multi-wavelength and neutrino data can we explore the physics powering these fascinating sources and properly guide multi-messenger follow-up programs.

11.9 CRITICAL OUTLOOK

In this section, we critically scrutinize our study, providing an overview of our main findings. We also discuss future directions to improve our analysis. Notably, a similar discussion is outlined in Secs.11.2.2 and 11.6 of the original publication.

11.9.1 *Overview and main findings*

As the number of high-energy neutrino events detected at IceCube in space and time coincidence with transient sources increases, several studies attempt to link the high-energy neutrino signal with the properties of the optical lightcurve (e.g., Refs. [593, 680]). However, this assumption is not motivated and the optical signal alone may not be optimal for high-energy neutrino searches. As a result, *it remains unclear which electromagnetic waveband exhibits a stronger correlation with high-energy neutrinos*. Similarly, *the way multi-messenger observations can be combined to break the degeneracies in the parameter space of the transient properties is yet to be addressed*. In our study, we tackle these open questions. Our work marks the first *ab initio* theoretical model of the correlations between high-energy neutrinos and the observable electromagnetic wavebands. The findings in this study provide a pivotal roadmap to conduct informed follow-up high-energy neutrino searches from astrophysical transients.

In order to assess the correlation between electromagnetic radiation and high-energy neutrinos, we perform back-of-the-envelope calculations of the fraction of the outflow kinetic energy radiated across the observable electromagnetic wavebands and in neutrinos. Our focus is on transients stemming from collapsing massive stars, including SNe Ib/c, SNe Ib/c broad line harboring jets, SNe II-P, SNe IIn, SLSNe and LFBOTs. The ejected spherical outflow can be heated through radioactive decay of ^{56}Ni, H recombination or activity of a central engine. We also consider interactions of the outflow with a dense CSM and shock breakout from the stellar envelope as viable heating sources. Finally, we consider the possibility of a jetted component harbored within the outflow. For each heating process, we calculate the observed lightcurve by relying on the model outlined in Ref. [129] and estimate the corresponding energy radiated across all the wavebands. As for high-energy neutrinos, we model their production in the magnetar wind, at interactions with the CSM surrounding the progenitor star and along the jet.

Our findings reveal that the majority of the heating processes emit the bulk of radiation in the UVOIR band, while the shock breakout produces a flash of light in the UV/X-ray bands depending on the progenitor star. However, a significant fraction of energy can be radiated in the radio and/or in the X-ray bands through synchrotron or bremsstrahlung processes, respectively, when the collapsing star is surrounded by a dense CSM. Importantly, we highlight that the physical parameters underlying the outflow dynamics, namely its kinetic energy and velocity, cannot be inferred by relying on optical data only. Thus, we suggest that

combining radio and optical data is crucial when the observed bolometric lightcurve is powered by CSM interactions. Likewise, when the bolometric lightcurve is powered by the spindown of a central magnetar, X-ray/non-thermal data should be combined with the UVOIR ones to break the degeneracy among the spin period and magnetic field.

Intriguingly, we find that bright radio transients whose signal is consistent with synchrotron radiation produced through CSM interactions are promising sources of high-energy neutrinos. In this case, for each doublet $(n_{\rm CSM}, \beta_{\rm sh})$ inferred from radio data, the total energy radiated in neutrinos can be unequivocally localized in the plane spanned by these two parameters. The direct correlation existing between radio synchrotron photons and high-energy neutrinos encourages follow-up neutrino searches from transients whose optical lightcurve exhibits strong signs of CSM interactions. These findings are further supported by the promising detection prospects of neutrinos produced at CSM interactions for SLSNe located at $d_L \lesssim 4$ Mpc, for which we anticipate that $\gtrsim 10$ neutrinos are expected at IceCube.

Similarly, when the bolometric lightcurve of the transient is powered by the spindown of a central magnetar we find that the high-energy neutrino signal is correlated with the UVOIR lightcurve. In this framework, more than 10 neutrino events from the magnetar wind are expected at IceCube-Gen2 radio from SLSNe (LFBOTs) at $d_L \lesssim 5(2)$ Mpc.

Our findings provide a pivotal roadmap for combining multi-wavelength and high-energy neutrino data to break the degeneracies affecting the optical ligthcurve. Importantly, our research demonstrates the potential of high-energy neutrinos to unveil the origin of transients emerging from collapsing massive stars, when combined with electromagnetic observations in a unified framework. In light of these findings, our work urges follow-up programs that combine UVOIR, radio and X-ray data to optimize the chances of serendipitous detection of electromagnetic and neutrino signals from collapsing transients.

11.9.2 *Future research directions*

In the following, we outline possible future directions to strengthen our results:

1. *Modelling of the radiation through the transport equation.* The simplified one-zone model outlined in Ref. [129] does not fully capture the propagation of radiation through the outflow. In order to estimate the non-thermal component, expected to emerge at times considerably beyond the peak of

the bolometric lightcurve, we suggest solving the coupled transport equations for photons, electrons, protons, neutrinos and intermediate particle species.

2. *Relaxing the approximation of constant velocity of the outflow*. This assumption is valid as long as the heating source injects an amount of energy smaller than the ejecta kinetic energy. Furthermore, the outflow can be decelerated by the CSM, if the mass of the latter is larger than the one of the ejecta. The constraint of constant velocity may be relaxed to explore a larger part of the parameter space.

3. *Considering range of values for the transient parameters.* We carried out our study by assuming average parameters for each class of transients, as listed in Table 11. In order to assess the dependence of our results on the specific choice of parameters, error bands spanning the wide range of values inferred from observations could be included in a future study.

In summary, our study scrutinizes the transients considered throughout the thesis within a multi-messenger framework. Our findings not only outline the most optimal strategies to connect multi-wavelength observations and high-energy neutrino data, but they also urge to optimize the detection techniques in the radio, UV and X-ray bands. This final work contained in the thesis further emphasizes that we can only delve into the physics powering transients by harnessing both multi-wavelength and neutrino data.

Part IV

SUMMARY AND CONCLUSIONS

12

SUMMARY AND CONCLUSIONS

In this thesis, we investigate the potential of combining high-energy neutrinos with multi-wavelength data to probe the mechanisms powering some of the most powerful transient phenomena occurring in the cosmos: long gamma-ray bursts (GRBs), supernovae (SNe), and luminous fast blue optical transients (LFBOTs). In the following paragraphs, we summarize the main findings of the works contained in Parts ii and iii of the thesis.

Our primary focus is on the multi-messenger emission from long-duration GRBs, which we extensively scrutinize in Part ii. The shaping of the GRB multi-messenger signal may start well below the jet photosphere and proceed over a wide range of radii. Yet, the innermost regions of GRB outflows are electromagnetically inaccessible, as photons are absorbed due to the large densities. On the contrary, high-energy neutrinos can escape unhindered from dense regions and provide us with unique insights into the jet physics below the photosphere. Pioneering a novel approach, in Chapter 7 we leverage outputs from state-of-the-art general relativity magneto-hydrodynamic (GRMHD) simulations to self-consistently model the production of subphotospheric high-energy neutrinos in collapsar jets. Up to now, this signal has been modeled analytically, hence overlooking the mixing between the jet and the cocoon. The crucial finding of this work is that, when the mixing is taken into account, subphotospheric neutrinos with energies $\lesssim O(10^5)$ TeV can be produced only if the jet is magnetized, through collisionless sub-shocks and magnetic reconnection. Contrary to previous works, we conclude that optically thick collapsar jets are unlikely to produce the bulk of the high-energy neutrino diffuse flux detected at IceCube. Importantly, our findings underscore the need for more advanced models of particle production and acceleration below the jet photosphere, a result achievable only by post-processing the outputs of GRMHD simulations.

High-energy neutrinos can not only provide valuable insights into opaque regions of GRB jets but also have the potential to probe the circumburst medium (CBM) where the burst propagates. This is particularly relevant in the case of GRB afterglows, broadly believed to be associated with the interaction of the jet with the CBM. Yet, GRB afterglows display a rich array of features that cannot be accommodated within

the standard model. Among these features, in Chapter 8 we focus on the optical jump, namely the sudden rebrightening observed in the optical light curve of some GRB afterglows. We model the jump through the late collision of two relativistic shells and inspect the corresponding signature induced in the high-energy neutrino signal. Our work reveals that the total number of emitted neutrinos in the presence of an optical jump increases up to one order of magnitude compared to the standard afterglow case. Importantly, this result holds as long as the burst propagates in a constant density interstellar medium (ISM), whereas no significant change in the neutrino signal is expected for a GRB jet expanding in a wind-like medium. Thus, our work unveils that high-energy neutrinos can probe the environment where the burst propagates, whereas electromagnetic models may be degenerate with respect to the nature and density of the CBM.

An additional puzzling and yet intriguing feature is the very-high-energy (VHE, $\gtrsim$ 100GeV) emission observed at late times deep in the afterglow of some GRBs, which we inspect in Chapter 9. By making use of radio, optical, and X-ray data of a sample of VHE bursts, we infer that these bursts may occur in environments with low densities, possibly connected to low metallicity progenitors. While these results may have significant implications for the origin of VHE GRBs, high-energy neutrinos cannot be used to further constrain the afterglow properties of VHE GRBs, due to poor statistics. However, the detection of high-energy neutrinos with the upcoming IceCube-Gen2 radio will play a pivotal role in pinpointing the mechanism responsible for the emission of VHE photons. Notably, the findings of Chapters 8 and 9 highlight the imperative need to combine multi-wavelength data with high-energy neutrino signals to gain a deeper understanding of the puzzling processes occurring during GRB afterglows. Upcoming telescopes with improved sensitivity will allow us to collect more afterglow data, shedding new light on the interaction of GRB jets with the CBM.

Besides GRBs, high-energy neutrinos may be produced in a multitude of emerging classes of high-energy transients, whose multi-messenger emission is inspected in Part iii. Among these transients, LFBOTs stand out for their intriguing properties resembling both SNe and GRBs. Despite their growing number, the nature of LFBOTs remains elusive, and a multi-messenger approach is crucial to gain a fresh perspective. In Chapter 10, we investigate for the first time high-energy neutrino production in LFBOTs within two theoretical frameworks: the cocoon model and the merger model. In both scenarios, we find that high-energy neutrinos can be produced at the mildly-relativistic shock between the fast outflow and the circumstellar medium (CSM). An additional bright neutrino signal is expected from the choked jet, should it be harbored within LFBOTs and pointing toward us. Importantly, our analysis reveals that existing IceCube neutrino

events in the direction of AT2018cow— the first LFBOT ever detected— significantly constrain the parameter space accessible in the choked jet scenario, otherwise allowed by electromagnetic observations. Furthermore, the high-energy neutrino signals produced through CSM interactions and through shocks in the choked jet are significantly different. Hence, the remarkable finding of this work is the capability of high-energy neutrinos to disentangle the mechanism powering LFBOTs, advocating for targeted searches for high-energy neutrinos in the direction of future LFBOT sources.

We conclude this thesis by acknowledging that, despite the increasing number of observed astrophysical transients, the observable electromagnetic waveband displaying the strongest correlation with high-energy neutrinos remains unknown. To tackle this open question, in Chapter 11 we outline a strategy to carry out informed follow-up neutrino observations of transients stemming from collapsing massive stars, including SNe Ib/c (BL), SNe IIP, SNe IIn, SLSNe, and LFBOTs. While the properties of the outflow cannot be accurately deduced solely from optical data, our findings emphasize the crucial role played by radio and X-ray observations in complementing the information obtained from the optical light curve. Importantly, our work unveils that bright radio sources are promising factories of high-energy neutrinos and that a strong link between the radio and neutrino signals exists. Likewise, if high-energy neutrinos are detected in space and time coincidence with astrophysical transients, our findings further confirm that these particles can be used to disentangle the degeneracies affecting electromagnetic models. As we prepare for the promising future of time-domain and multi-messenger astronomy, this work provides a pivotal roadmap for seamlessly integrating multi-wavelength and neutrino data.

The results presented in this thesis confirm the role of high-energy neutrinos as unparalleled cosmic messengers. Most importantly, our results prove that only by skillfully combining high-energy neutrino observations with multi-wavelength electromagnetic data can we tackle fundamental questions on the most energetic phenomena occurring in the cosmos. Although many challenges are ahead, the full potential of multi-messenger astronomy is poised to be unleashed soon, thanks to the multitude of upcoming telescopes with unprecedented sensitivity on the horizon.

Part V

APPENDICES

A

SUBPHOTOSPHERIC NEUTRINOS APPENDIX

A.1 PHOTON THERMALIZATION

Electrons are assumed to be accelerated to a power-law distribution $N(\gamma'_e) \propto \gamma'^{-k_e}_e$, where k_e is the electron spectral index. Both at collisionless sub-shocks and at magnetic reconnection sites, they are expected to cool through the emission of synchrotron radiation [259, 260, 271].

The synchrotron spectrum is defined in terms of three characteristic electron Lorentz factors: the minimum, the cooling and the self-absorption Lorentz factors ($\gamma'_{e,\rm min}$, $\gamma'_{e,\rm cool}$, and $\gamma'_{e,\rm abs}$), respectively. These are defined as [107, 343, 369, 681, 682]:

$$\gamma'_{e,\rm min} = \varepsilon_d \varepsilon_e \frac{m_p}{m_e} \frac{k_e - 2}{k_e - 1} , \tag{A.1}$$

$$\gamma'_{e,\rm cool} = \frac{6\pi m_e c}{\sigma_T B'^2 t'_{\rm dyn}} \tag{A.2}$$

$$\gamma'_{e,\rm abs} = \left(\frac{\varepsilon_{\rm abs}}{\varepsilon_B \alpha}\right)^{1/7} \left(\frac{B'}{B_Q}\right)^{-1/7} , \tag{A.3}$$

where ε_e and ε_B are the fractions of the dissipated energy that is stored in accelerated electrons and into magnetic field, respecitvely. With $\varepsilon_{\rm abs}$ we denote the fraction of energy that goes into accelerated electrons radiating at $\gamma'_{e,\rm abs}$; σ_T is the Thompson cross-section, $\alpha = 1/137$ is the fine-structure constant, m_e the electron mass and $B_Q = 4.41 \times 10^{13}$ G. The dynamical time scale of the acceleration process is $t'_{\rm dyn} = R/(2c\langle\Gamma_j\rangle)$, where R is the radius at which the process takes place.

Motivated by the results of particle in cell simulations, as for mildly magnetized sub-shocks, we assume $\varepsilon_e = 5 \times 10^{-4}$, $\varepsilon_B = 0.1$ [288] and $k_e = 2.5$ [85]. In the case of magnetic reconnection, k_e is given by Eq. 7.20 and $\varepsilon_e \approx 1 - \varepsilon_p$, with ε_p given by Eq. 7.21. Finally, following Ref. [682], we assume $\varepsilon_{\rm abs} = 0.1\varepsilon_e$. With this choice of parameters, we get that electrons are always in the fast-cooling regime, namely $\gamma'_{e,\rm min} \gg \gamma'_{e,\rm cool}$, both for internal sub-shocks and magnetic reconnection.

The characteristic Lorentz factors in Eqs. A.1, A.2, and A.3 result in three break energies in the photon spectrum, given by

$$E'_\gamma(\gamma'_e) = \frac{3}{2}\frac{\hbar e}{m_e c}\gamma'_e B' \,. \tag{A.4}$$

In particular, the self-absorption frequency $\nu'_{\gamma,\rm abs} = E'_{\gamma,\rm abs}/h$ gives an estimation of the time over which the synchrotron spectrum becomes self-absorbed and relaxes to a black-body: $t'_{\gamma,\rm abs} = \nu^{-1}_{\rm abs}$.

The main goal of this paper is to compute the neutrino production when the jet is optically thick. Hence, we need to check whether the synchrotron photons thermalize before undergoing $p\gamma$ interactions, whose cooling time can be approximated by

$$t'_{p\gamma} \simeq (n'_{\gamma,\rm synch}\sigma_{p\gamma} f_{p\gamma} c)^{-1} \,. \tag{A.5}$$

Here, $\sigma_{p\gamma} \simeq 10^{-28}$ cm^2 and $f_{p\gamma} \approx 0.2$ are the cross-section and the multiplicity of $p\gamma$ interactions, respectively [399]; $n'_{\gamma,\rm synch}$ is the number of synchrotron photons defined as in Eq. 6 of Ref. [682], with the appropriate energy density of the outflow. The latter is obtained from our benchmark simulations.

As an example, we get $t'_{\gamma,\rm abs} \simeq 2.2 \times 10^{-19}$ s at sub-shocks for the jet with $\sigma_0 = 15$. The photo-hadronic cooling time at the same position is $t'_{p\gamma} \simeq 5 \times 10^{-5}$ s, namely self-absorption is much faster than $p\gamma$ interactions. Similar results hold also for $\sigma_0 = 200$, both for internal sub-shocks and magnetic reconnection processes. Hence, we can safely assume a black-body spectrum in the optically thick region of the outflow.

A.2 PROTON AND MESON COOLING RATES

The comoving acceleration rate of protons is

$$t'^{-1}_{p,\rm acc} = \frac{ceB'}{\xi E'_p} \,, \tag{A.6}$$

where B' is the magnetic field in the acceleration region and it is shown in Fig. 25, $e = \sqrt{\hbar\alpha c}$ is the electric charge, with $\hbar$ being the reduced Planck constant, and α is the fine structure constant. ξ corresponds to the number of gyroradii required for accelerating protons; following Ref. [390], we assume $\xi = 10$.

Accelerated protons undergo several energy loss procceses, parametrized through the total cooling rate:

$$t'^{-1}_{p,\rm cool} = t'^{-1}_{p,\rm ad} + t'^{-1}_{p,p\gamma} + t'^{-1}_{p,pp} + t'^{-1}_{p,\rm BH} + t'^{-1}_{p,\rm IC} + t'^{-1}_{p,\rm sync} \,, \tag{A.7}$$

where $t'^{-1}_{p,\rm ad}$, $t'^{-1}_{p,p\gamma}$, $t'^{-1}_{p,pp}$, $t'^{-1}_{\rm BH}$, $t'^{-1}_{p,\rm IC}$, and $t'^{-1}_{p,\rm sync}$ are the adiabatic, photo-hadronic ($p\gamma$), hadronic (pp), Bethe-Heitler (BH, $p\gamma \to pe^+e^-$), inverse Compton (IC) and synchrotron cooling rates, defined as [103, 390, 399]:

$$t'^{-1}_{\rm ad} = \frac{2c\Gamma}{R} , \tag{A.8}$$

$$t'^{-1}_{p\gamma} = \frac{c}{2\gamma'^2_p}\int_{E_{\rm th}}^{\infty} dE'_\gamma \frac{n'_\gamma(E'_\gamma)}{E'^2_\gamma}\int_{E_{\rm th}}^{2\gamma'_p E'_\gamma} dE_r E_r \sigma_{p\gamma}(E_r) K_{p\gamma}(E_r) , \tag{A.9}$$

$$t'^{-1}_{pp} = cn'_{p,j}\sigma_{pp}K_{pp} , \tag{A.10}$$

$$t'^{-1}_{p,\rm BH} = \frac{7m_e\alpha\sigma_T c}{9\sqrt{2}\pi m_p \gamma'^2_p}\int_{\gamma'^{-1}_p}^{\frac{E'_{\gamma,\rm max}}{m_e c^2}} d\epsilon' \frac{n'_\gamma(\epsilon')}{\epsilon'^2}\left\{(2\gamma'_p\epsilon')^{3/2}\left[\ln(\gamma'_p\epsilon') - \frac{2}{3}\right] + \frac{2^{5/2}}{3}\right\} , \tag{A.11}$$

$$t'^{-1}_{p,\rm IC} = \frac{3(m_e c^2)^2\sigma_T c}{16\gamma'^2_p(\gamma'_p - 1)\beta'_p}\int_{E'_{\gamma,\rm min}}^{E'_{\gamma,\rm max}} \frac{dE'_\gamma}{E'^2_\gamma} F(E'_\gamma, \gamma'_p) n'_\gamma(E'_\gamma) , \tag{A.12}$$

$$t'^{-1}_{p,\rm sync} = \frac{4\sigma_T m_e^2 E'_p B'^2}{3m_p^4 c^3 8\pi} . \tag{A.13}$$

Here, $\gamma'_p = E'_p/m_p c^2$ is the proton Lorentz factor, $E_{\rm th} = 0.150$ GeV is the photo-pion production energy threshold, and $\epsilon' = E'_\gamma/m_e c^2$. The comoving proton density $n'_{p,j}$ is given by Eq. 7.9. The energy dependent cross-sections $\sigma_{p\gamma}$ and σ_{pp} are provided by Ref. [277]. The inelasticity for $p\gamma$ interactions is taken from Ref. [103]:

$$K_{p\gamma}(E_r) = \begin{cases} 0.2 & E_{\rm th} < E_r < 1 \text{ GeV} \\ 0.6 & E_r > 1 \text{ GeV} , \end{cases} \tag{A.14}$$

where $E_r = \gamma'_p E'_\gamma(1 - \beta'_p \cos\theta')$ is the relative energy between a photon with energy E'_γ and a proton with Lorentz factor γ'_p, moving in the comoving frame of the interaction region along the directions defined by the angle θ'. The inelasticity for pp interactions is $K_{pp} = 0.5$. Finally, the function $F(E'_\gamma, \gamma'_p)$ is defined as in Ref. [400], replacing $m_e \to m_p$.

As an example, Fig. 62 shows the proton cooling rates for the optically thick region of our jet with $\sigma_0 = 15$, at the internal sub-shock radius $R_{\rm SS} = 2.5 \times 10^9$ cm. Protons mainly cool through $p\gamma$ interactions, while pp interactions become relevant for $E'_p \lesssim 100$ GeV. Synchrotron losses are important for $E'_p \gtrsim 10^6$ GeV. Similar results hold for $\sigma_0 = 200$, both for collisionless sub-shocks and magnetic reconnection events.

Before decaying, mesons undergo several cooling processes as well. In particular, they suffer adiabatic, synchrotron and hadronic losses, the latter affecting only pions and kaons with the cross-section $\sigma_{\rm h} = 5 \times 10^{-26}$ cm^2 [277]. Their cooling rates are defined as for protons, with the replacement $m_p \to m_{\pi,K,\mu}$. The meson cooling times are shown in the right panel of Fig 62 for internal sub-shocks ($\sigma_0 = 15$). Pions and kaons substantially suffer hadronic losses, while muons mainly cool through synchrotron radiation.

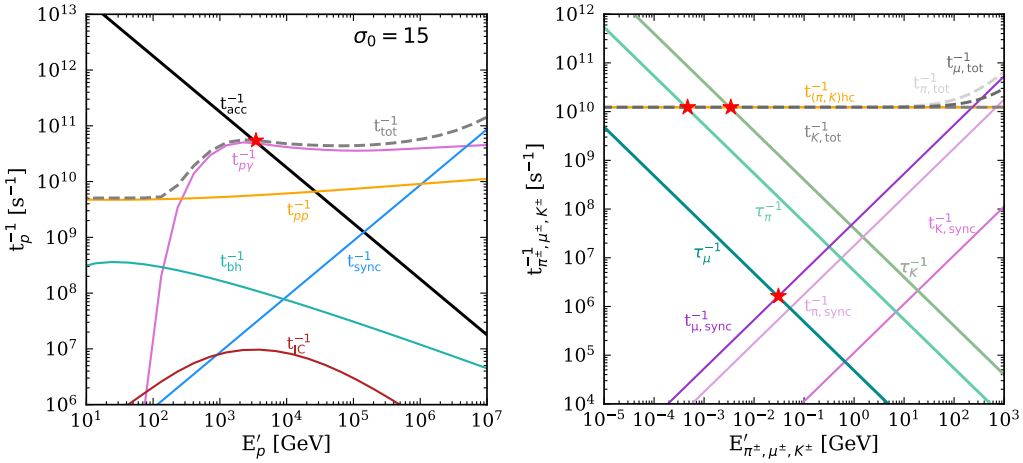

Figure 62: *Left panel*: Comoving cooling rates of protons for our benchmark jet with $\sigma_0 = 15$, calculated for internal sub-shocks at $R_{SS} = 2.5 \times 10^9$ cm. The red star marks the maximum energy at which protons can be accelerated. Protons mainly cool through $p\gamma$ interactions, while pp interactions become important for $E'_p \lesssim 10^2$ GeV. *Right panel*: Same as the left panel, but for secondary mesons. Kaons and pions mainly cool through hadronic processes, while muons undergo strong synchrotron losses. Similar results hold for $\sigma_0 = 200$.

A.3 PARTICLE ACCELERATION IN THE COCOON AND AT THE INTERFACE BETWEEN THE COCOON AND COUNTER-COCOON

While propagating inside the star, the jet inflates a high-pressure region called cocoon. After breaking out, the cocoon expands and engulfs the whole star whether the jet is successful or not. In some cases the fastest component moves with mildly relativistic velocities [683, 684]. Particle acceleration at internal shocks in the cocoon was assumed to take place in Ref. [685]. However, as shown in Fig. 24, the innermost regions of the cocoon are non-relativistic with $\langle \Gamma_c \rangle \simeq 1$, preventing the formation of strong mildly relativistic shocks. Furthermore, we can see from Fig. 26 that the optical depth of the cocoon is extremely large up to $R \simeq 4 \times 10^{11}$ cm; collisionless internal shocks are unlikely to take place. Following Sec. 7.4.1, we deduce from Fig. 24 that the cocoon average magnetization is not large enough to trigger magnetic reconnection. Hence, we conclude that particle acceleration in the cocoon is disfavored, contrary to what pointed out in Ref. [685].

The simulations of Ref. [222] also show interactions between the cocoon and the counter-cocoon both inside and outside the stellar progenitor, as sketched in Fig. 63. The interaction outside the star takes place in the form of a shock, occurring at $R \simeq 2R_\star = 8 \times 10^{10}$ cm. Nevertheless, the outflow is optically thick at this radius (see Fig. 26) and the corresponding magnetization is $\sigma \simeq 10^{-2}$ (see Fig. 24). Hence, there is no

mechanism able to efficiently accelerate particles at the shock between the cocoon and counter-cocoon shock.

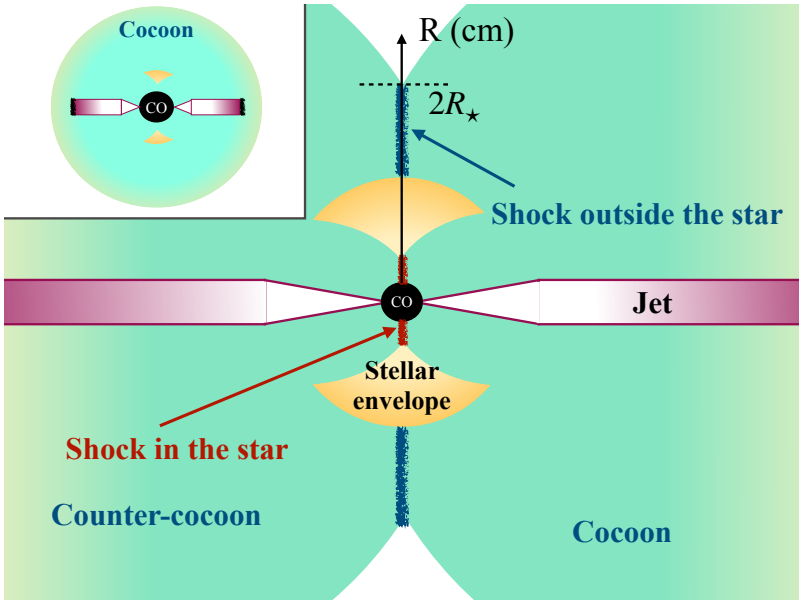

Figure 63: Sketch of the interaction between the cocoon and the counter-cocoon, after the cocoon (aqua) breaks out from the star (orange), expands and engulfs the progenitor star. The inset plot on the top left corner displays a late-time snapshot, when the cocoon engulfs the star. The cocoon and its counterpart interact inside the star (red line) and outside (blue line) at $R \simeq 2R_\star$. Interactions take place in the form of shocks. The large optical depth and very low magnetization of these regions of the outflow inhibit the formation of collissionless shocks and particle acceleration.

A.4 SUCCESSFUL JETS

The jet is successful when its energy and Lorentz factor are such that the jet drills out of the stellar envelope, eventually reaching the photosphere, as sketched in the right panel of Fig. 32. In this Appendix, we briefly discuss this case for completeness and in order to help the reader to compare the related neutrino emission to the subphotospheric one; the latter being the main focus of this work.

In our benchmark simulations, the jet breaks out from the star for both $\sigma_0 = 15$ and $\sigma_0 = 200$; the photospheric radius is $R_{\rm PH} \gtrsim 10^{12}$ cm. The position of the photospheric radius is independent on the jet magnetization, since the jet mimics a hydrodynamic one upon its breakout from the star.

The scenario of successful jets is of particular interest for GRBs. Once the jet reaches the photosphere, it produces the gamma-ray and neutrino bursts eventually observable on Earth. The gamma-ray signal corresponds to the GRB prompt emission, whose origin is still under debate [686, 687]. The findings of

Ref. [222] hint towards a hybrid composition of the jet, since both internal shocks and magnetic reconnection may contribute to energy dissipation.

Because of the strong energy dissipation occurring below the photosphere, the prompt signal originates from a non-thermal spectrum at $R_{\rm PH}$. The spectral peak and the low-energy part below it are determined by quasi-thermal Comptonization of photons by electrons accelerated to mildly relativistic velocities in the regions of the outflow with $1 \lesssim \tau \lesssim 100$ [688, 689]. Further dissipation may occur above the photosphere, for example through internal shocks. GRBs with a dissipative photosphere plus internal shocks has been widely discussed in the literature, see e.g. Refs. [231, 369, 690–695]. A summary of the neutrino signal from GRBs for various mechanisms proposed to model the prompt emission is provided in Ref. [231].

B

GRB OPTICAL JUMP APPENDIX

B.1 A MODEL FOR THE LATE COLLISION AND MERGER OF TWO RELATIVISTIC SHELLS

In this appendix, we revisit the relativistic shock jump conditions. We then model the dynamical merger of two relativistic shells. In the following, we rely on the assumption of thin shells, for which the reverse shock is at most mildly relativistic. We further assume that the reverse shock has already crossed the ejecta, hence we focus on the forward shock only.

The first ultrarelativistic, isotropic shell launched by the central engine starts to be decelerated by the ambient medium when it acquires a mass comparable to m_0/Γ_0, with m_0 being the initial mass of the jet and Γ_0 its initial Lorentz factor [107]. The number of particles, momentum and energy are conserved across the forward shock; this leads to the Rankine-Hugoniot jump conditions at the shock front, see e.g. [382, 696], which in the fluid rest frame read as:

$$w' = (\Gamma_u - 1) n' \frac{h_u}{n_u} , \tag{B.1}$$

$$n' = \frac{2\Gamma_{\mathrm{sh},u}^2}{\Gamma_u} n_u , \tag{B.2}$$

$$\Gamma_u^2 = \frac{1}{2}\Gamma_{\mathrm{sh},u}^2 ; \tag{B.3}$$

where u refers to the upstream quantities, while the primed quantities are measured in the downstream region. Here h_u is the enthalpy density of the upstream medium, which corresponds to the cold CBM, therefore $h_u \equiv \rho_u = n_u m_p c^2$. The quantities w', ρ', and n' denote the comoving pressure, internal energy density, density and number of particles, respectively. $\Gamma_{\mathrm{sh},u}$ is the Lorentz factor of the shock in the frame of the unshocked external medium and Γ_u is the Lorentz factor of the shocked region measured in the same frame. Since the upstream medium is the unshocked CBM, assumed to be at rest in the stellar reference frame, the Lorentz factors in these frames satisfy the equivalence $\tilde{\Gamma} \equiv \Gamma_u$. Therefore, as for the Lorentz factors, hereafter we do not distinguish between the stellar and the unshocked CBM frames and simply denote them as Γ. The shock heats the matter, so that the region behind the shock is a hot plasma for which the equation

of state $p' = (\hat{\gamma} - 1)w'$ holds, being $\hat{\gamma}$ the adiabatic index of the fluid and p' its comoving pressure . For a hot fluid $\hat{\gamma} = 4/3$, therefore the equation of state reads $p' = w'/3$. Using the shock jump conditions, we can rewrite the first equation in Eq. B.3:

$$w' = 4\Gamma(\Gamma - 1)\rho_u = 4\Gamma(\Gamma - 1)n_u m_p c^2 \,, \tag{B.4}$$

which corresponds to Eq. 8.16. Note that from Eq. B.3 one obtains that the plasma behind the shock moves with a velocity $\Gamma = \Gamma_{\rm sh}/\sqrt{2}$. This region of hot plasma corresponds to a blastwave decelerated to the BM solution [382], i.e. our slow shell.

The details of the collision between the slow and the fast shells depend on the hydrodynamical modeling (see, e.g., [360]) and are beyond the scope of this paper. We refer the interested reader to Ref. [363] for a semi-analytic treatment of the shell collision including the reverse shock. Here, we rely on a simplified collision model, expanding on the one adopted to model the internal shock [292, 697]. The main difference with respect to the internal shock prescription is that our slow shell is hot and continuously sweeps up material from the CBM. As a result, we need to include its internal energy at the collision time [698] as well as the mass swept up by the slow shell from the CBM until the time of the collision.

In the following, we focus on a merger whose duration is smaller than the dynamical time, considering that the jet has an opening angle θ_j small enough such that the merger process can be approximated as planar. Hence, the comoving volume of the shells can be expressed as $V' \simeq \pi\theta_j^2 R^2 l'$, where l' is the width of the shell. This assumption is valid as long as the Lorentz factor $\Gamma \gg 1$.

In order to obtain the total energy and momentum of the slow shell at a fixed time t, we introduce the energy-momentum tensor of a relativistic fluid in the laboratory frame [107, 698]:

$$\tilde{T}^{\mu\nu} = (\rho' c^2 + w' + p')\tilde{u}^\mu \tilde{u}^\nu + p'\eta^{\mu\nu} \,, \tag{B.5}$$

where $\tilde{u}^\mu = \Gamma(1, \vec{\tilde{v}}/c)$ is the adimensional 4-velocity of the fluid in the laboratory frame, $\eta^{\mu\nu} = \mathrm{diag}(-1, 1, 1, 1)$ the Minkowski flat space-time and $p' = w'/3$, since we only consider the relativistic shock case. From the component with $\mu = \nu = 0$ in Eq. B.5, we obtain the energy density in the blastwave at the fixed time t:

$$\tilde{T}^{00} = \Gamma^2(\rho' c^2 + w' + p') - p' = \Gamma^2 \rho' c^2 + (\hat{\gamma}\Gamma^2 - \hat{\gamma} + 1)w' \,. \tag{B.6}$$

The total energy of the slow shell in the laboratory frame is computed by integrating Eq. B.6 over $\tilde{V} = V'/\Gamma$, where V' is defined as described previously. By denoting the total internal energy of the slow shell in the comoving frame as $W' = w'V'$, its total energy is [698]:

$$\tilde{E} = \Gamma c^2 m + \frac{\hat{\gamma}\Gamma^2 - \hat{\gamma} + 1}{\Gamma} W' = \Gamma c^2 m + \Gamma_{\rm eff} W' \,, \tag{B.7}$$

where m is the mass of the slow shell given by Eq. 8.7. Furthermore, the effective Lorentz factor of the slow shell $\Gamma_{\rm eff}$ in Eq. B.7 is

$$\Gamma_{\rm eff} = \frac{\hat{\gamma}\Gamma^2 - \hat{\gamma} + 1}{\Gamma} \simeq \hat{\gamma}\Gamma = \frac{4}{3}\Gamma \,, \tag{B.8}$$

where we have done the approximation $\Gamma \gg 1$ (valid in the time window we are looking at) and the relativistic $\hat{\gamma} = 4/3$ has been adopted.

Similarly, taking the $(\mu = 1, \nu = 0)$ component in Eq. B.5, the 4-momentum density of the slow shell at a fixed time t is

$$\tilde{T}^{10} = \Gamma^2 \frac{\tilde{v}^1}{c} (\rho' c^2 + w' + p') \,, \tag{B.9}$$

where $\eta^{10} = 0$. The 1-st component of the total momentum of the slow shell is $\tilde{P}^1 = 1/c \int_{\tilde{V}} \tilde{T}^{10} d\tilde{V}$, from which:

$$\tilde{P} = c\Gamma\beta \left(m + \hat{\gamma} \frac{W'}{c^2} \right) = c\sqrt{\Gamma^2 - 1} \left(m + \frac{\hat{\gamma} W'}{c^2} \right) \,. \tag{B.10}$$

Equations B.7 and B.10 represent the energy and momentum of the slow shell.

If the second shell is emitted with energy $\tilde{E}_f$ and Lorentz factor $\Gamma_f = $ const., its mass is $m_f = \tilde{E}_f/(\Gamma_f c^2)$. The fast shell is cold, since it propagates freely, thus its energy and momentum are

$$\tilde{E}_f = \Gamma_f m_f c^2 \;\; \text{and} \;\; \tilde{P}_f = c m_f \sqrt{\Gamma_f^2 - 1} \,. \tag{B.11}$$

In order to obtain the Lorentz factor and energy of the resulting merged shell right after the collision, we impose energy and momentum conservation:

$$\tilde{T}_f^{00} \tilde{V}_f + \tilde{T}^{00} \tilde{V} = \tilde{T}_m^{00} \tilde{V}_m^0 \,; \tag{B.12}$$

$$\tilde{T}_f^{i0} \tilde{V}_f + \tilde{T}^{10} \tilde{V} = \tilde{T}_m^{10} \tilde{V}_m^0 \,, \tag{B.13}$$

being $\tilde{T}_m^{\mu\nu}$ the energy-momentum tensor of the merged shell and $\tilde{V}_m^0$ its volume, both evaluated at the collision time. Hereafter, we denote all relevant quantities of the merged shell computed at the collision time with the

apex "0," in order to distinguish them from the ones describing its deceleration phase. Plugging Eqs. B.7-B.11 in Eq. B.12, we obtain:

$$\Gamma_f m_f + \Gamma m + \frac{\Gamma_{\rm eff} W'}{c^2} = \Gamma_m^0 m_m^0 + \frac{\Gamma_{m,\rm eff}^0 W_m'^0}{c^2} , \tag{B.14}$$

$$\sqrt{\Gamma_f^2 - 1} m_f + \sqrt{\Gamma^2 - 1}\left(m + \frac{\hat{\gamma} W'}{c^2}\right) = \sqrt{{\Gamma_m^0}^2 - 1}\left(m_m^0 + \frac{\hat{\gamma} W_m'^0}{c^2}\right) , \tag{B.15}$$

where Γ_m^0, $m_m^0 \equiv m + m_f$, $W_m'^0$ are the initial Lorentz factor, the initial mass and the comoving internal energy of the merged shell, respectively. $\Gamma_{m,\rm eff}^0$ is the effective Lorentz factor of the merged shell and is defined as in Eq. B.8 by replacing $\Gamma \rightarrow \Gamma_m^0$. Note that all the physical quantities of the merged shell are evaluated at the collision time, thus they describe its initial setup. Equations B.14 and B.15 have a simple solution in the relativistic case, i.e. for $\Gamma_f \gg 1$ and $\Gamma \gg 1$, which also implies $\Gamma_m^0 \gg 1$. Indeed, in this case $\Gamma_{\rm eff} \approx \hat{\gamma}\Gamma$ and $\Gamma_{m,\rm eff}^0 \approx \hat{\gamma}\Gamma_m^0$ so that we can rewrite Eqs. B.14 and B.15 as follows:

$$m_f \Gamma_f + \Gamma m_{\rm eff} = \Gamma_m^0 m_{m,\rm eff}^0 ; \tag{B.16}$$

$$m_f \sqrt{\Gamma_f^2 - 1} + m_{\rm eff}\sqrt{\Gamma^2 - 1} = m_{m,\rm eff}^0 \sqrt{{\Gamma_m^0}^2 - 1} , \tag{B.17}$$

where we have introduced the effective masses of the slow and merged shells: $m_{\rm eff} = m + \hat{\gamma} W'/c^2$ and $m_{m,\rm eff}^0 = m_m^0 + \hat{\gamma} W_m'^0/c^2$. After performing a Taylor expansion around $1/\Gamma_f$, $1/\Gamma$ and $1/\Gamma_m^0$ in Eq. B.16, we obtain the initial Lorentz factor of the merged shell:

$$\Gamma_m^0 \approx \sqrt{\frac{m_f \Gamma_f + m_{\rm eff}\Gamma}{m_f/\Gamma_f + m_{\rm eff}/\Gamma}} . \tag{B.18}$$

From energy conservation (Eq. B.16), we obtain the internal energy $\tilde{W}_m^0$ of the merged shell in the laboratory frame:

$$\tilde{W}_m^0 \equiv \Gamma_m^0 W_m'^0 = \frac{1}{\hat{\gamma}}\left[(m_f \Gamma_f + m\Gamma)c^2 - (m + m_f)\Gamma c^2\right] + \Gamma W' . \tag{B.19}$$

Equations B.18 and B.19 describe the initial conditions of the merged shell.

We assume that the shocks immediately cross the plasma. During the crossing, the resulting shell will be compressed, so that the correct expression of the initial width of the resulting merged shell is the one in Eq. 7 of Ref. [292]. In this paper, we make the simple assumption that its width is given by the sum of the widths of the slow shell $\tilde{l}$ and the fast shell $\tilde{l}_f$:

$$\tilde{l}_m^0 \simeq \tilde{l} + \tilde{l}_f . \tag{B.20}$$

This result differs from the one in Ref. [292] for a small numerical correction factor.

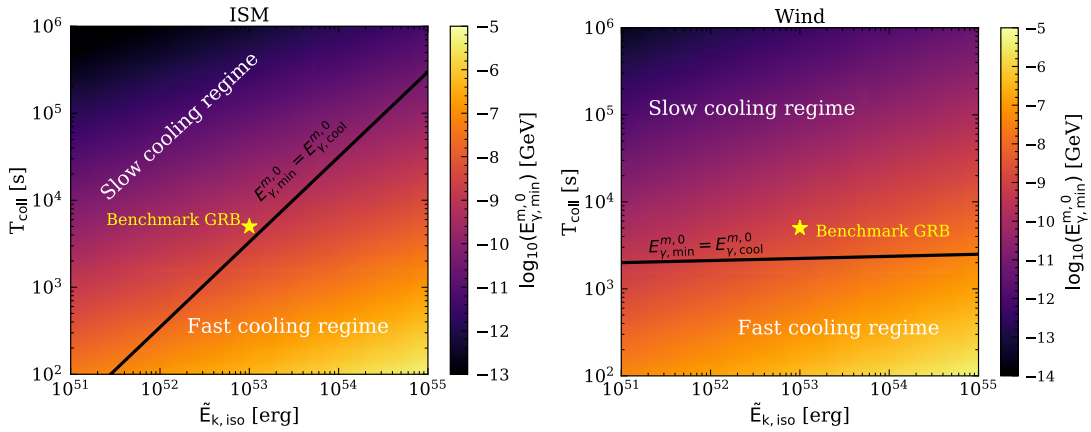

Figure 64: Contour plot of the minimum energy of the synchrotron photons emitted at the collision ($E^{m,0}_{\gamma,\rm min}$) in the plane spanned by ($\tilde{E}_{k,\rm iso}, T_{\rm coll}$), where $\tilde{E}_{k,\rm iso}$ is the isotropic kinetic energy of the slow shell and $T_{\rm coll}$ the collision time. The ISM (wind) scenario is shown on the left (right). The black solid line marks $E^{m,0}_{\gamma,\rm min} = E^{m,0}_{\gamma,\rm cool}$. For our set of parameters, electrons accelerated at the collision are in the slow cooling regime for the ISM and wind CBM scenarios.

After the merged shell forms, it interacts with the CBM. Even though in our model the merged shell is expected to produce a standard afterglow flux through its interaction with the CBM, its dynamics is slightly different from the one of the slow shell. This is because the merged shell is already hot and thus already has internal energy. Moreover, it also contains the matter material previously swept up by the slower shell. The total initial energy of the merged shell is:

$$\tilde{E}^0_{{\rm tot},m} \simeq \frac{4}{3}\tilde{W}^0_m + \Gamma^0_m m^0_m c^2 \ . \tag{B.21}$$

At the collision, a fraction $\epsilon^0_{e,m}$ of the internal energy $\tilde{W}^0_m$ goes into electrons and a fraction $\epsilon^0_{B,m}$ to the magnetic field. For our choice of parameters, electrons accelerated at the collision are in the slow cooling regime both in the ISM and wind scenarios, as shown in Fig. 64. Hence only a small fraction of electrons efficiently radiates, and all the internal energy $\tilde{W}^0_m$ stays in the merged shell. Nevertheless, it is worth stressing that even if the fast cooling condition should be satisfied and all the electrons should cool through synchrotron radiation, the fraction of energy carried away by photons is rather small ($\simeq$ 10–30% of the internal energy, depending on the assumptions on the microphysical parameter ϵ_e). Therefore, also in the fast cooling regime, most of the internal energy released at the collision stays in the merged shell as it is carried by protons which predominantly lose their energy via adiabatic cooling. Thus, the isotropic kinetic energy of the merged shell at the beginning of its deceleration is $\tilde{E}_{k,m} = \tilde{E}^0_{{\rm tot},m}$.

When the mass $m_{m,\rm swept}$ is swept up from the CBM by the expanding blastwave, conservation of energy reads as:

$$\Gamma_m^0\left(\frac{\tilde{E}_{k,m}}{\Gamma_m^0 c^2}\right) + m_{m,\rm swept} = \Gamma_m\left[\left(\frac{\tilde{E}_{k,m}}{\Gamma_m c^2}\right) + \hat{\gamma}\Gamma_m m_{m,\rm swept}\right], \tag{B.22}$$

where Γ_m is the Lorentz factor of the merged shell after the interaction with the medium and $m_{m,\rm swept}$ is the swept up mass dependent on the density profile of the external medium. The shell starts to be decelerated when the two terms on the right side of Eq. B.22 become comparable [107]:

$$m_{m,\rm swept} \simeq \frac{1}{\hat{\gamma}\Gamma_m}\left(\frac{\tilde{E}_{k,m}}{\Gamma_m^0 c^2}\right) \simeq \frac{1}{\Gamma_m^0}\left(\frac{\tilde{E}_{k,m}}{\Gamma_m^0 c^2}\right), \tag{B.23}$$

where we have considered that the Lorentz factor of the merged shell at the deceleration onset has been reduced to half of its initial value ($\Gamma_m \simeq \Gamma_0^m/2$) and we have neglected the numerical correction factor $2/3$.

By integrating the density profile between $R_{\rm coll} \equiv R(T_{\rm coll})$ and $R_{{\rm dec},m}$ and equating with Eq. B.23, we finally obtain:

$$\frac{4}{3}\pi n_0 m_p c^2 ({R_{{\rm dec},m}^{\rm ISM}}^3 - R_{\rm coll}^3) \simeq \frac{\tilde{E}_{k,m}}{{\Gamma_m^0}^2}, \tag{B.24}$$

$$4\pi A (R_{{\rm dec},m}^{\rm wind} - R_{\rm coll}) m_p c^2 \simeq \frac{\tilde{E}_{k,m}}{{\Gamma_m^0}^2}, \tag{B.25}$$

for the ISM and wind scenarios, respectively. Thus the deceleration radius for the merged shell is

$$R_{{\rm dec},m}^{\rm ISM} \simeq \left(\frac{3\tilde{E}_{k,m}}{8\pi n_0 m_p c^2 {\Gamma_m^0}^2} + R_{\rm coll}^3\right)^{1/3}, \tag{B.26}$$

$$R_{{\rm dec},m}^{\rm wind} \simeq \frac{\tilde{E}_{k,m}}{4\pi A m_p c^2 {\Gamma_m^0}^2} + R_{\rm coll}\,. \tag{B.27}$$

Finally, the deceleration time of the merged shell is

$$T_{{\rm dec},m}^{\rm ISM,wind} \simeq \frac{R_{{\rm dec},m}^{\rm ISM,wind}(1+z)}{2{\Gamma_m^0}^2 c}\,. \tag{B.28}$$

From $T_{{\rm dec},m}^{\rm ISM,wind}$ on, the merged shell follows the standard BM solution. In particular, the temporal evolution of its Lorentz factor Γ_m is described by Eq. 8.3, by considering Eq. B.28 for the deceleration time and replacing $\Gamma_0 \rightarrow \Gamma_m^0$.

B.2 DEGENERACIES AMONG THE PARAMETERS CHARACTERISTIC OF THE MERGING SHELLS

The two shells in our model collide when their position relative to the central engine coincides, i.e. when $R(T_{\rm coll}) = R_f(T_{\rm coll})$ (see Eqs. 8.5 and 8.11) [365]:

$$\frac{8\Gamma^2 T_{\rm coll} c}{(1+z)} = \frac{2\Gamma_f^2 (T_{\rm coll} - \Delta_T) c}{(1+z)} \,. \tag{B.29}$$

The collision of the two shells entails degeneracies among the parameters characteristic of the merging shells. One of these degeneracies occurs between the Lorentz factor of the fast shell Γ_f and the time delay Δ_T relative to the emission time of the first shell. Indeed, from Eq. B.29:

$$\Gamma_f = 2\Gamma(T_{\rm coll}) \left(1 - \frac{\Delta_T}{T_{\rm coll}}\right)^{-1/2} , \tag{B.30}$$

i.e. a shell launched with a large Δ_T can reach the first slow shell at the same collision time $T_{\rm coll}$ of a shell launched with a smaller delay and smaller Γ_f. This degeneracy can be better understood by looking at the left panel of Fig. 65 for our benchmark GRB (see Table 1).

A shortcoming of our model is that it is not possible to distinguish between Γ_f and Δ_T, if no other information is available except for the amplitude of the optical jump. Perhaps, an analysis of the reverse shock may break this degeneracy, but it is out of the scope of this paper. Hence, in this work, we take $\Delta_T / T_{\rm coll} \ll 1$, meaning that the emission of the second shell would occur shortly after the explosion.

Another degeneracy in our model is in the definition of Γ (see Eqs. 8.3). The same value of Γ can be obtained for different $(\tilde{E}_{k,\rm iso}, n_0)$ pairs for the ISM scenario or $(\tilde{E}_k, A_\star)$ for the wind scenario. Once the collision time has been fixed, this results in the same value of Γ_m^0, as displayed in the right panel of Fig. 65 for the ISM case. Similar results are obtained in the case of a wind environment, by replacing $n_0 \to A_\star$ (results not shown here). We do not exclude any region of the parameter space in Fig. 65, since there are not observational constraints for the jump component. In principle, $\tilde{E}_{k,\rm iso}$ can be estimated from modeling the afterglow or by assuming that it is in the same order as $\tilde{E}_{\gamma,\rm iso}$, see e.g. [699].

Even though the same Γ and Γ_m^0 can be obtained at a fixed time for different values of the energy and density of the external environment, the degeneracy is not observable in the resulting spectrum. Indeed, there are other parameters (e.g. the break frequencies and magnetic field) that strictly depend on the density of the environment and thus allow to break this degeneracy—see Fig. 66 for the ISM scenario (similar conclusions hold for the wind scenario, results not shown here).

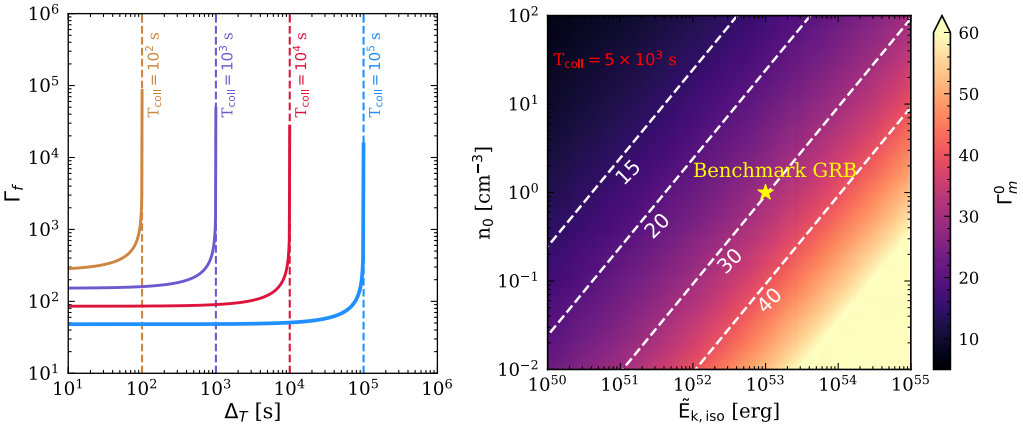

Figure 65: *Left:* Isocontours of $T_{\rm coll}$ in the plane spanned by Δ_T and Γ_f in the ISM scenario. The function Γ_f diverges when $\Delta_T \to T_{\rm coll}$. *Right:* Contour plot of Γ_m^0 in the plane spanned by $\tilde{E}_{k,\rm iso}$ and n_0 (ISM scenario) for $T_{\rm coll} = 5 \times 10^4$ s. The red dashed lines denote $\Gamma_m^0 = 15$, 20, 30, and 40. The yellow stars mark our benchmark GRB (Table 1). Similar results also hold for the wind case, both for the degeneracy between Γ_f and Δ_T and for Γ_m^0, by replacing $n_0 \to A_\star$.

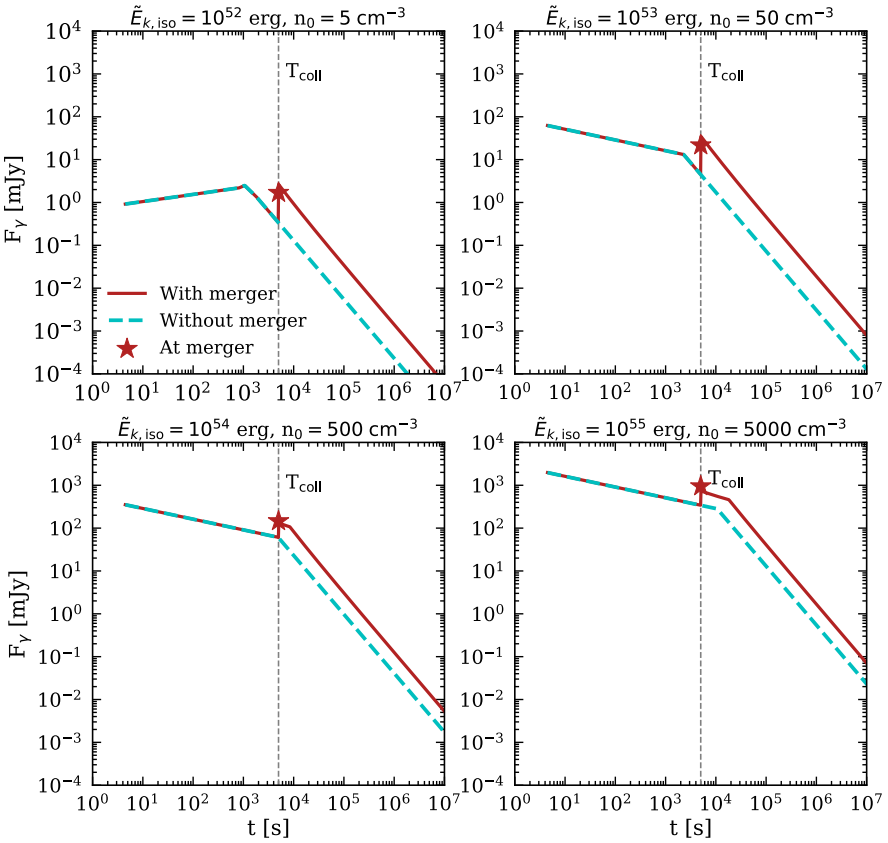

Figure 66: Light curves, generated from different $(\tilde{E}_{k,\rm iso}, n_0)$ pairs in the ISM scenario, with the same Γ_m^0 ($z = 1$ for all the panels). Each pair leads to a different light curve, both in the absence (cyan dashed line) and in the presence (brown solid line) of the shell merger. The flux at the optical jump (marked by a brown star) is different for each $(\tilde{E}_{k,\rm iso}, n_0)$ pair. Similar conclusions hold for the wind scenario.

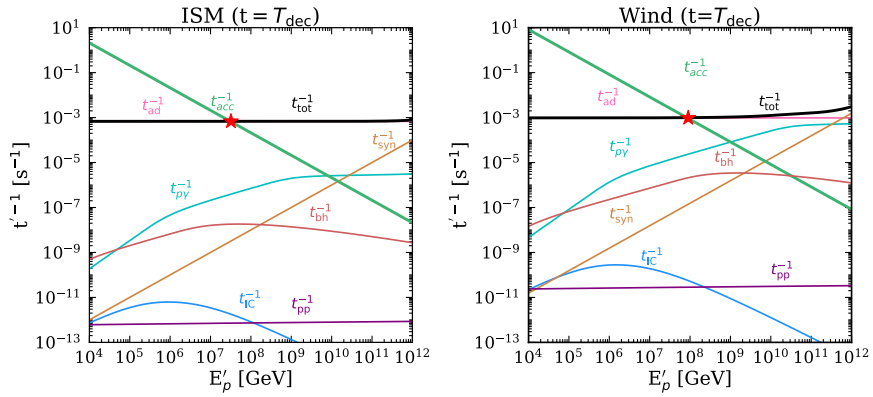

Figure 67: Inverse cooling timescales of protons as functions of the comoving proton energy at the deceleration time T_{dec} for our benchmark GRB (Table 1) placed at $z = 1$ in the ISM (left panel) and wind (right panel) scenarios . The red star marks the maximum energy up to which protons can be accelerated. The main cooling process for the ISM scenario is the adiabatic one; for the wind scenario, adiabatic cooling dominates at lower energies, while synchrotron and the $p\gamma$ interactions become important at higher energies.

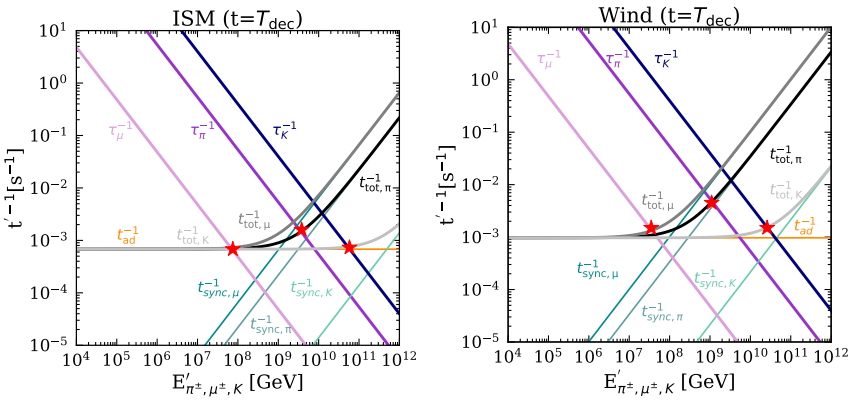

Figure 68: Same as Fig. 67 but for $\pi^\pm$, $\mu^\pm$, and $K^\pm$. For the ISM scenario, adiabatic cooling is the most important process for kaons and muons, while synchrotron losses are important for pions. For the wind scenario, both synchrotron and adiabatic cooling are relevant for pions and muons. In both scenarios, the cooling of kaons occurs at energies larger than the maximum proton energy $E'_{p,\max}$; thus, their cooling is negligible.

B.3 COOLING TIMESCALES OF PROTONS AND MESONS

In order to compute the neutrino energy distributions, we need to take into account the main cooling processes for accelerated protons, $\pi^\pm$, $\mu^\pm$, and $K^\pm$. The proton inverse cooling timescales for our benchmark GRB (see Table 1) are shown in Fig. 67 at $t = T_{dec}$ for the ISM and wind scenarios. Both in the ISM scenario (left panel) and in the wind scenario (right panel), the main cooling process for protons is the adiabatic one, that defines $E'_{p,\max}$. The adiabatic timescale decreases with time, as a consequence of the fact that Γ of the shell decreases, while its radius increases. Concerning the $\pi^\pm, \mu^\pm, K^\pm$, the cooling time scales for the slow shell at $t = T_{dec}$ are shown in Fig.68. For the ISM scenario, adiabatic cooling can be important, yet not relevant, for muons at the onset of the deceleration. Pions and kaons, instead, are expected to cool at energies larger than

the maximum proton energy. Thus, their cooling does not affect the resulting neutrino energy distribution. For the wind case, the cooling timescales of mesons at $t = T_{\rm dec}$ are shown in Fig. 68. In this scenario, muons cool at energies lower than the maximum energy of protons, affecting the neutrino energy distribution. For our benchmark GRB, kaons always cool at energies that are higher than the maximum proton energy. Thus, their contribution is negligible. In both scenarios, the cooling of secondary particles becomes less relevant at larger times and it does not affect the shape of the resulting neutrino distribution.

C

VERY HIGH ENERGY GRB AFTERGLOW

C.1 PHOTON ENERGY DISTRIBUTION

The total distribution of target photons is

$$n'^{\rm tot}_{\gamma}(E'_{\gamma}) = n'^{\rm sync}_{\gamma}(E'_{\gamma}) + n'^{\rm VHE}_{\gamma}(E'_{\gamma}) \,, \tag{C.1}$$

where $n'^{\rm sync}_{\gamma}$ is the synchrotron component defined in Eqs. 9.12 (including SSC corrections, see [109]) and 9.13 and $n'^{\rm VHE}_{\gamma}$ is the VHE part of the photon energy distribution.

We model the VHE component of the photon spectrum both with SSC radiatio. The SSC component is obtained by following the prescription in [110]. We include the Klein-Nishina regime by introducing a cut-off in the photon spectrum at the Klein-Nishina energy [479]. The latter, can be expressed as [479]:.

$$E_{\rm KN} = \begin{cases} 0.3 \text{ TeV } 6 \frac{k_e - 2}{k_e - 1} \text{"}_{e,-1} E_{54}^{1/4} n_{-1}^{-1/4} t_2^{-3/4} & \text{fl}_{\rm min} > \text{fl}_{\rm cool} \\ 0.1 \text{ TeV} \frac{1}{1+Y} \text{"}_{B,-2}^{-1} E_{54}^{-1/4} n_{-1}^{-3/4} t_{10\text{ hr}}^{-1/4} & \text{fl}_{\rm min} < \text{fl}_{\rm cool} \,, \end{cases} \tag{C.2}$$

where Y is the Compton parameter [109], $\gamma_{\rm min}$ is given by Eq. 9.8, while $\gamma_{\rm cool}$ is given by dividing Eq. 9.9 by $1+Y$ [109]. We are using the notation $X_y = X/10^y$. Therefore, the cutoff $E_{\rm KN}$ varies over time and is usually larger at the onset of the afterglow. This is a good approximation, since the VHE photons predominantly interact with low-energy protons, and the neutrinos produced in these interactions do not affect substantially the high-energy neutrino signal.

C.2 HADRONIC INTERACTIONS

Because of the relatively small baryon density, pp interactions are subleading during the afterglow and only efficient in the innermost regions of the outflow [228–230]. Hence, the main channels for neutrino production are

$$p + \gamma \quad \rightarrow \quad \Delta \rightarrow n + \pi^+, p + \pi^0 \tag{C.3}$$

$$p + \gamma \quad \rightarrow \quad K^+ + \Lambda/\Sigma \, . \tag{C.4}$$

Neutral pions decay into gamma-rays $\pi^0 \longrightarrow 2\gamma$, while neutrinos are produced through the charged pion decay $\pi^+ \longrightarrow \nu_\mu + \mu^+$ followed by $\mu^+ \longrightarrow \bar{\nu}_\mu + \nu_e + e^+$, and through $n \rightarrow p + e^- + \bar{\nu}_e$. Antineutrinos are also produced in the corresponding antiparticle channels; however, in this work, we do not distinguish between particle and antiparticles.

C.2.1 *Proton energy distribution*

Protons are assumed to be accelerated together with electrons at the forward shock driven by the blastwave in the cold CBM. Their comoving energy distribution is assumed to be [in units of GeV^{-1} cm^{-3}]

$$n'_p(E'_p) = A'_p E_p^{'-k_p} \exp\left[-\left(\frac{E'_p}{E'_{p,\mathrm{max}}}\right)^{\alpha_p}\right] \Theta(E'_p - E'_{p,\mathrm{min}}) \, , \tag{C.5}$$

where Θ is the Heaviside function, $E'_{p,\mathrm{min}} = \Gamma m_p c^2$ [226, 372, 373] is the minimum energy of accelerated protons and E'_{max} is the maximum energy at which protons can be accelerated. The latter is fixed by equating the acceleration time scale of protons with their total cooling time, which takes into account all the energy loss mechanisms for accelerated protons. We refer the interested reader to Sec. 4 of [233] for a detailed discussion.

Finally, $A'_p = \varepsilon_p \xi_p u' [\int_{E'_{p,\mathrm{min}}}^{E'_{p,\mathrm{max}}} dE'_p E'_p n'_p(E'_p)]^{-1}$ is the normalization constant. Here, u' is the blastwave energy density defined in Eq. 9.6, $\varepsilon_p \lesssim 1 - \varepsilon_e - \varepsilon_B$ is the fraction of this energy which is stored into accelerated protons and ξ_p is the fraction of accelerated protons.

The proton spectral index k_p depends on the model invoked for particle acceleration. It is expected to be $k_p \simeq 2$ [398] in the non-relativistic shock diffusive acceleration theory, while $k_p \simeq 2.2$ is expected from

Monte-Carlo simulations of ultra-relativistic shocks [85]. The constant $\alpha_p = 2$ mimics the exponential cutoff in the photon energy distribution [115].

C.3 ADDITIONAL CONSTRAINTS ON THE PROPERTIES OF THE CIRCUMBURST MEDIUM

Both the range of $\tilde{E}_{k,\rm iso}$ allowed by the arguments in Sec. 9.4.2 and the CBM density could span several orders of magnitude. A priori, it is not obvious whether our sample of VHE bursts (despite being based on a small number of bursts) shares common properties in terms of CMB densities with other GRBs without observed VHE emission.

[493] performed a scan of the parameter space allowed for the blastwave isotropic energy and the CBM density for a selected set of GRBs not detected in the VHE regime. We stress that, in this appendix, we assume that our sample of VHE GRBs (Table 3) can be modelled by relying on the same assumptions as in [493] for the microphysical parameters. We also include GRB 130427A observed at $z = 0.34$, with $\tilde{E}_{\gamma,\rm iso} \simeq 8 \times 10^{53}$ erg [700, 701]. Even though this burst has not been detected in the TeV range, it has been observed by *Fermi*-LAT during the afterglow phase, with photons up to $O(10)$ GeV about 9 hours after the trigger [701]. Being among the most investigated events of this class, we consider GRB 130427A as representative of the HE sample observed by *Fermi*-LAT [166].

In light of the existing uncertainties on the microphysical parameters and in order to enable a comparison with the standard bursts of [493] and the VHE ones considered in this work, we relax the values of the microphysical parameters considered in the main text and in Fig. 46. Our goal is to assess whether particular properties are preferred by GRBs emitting VHE photons with respect to standard GRBs.

Once the CBM type is fixed (ISM or wind), following [493], we focus at 11 hours (as measured on Earth) after the trigger of the burst. At this time, two scenarios are possible: either $\nu_R < \nu_{\gamma,\rm cool} < \nu_X$ or $\nu_X < \nu_{\gamma,\rm cool}$, where ν_R and ν_X are the observed effective frequencies in the optical R and X-ray bands, respectively. In the former case, we can infer the properties of the blastwave responsible for the afterglow emission [383, 472, 493]:

$$\frac{\Phi_R^{\rm obs}}{\Phi_X^{\rm obs}} = \left(\frac{\nu_R}{\nu_X}\right)^{-k_e/2} \nu_R^{1/2} \nu_{\gamma,\rm cool}^{-1/2} \,, \tag{C.6}$$

Table 14: Temporal optical index α_O obtained for the three considered VHE bursts and GRB 130427A, with relative References.

Burst	α_O	References
GRB 180720B	1.2	[470]
GRB 190114C	0.76	[476]
GRB 221009A	0.52	[464]
GRB 130427A	1.36	[377]

where $\Phi_R^{\rm obs}$ and $\Phi_X^{\rm obs}$ are the fluxes observed at 11 hours in the R and X-ray bands, respectively [both in units erg cm^{-2} s^{-1}]. By replacing $\nu_{\gamma,\rm cool}$ in Eq. C.6 with Eq. 9.11, we obtain a relation between $\tilde{E}_{k,\rm iso}$ and n_0 or $A/(3\times10^{35})$.

If $\nu_X < \nu_{\gamma,\rm cool}$, the blastwave parameters can be inferred from the flux observed in the R band. Plugging $\Phi_{\nu,R}^{\rm obs}$ in the left hand side of Eq. 9.15 and evaluating the right hand side of Eq. 9.15 at $\nu_\gamma \equiv \nu_R$ provides us with a relation between $\tilde{E}_{k,\rm iso}$ and n_0 $[A/(3\times10^{35})]$ [383, 472]; see also Eqs. 6–7 in [493].

The flux in the R band is obtained by converting the AB magnitude through the following relation [702]:

$$m_{\rm AB} = -2.5\log_{10}\left(\frac{\Phi_{\nu,R}^{\rm obs}}{3631}\right), \tag{C.7}$$

where $\Phi_{\nu,R}^{\rm obs}$ is the observed flux [in units of Jy]. The AB magnitudes are extracted from the [703]. The flux at 11 hours is extrapolated by evolving $\Phi_{\nu,R}^{\rm obs} \propto t^{-\alpha_O}$, with α_O being the temporal spectral index in the optical band reported in Table 14. Note that these values do not include the intrinsic host galaxy extinction; hence, the value of $\Phi_{\nu,R}^{\rm obs}$ that we use is a lower limit of the real flux. We warn the reader that the value of α_O obtained for GRB 190114C from the standard closure relations and reported in Table 14 does not reproduce the optical lightcurve and the spectral energy distribution simultaneously and satisfactorily. This hints that the standard afterglow model may not be adequate to model this GRB. Time-varying microphysical parameters might be more appropriate for this burst [462]; in this case our results would no longer hold.

We fix the electron spectral index (k_e) as indicated in Table 3. In particular, for GRB 190114C we fix the value $k_e = 2.2$, while we checked that the results are not very sensitive to the variation of k_e. Furthermore, we assume that the isotropic energy left in the blastwave after the prompt emission is $\tilde{E}_{k,\rm iso} \equiv \tilde{E}_{\gamma,\rm iso}$ [493]. This implies a prompt efficiency of $\approx 50\%$, which might be optimistic [478] and should be rather interpreted as a lower limit on $\tilde{E}_{k,\rm iso}$.

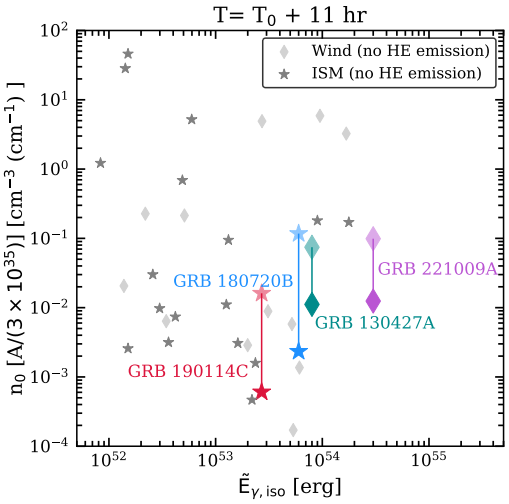

Figure 69: VHE GRBs in Table 3 (each distinguished by a different color) in the plane spanned by the isotropic gamma-ray energy $\tilde{E}_{\gamma,\mathrm{iso}}$ and CBM density [n_0 or A/(3×10^{35})]. Following [493], we fix $\tilde{E}_{k,\mathrm{iso}} = \tilde{E}_{\gamma,\mathrm{iso}}$, $\varepsilon_e = 0.1$ and $\varepsilon_B = 10^{-4}$–10^{-5} for the lower (opaque markers) and upper limits (shadowed markers), respectively. The stars denote bursts occurring in an ISM, while the diamonds correspond to bursts occurring in a wind-like CBM. The gray stars and diamonds correspond to the bursts analyzed in [493] occurring in an ISM and a wind-like CBM, respectively, for $\varepsilon_e = 10^{-1}$ and $\varepsilon_B = 10^{-4}$. The VHE GRBs in our sample favor low density CBM, for ε_B compatible with the SSC model; see main text for details.

In both the aforementioned regimes, the microphysical parameters ε_e and ε_B should be fixed. [493] assumes $\varepsilon_e = 0.1$ and $\varepsilon_B = 10^{-1}$–10^{-4} for all GRBs in their sample, and they conclude that $\varepsilon_B \simeq 10^{-4}$ is preferred to avoid unphysical values of the CBM density. The parameters $\varepsilon_e = 0.1$ and $\varepsilon_B = 10^{-5}$–10^{-4} are also consistent with the typical values required for modelling the VHE emission through the SSC mechanism [e.g. 492]. We first rely on the same choice of the microphysical parameters of [493] to favor a direct comparison between the properties of the VHE bursts and the standard ones and, to this purpose, we use $\varepsilon_e = 0.1$ and $\varepsilon_B = 10^{-2}$–10^{-4}. Then, we assume $\varepsilon_B = 10^{-5}$, while keeping $\varepsilon_e = 0.1$, since this value is allowed in the context of the SSC model. This procedure allows us to obtain upper and lower limits for the CBM densities for the two underlying mechanisms.

Figure 69 summarizes our findings for $\varepsilon_B = 10^{-5}$–10^{-4}. We include GRB 130427A in the plot, as representative of the GRBs detected in the HE regime during the afterglow; see Sec. 9.2. The results obtained by adopting $\varepsilon_B = 10^{-4}$ can be directly compared to the ones of [493], as shown in Fig. 69 (gray markers). Intriguingly, the bursts detected in the VHE regime cluster in the region of the parameter space corresponding to large isotropic energy emitted in gamma-rays and relatively small CBM densities [$10^{-3} \lesssim n_0 \lesssim 10^{-1}$ and $10^{-5} \lesssim A/(3\times10^{35}) \lesssim 10^{-1}$], consistently with our findings displayed in Fig. 46.

The case with $\varepsilon_B = 10^{-5}$ cannot be compared with the results in [493] directly. Nevertheless, we consider it as representative of the SSC model [492]: since $n_0 \propto \varepsilon_B^{-(k_e+1)/2}$ [$A \propto \varepsilon_B^{-(k_e+1)/4}$], we expect the density to increase as ε_B decreases, while keeping fixed $\tilde{E}_{k,\rm iso}$. It is worth noticing that decreasing ε_e implies an increase in the CBM density, because $n_0 \propto \varepsilon_e^{(1-k_e)/2}$ [$A \propto \varepsilon_e^{(1-k_e)}$], for the ISM [wind] scenario. For example, for $\varepsilon_e = 10^{-2}$ and $\varepsilon_B = 10^{-2}$, one obtains results similar to the lower limits in Fig. 46. On the contrary, assuming $\varepsilon_e = 10^{-2}$ and $\varepsilon_B = 10^{-4}$, shifts the points in Fig. 69 to larger densities, i.e. $n_0[A/(3\times10^{35})] \gtrsim 1$. Nevertheless, the multi-wavelength fits in the literature suggest $\varepsilon_e \simeq 0.1$. Hence, the densities obtained in Fig. 69 might be preferred.

We stress that the results in Fig. 69 cannot be directly compared to the ones in Fig. 46, since in the former we fix $\tilde{E}_{k,\rm iso} = \tilde{E}_{\gamma,\rm iso}$, while in the latter $\tilde{E}_{k,\rm iso}$ is a free parameter. In Fig. 46 the scaling of the CBM density with ε_e and ε_B is not trivial, since the isotropic kinetic energy is also changing with the other model parameters.

Note that, $10^{-3} \lesssim \varepsilon_B \lesssim 10^{-1}$ (with $\varepsilon_e = 10^{-1}$) leads to $10^{-8} \lesssim n\ [A/(3\times10^{35})] \lesssim 10^{-6}$, which is too low to be realistic [493]. This result might be biased by theoretical limitations of the closure relations and by the assumption $\xi_e = 1$. While the arguments in Sec. 9.4 are not constraining for GRB 180720B, we conclude from Fig. 69 that low densities might be preferred for VHE bursts for typical microphysical parameters consistent with a SSC scenario, as also found in [479].

D

LUMINOUS FAST BLUE OPTICAL TRANSIENTS APPENDIX

D.1 PROTON AND MESON COOLING TIMES

For the choked jet case the acceleration time scale of protons is

$$t'^{-1}_{\rm acc} = \frac{ceB'}{\xi E'_p} \ , \tag{D.1}$$

where $e = \sqrt{\hbar\alpha c}$ is the electric charge with $\alpha = 1/137$ being the fine structure constant and $\hbar$ is the reduced Planck constant. ξ defines the number of gyroradii needed for accelerating protons, and we assume $\xi = 10$ [390]. Finally, B' is the magnetic field generated at the internal shock, see main text.

For CSM interaction, the acceleration timescale is obtained in the Bohm limit [704]

$$t'^{-1}_{\rm acc} \simeq \frac{3eB'v^2_{\rm sh}}{20\gamma_p m_p c^3} \ , \tag{D.2}$$

where $B' \equiv \tilde{B}$ is the magnetic field in the shocked interacting shell, see main text. Protons accelerated at the

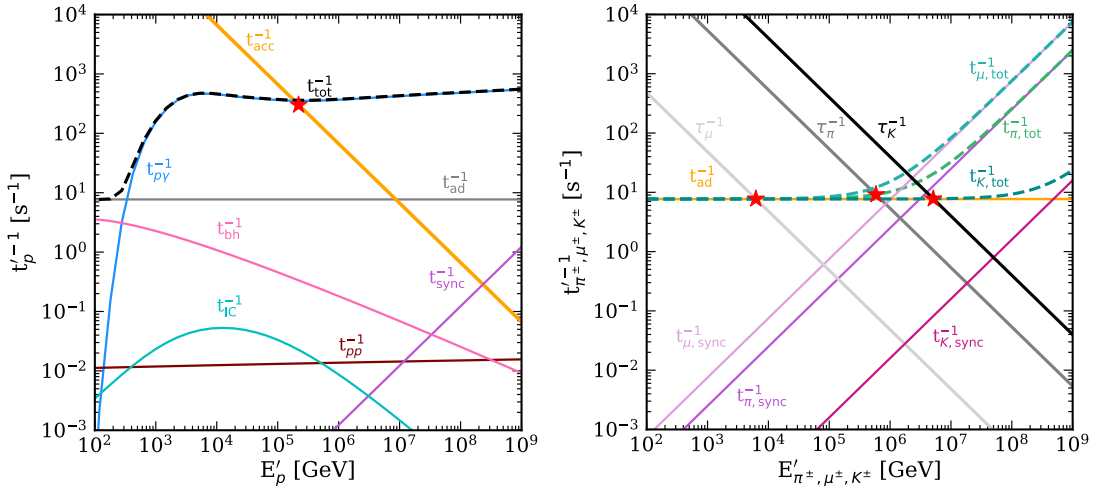

Figure 70: Cooling times of protons accelerated (left panel) and charged mesons (right panel) in the internal shock scenario as functions of the particle energy. Results are shown for $\tilde{L}_{\rm iso} = 5 \times 10^{49}$ erg s^{-1}, $\tilde{t}_j = 20$ s and $\Gamma = 100$. The total cooling time is plotted with a dashed black line. For protons, $p\gamma$ interactions are the most efficient energy loss mechanism and they define the maximum energy of accelerated protons, marked with a red star. For mesons, adiabatic losses are the only relevant energy loss mechanism. The maximum energy that mesons can achieve before decaying is marked by a red star.

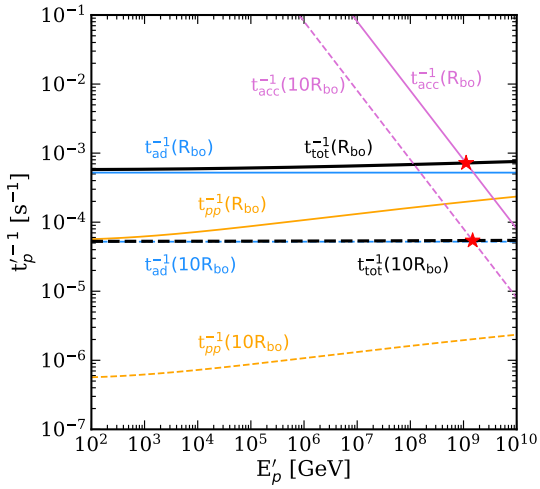

Figure 71: Cooling times of protons accelerated at the forward shock between the fast ejecta and the CSM as functions of the proton energy. We show the results at $R_{\rm bo}$ and $10 \times R_{\rm bo}$ for $v_{\rm ej} = 0.55c$, $M_{\rm ej} = 3.7 \times 10^{-2} M_\odot$ and $M_{\rm CSM} = 10^{-1} M_\odot$. Adiabatic cooling is the most important energy loss mechanism, while pp interactions are more competitive at the beginning of the evolution of the ejecta, but they rapidly drop. The red star marks the maximum energy that protons can reach in the shocked plasma shell.

shocks undergo several energy loss processes. The total cooling time is

$$t'^{-1}_{p,\rm cool} = t'^{-1}_{\rm ad} + t'^{-1}_{p,\rm sync} + t'^{-1}_{p\rm fl} + t'^{-1}_{pp} + t'^{-1}_{p,\rm BH} + t'^{-1}_{p,\rm IC} \,, \tag{D.3}$$

where $t'^{-1}_{\rm ad}$, $t'^{-1}_{p,\rm sync}$, $t'^{-1}_{p\gamma}$, t'^{-1}_{pp}, $t'^{-1}_{p,\rm BH}$, $t'^{-1}_{p,\rm IC}$ are the adiabatic, synchrotron, photo-hadronic ($p\gamma$), hadronic (pp), Bethe-Heitler (BH, $p\gamma \to pe^+e^-$) and inverse Compton (IC) cooling timescales, respectively.

These are defined as follows [103, 390, 399]:

$$t'^{-1}_{\rm ad} = \frac{v}{R} \,, \tag{D.4}$$

$$t'^{-1}_{p,\rm sync} = \frac{4\sigma_T m_e^2 E'_p B'^2}{3 m_p^4 c^3 8\pi} \,, \tag{D.5}$$

$$t'^{-1}_{p\gamma} = \frac{c}{2\gamma'^2_p} \int_{E_{\rm th}}^{\infty} dE'_\gamma \frac{n'_\gamma(E'_\gamma)}{E'^2_\gamma} \int_{E_{\rm th}}^{2\gamma'_p E'_\gamma} dE_r E_r \sigma_{p\gamma}(E_r) K_{p\gamma}(E_r) \,, \tag{D.6}$$

$$t'^{-1}_{pp} = c n'_p \sigma_{pp} K_{pp} \,, \tag{D.7}$$

$$t'^{-1}_{p,\rm BH} = \frac{7 m_e \alpha \sigma_T c}{9\sqrt{2}\pi m_p \gamma'^2_p} \int_{\gamma'^{-1}_p}^{\frac{E'_{\gamma,\rm max}}{m_e c^2}} d\epsilon' \frac{n'_\gamma(\epsilon')}{\epsilon'^2} \left\{ (2\gamma'_p \epsilon')^{3/2} \left[\ln(\gamma'_p \epsilon') - \frac{2}{3} \right] + \frac{2^{5/2}}{3} \right\} , \tag{D.8}$$

$$t'^{-1}_{p,\rm IC} = \frac{3(m_e c^2)^2 \sigma_T c}{16 \gamma'^2_p (\gamma'_p - 1) \beta'_p} \int_{E'_{\gamma,\rm min}}^{E'_{\gamma,\rm max}} \frac{dE'_\gamma}{E'^2_\gamma} F(E'_\gamma, \gamma'_p) n'_\gamma(E'_\gamma) \,, \tag{D.9}$$

where $v = 2c\Gamma$ for the choked jet and $v = v_{\rm sh}$ for CSM interactions, $\gamma_p = E'_p / m_p c^2$, $\epsilon' = E'_\gamma / m_e c^2$, $E_{\rm th} = 0.150$ GeV is the energy threshold for photo-pion production, and $\beta'_p \approx 1$ for relativistic particles. The function $F(E'_\gamma, \gamma'_p)$ follows the definition provided in [400], replacing $m_e \to m_p$. The cross sections for $p\gamma$

and pp interactions, $\sigma_{p\gamma}$ and σ_{pp}, can be found in [277]. The function $K_{p\gamma}(E_r)$ is the $p\gamma$ inelasticity, given by Eq. 9.9 of [103]:

$$K_{p\gamma}(E_r) = \begin{cases} 0.2 & E_{\rm th} < E_r < 1\ {\rm GeV} \\ 0.6 & E_r > 1\ {\rm GeV} \end{cases} \tag{D.10}$$

where $E_r = \gamma'_p E'_\gamma (1 - \beta'_p \cos\theta')$ is the relative energy between a proton with Lorentz factor γ'_p and a photon with energy E'_γ, whose directions form an angle θ' in the comoving frame of the interaction region. The comoving proton density is $n'_p = 4\tilde{L}_j/(4\pi R_{\rm IS}^2 c m_p c^3 \theta_j^2)$ for the choked jet, and $n'_p = \tilde{n}_p = 4 n_{p,{\rm CSM}} m_p c^2$ for CSM interaction. The inelasticity of pp interactions is $K_{pp} = 0.5$ and $n'_\gamma(E'_\gamma)$ is the photon target for accelerated protons.

At the internal shock, secondary charged mesons undergo energy losses before decaying; in turn, affecting the neutrino spectrum. In Fig. 70, we show an example obtained for $\tilde{L}_j = 2 \times 10^{47}$ erg s^{-1}, $\tilde{t}_j = 20$ s and $\Gamma = 100$. We note that, in the choked jet, $p\gamma$ interactions are the main energy loss channel for protons, while secondaries mainly cool through adiabatic losses. Kaons cool at energy much higher than the maximum proton energy, therefore their cooling does not affect the neutrino spectrum [238, 274–276].

As for CSM interaction, the only relevant cooling processes for protons are hadronic cooling (pp interactions) and adiabatic cooling. The photons produced at the external shock between the ejecta and the CSM have energies in the radio band, i.e. at low energies. Therefore interactions between protons and photons are negligible, consistently with [131, 298]. For CSM interaction, $t'^{-1}_{\rm cool} = t'^{-1}_{pp} + t'^{-1}_{\rm ad}$ (note that since shocks are non-relativistic, there is no difference between the comoving frame of the shock and the CO frame for CSM interaction). The proton cooling times are shown at $R_{\rm bo}$ and $10R_{\rm bo}$ in Fig. 71 for $v_{\rm ej} = 0.55c$, $M_{\rm ej} = 3.7 \times 10^{-2} M_\odot$ and $M_{\rm CSM} = 10^{-1} M_\odot$. We note that the pp interactions are more efficient at earlier times, though they are less important than adiabatic losses throughout the ejecta evolution, as expected because of the low densities of the CSM.

E

FOLLOW-UP SEARCHES APPENDIX

E.1 INTERACTION RATES OF ACCELERATED PROTONS

In this appendix we summarize the interaction rates of protons accelerated in the magnetar wind as well as at CSM interactions or in a jetted outflow.

E.1.1 *Magnetar wind*

The energy deposited by the spin down is partially deposited into kinetic energy of the outflow, with the remaining energy being used to produce thermal and non-thermal radiation. Therefore, protons accelerated in the magnetar wind interact through $p\gamma$ interactions both with thermal and non-thermal photons in the wind nebula. The corresponding interaction rates are [132]:

$$t_{p\gamma,\rm th}^{-1} = 7.7\times10^{-5} t_{5.5}^{-15/8} B_{14}^{-3/4} \beta_w^{-15/8} \ \rm s\ , \tag{E.1}$$

$$t_{p\gamma,\rm nth}^{-1} = 2.4\times10^{-5} t_{5.5}^{-27/8} B_{14}^{-7/4} \beta_w^{-19/8} \ \rm s\ , \tag{E.2}$$

where $\beta_w \simeq 1 M_{\rm ej,-2}^{-1/2} P_{\rm spin,-3}^{-1}$ is the wind velocity after its acceleration, at times $t \gg t_{\rm sd}$, where $t_{\rm sd}$ is the spin-down time defined as in Eq. 11.10.

The interaction rate for pp interactions is

$$t_{pp}^{-1} = 6.25\times10^{-9} M_{\rm ej,-2}^{-1} t_{5.5}^{3} \beta_w^{3} \ \rm s\ . \tag{E.3}$$

Pions are created in the wind nebula at a rate

$$t_{\pi,\rm cre}^{-1} = t_{p\gamma,\rm th}^{-1} + t_{p\gamma,\rm nth}^{-1} + t_{pp}^{-1}\ . \tag{E.4}$$

The only proton cooling process competing with pion production is the synchrotron cooling, whose characteristic time is

$$t_{p,\rm rad} = 5.6\times10^{-6} \eta_{-1}^{-1} t_{5.5}^{5} B_{14}^{3} \beta_w^{3} \epsilon_{B,-2}^{-1} \ \rm s. \tag{E.5}$$

Thus, pion creation in the wind nebula is suppressed by a factor

$$f_{\rm sup}^{p} = \min\left(1, \frac{t_{\rm ad}}{t_{\pi,\rm cre}}, \frac{t_{p,\rm rad}}{t_{\pi,\rm cre}}\right) \tag{E.6}$$

where $t_{\rm ad} \simeq R/\beta_w c$ is the adiabatic expansion time scale of the wind nebula.

The onset of neutrino production corresponds to the time when efficient photopion production starts, namely when $t_{p,\rm rad}^{-1} \equiv t_{\pi,\rm cre}^{-1}$. Similarly, neutrino production ends at the time when photopion processes are no longer efficient, i.e. $t_{\pi,\rm cre}^{-1} \equiv t_{\rm cross}^{-1}$.

Before decaying, secondary pions and muons also cool. Their cooling affects the neutrino signal through the following suppression factors:

$$f_{\rm sup}^{\pi} = 0.3\eta_{-1}^{-2} B_{14}^{4} \epsilon_{B,-2}^{-1} t_{5.5}^{6} \,, \tag{E.7}$$

$$f_{\rm sup}^{\mu} = 1.5\times10^{-3} \eta_{-1}^{-2} B_{14}^{4} \beta_w^{3} \epsilon_{B,-2}^{-1} t_{5.5}^{6} \,. \tag{E.8}$$

E.1.2 *CSM interactions and jets*

In the case of non-relativistic and mildly relativistic shocks—such as the external shock driven by the outflow as it expands in the CSM—the proton acceleration rate is obtained from the Bohm limit [704]

$$t_{\rm acc}^{\prime -1} \simeq \frac{3eBv_{\rm sh}^{2}}{20\gamma_p m_p c^{3}} \,, \tag{E.9}$$

where $e = \sqrt{\hbar\alpha c}$ is the elementary electric charge, $\alpha = 1/137$ is the fine structure constant and $\hbar$ is the reduced Planck constant; for non-relativistic shocks, the comoving frame of the outflow and the center of explosion frame coincide—we carry out the calculations in the comoving frame of the outflow and we denote quantities with X'. The magnetic field B is defined as in Sec. 11.2 and γ_p is the proton Lorentz factor.

In the case of relativistic and mildly relativistic outflows, the proton acceleration rate is

$$t_{\rm acc}^{\prime -1} = \frac{ceB'}{\xi E_p'} \,, \tag{E.10}$$

where ξ represents the number of gyroradii needed for accelerating protons. We assume $\xi = 10$ [390]. Finally, B' is the magnetic field along the jet, which depends on the energy dissipation mechanism [231].

The total cooling rate of accelerated protons is

$$t_{p,\rm cool}^{\prime -1} = t_{\rm ad}^{\prime -1} + t_{p,\rm sync}^{\prime -1} + t_{p\rm fl}^{\prime -1} + t_{pp}^{\prime -1} + t_{p,\rm BH}^{\prime -1} + t_{p,\rm IC}^{\prime -1} \,, \tag{E.11}$$

where $t'^{-1}_{\rm ad}$, $t'^{-1}_{p,\rm sync}$, $t'^{-1}_{p\gamma}$, t'^{-1}_{pp}, $t'^{-1}_{p,\rm BH}$, $t'^{-1}_{p,\rm IC}$ are the adiabatic, synchrotron, photo-hadronic ($p\gamma$), hadronic (pp), Bethe-Heitler (BH, $p\gamma \to pe^+e^-$) and inverse Compton (IC) cooling rates, respectively, defined as follows [103, 390, 399]:

$$t'^{-1}_{\rm ad} = \frac{v}{R}\,, \tag{E.12}$$

$$t'^{-1}_{p,\rm sync} = \frac{4\sigma_T m_e^2 E'_p B'^2}{3m_p^4 c^3 8\pi}\,, \tag{E.13}$$

$$t'^{-1}_{p\gamma} = \frac{c}{2\gamma'^2_p}\int_{E_{\rm th}}^{\infty} dE'_\gamma \frac{n'_\gamma(E'_\gamma)}{E'^2_\gamma} \times \int_{E_{\rm th}}^{2\gamma'_p E'_\gamma} dE_r E_r \times \sigma_{p\gamma}(E_r) K_{p\gamma}(E_r)\,, \tag{E.14}$$

$$t'^{-1}_{pp} = cn'_p \sigma_{pp} K_{pp}\,, \tag{E.15}$$

$$t'^{-1}_{p,\rm BH} = \frac{7m_e \alpha \sigma_T c}{9\sqrt{2}\pi m_p \gamma'^2_p}\int_{\gamma'^{-1}_p}^{\frac{E'_{\gamma,\rm max}}{m_e c^2}} d\epsilon' \frac{n'_\gamma(\epsilon')}{\epsilon'^2} \times\left\{(2\gamma'_p\epsilon')^{3/2}\left[\ln(\gamma'_p\epsilon') - \frac{2}{3}\right] + \frac{2^{5/2}}{3}\right\}, \tag{E.16}$$

$$t'^{-1}_{p,\rm IC} = \frac{3(m_e c^2)^2 \sigma_T c}{16\gamma'^2_p(\gamma'_p - 1)\beta'_p}\int_{E'_{\gamma,\rm min}}^{E'_{\gamma,\rm max}} \frac{dE'_\gamma}{E'^2_\gamma} \times F(E'_\gamma, \gamma'_p) n'_\gamma(E'_\gamma)\,, \tag{E.17}$$

where $v = 2c\Gamma$ for the jetted outflow and $v = v_{\rm sh}$ for CSM interactions, $\gamma_p = E'_p/m_p c^2$ is the proton Lorentz factor, $\epsilon' = E'_\gamma/m_e c^2$, $E_{\rm th} = 0.150$ GeV is the energy threshold for photo-pion production, and $\beta'_p \approx 1$ for relativistic particles. The function $F(E'_\gamma, \gamma'_p)$ is defined in Ref. [400], with the replacement $m_e \to m_p$. The cross sections for $p\gamma$ and pp interactions, $\sigma_{p\gamma}$ and σ_{pp} are taken from Ref. [277]. The function $K_{p\gamma}(E_r)$ is the inelasticity of $p\gamma$ interactions defined in Eq. 9.9 of [103]:

$$K_{p\gamma}(E_r) = \begin{cases} 0.2 & E_{\rm th} < E_r < 1\ {\rm GeV} \\ 0.6 & E_r > 1\ {\rm GeV}\,, \end{cases} \tag{E.18}$$

with $E_r = \gamma'_p E'_\gamma(1 - \beta'_p \cos\theta')$ being the relative energy between a proton with Lorentz factor γ'_p and a photon with energy E'_γ, which move in the comoving frame of the interaction region along directions which form an angle θ'. The comoving proton density is $n'_p = E_{\rm iso}/(4\pi R_j^2 c t_j \Gamma^2)$ for the jetted outflow, and $n'_p = 4n_{p,\rm CSM} m_p c^2$ for CSM interaction. The inelasticity of pp interactions is $K_{pp} = 0.5$ and $n'_\gamma(E'_\gamma)$ is the photon target for accelerated protons, defined in the main text for the jetted and spherical outflow. Before decaying, also secondary pions and muons cool through synchrotron, adiabatic and hadronic energy losses. Their cooling rates are defined as for protons, but replacing $m_p \to m_x$, with m_x being the mass of the x secondary particle.

E.2 RADIATIVE SHOCKS

When the gas behind the shock immediately cools in a thin shell, the shocks are radiative. This happens when the CSM density is very large [298, 628]. Also in the radiative regime the dynamical timescale for the forward shock driven by the outflow in the optically thin CSM is $t_{\rm dyn} = R/v_{\rm sh}$.

When the forward shock breaks out from the dense CSM shell, bremmstrahlung becomes the leading mechanisms for photon production and electrons mainly cool through free-free emission. The timescale for this process reads

$$t_{\rm ff} = \frac{3 n_e k_B T_e}{2\Lambda_{\rm ff}(n_e, T_e)} \,, \tag{E.19}$$

where $\Lambda_{\rm ff}$ is the free-free cooling rate [705], $k_B T_e = 3/16 \mu_p m_p v_{\rm sh}^2$ is the post-shock temperature of the gas, with $\mu_p \simeq 0.62$ being the mean molecular weight for a fully-ionized gas. The post-shock electron density is $n_e = 4\rho_{\rm CSM} m_p/\mu_e$ and $\mu_e \simeq 1.18$. Finally, $L_{\rm sh} = 2\pi R_{\rm CSM}^2 \rho_{\rm CSM}(R_{\rm CSM}) v_{\rm sh}^3$ is the total kinetic shock power computed at the CSM edge.

BIBLIOGRAPHY

[1] Karl G. Jansky. “Radio Waves from Outside the Solar System”. In: *Nature* 132.3323 (July 1933), p. 66. DOI: 10.1038/132066a0.

[2] W. L. Kraushaar and G. W. Clark. “Search for Primary Cosmic Gamma Rays with the Satellite Explorer XI”. In: *Phys. Rev. Lett.* 8.3 (Feb. 1962), pp. 106–109. DOI: 10.1103/PhysRevLett.8.106.

[3] S. A. Rodney et al. “Two peculiar fast transients in a strongly lensed host galaxy”. In: *Nature Astronomy* 2 (Apr. 2018), pp. 324–333. DOI: 10.1038/s41550-018-0405-4. arXiv: 1707.02434 [astro-ph.GA].

[4] Victor F. Hess. “Über Beobachtungen der durchdringenden Strahlung bei sieben Freiballonfahrten”. In: *Phys. Z.* 13 (1912), pp. 1084–1091.

[5] John N. Bahcall and R. Davis. “Solar Neutrinos - a Scientific Puzzle”. In: *Science* 191 (1976), pp. 264–267. DOI: 10.1126/science.191.4224.264.

[6] R. M. Bionta et al. “Observation of a neutrino burst in coincidence with supernova 1987A in the Large Magellanic Cloud”. In: *Phys. Rev. Lett.* 58.14 (Apr. 1987), pp. 1494–1496. DOI: 10.1103/PhysRevLett.58.1494.

[7] K. Hirata et al. “Observation of a neutrino burst from the supernova SN1987A”. In: *Phys. Rev. Lett.* 58.14 (Apr. 1987), pp. 1490–1493. DOI: 10.1103/PhysRevLett.58.1490.

[8] M. G. Aartsen et al. “Evidence for High-Energy Extraterrestrial Neutrinos at the IceCube Detector”. In: *Science* 342 (2013), p. 1242856. DOI: 10.1126/science.1242856. arXiv: 1311.5238 [astro-ph.HE].

[9] B. P. Abbott et al. “Observation of Gravitational Waves from a Binary Black Hole Merger”. In: *Phys. Rev. Lett.* 116.6 (2016), p. 061102. DOI: 10.1103/PhysRevLett.116.061102. arXiv: 1602.03837 [gr-qc].

[10] Floyd W. Stecker and Tonia M. Venters. "Components of the Extragalactic Gamma Ray Background". In: *Astrophys. J.* 736 (2011), p. 40. DOI: 10.1088/0004-637X/736/1/40. arXiv: 1012.3678 [astro-ph.HE].

[11] Floyd W. Stecker, Sean T. Scully, and Matthew A. Malkan. "An Empirical Determination of the Intergalactic Background Light from UV to FIR Wavelengths Using FIR Deep Galaxy Surveys and the Gamma-ray Opacity of the Universe". In: *Astrophys. J.* 827.1 (2016). [Erratum: Astrophys.J. 863, 112 (2018)], p. 6. DOI: 10.3847/0004-637X/827/1/6. arXiv: 1605.01382 [astro-ph.HE].

[12] A. M. Hillas. "The Origin of Ultrahigh-Energy Cosmic Rays". In: *Ann. Rev. Astron. Astrophys.* 22 (1984), pp. 425–444. DOI: 10.1146/annurev.aa.22.090184.002233.

[13] M. G. Aartsen et al. "The IceCube Neutrino Observatory: Instrumentation and Online Systems". In: *JINST* 12.03 (2017), P03012. DOI: 10.1088/1748-0221/12/03/P03012. arXiv: 1612.05093 [astro-ph.IM].

[14] Guillem Megias Homar, Joshua M. Meyers, and Steven M. Kahn. "Prompt Detection of Fast Optical Bursts with the Vera C. Rubin Observatory". In: *Astrophys. J.* 950.1 (2023), p. 21. DOI: 10.3847/1538-4357/accb93. arXiv: 2303.02525 [astro-ph.HE].

[15] Y. Shvartzvald et al. "ULTRASAT: A wide-field time-domain UV space telescope". In: (Apr. 2023). arXiv: 2304.14482 [astro-ph.IM].

[16] M. G. Aartsen et al. "IceCube-Gen2: the window to the extreme Universe". In: *J. Phys. G* 48.6 (2021), p. 060501. DOI: 10.1088/1361-6471/abbd48. arXiv: 2008.04323 [astro-ph.HE].

[17] Jaime Álvarez-Muñiz et al. "The Giant Radio Array for Neutrino Detection (GRAND): Science and Design". In: *Sci. China Phys. Mech. Astron.* 63.1 (2020), p. 219501. DOI: 10.1007/s11433-018-9385-7. arXiv: 1810.09994 [astro-ph.HE].

[18] A. V. Olinto et al. "The POEMMA (Probe of Extreme Multi-Messenger Astrophysics) observatory". In: *JCAP* 06 (2021), p. 007. DOI: 10.1088/1475-7516/2021/06/007. arXiv: 2012.07945 [astro-ph.IM].

[19] Riccardo Giacconi et al. "Evidence for x Rays From Sources Outside the Solar System". In: *Phys. Rev. Lett.* 9 (1962), pp. 439–443. DOI: 10.1103/PhysRevLett.9.439.

[20] M. Ted Ressell and Michael S. Turner. "The Grand Unified Photon Spectrum: A Coherent View of the Diffuse Extragalactic Background Radiation". In: *Comments on Astrophysics* 14 (Jan. 1990), p. 323.

[21] Ruth Durrer. "The cosmic microwave background: the history of its experimental investigation and its significance for cosmology". In: *Class. Quant. Grav.* 32.12 (2015), p. 124007. DOI: 10.1088/0264-9381/32/12/124007. arXiv: 1506.01907 [astro-ph.CO].

[22] Asantha Cooray. "Extragalactic Background Light: Measurements and Applications". In: (Feb. 2016). arXiv: 1602.03512 [astro-ph.CO].

[23] Alessandro De Angelis, Giorgio Galanti, and Marco Roncadelli. "Transparency of the Universe to gamma rays". In: *Mon. Not. Roy. Astron. Soc.* 432 (2013), pp. 3245–3249. DOI: 10.1093/mnras/stt684. arXiv: 1302.6460 [astro-ph.HE].

[24] M. Tanabashi et al. "Review of Particle Physics". In: *Phys. Rev. D* 98.3 (2018), p. 030001. DOI: 10.1103/PhysRevD.98.030001.

[25] G. T. Zatsepin and V. A. Kuzmin. "Upper limit of the spectrum of cosmic rays". In: *JETP Lett.* 4 (1966), pp. 78–80.

[26] Kenneth Greisen. "End to the cosmic ray spectrum?" In: *Phys. Rev. Lett.* 16 (1966), pp. 748–750. DOI: 10.1103/PhysRevLett.16.748.

[27] W. Pauli. "Dear radioactive ladies and gentlemen". In: *Phys. Today* 31N9 (1978), p. 27.

[28] E. Fermi. "An attempt of a theory of beta radiation. 1." In: *Z. Phys.* 88 (1934), pp. 161–177. DOI: 10.1007/BF01351864.

[29] Frederick Reines and Clyde L. Cowan. "The neutrino". In: *Nature* 178 (1956), pp. 446–449. DOI: 10.1038/178446a0.

[30] K. S. Hirata et al. "Observation of a small atmospheric muon-neutrino / electron-neutrino ratio in Kamiokande". In: *Phys. Lett. B* 280 (1992), pp. 146–152. DOI: 10.1016/0370-2693(92)90788-6.

[31] Y. Fukuda et al. "Evidence for oscillation of atmospheric neutrinos". In: *Phys. Rev. Lett.* 81 (1998), pp. 1562–1567. DOI: 10.1103/PhysRevLett.81.1562. arXiv: hep-ex/9807003.

[32] Edoardo Vitagliano, Irene Tamborra, and Georg Raffelt. "Grand Unified Neutrino Spectrum at Earth: Sources and Spectral Components". In: *Rev. Mod. Phys.* 92 (2020), p. 45006. DOI: 10.1103/RevModPhys.92.045006. arXiv: 1910.11878 [astro-ph.HE].

[33] B. T. Cleveland et al. "Measurement of the solar electron neutrino flux with the Homestake chlorine detector". In: *Astrophys. J.* 496 (1998), pp. 505–526. DOI: 10.1086/305343.

[34] Francis Halzen and Spencer R. Klein. "IceCube: An Instrument for Neutrino Astronomy". In: *Rev. Sci. Instrum.* 81 (2010), p. 081101. DOI: 10.1063/1.3480478. arXiv: 1007.1247 [astro-ph.HE].

[35] M. G. Aartsen et al. "Time-Integrated Neutrino Source Searches with 10 Years of IceCube Data". In: *Phys. Rev. Lett.* 124.5 (2020), p. 051103. DOI: 10.1103/PhysRevLett.124.051103. arXiv: 1910.08488 [astro-ph.HE].

[36] P. Meszaros. "Astrophysical Sources of High Energy Neutrinos in the IceCube Era". In: *Ann. Rev. Nucl. Part. Sci.* 67 (2017), pp. 45–67. DOI: 10.1146/annurev-nucl-101916-123304. arXiv: 1708.03577 [astro-ph.HE].

[37] Markus Ahlers and Francis Halzen. "Opening a New Window onto the Universe with IceCube". In: *Prog. Part. Nucl. Phys.* 102 (2018), pp. 73–88. DOI: 10.1016/j.ppnp.2018.05.001. arXiv: 1805.11112 [astro-ph.HE].

[38] S. Hild et al. "Sensitivity Studies for Third-Generation Gravitational Wave Observatories". In: *Class. Quant. Grav.* 28 (2011), p. 094013. DOI: 10.1088/0264-9381/28/9/094013. arXiv: 1012.0908 [gr-qc].

[39] Pau Amaro-Seoane et al. "Laser Interferometer Space Antenna". In: *arXiv e-prints*, arXiv:1702.00786 (Feb. 2017), arXiv:1702.00786. DOI: 10.48550/arXiv.1702.00786. arXiv: 1702.00786 [astro-ph.IM].

[40] Gemma Janssen et al. "Gravitational wave astronomy with the SKA". In: *PoS* AASKA14 (2015). Ed. by Tyler L. Bourke et al., p. 037. DOI: 10.22323/1.215.0037. arXiv: 1501.00127 [astro-ph.IM].

[41] B. P. Abbott et al. "Gravitational Waves and Gamma-rays from a Binary Neutron Star Merger: GW170817 and GRB 170817A". In: *Astrophys. J. Lett.* 848.2 (2017), p. L13. DOI: 10.3847/2041-8213/aa920c. arXiv: 1710.05834 [astro-ph.HE].

[42] Y. Hayato et al. “Search for Neutrinos in Super-Kamiokande Associated with the GW170817 Neutron-star Merger”. In: *Astrophys. J. Lett.* 857.1 (2018), p. L4. DOI: 10.3847/2041-8213/aabaca. arXiv: 1802.04379 [astro-ph.HE].

[43] A. Albert et al. “Search for High-energy Neutrinos from Binary Neutron Star Merger GW170817 with ANTARES, IceCube, and the Pierre Auger Observatory”. In: *Astrophys. J. Lett.* 850.2 (2017), p. L35. DOI: 10.3847/2041-8213/aa9aed. arXiv: 1710.05839 [astro-ph.HE].

[44] R. Abbasi et al. “Evidence for neutrino emission from the nearby active galaxy NGC 1068”. In: *Science* 378.6619 (2022), pp. 538–543. DOI: 10.1126/science.abg3395. arXiv: 2211.09972 [astro-ph.HE].

[45] M. Ackermann et al. “GeV Observations of Star-forming Galaxies with the Fermi Large Area Telescope”. In: *Astrophys. J.* 755.2, 164 (Aug. 2012), p. 164. DOI: 10.1088/0004-637X/755/2/164. arXiv: 1206.1346 [astro-ph.HE].

[46] S. Abdollahi et al. “Fermi Large Area Telescope Fourth Source Catalog”. In: *Astrophys. J.* 247.1, 33 (Mar. 2020), p. 33. DOI: 10.3847/1538-4365/ab6bcb. arXiv: 1902.10045 [astro-ph.HE].

[47] Kohta Murase. “Hidden Hearts of Neutrino Active Galaxies”. In: *Astrophys. J. Lett.* 941.1 (2022), p. L17. DOI: 10.3847/2041-8213/aca53c. arXiv: 2211.04460 [astro-ph.HE].

[48] R. Abbasi et al. “Observation of high-energy neutrinos from the Galactic plane”. In: *Science* 380.6652 (2023), adc9818. DOI: 10.1126/science.adc9818. arXiv: 2307.04427 [astro-ph.HE].

[49] M. G. Aartsen et al. “Multimessenger observations of a flaring blazar coincident with high-energy neutrino IceCube-170922A”. In: *Science* 361.6398 (2018), eaat1378. DOI: 10.1126/science.aat1378. arXiv: 1807.08816 [astro-ph.HE].

[50] M. G. Aartsen et al. “Neutrino emission from the direction of the blazar TXS 0506+056 prior to the IceCube-170922A alert”. In: *Science* 361.6398 (2018), pp. 147–151. DOI: 10.1126/science.aat2890. arXiv: 1807.08794 [astro-ph.HE].

[51] IceCube Collaboration. “IceCube-211208A - IceCube observation of a high-energy neutrino candidate track-like event”. In: *GRB Coordinates Network* 31191 (Dec. 2021), p. 1.

[52] Zh. A. Dzhilkibaev, O. Suvorova, and Baikal-GVD Collaboration. "Baikal-GVD observation of a high-energy neutrino candidate event from the blazar PKS 0735+17 at the day of the IceCube-211208A neutrino alert from the same direction". In: *The Astronomer's Telegram* 15112 (Dec. 2021), p. 1.

[53] V. B. Petkov et al. "Baksan Underground Scintillation Telescope observation of a GeV neutrino candidate event at the time of a gamma-ray flare of the blazar PKS 0735+17, a possible source of coinciding IceCube and Baikal high-energy neutrinos". In: *The Astronomer's Telegram* 15143 (Dec. 2021), p. 1.

[54] F. Filippini et al. "Search for neutrino counterpart to the blazar PKS0735+178 potentially associated with IceCube-211208A and Baikal-GVD-211208A with the KM3NeT neutrino detectors." In: *The Astronomer's Telegram* 15290 (Mar. 2022), p. 1.

[55] Xavier Rodrigues et al. "Leptohadronic Blazar Models Applied to the 2014–2015 Flare of TXS 0506+056". In: *Astrophys. J. Lett.* 874.2 (2019), p. L29. DOI: 10.3847/2041-8213/ab1267. arXiv: 1812.05939 [astro-ph.HE].

[56] Maria Petropoulou et al. "Multi-Epoch Modeling of TXS 0506+056 and Implications for Long-Term High-Energy Neutrino Emission". In: *Astrophys. J.* 891 (2020), p. 115. DOI: 10.3847/1538-4357/ab76d0. arXiv: 1911.04010 [astro-ph.HE].

[57] Sargis Gasparyan, Damien Bégué, and Narek Sahakyan. "Time-dependent lepto-hadronic modelling of the emission from blazar jets with SOPRANO: the case of TXS 0506 + 056, 3HSP J095507.9 + 355101, and 3C 279". In: *Mon. Not. Roy. Astron. Soc.* 509.2 (2021), pp. 2102–2121. DOI: 10.1093/mnras/stab2688. arXiv: 2110.01549 [astro-ph.HE].

[58] I. Bartos et al. "The IceCube Pie Chart: Relative Source Contributions to the Cosmic Neutrino Flux". In: *Astrophys. J.* 921.1 (2021), p. 45. DOI: 10.3847/1538-4357/ac1c7b. arXiv: 2105.03792 [astro-ph.HE].

[59] Robert Stein et al. "A tidal disruption event coincident with a high-energy neutrino". In: *Nature Astron.* 5.5 (2021), pp. 510–518. DOI: 10.1038/s41550-020-01295-8. arXiv: 2005.05340 [astro-ph.HE].

[60] R. Chornock et al. “Transient Classification Report for 2019-06-15”. In: *Transient Name Server Classification Report* 2019-1016 (June 2019), p. 1.

[61] Sjoert van Velzen et al. “Establishing accretion flares from massive black holes as a major source of high-energy neutrinos”. In: (Nov. 2021). arXiv: 2111.09391 [astro-ph.HE].

[62] IceCube Collaboration. “IceCube-200530A - IceCube observation of a high-energy neutrino candidate event”. In: *GRB Coordinates Network* 27865 (May 2020), p. 1.

[63] Simeon Reusch et al. “IceCube-200530A: Candidate Counterparts from the Zwicky Transient Facility”. In: *GRB Coordinates Network* 27872 (May 2020), p. 1.

[64] L. Yan et al. “Spectroscopic Classifications of Eighteen Superluminous Supernovae from the Zwicky Transient Facility”. In: *Transient Name Server AstroNote* 45 (July 2019), p. 1.

[65] Tetyana Pitik et al. “Is the High-energy Neutrino Event IceCube-200530A Associated with a Hydrogen-rich Superluminous Supernova?” In: *Astrophys. J.* 929.2 (Oct. 2022), p. 163. DOI: 10.3847/1538-4357/ac5ab1. arXiv: 2110.06944 [astro-ph.HE].

[66] Erik Blaufuss. “AT2018cow: IceCube neutrino search”. In: *The Astronomer’s Telegram* 11785 (June 2018), p. 1.

[67] Jonathan Granot, Dafne Guetta, and Ramandeep Gill. “Lessons from the Short GRB 170817A: The First Gravitational-wave Detection of a Binary Neutron Star Merger”. In: *Astrophys. J. Lett.* 850.2 (2017), p. L24. DOI: 10.3847/2041-8213/aa991d. arXiv: 1710.06407 [astro-ph.HE].

[68] E. Troja et al. “A year in the life of GW 170817: the rise and fall of a structured jet from a binary neutron star merger”. In: *Mon. Not. Roy. Astron. Soc.* 489.2 (2019), pp. 1919–1926. DOI: 10.1093/mnras/stz2248. arXiv: 1808.06617 [astro-ph.HE].

[69] Iair Arcavi et al. “Optical emission from a kilonova following a gravitational-wave-detected neutron-star merger”. In: *Nature* 551 (2017), p. 64. DOI: 10.1038/nature24291. arXiv: 1710.05843 [astro-ph.HE].

[70] B. P. Abbott et al. “Multi-messenger Observations of a Binary Neutron Star Merger”. In: *Astrophys. J. Lett.* 848.2 (2017), p. L12. DOI: 10.3847/2041-8213/aa91c9. arXiv: 1710.05833 [astro-ph.HE].

[71] E. Pian et al. “Spectroscopic identification of r-process nucleosynthesis in a double neutron star merger”. In: *Nature* 551 (2017), pp. 67–70. DOI: 10.1038/nature24298. arXiv: 1710.05858 [astro-ph.HE].

[72] N. R. Tanvir et al. “The Emergence of a Lanthanide-Rich Kilonova Following the Merger of Two Neutron Stars”. In: *Astrophys. J. Lett.* 848.2 (2017), p. L27. DOI: 10.3847/2041-8213/aa90b6. arXiv: 1710.05455 [astro-ph.HE].

[73] Jillian C. Rastinejad et al. “A kilonova following a long-duration gamma-ray burst at 350 Mpc”. In: *Nature* 612.7939 (2022), pp. 223–227. DOI: 10.1038/s41586-022-05390-w. arXiv: 2204.10864 [astro-ph.HE].

[74] James H. Gillanders et al. “Heavy element nucleosynthesis associated with a gamma-ray burst”. In: (Aug. 2023). arXiv: 2308.00633 [astro-ph.HE].

[75] A. Marcowith et al. “The microphysics of collisionless shock waves”. In: *Rept. Prog. Phys.* 79 (2016), p. 046901. DOI: 10.1088/0034-4885/79/4/046901. arXiv: 1604.00318 [astro-ph.HE].

[76] Frank M. Rieger and Peter Duffy. “Shear acceleration in relativistic astrophysical jets”. In: *Astrophys. J.* 617 (2004), pp. 155–161. DOI: 10.1086/425167. arXiv: astro-ph/0410269.

[77] Dimitrios Giannios. “UHECRs from magnetic reconnection in relativistic jets”. In: *Mont. Notic. Roy. Astron. Soc.* 408.1 (Oct. 2010), pp. L46–L50. DOI: 10.1111/j.1745-3933.2010.00925.x. arXiv: 1007.1522 [astro-ph.HE].

[78] Enrico Fermi. “On the Origin of the Cosmic Radiation”. In: *Physical Review* 75.8 (Apr. 1949), pp. 1169–1174. DOI: 10.1103/PhysRev.75.1169.

[79] E. Fermi. “Galactic Magnetic Fields and the Origin of Cosmic Radiation.” In: *Astrophys. J.* 119 (Jan. 1954), p. 1. DOI: 10.1086/145789.

[80] Malcolm S. Longair. *High Energy Astrophysics*. 3rd ed. Cambridge University Press, 2011. DOI: 10.1017/CBO9780511778346.

[81] A. R. Bell. “The acceleration of cosmic rays in shock fronts - I.” In: *Mon. Not. Roy. Astron. Soc.* 182 (Jan. 1978), pp. 147–156. DOI: 10.1093/mnras/182.2.147.

[82] Yves A. Gallant and Abraham Achterberg. "Ultra-high-energy cosmic ray acceleration by relativistic blast waves". In: *Mon. Not. Roy. Astron. Soc.* 305 (1999), p. 6. DOI: 10.1046/j.1365-8711.1999.02566.x. arXiv: astro-ph/9812316.

[83] Martin Lemoine, Guy Pelletier, and Benoit Revenu. "On the efficiency of Fermi acceleration at relativistic shocks". In: *Astrophys. J. Lett.* 645 (2006), pp. L129–L132. DOI: 10.1086/506322. arXiv: astro-ph/0606005.

[84] Anatoly Spitkovsky. "Particle acceleration in relativistic collisionless shocks: Fermi process at last?" In: *Astrophys. J. Lett.* 682 (2008), p. L5. DOI: 10.1086/590248. arXiv: 0802.3216 [astro-ph].

[85] Lorenzo Sironi, Anatoly Spitkovsky, and Jonathan Arons. "The Maximum Energy of Accelerated Particles in Relativistic Collisionless Shocks". In: *Astrophys. J.* 771 (2013), p. 54. DOI: 10.1088/0004-637X/771/1/54. arXiv: 1301.5333 [astro-ph.HE].

[86] Martin Lemoine and Benoit Revenu. "Relativistic Fermi acceleration with shock compressed turbulence". In: *Mon. Not. Roy. Astron. Soc.* 366 (2006), pp. 635–644. DOI: 10.1111/j.1365-2966.2005.09912.x. arXiv: astro-ph/0510522.

[87] Eli Waxman and Abraham Loeb. "TeV neutrinos and GeV photons from shock breakout in supernovae". In: *Phys. Rev. Lett.* 87 (2001), p. 071101. DOI: 10.1103/PhysRevLett.87.071101. arXiv: astro-ph/0102317.

[88] Amir Levinson and Omer Bromberg. "Relativistic Photon Mediated Shocks". In: *Phys. Rev. Lett.* 100 (2008), p. 131101. DOI: 10.1103/PhysRevLett.100.131101. arXiv: 0711.3281 [astro-ph].

[89] Andrei M. Beloborodov. "Sub-photospheric shocks in relativistic explosions". In: *Astrophys. J.* 838.2 (2017), p. 125. DOI: 10.3847/1538-4357/aa5c8c. arXiv: 1604.02794 [astro-ph.HE].

[90] Masaaki Yamada. *Magnetic Reconnection. A Modern Synthesis of Theory, Experiment, and Observations*. 2022.

[91] P. A. Sweet. "The Neutral Point Theory of Solar Flares". In: *Electromagnetic Phenomena in Cosmical Physics*. Ed. by B. Lehnert. Vol. 6. Jan. 1958, p. 123.

[92] E. N. Parker. "The Solar-Flare Phenomenon and the Theory of Reconnection and Annihiliation of Magnetic Fields." In: *Astrophys. J.* 8 (July 1963), p. 177. DOI: 10.1086/190087.

[93] H. E. Petschek. "Magnetic Field Annihilation". In: *NASA Special Publication*. Vol. 50. 1964, p. 425.

[94] Masaaki Yamada, Russell Kulsrud, and Hantao Ji. "Magnetic reconnection". In: *Rev. Mod. Phys.* 82 (1 2010), pp. 603–664. DOI: 10.1103/RevModPhys.82.603. URL: https://link.aps.org/doi/10.1103/RevModPhys.82.603.

[95] Eric G. Blackman and George B. Field. "Kinematics of relativistic magnetic reconnection". In: *Phys. Rev. Let.* 72.4 (Jan. 1994), pp. 494–497. DOI: 10.1103/PhysRevLett.72.494.

[96] Dmitri A. Uzdensky. "Magnetic Reconnection in Extreme Astrophysical Environments". In: *SSR* 160.1-4 (Oct. 2011), pp. 45–71. DOI: 10.1007/s11214-011-9744-5. arXiv: 1101.2472 [astro-ph.HE].

[97] Lorenzo Sironi, Maria Petropoulou, and Dimitrios Giannios. "Relativistic Jets Shine through Shocks or Magnetic Reconnection?" In: *Mon. Not. Roy. Astron. Soc.* 450.1 (2015), pp. 183–191. DOI: 10.1093/mnras/stv641. arXiv: 1502.01021 [astro-ph.HE].

[98] Fan Guo et al. "Efficient Production of High-energy Nonthermal Particles During Magnetic Reconnection in a Magnetically Dominated Ion–electron Plasma". In: *Astrophys. J. Lett.* 818.1 (2016), p. L9. DOI: 10.3847/2041-8205/818/1/L9. arXiv: 1511.01434 [astro-ph.HE].

[99] G. R. Werner et al. "Non-thermal particle acceleration in collisionless relativistic electron–proton reconnection". In: *Mon. Not. Roy. Astron. Soc.* 473.4 (2018), pp. 4840–4861. DOI: 10.1093/mnras/stx2530. arXiv: 1612.04493 [astro-ph.HE].

[100] Lorenzo Sironi and Anatoly Spitkovsky. "Relativistic Reconnection: an Efficient Source of Non-Thermal Particles". In: *Astrophys. J. Lett.* 783 (2014), p. L21. DOI: 10.1088/2041-8205/783/1/L21. arXiv: 1401.5471 [astro-ph.HE].

[101] Fan Guo et al. "Formation of Hard Power-laws in the Energetic Particle Spectra Resulting from Relativistic Magnetic Reconnection". In: *Phys. Rev. Lett.* 113 (2014), p. 155005. DOI: 10.1103/PhysRevLett.113.155005. arXiv: 1405.4040 [astro-ph.HE].

[102] Maria Petropoulou et al. "Relativistic Magnetic Reconnection in Electron-Positron-Proton Plasmas: Implications for Jets of Active Galactic Nuclei". In: *Astrophys. J.* 880 (June 2019), p. 37. DOI: 10.3847/1538-4357/ab287a. arXiv: 1906.03297 [astro-ph.HE].

[103] Charles D. Dermer and Govind Menon. *High Energy Radiation from Black Holes: Gamma Rays, Cosmic Rays, and Neutrinos*. Princeton U. Pr., USA, 2009.

[104] Malcolm S. Longair. *High Energy Astrophysics*. 2011.

[105] Gabriele Ghisellini. *Radiative Processes in High Energy Astrophysics*. Vol. 873. 2013. DOI: 10.1007/978-3-319-00612-3.

[106] Damien Bégué and Asaf Pe'er. "Poynting flux dominated jets challenged by their photospheric emission". In: *Astrophys. J.* 802.2 (2015), p. 134. DOI: 10.1088/0004-637X/802/2/134. arXiv: 1410.2730 [astro-ph.HE].

[107] Bing Zhang. *The Physics of Gamma-Ray Bursts*. Cambridge University Press, UK, 2018. DOI: 10.1017/9781139226530.

[108] H. Abdalla et al. "Revealing x-ray and gamma ray temporal and spectral similarities in the GRB 190829A afterglow". In: *Science* 372.6546 (2021), pp. 1081–1085. DOI: 10.1126/science.abe8560. arXiv: 2106.02510 [astro-ph.HE].

[109] Re'em Sari and Ann A. Esin. "On the Synchrotron self-compton emission from relativistic shocks and its implications for gamma-ray burst afterglows". In: *Astrophys. J.* 548 (2001), pp. 787–799. DOI: 10.1086/319003. arXiv: astro-ph/0005253.

[110] He Gao et al. "Compton scattering of self-absorbed synchrotron emission". In: *Mon. Not. Roy. Astron. Soc.* 435.3 (Nov. 2013), pp. 2520–2531. DOI: 10.1093/mnras/stt1461. arXiv: 1204.1386 [astro-ph.HE].

[111] Leonel Morejon et al. "Improved photomeson model for interactions of cosmic ray nuclei". In: *JCAP* 11 (2019), p. 007. DOI: 10.1088/1475-7516/2019/11/007. arXiv: 1904.07999 [astro-ph.HE].

[112] R. Abbasi et al. "The IceCube high-energy starting event sample: Description and flux characterization with 7.5 years of data". In: *Phys. Rev. D* 104 (2021), p. 022002. DOI: 10.1103/PhysRevD.104.022002. arXiv: 2011.03545 [astro-ph.HE].

[113] M. Ackermann et al. "The spectrum of isotropic diffuse gamma-ray emission between 100 MeV and 820 GeV". In: *Astrophys. J.* 799 (2015), p. 86. DOI: 10.1088/0004-637X/799/1/86. arXiv: 1410.3696 [astro-ph.HE].

[114] Valerio Verzi. "Measurement of the energy spectrum of ultra-high energy cosmic rays using the Pierre Auger Observatory". In: *PoS* ICRC2019 (2020), p. 450. DOI: 10.22323/1.358.0450.

[115] S. Hümmer et al. “Simplified models for photohadronic interactions in cosmic accelerators”. In: *Astrophys. J.* 721 (2010), pp. 630–652. DOI: 10.1088/0004-637X/721/1/630. arXiv: 1002.1310 [astro-ph.HE].

[116] S. R. Kelner, Felex A. Aharonian, and V. V. Bugayov. “Energy spectra of gamma-rays, electrons and neutrinos produced at proton-proton interactions in the very high energy regime”. In: *Phys. Rev. D* 74 (2006). [Erratum: Phys.Rev.D 79, 039901 (2009)], p. 034018. DOI: 10.1103/PhysRevD.74.034018. arXiv: astro-ph/0606058.

[117] S. R. Kelner and F. A. Aharonian. “Energy spectra of gamma-rays, electrons and neutrinos produced at interactions of relativistic protons with low energy radiation”. In: *Phys. Rev. D* 78 (2008). [Erratum: Phys.Rev.D 82, 099901 (2010)], p. 034013. DOI: 10.1103/PhysRevD.82.099901. arXiv: 0803.0688 [astro-ph].

[118] A. Mucke et al. “SOPHIA: Monte Carlo simulations of photohadronic processes in astrophysics”. In: *Comput. Phys. Commun.* 124 (2000), pp. 290–314. DOI: 10.1016/S0010-4655(99)00446-4. arXiv: astro-ph/9903478.

[119] Klaus Werner, Fu-Ming Liu, and Tanguy Pierog. “Parton ladder splitting and the rapidity dependence of transverse momentum spectra in deuteron-gold collisions at RHIC”. In: *Phys. Rev. C* 74 (2006), p. 044902. DOI: 10.1103/PhysRevC.74.044902. arXiv: hep-ph/0506232.

[120] M. G. Aartsen et al. “Search for correlations between the arrival directions of IceCube neutrino events and ultrahigh-energy cosmic rays detected by the Pierre Auger Observatory and the Telescope Array”. In: *JCAP* 01 (2016), p. 037. DOI: 10.1088/1475-7516/2016/01/037. arXiv: 1511.09408 [astro-ph.HE].

[121] Eli Waxman and John N. Bahcall. “High-energy neutrinos from astrophysical sources: An Upper bound”. In: *Phys. Rev. D* 59 (1999), p. 023002. DOI: 10.1103/PhysRevD.59.023002. arXiv: hep-ph/9807282.

[122] Kohta Murase, Dafne Guetta, and Markus Ahlers. “Hidden Cosmic-Ray Accelerators as an Origin of TeV-PeV Cosmic Neutrinos”. In: *Phys. Rev. Lett.* 116.7 (2016), p. 071101. DOI: 10.1103/PhysRevLett.116.071101. arXiv: 1509.00805 [astro-ph.HE].

[123] Prantik Sarmah et al. “High energy particles from young supernovae: gamma-ray and neutrino connections”. In: *JCAP* 08.08 (Apr. 2022), p. 011. DOI: 10.1088/1475-7516/2022/08/011. arXiv: 2204.03663 [astro-ph.HE].

[124] Markus Ackermann et al. “Astrophysics Uniquely Enabled by Observations of High-Energy Cosmic Neutrinos”. In: *Bull. Am. Astron. Soc.* 51 (2019), p. 185. arXiv: 1903.04334 [astro-ph.HE].

[125] Philipp Mertsch, Mohamed Rameez, and Irene Tamborra. “Detection prospects for high energy neutrino sources from the anisotropic matter distribution in the local universe”. In: *JCAP* 03 (2017), p. 011. DOI: 10.1088/1475-7516/2017/03/011. arXiv: 1612.07311 [astro-ph.HE].

[126] Avishay Gal-Yam. “The Most Luminous Supernovae”. In: *Ann. Rev. Astron. Astrophys.* 57 (2019), pp. 305–333. DOI: 10.1146/annurev-astro-081817-051819. arXiv: 1812.01428 [astro-ph.HE].

[127] Hans-Thomas Janka. “Explosion Mechanisms of Core-Collapse Supernovae”. In: *Ann. Rev. Nucl. Part. Sci.* 62 (2012), pp. 407–451. DOI: 10.1146/annurev-nucl-102711-094901. arXiv: 1206.2503 [astro-ph.SR].

[128] Adam Burrows and David Vartanyan. “Core-Collapse Supernova Explosion Theory”. In: *Nature* 589.7840 (2021), pp. 29–39. DOI: 10.1038/s41586-020-03059-w. arXiv: 2009.14157 [astro-ph.SR].

[129] V. Ashley Villar et al. “Theoretical Models of Optical Transients. I. A Broad Exploration of the Duration-Luminosity Phase Space”. In: *Astrophys. J.* 849 (2017), p. 70. DOI: 10.3847/1538-4357/aa8fcb. arXiv: 1707.08132 [astro-ph.HE].

[130] H. Th. Janka. “Neutrino Emission from Supernovae”. In: (Feb. 2017). DOI: 10.1007/978-3-319-21846-5_4. arXiv: 1702.08713 [astro-ph.HE].

[131] Kohta Murase et al. “New Class of High-Energy Transients from Crashes of Supernova Ejecta with Massive Circumstellar Material Shells”. In: *Phys. Rev. D* 84 (2011), p. 043003. DOI: 10.1103/PhysRevD.84.043003. arXiv: 1012.2834 [astro-ph.HE].

[132] Ke Fang and Brian D. Metzger. “High-Energy Neutrinos from Millisecond Magnetars formed from the Merger of Binary Neutron Stars”. In: *Astrophys. J.* 849.2 (2017), p. 153. DOI: 10.3847/1538-4357/aa8b6a. arXiv: 1707.04263 [astro-ph.HE].

[133] Pawan Kumar and Bing Zhang. "The physics of gamma-ray bursts \& relativistic jets". In: *Phys. Rept.* 561 (2014), pp. 1–109. DOI: 10.1016/j.physrep.2014.09.008. arXiv: 1410.0679 [astro-ph.HE].

[134] Tsvi Piran. "The physics of gamma-ray bursts". In: *Rev. Mod. Phys.* 76 (2004), pp. 1143–1210. DOI: 10.1103/RevModPhys.76.1143. arXiv: astro-ph/0405503.

[135] Bing Zhang. "Gamma-Ray Bursts in the Swift Era". In: *Chin. J. Astron. Astrophys.* 7 (2007), pp. 1–50. DOI: 10.1088/1009-9271/7/1/01. arXiv: astro-ph/0701520.

[136] P. Meszaros and M. J. Rees. "Optical and long wavelength afterglow from gamma-ray bursts". In: *Astrophys. J.* 476 (1997), pp. 232–237. DOI: 10.1086/303625. arXiv: astro-ph/9606043.

[137] Eli Waxman. "GRB afterglow: Supporting the cosmological fireball model, constraining parameters, and making predictions". In: *Astrophys. J. Lett.* 485 (1997), p. L5. DOI: 10.1086/310809. arXiv: astro-ph/9704116.

[138] Eli Waxman. "Gamma-ray burst afterglow: Confirming the cosmological fireball model". In: *Astrophys. J. Lett.* 489 (1997), pp. L33–L36. DOI: 10.1086/310960. arXiv: astro-ph/9705229.

[139] Eli Waxman. "Cosmological gamma-ray bursts and the highest energy cosmic rays". In: *Phys. Rev. Lett.* 75 (1995), pp. 386–389. DOI: 10.1103/PhysRevLett.75.386. arXiv: astro-ph/9505082.

[140] M. G. Aartsen et al. "Extending the search for muon neutrinos coincident with gamma-ray bursts in IceCube data". In: *Astrophys. J.* 843.2, 112 (July 2017), p. 112. DOI: 10.3847/1538-4357/aa7569. arXiv: 1702.06868 [astro-ph.HE].

[141] R. Abbasi et al. "IceCube Data for Neutrino Point-Source Searches Years 2008-2018". In: *arXiv e-prints*, arXiv:2101.09836 (Jan. 2021), arXiv:2101.09836. DOI: 10.21234/CPKQ-K003. arXiv: 2101.09836 [astro-ph.HE].

[142] Francesco Lucarelli et al. "Neutrino search from γ-ray bursts during the prompt and X-ray afterglow phases using 10 years of IceCube public data". In: *Astron. Astrophys.* 672, arXiv:2208.13792 (Aug. 2023), A102. DOI: 10.1051/0004-6361/202244815. arXiv: 2208.13792 [astro-ph.HE].

[143] M. R. Drout et al. "Rapidly-Evolving and Luminous Transients from Pan-STARRS1". In: *Astrophys. J.* 794.1 (2014), p. 23. DOI: 10.1088/0004-637X/794/1/23. arXiv: 1405.3668 [astro-ph.HE].

[144] Iair Arcavi et al. “Rapidly Rising Transients in the Supernova—superluminous Supernova gap”. In: *Astrophys. J.* 819.1 (2016), p. 35. DOI: 10.3847/0004-637X/819/1/35. arXiv: 1511.00704 [astro-ph.CO].

[145] Masaomi Tanaka et al. “Rapidly Rising Transients From the Subaru Hyper Suprime-cam Transient Survey”. In: *Astrophys. J.* 819.1 (2016), p. 5. DOI: 10.3847/0004-637X/819/1/5. arXiv: 1601.03261 [astro-ph.HE].

[146] Anna Y. Q. Ho et al. “A Search for Extragalactic Fast Blue Optical Transients in ZTF and the Rate of AT2018cow-like Transients”. In: *Astrophys. J.* 949.2 (May 2023), p. 120. DOI: 10.3847/1538-4357/acc533. arXiv: 2105.08811 [astro-ph.HE].

[147] Anna Y. Q. Ho et al. “AT2018cow: a luminous millimeter transient”. In: *Astrophys. J.* 871.1 (2019), p. 73. DOI: 10.3847/1538-4357/aaf473. arXiv: 1810.10880 [astro-ph.HE].

[148] R. Margutti et al. “An Embedded X-Ray Source Shines through the Aspherical AT 2018cow: Revealing the Inner Workings of the Most Luminous Fast-evolving Optical Transients”. In: *Astrophys. J.* 872.1 (2019), p. 18. DOI: 10.3847/1538-4357/aafa01. arXiv: 1810.10720 [astro-ph.HE].

[149] Daniel A. Perley et al. “The Fast, Luminous Ultraviolet Transient AT2018cow: Extreme Supernova, or Disruption of a Star by an Intermediate-Mass Black Hole?” In: *Mon. Not. Roy. Astron. Soc.* 484.1 (2019), pp. 1031–1049. DOI: 10.1093/mnras/sty3420. arXiv: 1808.00969 [astro-ph.HE].

[150] Yuhan Yao et al. “The X-Ray and Radio Loud Fast Blue Optical Transient AT2020mrf: Implications for an Emerging Class of Engine-driven Massive Star Explosions”. In: *Astrophys. J.* 934.2 (Dec. 2022), p. 104. DOI: 10.3847/1538-4357/ac7a41. arXiv: 2112.00751 [astro-ph.HE].

[151] Joe S. Bright et al. “Radio and X-Ray Observations of the Luminous Fast Blue Optical Transient AT 2020xnd”. In: *Astrophys. J.* 926.2 (2022), p. 112. DOI: 10.3847/1538-4357/ac4506. arXiv: 2110.05514 [astro-ph.HE].

[152] D. L. Coppejans et al. “A mildly relativistic outflow from the energetic, fast-rising blue optical transient CSS161010 in a dwarf galaxy”. In: *Astrophys. J. Lett.* 895.1 (2020), p. L23. DOI: 10.3847/2041-8213/ab8cc7. arXiv: 2003.10503 [astro-ph.HE].

[153] Ore Gottlieb, Alexander Tchekhovskoy, and Raffaella Margutti. "Shocked jets in CCSNe can power the zoo of fast blue optical transients". In: *Mon. Not. Roy. Astron. Soc.* 513.3 (2022), pp. 3810–3817. DOI: 10.1093/mnras/stac910. arXiv: 2201.04636 [astro-ph.HE].

[154] Brian D. Metzger. "Luminous Fast Blue Optical Transients and Type Ibn/Icn SNe from Wolf-Rayet/Black Hole Mergers". In: *Astrophys. J.* 932.2 (2022), p. 84. DOI: 10.3847/1538-4357/ac6d59. arXiv: 2203.04331 [astro-ph.HE].

[155] Anna Y. Q. Ho et al. "Minutes-duration Optical Flares with Supernova Luminosities". In: (Nov. 2023). DOI: 10.1038/s41586-023-06673-6. arXiv: 2311.10195 [astro-ph.HE].

[156] Anna Y. Q. Ho et al. "Cosmological Fast Optical Transients with the Zwicky Transient Facility: A Search for Dirty Fireballs". In: (Jan. 2022). DOI: 10.3847/1538-4357/ac8bd0. arXiv: 2201.12366 [astro-ph.HE].

[157] Richard Dekany et al. "The Zwicky Transient Facility: Observing System". In: *Publ. Astron. Soc. Pac.* 132 (2020), p. 038001. DOI: 10.1088/1538-3873/ab4ca2. arXiv: 2008.04923 [astro-ph.IM].

[158] C. S. Kochanek et al. "The All-Sky Automated Survey for Supernovae (ASAS-SN) Light Curve Server v1.0". In: *Pub. of the Astron. Soc. of the Pac.* 129.980 (Oct. 2017), p. 104502. DOI: 10.1088/1538-3873/aa80d9. arXiv: 1706.07060 [astro-ph.SR].

[159] K. C. Chambers et al. "The Pan-STARRS1 Surveys". In: *arXiv e-prints*, arXiv:1612.05560 (Dec. 2016), arXiv:1612.05560. DOI: 10.48550/arXiv.1612.05560. arXiv: 1612.05560 [astro-ph.IM].

[160] D. O. Jones et al. "The Young Supernova Experiment: Survey Goals, Overview, and Operations". In: *Astrophys. J.* 908.2 (2021), p. 143. DOI: 10.3847/1538-4357/abd7f5. arXiv: 2010.09724 [astro-ph.HE].

[161] Kelly M. Hambleton et al. "Rubin Observatory LSST Transients and Variable Stars Roadmap". In: (Aug. 2022). arXiv: 2208.04499 [astro-ph.IM].

[162] M. Lacy et al. "The Karl G. Jansky Very Large Array Sky Survey (VLASS). Science case and survey design". In: *Publ. Astron. Soc. Pac.* 132.1009 (2020), p. 035001. DOI: 10.1088/1538-3873/ab63eb. arXiv: 1907.01981 [astro-ph.IM].

[163] J. P. Macquart et al. "Fast Transients at Cosmological Distances with the SKA". In: *Advancing Astrophysics with the Square Kilometre Array (AASKA14)*. Jan. 2015, 55, p. 55. DOI: 10.22323/1.215.0055. arXiv: 1501.07535 [astro-ph.HE].

[164] David N. Burrows et al. "The Swift X-ray Telescope". In: *Space Sci. Rev.* 120 (2005), p. 165. DOI: 10.1007/s11214-005-5097-2. arXiv: astro-ph/0508071.

[165] Charles Meegan et al. "The Fermi Gamma-ray Burst Monitor". In: *Astrophys. J.* 702.1 (Sept. 2009), pp. 791–804. DOI: 10.1088/0004-637X/702/1/791. arXiv: 0908.0450 [astro-ph.IM].

[166] M. Ajello et al. "A Decade of Gamma-Ray Bursts Observed by Fermi-LAT: The Second GRB Catalog". In: *Astrophys. J.* 878.1 (2019), p. 52. DOI: 10.3847/1538-4357/ab1d4e. arXiv: 1906.11403 [astro-ph.HE].

[167] Jamie Holder et al. "The first VERITAS telescope". In: *Astropart. Phys.* 25 (2006), pp. 391–401. DOI: 10.1016/j.astropartphys.2006.04.002. arXiv: astro-ph/0604119.

[168] G. Hermann. "The HESS array: A new system of 100-GeV IACTs for stereoscopic observations". In: *32nd Rencontres de Moriond: High-Energy Phenomena in Astrophysics*. 1997, pp. 141–146.

[169] Daniel Mazin et al. "Upgrade of the MAGIC telescopes". In: *arXiv e-prints*, arXiv:1410.5073 (Oct. 2014), arXiv:1410.5073. DOI: 10.48550/arXiv.1410.5073. arXiv: 1410.5073 [astro-ph.IM].

[170] Andrea Addazi et al. "The Large High Altitude Air Shower Observatory (LHAASO) Science Book (2021 Edition)". In: *Chin. Phys. C* 46 (2022), pp. 035001–035007. arXiv: 1905.02773 [astro-ph.HE].

[171] Jürgen Knödlseder. "The Cherenkov Telescope Array". In: *16th Rencontres du Vietnam: Theory meeting experiment: Particle Astrophysics and Cosmology*. Apr. 2020, arXiv:2004.09213, arXiv:2004.09213. arXiv: 2004.09213 [astro-ph.IM].

[172] Giulio Lucchetta et al. "Introducing the MeVCube concept: a CubeSat for MeV observations". In: *JCAP* 08.08 (2022), p. 013. DOI: 10.1088/1475-7516/2022/08/013. arXiv: 2204.01325 [astro-ph.IM].

[173] R. Abbasi et al. "The Design and Performance of IceCube DeepCore". In: *Astropart. Phys.* 35 (2012), pp. 615–624. DOI: 10.1016/j.astropartphys.2012.01.004. arXiv: 1109.6096 [astro-ph.IM].

[174] S. W. Barwick et al. “Radio detection of air showers with the ARIANNA experiment on the Ross Ice Shelf”. In: *Astropart. Phys.* 90 (2017), pp. 50–68. DOI: 10.1016/j.astropartphys.2017.02.003. arXiv: 1612.04473 [astro-ph.IM].

[175] P. Allison et al. “Performance of two Askaryan Radio Array stations and first results in the search for ultrahigh energy neutrinos”. In: *Phys. Rev. D* 93.8 (2016), p. 082003. DOI: 10.1103/PhysRevD.93.082003. arXiv: 1507.08991 [astro-ph.HE].

[176] J. A. Aguilar et al. “Design and Sensitivity of the Radio Neutrino Observatory in Greenland (RNO-G)”. In: *JINST* 16.03 (2021). [Erratum: JINST 18, E03001 (2023)], P03025. DOI: 10.1088/1748-0221/16/03/P03025. arXiv: 2010.12279 [astro-ph.IM].

[177] P. W. Gorham et al. “The Antarctic Impulsive Transient Antenna Ultra-high Energy Neutrino Detector Design, Performance, and Sensitivity for 2006-2007 Balloon Flight”. In: *Astropart. Phys.* 32 (2009), pp. 10–41. DOI: 10.1016/j.astropartphys.2009.05.003. arXiv: 0812.1920 [astro-ph].

[178] Matteo Agostini et al. “The Pacific Ocean Neutrino Experiment”. In: *Nature Astron.* 4.10 (2020), pp. 913–915. DOI: 10.1038/s41550-020-1182-4. arXiv: 2005.09493 [astro-ph.HE].

[179] S. Adrian-Martinez et al. “Letter of intent for KM3NeT 2.0”. In: *J. Phys. G* 43.8 (2016), p. 084001. DOI: 10.1088/0954-3899/43/8/084001. arXiv: 1601.07459 [astro-ph.IM].

[180] M. Ageron et al. “ANTARES: the first undersea neutrino telescope”. In: *Nucl. Instrum. Meth. A* 656.1 (Nov. 2011), pp. 11–38. DOI: 10.1016/j.nima.2011.06.103. arXiv: 1104.1607 [astro-ph.IM].

[181] A. D. Avrorin et al. “High-Energy Neutrino Astronomy and the Baikal-GVD Neutrino Telescope”. In: *Phys. At. Nucl.* 84.4 (2021), pp. 513–518. DOI: 10.1134/S1063778821040062. arXiv: 2011.09209 [astro-ph.HE].

[182] K. Abe et al. “Hyper-Kamiokande Design Report”. In: (May 2018). arXiv: 1805.04163 [physics.ins-det].

[183] Markus Ackermann et al. “High-energy and ultra-high-energy neutrinos: A Snowmass white paper”. In: *JHEAp* 36 (2022), pp. 55–110. DOI: 10.1016/j.jheap.2022.08.001. arXiv: 2203.08096 [hep-ph].

[184] Markus Ahlers, Klaus Helbing, and Carlos Pérez de los Heros. "Probing Particle Physics with IceCube". In: *Eur. Phys. J. C* 78.11 (2018), p. 924. DOI: 10.1140/epjc/s10052-018-6369-9. arXiv: 1806.05696 [astro-ph.HE].

[185] Ray W. Klebesadel, Ian B. Strong, and Roy A. Olson. "Observations of Gamma-Ray Bursts of Cosmic Origin". In: *Astrophys. J. Lett.* 182 (1973), pp. L85–L88. DOI: 10.1086/181225.

[186] Tsvi Piran, Amotz Shemi, and Ramesh Narayan. "Hydrodynamics of relativistic fireballs". In: *Mon. Not. Roy. Astron. Soc.* 263 (1993), p. 861. DOI: 10.1093/mnras/263.4.861. arXiv: astro-ph/9301004.

[187] Roger D. Blandford and Roman L. Znajek. "Electromagnetic extraction of energy from Kerr black holes." In: *Mon. Not. Roy. Astron. Soc.* 179.3 (May 1977), pp. 433–456. ISSN: 0035-8711. DOI: 10.1093/mnras/179.3.433. eprint: https://academic.oup.com/mnras/article-pdf/179/3/433/9333653/mnras179-0433.pdf. URL: https://doi.org/10.1093/mnras/179.3.433.

[188] Tsvi Piran et al. "Relativistic Jets in Core Collapse Supernovae". In: *Astrophys. J. Lett.* 871.2 (2019), p. L25. DOI: 10.3847/2041-8213/aaffce. arXiv: 1704.08298 [astro-ph.HE].

[189] Noam Soker. "Review: The role of jets in exploding supernovae and in shaping their remnants". In: Aug. 2022. arXiv: 2208.04875 [astro-ph.HE].

[190] Takami Kuroda et al. "Magnetorotational Explosion of A Massive Star Supported by Neutrino Heating in General Relativistic Three Dimensional Simulations". In: *Astrophys. J.* 896.2 (2020), p. 102. DOI: 10.3847/1538-4357/ab9308. arXiv: 2003.02004 [astro-ph.HE].

[191] Maria Petropoulou et al. "Deciphering the properties of the central engine in GRB collapsars". In: *Mon. Not. Roy. Astron. Soc.* 496.3 (2020), pp. 2910–2921. DOI: 10.1093/mnras/staa1695. arXiv: 2006.07482 [astro-ph.HE].

[192] Tong Liu, Wei-Min Gu, and Bing Zhang. "Neutrino-dominated accretion flows as the central engine of gamma-ray bursts". In: *New Astron. Rev.* 79 (2017), pp. 1–25. DOI: 10.1016/j.newar.2017.07.001. arXiv: 1705.05516 [astro-ph.HE].

[193] Edo Berger. "Short-Duration Gamma-Ray Bursts". In: *Ann. Rev. Astron. Astrophys.* 52 (2014), pp. 43–105. DOI: 10.1146/annurev-astro-081913-035926. arXiv: 1311.2603 [astro-ph.HE].

[194] Péter Mészáros and Martin J. Rees. "Poynting jets from black holes and cosmological gamma-ray bursts". In: *Astrophys. J. Lett.* 482 (1997), pp. L29–L32. DOI: 10.1086/310692. arXiv: astro-ph/9609065.

[195] Wen-Xin Chen and Andrei M. Beloborodov. "Neutrino-Cooled Accretion Disks around Spinning Black Hole". In: *Astrophys. J.* 657 (2007), pp. 383–399. DOI: 10.1086/508923. arXiv: astro-ph/0607145.

[196] David Eichler et al. "Nucleosynthesis, Neutrino Bursts and Gamma-Rays from Coalescing Neutron Stars". In: *Nature* 340 (1989), pp. 126–128. DOI: 10.1038/340126a0.

[197] Robert Popham, Stan E. Woosley, and Chris Fryer. "Hyperaccreting black holes and gamma-ray bursts". In: *Astrophys. J.* 518 (1999), pp. 356–374. DOI: 10.1086/307259. arXiv: astro-ph/9807028.

[198] Paolo A. Mazzali et al. "The metamorphosis of Supernova SN2008D/XRF080109: a link between Supernovae and GRBs/Hypernovae". In: *Science* 321 (2008), p. 1185. DOI: 10.1126/science.1158088. arXiv: 0807.1695 [astro-ph].

[199] Raffaella Margutti et al. "Relativistic supernovae have shorter-lived central engines or more extended progenitors: the case of SN\,2012ap". In: *Astrophys. J.* 797.2 (2014), p. 107. DOI: 10.1088/0004-637X/797/2/107. arXiv: 1402.6344 [astro-ph.HE].

[200] Ehud Nakar. "A unified picture for low-luminosity and long gamma-ray bursts based on the extended progenitor of llgrb 060218/SN 2006aj". In: *Astrophys. J.* 807.2 (2015), p. 172. DOI: 10.1088/0004-637X/807/2/172. arXiv: 1503.00441 [astro-ph.HE].

[201] Omer Bromberg et al. "The Propagation of Relativistic Jets in External Media". In: *Astrophys. J.* 740.2, 100 (Oct. 2011), p. 100. DOI: 10.1088/0004-637X/740/2/100. arXiv: 1107.1326 [astro-ph.HE].

[202] Andrew I. MacFadyen, Stan E. Woosley, and Alexander Heger. "Supernovae, jets, and collapsars". In: *Astrophys. J.* 550 (2001), p. 410. DOI: 10.1086/319698. arXiv: astro-ph/9910034.

[203] Enrico Ramirez-Ruiz, Annalisa Celotti, and Martin J. Rees. "Events in the life of a cocoon surrounding a light, collapsar jet". In: *Mon. Not. Roy. Astron. Soc.* 337 (2002), p. 1349. DOI: 10.1046/j.1365-8711.2002.05995.x. arXiv: astro-ph/0205108.

[204] Weiqun Zhang, Stan E. Woosley, and Andrew I. MacFadyen. "Relativistic jets in collapsars". In: *Astrophys. J.* 586 (2003), pp. 356–371. DOI: 10.1086/367609. arXiv: astro-ph/0207436.

[205] Davide Lazzati and Mitchell Begelman. "Universal GRB jets from jet-cocoon interaction in massive stars". In: *Astrophys. J.* 629 (2005), pp. 903–907. DOI: 10.1086/430877. arXiv: astro-ph/0502084.

[206] Diego López-Cámara et al. "Three-dimensional Adaptive Mesh Refinement Simulations of Long-duration Gamma-Ray Burst Jets inside Massive Progenitor Stars". In: *Astrophys. J.* 767.1, 19 (Apr. 2013), p. 19. DOI: 10.1088/0004-637X/767/1/19. arXiv: 1212.0539 [astro-ph.HE].

[207] Diego López-Cámara, Davide Lazzati, and Brian J. Morsony. "Three-dimensional Simulations of Long Duration Gamma-ray Burst Jets: Timescales From Variable Engines". In: *Astrophys. J.* 826.2 (2016), p. 180. DOI: 10.3847/0004-637X/826/2/180. arXiv: 1603.02350 [astro-ph.HE].

[208] Hirotaka Ito et al. "Photospheric Emission from Collapsar Jets in 3D Relativistic Hydrodynamics". In: *Astrophys. J. Lett.* 814.2 (2015), p. L29. DOI: 10.1088/2041-8205/814/2/L29. arXiv: 1511.03443 [astro-ph.HE].

[209] Hirotaka Ito et al. "The photospheric origin of the Yonetoku relation in gamma-ray bursts". In: *Nature Commun.* 10.1 (2019), p. 1504. DOI: 10.1038/s41467-019-09281-z. arXiv: 1806.00590 [astro-ph.HE].

[210] Richard Harrison, Ore Gottlieb, and Ehud Nakar. "Numerically calibrated model for propagation of a relativistic unmagnetized jet in dense media". In: *Mon. Not. Roy. Astron. Soc.* 477.2 (June 2018), pp. 2128–2140. DOI: 10.1093/mnras/sty760. arXiv: 1707.06234 [astro-ph.HE].

[211] Ore Gottlieb, Amir Levinson, and Ehud Nakar. "High efficiency photospheric emission entailed by formation of a collimation shock in gamma-ray bursts". In: *Mon. Not. Roy. Astron. Soc.* 488.1 (2019), pp. 1416–1426. DOI: 10.1093/mnras/stz1828. arXiv: 1904.07244 [astro-ph.HE].

[212] Ore Gottlieb, Amir Levinson, and Ehud Nakar. "Intermittent hydrodynamic jets in collapsars do not produce GRBs". In: *Mon. Not. Roy. Astron. Soc.* 495.1 (2020), pp. 570–577. DOI: 10.1093/mnras/staa1216. arXiv: 2002.12384 [astro-ph.HE].

[213] Ore Gottlieb, Ehud Nakar, and Omer Bromberg. "The structure of hydrodynamic γ-ray burst jets". In: *Mon. Not. Roy. Astron. Soc.* 500.3 (2020), pp. 3511–3526. DOI: 10.1093/mnras/staa3501. arXiv: 2006.02466 [astro-ph.HE].

[214] Norita Kawanaka, Tsvi Piran, and Julian H. Krolik. "Jet Luminosity from Neutrino-dominated Accretion Flows in Gamma-Ray Bursts". In: *Astrophys. J.* 766.1, 31 (Mar. 2013), p. 31. DOI: 10.1088/0004-637X/766/1/31. arXiv: 1211.5110 [astro-ph.HE].

[215] Mingbin Leng and Dimitrios Giannios. "Testing the neutrino annihilation model for launching GRB jets". In: *Mon. Not. Roy. Astron. Soc.* 445 (2014), p. 1. DOI: 10.1093/mnrasl/slu122. arXiv: 1408.4509 [astro-ph.HE].

[216] Oliver Just et al. "Neutron-star merger ejecta as obstacles to neutrino-powered jets of gamma-ray bursts". In: *Astrophys. J. Lett.* 816.2 (2016), p. L30. DOI: 10.3847/2041-8205/816/2/L30. arXiv: 1510.04288 [astro-ph.HE].

[217] Adam Burrows et al. "Simulations of Magnetically-Driven Supernova and Hypernova Explosions in the Context of Rapid Rotation". In: *Astrophys. J.* 664 (2007), pp. 416–434. DOI: 10.1086/519161. arXiv: astro-ph/0702539.

[218] Andrea Mignone et al. "High-resolution 3D relativistic MHD simulations of jets". In: *Mon. Not. Roy. Astron. Soc.* 402.1 (Feb. 2010), pp. 7–12. DOI: 10.1111/j.1365-2966.2009.15642.x. arXiv: 0908.4523 [astro-ph.CO].

[219] Oliver Porth. "Three-dimensional structure of relativistic jet formation". In: *Mon. Not. Roy. Astron. Soc.* 429.3 (Mar. 2013), pp. 2482–2492. DOI: 10.1093/mnras/sts519. arXiv: 1212.0676 [astro-ph.HE].

[220] Omer Bromberg and Alexander Tchekhovskoy. "Relativistic MHD simulations of core-collapse GRB jets: 3D instabilities and magnetic dissipation". In: *Mon. Not. Roy. Astron. Soc.* 456.2 (2016), pp. 1739–1760. DOI: 10.1093/mnras/stv2591. arXiv: 1508.02721 [astro-ph.HE].

[221] Edoardo Striani et al. "MHD simulations of three-dimensional resistive reconnection in a cylindrical plasma column". In: *Mon. Not. Roy. Astron. Soc.* 462.3 (Nov. 2016), pp. 2970–2979. DOI: 10.1093/mnras/stw1848. arXiv: 1607.07323 [astro-ph.HE].

[222] Ore Gottlieb et al. “Black Hole to Photosphere: 3D GRMHD Simulations of Collapsars Reveal Wobbling and Hybrid Composition Jets”. In: *Astrophys. J. Lett.* 933.1 (2022), p. L9. DOI: 10.3847/2041-8213/ac7530. arXiv: 2204.12501 [astro-ph.HE].

[223] Ore Gottlieb et al. “Black hole to breakout: 3D GRMHD simulations of collapsar jets reveal a wide range of transients”. In: *Mon. Not. Roy. Astron. Soc.* 510.4 (2022), pp. 4962–4975. DOI: 10.1093/mnras/stab3784. arXiv: 2109.14619 [astro-ph.HE].

[224] Eli Waxman and John N. Bahcall. “High-energy neutrinos from cosmological gamma-ray burst fireballs”. In: *Phys. Rev. Lett.* 78 (1997), pp. 2292–2295. DOI: 10.1103/PhysRevLett.78.2292. arXiv: astro-ph/9701231.

[225] Dafne Guetta et al. “Neutrinos from individual gamma-ray bursts in the BATSE catalog”. In: *Astropart. Phys.* 20 (2004), pp. 429–455. DOI: 10.1016/S0927-6505(03)00211-1. arXiv: astro-ph/0302524.

[226] Charles D. Dermer. “Neutrino, neutron, and cosmic ray production in the external shock model of gamma-ray bursts”. In: *Astrophys. J.* 574 (2002), pp. 65–87. DOI: 10.1086/340893. arXiv: astro-ph/0005440.

[227] Kai Wang et al. “Hadronic origin of prompt high-energy emission of gamma-ray bursts revisited: in the case of a limited maximum proton energy”. In: *Astrophys. J.* 857.1 (2018), p. 24. DOI: 10.3847/1538-4357/aab667. arXiv: 1803.04112 [astro-ph.HE].

[228] Soebur Razzaque, Péter Mészáros, and Eli Waxman. “Neutrino tomography of gamma-ray bursts and massive stellar collapses”. In: *Phys. Rev. D* 68 (2003), p. 083001. DOI: 10.1103/PhysRevD.68.083001. arXiv: astro-ph/0303505.

[229] Brian D. Metzger, Dimitrios Giannios, and Shunsaku Horiuchi. “Heavy nuclei synthesized in gamma-ray burst outflows as the source of ultrahigh energy cosmic rays”. In: *Mon. Not. Roy. Astron. Soc.* 415.3 (Aug. 2011), pp. 2495–2504. DOI: 10.1111/j.1365-2966.2011.18873.x. arXiv: 1101.4019 [astro-ph.HE].

[230] Jonas Heinze et al. “Systematic parameter space study for the UHECR origin from GRBs in models with multiple internal shocks”. In: *Mon. Not. Roy. Astron. Soc.* 498.4 (2020), pp. 5990–6004. DOI: 10.1093/mnras/staa2751. arXiv: 2006.14301 [astro-ph.HE].

[231] Tetyana Pitik, Irene Tamborra, and Maria Petropoulou. "Neutrino signal dependence on gamma-ray burst emission mechanism". In: *JCAP* 05 (2021), p. 034. DOI: 10.1088/1475-7516/2021/05/034. arXiv: 2102.02223 [astro-ph.HE].

[232] Eli Waxman and John N. Bahcall. "Neutrino afterglow from gamma-ray bursts: Similar to 10**18-eV". In: *Astrophys. J.* 541 (2000), pp. 707–711. DOI: 10.1086/309462. arXiv: hep-ph/9909286.

[233] Ersilia Guarini et al. "Multi-messenger detection prospects of gamma-ray burst afterglows with optical jumps". In: *JCAP* 06.06 (2022), p. 034. DOI: 10.1088/1475-7516/2022/06/034. arXiv: 2112.07690 [astro-ph.HE].

[234] Ersilia Guarini, Irene Tamborra, and Raffaella Margutti. "Neutrino Emission from Luminous Fast Blue Optical Transients". In: *Astrophys. J.* 935.2 (2022), p. 157. DOI: 10.3847/1538-4357/ac7fa0. arXiv: 2205.12282 [astro-ph.HE].

[235] Nicholas Senno, Kohta Murase, and Péter Mészáros. "Choked Jets and Low-Luminosity Gamma-Ray Bursts as Hidden Neutrino Sources". In: *Phys. Rev. D* 93.8 (2016), p. 083003. DOI: 10.1103/PhysRevD.93.083003. arXiv: 1512.08513 [astro-ph.HE].

[236] Ore Gottlieb and Noemie Globus. "The Role of Jet–Cocoon Mixing, Magnetization, and Shock Breakout in Neutrino and Cosmic-Ray Emission from Short Gamma-Ray Bursts". In: *Astrophys. J. Lett.* 915.1 (2021), p. L4. DOI: 10.3847/2041-8213/ac05c5. arXiv: 2105.01076 [astro-ph.HE].

[237] Irene Tamborra and Shin'ichiro Ando. "Inspecting the supernova–gamma-ray-burst connection with high-energy neutrinos". In: *Phys. Rev. D* 93.5 (2016), p. 053010. DOI: 10.1103/PhysRevD.93.053010. arXiv: 1512.01559 [astro-ph.HE].

[238] Irene Tamborra and Shin'ichiro Ando. "Diffuse emission of high-energy neutrinos from gamma-ray burst fireballs". In: *JCAP* 09 (2015), p. 036. DOI: 10.1088/1475-7516/2015/9/036. arXiv: 1504.00107 [astro-ph.HE].

[239] Peter B. Denton and Irene Tamborra. "Exploring the Properties of Choked Gamma-ray Bursts with IceCube's High-energy Neutrinos". In: *Astrophys. J.* 855.1 (2018), p. 37. DOI: 10.3847/1538-4357/aaab4a. arXiv: 1711.00470 [astro-ph.HE].

[240] Cecilia Lunardini and Walter Winter. "High Energy Neutrinos from the Tidal Disruption of Stars". In: *Phys. Rev. D* 95.12 (2017), p. 123001. DOI: 10.1103/PhysRevD.95.123001. arXiv: 1612.03160 [astro-ph.HE].

[241] Walter Winter and Cecilia Lunardini. "A concordance scenario for the observed neutrino from a tidal disruption event". In: *Nature Astron.* 5.5 (2021), pp. 472–477. DOI: 10.1038/s41550-021-01343-x. arXiv: 2005.06097 [astro-ph.HE].

[242] Lixin Dai and Ke Fang. "Can tidal disruption events produce the IceCube neutrinos?" In: *Mon. Not. Roy. Astron. Soc.* 469.2 (2017), pp. 1354–1359. DOI: 10.1093/mnras/stx863. arXiv: 1612.00011 [astro-ph.HE].

[243] Jin Matsumoto, Serguei S. Komissarov, and Konstantinos N. Gourgouliatos. "Magnetic inhibition of the recollimation instability in relativistic jets". In: *Mon. Not. Roy. Astron. Soc.* 503.4 (2021), pp. 4918–4929. DOI: 10.1093/mnras/stab828. arXiv: 2010.11012 [astro-ph.HE].

[244] Ore Gottlieb et al. "The structure of weakly magnetized γ-ray burst jets". In: *Mon. Not. Roy. Astron. Soc.* 498.3 (2020), pp. 3320–3333. DOI: 10.1093/mnras/staa2567. arXiv: 2007.11590 [astro-ph.HE].

[245] Ore Gottlieb et al. "Intermittent mildly magnetized jets as the source of GRBs". In: *Mon. Not. Roy. Astron. Soc.* 504.3 (2021), pp. 3947–3955. DOI: 10.1093/mnras/stab1068. arXiv: 2102.00005 [astro-ph.HE].

[246] Bing Zhang and Huirong Yan. "The Internal-Collision-Induced Magnetic Reconnection and Turbulence (ICMART) Model of Gamma-Ray Bursts". In: *Astrophys. J.* 726 (2011), p. 90. DOI: 10.1088/0004-637X/726/2/90. arXiv: 1011.1197 [astro-ph.HE].

[247] Kohta Murase and Kunihito Ioka. "TeV–PeV Neutrinos from Low-Power Gamma-Ray Burst Jets inside Stars". In: *Phys. Rev. Lett.* 111.12 (2013), p. 121102. DOI: 10.1103/PhysRevLett.111.121102. arXiv: 1306.2274 [astro-ph.HE].

[248] Hao-Ning He et al. "Neutrinos from Choked Jets Accompanied by Type-II Supernovae". In: *Astrophys. J.* 856.2 (2018), p. 119. DOI: 10.3847/1538-4357/aab360. arXiv: 1803.07478 [astro-ph.HE].

[249] Shigeo S. Kimura et al. "Transejecta high-energy neutrino emission from binary neutron star mergers". In: *Phys. Rev. D* 98.4 (2018), p. 043020. DOI: 10.1103/PhysRevD.98.043020. arXiv: 1805.11613 [astro-ph.HE].

[250] Xiang-Yu Wang and Zi-Gao Dai. "Prompt TeV neutrinos from dissipative photospheres of gamma-ray bursts". In: *Astrophys. J. Lett.* 691 (2009), pp. L67–L71. DOI: 10.1088/0004-637X/691/2/L67. arXiv: 0807.0290 [astro-ph].

[251] Kohta Murase, Kazumi Kashiyama, and Peter Mészáros. "Subphotospheric Neutrinos from Gamma-Ray Bursts: The Role of Neutrons". In: *Phys. Rev. Lett.* 111 (2013), p. 131102. DOI: 10.1103/PhysRevLett.111.131102. arXiv: 1301.4236 [astro-ph.HE].

[252] Soebur Razzaque, Péter Mészáros, and Eli Waxman. "TeV neutrinos from core collapse supernovae and hypernovae". In: *Phys. Rev. Lett.* 93 (2004). [Erratum: Phys.Rev.Lett. 94, 109903 (2005)], p. 181101. DOI: 10.1103/PhysRevLett.94.109903. arXiv: astro-ph/0407064.

[253] Michela Fasano et al. "Estimating the neutrino flux from choked gamma-ray bursts". In: *JCAP* 09 (2021), p. 044. DOI: 10.1088/1475-7516/2021/09/044. arXiv: 2101.03502 [astro-ph.HE].

[254] Aldana Grichener and Noam Soker. "Common envelope jets supernovae with a black hole companion as possible high-energy neutrino sources". In: *Mon. Not. Roy. Astron. Soc.* 507.2 (2021), pp. 1651–1661. DOI: 10.1093/mnras/stab2233. arXiv: 2101.05118 [astro-ph.HE].

[255] Shin'ichiro Ando and John F. Beacom. "Revealing the supernova-gamma-ray burst connection with TeV neutrinos". In: *Phys. Rev. Lett.* 95 (2005), p. 061103. DOI: 10.1103/PhysRevLett.95.061103. arXiv: astro-ph/0502521.

[256] Peter B. Denton and Irene Tamborra. "The Bright and Choked Gamma-Ray Burst Contribution to the IceCube and ANTARES Low-Energy Excess". In: *JCAP* 04 (2018), p. 058. DOI: 10.1088/1475-7516/2018/04/058. arXiv: 1802.10098 [astro-ph.HE].

[257] Georg Drenkhahn and Hendrik C. Spruit. "Efficient acceleration and radiation in Poynting flux powered GRB outflows". In: *Astron. Astrophys.* 391 (2002), p. 1141. DOI: 10.1051/0004-6361:20020839. arXiv: astro-ph/0202387.

[258] Georg Drenkhahn. "Acceleration of GRB outflows by Poynting flux dissipation". In: *Astron. Astrophys.* 387 (2002), p. 714. DOI: 10.1051/0004-6361:20020390. arXiv: astro-ph/0112509.

[259] Paz Beniamini and Dimitrios Giannios. "Prompt Gamma Ray Burst emission from gradual magnetic dissipation". In: *Mon. Not. Roy. Astron. Soc.* 468.3 (2017), pp. 3202–3211. DOI: 10.1093/mnras/stx717. arXiv: 1703.07380 [astro-ph.HE].

[260] Ramandeep Gill, Jonathan Granot, and Paz Beniamini. "GRB Spectrum from Gradual Dissipation in a Magnetized Outflow". In: *Mon. Not. Roy. Astron. Soc.* 499.1 (2020), pp. 1356–1372. DOI: 10.1093/mnras/staa2870. arXiv: 2008.10729 [astro-ph.HE].

[261] Matthew Liska et al. "H-AMR: A New GPU-accelerated GRMHD Code for Exascale Computing With 3D Adaptive Mesh Refinement and Local Adaptive Time-stepping". In: (Dec. 2019). arXiv: 1912.10192 [astro-ph.HE].

[262] En-Wei Liang et al. "A Comprehensive Analysis of the Swift/XRT Data. 3. Jet Break Candidates in the X-ray and Optical Afterglow Lightcurves". In: *Astrophys. J.* 675 (2008), p. 528. DOI: 10.1086/524701. arXiv: 0708.2942 [astro-ph].

[263] Ore Gottlieb et al. "Jet-Inflated Cocoons in Dying Stars: New LIGO-Detectable Gravitational Wave Sources". In: (Sept. 2022). arXiv: 2209.09256 [astro-ph.HE].

[264] William S. Paciesas et al. "The Fermi GBM Gamma-Ray Burst Catalog: The First Two Years". In: *Astrophys. J. Suppl.* 199 (2012), p. 18. DOI: 10.1088/0067-0049/199/1/18. arXiv: 1201.3099 [astro-ph.HE].

[265] Anna Y. Q. Ho et al. "The Koala: A Fast Blue Optical Transient with Luminous Radio Emission from a Starburst Dwarf Galaxy at $z = 0.27$". In: *Astrophys. J.* 895.1 (2020), p. 49. DOI: 10.3847/1538-4357/ab8bcf. arXiv: 2003.01222 [astro-ph.HE].

[266] Tsvi Piran. "Gamma-ray bursts and the fireball model". In: *Phys. Rept.* 314 (1999), pp. 575–667. DOI: 10.1016/S0370-1573(98)00127-6. arXiv: astro-ph/9810256.

[267] Péter Mészáros. "Gamma-Ray Bursts". In: *Rept. Prog. Phys.* 69 (2006), pp. 2259–2322. DOI: 10.1088/0034-4885/69/8/R01. arXiv: astro-ph/0605208.

[268] Hendrik C. Spruit, Frédéric Daigne, and Georg Drenkhahn. "Large scale magnetic fields and their dissipation in grb fireballs". In: *Astron. Astrophys.* 369 (2001), p. 694. DOI: 10.1051/0004-6361:20010131. arXiv: astro-ph/0004274.

[269] Dimitrios Giannios. "Prompt GRB emission from gradual energy dissipation". In: *Astron. Astrophys.* 480 (2008), p. 305. DOI: 10.1051/0004-6361:20079085. arXiv: 0711.2632 [astro-ph].

[270] Daniel Kagan et al. "Relativistic magnetic reconnection in pair plasmas and its astrophysical applications". In: *Space Sci. Rev.* 191.1-4 (2015), pp. 545–573. DOI: 10.1007/s11214-014-0132-9. arXiv: 1412.2451 [astro-ph.HE].

[271] Lorenzo Sironi and Anatoly Spitkovsky. "Synthetic Spectra from Particle-In-Cell Simulations of Relativistic Collisionless Shocks". In: *Astrophys. J.* 707.1 (Dec. 2009), pp. L92–L96. DOI: 10.1088/0004-637X/707/1/L92. arXiv: 0908.3193 [astro-ph.HE].

[272] Atul Chhotray and Davide Lazzati. "Gamma-ray burst spectra and spectral correlations from sub-photospheric Comptonization". In: *Astrophys. J.* 802.2 (2015), p. 132. DOI: 10.1088/0004-637X/802/2/132. arXiv: 1502.03055 [astro-ph.HE].

[273] Paolo Lipari, Maurizio Lusignoli, and Davide Meloni. "Flavor Composition and Energy Spectrum of Astrophysical Neutrinos". In: *Phys. Rev. D* 75 (2007), p. 123005. DOI: 10.1103/PhysRevD.75.123005. arXiv: 0704.0718 [astro-ph].

[274] Hao-Ning He et al. "Icecube non-detection of GRBs: Constraints on the fireball properties". In: *Astrophys. J.* 752 (2012), p. 29. DOI: 10.1088/0004-637X/752/1/29. arXiv: 1204.0857 [astro-ph.HE].

[275] Katsuaki Asano and S. Nagataki. "Very high energy neutrinos originating from kaons in gamma-ray bursts". In: *Astrophys. J. Lett.* 640 (2006), pp. L9–L12. DOI: 10.1086/503291. arXiv: astro-ph/0603107.

[276] Maria Petropoulou, Dimitrios Giannios, and Stavros Dimitrakoudis. "Implications of a PeV neutrino spectral cutoff in GRB models". In: *Mon. Not. Roy. Astron. Soc.* 445.1 (2014), pp. 570–580. DOI: 10.1093/mnras/stu1757. arXiv: 1405.2091 [astro-ph.HE].

[277] Piotr A. Zyla et al. "Review of Particle Physics". In: *PTEP* 2020.8 (Aug. 2020). 083C01, p. 083C01. ISSN: 2050-3911. DOI: 10.1093/ptep/ptaa104. eprint: https://academic.oup.com/ptep/article-pdf/2020/8/083C01/34673722/ptaa104.pdf. URL: https://doi.org/10.1093/ptep/ptaa104.

[278] Yasaman Farzan and Alexei Yu. Smirnov. "Coherence and oscillations of cosmic neutrinos". In: *Nucl. Phys. B* 805 (2008), pp. 356–376. DOI: 10.1016/j.nuclphysb.2008.07.028. arXiv: 0803.0495 [hep-ph].

[279] Luis A. Anchordoqui et al. "Cosmic Neutrino Pevatrons: A Brand New Pathway to Astronomy, Astrophysics, and Particle Physics". In: *JHEAp* 1-2 (2014), pp. 1–30. DOI: 10.1016/j.jheap.2014.01.001. arXiv: 1312.6587 [astro-ph.HE].

[280] Philipp Baerwald, Svenja Hümmer, and Walter Winter. "Systematics in the Interpretation of Aggregated Neutrino Flux Limits and Flavor Ratios from Gamma-Ray Bursts". In: *Astropart. Phys.* 35 (2012), pp. 508–529. DOI: 10.1016/j.astropartphys.2011.11.005. arXiv: 1107.5583 [astro-ph.HE].

[281] Ivan Esteban et al. "The fate of hints: updated global analysis of three-flavor neutrino oscillations". In: *JHEP* 09 (2020), p. 178. DOI: 10.1007/JHEP09(2020)178. arXiv: 2007.14792 [hep-ph].

[282] Páll Jakobsson et al. "The optically unbiased GRB host (TOUGH) survey. III. Redshift distribution". In: *Astrophys. J.* 752.1, 62 (June 2012), p. 62. DOI: 10.1088/0004-637X/752/1/62. arXiv: 1205.3490 [astro-ph.CO].

[283] Krzysztof Nalewajko et al. "On the distribution of particle acceleration sites in plasmoid-dominated relativistic magnetic reconnection". In: *Astrophys. J.* 815.2 (2015), p. 101. DOI: 10.1088/0004-637X/815/2/101. arXiv: 1508.02392 [astro-ph.HE].

[284] Maria Petropoulou and Lorenzo Sironi. "The steady growth of the high-energy spectral cut-off in relativistic magnetic reconnection". In: *Mon. Not. Roy. Astron. Soc.* 481.4 (2018), pp. 5687–5701. DOI: 10.1093/mnras/sty2702. arXiv: 1808.00966 [astro-ph.HE].

[285] Patrick Kilian et al. "Exploring the acceleration mechanisms for particle injection and power-law formation during trans-relativistic magnetic reconnection". In: *Astrophys. J.* 899.2 (2020), p. 151. DOI: 10.3847/1538-4357/aba1e9. arXiv: 2001.02732 [astro-ph.HE].

[286] Martin J. Rees and Péter Mészáros. "Unsteady outflow models for cosmological gamma-ray bursts". In: *Astrophys. J. Lett.* 430 (1994), pp. L93–L96. DOI: 10.1086/187446. arXiv: astro-ph/9404038.

[287] Amir Levinson and Ehud Nakar. "Physics of radiation mediated shocks and its applications to GRBs, supernovae, and neutron star mergers". In: *Phys. Rept.* 866 (2020), pp. 1–46. DOI: 10.1016/j.physrep.2020.04.003. arXiv: 1909.10288 [astro-ph.HE].

[288] Patrick Crumley et al. "Kinetic simulations of mildly relativistic shocks – I. Particle acceleration in high Mach number shocks". In: *Mon. Not. Roy. Astron. Soc.* 485.4 (2019), pp. 5105–5119. DOI: 10.1093/mnras/stz232. arXiv: 1809.10809 [astro-ph.HE].

[289] Petar Mimica and Miguel A. Aloy. "On the dynamic efficiency of internal shocks in magnetized relativistic outflows". In: *Mont. Not. Roy. Astron. Soc.* 401.1 (Jan. 2010), pp. 525–532. DOI: 10.1111/j.1365-2966.2009.15669.x. arXiv: 0909.1328 [astro-ph.HE].

[290] Serguei S. Komissarov. "Shock dissipation in magnetically dominated impulsive flows". In: *Mon. Not. Roy. Astron. Soc.* 422.1 (May 2012), pp. 326–346. DOI: 10.1111/j.1365-2966.2012.20609.x. arXiv: 1201.3469 [astro-ph.HE].

[291] Frédéric Daigne and Robert Mochkovitch. "Gamma-ray bursts from internal shocks in a relativistic wind: temporal and spectral properties". In: *Mon. Not. Roy. Astron. Soc.* 296 (1998), p. 275. DOI: 10.1046/j.1365-8711.1998.01305.x. arXiv: astro-ph/9801245.

[292] Shiho Kobayashi, Tsvi Piran, and Re'em Sari. "Can internal shocks produce the variability in GRBs?" In: *Astrophys. J.* 490 (1997), pp. 92–98. DOI: 10.1086/512791. arXiv: astro-ph/9705013.

[293] Andrew Levan et al. "Gamma-ray burst progenitors". In: *Space Sci. Rev.* 202.1-4 (2016), pp. 33–78. DOI: 10.1007/s11214-016-0312-x. arXiv: 1611.03091 [astro-ph.HE].

[294] Avishai Gilkis and Iair Arcavi. "How much hydrogen is in Type Ib and IIb supernova progenitors?" In: *Mon. Not. Roy. Astron. Soc.* 511.1 (2022), pp. 691–712. DOI: 10.1093/mnras/stac088. arXiv: 2111.04432 [astro-ph.SR].

[295] Emanuele Sobacchi et al. "A common central engine for long gamma-ray bursts and Type Ib/c supernovae". In: *Mon. Not. Roy. Astron. Soc.* 472.1 (2017), pp. 616–627. DOI: 10.1093/mnras/stx2083. arXiv: 1705.00281 [astro-ph.HE].

[296] Miika Pursiainen et al. "Rapidly Evolving Transients in the Dark Energy Survey". In: *Mon. Not. Roy. Astron. Soc.* 481.1 (2018), pp. 894–917. DOI: 10.1093/mnras/sty2309. arXiv: 1803.04869 [astro-ph.HE].

[297] Michael F. Bietenholz et al. “AT 2018cow VLBI: no long-lived relativistic outflow”. In: *Mon. Not. Roy. Astron. Soc.* 491.4 (2020), pp. 4735–4741. DOI: 10.1093/mnras/stz3249. arXiv: 1911.08778 [astro-ph.HE].

[298] Ke Fang et al. “High-energy Neutrinos and Gamma Rays from Nonrelativistic Shock-powered Transients”. In: *Astrophys. J.* 904.1 (2020), p. 4. DOI: 10.3847/1538-4357/abbc6e. arXiv: 2007.15742 [astro-ph.HE].

[299] Christopher D. Matzner and Christopher F. McKee. “The expulsion of stellar envelopes in core-collapse supernovae”. In: *Astrophys. J.* 510 (1999), p. 379. DOI: 10.1086/306571. arXiv: astro-ph/9807046.

[300] Péter Mészáros and Martin J. Rees. “Collapsar jets, bubbles and fe lines”. In: *Astrophys. J. Lett.* 556 (2001), pp. L37–L40. DOI: 10.1086/322934. arXiv: astro-ph/0104402.

[301] Tony Pan, Daniel J. Patnaude, and Abraham Loeb. “Super-luminous X-ray Emission from the Interaction of Supernova Ejecta with Dense Circumstellar Shells”. In: *Mon. Not. Roy. Astron. Soc.* 433 (2013), p. 838. DOI: 10.1093/mnras/stt780. arXiv: 1303.6958 [astro-ph.HE].

[302] Kazumi Kashiyama et al. “High-energy Neutrino and Gamma-Ray Transients from Trans-relativistic Supernova Shock Breakouts”. In: *"Astrophys. J. L."* 769.1, L6 (May 2013), p. L6. DOI: 10.1088/2041-8205/769/1/L6. arXiv: 1210.8147 [astro-ph.HE].

[303] Joseph A. Formaggio and Geralyn P. Zeller. “From eV to EeV: Neutrino Cross Sections Across Energy Scales”. In: *Rev. Mod. Phys.* 84 (2012), pp. 1307–1341. DOI: 10.1103/RevModPhys.84.1307. arXiv: 1305.7513 [hep-ex].

[304] Olga Mena, Irina Mocioiu, and Soebur Razzaque. “Oscillation effects on high-energy neutrino fluxes from astrophysical hidden sources”. In: *Phys. Rev. D* 75 (2007), p. 063003. DOI: 10.1103/PhysRevD.75.063003. arXiv: astro-ph/0612325.

[305] Soebur Razzaque and A. Yu. Smirnov. “Flavor conversion of cosmic neutrinos from hidden jets”. In: *JHEP* 03 (2010), p. 031. DOI: 10.1007/JHEP03(2010)031. arXiv: 0912.4028 [hep-ph].

[306] Jose Carpio and Kohta Murase. “Oscillation of high-energy neutrinos from choked jets in stellar and merger ejecta”. In: *Phys. Rev. D* 101.12 (2020), p. 123002. DOI: 10.1103/PhysRevD.101.123002. arXiv: 2002.10575 [astro-ph.HE].

[307] Sarira Sahu and Bing Zhang. "Effect of Resonant Neutrino Oscillation on TeV Neutrino Flavor Ratio from Choked GRBs". In: *Res. Astron. Astrophys.* 10 (2010), pp. 943–949. DOI: 10.1088/1674-4527/10/10/001. arXiv: 1007.4582 [hep-ph].

[308] Euan Richard et al. "Measurements of the atmospheric neutrino flux by Super-Kamiokande: energy spectra, geomagnetic effects, and solar modulation". In: *Phys. Rev. D* 94.5 (2016), p. 052001. DOI: 10.1103/PhysRevD.94.052001. arXiv: 1510.08127 [hep-ex].

[309] Mark G. Aartsen et al. "Measurement of the Atmospheric ν_e Spectrum with IceCube". In: *Phys. Rev. D* 91 (2015), p. 122004. DOI: 10.1103/PhysRevD.91.122004. arXiv: 1504.03753 [astro-ph.HE].

[310] Mark G. Aartsen et al. "Development of a General Analysis and Unfolding Scheme and its Application to Measure the Energy Spectrum of Atmospheric Neutrinos with IceCube". In: *Eur. Phys. J. C* 75.3 (2015), p. 116. DOI: 10.1140/epjc/s10052-015-3330-z. arXiv: 1409.4535 [astro-ph.HE].

[311] I. Bartos et al. "Detection Prospects for GeV Neutrinos from Collisionally Heated Gamma-ray Bursts with IceCube/DeepCore". In: *Phys. Rev. Lett.* 110.24 (2013), p. 241101. DOI: 10.1103/PhysRevLett.110.241101. arXiv: 1301.4232 [astro-ph.HE].

[312] Angela Zegarelli et al. "Detection prospects for multi-GeV neutrinos from collisionally heated GRBs". In: *Phys. Rev. D* 105.8 (2022), p. 083023. DOI: 10.1103/PhysRevD.105.083023. arXiv: 2112.14188 [astro-ph.HE].

[313] Mark G. Aartsen et al. "Observation and Characterization of a Cosmic Muon Neutrino Flux from the Northern Hemisphere using six years of IceCube data". In: *Astrophys. J.* 833.1 (2016), p. 3. DOI: 10.3847/0004-637X/833/1/3. arXiv: 1607.08006 [astro-ph.HE].

[314] Victor Branco Valera, Mauricio Bustamante, and Christian Glaser. "The ultra-high-energy neutrino-nucleon cross section: measurement forecasts for an era of cosmic EeV-neutrino discovery". In: *JHEP* 06 (2022), p. 105. DOI: 10.1007/JHEP06(2022)105. arXiv: 2204.04237 [hep-ph].

[315] Ko Abe et al. "Letter of Intent: The Hyper-Kamiokande Experiment — Detector Design and Physics Potential —". In: (Sept. 2011). arXiv: 1109.3262 [hep-ex].

[316] Jianming Bian et al. "Hyper-Kamiokande Experiment: A Snowmass White Paper". In: *2022 Snowmass Summer Study*. Mar. 2022. arXiv: 2203.02029 [hep-ex].

[317] Christopher Wiebusch. "Physics Capabilities of the IceCube DeepCore Detector". In: (July 2009). arXiv: 0907.2263 [astro-ph.IM].

[318] A. de Ugarte Postigo et al. "GRB 221009A: Redshift from X-shooter/VLT". In: *GRB Coordinates Network* 32648 (Oct. 2022), p. 1.

[319] Aya Ishihara. "The IceCube Upgrade - Design and Science Goals". In: *PoS* ICRC2019 (2021), p. 1031. DOI: 10.22323/1.358.1031. arXiv: 1908.09441 [astro-ph.HE].

[320] M. G. Aartsen et al. "Neutrino astronomy with the next generation IceCube Neutrino Observatory". In: (Nov. 2019). arXiv: 1911.02561 [astro-ph.HE].

[321] Jose Carpio. "Neutrino production in magnetised jets". In: *Transient Tuesday Seminars, Niels Bohr Institute, U. of Copenhagen* (2022). URL: https://drive.google.com/file/d/172rg7HpilNPVH80Lc07N31ksghq1Sri9/view.

[322] Mukul Bhattacharya et al. "High-energy neutrino emission from magnetised jets of rapidly rotating protomagnetars". In: (Oct. 2022). arXiv: 2210.08029 [astro-ph.HE].

[323] Chryssa Kouveliotou et al. "Identification of two classes of gamma-ray bursts". In: *Astrophys. J. Lett.* 413 (Aug. 1993), pp. L101–104. DOI: 10.1086/186969.

[324] N. Gehrels, E. Ramirez-Ruiz, and Derek B. Fox. "Gamma-Ray Bursts in the Swift Era". In: *Ann. Rev. Astron. Astrophys.* 47.1 (Sept. 2009), pp. 567–617. DOI: 10.1146/annurev.astro.46.060407.145147. arXiv: 0909.1531 [astro-ph.HE].

[325] S. E. Woosley. "Gamma-ray bursts from stellar mass accretion disks around black holes". In: *Astrophys. J.* 405 (Mar. 1993), p. 273. DOI: 10.1086/172359.

[326] A. MacFadyen and S. E. Woosley. "Collapsars: Gamma-ray bursts and explosions in 'failed supernovae'". In: *Astrophys. J.* 524 (1999), p. 262. DOI: 10.1086/307790. arXiv: astro-ph/9810274.

[327] S. E. Woosley and J. S. Bloom. "The Supernova Gamma-Ray Burst Connection". In: *Ann. Rev. Astron. Astrophys.* 44 (2006), pp. 507–556. DOI: 10.1146/annurev.astro.43.072103.150558. arXiv: astro-ph/0609142.

[328] J. L. Atteia et al. “The maximum isotropic energy of gamma-ray bursts”. In: *Astrophys. J.* 837.2 (2017). [Erratum: Astrophys.J. 852, 144 (2018)], p. 119. DOI: 10.3847/1538-4357/aa5ffa. arXiv: 1702.02961 [astro-ph.HE].

[329] D. Band et al. “BATSE Observations of Gamma-Ray Burst Spectra. I. Spectral Diversity”. In: *Astrophys. J.* 413 (1993), p. 281. DOI: 10.1086/172995.

[330] David Gruber et al. “The Fermi GBM Gamma-Ray Burst Spectral Catalog: Four Years Of Data”. In: *Astrophys. J. Suppl.* 211 (2014), p. 12. DOI: 10.1088/0067-0049/211/1/12. arXiv: 1401.5069 [astro-ph.HE].

[331] A. von Kienlin et al. “The Fourth Fermi-GBM Gamma-Ray Burst Catalog: A Decade of Data”. In: *Astrophys. J.* 893 (2020), p. 46. DOI: 10.3847/1538-4357/ab7a18. arXiv: 2002.11460 [astro-ph.HE].

[332] V. A. Acciari et al. “Observation of inverse Compton emission from a long γ-ray burst”. In: *Nature* 575.7783 (2019), pp. 459–463. DOI: 10.1038/s41586-019-1754-6. arXiv: 2006.07251 [astro-ph.HE].

[333] H. Abdalla et al. “A very-high-energy component deep in the γ-ray burst afterglow”. In: *Nature* 575.7783 (2019), pp. 464–467. DOI: 10.1038/s41586-019-1743-9. arXiv: 1911.08961 [astro-ph.HE].

[334] J. I. Katz and T. Piran. “Persistent Counterparts to Gamma-Ray Bursts”. In: *Astrophys. J.* 490.2 (1997), pp. 772–778. DOI: 10.1086/304913.

[335] S. D. Barthelmy et al. “Discovery of an afterglow extension of the prompt phase of two gamma ray bursts observed by swift”. In: *Astrophys. J. Lett.* 635 (2005), pp. L133–L136. DOI: 10.1086/499432. arXiv: astro-ph/0511576.

[336] Da-Bin Lin et al. “Steep Decay Phase Shaped by the Curvature Effect. I. Flux Evolution”. In: *Astrophys. J.* 840.2 (2017), p. 95. DOI: 10.3847/1538-4357/aa6d61. arXiv: 1704.04233 [astro-ph.HE].

[337] Paul T. O’Brien et al. “The early x-ray emission from grbs”. In: *Astrophys. J.* 647 (2006), pp. 1213–1237. DOI: 10.1086/505457. arXiv: astro-ph/0601125.

[338] R. Margutti et al. "On the average gamma-ray burst X-ray flaring activity". In: *MNRAS* 410.2 (Jan. 2011), pp. 1064–1075. DOI: 10.1111/j.1365-2966.2010.17504.x. arXiv: 1009.0172 [astro-ph.HE].

[339] G. Chincarini et al. "Unveiling the origin of X-ray flares in gamma-ray bursts". In: *MNRAS* 406.4 (Aug. 2010), pp. 2113–2148. DOI: 10.1111/j.1365-2966.2010.17037.x. arXiv: 1004.0901 [astro-ph.HE].

[340] J. A. Nousek et al. "Evidence for a Canonical Gamma-Ray Burst Afterglow Light Curve in the Swift XRT Data". In: *Astrophys. J.* 642.1 (2006), pp. 389–400. DOI: 10.1086/500724. arXiv: astro-ph/0508332 [astro-ph].

[341] Bing Zhang et al. "Physical processes shaping GRB x-ray afterglow lightcurves: Theoretical implications from the SWIFT XRT observations". In: *Astrophys. J.* 642 (2006), pp. 354–370. DOI: 10.1086/500723. arXiv: astro-ph/0508321.

[342] A. Melandri et al. "The Early-Time Optical Properties of Gamma-Ray Burst Afterglows". In: *Astrophys. J.* 686.2 (2008), pp. 1209–1230. DOI: 10.1086/591243. arXiv: 0804.0811 [astro-ph].

[343] Re'em Sari and Tsvi Piran. "GRB 990123: The optical flash and the fireball model". In: *Astrophys. J. Lett.* 517.2 (1999), p. L109. DOI: 10.1086/312039. arXiv: astro-ph/9902009 [astro-ph].

[344] J. Japelj et al. "Phenomenology of Reverse-shock Emission in the Optical Afterglows of Gamma-Ray Bursts". In: *Astrophys. J.* 785.2, 84 (2014), p. 84. DOI: 10.1088/0004-637X/785/2/84. arXiv: 1402.3701 [astro-ph.HE].

[345] T. Krühler et al. "Correlated Optical and X-Ray Flares in the Afterglow of XRF 071031". In: *Astrophys. J.* 697.1 (2009), pp. 758–768. DOI: 10.1088/0004-637X/697/1/758. arXiv: 0903.1184 [astro-ph.HE].

[346] Liang Li et al. "A Comprehensive Study of Gamma-Ray Burst Optical Emission. I. Flares and Early Shallow-decay Component". In: *Astrophysical Journal* 758.1, 27 (2012), p. 27. DOI: 10.1088/0004-637X/758/1/27. arXiv: 1203.2332 [astro-ph.HE].

[347] J. S. Bloom et al. "The Unusual afterglow of GRB 980326: Evidence for the gamma-ray burst - supernova connection". In: *Nature* 401 (1999), p. 453. DOI: 10.1038/46744. arXiv: astro-ph/9905301.

[348] Lazzati, D. et al. “The optical afterglow of GRB 000911: Evidence for an associated supernova?*”. In: *Astron. Astrophys.* 378.3 (2001), pp. 996–1002. DOI: 10.1051/0004-6361:20011282. URL: https://doi.org/10.1051/0004-6361:20011282.

[349] Vikram Rana et al. “Multi-wavelength Study of GRB 060906”. In: *American Astronomical Society Meeting Abstracts #213*. Vol. 213. American Astronomical Society Meeting Abstracts. Dec. 2009, 610.03, p. 610.03.

[350] A. Volnova et al. “GRB 100901A: optical observations in Mondy and r-light curve.” In: *GRB Coordinates Network* 11270 (Jan. 2010), p. 1.

[351] M. Nardini et al. “On the nature of the extremely fast optical rebrightening of the afterglow of GRB 081029”. In: *Astron. Astrophys* 531, A39 (2011), A39. DOI: 10.1051/0004-6361/201116814. arXiv: 1105.0917 [astro-ph.HE].

[352] J. Greiner et al. “The unusual afterglow of the Gamma-Ray Burst 100621A”. In: *Astron. Astrophys.* 560 (2013), A70. DOI: 10.1051/0004-6361/201321284. arXiv: 1304.5852 [astro-ph.HE].

[353] M. Nardini et al. “Afterglow rebrightenings as a signature of a long-lasting central engine activity? The emblematic case of GRB 100814A”. In: *Astron. Astrophys.* 562 (2014), A29. DOI: 10.1051/0004-6361/201321525. arXiv: 1312.1335 [astro-ph.HE].

[354] En-Wei Liang et al. “A Comprehensive Study of Gamma-Ray Burst Optical Emission. II. Afterglow Onset and Late Re-brightening Components”. In: *Astrophysical Journal* 774.1, 13 (2013), p. 13. DOI: 10.1088/0004-637X/774/1/13. arXiv: 1210.5142 [astro-ph.HE].

[355] Davide Lazzati et al. “The Afterglow of GRB 021004: Surfing on density waves”. In: *Astron. Astrophys.* 396 (2002), pp. L5–L10. DOI: 10.1051/0004-6361:20021618. arXiv: astro-ph/0210333.

[356] Xiaohu Wang and Abraham Loeb. “Variability of GRB afterglows due to interstellar turbulence”. In: *Astrophys. J.* 535 (2000), p. 788. DOI: 10.1086/308888. arXiv: astro-ph/9910477.

[357] Ehud Nakar and Jonathan Granot. “Smooth Light Curves from a Bumpy Ride: Relativistic Blast Wave Encounters a Density Jump”. In: *Mon. Not. R. Astron. Soc.* 380 (2007), pp. 1744–1760. DOI: 10.1111/j.1365-2966.2007.12245.x. arXiv: astro-ph/0606011.

[358] H. J. van Eerten and R. A. M. J. Wijers. "Gamma-Ray Burst afterglow scaling coefficients for general density profile via post-processing of blastwave solutions". In: *Mon. Not. R. Astron. Soc.* 394 (2009), p. 2164. DOI: 10.1111/j.1365-2966.2009.14482.x. arXiv: 0810.2250 [astro-ph].

[359] H. J. van Eerten et al. "No visible optical variability from a relativistic blast wave encountering a wind-termination shock". In: *Mon. Not. R. Astron. Soc.* 398.1 (Sept. 2009), p. 63. DOI: 10.1111/j.1745-3933.2009.00711.x. arXiv: 0906.3629 [astro-ph.HE].

[360] A. Vlasis et al. "Two-shell collisions in the gamma-ray burst afterglow phase". In: *Mon. Not. R. Astron. Soc* 415.1 (2011), pp. 279–291. DOI: 10.1111/j.1365-2966.2011.18696.x.

[361] Kunihito Ioka, Shiho Kobayashi, and Bing Zhang. "Long-acting engine or strong temporal anisotropy inferred from variabilities of gamma-ray burst afterglows". In: *Astrophys. J.* 631 (2005), p. 429. DOI: 10.1086/432567. arXiv: astro-ph/0409376.

[362] Rosalba Perna, Philip J. Armitage, and Bing Zhang. "Flares in long and short gamma-ray bursts: a common origin in a hyperaccreting accretion disk". In: *Astrophys. J. Lett.* 636 (2005), pp. L29–L32. DOI: 10.1086/499775. arXiv: astro-ph/0511506.

[363] Pawan Kumar and Tsvi Piran. "Some observational consequences of grb shock models". In: *Astrophys. J.* 523 (1999), p. 286. DOI: 10.1086/308537. arXiv: astro-ph/9906002.

[364] Jonathan Granot, Ehud Nakar, and Tsvi Piran. "The variable light curve of GRB 030329: The case for refreshed shocks". In: *Nature* 426 (2003), pp. 138–139. DOI: 10.1038/426138a. arXiv: astro-ph/0304563.

[365] Tanmoy Laskar et al. "A VLA Study of High-redshift GRBs. I. Multiwavelength Observations and Modeling of GRB 140311A". In: *Astrophys. J.* 858.1 (2018), p. 65. DOI: 10.3847/1538-4357/aab8f5. arXiv: 1707.05358 [astro-ph.HE].

[366] P. Mészáros. "Gamma Ray Bursts as Neutrino Sources". In: *Neutrino Astronomy: Current Status, Future Prospects*. 2017, pp. 1–14. DOI: 10.1142/9789814759410_0001. arXiv: 1511.01396 [astro-ph.HE].

[367] E. Waxman. "The Origin of IceCube's Neutrinos: Cosmic Ray Accelerators Embedded in Star Forming Calorimeters". In: *Neutrino Astronomy: Current Status, Future Prospects*. 2017, pp. 33–45. DOI: 10.1142/9789814759410_0003. arXiv: 1511.00815 [astro-ph.HE].

[368] Kohta Murase. "Active Galactic Nuclei as High-Energy Neutrino Sources". In: *Neutrino Astronomy: Current Status, Future Prospects*. Ed. by Thomas Gaisser and Albrecht Karle. 2017, pp. 15–31. DOI: 10.1142/9789814759410_0002. arXiv: 1511.01590 [astro-ph.HE].

[369] Kenji Toma, Xuefeng Wu, and Péter Mészáros. "Photosphere-internal shock model of gamma-ray bursts: case studies of Fermi/LAT bursts". In: *Mont. Not. Roy. Astron. Soc.* 415.2 (Aug. 2011), pp. 1663–1680. DOI: 10.1111/j.1365-2966.2011.18807.x. arXiv: 1002.2634 [astro-ph.HE].

[370] Mario Vietri. "On the acceleration of ultrahigh-energy cosmic rays in gamma-ray bursts". In: *Astrophys. J.* 453 (1995), pp. 883–889. DOI: 10.1086/176448. arXiv: astro-ph/9506081.

[371] Zhuo Li, Z. G. Dai, and T. Lu. "Long term neutrino afterglows from gamma-ray bursts". In: *Astron. Astrophys.* 396 (2002), pp. 303–308. DOI: 10.1051/0004-6361:20021397. arXiv: astro-ph/0208435.

[372] Soebur Razzaque. "Long-lived PeV–EeV neutrinos from gamma-ray burst blastwave". In: *Phys. Rev. D* 88.10 (2013), p. 103003. DOI: 10.1103/PhysRevD.88.103003. arXiv: 1307.7596 [astro-ph.HE].

[373] Kohta Murase. "High energy neutrino early afterglows gamma-ray bursts revisited". In: *Phys. Rev. D* 76 (2007), p. 123001. DOI: 10.1103/PhysRevD.76.123001. arXiv: 0707.1140 [astro-ph].

[374] Markus Ahlers and Francis Halzen. "High-energy cosmic neutrino puzzle: a review". In: *Rept. Prog. Phys.* 78.12 (2015), p. 126901. DOI: 10.1088/0034-4885/78/12/126901. URL: https://doi.org/10.1088/0034-4885/78/12/126901.

[375] R. Abbasi et al. "Measurement of Astrophysical Tau Neutrinos in IceCube's High-Energy Starting Events". In: *Eur. Phys. J. C* 82.11 (Nov. 2020), p. 1031. DOI: 10.1140/epjc/s10052-022-10795-y. arXiv: 2011.03561 [hep-ex].

[376] Tonia M. Venters et al. "POEMMA's Target of Opportunity Sensitivity to Cosmic Neutrino Transient Sources". In: *Phys. Rev. D* 102 (2020), p. 123013. DOI: 10.1103/PhysRevD.102.123013. arXiv: 1906.07209 [astro-ph.HE].

[377] A. Panaitescu, W. T. Vestrand, and P. Wozniak. "An external-shock model for GRB afterglow 130427A". In: *Mon. Not. R. Astron. Soc.* 436 (2013), p. 3106. DOI: 10.1093/mnras/stt1792. arXiv: 1311.5867 [astro-ph.HE].

[378] D. A. Perley et al. "The Afterglow of GRB 130427A from 1 to 10^16 GHz". In: *Astrophys. J.* 781 (2014), p. 37. DOI: 10.1088/0004-637X/781/1/37. arXiv: 1307.4401 [astro-ph.HE].

[379] M. De Pasquale et al. "The 80 Ms follow-up of the X-ray afterglow of GRB 130427A challenges the standard forward shock model". In: *Mon. Not. Roy. Astron. Soc.* 462.1 (2016), pp. 1111–1122. DOI: 10.1093/mnras/stw1704. arXiv: 1602.04158 [astro-ph.HE].

[380] Abraham D. Falcone et al. "The giant x-ray flare of grb 050502b: evidence for late-time internal engine activity". In: *Astrophys. J.* 641 (2006), pp. 1010–1017. DOI: 10.1086/500655. arXiv: astro-ph/0512615.

[381] Patrizia Romano et al. "X-ray flare in xrf 050406: evidence for prolonged engine activity". In: *Astron. Astrophys.* 450 (2006), pp. 59–68. DOI: 10.1051/0004-6361:20054172. arXiv: astro-ph/0601173.

[382] R. D. Blandford and C. F. McKee. "Fluid dynamics of relativistic blast waves". In: *Physics of Fluids* 19 (Aug. 1976), pp. 1130–1138. DOI: 10.1063/1.861619.

[383] Re'em Sari, Tsvi Piran, and Ramesh Narayan. "Spectra and light curves of gamma-ray burst afterglows". In: *Astrophys. J. Lett.* 497 (1998), p. L17. DOI: 10.1086/311269. arXiv: astro-ph/9712005.

[384] Roger A. Chevalier and Zhi-Yun Li. "Wind interaction models for gamma-ray burst afterglows: The Case for two types of progenitors". In: *Astrophys. J.* 536 (2000), pp. 195–212. DOI: 10.1086/308914. arXiv: astro-ph/9908272.

[385] R. A. Chevalier and Z. Y. Li. "Gamma-ray burst environments and progenitors". In: *Astrophys. J. Lett.* 520 (1999), pp. L29–L32. DOI: 10.1086/312147. arXiv: astro-ph/9904417.

[386] G. Ghisellini, G. Ghirlanda, and L. Nava. "GeV emission from Gamma Ray Bursts: a radiative fireball?" In: *Mon. Not. R. Astron. Soc.* 403 (2010), p. 926. DOI: 10.1111/j.1365-2966.2009.16171.x. arXiv: 0910.2459 [astro-ph.HE].

[387] Evgeny Derishev and Tsvi Piran. "GRB Afterglow Parameters in the Era of TeV Observations: The Case of GRB 190114C". In: *Astrophys. J.* 923.2 (2021), p. 135. DOI: 10.3847/1538-4357/ac2dec. arXiv: 2106.12035 [astro-ph.HE].

[388] Eli Waxman. "High-energy cosmic rays and neutrinos from cosmological gamma-ray burst fireballs". In: *Phys. Scripta T* 85 (2000). Ed. by L. Bergström, C. Fransson, and P. Carlson, pp. 117–126. DOI: 10.1238/Physica.Topical.085a00117. arXiv: astro-ph/9911395.

[389] A. Panaitescu and P. Kumar. "Analytic light-curves of gamma-ray burst afterglows: homogeneous versus wind external media". In: *Astrophys. J.* 543 (2000), p. 66. DOI: 10.1086/317090. arXiv: astro-ph/0003246.

[390] Shan Gao, Katsuaki Asano, and Péter Mészáros. "High Energy Neutrinos from Dissipative Photospheric Models of Gamma Ray Bursts". In: *JCAP* 11.11, 058 (Nov. 2012), p. 058. DOI: 10.1088/1475-7516/2012/11/058. arXiv: 1210.1186 [astro-ph.HE].

[391] Donald C. Warren et al. "Synchrotron self-absorption in GRB afterglows: the effects of a thermal electron population". In: *Mon. Not. Roy. Astron. Soc.* 480.3 (2018), pp. 4060–4068. DOI: 10.1093/mnras/sty2138. arXiv: 1804.06030 [astro-ph.HE].

[392] Jessymol K. Thomas, Reetanjali Moharana, and Soebur Razzaque. "Ultrahigh energy neutrino afterglows of nearby long duration gamma-ray bursts". In: *Phys. Rev. D* 96.10 (2017), p. 103004. DOI: 10.1103/PhysRevD.96.103004. arXiv: 1710.04024 [astro-ph.HE].

[393] R. A. M. J. Wijers and T. J. Galama. "Physical parameters of GRB 970508 and GRB 971214 from their afterglow synchrotron emission". In: *Astrophys. J.* 523 (1999), pp. 177–186. DOI: 10.1086/307705. arXiv: astro-ph/9805341.

[394] J. G. Kirk et al. "Particle acceleration at ultrarelativistic shocks: an eigenfunction method". In: *Astrophys. J.* 542 (2000), p. 235. DOI: 10.1086/309533. arXiv: astro-ph/0005222.

[395] P. A. Curran et al. "On the Electron Energy Distribution Index of Swift Gamma-ray Burst Afterglows". In: *Astrophys. J. Letter* 716.2 (June 2010), pp. L135–L139. DOI: 10.1088/2041-8205/716/2/L135. arXiv: 0908.0891 [astro-ph.HE].

[396] J. Greiner et al. "The nature of "dark" gamma-ray bursts". In: *Astronomy and Astrophysics* 526, A30 (Feb. 2011), A30. DOI: 10.1051/0004-6361/201015458. arXiv: 1011.0618 [astro-ph.HE].

[397] S. R. Oates et al. "A statistical comparison of the optical/UV and X-ray afterglows of gamma-ray bursts using the Swift Ultraviolet Optical and X-ray Telescopes". In: *MNRAS* 412.1 (Mar. 2011), pp. 561–579. DOI: 10.1111/j.1365-2966.2010.17928.x. arXiv: 1010.6212 [astro-ph.HE].

[398] James Matthews, Anthony Bell, and Katherine Blundell. "Particle acceleration in astrophysical jets". In: *New Astron. Rev.* 89 (2020), p. 101543. DOI: 10.1016/j.newar.2020.101543. arXiv: 2003.06587 [astro-ph.HE].

[399] Soebur Razzaque, Péter Mészáros, and Eli Waxman. "High energy neutrinos from a slow jet model of core collapse supernovae". In: *Mod. Phys. Lett. A* 20 (2005), pp. 2351–2368. DOI: 10.1142/S0217732305018414. arXiv: astro-ph/0509729.

[400] Frank C. Jones. "Inverse Compton Scattering of Cosmic-Ray Electrons". In: *Physical Review* 137.5B (5B Mar. 1965), pp. 1306–1311. DOI: 10.1103/PhysRev.137.B1306. URL: https://link.aps.org/doi/10.1103/PhysRev.137.B1306.

[401] Kevin Cahill. "Flat Space, Dark Energy, and the Cosmic Microwave Background". In: *Eur. J. Phys.* 41.3 (2020), p. 035603. DOI: 10.1088/1361-6404/ab738d. arXiv: 2002.11464 [physics.gen-ph].

[402] S. B. Cenko et al. "The Collimation and Energetics of the Brightest Swift Gamma-ray Bursts". In: *Astrophys. J.* 711.2 (2010), pp. 641–654. DOI: 10.1088/0004-637X/711/2/641. arXiv: 0905.0690 [astro-ph.HE].

[403] Rasha Abbasi et al. "Searches for Neutrinos from Precursors and Afterglows of Gamma-Ray Bursts using the IceCube Neutrino Observatory". In: *PoS* ICRC2021 (2021), p. 1118. DOI: 10.22323/1.395.1118. arXiv: 2107.08870 [astro-ph.HE].

[404] W. S. Paciesas et al. "The Fourth batse gamma-ray burst catalog (revised)". In: *Astrophys. J. Suppl.* 122 (1999), pp. 465–495. DOI: 10.1086/313224. arXiv: astro-ph/9903205.

[405] P. Giommi et al. "3HSP J095507.9+355101: a flaring extreme blazar coincident in space and time with IceCube-200107A". In: *Astron. Astrophys.* 640 (2020), p. L4. DOI: 10.1051/0004-6361/202038423. arXiv: 2003.06405 [astro-ph.HE].

[406] A. Franckowiak et al. "Patterns in the Multiwavelength Behavior of Candidate Neutrino Blazars". In: *Astrophys. J.* 893.2 (2020), p. 162. DOI: 10.3847/1538-4357/ab8307. arXiv: 2001.10232 [astro-ph.HE].

[407] S. Garrappa et al. "Investigation of two Fermi-LAT gamma-ray blazars coincident with high-energy neutrinos detected by IceCube". In: *Astrophys. J.* 880.2 (2019), 880:103. DOI: 10.3847/1538-4357/ab2ada. arXiv: 1901.10806 [astro-ph.HE].

[408] F. Krauß et al. “Fermi/LAT counterparts of IceCube neutrinos above 100 TeV”. In: *Astron. Astrophys.* 620 (2018), A174. DOI: 10.1051/0004-6361/201834183. arXiv: 1810.08482 [astro-ph.HE].

[409] M. Kadler et al. “Coincidence of a high-fluence blazar outburst with a PeV-energy neutrino event”. In: *Nature Phys.* 12.8 (2016), pp. 807–814. DOI: 10.1038/NPHYS3715. arXiv: 1602.02012 [astro-ph.HE].

[410] Simeon Reusch et al. “Candidate Tidal Disruption Event AT2019fdr Coincident with a High-Energy Neutrino”. In: *Phys. Rev. Lett.* 128.22 (Nov. 2022), p. 221101. DOI: 10.1103/PhysRevLett.128.221101. arXiv: 2111.09390 [astro-ph.HE].

[411] A. Albert et al. “Constraining the contribution of Gamma-Ray Bursts to the high-energy diffuse neutrino flux with 10 yr of ANTARES data”. In: *Mon. Not. R. Astron. Soc.* 500.4 (2020), pp. 5614–5628. DOI: 10.1093/mnras/staa3503. arXiv: 2008.02127 [astro-ph.HE].

[412] Soebur Razzaque and Lili Yang. “PeV-EeV neutrinos from GRB blast waves in IceCube and future neutrino telescopes”. In: *Phys. Rev. D* 91 (2015), p. 043003. DOI: 10.1103/PhysRevD.91.043003. arXiv: 1411.7491 [astro-ph.HE].

[413] Gang Guo, Yong-Zhong Qian, and Meng-Ru Wu. “Neutrino Production Associated with Late Bumps in Gamma-Ray Bursts and Potential Contribution to Diffuse Flux at IceCube”. In: *Astrophys. J.* 890 (2020), p. 83. DOI: 10.3847/1538-4357/ab6bcf. arXiv: 1911.07568 [astro-ph.HE].

[414] Kohta Murase and Shigehiro Nagataki. “High Energy Neutrino Flash from Far-UV/X-ray Flares of Gamma-Ray Bursts”. In: *Phys. Rev. Lett.* 97 (2006), p. 051101. DOI: 10.1103/PhysRevLett.97.051101. arXiv: astro-ph/0604437.

[415] Yizhong Fan and Tsvi Piran. “Sub-gev flashes in gamma-ray burst afterglows as probes of underlying bright uv flares”. In: *Mon. Not. R. Astron. Soc.* 370 (2006), pp. L24–L28. DOI: 10.1111/j.1745-3933.2006.00181.x. arXiv: astro-ph/0601619.

[416] Rasha Abbasi et al. “Sensitivity studies for the IceCube-Gen2 radio array”. In: *PoS* ICRC2021 (2021), p. 1183. DOI: 10.22323/1.395.1183. arXiv: 2107.08910 [astro-ph.HE].

[417] M. G. Aartsen et al. “IceCube Search for Neutrinos Coincident with Compact Binary Mergers from LIGO-Virgo’s First Gravitational-wave Transient Catalog”. In: *Astrophys. J. Lett.* 898.1, L10 (July 2020), p. L10. DOI: 10.3847/2041-8213/ab9d24. arXiv: 2004.02910 [astro-ph.HE].

[418] P. Allison et al. “Design and Initial Performance of the Askaryan Radio Array Prototype EeV Neutrino Detector at the South Pole”. In: *Astropart. Phys.* 35 (2012), pp. 457–477. DOI: 10.1016/j.astropartphys.2011.11.010. arXiv: 1105.2854 [astro-ph.IM].

[419] S. W. Barwick et al. “A First Search for Cosmogenic Neutrinos with the ARIANNA Hexagonal Radio Array”. In: *Astropart. Phys.* 70 (2015), pp. 12–26. DOI: 10.1016/j.astropartphys.2015.04.002. arXiv: 1410.7352 [astro-ph.HE].

[420] S. W. Barwick et al. “Design and Performance of the ARIANNA HRA-3 Neutrino Detector Systems”. In: *IEEE Trans. Nucl. Sci.* 62.5 (2015), pp. 2202–2215. DOI: 10.1109/TNS.2015.2468182. arXiv: 1410.7369 [astro-ph.IM].

[421] P. W. Gorham et al. “Observational Constraints on the Ultra-high Energy Cosmic Neutrino Flux from the Second Flight of the ANITA Experiment”. In: *Phys. Rev. D* 82 (2010). [Erratum: Phys.Rev.D 85, 049901 (2012)], p. 022004. DOI: 10.1103/PhysRevD.82.022004. arXiv: 1003.2961 [astro-ph.HE].

[422] K. Kotera, D. Allard, and A. V. Olinto. “Cosmogenic Neutrinos: parameter space and detectabilty from PeV to ZeV”. In: *JCAP* 10 (2010), p. 013. DOI: 10.1088/1475-7516/2010/10/013. arXiv: 1009.1382 [astro-ph.HE].

[423] Klaes Møller, Peter B. Denton, and Irene Tamborra. “Cosmogenic Neutrinos Through the GRAND Lens Unveil the Nature of Cosmic Accelerators”. In: *JCAP* 05 (2019), p. 047. DOI: 10.1088/1475-7516/2019/05/047. arXiv: 1809.04866 [astro-ph.HE].

[424] Arjen van Vliet, Rafael Alves Batista, and Jörg R. Hörandel. “Determining the fraction of cosmic-ray protons at ultrahigh energies with cosmogenic neutrinos”. In: *Phys. Rev. D* 100.2 (2019), p. 021302. DOI: 10.1103/PhysRevD.100.021302. arXiv: 1901.01899 [astro-ph.HE].

[425] Claire Guépin et al. “Ultra-High Energy Cosmic Rays and Neutrinos from Tidal Disruptions by Massive Black Holes”. In: *Astron. Astrophys.* 616 (2018). [Erratum: Astron.Astrophys. 636, C3 (2020)], A179. DOI: 10.1051/0004-6361/201732392. arXiv: 1711.11274 [astro-ph.HE].

[426] Ke Fang et al. “Testing the Newborn Pulsar Origin of Ultrahigh Energy Cosmic Rays with EeV Neutrinos”. In: *Phys. Rev. D* 90.10 (2014). [Erratum: Phys.Rev.D 92, 129901 (2015)], p. 103005. DOI: 10.1103/PhysRevD.90.103005. arXiv: 1311.2044 [astro-ph.HE].

[427] J. Greiner et al. "GROND - a 7-channel imager". In: *Publ. Astron. Soc. Pac.* 120 (2008), p. 405. DOI: 10.1086/587032. arXiv: 0801.4801 [astro-ph].

[428] S. Poolakkil et al. "The Fermi-GBM Gamma-Ray Burst Spectral Catalog: 10 yr of Data". In: *Astrophys. J.* 913.1 (2021), p. 60. DOI: 10.3847/1538-4357/abf24d. arXiv: 2103.13528 [astro-ph.HE].

[429] L. A. Ford et al. "BATSE observations of gamma-ray burst spectra. 2. Peak energy evolution in bright, long bursts". In: *Astrophys. J.* 439 (1995), p. 307. DOI: 10.1086/175174. arXiv: astro-ph/9407090.

[430] V. A. Acciari et al. "Teraelectronvolt emission from the γ-ray burst GRB 190114C". In: *Nature* 575.7783 (2019), pp. 455–458. DOI: 10.1038/s41586-019-1750-x. arXiv: 2006.07249 [astro-ph.HE].

[431] Yusuke Suda et al. "Observation of a relatively low luminosity long duration GRB 201015A by the MAGIC telescopes". In: *PoS* ICRC2021 (2021), p. 797. DOI: 10.22323/1.395.0797.

[432] Satoshi Fukami et al. "Very-high-energy gamma-ray emission from GRB 201216C detected by MAGIC". In: *PoS* ICRC2021 (2021), p. 788. DOI: 10.22323/1.395.0788.

[433] Yong Huang et al. "LHAASO observed GRB 221009A with more than 5000 VHE photons up to around 18 TeV". In: *GRB Coordinates Network* 32677 (Oct. 2022), p. 1.

[434] P. Meszaros, M. J. Rees, and H. Papathanassiou. "Spectral properties of blast wave models of gamma-ray burst sources". In: *Astrophys. J.* 432 (1994), pp. 181–193. DOI: 10.1086/174559. arXiv: astro-ph/9311071.

[435] Charles D. Dermer, James Chiang, and Kurt E. Mitman. "Beaming, baryon-loading, and the synchrotron self-compton component in gamma-ray burst blast waves energized by external shocks". In: *Astrophys. J.* 537 (2000), p. 785. DOI: 10.1086/309061. arXiv: astro-ph/9910240.

[436] Peter Meszaros. "Theories of gamma-ray bursts". In: *Ann. Rev. Astron. Astrophys.* 40 (2002), pp. 137–169. DOI: 10.1146/annurev.astro.40.060401.093821. arXiv: astro-ph/0111170.

[437] G. Ghisellini and A. Celotti. "Quasi-thermal comptonization and gamma-ray bursts". In: *Astrophys. J. Lett.* 511 (1999), p. L93. DOI: 10.1086/311845. arXiv: astro-ph/9812079.

[438] J. Chiang and C. D. Dermer. "Synchrotron and ssc emission and the blast-wave model of gamma-ray bursts". In: *Astrophys. J.* 512 (1999), p. 699. DOI: 10.1086/306789. arXiv: astro-ph/9803339.

[439] Ehud Nakar, Shin'ichiro Ando, and Re'em Sari. "Klein-Nishina Effects on Optically Thin Synchrotron and Synchrotron Self-Compton Spectrum". In: *Astrophys. J.* 703.1 (Sept. 2009), pp. 675–691. DOI: 10.1088/0004-637X/703/1/675. arXiv: 0903.2557 [astro-ph.HE].

[440] Ruo-Yu Liu, Xiang-Yu Wang, and Xue-Feng Wu. "Interpretation of the unprecedentedly long-lived high-energy emission of GRB 130427A". In: *Astrophys. J. Lett.* 773 (2013), p. L20. DOI: 10.1088/2041-8205/773/2/L20. arXiv: 1306.5207 [astro-ph.HE].

[441] N. Fraija et al. "Synchrotron self-Compton as a likely mechanism of photons beyond the synchrotron limit in GRB 190114C". In: *Astrophys. J.* 883 (2019), p. 162. DOI: 10.3847/1538-4357/ab3ec4. arXiv: 1907.06675 [astro-ph.HE].

[442] Katsuaki Asano, Kohta Murase, and Kenji Toma. "Probing Particle Acceleration through Broadband Early Afterglow Emission of MAGIC Gamma-Ray Burst GRB 190114C". In: *Astrophys. J.* 905.2 (2020), p. 105. DOI: 10.3847/1538-4357/abc82c. arXiv: 2007.06307 [astro-ph.HE].

[443] Dmitry Khangulyan, Andrew M. Taylor, and Felix Aharonian. "The formation of hard VHE spectra from GRB afterglow via Two-Zone Synchrotron Self-Compton Emission". In: *arXiv e-prints*, arXiv:2301.08578 (Jan. 2023), arXiv:2301.08578. DOI: 10.48550/arXiv.2301.08578. arXiv: 2301.08578 [astro-ph.HE].

[444] Markus Bottcher and Charles D. Dermer. "High-energy gamma-rays from ultrahigh-energy cosmic ray protons in gamma-ray bursts". In: *Astrophys. J. Lett.* 499 (1998), pp. L131–L134. DOI: 10.1086/311366. arXiv: astro-ph/9801027.

[445] Katsuaki Asano, Susumu Inoue, and Péter Mészáros. "Prompt High-Energy Emission from Proton-Dominated Gamma-Ray Bursts". In: *Astrophys. J.* 699 (2009), pp. 953–957. DOI: 10.1088/0004-637X/699/2/953. arXiv: 0807.0951 [astro-ph].

[446] Soebur Razzaque, Charles D. Dermer, and Justin D. Finke. "Synchrotron radiation from ultra-high energy protons and the Fermi observations of GRB 080916C". In: *Open Astron. J.* 3 (2010), pp. 150–155. DOI: 10.2174/1874381101003010150. arXiv: 0908.0513 [astro-ph.HE].

[447] S. Gagliardini et al. "On the hadronic origin of the TeV radiation from GRB 190114C". In: *arXiv e-prints*, arXiv:2209.01940 (Sept. 2022), arXiv:2209.01940. arXiv: 2209.01940 [astro-ph.HE].

[448] Hebzibha Isravel, Asaf Pe'er, and Damien Bégué. "Proton Synchrotron Origin of the Very High Energy Emission of GRB 190114C". In: *arXiv e-prints*, arXiv:2210.02363 (Oct. 2022), arXiv:2210.02363. arXiv: 2210.02363 [astro-ph.HE].

[449] Sarira Sahu and Carlos E. López Fortín. "Origin of sub-TeV afterglow emission from gamma-ray bursts GRB 190114C and GRB 180720B". In: *Astrophys. J. Lett.* 895.2 (2020), p. L41. DOI: 10.3847/2041-8213/ab93da. arXiv: 2005.12383 [astro-ph.HE].

[450] Sarira Sahu, Isabel Abigail Valadez Polanco, and Subhash Rajpoot. "Very High-energy Afterglow Emission of GRB 190829A: Evidence for Its Hadronic Origin?" In: *Astrophys. J.* 929.1 (2022), p. 70. DOI: 10.3847/1538-4357/ac5cc6. arXiv: 2204.04822 [astro-ph.HE].

[451] S. Schulze et al. "The circumburst density profile around GRB progenitors". In: *Gamma Ray Bursts 2010*. Ed. by J. E. McEnery, J. L. Racusin, and N. Gehrels. Vol. 1358. American Institute of Physics Conference Series. Aug. 2011, pp. 165–168. DOI: 10.1063/1.3621763.

[452] Paul A Crowther. "Physical Properties of Wolf-Rayet Stars". In: *Ann. Rev. Astron. Astrophys.* 45 (2007), pp. 177–219. DOI: 10.1146/annurev.astro.45.051806.110615. arXiv: astro-ph/0610356.

[453] D. Frederiks et al. "Konus-Wind observation of GRB 180720B." In: *GRB Coordinates Network* 23011 (Jan. 2018), p. 1.

[454] R. Hamburg et al. "GRB 190114C: Fermi GBM detection." In: *GRB Coordinates Network* 23707 (Jan. 2019), p. 1.

[455] D. Frederiks et al. "Konus-Wind detection of GRB 221009A". In: *GRB Coordinates Network* 32668 (Oct. 2022), p. 1.

[456] D. A. Kann and J. F. Agui Fernandez. "GRB 221009A: Armchair Energetics". In: *GRB Coordinates Network* 32762 (Oct. 2022), p. 1.

[457] Zi-Qing Xia et al. "GRB 221009A: a 397.7 GeV photon observed by Fermi-LAT at 0.4 day after the GBM trigger". In: *GRB Coordinates Network* 32748 (Oct. 2022), p. 1.

[458] F. Aharonian et al. "H.E.S.S. follow-up observations of GRB221009A". In: *arXiv e-prints* (Mar. 2023). arXiv: 2303.10558 [astro-ph.HE].

[459] D. Frederiks et al. "Konus-Wind detection of GRB 201216C". In: *GRB Coordinates Network* 29084 (Dec. 2020), p. 1.

[460] O. J. Roberts and C. Meegan. "GRB 180720B: Fermi GBM observation." In: *GRB Coordinates Network* 22981 (Jan. 2018), p. 1.

[461] J. D. Gropp et al. "GRB 190114C: Swift detection of a very bright burst with a bright optical counterpart." In: *GRB Coordinates Network* 23688 (Jan. 2019), p. 1.

[462] K. Misra et al. "Low frequency view of GRB 190114C reveals time varying shock micro-physics". In: *Mon. Not. Roy. Aastron. Soc.* 504.4 (Nov. 2019), pp. 5685–5701. DOI: 10.1093/mnras/stab1050. arXiv: 1911.09719 [astro-ph.HE].

[463] S. Lesage et al. "GRB 221009A: Fermi GBM observation". In: *GRB Coordinates Network* 32642 (Oct. 2022), p. 1.

[464] S. Belkin et al. "GRB 221009A (Swift J1913.1+1946): Mondy optical observations". In: *GRB Coordinates Network* 32645 (Oct. 2022), p. 1.

[465] Eli Waxman. "Angular size and emission time scales of relativistic fireballs". In: *Astrophys. J. Lett.* 491 (1997), p. L19. DOI: 10.1086/311057. arXiv: astro-ph/9709190.

[466] Z. G. Dai and T. Lu. "Gamma-ray burst afterglows: Effects of radiative corrections and nonuniformity of the surrounding medium". In: *Mon. Not. Roy. Astron. Soc.* 298 (1998), pp. 87–92. DOI: 10.1046/j.1365-8711.1998.01681.x. arXiv: astro-ph/9806305.

[467] Jia Ren, Yun Wang, and Lu-Lu Zhang. "Very High Energy Afterglow Emission of GRB~221009A: Lessons Learned from the Brightest Long Gamma-ray Burst in a Wind Environment". In: *arXiv e-prints*, arXiv:2210.10673 (Oct. 2022), arXiv:2210.10673. arXiv: 2210.10673 [astro-ph.HE].

[468] *Swift* Burst Analyser. *BAT-XRT-UVOT light curves*. 2022. URL: https://www.swift.ac.uk/burst_analyser/.

[469] I. Sfaradi et al. "GRB 180720B: AMI-LA 15.5 GHz observation." In: *GRB Coordinates Network* 23037 (Jan. 2018), p. 1.

[470] N. Fraija et al. "Modeling the observations of GRB 180720B: From radio to sub-TeV gamma-rays". In: *Astrophys. J.* 885.1, 29 (May 2019), p. 29. DOI: 10.3847/1538-4357/ab3e4b. arXiv: 1905.13572 [astro-ph.HE].

[471] Wael Farah et al. "GRB221009A/Swift J1913.1+1946: ATA follow-up observations". In: *GRB Coordinates Network* 32655 (Oct. 2022), p. 1.

[472] Asaf Pe'er and Eli Waxman. "High energy photon emission in the early afterglow of GRB's". In: *Astrophys. J.* 633 (2005). [Erratum: Astrophys.J. 638, 1187 (2006)], pp. 1018–1026. DOI: 10.1086/468175. arXiv: astro-ph/0407084.

[473] Matthew G. Baring and Alice K. Harding. "The Escape of high-energy photons from gamma-ray bursts". In: *Astrophys. J.* 491 (1997), p. 663. DOI: 10.1086/304982. arXiv: astro-ph/9711217.

[474] Yoram Lithwick and Re'em Sari. "Lower limits on Lorentz factors in gamma-ray bursts". In: *Astrophys. J.* 555 (2001), pp. 540–545. DOI: 10.1086/321455. arXiv: astro-ph/0011508.

[475] R. Hascoët et al. "Do Fermi Large Area Telescope observations imply very large Lorentz factors in gamma-ray burst outflows?" In: *Mon. Not. Roy. Astron. Soc.* 421.1 (Mar. 2012), pp. 525–545. DOI: 10.1111/j.1365-2966.2011.20332.x. arXiv: 1107.5737 [astro-ph.HE].

[476] N. Fraija et al. "Analysis and Modeling of the Multi-wavelength Observations of the Luminous GRB 190114C". In: *Astrophys. J. Lett.* 879.2 (2019), p. L26. DOI: 10.3847/2041-8213/ab2ae4. arXiv: 1904.06976 [astro-ph.HE].

[477] David Eichler and Eli Waxman. "The Efficiency of electron acceleration in collisionless shocks and GRB energetics". In: *Astrophys. J.* 627 (2005), pp. 861–867. DOI: 10.1086/430596. arXiv: astro-ph/0502070.

[478] Paz Beniamini, Lara Nava, and Tsvi Piran. "A revised analysis of gamma-ray bursts' prompt efficiencies". In: *Mon. Not. Roy. Astron. Soc.* 461.1 (2016), pp. 51–59. DOI: 10.1093/mnras/stw1331. arXiv: 1606.00311 [astro-ph.HE].

[479] Xiang-Yu Wang et al. "Synchrotron self-Compton emission from external shocks as the origin of the sub-TeV emission in GRB 180720B and GRB 190114C". In: *Astrophys. J.* 884.2, 117 (May 2019), p. 117. DOI: 10.3847/1538-4357/ab426c. arXiv: 1905.11312 [astro-ph.HE].

[480] Yuri Sato et al. "Two-component jet model for multi-wavelength afterglow emission of the extremely energetic burst GRB 221009A". In: *arXiv e-prints* (Dec. 2022). arXiv: 2212.09266 [astro-ph.HE].

[481] Robert Filgas et al. "GRB 091127: The cooling break race on magnetic fuel". In: *Astron. Astrophys.* 535 (2011), A57. DOI: 10.1051/0004-6361/201117695. arXiv: 1109.2810 [astro-ph.HE].

[482] Tanmoy Laskar et al. "The Radio to GeV Afterglow of GRB 221009A". In: *Astrophys. J. Lett.* 946.1 (2023), p. L23. DOI: 10.3847/2041-8213/acbfad. arXiv: 2302.04388 [astro-ph.HE].

[483] G. Ghirlanda et al. “Bulk Lorentz factors of Gamma-Ray Bursts”. In: *Astron. Astrophys.* 609 (2018), A112. DOI: 10.1051/0004-6361/201731598. arXiv: 1711.06257 [astro-ph.HE].

[484] Romain Hascoët et al. “Estimates for Lorentz factors of gamma-ray bursts from early optical afterglow observations”. In: *Astrophys. J.* 782 (2014), p. 5. DOI: 10.1088/0004-637X/782/1/5. arXiv: 1304.5813 [astro-ph.HE].

[485] Kohta Murase et al. “Neutrinos from the Brightest Gamma-Ray Burst?” In: *Astrophys. J. Lett.* 941.1 (2022), p. L10. DOI: 10.3847/2041-8213/aca3ae. arXiv: 2210.15625 [astro-ph.HE].

[486] Ruo-Yu Liu, Hai-Ming Zhang, and Xiang-Yu Wang. “Constraints on the Model of Gamma-ray Bursts and Implications from GRB 221009A: GeV gamma rays v.s. High-energy Neutrinos”. In: *arXiv e-prints*, arXiv:2211.14200 (Nov. 2022), arXiv:2211.14200. arXiv: 2211.14200 [astro-ph.HE].

[487] Shunke Ai and He Gao. “Model Constraints Based on the IceCube Neutrino Nondetection of GRB 221009A”. In: *Astrophys. J.* 944.2 (2023), p. 115. DOI: 10.3847/1538-4357/acb3bf. arXiv: 2210.14116 [astro-ph.HE].

[488] Liang Li et al. “A Cosmological Fireball with 16% Gamma-Ray Radiative Efficiency”. In: *Astrophys. J. Lett.* 944.2, L57 (Feb. 2023), p. L57. DOI: 10.3847/2041-8213/acb99d. arXiv: 2212.02141 [astro-ph.HE].

[489] R. Abbasi et al. “Searches for Neutrinos from Gamma-Ray Bursts Using the IceCube Neutrino Observatory”. In: *Astrophys. J.* 939.2 (2022), p. 116. DOI: 10.3847/1538-4357/ac9785. arXiv: 2205.11410 [astro-ph.HE].

[490] IceCube Collaboration. “GRB 221009A: Upper limits from a neutrino search with IceCube”. In: *GRB Coordinates Network* 32665 (Oct. 2022), p. 1.

[491] Annika Rudolph et al. “Multi-messenger Model for the Prompt Emission from GRB 221009A”. In: *Astrophys. J. Lett.* 944.2, L34 (Feb. 2023), p. L34. DOI: 10.3847/2041-8213/acb6d7. arXiv: 2212.00766 [astro-ph.HE].

[492] N. Fraija et al. “Synchrotron Self-Compton Afterglow Closure Relations and Fermi-LAT-detected Gamma-Ray Bursts”. In: *Astrophys. J.* 934.2 (2022), p. 188. DOI: 10.3847/1538-4357/ac7a9c. arXiv: 2206.11490 [astro-ph.HE].

[493] B. P. Gompertz, A. S. Fruchter, and A. Pe'er. "The Environments of the Most Energetic Gamma-Ray Bursts". In: *Astrophys. J.* 866.2 (2018), p. 162. DOI: 10.3847/1538-4357/aadba8. arXiv: 1802.07730 [astro-ph.HE].

[494] He Gao et al. "A Complete Reference of the Analytical Synchrotron External Shock Models of Gamma-Ray Bursts". In: *New Astron. Rev.* 57 (2013), pp. 141–190. DOI: 10.1016/j.newar.2013.10.001. arXiv: 1310.2181 [astro-ph.HE].

[495] A. Panaitescu and P. Kumar. "Properties of Relativistic Jets in Gamma-Ray Burst Afterglows". In: *Astrophys. J.* 571.2 (June 2002), pp. 779–789. DOI: 10.1086/340094.

[496] N. Mirabal et al. "Time dependent optical spectroscopy of GRB 010222: Clues to the GRB environment". In: *Astrophys. J.* 578 (2002), pp. 818–832. DOI: 10.1086/342619. arXiv: astro-ph/0207009.

[497] John Scalo and J. Craig Wheeler. "Pre-existing superbubbles as the sites of gamma-ray bursts". In: *Astrophys. J.* 562 (2001), p. 664. DOI: 10.1086/323858. arXiv: astro-ph/0105369.

[498] Jorick S. Vink, Alex de Koter, and Henny J. G. L. M. Lamers. "Mass-loss predictions for o and b stars as a function of metallicity". In: *Astron. Astrophys.* 369 (2001), pp. 574–588. DOI: 10.1051/0004-6361:20010127. arXiv: astro-ph/0101509.

[499] D. A. Perley et al. "A Population of Massive, Luminous Galaxies Hosting Heavily Dust-Obscured Gamma-Ray Bursts: Implications for the Use of GRBs as Tracers of Cosmic Star Formation". In: *Astrophys. J.* 778 (2013), p. 128. DOI: 10.1088/0004-637X/778/2/128. arXiv: 1301.5903 [astro-ph.CO].

[500] D. A. Perley et al. "The Swift GRB Host Galaxy Legacy Survey. II. Rest-frame Near-IR Luminosity Distribution and Evidence for a Near-solar Metallicity Threshold". In: *Astrophys. J.* 817.1 (2016), p. 8. DOI: 10.3847/0004-637X/817/1/8. arXiv: 1504.02479 [astro-ph.GA].

[501] Hüsne Dereli-Bégué et al. "A wind environment and Lorentz factors of tens explain gamma-ray bursts X-ray plateau". In: *Nature Commun.* 13.1 (2022), p. 5611. DOI: 10.1038/s41467-022-32881-1. arXiv: 2207.11066 [astro-ph.HE].

[502] Tanima Mondal et al. “Probing Gamma-Ray Burst afterglows with the Cherenkov Telescope Array”. In: *arXiv e-prints*, arXiv:2212.07874 (Dec. 2022), arXiv:2212.07874. arXiv: 2212.07874 [astro-ph.HE].

[503] Zhen Cao et al. “Very high energy gamma-ray emission beyond 10 TeV from GRB 221009A”. In: (Oct. 2023). arXiv: 2310.08845 [astro-ph.HE].

[504] Dovi Poznanski et al. “An Unusually Fast-Evolving Supernova”. In: *Science* 327.5961 (Jan. 2010), p. 58. DOI: 10.1126/science.1181709. arXiv: 0911.2699 [astro-ph.SR].

[505] Cosimo Inserra. “Observational properties of extreme supernovae”. In: *Nature Astron.* 3.8 (2019), pp. 697–705. DOI: 10.1038/s41550-019-0854-4. arXiv: 1908.02314 [astro-ph.HE].

[506] Maryam Modjaz, Claudia P. Gutierrez, and Iair Arcavi. “New Regimes in the Observation of Core-Collapse Supernovae”. In: *Nature Astron.* 3.8 (2019), pp. 717–724. DOI: 10.1038/s41550-019-0856-2. arXiv: 1908.02476 [astro-ph.HE].

[507] P. J. Vallely et al. “High-Cadence, Early-Time Observations of Core-Collapse Supernovae From the TESS Prime Mission”. In: *Mon. Not. Roy. Astron. Soc.* 500.4 (2020), pp. 5639–5656. DOI: 10.1093/mnras/staa3675. arXiv: 2010.06596 [astro-ph.HE].

[508] Ning-Chen Sun et al. “A hot and luminous source at the site of the fast transient AT2018cow at 2-3 years after its explosion”. In: (Mar. 2022). DOI: 10.1093/mnrasl/slac023. arXiv: 2203.01960 [astro-ph.HE].

[509] Dheeraj R. Pasham et al. “Evidence for a compact object in the aftermath of the extragalactic transient AT2018cow”. In: *Nature Astron.* 6.2 (2022), pp. 249–258. DOI: 10.1038/s41550-021-01524-8. arXiv: 2112.04531 [astro-ph.HE].

[510] Ori D. Fox and Nathan Smith. “Signatures of circumstellar interaction in the unusual transient AT 2018cow”. In: *Mon. Not. Roy. Astron. Soc.* 488.3 (2019), pp. 3772–3782. DOI: 10.1093/mnras/stz1925. arXiv: 1903.01535 [astro-ph.HE].

[511] C. Pellegrino et al. “Circumstellar Interaction Powers the Light Curves of Luminous Rapidly Evolving Optical Transients”. In: *Astrophys. J.* 926.2 (2022), p. 125. DOI: 10.3847/1538-4357/ac3e63. arXiv: 2110.15370 [astro-ph.HE].

[512] Shing-Chi Leung et al. "A Model for the Fast Blue Optical Transient AT2018cow: Circumstellar Interaction of a Pulsational Pair-instability Supernova". In: *Astrophys. J.* 903.1 (2020), p. 66. DOI: 10.3847/1538-4357/abba33. arXiv: 2008.11404 [astro-ph.HE].

[513] Danfeng Xiang et al. "The Peculiar Transient AT2018cow: A Possible Origin of A Type Ibn/IIn Supernova". In: *Astrophys. J.* 910.1 (2021), p. 42. DOI: 10.3847/1538-4357/abdeba. arXiv: 2101.08009 [astro-ph.HE].

[514] Chun Chen and Rong-Feng Shen. "Radiative Diffusion in a Time-dependent Outflow: a Model for Fast Blue Optical Transients". In: *Res. Astron. Astrophys.* 22.3 (2022), p. 035017. DOI: 10.1088/1674-4527/ac488a. arXiv: 2201.12534 [astro-ph.HE].

[515] Diego Calderón, Ondřej Pejcha, and Paul C. Duffell. "Moving-mesh radiation-hydrodynamic simulations of wind-reprocessed transients". In: *Mon. Not. Roy. Astron.* 507.1 (Oct. 2021), pp. 1092–1105. DOI: 10.1093/mnras/stab2219. arXiv: 2105.08735 [astro-ph.SR].

[516] Anthony L. Piro and Wenbin Lu. "Wind-reprocessed Transients". In: *Astrophys. J.* 894.1 (2020), p. 2. DOI: 10.3847/1538-4357/ab83f6. arXiv: 2001.08770 [astro-ph.HE].

[517] Kohki Uno and Keiichi Maeda. "A Wind-Driven Model: Application to Peculiar Transients AT2018cow and iPTF14hls". In: (Mar. 2020). DOI: 10.3847/1538-4357/ab9632. arXiv: 2003.05795 [astro-ph.HE].

[518] Liang-Duan Liu et al. "Photospheric Radius Evolution of Homologous Explosions". In: *Astrophys. J. Lett.* 868.2 (2018), p. L24. DOI: 10.3847/2041-8213/aaeff6. arXiv: 1809.05048 [astro-ph.HE].

[519] N. Paul M. Kuin et al. "Swift spectra of AT2018cow: A White Dwarf Tidal Disruption Event?" In: *Mon. Not. Roy. Astron. Soc.* 487.2 (2019), pp. 2505–2521. DOI: 10.1093/mnras/stz053. arXiv: 1808.08492 [astro-ph.HE].

[520] Noam Soker, Aldana Grichener, and Avishai Gilkis. "Diversity of common envelope jets supernovae and the fast transient AT2018cow". In: *Mon. Not. Roy. Astron. Soc.* 484 (2019), p. 4972. DOI: 10.1093/mnras/stz364. arXiv: 1811.11106 [astro-ph.HE].

[521] Noam Soker. "A Common Envelope Jets Supernova (CEJSN) Impostor Scenario for Fast Blue Optical Transients". In: *Research in Astronomy and Astrophysics* 22.5, 055010 (May 2022), p. 055010. DOI: 10.1088/1674-4527/ac5b40. arXiv: 2201.07728 [astro-ph.HE].

[522] Kazumi Kashiyama and Eliot Quataert. "Fast Luminous Blue Transients from Newborn Black Holes". In: *Mon. Not. Roy. Astron. Soc.* 451.3 (2015), pp. 2656–2662. DOI: 10.1093/mnras/stv1164. arXiv: 1504.05582 [astro-ph.HE].

[523] Eliot Quataert, Daniel Lecoanet, and Eric R. Coughlin. "Black Hole Accretion Discs and Luminous Transients in Failed Supernovae from Non-Rotating Supergiants". In: *Mon. Not. Roy. Astron. Soc.* 485.1 (2019), pp. L83–L88. DOI: 10.1093/mnrasl/slz031. arXiv: 1811.12427 [astro-ph.SR].

[524] Maxim Lyutikov and Silvia Toonen. "FBOTs and AT2018cow following electron-capture collapse of merged white dwarfs". In: *Mon. Not. Roy. Astron. Soc.* 487 (2019), p. 5618. DOI: 10.1093/mnras/stz1640. arXiv: 1812.07569 [astro-ph.HE].

[525] Maxim Lyutikov. "On the nature of Fast Blue Optical Transients". In: (Apr. 2022). arXiv: 2204.08366 [astro-ph.HE].

[526] R. Abbasi et al. "Follow-up of Astrophysical Transients in Real Time with the IceCube Neutrino Observatory". In: *Astrophys. J.* 910.1 (2021), p. 4. DOI: 10.3847/1538-4357/abe123. arXiv: 2012.04577 [astro-ph.HE].

[527] Victor A. Acciari et al. "Searching for VHE gamma-ray emission associated with IceCube neutrino alerts using FACT, H.E.S.S., MAGIC, and VERITAS". In: *Proceedings of 37th International Cosmic Ray Conference — PoS(ICRC2021)*. Vol. 395. 2021, p. 960. DOI: 10.22323/1.395.0960. arXiv: 2109.04350 [astro-ph.HE].

[528] Jannis Necker et al. "ASAS-SN follow-up of IceCube high-energy neutrino alerts". In: (Apr. 2022). arXiv: 2204.00500 [astro-ph.HE].

[529] Robert Stein et al. "Neutrino follow-up with the Zwicky Transient Facility: Results from the first 24 campaigns". In: *Mon. Roy. Astron. Soc.* 521.4 (Mar. 2022), pp. 5046–5063. DOI: 10.1093/mnras/stad767. arXiv: 2203.17135 [astro-ph.HE].

[530] Ke Fang et al. “Multimessenger Implications of AT2018cow: High-energy Cosmic-Ray and Neutrino Emissions from Magnetar-powered Superluminous Transients”. In: *Astrophys. J.* 878.1 (2019), p. 34. DOI: 10.3847/1538-4357/ab1b72. arXiv: 1812.11673 [astro-ph.HE].

[531] Peter Meszaros and Eli Waxman. “TeV neutrinos from successful and choked gamma-ray bursts”. In: *Phys. Rev. Lett.* 87 (2001), p. 171102. DOI: 10.1103/PhysRevLett.87.171102. arXiv: astro-ph/0103275.

[532] D. Xiao and Z. G. Dai. “Neutrino Emission in the Jet Propagation Process”. In: *Astrophys. J.* 790.1 (2014), p. 59. DOI: 10.1088/0004-637X/790/1/59. arXiv: 1406.2792 [astro-ph.HE].

[533] M. Petropoulou et al. “Point-source and diffuse high-energy neutrino emission from Type IIn supernovae”. In: *Mon. Not. Roy. Astron. Soc.* 470.2 (2017), pp. 1881–1893. DOI: 10.1093/mnras/stx1251. arXiv: 1705.06752 [astro-ph.HE].

[534] Maria Petropoulou, Atish Kamble, and Lorenzo Sironi. “Radio synchrotron emission from secondary electrons in interaction-powered supernovae”. In: *Mon. Not. Roy. Astron. Soc.* 460.1 (2016), pp. 44–66. DOI: 10.1093/mnras/stw920. arXiv: 1603.00891 [astro-ph.HE].

[535] Boaz Katz, Nir Sapir, and Eli Waxman. “X-rays, gamma-rays and neutrinos from collisoinless shocks in supernova wind breakouts”. In: *arXiv e-prints*, arXiv:1106.1898 (June 2011), arXiv:1106.1898. arXiv: 1106.1898 [astro-ph.HE].

[536] Kohta Murase, Todd A. Thompson, and Eran O. Ofek. “Probing Cosmic-Ray Ion Acceleration with Radio-Submm and Gamma-Ray Emission from Interaction-Powered Supernovae”. In: *Mon. Not. Roy. Astron. Soc.* 440.3 (2014), pp. 2528–2543. DOI: 10.1093/mnras/stu384. arXiv: 1311.6778 [astro-ph.HE].

[537] Martina Cardillo, Elena Amato, and Pasquale Blasi. “On the cosmic ray spectrum from type II Supernovae expanding in their red giant presupernova wind”. In: *Astropart. Phys.* 69 (2015), pp. 1–10. DOI: 10.1016/j.astropartphys.2015.03.002. arXiv: 1503.03001 [astro-ph.HE].

[538] V. N. Zirakashvili and V. S. Ptuskin. “Type IIn supernovae as sources of high energy astrophysical neutrinos”. In: *Astropart. Phys.* 78 (2016), pp. 28–34. DOI: 10.1016/j.astropartphys.2016.02.004. arXiv: 1510.08387 [astro-ph.HE].

[539] Kohta Murase et al. “High-Energy Neutrino and Gamma-Ray Emission from Tidal Disruption Events”. In: *Astrophys. J.* 902.2 (2020), p. 108. DOI: 10.3847/1538-4357/abb3c0. arXiv: 2005.08937 [astro-ph.HE].

[540] B. Theodore Zhang and Kohta Murase. “Ultrahigh-energy cosmic-ray nuclei and neutrinos from engine-driven supernovae”. In: *Phys. Rev. D* 100.10 (2019), p. 103004. DOI: 10.1103/PhysRevD.100.103004. arXiv: 1812.10289 [astro-ph.HE].

[541] Kohta Murase and Imre Bartos. “High-Energy Multimessenger Transient Astrophysics”. In: *Ann. Rev. Nucl. Part. Sci.* 69 (2019), pp. 477–506. DOI: 10.1146/annurev-nucl-101918-023510. arXiv: 1907.12506 [astro-ph.HE].

[542] Reem Sari and Tsvi Piran. “Hydrodynamic time scales and temporal structure of GRBs”. In: *Astrophys. J. Lett.* 455 (1995), p. L143. DOI: 10.1086/309835. arXiv: astro-ph/9508081.

[543] M. A. Malkov and L. O’C. Drury. “Nonlinear theory of diffusive acceleration of particles by shock waves”. In: *Reports on Progress in Physics* 64.4 (Apr. 2001), pp. 429–481. DOI: 10.1088/0034-4885/64/4/201.

[544] D. Guetta, M. Spada, and E. Waxman. “Efficiency and spectrum of internal gamma-ray burst shocks”. In: *Astrophys. J.* 557 (2001), p. 399. DOI: 10.1086/321543. arXiv: astro-ph/0011170.

[545] Nayana A. J. and Poonam Chandra. “uGMRT Observations of a Fast and Blue Optical Transient—AT 2018cow”. In: *Astrophys. J. Lett.* 912.1 (2021), p. L9. DOI: 10.3847/2041-8213/abed55. arXiv: 2103.06008 [astro-ph.HE].

[546] Donald C. Ellison et al. “Particle Acceleration in Supernova Remnants and the Production of Thermal and Nonthermal Radiation”. In: *Astrophys. J.* 661 (2007), pp. 879–891. DOI: 10.1086/517518. arXiv: astro-ph/0702674.

[547] Daniel J. Patnaude and Robert A. Fesen. “Proper Motions and Brightness Variations of Nonthermal X-ray Filaments in the Cassiopeia A Supernova Remnant”. In: *Astrophys. J.* 697 (2009), pp. 535–543. DOI: 10.1088/0004-637X/697/1/535. arXiv: 0808.0692 [astro-ph].

[548] K. M. Schure et al. “Time-dependent particle acceleration in supernova remnants in different environments”. In: *Mon. Not. Roy. Astron.* 406.4 (Aug. 2010), pp. 2633–2649. DOI: 10.1111/j.1365-2966.2010.16857.x. arXiv: 1004.2766 [astro-ph.HE].

[549] Akihiro Suzuki, Takashi J. Moriya, and Tomoya Takiwaki. "A Systematic Study on the Rise Time–Peak Luminosity Relation for Bright Optical Transients Powered by Wind Shock Breakout". In: *Astrophys. J.* 899.1 (2020), p. 56. DOI: 10.3847/1538-4357/aba0ba. arXiv: 2006.16494 [astro-ph.HE].

[550] P. Slane et al. "A CR-hydro-NEI Model of the Structure and Broadband Emission from Tycho's Supernova Remnant". In: *Astrophys. J.* 783.1, 33 (Mar. 2014), p. 33. DOI: 10.1088/0004-637X/783/1/33.

[551] Toshiki Sato et al. "X-Ray Measurements of the Particle Acceleration Properties at Inward Shocks in Cassiopeia A". In: *Astrophys. J.* 853.1, 46 (Jan. 2018), p. 46. DOI: 10.3847/1538-4357/aaa021. arXiv: 1710.06992 [astro-ph.HE].

[552] Boaz Katz, Nir Sapir, and Eli Waxman. "X-rays, gamma-rays and neutrinos from collisoinless shocks in supernova wind breakouts". In: (June 2011). arXiv: 1106.1898 [astro-ph.HE].

[553] Eric R. Coughlin. "Energy-conserving, Relativistic Corrections to Strong Shock Propagation". In: (May 2019). DOI: 10.3847/1538-4357/ab29e6. arXiv: 1905.11991 [astro-ph.HE].

[554] Ben Margalit and Eliot Quataert. "Thermal Electrons in Mildly Relativistic Synchrotron Blast Waves". In: *Astrophys. J. Lett.* 923.1 (2021), p. L14. DOI: 10.3847/2041-8213/ac3d97. arXiv: 2111.00012 [astro-ph.HE].

[555] S. J. Prentice et al. "The Cow: discovery of a luminous, hot and rapidly evolving transient". In: *Astrophys. J. Lett.* 865.1 (2018), p. L3. DOI: 10.3847/2041-8213/aadd90. arXiv: 1807.05965 [astro-ph.HE].

[556] Jonathan Granot. "The Structure and Dynamics of GRB Jets". In: *Rev. Mex. Astron. Astrof. Ser. Conf.* 27 (2007), pp. 140–165. arXiv: astro-ph/0610379.

[557] J. P. Ostriker and J. E. Gunn. "On the Nature of Pulsars. I. Theory". In: *Astrophys. J.* 157 (Sept. 1969), p. 1395. DOI: 10.1086/150160.

[558] Akira Mizuta and Kunihito Ioka. "Opening Angles of Collapsar Jets". In: *Astrophys. J.* 777 (2013), p. 162. DOI: 10.1088/0004-637X/777/2/162. arXiv: 1304.0163 [astro-ph.HE].

[559] Jonathan C. Tan, Christopher D. Matzner, and Christopher F. McKee. "Trans-relativistic blast waves in supernovae as gamma-ray burst progenitors". In: *Astrophys. J.* 551 (2001), p. 946. DOI: 10.1086/320245. arXiv: astro-ph/0012003.

[560] Lorenzo Sironi and Anatoly Spitkovsky. "Particle Acceleration in Relativistic Magnetized Collisionless Electron-Ion Shocks". In: *Astrophys. J.* 726.2, 75 (Jan. 2011), p. 75. DOI: 10.1088/0004-637X/726/2/75. arXiv: 1009.0024 [astro-ph.HE].

[561] Rudolf Kippenhahn, Alfred Weigert, and Achim Weiss. *Stellar structure and evolution*. Vol. 192. Springer, 1990.

[562] Damiano Caprioli and Anatoly Spitkovsky. "Simulations of Ion Acceleration at Non-relativistic Shocks. I. Acceleration Efficiency". In: *Astrophys. J.* 783 (2014), p. 91. DOI: 10.1088/0004-637X/783/2/91. arXiv: 1310.2943 [astro-ph.HE].

[563] B. D. Metzger et al. "The protomagnetar model for gamma-ray bursts". In: *Mon. Not. Roy. Astron.* 413.3 (May 2011), pp. 2031–2056. DOI: 10.1111/j.1365-2966.2011.18280.x. arXiv: 1012.0001 [astro-ph.HE].

[564] Steven J. Sturner et al. "Temporal Evolution of Nonthermal Spectra from Supernova Remnants". In: *Astrophys. J.* 490.2 (Dec. 1997), pp. 619–632. DOI: 10.1086/304894.

[565] Justin D. Finke and Charles D. Dermer. "Cosmic-Ray Electron Evolution in the Supernova Remnant RX J1713.7-3946". In: *Astrophys. J.* 751.1, 65 (May 2012), p. 65. DOI: 10.1088/0004-637X/751/1/65. arXiv: 1203.4242 [astro-ph.HE].

[566] N. Aghanim et al. "Planck 2018 results. VI. Cosmological parameters". In: *Astron. Astrophys.* 641 (2020). [Erratum: Astron.Astrophys. 652, C4 (2021)], A6. DOI: 10.1051/0004-6361/201833910. arXiv: 1807.06209 [astro-ph.CO].

[567] Robert Stein. "Search for Neutrinos from Populations of Optical Transients". In: *PoS* ICRC2019 (2020), p. 1016. DOI: 10.22323/1.358.1016. arXiv: 1908.08547 [astro-ph.HE].

[568] M. G. Aartsen et al. "Searches for Extended and Point-like Neutrino Sources with Four Years of IceCube Data". In: *Astrophys. J.* 796.2 (2014), p. 109. DOI: 10.1088/0004-637X/796/2/109. arXiv: 1406.6757 [astro-ph.HE].

[569] Kohta Murase, Peter Meszaros, and Bing Zhang. "Probing the birth of fast rotating magnetars through high-energy neutrinos". In: *Phys. Rev. D* 79 (2009), p. 103001. DOI: 10.1103/PhysRevD.79.103001. arXiv: 0904.2509 [astro-ph.HE].

[570] M. G. Aartsen et al. “All-sky Search for Time-integrated Neutrino Emission from Astrophysical Sources with 7 yr of IceCube Data”. In: *Astrophys. J.* 835.2 (2017), p. 151. DOI: 10.3847/1538-4357/835/2/151. arXiv: 1609.04981 [astro-ph.HE].

[571] Todor Stanev. *High energy cosmic rays*. Springer Science & Business Media, 2010.

[572] T. K. Gaisser and M. Honda. “Flux of atmospheric neutrinos”. In: *Ann. Rev. Nucl. Part. Sci.* 52 (2002), pp. 153–199. DOI: 10.1146/annurev.nucl.52.050102.090645. arXiv: hep-ph/0203272.

[573] Thomas K. Gaisser. “Atmospheric Neutrinos”. In: (Oct. 2019). arXiv: 1910.08851 [astro-ph.HE].

[574] Nora L. Strotjohann, Marek Kowalski, and Anna Franckowiak. “Eddington bias for cosmic neutrino sources”. In: *Astron. Astrophys.* 622 (2019), p. L9. DOI: 10.1051/0004-6361/201834750. arXiv: 1809.06865 [astro-ph.HE].

[575] Hasan Yuksel et al. “Revealing the High-Redshift Star Formation Rate with Gamma-Ray Bursts”. In: *Astrophys. J. Lett.* 683 (2008), pp. L5–L8. DOI: 10.1086/591449. arXiv: 0804.4008 [astro-ph].

[576] Irene Tamborra, Shin’ichiro Ando, and Kohta Murase. “Star-forming galaxies as the origin of diffuse high-energy backgrounds: Gamma-ray and neutrino connections, and implications for starburst history”. In: *JCAP* 09 (2014), p. 043. DOI: 10.1088/1475-7516/2014/09/043. arXiv: 1404.1189 [astro-ph.HE].

[577] Fabio Zandanel et al. “High-energy gamma-ray and neutrino backgrounds from clusters of galaxies and radio constraints”. In: *Astron. Astrophys.* 578 (2015), A32. DOI: 10.1051/0004-6361/201425249. arXiv: 1410.8697 [astro-ph.HE].

[578] Xiang-Yu Wang and Ruo-Yu Liu. “Tidal disruption jets of supermassive black holes as hidden sources of cosmic rays: explaining the IceCube TeV-PeV neutrinos”. In: *Phys. Rev. D* 93.8 (2016), p. 083005. DOI: 10.1103/PhysRevD.93.083005. arXiv: 1512.08596 [astro-ph.HE].

[579] Nicholas Senno, Kohta Murase, and Peter Mészáros. “High-energy Neutrino Flares from X-Ray Bright and Dark Tidal Disruption Events”. In: *Astrophys. J.* 838.1 (2017), p. 3. DOI: 10.3847/1538-4357/aa6344. arXiv: 1612.00918 [astro-ph.HE].

[580] M. G. Aartsen et al. “Differential limit on the extremely-high-energy cosmic neutrino flux in the presence of astrophysical background from nine years of IceCube data”. In: *Phys. Rev. D* 98.6 (2018), p. 062003. DOI: 10.1103/PhysRevD.98.062003. arXiv: 1807.01820 [astro-ph.HE].

[581] G. Migliori et al. “Roaring to softly whispering: Persistent X-ray emission at the location of the Fast Blue Optical Transient AT2018cow ∼3.7 yrs after discovery and implications on accretion-powered scenarios”. In: (Sept. 2023). arXiv: 2309.15678 [astro-ph.HE].

[582] J. Moran-Fraile et al. “Self-consistent MHD simulation of jet launching in a neutron star - white dwarf merger”. In: (Oct. 2023). arXiv: 2310.08623 [astro-ph.HE].

[583] Yuki Kaneko et al. “Prompt and Afterglow Emission Properties of Gamma-Ray Bursts with Spectroscopically Identified Supernovae”. In: *Astrophys. J.* 654 (2006), pp. 385–402. DOI: 10.1086/508324. arXiv: astro-ph/0607110.

[584] R. M. Quimby et al. “Hydrogen-poor superluminous stellar explosions”. In: *Nature* 474 (2011), p. 487. DOI: 10.1038/nature10095. arXiv: 0910.0059 [astro-ph.CO].

[585] D. Milisavljevic et al. “Metamorphosis of SN 2014C: Delayed Interaction Between a Hydrogen Poor Core-collapse Supernova and a Nearby Circumstellar Shell”. In: *Astrophys. J.* 815.2 (2015), p. 120. DOI: 10.1088/0004-637X/815/2/120. arXiv: 1511.01907 [astro-ph.HE].

[586] Raffaella Margutti et al. “Ejection of the Massive Hydrogen-rich Envelope Time with the Collapse of the Stripped SN 2014C”. In: *Astrophys. J.* 835.2 (2017), p. 140. DOI: 10.3847/1538-4357/835/2/140. arXiv: 1601.06806 [astro-ph.HE].

[587] Peter W. A. Roming et al. “The Swift Ultra-Violet/Optical Telescope”. In: *Space Sci. Rev.* 120 (2005), pp. 95–142. DOI: 10.1007/s11214-005-5095-4. arXiv: astro-ph/0507413.

[588] B. P. Abbott et al. “GW170817: Observation of Gravitational Waves from a Binary Neutron Star Inspiral”. In: *Phys. Rev. Lett.* 119.16 (2017), p. 161101. DOI: 10.1103/PhysRevLett.119.161101. arXiv: 1710.05832 [gr-qc].

[589] Matteo Sanguineti. “Status and physics results of the KM3NeT experiment”. In: *Nuovo Cim. C* 46.1 (2023), p. 4. DOI: 10.1393/ncc/i2023-23004-3.

[590] Claire Guépin and Kumiko Kotera. “Can we observe neutrino flares in coincidence with explosive transients?” In: *Astron. Astrophys.* 603 (2017), A76. DOI: 10.1051/0004-6361/201630326. arXiv: 1701.07038 [astro-ph.HE].

[591] Claire Guépin, Kumiko Kotera, and Foteini Oikonomou. "High-energy neutrino transients and the future of multi-messenger astronomy". In: *Nature Rev. Phys.* 4.11 (2022), pp. 697–712. DOI: 10.1038/s42254-022-00504-9. arXiv: 2207.12205 [astro-ph.HE].

[592] Tetyana Pitik et al. "Optically Informed Searches of High-Energy Neutrinos from Interaction-Powered Supernovae". In: *Mon. Not. Roy. Astron. Soc.* 524 (2023), p. 3. DOI: 10.1093/mnras/stad2025. arXiv: 2306.01833 [astro-ph.HE].

[593] E. Kankare et al. "Search for transient optical counterparts to high-energy IceCube neutrinos with Pan-STARRS1". In: *Astron. Astrophys.* 626 (2019), A117. DOI: 10.1051/0004-6361/201935171. arXiv: 1901.11080 [astro-ph.HE].

[594] Jannis Necker et al. "ASAS-SN follow-up of IceCube high-energy neutrino alerts". In: *Mon. Roy. Astron. Soc.* 516.2 (Oct. 2022), pp. 2455–2469. DOI: 10.1093/mnras/stac2261. arXiv: 2204.00500 [astro-ph.HE].

[595] R. Abbasi et al. "Constraining High-energy Neutrino Emission from Supernovae with IceCube". In: *Astrophys. J. Lett.* 949.1, L12 (May 2023), p. L12. DOI: 10.3847/2041-8213/acd2c9. arXiv: 2303.03316 [astro-ph.HE].

[596] W. B. Atwood et al. "The Large Area Telescope on the Fermi Gamma-Ray Space Telescope Mission". In: *Astrophys. J.* 697.2 (June 2009), pp. 1071–1102. DOI: 10.1088/0004-637X/697/2/1071. arXiv: 0902.1089 [astro-ph.IM].

[597] Simone Garrappa et al. "Fermi-LAT realtime follow-ups of high-energy neutrino alerts". In: *PoS* ICRC2021 (2021), p. 956. DOI: 10.22323/1.395.0956. arXiv: 2112.11586 [astro-ph.HE].

[598] W. D. Arnett. "Analytic solutions for light curves of supernovae of Type II". In: *Astrophys. J.* 237 (Apr. 1980), pp. 541–549. DOI: 10.1086/157898.

[599] Emmanouil Chatzopoulos, J. Craig Wheeler, and Jozsef Vinko. "Generalized Semi-Analytical Models of Supernova Light Curves". In: *Astrophys. J.* 746 (2012), p. 121. DOI: 10.1088/0004-637X/746/2/121. arXiv: 1111.5237 [astro-ph.HE].

[600] Stuart A. Sim. "Spectra of Supernovae During the Photospheric Phase". In: *Handbook of Supernovae*. Ed. by Athem W. Alsabti and Paul Murdin. 2017, p. 769. DOI: 10.1007/978-3-319-21846-5_28.

[601] Eran O. Ofek et al. "SN 2010jl: Optical to Hard X-Ray Observations Reveal an Explosion Embedded in a Ten Solar Mass Cocoon". In: *Astrophys. J.* 781 (2014), p. 42. DOI: 10.1088/0004-637X/781/1/42. arXiv: 1307.2247 [astro-ph.HE].

[602] William H. Lee and Enrico Ramirez-Ruiz. "Accretion modes in collapsars: prospects for grb production". In: *Astrophys. J.* 641 (2006), pp. 961–971. DOI: 10.1086/500533. arXiv: astro-ph/0509307.

[603] Brian D. Metzger, Paz Beniamini, and Dimitrios Giannios. "Effects of Fallback Accretion on Protomagnetar Outflows in Gamma-Ray Bursts and Superluminous Supernovae". In: *Astrophys. J.* 857.2 (2018), p. 95. DOI: 10.3847/1538-4357/aab70c. arXiv: 1802.07750 [astro-ph.HE].

[604] B. D. Metzger, A. L. Piro, and E. Quataert. "Time-Dependent Models of Accretion Disks Formed from Compact Object Mergers". In: *Mon. Not. Roy. Astron. Soc.* 390 (2008), p. 781. DOI: 10.1111/j.1365-2966.2008.13789.x. arXiv: 0805.4415 [astro-ph].

[605] Brian D. Metzger. "Kilonovae". In: *Living Rev. Rel.* 23.1 (2020), p. 1. DOI: 10.1007/s41114-019-0024-0. arXiv: 1910.01617 [astro-ph.HE].

[606] Diego Lopez-Camara, William H. Lee, and Enrico Ramirez-Ruiz. "GRB production and SN signatures in slowly rotating collapsars". In: *Astrophys. J.* 692 (2009), pp. 804–815. DOI: 10.1088/0004-637X/692/1/804. arXiv: 0808.0462 [astro-ph].

[607] Jason Dexter and Daniel Kasen. "Supernova Light Curves Powered by Fallback Accretion". In: *Astrophys. J.* 772 (2013), p. 30. DOI: 10.1088/0004-637X/772/1/30. arXiv: 1210.7240 [astro-ph.HE].

[608] Roger A. Chevalier. "Neutron Star Accretion in a Supernova". In: *Astrophys. J.* 346 (Nov. 1989), p. 847. DOI: 10.1086/168066.

[609] Daniel Kasen and Lars Bildsten. "Supernova Light Curves Powered by Young Magnetars". In: *Astrophys. J.* 717 (2010), pp. 245–249. DOI: 10.1088/0004-637X/717/1/245. arXiv: 0911.0680 [astro-ph.HE].

[610] James M. Lattimer and Bernard F. Schutz. "Constraining the equation of state with moment of inertia measurements". In: *Astrophys. J.* 629 (2005), pp. 979–984. DOI: 10.1086/431543. arXiv: astro-ph/0411470.

[611] W. D. Arnett. "On the theory of type I supernovae." In: *Astrophys. J. Lett.* 230 (May 1979), pp. L37–L40. DOI: 10.1086/182957.

[612] J. Craig Wheeler, V. Johnson, and A. Clocchiatti. "Analysis of Late–time Light Curves of Type IIb, Ib and Ic Supernovae". In: *Mon. Not. Roy. Astron. Soc.* 450.2 (2015), pp. 1295–1307. DOI: 10.1093/mnras/stv650. arXiv: 1411.5975 [astro-ph.SR].

[613] Mario Hamuy. "Observed and physical properties of core-collapse supernovae". In: *Astrophys. J.* 582 (2003), pp. 905–914. DOI: 10.1086/344689. arXiv: astro-ph/0209174.

[614] S. J. Smartt et al. "The death of massive stars - I. Observational constraints on the progenitors of type II-P supernovae". In: *Mon. Not. Roy. Astron. Soc.* 395 (2009), p. 1409. DOI: 10.1111/j.1365-2966.2009.14506.x. arXiv: 0809.0403 [astro-ph].

[615] N. E. Sanders et al. "Towards Characterization of the Type IIP Supernova Progenitor Population: a Statistical Sample of Light Curves from Pan-STARRS1". In: *Astrophys. J.* 799.2 (2015), p. 208. DOI: 10.1088/0004-637X/799/2/208. arXiv: 1404.2004 [astro-ph.HE].

[616] Adam Rubin et al. "Type II supernova energetics and comparison of light curves to shock-cooling models". In: *Astrophys. J.* 820.1 (2016), p. 33. DOI: 10.3847/0004-637X/820/1/33. arXiv: 1512.00733 [astro-ph.HE].

[617] Daniel Kasen and S. E. Woosley. "Type II Supernovae: Model Light Curves and Standard Candle Relationships". In: *Astrophys. J.* 703.2 (Oct. 2009), p. 2205. DOI: 10.1088/0004-637X/703/2/2205. arXiv: 0910.1590 [astro-ph.CO].

[618] Morgan MacLeod et al. "Lessons from the Onset of a Common Envelope Episode: the Remarkable M31 2015 Luminous Red Nova Outburst". In: *Astrophys. J.* 835.2, 282 (Feb. 2017), p. 282. DOI: 10.3847/1538-4357/835/2/282. arXiv: 1605.01493 [astro-ph.SR].

[619] Daniel Kasen and Enrico Ramirez-Ruiz. "Optical Transients from the Unbound Debris of Tidal Disruption". In: *Astrophys. J.* 714.1 (May 2010), pp. 155–162. DOI: 10.1088/0004-637X/714/1/155. arXiv: 0911.5358 [astro-ph.HE].

[620] Ehud Nakar and Re'em Sari. "Early supernovae light-curves following the shock-breakout". In: *Astrophys. J.* 725 (2010), pp. 904–921. DOI: 10.1088/0004-637X/725/1/904. arXiv: 1004.2496 [astro-ph.HE].

[621] Ehud Nakar and Re'em Sari. "Relativistic shock breakouts - a variety of gamma-ray flares: from low luminosity gamma-ray bursts to type Ia supernovae". In: *Astrophys. J.* 747 (2012), p. 88. DOI: 10.1088/0004-637X/747/2/88. arXiv: 1106.2556 [astro-ph.HE].

[622] Eli Waxman and Boaz Katz. "Shock breakout theory". In: *Handbook of Supernovae*. Ed. by Athem W. Alsabti and Paul Murdin. 2017, p. 967. DOI: 10.1007/978-3-319-21846-5_33.

[623] A. M. Soderberg et al. "An Extremely Luminous X-ray Outburst Marking the Birth of a Normal Supernova". In: *Nature* 453 (2008), pp. 469–474. DOI: 10.1038/nature06997. arXiv: 0802.1712 [astro-ph].

[624] Dennis Alp and Josefin Larsson. "Blasts from the Past: Supernova Shock Breakouts among X-Ray Transients in the XMM-Newton Archive". In: *Astrophys. J.* 896.1 (2020), p. 39. DOI: 10.3847/1538-4357/ab91ba. arXiv: 2004.09519 [astro-ph.HE].

[625] Giovanni Novara et al. "A Supernova Candidate at z = 0.092 in XMM–Newton Archival Data". In: *Astrophys. J.* 898.1 (2020), p. 37. DOI: 10.3847/1538-4357/ab98f8. arXiv: 2004.10665 [astro-ph.HE].

[626] Roger A. Chevalier and Claes Fransson. "Thermal and non-thermal emission from circumstellar interaction". In: *Handbook of Supernovae*. Ed. by Athem W. Alsabti and Paul Murdin. 2017, p. 875. DOI: 10.1007/978-3-319-21846-5_34.

[627] Roger A. Chevalier and Christopher M. Irwin. "Shock Breakout in Dense Mass Loss: Luminous Supernovae". In: *Astrophys. J. Lett.* 729 (2011), p. L6. DOI: 10.1088/2041-8205/729/1/L6. arXiv: 1101.1111 [astro-ph.HE].

[628] Ben Margalit, Eliot Quataert, and Anna Y. Q. Ho. "Optical to X-Ray Signatures of Dense Circumstellar Interaction in Core-collapse Supernovae". In: *Astrophys. J.* 928.2 (2022), p. 122. DOI: 10.3847/1538-4357/ac53b0. arXiv: 2109.09746 [astro-ph.HE].

[629] Roger A. Chevalier. "Synchrotron Self-Absorption in Radio Supernovae". In: *Astrophys. J.* 499.2 (May 1998), pp. 810–819. DOI: 10.1086/305676.

[630] Pawan Kumar, Ramesh Narayan, and Jarrett L. Johnson. "Mass Fall-back and Accretion in the Central Engine of Gamma-Ray Bursts". In: *Mon. Not. Roy. Astron. Soc.* 388 (2008), p. 1729. DOI: 10.1111/j.1365-2966.2008.13493.x. arXiv: 0807.0441 [astro-ph].

[631] Enrico Ramirez-Ruiz et al. “An Off-axis model for GRB 031203”. In: *Astrophys. J. Lett.* 625 (2005), pp. L91–L94. DOI: 10.1086/431237. arXiv: astro-ph/0412145.

[632] Robert G. Izzard, Enrico Ramirez-Ruiz, and Christopher A. Tout. “Formation rates of core collapse SNe and GRBs”. In: *Mon. Not. Roy. Astron. Soc.* 348 (2004), p. 1215. DOI: 10.1111/j.1365-2966.2004.07436.x. arXiv: astro-ph/0311463.

[633] Mariusz Tarnopolski. “Analysis of Fermi gamma-ray burst duration distribution”. In: *Astron. Astrophys.* 581 (2015), A29. DOI: 10.1051/0004-6361/201526415. arXiv: 1506.07324 [astro-ph.HE].

[634] Keiichi Maeda, Akihiro Suzuki, and Luca Izzo. “Diagnosing The Ejecta Properties of Engine-Driven Supernovae from Observables in Their Initial Phase”. In: *Mon. Roy. Astron. Soc.* 522.2 (June 2023), pp. 2267–2278. DOI: 10.1093/mnras/stad1075. arXiv: 2304.04146 [astro-ph.HE].

[635] Ersilia Guarini, Irene Tamborra, and Ore Gottlieb. “State-of-the-art collapsar jet simulations imply undetectable subphotospheric neutrinos”. In: *Phys. Rev. D* 107.2 (2023), p. 023001. DOI: 10.1103/PhysRevD.107.023001. arXiv: 2210.03757 [astro-ph.HE].

[636] C. F. Kennel and F. V. Coroniti. “Magnetohydrodynamic model of Crab nebula radiation.” In: *Astrophys. J.* 283 (Aug. 1984), pp. 710–730. DOI: 10.1086/162357.

[637] Daniel Brethauer et al. “Seven Years of Coordinated Chandra–NuSTAR Observations of SN 2014C Unfold the Extreme Mass-loss History of Its Stellar Progenitor”. In: *Astrophys. J.* 939.2 (2022), p. 105. DOI: 10.3847/1538-4357/ac8b14. arXiv: 2206.00842 [astro-ph.HE].

[638] Nathan Smith. “Mass Loss: Its Effect on the Evolution and Fate of High-Mass Stars”. In: *Ann. Rev. Astron. Astrophys.* 52 (2014), pp. 487–528. DOI: 10.1146/annurev-astro-081913-040025. arXiv: 1402.1237 [astro-ph.SR].

[639] Alexander Gagliano et al. “An Early-time Optical and Ultraviolet Excess in the Type-Ic SN 2020oi”. In: *Astrophys. J.* 924.2 (2022), p. 55. DOI: 10.3847/1538-4357/ac35ec. arXiv: 2105.09963 [astro-ph.HE].

[640] Moo-Keon Jung, Sung-Chul Yoon, and Hyun-Jeong Kim. “Effects of Winds on the Optical Properties of Type Ib and Ic Supernova Progenitors”. In: *Astrophys. J.* 925.2 (2022), p. 216. DOI: 10.3847/1538-4357/ac3f33. arXiv: 2112.00272 [astro-ph.SR].

[641] Enrico Ramirez-Ruiz et al. “The State of the circumstellar medium surrounding gamma-ray burst sources and its effect on the afterglow appearance”. In: *Astrophys. J.* 631 (2005), pp. 435–445. DOI: 10.1086/432433. arXiv: astro-ph/0412446.

[642] Prantik Sarmah et al. “Gamma-rays and neutrinos from supernovae of Type Ib/c with late time emission”. In: (Mar. 2023). arXiv: 2303.13576 [astro-ph.HE].

[643] E. Berger, S. R. Kulkarni, and R. A. Chevalier. “The radio evolution of the ordinary type Ic SN 2002ap”. In: *Astrophys. J. Lett.* 577 (2002), pp. L5–L8. DOI: 10.1086/344045. arXiv: astro-ph/0206183.

[644] D. Milisavljevic et al. “The Broad-Lined Type Ic SN 2012ap and the Nature of Relativistic Supernovae Lacking a Gamma-ray Burst Detection”. In: *Astrophys. J.* 799.1 (2015), p. 51. DOI: 10.1088/0004-637X/799/1/51. arXiv: 1408.1606 [astro-ph.HE].

[645] Giuliano Pignata et al. “SN 2009bb: a Peculiar Broad-Lined Type Ic Supernova”. In: *Astrophys. J.* 728 (2011), p. 14. DOI: 10.1088/0004-637X/728/1/14. arXiv: 1011.6126 [astro-ph.SR].

[646] K. S. Kawabata et al. “Optical spectropolarimetry of SN 2002AP: A High velocity asymmetric explosion”. In: *Astrophys. J. Lett.* 580 (2002), pp. L39–L42. DOI: 10.1086/345545. arXiv: astro-ph/0205414.

[647] Tomoyasu Hayakawa and Keiichi Maeda. “A collapsar model with disk wind: Implications for supernovae associated with Gamma-Ray Bursts”. In: *Astrophys. J.* 854.1 (2018), p. 43. DOI: 10.3847/1538-4357/aaa76c. arXiv: 1801.09681 [astro-ph.HE].

[648] Robert C. Duncan and Christopher Thompson. “Formation of very strongly magnetized neutron stars - implications for gamma-ray bursts”. In: *Astrophys. J. Lett.* 392 (1992), p. L9. DOI: 10.1086/186413.

[649] Paolo A. Mazzali et al. “A Neutron Star-driven XRF associated with SN 2006aj”. In: *Nature* 442 (2006), pp. 1018–1020. DOI: 10.1038/nature05081. arXiv: astro-ph/0603567.

[650] Tatsuya Nakaoka et al. “The Low-luminosity Type IIP Supernova 2016bkv with Early-phase Circumstellar Interaction”. In: *Astrophys. J.* 859.2 (2018), p. 78. DOI: 10.3847/1538-4357/aabee7. arXiv: 1804.06065 [astro-ph.GA].

[651] O. Yaron et al. “Confined Dense Circumstellar Material Surrounding a Regular Type II Supernova: The Unique Flash-Spectroscopy Event of SN 2013fs”. In: *Nature Phys.* 13 (2017), p. 510. DOI: 10.1038/nphys4025. arXiv: 1701.02596 [astro-ph.HE].

[652] Christopher Bullivant et al. “SN 2013fs and SN 2013fr: exploring the circumstellar-material diversity in Type II supernovae”. In: *Mon. Not. Roy. Astron. Soc.* 476.2 (2018), pp. 1497–1518. DOI: 10.1093/mnras/sty045. arXiv: 1801.01532 [astro-ph.HE].

[653] Viktoriya Morozova, Anthony L. Piro, and Stefano Valenti. “Unifying Type II Supernova Light Curves with Dense Circumstellar Material”. In: *Astrophys. J.* 838.1 (2017), p. 28. DOI: 10.3847/1538-4357/aa6251. arXiv: 1610.08054 [astro-ph.HE].

[654] Gururaj A. Wagle and Alak Ray. “Type IIP Supernova Progenitors. II. Stellar Mass and Obscuration by the Dust in the Circumstellar Medium”. In: *Astrophys. J.* 889.2, 86 (Feb. 2020), p. 86. DOI: 10.3847/1538-4357/ab5d2c. arXiv: 1911.12831 [astro-ph.HE].

[655] Tomás Müller et al. “The Nickel Mass Distribution of Normal Type II Supernovae”. In: *Astrophys. J.* 841.2 (2017), p. 127. DOI: 10.3847/1538-4357/aa72f1. arXiv: 1702.00416 [astro-ph.SR].

[656] Vikram V. Dwarkadas. “On the Lack of X-ray Bright Type IIP Supernovae”. In: *Mon. Not. Roy. Astron. Soc.* 440.3 (2014), pp. 1917–1924. DOI: 10.1093/mnras/stu347. arXiv: 1402.5150 [astro-ph.HE].

[657] Nathan Smith. “Interacting Supernovae: Types IIn and Ibn”. In: *Handbook of Supernovae*. Ed. by Athem W. Alsabti and Paul Murdin. 2017, p. 403. DOI: 10.1007/978-3-319-21846-5_38.

[658] F. Taddia et al. “Carnegie Supernova Project: Observations of Type IIn supernovae”. In: *Astron. Astrophys.* 555 (2013), A10. DOI: 10.1051/0004-6361/201321180. arXiv: 1304.3038 [astro-ph.CO].

[659] Takashi J. Moriya et al. “Mass-loss histories of Type IIn supernova progenitors within decades before their explosion”. In: *Mon. Not. Roy. Astron. Soc.* 439.3 (2014), pp. 2917–2926. DOI: 10.1093/mnras/stu163. arXiv: 1401.4893 [astro-ph.SR].

[660] Takashi J. Moriya, Elena I. Sorokina, and Roger A. Chevalier. “Superluminous supernovae”. In: *Space Sci. Rev.* 214.2 (2018), p. 59. DOI: 10.1007/s11214-018-0493-6. arXiv: 1803.01875 [astro-ph.HE].

[661] Avishay Gal-Yam. “Luminous Supernovae”. In: *Science* 337 (2012), p. 927. DOI: 10.1126/science.1203601. arXiv: 1208.3217 [astro-ph.CO].

[662] Nathan Smith et al. “Spectral Evolution of the Extraordinary Type IIn Supernova 2006gy”. In: *Astrophys. J.* 709.2 (Feb. 2010), pp. 856–883. DOI: 10.1088/0004-637X/709/2/856. arXiv: 0906.2200 [astro-ph.HE].

[663] T. W. Chen et al. “The evolution of superluminous supernova LSQ14mo and its interacting host galaxy system”. In: *Astron. Astrophys.* 602 (2017), A9. DOI: 10.1051/0004-6361/201630163. arXiv: 1611.09910 [astro-ph.SR].

[664] C. Inserra et al. “Complexity in the light curves and spectra of slow-evolving superluminous supernovae”. In: *Mon. Not. Roy. Astron. Soc.* 468.4 (2017), pp. 4642–4662. DOI: 10.1093/mnras/stx834. arXiv: 1701.00941 [astro-ph.HE].

[665] Justyn R. Maund et al. “A flash of polarized optical light points to an aspherical ‘cow’”. In: *Mon. Not. Roy. Astron. Soc.* 521.3 (2023), pp. 3323–3332. DOI: 10.1093/mnras/stad539. arXiv: 2303.00787 [astro-ph.SR].

[666] A. R. Bell and S. G. Lucek. “Cosmic ray acceleration to very high energy through the non-linear amplification by cosmic rays of the seed magnetic field”. In: *Mon. Not. Roy. Astron. Soc.* 321.3 (Mar. 2001), pp. 433–438. DOI: 10.1046/j.1365-8711.2001.04063.x.

[667] F. Aharonian. “Discovery of gamma-ray emission from the shell-type supernova remnant RCW 86 with H.E.S.S”. In: *Astrophys. J.* 692 (2009), pp. 1500–1505. DOI: 10.1088/0004-637X/692/2/1500. arXiv: 0810.2689 [astro-ph].

[668] E. A. Helder et al. “Measuring the Cosmic-Ray Acceleration Efficiency of a Supernova Remnant”. In: *Science* 325.5941 (Aug. 2009), p. 719. DOI: 10.1126/science.1173383. arXiv: 0906.4553 [astro-ph.GA].

[669] Roger A. Chevalier and Claes Fransson. “Emission from Circumstellar Interaction in Normal Type II Supernovae”. In: *Astrophys. J.* 420 (Jan. 1994), p. 268. DOI: 10.1086/173557.

[670] Jonathan Granot and Enrico Ramirez-Ruiz. “The case for a misaligned relativistic jet from sn 2001em”. In: *Astrophys. J. Lett.* 609 (2004), pp. L9–L12. DOI: 10.1086/422516. arXiv: astro-ph/0403421.

[671] Jakob van Santen et al. *toise: Performance estimator for high-energy neutrino detectors*. Astrophysics Source Code Library, record ascl:2208.024. Aug. 2022. ascl: 2208.024.

[672] Nathan Smith et al. “Observed Fractions of Core-Collapse Supernova Types and Initial Masses of their Single and Binary Progenitor Stars”. In: *Mon. Not. Roy. Astron. Soc.* 412 (2011), p. 1522. DOI: 10.1111/j.1365-2966.2011.17229.x. arXiv: 1006.3899 [astro-ph.HE].

[673] Alessandra Corsi and Davide Lazzati. “Gamma-ray burst jets in supernovae”. In: *New Astron. Rev.* 92, 101614 (June 2021), p. 101614. DOI: 10.1016/j.newar.2021.101614.

[674] Amy Lien et al. “Probing the Cosmic Gamma-Ray Burst Rate with Trigger Simulations of the Swift Burst Alert Telescope”. In: *Astrophys. J.* 783.1 (2014), p. 24. DOI: 10.1088/0004-637X/783/1/24. arXiv: 1311.4567 [astro-ph.HE].

[675] Francisco Virgili, Enwei Liang, and Bing Zhang. “Low-Luminosity Gamma-Ray Bursts as a Distinct GRB Population:A Monte Carlo Analysis”. In: *Mon. Not. Roy. Astron. Soc.* 392 (2009), p. 91. DOI: 10.1111/j.1365-2966.2008.14063.x. arXiv: 0801.4751 [astro-ph].

[676] Robert M. Quimby et al. “Rates of Superluminous Supernovae at z~0.2”. In: *Mon. Not. Roy. Astron. Soc.* 431 (2013), p. 912. DOI: 10.1093/mnras/stt213. arXiv: 1302.0911 [astro-ph.CO].

[677] Daniel Mazin. “The Cherenkov Telescope Array”. In: *PoS* ICRC2019 (2020), p. 741. DOI: 10.22323/1.358.0741. arXiv: 1907.08530 [astro-ph.IM].

[678] Grant J. Mathews et al. “Supernova Relic Neutrinos and the Supernova Rate Problem: Analysis of Uncertainties and Detectability of ONeMg and Failed Supernovae”. In: *Astrophys. J.* 790 (2014), p. 115. DOI: 10.1088/0004-637X/790/2/115. arXiv: 1405.0458 [astro-ph.CO].

[679] M. G. Aartsen et al. “The IceCube Realtime Alert System”. In: *Astropart. Phys.* 92 (2017), pp. 30–41. DOI: 10.1016/j.astropartphys.2017.05.002. arXiv: 1612.06028 [astro-ph.HE].

[680] Rasha Abbasi et al. “Search for High-Energy Neutrinos from TDE-like Flares with IceCube”. In: *PoS* ICRC2023 (2023), p. 1478. DOI: 10.22323/1.444.1478. arXiv: 2307.15531 [astro-ph.HE].

[681] Shiho Kobayashi and Bing Zhang. “Early optical afterglows from wind-type gamma-ray bursts”. In: *Astrophys. J.* 597 (2003), pp. 455–458. DOI: 10.1086/378283. arXiv: astro-ph/0304086.

[682] Christopher Thompson, Peter Mészáros, and Martin J. Rees. “Thermalization in Relativistic Outflows and the Correlation between Spectral Hardness and Apparent Luminosity in Gamma-ray Bursts”. In: *Astrophys. J.* 666 (2007), pp. 1012–1023. DOI: 10.1086/518551. arXiv: astro-ph/0608282.

[683] Ehud Nakar and Tsvi Piran. "The Observable Signatures of GRB Cocoons". In: *Astrophys. J.* 834.1 (2017), p. 28. DOI: 10.3847/1538-4357/834/1/28. arXiv: 1610.05362 [astro-ph.HE].

[684] Ore Gottlieb and Ehud Nakar. "The propagation of relativistic jets in expanding media". In: *Mon. Not. Roy. Astron. Soc.* 517.2 (2022), pp. 1640–1666. DOI: 10.1093/mnras/stac2699. arXiv: 2106.03860 [astro-ph.HE].

[685] Di Xiao, Zi-Gao Dai, and Peter Mészáros. "Prompt Neutrino Emission of Gamma-Ray Bursts in the Dissipative Photospheric Scenario Revisited: Possible Contributions from Cocoons". In: *Astrophys. J.* 843.1 (2017), p. 17. DOI: 10.3847/1538-4357/aa76e5. arXiv: 1706.01293 [astro-ph.HE].

[686] Željka Bošnjak, Rodolfo Barniol Duran, and Asaf Pe'er. "The GRB Prompt Emission: An Unsolved Puzzle". In: *Galaxies* 10.2 (Feb. 2022), p. 38. DOI: 10.3390/galaxies10020038.

[687] Bing Zhang. "Gamma-Ray Burst Prompt Emission". In: *Int. J. Mod. Phys. D* 23 (2014). Ed. by Remo Ruffini, Robert Jantzen, and Kjell Rosquist, p. 1430002. DOI: 10.1142/S021827181430002X. arXiv: 1402.7022 [astro-ph.HE].

[688] Dimitrios Giannios and Henk C. Spruit. "Spectral and timing properties of a dissipative GRB photosphere". In: *Astron. Astrophys.* 469 (2007), pp. 1–9. DOI: 10.1051/0004-6361:20066739. arXiv: astro-ph/0611385.

[689] Christopher Thompson and Ramandeep Gill. "Hot Electromagnetic Outflows. III. Displaced Fireball in a Strong Magnetic Field". In: *Astrophys. J.* 791 (2014), p. 46. DOI: 10.1088/0004-637X/791/1/46. arXiv: 1310.2480 [astro-ph.HE].

[690] Chris Thompson. "A model of gamma-ray bursts." In: *Mon. Not. Roy. Soc.* 270 (Oct. 1994), pp. 480–498. DOI: 10.1093/mnras/270.3.480.

[691] Dimitrios Giannios. "Prompt emission spectra from the photosphere of a grb". In: *Astron. Astrophys.* 457 (2006), pp. 763–770. DOI: 10.1051/0004-6361:20065000. arXiv: astro-ph/0602397.

[692] Indrek Vurm, Yuri Lyubarsky, and Tsvi Piran. "On Thermalization in Gamma-Ray Burst Jets and the Peak Energies of Photospheric Spectra". In: *Astrophys. J.* 764.2, 143 (Feb. 2013), p. 143. DOI: 10.1088/0004-637X/764/2/143. arXiv: 1209.0763 [astro-ph.HE].

[693] Ramandeep Gill and Christopher Thompson. "Non-thermal Gamma-ray Emission from Delayed Pair Breakdown in a Magnetized and Photon-rich Outflow". In: *Astrophys. J.* 796.2 (2014), p. 81. DOI: 10.1088/0004-637X/796/2/81. arXiv: 1406.4774 [astro-ph.HE].

[694] Martin J. Rees and Péter Mészáros. "Dissipative photosphere models of gamma-ray bursts and x-ray flashes". In: *Astrophys. J.* 628 (2005), pp. 847–852. DOI: 10.1086/430818. arXiv: astro-ph/0412702.

[695] Andrei M. Beloborodov. "Regulation of the Spectral Peak in Gamma-Ray Bursts". In: *Astrophys. J.* 764.2, 157 (Feb. 2013), p. 157. DOI: 10.1088/0004-637X/764/2/157. arXiv: 1207.2707 [astro-ph.HE].

[696] A. H. Taub. "Relativistic Rankine-Hugoniot Equations". In: *Phys. Rev.* 74 (1948), pp. 328–334. DOI: 10.1103/PhysRev.74.328.

[697] Mauricio Bustamante et al. "Multi-messenger light curves from gamma-ray bursts in the internal shock model". In: *Astrophys. J.* 837.1 (2017), p. 33. DOI: 10.3847/1538-4357/837/1/33. arXiv: 1606.02325 [astro-ph.HE].

[698] L. Nava et al. "Afterglow emission in gamma-ray bursts - I. Pair-enriched ambient medium and radiative blast waves". In: *Mon. Not. R. Astron. Soc.* 433.3 (2013), pp. 2107–2121. DOI: 10.1093/mnras/stt872. arXiv: 1211.2806 [astro-ph.HE].

[699] S. B. Cenko et al. "Afterglow Observations of Fermi Large Area Telescope Gamma-ray Bursts and the Emerging Class of Hyper-energetic Events". In: *Astrophys. J.* 732.1, 29 (May 2011), p. 29. DOI: 10.1088/0004-637X/732/1/29. arXiv: 1004.2900 [astro-ph.HE].

[700] S. Golenetskii et al. "Konus-wind observation of GRB 130427A." In: *GRB Coordinates Network* 14487 (Jan. 2013), p. 1.

[701] Sylvia Zhu et al. "Fermi-LAT Observations of the Gamma-ray Burst GRB 130427A". In: *Science* 343 (2014), p. 42. DOI: 10.1126/science.1242353. arXiv: 1311.5623 [astro-ph.HE].

[702] M. Fukugita et al. "The Sloan Digital Sky Survey Photometric System". In: *Astron. J.* 111 (Apr. 1996), p. 1748. DOI: 10.1086/117915.

[703] GCN circular archive. *The Gamma-Ray Coordinates Network*. 2022. URL: https://gcn.gsfc.nasa.gov/gcn/gcn3_archive.html.

[704] R. J. Protheroe and R. W. Clay. “Ultra High Energy Cosmic Rays”. In: *Publications of the Astronomical Society of Australia* 21.1 (2004), 1?22. DOI: 10.1071/AS03047.

[705] Bruce T. Draine. *Physics of the Interstellar and Intergalactic Medium*. Princeton University Press, 2011.